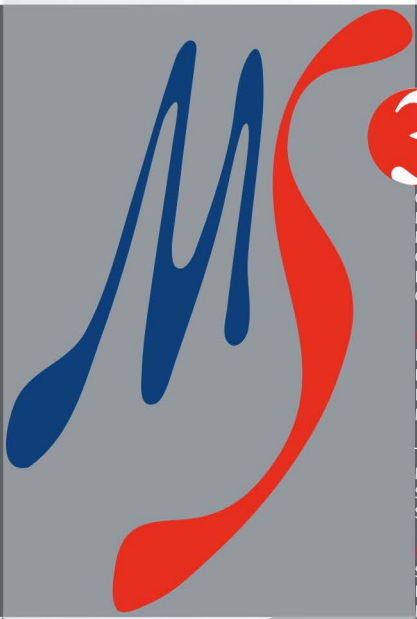

ОДИННАДЦАТЫЙ
МОСКОВСКИЙ
МЕЖДУНАРОДНЫЙ
СИМПОЗИУМ
ПО ИССЛЕДОВАНИЯМ
СОЛНЕЧНОЙ СИСТЕМЫ

5–9 ОКТЯБРЯ 2020
ИНСТИТУТ
КОСМИЧЕСКИХ
ИССЛЕДОВАНИЙ
МОСКВА

THE ELEVENTH
MOSCOW
SOLAR SYSTEM
SYMPOSIUM

5–9 OCTOBER 2020
SPACE RESEARCH
INSTITUTE
MOSCOW

11

RUSSIAN
FOUNDATION
FOR BASIC
RESEARCH
RFBR
PROJECT
20-02-22024

ОДИННАДЦАТЫЙ МОСКОВСКИЙ СИМПОЗИУМ ПО ИССЛЕДОВАНИЯМ СОЛНЕЧНОЙ СИСТЕМЫ 11M-S^3

октябрь 5-9, 2020
ИНСТИТУТ КОСМИЧЕСКИХ ИССЛЕДОВАНИЙ РОССИЙСКОЙ АКАДЕМИИ НАУК
МОСКВА, РОССИЯ

THE ELEVENTH MOSCOW SOLAR SYSTEM SYMPOSIUM 11M-S^3

october 5-9, 2020
SPACE RESEARCH INSTITUTE OF RUSSIAN ACADEMY OF SCIENCES
MOSCOW, RUSSIA

спонсоры:
- Российский Фонд Фундаментальных Исследований (РФФИ)
- Институт Космических Исследований РАН

sponsored by:
- Russian Foundation for Basic Research (RFBR)
- Space Research Institute RAS

ISBN- 978-5-00015-050-4
DOI: 0.21046/11MS3-2020

TABLE OF CONTENT

THE ELEVENTH MOSCOW SOLAR SYSTEM SYMPOSIUM 11M-S^3

SPACE RESEARCH INSTITUTE
MOSCOW, RUSSIA
October 5-9, 2020

Starting from 2010, the Space Research Institute holds annual international symposia on Solar system exploration. Main topics of these symposia include wide range of problems related to formation and evolution of Solar system, planetary systems of other stars; exploration of Solar system planets, their moons, small bodies; interplanetary environment, astrobiology problems. Experimental planetary studies, science instruments and preparation for space missions are also considered at these symposia.

The Eleventh Moscow international Solar System Symposium (11M-S3) will be held from October 5 till 9, 2020.

Subject matter of this symposium will cover many problems of the Solar system science with the central topic "Moon, Mars and Venus research". This topic relates to scientific problems of several missions: «Mars Express», «Venus Express», the missions under development in Russia: "Luna-Glob", "Luna-Resource", "ExoMars ".

THE FOLLOWING SESSIONS WILL BE HELD DURING THE SYMPOSIUM:

- Session: MARS
- Session: VENUS
- Session: MOON AND MERCURY
- Session: GIANT PLANETS
- Session: SMALL BODIES (INCLUDING COSMIC DUST)
- Session: EXTRASOLAR PLANETS
- Session: ASTROBIOLOGY
- Session: SOLAR WIND INTERACTIONS WITH PLANETS AND SMALL BODIES

In light of COVID-19 travel restrictions the Symposium will be held both «face-to- face» and «virtual» formats.

For all «face-to- face» participants in Space Research Institute (IKI) the masks as well as social distancing will still be obligatory!

Space Research Institute holds this symposium with participation of the following organizations:

- Russian Foundation for Basic Research, Russia
- Vernadsky Institute of Geochemistry and Analytical Chemistry, Russia
- Brown University, USA

Symposium website: **https://ms2020.cosmos.ru**
Contact email address: **ms2020@cosmos.ru**

Мероприятие проводится при финансовой поддержке Российской академии наук,

Российского фонда фундаментальных исследований, проект №20-02-22024

PROGRAM COMMITTEE

chair:
acad. **ZELENYI L.M.** IKI RAS

members:
BAZILEVSKIY A.T. GEOHI RAS
BIBRING J.-P. IAS,CNRS, France
BOLTON S.J. Southwest Research Institute, USA
BOROVIN G.K. Keldysh AMI RAS
DUXBURY T. George Mason University, USA
HEAD III J. Brown University, USA
KORABLEV O.I. IKI RAS
KOSTITSYN Y.A. GEOHI RAS
MAROV M.Ya. GEOHI RAS
MITROFANOV I.G. IKI RAS
RODIN A.V. IKI RAS
SHEVCHENKO V.V. GAISH MSU
SMIRNOV V.M. IRE RAS
SVEDHEM H. ESTEC, ESA
TAVROV A.V. IKI RAS
TITOV D. ESTEC, ESA
VAISBERG O.L. IKI RAS
VOROBYOVA E.A. MSU
WU Ji National Space Science Center, China
ZHARKOV V.N. IFZ RAS
ZAKHAROV A.V. IKI RAS
ZASOVA L.V. IKI RAS

secretary:
ROSTE O.Z. IKI RAS, ms3@iki.rssi.ru

overview 11M-S^3 program
THE ELEVENTH MOSCOW SOLAR SYSTEM SYMPOSIUM (11M-S^3)

IKI RAS, 5-9 October 2020

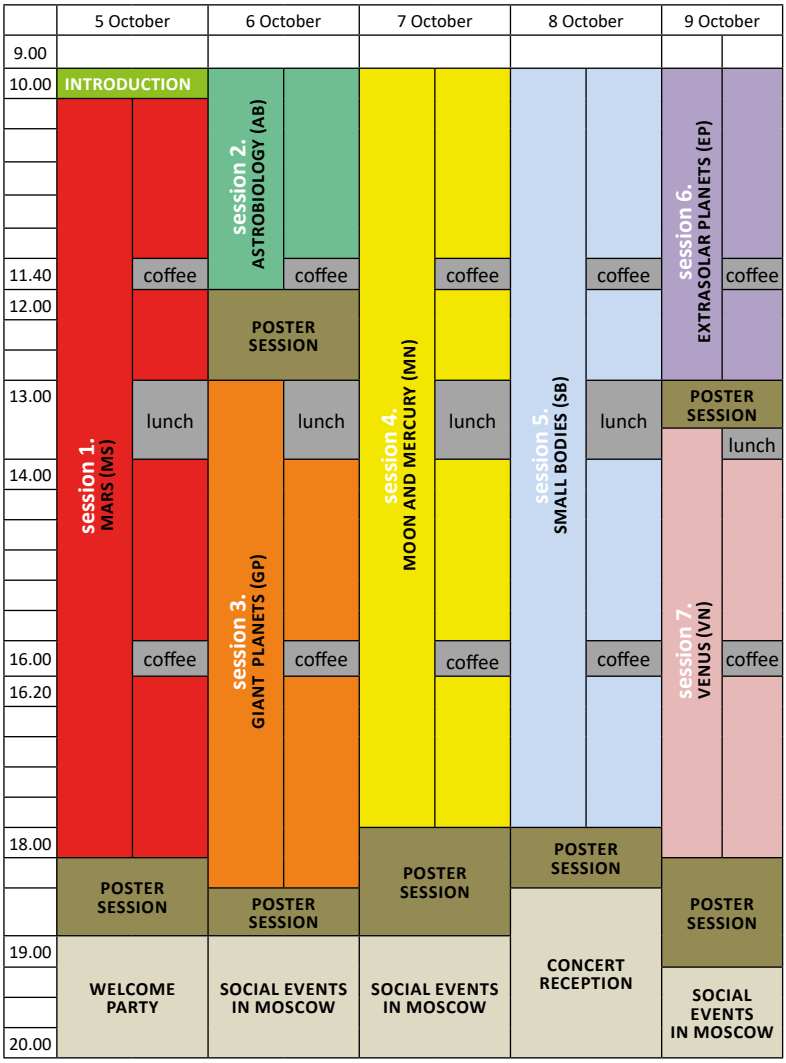

11M-S^3 SCIENTIFIC PROGRAM

	Monday, 5 October 2020		
	Lev ZELENYI	Opening Remarks	10.00-10.15
	session 1. MARS **convener: Oleg KORABLEV** **conference hall, second floor**		**10.15-18.30**
11MS3-MS-01	**Nikolay ABRAMOV et al**	Ground testing of the landing platform television system of the ExoMars-2020 spacecraft	10.15-10.30
11MS3-MS-02	**Sergei NIKIFOROV et al**	Water content in the Martian subsurface along the NASA MSL traverse by neutron measurements	10.30-10.45
11MS3-MS-03	**Alexey MALAKHOV et al**	Local water-rich areas in equatorial region of Mars as seen by FREND neutron spectrometer	10:45-11:00
11MS3-MS-04	**Pascal ROSENBLATT et al**	Measurements of Mars' CO2 seasonal mass deposits at polar caps: a comparison between gravity and Neutron flux data	11.00-11:15
11MS3-MS-05	**Jordanka SEMKOVA et al**	Radiation environment in the interplanetary space and Mars' orbit according FREND's Liulin-MO dosimeter aboard ExoMars TGO data	11.15-11.30
11MS3-MS-06	**Maria-Paz ZORZANO et al**	Comparison of space weather on Mars and Earth, towards a global monitoring: a feasibility study for ExoMars, using InSight and MSL	11.30-11.45
	coffee-break		11.45-12.15
11MS3-MS-07	**Dmitrij TITOV et al**	Mars Express science highlights and future plans	12.15-12:30
11MS3-MS-08	**Salvador JIMENEZ et al**	Solar wind at Mars and magnetic field interactions	12.30-12.45
11MS3-MS-09	**Luis VÁZQUEZ**	From Space and Radiation to New Materials	12.45-13.00
11MS3-MS-10	**Marina DÍAZ MICHELENA et al**	Drone magnetometry: a new approach to study present and past conditions in the planetary bodies	13:00-13:15
11MS3-MS-11	**Anatoliy PAVLOV et al**	Combination of methane spontaneous emission and ion-molecular reactions as a possible way to explain the variations of methane concentration in Martian atmosphere	13:15-13:30

	lunch		**13.30-14.30**
11MS3-MS-12	**Valery SHEMATOVICH and E.S. KALINICHEVA**	Atmospheric escape of atomic oxygen during the auroral events at Mars	14.30-14.45
11MS3-MS-13	**Boris IVANOV**	Martian dust activation due to air shock waves from small impacts	14.45-15.00
11MS3-MS-14	**Pavel VLASOV et al**	Diurnal and seasonal evolution of Martian atmospheric thermal structure from ACS-TIRVIM experiment onboard TGO ExoMars	15.00-15.15
11MS3-MS-15	**Denis BELYAEV et al**	Upper mesospheric water on Mars as measured by ACS TGO solar occultations	15.15-15.30
11MS3-MS-16	**Alexander TROKHIMOVSKIY et al**	First detection of HCl in the atmosphere of Mars by ACS TGO	15.30-15.45
11MS3-MS-17	**Vladimir Krasnopolsky**	Photochemistry of HCl in the Martian Atmosphere	15.45-16.00
	coffee-break		**16.00-16.30**
11MS3-MS-18	**Mikhail IVANOV and H. HIESINGER**	Topographic characteristics and chronology of the Uzboi-Ladon fluvial system on Mars	16.30-16.45
11MS3-MS-19	**Jessica FLAHAUT et al**	Identification and characterization of new feldspar-bearing rocks in the walls of Valles Marineris, Mars	16.45-17.00
11MS3-MS-20	**James W. HEAD and Lionel WILSON**	Sulfates on Mars: a pyroclastic airfall model for origin, emplacement, and initial alteration of Valles Marineris interior layered deposits	17.00-17.15
11MS3-MS-21	**James W. HEAD et al**	Geologic and climatologic history of early Mars: Recent developments, unknowns and directions for the next decade	17:15-17:45
11MS3-MS-22	**James L. DICKSON et al**	The formation of young Gullies on Mars by the melting and boiling of water at high obliquity	17.45-18.00
11MS3-MS-23	**Benjamin BOATWRIGHT and James W. HEAD**	Mars Crater Modification in the Late Noachian: Evidence for Cold-Based Crater Wall Glaciation and Endorheic Basin Formation	18:00-18:15
11MS3-MS-24	**Ashley PALUMBO and James W. HEAD**	Large impact basin-related climatic and surface effects on Mars: Argyre basin as a case study	18:15-18:30

	POSTER SESSION , session MARS	
	ONLINE DISCUSSION	**18.30-19.00**
11MS3- MS-PS-01	**Elizaveta FEDOROVA et al**	Analysis of H2O transmission spectra in the Martian atmosphere as measured by the ACS-TIRVIM solar occultations
11MS3- MS-PS-02	**Ekaterina STARICHENKO et al**	Gravity wave activity in the Martian atmosphere at altitudes 10 - 160 km from ACS/TGO solar occultations
11MS3- MS-PS-03	**Anton SALNIKOV et al**	Analysis of the magnetic field data of Mars
11MS3- MS-PS-04	**Tamara GUDKOVA et al**	Effect of third- and higher-order tide on the estimate of dissipative factor for Mars
11MS3- MS-PS-05	**Elena PODOBNAYA et al**	Fresh Martian impact clusters
11MS3- MS-PS-06	**Vincent PAYET et al**	Automated denoising for mineral indentification on hyperspectral data
11MS3- MS-PS-07	**Marie BARTHEZ et al**	VNIR Spectroscopic analysis of analogue feldspathic rocks as a reference for the interpretation of Mars data
11MS3- MS-PS-08	**Gen ITO et al**	Mineral mapping in Altiplano-Puna volcanic complex for Mars analog study
11MS3- MS-PS-09	**Jose Luis VAZQUEZ-POLETTI et al**	Advances in cloud computing for Mars data processing
11MS3- MS-PS-10	**Maria Pilar VELASCO et al**	Mathematical advances in fractional models for the Martian atmospheric dust dynamics
11MS3- MS-PS-11	**Imant VINOGRADOV et al**	Martian multichannel diode laser spectrometer experiment for the ExoMars-2022 lander mission: M-DLS instrument fabrication and laboratory calibration results
11MS3- MS-PS-12	**Kirill ZAKHARCHENKO et al**	Diamond Detectors of Space Radiation: the Ways to counter the Polarization Effect

	Tuesday, 6 October 2020		
	session 2. ASTROBIOLOGY **conveners: Elena VOROBYOVA,** **Oleg KOTSYURBENKO** **conference hall, second floor**		**10.00-12.00**
11MS3-AB-01	**Richard B. HOOVER**	Life in ice: implications to life on the Moon and small Solar System bodies	10.00-10.15
11MS3-AB-02	**Maxim ZAITSEV et al**	On the formation and transformation of organic matter in the Solar System	10.15-10.30
11MS3-AB-03	**Peter WURZ et al**	A novel and compact laser desorption – mass spectrometry system for sensitive in situ detection of amino acids on extraterrestrial surfaces	10.30-10.45
11MS3-AB-04	**Sergey BULAT et al**	New microbial finds in the subglacial antarctic lake Vostok	10.45-11.00
11MS3-AB-05	**Nikita DEMIDOV et al**	Sources of materials for the western delta of Jezero crater (Mars), astrobiological implication	11.00-11.15
11MS3-AB-06	**Zohreh ASHRAFZADEH et al**	The effect of cosmic rays on the human hippocampus	11.15-11.30
	coffee-break		**11.30-12.00**
	POSTER SESSION , session ASTROBIOLOGY **ONLINE DISCUSSION**		**12.00-12.20**
11MS3-AB-PS-1	**Vladimir CHEPTSOV et al**	The stability of enzymes to the effect of ionizing radiation under simulated extraterrestrial conditions	
11MS3-AB-PS-2	**Elizaveta SUKHOVA et al**	Resistance of DT57C bacteriophage to irradiation by high-energy electrons	
11MS3-AB-PS-3	**Andrey BELOV et al**	Microbial communities of Novaya Zemlya permafrost: physiological properties and astrobiological implication	
	POSTER SESSION, **session SOLAR WIND INTERACTIONS WITH PLANETS AND SMALL BODIES** **convener: Oleg VAISBERG** **ONLINE DISCUSSION**		**12.20-13.00**
11MS3-SW-PS-01	**Valery SHEMATOVICH and D.V. BISIKALO**	Efficiency of charge exchange between solar wind protons and the extended hydrogen corona of Mars	

11MS3-SW-PS-02	**Vladimir GUBENKO and I.A. KIRILLOVCH**	Solar wind interaction with the Earth's high-latitude ionosphere during geomagnetic storm in june 2015 by the radio occultation data	
11MS3-SW-PS-03	**Natalia BULATOVA**	On the movement of ensembles of objects by the spatio-temporal technology	
11MS3-SW-PS-04	**Ilia MIROSHNICHENKO et al**	The influence of the parent star Lyα radiation on absorption in the Hα line of the hot atmospheres HD189733b AND HD 209458b	
11MS3-SW-PS-05	**Tatiana MOROZOVA and Sergey POPEL**	Dusty plasma processes associated with meteor showers in the Earth's atmosphere	
11MS3-SW-PS-06	**Rico FAUSCH et al**	CHESS – constellation of CubeSats: analyzing the drivers of the Earth's exosphere with MS and GNSS	
11MS3-SW-PS-07	**Igor MINAEV et al**	Neutrino Telescope and the Sun	
	lunch		**13.00-14.00**
	session 3. GIANT PLANETS **convener: Scott BOLTON** conference hall, second floor		**14.00-18.40**
11MS3-GP-01	**Michel BLANC et al**	Science goals and mission objectives for the future exploration of ice giants systems - a Horizon 2061 perspective	14.00-14.20
11MS3-GP-02	**Michel BLANC et al**	A preliminary study of MIT coupling at Jupiter based on Juno observations and modelling tools	14.20-14.40
11MS3-GP-03	**Yohai KASPI et al**	Comparison of the deep atmospheric dynamics of Jupiter and Saturn in light of the Juno and Cassini gravity measurements	14.40-15.00
11MS3-GP-04	**Alessandro MURA et al**	Infrared observations of Jupiter's aurorae and atmosphere	15.00-15.20
11MS3-GP-05	**Leigh N. FLETCHER et al**	Jupiter's temperate belt/zone contrasts at depth revealed by Juno	15.20-15.40
11MS3-GP-06	**Tatiana SALNIKOVA and S. STEPANOV**	Peculiar movement of a pair of Saturn satellites	15.40-16.00
	coffee-break		**16.00-16.20**
11MS3-GP-07	**Scott BOLTON and the Juno Science Team**	Overview of Juno results at Jupiter	16.20-16.40

11MS3-GP-08	**Scott BOLTON and the Juno MWR Team**	The depth of Jupiter's storms	16.40-17.00
11MS3-GP-09	**Jack CONNERNEY et al**	Juno's exploration of Jupiter's magnetic field and magnetosphere	17.00-17.20
11MS3-GP-10	**Philip VALEK et al**	In situ observations above the Jovian ionosphere by Juno JADE-I	17.20-17.40
11MS3-GP-11	**Steven LEVIN and the Juno MWR Team**	Latest results from the Juno Microwave Radiometer at Jupiter	17.40-18.00
11MS3-GP-12	**Steven LEVIN and the Juno MWR Team**	The global abundance of water in Jupiter's atmosphere: a progress report	18.00-18.20
11MS3-GP-13	**Heidi BECKER et al**	Observations of Jupiter's atmosphere by Juno's Stellar Reference Unit	18.20-18.40
	POSTER SESSION , session Giant Planets		
	ONLINE DISCUSSION		**18.40-19.00**
11MS3-GP-PS-1	**Anna DUNAEVA et al**	Carbon dioxide clathrates in the Titan interiors	
11MS3-GP-PS-2	**Victor KRONROD et al**	Thermal evolution of rocky cores of the icy giant satellites	
11MS3-GP-PS-3	**Petr LYSENKO et al**	Some interesting features of the methane and ammonia absorption bands behavior on Jupiter	

	Wednesday, 7 October 2020		
	session 4. MOON AND MERCURY **conveners: Igor MITROFANOV, Maxim LITVAK** conference hall, second floor		**10.00-18.00**
11MS3-MN-01	**Johannes BENKHOFF**	Update on BepiColombo and first results from measurements during cruise	10.00-10.20
11MS3-MN-02	**Alexander KOZYREV et al**	First results of the monitoring of cosmic gamma-ray bursts by the MGNS instrument onboard ESA BepiColombo mission to Mercury	10.20-10.40
11MS3-MN-03	**Ekaterina FEOKTISTOVA et al**	Compilation of a new global catalog of Mercury's craters	10.40-11.00
11MS3-MN-04	**Igor MITROFANOV**	Human and Robotic Lunar Exploration	11.00-11.20
11MS3-MN-05	**Maxim LITVAK**	The reconnaissance of lunar resources	11.20-11.40
	coffee-break		**11.40-12.00**
11MS3-MN-06	**Lev ZELENYI et al**	Dust and dusty plasmas at the Moon. Challenges of modeling and measurements	12.00-12.20
11MS3-MN-07	**Alexander BASILEVSKY et al**	50 years of Lunokhod-1: past, present and future of planetary rovers	12.20-12.40
11MS3-MN-08	**Marine JOULAUD et al**	Candidate landing sites and possible traverses at the South Pole of the Moon for the LUVMI-X rover	12.40-13.00
	lunch		**13.00-14.00**
11MS3-MN-09	**Anatoly PETRUKOVICH et al**	Russian Luna-26 orbiter mission: science and implementation	14.00-14.20
11MS3-MN-10	**Vladislav TRETYAKOV et al**	Overview of Luna-27 science instruments	14.20-14.40
11MS3-MN-11	**David HEATHER et al**	ESA's PROSPECT payload on Luna-27: Development Status	14.40-15.00
11MS3-MN-12	**Artem NOSOV et al**	Lunar rover and soil intake system for Luna-28	15.00-15.20
11MS3-MN-13	**Tatiana TOMILINA et al**	Technology of 3D printing on the Moon	15.20-15.40
11MS3-MN-14	**Anton SANIN et al**	The concept of gamma-ray spectrometer with tagged charged particles of galactic cosmic ray for lunar resource investigations	15.40-16.00
	coffee-break		**16.00-16.20**
11MS3-MN-15	**James W.HEAD et al**	Volcanically-Induced Transient Atmospheres on the Moon: Assessment of Duration, Significance and Contributions to Polar Volatile Traps	16.20-16.40

11MS3-MN-16	**Nicolas BOTT et al**	Unveiling the mineralogical composition of lunar farside mare basalts	16.40-17.00
11MS3-MN-17	**Yuqi QIAN et al**	Young Mare Basalts in the Chang'e-5 Landing Region, Northern Oceanus Procellarum	17.00-17.20
11MS3-MN-18	**Jingyi ZHANG et al**	The Origin of the Lunar Procellarum KREEP Terrane (PKT): Stratigraphic Evidence and Implications for Lunar Geological and Thermal Evolution	17.20-17.40
11MS3-MN-19	**Carle PIETERS et al**	Why Go Forward to the Moon? Because It Is an Integral Part of the Earth-Moon System	17.40-18.00
	POSTER SESSION , session MOON AND MERCURY		
	ONLINE DISCUSSION		**18.00-19.00**
11MS3-MN-PS-1	**Alexander GUSEV et al**	Geological exploration of the Moon: strategies, concepts, approaches	
11MS3-MN-PS-2	**Ekaterina KRONROD et al**	Calculation of internal structure and physical properties of the lowermost lunar mantle from geophysical and geochemical data	
11MS3-MN-PS-3	**Jun CHU et al**	Chronology of volcanism in the Moscoviense basin	
11MS3-MN-PS-4	**Gennady KOCHEMASOV**	Swirls as intergrowths of light magnesian silicates (predominantly enstatite) and native iron	
11MS3-MN-PS-5	**Le QIAO et al**	Hyginus Crater and Graben: Dike Emplacement and Evolution, Magmatic Foam Extrusions, and Irregular Mare Patches	
11MS3-MN-PS-6	**Sergei IPATOV et al**	Estimates of the number of near-Earth objects based on the number of lunar craters formed during the last billion years	
11MS3-MN-PS-7	**Alexander BASILEVSKY and G.G. MICHAEL**	Morphology and age of lunar crater Ina	
11MS3-MN-PS-8	**Ekaterina GRISHAKINA and Mikhail IVANOV**	Rock abundance in the Plaskett lunar crater	
11MS3-MN-PS-9	**Ekaterina FEOKTISTOVA and Sergei IPATOV**	Depths of the Copernicans craters located on lunar maria and highlands	
11MS3-MN-PS-10	**Alexandr KRASILNIKOV et al**	Estimates of the model thickness of the crater ejecta in the South Polar region of the Moon	

11MS3-MN-PS-11	**Nikolay SLODARZH et al**	Morhometric features of craters in the southern polar region of the Moon
11MS3-MN-PS-12	**Azariy BARENBAUM and Michael SHPEKIN**	Problem of «South Pole-Aitken» basin formation
11MS3-MN-PS-13	**Svetlana PUGACHEVA et al**	The proposed landing site for the Luna-25 mission in the south pole region of the Moon
11MS3-MN-PS-14	**Nadezhda CHUJKOVA et al**	Evolution of the Moon and possible dynamics of its interior
11MS3-MN-PS-15	**Valerii BURMIN**	The optimal arrangement of seismic stations on the Moon for recording moonquakes
11MS3-MN-PS-16	**Nikita POPANDOPULO et al**	Study of the Dynamic Structure of the Near–Lunar Orbital Space
11MS3-MN-PS-17	**Imant VINOGRADOV et al**	Diode laser spectroscopy sensor DLS-L of the GC-L instrument for the Luna-Resource (Luna-27) mission: scientific targets, design options and future perspectives
11MS3-MN-PS-18	**Sergei KULIKOV et al**	Measurements of the electric and magnetic fields onboard the Luna-26 spacecraft
11MS3-MN-PS-19	**Alexander KOSOV et al**	Main features of Moon's radio beacon and orbiter Ka-band receiver, included into "Luna-Resource-1" project
11MS3-MN-PS-20	**Boris EPISHIN and Michael SHPEKIN**	Sunrise, sunset and culmination of stars and bodies of the solar system on the lunar sky
11MS3-MN-PS-21	**Gennady KOCHEMASOV**	Trembling Moon causing replenishment of its atmosphere and regolith layering

	Thursday, 8 October 2020		
	session 5. SMALL BODIES (including cosmic dust) **conveners: Alexander BASILEVSKY, Alexander ZAKHAROV** conference hall, second floor		**10.00-18.00**
11MS3-SB-01	**Ekaterina CHORNAYA et al.**	The 10 micron silicate feature in the Agglomerated Debris Particles	10.00-10.20
11MS3-SB-02	**Anton KOCHERGIN et al**	Blue color of disintegrating comet C/2019 Y4 (Atlas)	10.20-10.40
11MS3-SB-03	**Evgenij ZUBKO et al**	Characterizing primordial dust in comets: Implication to C/2019 Y4 (ATLAS)	10.40-11.00
11MS3-SB-04	**Evgeniya BLINKOVA et al**	Study of the dynamic structure of Leo-Meo regions of the near–earth orbital space	11.00-11.20
11MS3-SB-05	**Yuri SKOROV et al**	Activity of (6478) Gault during January 13 – March, 28, 2019	11.20-11.40
	coffee-break		**11.40-12.00**
11MS3- SB-06	**Tatyana GALUSHINA and Oksana LETNER**	The dynamics research of asteroids 3200 Phaethon and 2007 PR10 under the Yarkovsky effect influence	12.00-12.20
11MS3- SB-07	**Boris KONDRATYEV and V.S. KORNOUKHOV**	To the question of precession ring around dwarf planet Haumea	12.20-12.40
11MS3- SB-08	**Vladimir BUSAREV et al**	Interstellar comet 2I/ Borisov: the dust composition estimation	12.40-13.00
	lunch		**13.00-14.00**
11MS3- SB-09	**Vladimir BUSAREV et al**	Variability of the reflectance spectra of (1) Ceres and solar activity	14.00-14.20
11MS3- SB-10	**Mikhail MAROV et al**	Protoplanetary disk at the snowline: modeling clusters of refractory and ice particles	14.20-14.40
11MS3- SB-11	**Mikhail MAROV and Sergei IPATOV**	Migration of planetesimals to the Earth from the zone of the outer asteroid belt	14.40-15.00
11MS3- SB-12	**Tatiana SALNIKOVA and Alexander SAMOKHIN**	Probabilistic analysis of the cosmic masses accumulations in the Solar system	15.00-15.20
11MS3- SB-13	**Alexey BEREZHNOY et al**	Behavior of Fe-containing species during meteor events and in laser experiments	15.20-15.40
11MS3- SB-14	**Eva PLÁVALOVÁ and A. ROSAEV**	Estimation Yarkovsky effect in 355258 (2007 LY4) and 404118 (2013 AF40) young asteroid pair	15.40-16.00

	coffee-break		**16:00-16:20**
11MS3- SB-15	**Vladimir TCHERNYI et al**	About Importance of magnetic phenomena for the Saturn's rings origin	16.20-16.40
11MS3- SB-16	**Sergey POPEL et al**	Dust and dusty plasmas in the system of Mars	16.40-17.00
11MS3- SB-17	**Anna KARTASHOVA et al**	Meteoroid parameters from optical data	17.00-17.20
11MS3- SB-18	**Vladimir KRASNOPOLSKY**	On the methylacetylene abundance and nitrogen isotope ratio on Pluto	17.20-17.40
11MS3- SB-19	**Sergey VOROPAEV et al**	Models of h chondrites genesis and evolution: new findings	17.40-18.00
	POSTER SESSION , session SMALL BODIES (including cosmic dust)		
	ONLINE DISCUSSION		**18.00-18.30**
11MS3- SB-PS-1	**Olga SYUSINA and V.A. AVDYUSHEV**	Nonlinearity in inverse orbital problems for potentially hazardous asteroids	
11MS3- SB-PS-2	**Anton KOCHERGIN et al**	Cometary dust migrating through the Solar System	
11MS3- SB-PS-3	**Amirhossein DEHGHANI GHANATGHESTANI et al**	Applying UT to visual timing in occultation observations	
11MS3- SB-PS-4	**Arina SAVELOVA et al**	Estimation of some NEAs' composition by spectral method	
11MS3- SB-PS-5	**A. BERDYUGIN et al**	Negative polarization of asteroids (216) Kleopatra and (324) Bamberga	
11MS3- SB-PS-6	**Dmitry GLAZACHEV et al**	Scaling relations for spatial heterogeneity of shock wave effects from the impact of cosmic objects of different sizes	
11MS3- SB-PS-7	**Eduard KUZNETSOV et al**	Young asteroid family Rampo and cascade disruption	
11MS3- SB-PS-8	**Vladimir CHEPTSOV et al**	Formation of water and hydroxyl ions in simulated plasma of (micro)meteorite impact	
11MS3- SB-PS-9	**Artem KRIVENKO et al**	Features of mesuring the mechanical properties of meteorites L-Type	
11MS3- SB-PS-10	**Yulia REZNICHENKO et al**	Dust acoustic waves and solitons in Martian ionosphere	
11MS3- SB-PS-11	**Yulia IZVEKOVA et al**	On possibility of the existence of oscillations in Schumann cavity at Mars	
	CONCERT, RECEPTION		**18.30-20.30**

	Friday, 9 October 2020		
	session 6. EXTRASOLAR PLANETS **convener: Alexander TAVROV** conference hall, second floor		**9.00-13.00**
11MS3-EP-01	**Shingo KAMEDA et al**	Current status of Ultraviolet Spectrograph for Exoplanet (UVSPEX) for WSO-UV	9.00-9.15
11MS3-EP-02	**Maxim KHODACHENKO et al**	Exoplanetary dust phenomena in transit photometry	9.15-9.30
11MS3-EP-03	**Eva PLÁVALOVÁ**	Classification of Exoplanets	9.30-9.45
11MS3-EP-04	**Pegahsadat MIRSHAFIEKHOZANI et al**	Light curve analysis and radius study of 16 transiting exoplanets with ground-based data from ETD	9.45-10.00
11MS3-EP-05	**Anastasiia IVANOVA et al**	Detectability window regularization algorithm to account for observation selection in statistics of RV-exoplanets	10.00-10.10
11MS3-EP-06	**Vladislava ANANYEVA et al**	Radial velocity-exoplanets distributions by masses and by orbital periods	10.10-10.25
11MS3-EP-07	**Oleg YAKOVLEV et al**	Study of the mass distribution of transit exoplanets via mass-radius dependence	10.25-10.35
11MS3-EP-08	**Igor SAVANOV and E.S.DMITRIENKO**	Activity of two stars with planetary systems in Tuc-Hor group	10.35-10.50
11MS3-EP-09	**Valery SHEMATOVICH**	Non-thermal atmospheric loss for exoplanet GJ 436b: H_2 photodissociation input	10.50-11.05
11MS3-EP-10	**Ildar SHAIKHISLAMOV et al**	3D modeling of transit absorption of GJ3470B in hydrogen and helium lines	11.05-11.20
11MS3-EP-11	**Fatemeh DAVOUDI et al**	Study of transit timing variation in five hot jupiter planets	11.20-11.35
	coffee-break		**11.35-12.00**
11MS3-EP-12	**Evgeniya KALINICHEVA and Valery SHEMATOVICH**	Thermal atmospheric loss for close-in exoplanets	12.00-12.15
11MS3-EP-13	**Alexander PERMINOV and Eduard KUZNETSOV**	The Dynamical Evolution of Extrasolar Three-Planetary System GJ 3138	12.15-12.30
11MS3-EP-14	**Sergei IPATOV**	Probabilities of collisions of exoplanetesimals with exoplanets in the Proxima Centauri planetary system	12.30-12.45

11MS3-EP-15	**Valery KOTOV**	Motion of fast exoplanets and rotation of the Earth	12.45-13.00
	POSTER SESSION , session EXTRASOLA PLANETS		
	ONLINE DISCUSSION		**13.00-13.15**
11MS3-EP-PS-01	**Andrei YUDAEV et al**	Coronagraph with wavefront correction for exoplanet direct imaging	
11MS3-EP-PS-02	**Marina RUMENSKIKH et al**	Numerical simulation of helium-rich atmospheres of hot exoplanets	
11MS3-EP-PS-03	**Faezeh JAHEDIPARIZI et al**	Investigating the impact of exoplanets parameters on their habitability	
11MS3-EP-PS-04	**Zahra ZAREI et al**	Estimation of the Total Mass of Ten Exoplanets and their Host Stars Based on the Primary Transit Method	
11MS3-EP-PS-05	**Atila PORO et al**	Period Study by the Transit Method with Ground-Based Observations	
	lunch		**13.15-14.00**
	session 7. VENUS		**14.00-18.20**
	convener: Ludmila ZASOVA, Sanjay LIMAYE		
	conference hall, second floor		
11MS3-VN-01	**Mikhail RAZUMOVSKY et al**	Development of radiation block for non-hydrostatic GCM of Venus' Atmosphere	14.00-14.20
11MS3-VN-02	**Marina PATSAEVA et al**	Long-term variations of zonal wind speed at the cloud top level over mission time from VMC/ Venus Express and UVI/ Akatsuki UV images	14.20-14.40
11MS3-VN-03	**Dmitry GORINOV et al**	Horizontal winds in the lower clouds on the nightside of Venus from VIRTIS/VEx 1.74 μm data	14.40-15.00
11MS3-VN-04	**Ludmila ZASOVA**	Venera-D: a perspective planetary mission	15.00-15.20
11MS3-VN-05	**Vladislav ZUBKO et al**	Landing on the Venus surface with gravity assist	15.20-15.40
11MS3-VN-06	**Tibor KREMIC et al**	LLISSE: Development status	15.40-16.00
	coffee-break		**16.00-16.20**
11MS3-VN-07	**Sanjay LIMAYE et al**	Venus, an astrobiology target	16.20-16.40
11MS3-VN-08	**Michael WAY**	A Temperate Climate History of Venus	16:40-17:00
11MS3-VN-09	**Piero D'INCECCO et al**	The young volcanic rises as suitable landing sites for future Venus missions: scientific relevance in the debate between the equilibrium and catastrophic resurfacing hypotheses	17.00-17.20

11MS3-VN-10	**Lauren MACLELLAN et al**	Volcanic history of the Derceto Corona event, Astkhik Planum, Venus	17.20-17.40
11MS3-VN-11	**Richard ERNST et al**	Tesserae on Venus may preserve evidence of fluvial erosion	17.40-18.00
10MS3- VN-12	**Manuel DOMÍNGUEZ-PUMAR et al**	First experiments with a 3D heat flux sensor for planetary regolith	18.00-18.20
	POSTER SESSION , session Venus ONLINE DISCUSSION		**18.20-19.20**
11MS3-VN-PS-01	**Sara PORT et al**	Venus Surveyor for Planetary Exploration Research (VeSPER)	
11MS3-VN-PS-02	**Akos KERESZTURI**	Targets of high resolution radar analysis on Venus for the EnVision mission	
11MS3-VN-PS-03	**Jeffrey BALCERSKI et al**	LEAVES – a low-mass atmospheric sensor platform concept for distributed exploration at Venus	
11MS3-VN=PS-04	**Igor KHATUNTSEV et al**	Cloud level winds from VMC (Venus Express) and UVI (Akatsuki) imaging	
11MS3-VN-PS-05	**Vladimir OGIBALOV and Yu.L. BORDOVSKAYA**	Emissions in the IR CO2 bands outgoing the planetary atmosphere with macroscopic wind velocity gradient	
11MS3-VN-PS-06	**Vladimir ZHARKOV et al**	The choice of the reference surface for Venus	
11MS3-VN-PS-07	**Tamara MENSHCHIKOVA et al**	Data analysis of the gravity field of Venus	
11MS3-VN-PS-08	**Evgeniya GUSEVA and Mikhail IVANOV**	Results of geologic analysis of the coronae of different topographic categories on Venus	
11MS3-VN-PS-09	**Anastasia KOSENKOVA and Alexey MARTYNOV**	Investigation of design characteristics of a lander for maneueverable descent to the Venus surface	
11MS3-VN-PS-10	**Alexey MARTYNOV and Anastasia KOSENKOVA**	Some platforms to observe Venus as a system	

GROUND TESTING OF THE LANDING PLATFORM TELEVISION SYSTEM OF THE EXOMARS-2020 SPACECRAFT

N. F. Abramov, Ya. D. Elyashev, I. V. Polyanskiy, S. A. Prokhorova
Space Research Institute of the Russian Academy of Sciences,
Moscow 117997, *Russia*
(*abramov.n2@mail.ru*)

KEYWORDS:
ExoMars-2020, TSPP-EM, Mars, panoramic television imaging, landing platform, scientific payload

The paper describes the ground testing of the landing platform television system (TSPP-EM), designed as part of the complex of scientific instruments of the ExoMars-2020 spacecraft. Design features of TSPP-EM as well as imaging stages are considered. Among the construction features it is important to note that the optical axes of all four cameras (CAM-O/EM) are spaced by 90 degrees in the azimuthal plane. This makes it possible to completely overview the horizon line due to the overlapping fields of view of the cameras. The cameras are placed on the edges of the landing platform in close proximity to the outer boundary on special brackets.

They are able to take still images or sequenced set of frames separately or simultaneously. The data collection unit (BSD/EM) provides imaging in several modes, as well as collection, storage and subsequent transfer of the received data to the spacecraft housekeeping systems for sending to the Earth. BSD consists of two independent units: main and redundant, which may be operated in spare or mirroring mode. The results of testing ot TSPP-EM and calibration of four CAM-O/EM are given.

REFERENCES:

[1] Abramov N. F. et al. Remote television imaging from the landing platform of the ExoMars-2020 spacecraft // Sovremennye problemy distantsionnogo zondirovaniya Zemli iz kosmosa (Current problems in remote sensing of the earth from space). 2018. V. 15. No. 6. P. 188–200.

[2] Zhukov B. S., Zhukov S. B., Snetkova N. I., Teplukhina T. R., Proverka kharakteristik kamer televizionnoi sistemy navigatsii i nablyudeniya po resultatam naturnykh s'emok (On-Ground Tests of the Cameras of Television System for Navigation and Observation), 2-ya Vserossiiskaya nauchno-tekhnicheskaya konferentsiya "Sovremennye problemy orientatsii i navigatsii kosmicheskikh apparatov" (2nd All-Russia Scientific and Technological Conf. "Contemporary problems of spacecraft attitude determination and control"): Proc. Tarusa, 13–16 Sept., 2010. M.: IKI RAN, 2011. P. 308–318.

[3] Elyashev Ya. D., Bessonov R. V., Polyanskiy I. V., Prokhorova S. A., Zhukov B. S., Algoritmy raboty s'emochnykh kamer sluzhebnoi televizionnoi sistemy kosmicheskogo apparata "Luna-Glob" (Algorithmic Support of Service Television System (STS-L) for the Spacecraft Luna-Glob), 4-ya Vserossiiskaya nauchno-tekhnicheskaya konferentsiya "Sovremennye problemy orientatsii i navigatsii kosmicheskikh apparatov" (4th All-Russia Scientific and Technological Conf. "Contemporary problems of spacecraft attitude determi- nation and control"): Proc. Tarusa, 8–11 Sept., 2014. M.: IKI RAN, 2015. P. 181–205.

WATER CONTENT IN THE MARTIAN SUBSURFACE ALONG THE NASA MSL TRAVERSE BY NEUTRON MEASUREMENTS

S. Y. Nikiforov[1], I. G. Mitrofanov[1], M. L. Litvak[1], M. V. Djachkova[1], D. I. Lisov[1], A. B. Sanin[1]
Space Research Institute of the Russian Academy of Sciences, Moscow 117997, Russia

KEYWORDS:
Mars exploration, surface, neutron spectroscopy, water

INTRODUCTION:

Passive neutron sensing onboard Martian rovers is an advanced technique in planetary science. Such measurements provide investigations on hydrogen abundances and elements with high thermal neutron absorption cross sections down to ~60 cm of subsurface [1]. The presence of hydrogen (mostly water/ice) in subsurface significantly influences the neutron leakage spectrum due moderation and thermalization through collisions with hydrogen nuclei. As a result, the variations of neutron flux detected onboard in different energy bands correlate with subsurface hydrogen/water abundance.

Dynamic Albedo of Neutrons (DAN) is the first neutron spectrometer installed on the NASA's rover [2]. More than 7 years, NASA rover is successfully traversing across Mars surface exploring Gale crater.

This work will demonstrate scientific potential and results of passive neutron technique for Martian subsurface local features, based on the DAN instrument findings.

REFERENCES:

[1] Nikiforov, S. Y. et al. Assessment of water content in Martian subsurface along the traverse of the Curiosity rover based on passive measurements of the DAN instrument // Icarus. 2020. V. 346. Art. 113818. https://doi.org/10.1016/j.icarus.2020.113818
[2] Mitrofanov I. G. et al., (2012). Dynamic Albedo of Neutrons (DAN) experiment onboard NASA's Mars Science Laboratory // Space Science Reviews. 2020. V. 170. V. 1–4. P. 559–582. https://doi.org/10.1007/s11214-012-9924-y.

LOCAL WATER-RICH AREAS IN EQUATORIAL REGION OF MARS AS SEEN BY FREND NEUTRON SPECTROMETER

A. V. Malakhov, I. G. Mitrofanov, M. L. Litvak, A. B. Sanin, D. V. Golovin, A. A. Anikin, M. V. Djachkova, D. I. Lisov, N. V. Lukyanov, S. Yu. Nikiforov
Space Research Institute (*IKI*),
Moscow, *Russia*
(*malakhov@np.cosmos.ru*)

KEYWORDS:
Mars, hydrogen, water, neutron, regolith

FREND [1] is a neutron telescope onboard ESA's Trace Gas Orbiter [2], mapping Mars for hydrogen content in the upper 1 m of regolith. It's capable of mapping with high spatial resolution using its collimator module that narrows the field of view significantly, allowing for 60–200 km pixel size on the surface [1]. This size is comparable to local relief features or characteristic sizes of landing ellipses. This allows FREND to significantly improve theknowledge of Martian water resources compared to previous maps created with omnidirectional detectors with characteristic pixel size of 550 km [3].

In this study we present latest findings of small but water-rich "oases" close to equator identified by FREND. These are of particular interest since it is known that water is not stable close to equator, so special conditions need to be met in order to preserve it in the upper layer of the regolith [4]. These oases may be rich in remnants of past Martian life or signs of wet subsurface areas that can still preserve life. And of course, such locations are excellent resource providers for future exploration.

REFERENCES:

[1] Mitrofanov I. et al. Fine Resolution Epithermal Neutron Detector (FREND) onboard the ExoMars Trace Gas Orbiter // Space Science Reviews, 214, 86 (2018).
[2] Vago J. et al. ESA ExoMars program: The next step in exploring Mars // Solar System Research, 49, 7 (2015).
[3] Maurice S. et al. Mars Odyssey neutron data: 1. Data processing and models of water-equivalent-hydrogen distribution // Journal of Geophysical Research E: Planets, vol: 116 (11) pp.: E11008 (2011).
[4] Forget F. et al. Formation of glaciers on Mars by atmospheric precipitation at high obliquity // Science vol: 311 (5759) pp.: 368-371(2006).

MEASUREMENTS OF MARS' CO_2 SEASONAL MASS DEPOSITS AT POLAR CAPS: A COMPARISON BETWEEN GRAVITY AND NEUTRON FLUX DATA

P. Rosenblatt[1], M. Muñoz Fernández[2], J. C. Marty[3], H. Svedhem[4], L. Metcalfe[5]

[1] *Laboratoire de Planétologie et Géodynamique, 2 chemin de la Houssinière, 44300 Nantes, France* (*pascal.rosenblatt@univ-nantes.fr*)

[2] *HE Space for ESA/ESAC, Urbanización Villafranca del Castillo, Villanueva de la Cañada, 28692, Madrid, Spain*

[3] *CNES/GRGS, 14 Avenue E. Belin 31400 Toulouse, France*

[4] *European Space Research and Technology Centre, Keplerlaan 1, Postbus 299, 2200 AG Noordwijk, the Netherlands*

[5] *European Space Astronomy Centre, European Space Agency, Urbanización Villafranca del Castillo, Villanueva de la Cañada, 28692, Madrid, Spain*

KEYWORDS:
Mars CO_2 seasonal cycle, seasonal gravity changes, neutron flux data, Trace Gas Orbiter

INTRODUCTION:
Mars' frozen CO_2 completely sublimates at the northern cap in summer and condensates at the southern cap (which is then in the winter season). The seasonal variations of atmospheric pressure have been accurately measured at Lander sites [1], providing the CO_2 seasonal cycle in the atmosphere. This cycle has been accounted for by a Global Circulation Model (GCM) providing in turn predictions of the seasonal cycle of CO_2 deposits at polar caps [2, 3]. However, these deposits have not been monitored yet with high precision unlike the atmospheric pressure variations. In this study, we investigate how to improve the measurements of CO_2 mass deposits at the polar caps over seasons. Two independent approaches based on the gravity changes and on the Neutron flux variations are used. The results are then compared with the Global Circulation Model (GCM) predictions.

IMPROVING SEASONAL GRAVITY VARIATION ESTIMATES WITH THE TRACKING DATA OF ESA'S TRACE GAS ORBITER (TGO):
The CO_2 mass seasonal cycle is expected to produce detectable variations of Mars' gravity field. In turn, measurements of gravity changes should provide direct measurements of the seasonal CO_2 mass budget. However, CO_2 mass estimates at the polar caps, from gravity changes, show slight discrepancies with the GCM predictions [4]. This mass budget shows a deficit of mass deposits at the South pole (winter season) and an excess of accumulation of CO_2 ice at the North pole (fall season), which occurs sooner than predicted by the GCM (Figure 1). However, this slight discrepancy is just at the limit of the error bars on the seasonal mass budget estimates at the polar caps, preventing a better constraint of GCM predictions of CO_2 deposits at the polar caps [1]. This lack of resolution in the gravity changes solution is due to the error of the reconstructed orbit of near-polar orbiters [5]. In addition, the CO_2 ice polar caps extent needs to be monitored over the seasons to model the CO_2 mass deposits with gravity changes. This monitoring of the polar caps geometry uses Thermal Emissivity Spectrometer (TES) data, which also suffer from low-resolution [4].

A way to improve the time variable gravity field solution is to combine tracking data of orbiters with different inclinations. For the first time in the exploration of Mars, there are simultaneously in Mars orbit two near-polar orbiters (ODY) and Mars Reconnaissance Orbiter (MRO), and one non-polar orbiter (TGO) with an orbital inclination of 74 degrees. The even harmonics signal on this non-polar orbit is expected to be 5 times larger than it is on polar orbiters [5], thus allowing for improving the current gravity changes solution from tracking data [e. g. 6–8].

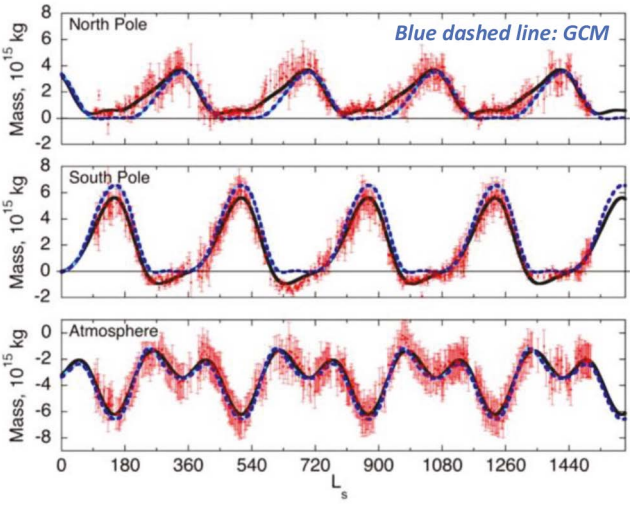

Fig. 1. Mars seasonal CO_2 mass budget derived from the seasonal variations of the gravity field determined with Mars Global surveyor (MGS) and Mars Odyssey (ODY) tracking data [4]. Red dots with error bars are time series determined every 5 days, the black solid line is the best fit of annual and sub-annual variation, and the blue dashed line corresponds to predictions from Global Circulation Model (GCM) simulations [3]. L_S is the angular position of the Sun over the course of one Martian year (L_S = 0° at Northern Spring/Southern fall season)

Monitoring the seasonal variations of the polar caps CO_2 deposits from Neutron flux data:

The high energy neutrons from cosmic rays regularly hit the surface of the planet and penetrate into the soil. There, they interact with hydrogen (essentially contained in water ice) and are re-emitted out of the soil. This re-emitted flux is however absorbed by the CO_2 deposits at the polar caps, hence the variations of the neutron flux measured by the HEND instrument reflect the variations of the CO_2 deposits over the seasons [9–11]. Based on specific calibration of the neutron flux, the surface density of the CO_2 deposits at the polar caps can be derived. Then, the integration of the surface density over the entire area of CO_2 deposits enables monitoring the polar caps mass at a given time in the season [10, 11]. This approach has provided polar caps mass estimates with a better resolution than gravity changes but it still shows discrepancies with GCM predictions (Figure 2), which may result in part from the calibration process from Neutron flux data of CO_2 deposits.

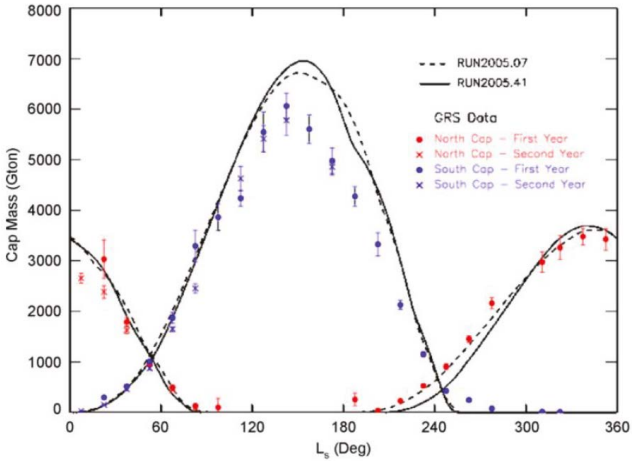

Fig. 2. Comparison between CO_2 mass deposits estimates from HEND/ODY Neutron flux data (blue and red dots with error bars) and predictions from GCMs [1]

Here, we propose to (re-)process the Neutron flux data of the instrument High Neutron Energy Detector (HEND) onboard ODY. The dataset is available in the Planetary Data System (PDS) and covers almost 10 Martian years (since 2002). The goal is to produce maps of estimated CO_2 polar caps (both mass and extent) with a spatial resolution of 5° in latitude and longitude and 15° in solar longitude. The CO_2 mass estimates will then be compared, and eventually combined, with the improved gravity estimates.

FROM GRAVITY AND NEUTRON DATA TO ATMOSPHERIC PHYSICS:
The GCMs include a detailed representation of the condensation and sublimation in the seasonal polar caps based on the local energy balance [12]. Estimating this balance is however challenging: first, CO_2 ice, snow and clouds can have exotic properties in the thermal infrared (highly variable emissivity) and in the visible (highly variable albedo). Second, the Martian high latitudes ground is characterized by the presence of a high-thermal-inertia ice-rich layer below a few centimeters of dry soil [13]. At seasonal scales, the hidden ice layer is able to store a significant amount of heat during summer and release it during fall and winter, hence significantly reducing the CO_2 condensation rate [13]. Thus, the modeled CO_2 cycle is tuned by adjusting GCM parameters such as the CO_2 ice varying albedos and the depth of the subsurface-ice rich layer [14]. For this purpose, the main dataset used is the seasonal atmospheric pressure variations measured by the Viking Landers which are assumed to provide a proxy for the global atmospheric mass variations. The seasonal variations of CO_2 in the atmosphere derived from the joint analysis of ODY/HEND data and TGO/ODY/MRO tracking data will precisely monitor the polar caps deposits' mass variations, allowing in turn to assess the use of the Viking pressure data points in the GCMs as a proxy for the global CO_2 seasonal cycle.

REFERENCES:
[1] Haberle et al., 2008. Planet. Space Sci., vol. 56, p. 251–255, 2008.
[2] Forget F. et al., 1999. J. Geophysical Research. 104 (E10), p. 24155–24176.
[3] Haberle et al. 1999. J. Geophysical Research. 104 (E4), 8957–8974.
[4] Smith et al., 2009. J. Geophysical Research., 114 (E5), doi:10.1029/2008JE003267.
[5] Rosenblatt et al., AGU fall meeting, Abstract 249478, 2018.
[6] Marty et al., 2013. AGU fall meeting, 2013.
[7] Konopliv A. S. et al., 2016. Icarus 274, 253–260.
[8] Genova A. et al., 2016. Icarus 272, 228–245.
[9] Litvak et al., Solar System Research, vol. 38, p. 167, 2004.
[10] Feldman et al., J. Geophysical Research., vol. 108, doi :10.1029/2003JE002101, 2003.
[11] Prettyman et al., J. Geophysical Research., vol. 109, doi :10.1029/2003JE002139, 2004.
[12] Forget et al. Icarus, vol. 131, p. 302, 1998.
[13] Boynton et al. Science, vol. 297, p. 81, 2002.
[14] Millour et al., Third International Workshop on Mars Polar energy balance and the CO_2 cycle, Contribution 1494, 2009.

RADIATION ENVIRONMENT IN THE INTERPLANETARY SPACE AND MARS' ORBIT ACCORDING FREND'S LIULIN-MO DOSIMETER ABOARD EXOMARS TGO DATA

J. Semkova[1], R. Koleva[1], V. Benghin[3], T. Dachev[1], Y. Matviichuk[1], B. Tomov[1], K. Krastev[1], S. Maltchev[1], P. Dimitrov[1], N. Bankov[1], I. Mitrofanov[2], A. Malakhov[2], D. Golovin[2], M. Mokrousov[2], A. Sanin[2], M. Litvak[2], A. Kozyrev[2], S. Nikiforov[2], D. Lisov[2], A. Anikin[2], V. Shurshakov[3], S. Drobyshev[3]

[1] *Space Research and Technology Institute*, *Bulgarian Academy of Sciences*, *Sofia*, *Bulgaria* (*jsemkova@stil.bas.bg*)
[2] *Space Research Institute*, *Russian Academy of Sciences*, *Moscow*, *Russia* (*mitrofanov@np.cosmos.ru*)
[3] *State Scientific Center of Russian Federation*, *Institute of Biomedical Problems*, *Russian Academy of Sciences*, *Moscow*, *Russia* (*v_benghin@mail.ru*)

KEYWORDS:
Mars, galactic cosmic rays, radiation environment, ExoMars, TGO, FREND, dosimeter, dose rate, particle flux

INTRODUCTION:
The dosimeter Liulin-MO [1] for measuring the radiation environment onboard the ExoMars TGO is a module of the Fine Resolution Epithermal Neutron Detector (FREND) [2].

In this work we present recent results from measurements of the charged particle fluxes, dose rates and estimation of radiation quality factors and dose equivalent rates at ExoMars TGO science orbit (circular orbit with 400 km altitude, 74° inclination, 2 hours orbit period), provided by Liulin-MO dosimeter since the beginning of science measurements in May 01, 2018. Since now the dosimeter has measured the dosimetric parameters of the galactic cosmic rays (GCR). Solar particle events were not registered. The measurements were taken during the declining and minimum of the Solar activity in 24th Solar cycle.

Compared are the data obtained during the transit to Mars and in Mars science orbit.

Investigated is the dependence of the flux distribution on Martian latitude and longitude.

Compared are the time profiles of the charged particles and neutron detections from Liulin-MO, FREND/TGO and HEND/Odyssey [3, 4] measured in Mars science orbit.

METHODOLOGY AND MEASURED PARAMETERS:
FREND contains four ^{3}He counters for neutrons with energies from 0.4 eV to 500 eV, one stilbene-based scintilator for high energy neutrons (up to 10 MeV) and the dosimetry module Liulin-MO. Liulin-MO consists of two dosimetric telescopes arranged in two perpendicular directions. The parameters, provided by Liulin-MO simultaneously for the two perpendicular directions have the following ranges: absorbed dose rate from 10^{-7} Gy·h^{-1} to 0.1 Gy·h^{-1}; particle flux in the range 0–10^4 cm^{-2}·s^{-1}; energy deposition spectrum and coincidence energy deposition spectrum in the range 0.08–190 MeV, LET spectra in water 0.13–177 keV/µm.

RADIATION ENVIRONMENT DATA IN MARS' SCIENCE ORBIT:
The fluxes and dose rates recorded in the perpendicular detectors B(A) and D(C) of Liulin-MO and the count rates of Oulu neutron monitor (http://cosmicrays.oulu.fi/) for the period from 1 May 2018 to 10 June 2020 are shown in Figure 1. An increase of all quantities — flux, dose rate and Oulu count rate due to solar cycle modulation is observed. In this period in the two perpendicular directions B(A) and D(C) the average values are: dose rate

14.8±1.5/15.4±1.5 mGy·h^{-1}, planar flux 3.11/3.21 cm^{-2}·s^{-1}, quality factor Q 3.5±0.26, dose equivalent rate 1.61±0.33/1.66±0.34 mSv·d^{-1}.

In TGO science orbit in May 2018 – July 2020, the flux is about 95 %, the dose rate is about 86 %, the dose equivalent rate is 72 % of those in February – March 2017 in high elliptic Mars orbit (practically in the free interplanetary space) — due to two competing effects: the Mars' shadow of GCR and the increase in GCR flux because of the decreased solar modulation.

A slight, but well expressed dependence of the flux distribution on Martian latitude and longitude is observed. This effect is currently under investigation as more statistics is necessary. The measured flux in TGO altitude consists of the primary GCR flux and the albedo flux from the interaction of the primary GCR with the surface and Mars atmosphere. The comparison of the existing flux data with the Mars topography shows that the lower fluxes in the northern hemisphere correspond to the lower elevations there. We suppose that the decrease of the flux in the northern part is due to a stronger attenuation of the albedo flux from the surface by Martian atmosphere there. It was shown that in the southern hemisphere the lower fluxes registered in the east and west part correspond to the increased crustal magnetic sources.

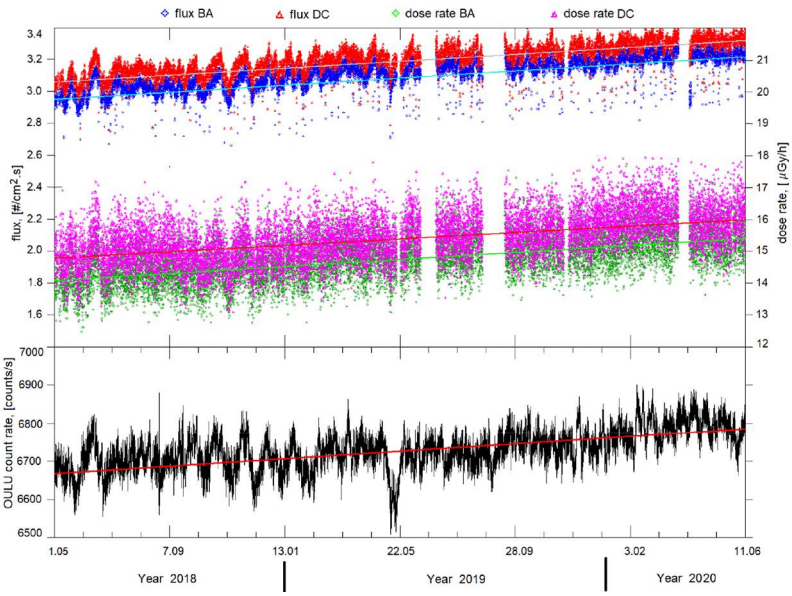

Fig. 1. Overview of GCR fluxes (top) and dose rates (middle) measured by Liulin-MO in Mars science orbit and Oulu neutron monitor count rates (bottom) in the period 01.05.2018–10.06.2020

We have compared time profiles of particles and neutron detections from Liulin-MO, FREND/TGO and HEND/Odyssey measured since May 2018. Similar to FREND, HEND/Odyssey is a neutron spectrometer based on ^{3}H proportional counters but with smaller sensitivity and without collimation a in FREND. For the comparison with Liulin-MO we have selected FREND and HEND count rates measured in ^{3}He detectors. The time profiles of GCR daily variations measured by Liulin-MO and HEND demonstrate good correlation both on a short time scale (days) and long term scale (months). The comparison between the normalised FREND total counts rate and HEND data accumulated in the energy channels mostly populated with counts from Martian neutron albedo also shows high correlation with each other both on short and long term scales. The difference in the long term variations between the profiles of GCR and the neutron albedo might be addressed to how the solar modulation changes directly the GCR flux and how it changes the emission of the neutron albedo produced by interaction with a matter in the Martian shallow subsurface.

ACKNOWLEDGEMENTS:
The work in Bulgaria is supported by the Contract No. 4000117692/16/NL/NDe funded by the Government of Bulgaria through an ESA Contract under the PECS (Plan for European Cooperating States) and by Project No. 129 for bilateral projects of the National Science Fund of Bulgaria and Russian Foundation for Basic Research. The work in Russia is supported by Grant 19-52-18009 for bilateral projects of the National Science Fund of Bulgaria and Russian Foundation for Basic Research in part of HEND data analysis, and Russian Science Foundation Grant 19-72-10144 in part of FREND data analysis.

REFERENCES:
[1] Semkova J. et al. Charged particles radiation measurements with Liulin–MO dosimeter of FREND instrument aboard ExoMars Trace Gas Orbiter during the transit and in high elliptic Mars orbit // Icarus. 2018. V. 303. P. 53–66. https://doi.org/10.1016/j.icarus.2017.12.034.
[2] Mitrofanov I. et al. Fine Resolution Epithermal Neutron Detector (FREND) onboard the Trace Gas Orbiter // Space Sciences Rev. 2018. V. 214. P. 86. https://doi.org/10.1007/s11214-018-0522-5.
[3] Mitrofanov I. et al. Maps of Subsurface Hydrogen from the High Energy Neutron Detector, Mars Odyssey // Science. 2002. V. 297. Iss. 5578. P. 78–81.
[4] Mitrofanov I. G. et al. Search for water in Martian soil using global neutron mapping by the Russian HEND instrument onboard the US 2001 Mars Odyssey spacecraft // Solar System Research. 2003. V. 37. Iss. 5. P. 366–377.

COMPARISON OF SPACE WEATHER ON MARS AND EARTH, TOWARDS A GLOBAL MONITORING: A FEASIBILITY STUDY FOR EXOMARS, USING INSIGHT AND MSL

M. P. Zorzano[1,2], J. Martín-Torres[2,3], J. A. Ramírez-Luque[4]
[1] *Centro de Astrobiología* (*CSIC-INTA*), *INTA*, *Torrejón de Ardoz*, *28850*, *Madrid*, *Spain*
[2] *School of Geosciences*, *University of Aberdeen*, *Aberdeen*, *AB24 3FX*, *UK*
[3] *Instituto Andaluz de Ciencias de la Tierra* (*CSIC-UGR*), *18100 Granada*, *Spain*
[4] *Department of Computer Science*, *Electrical and Space Engineering*, *Luleå University of Technology*, *Luleå*, *Sweden*

KEYWORDS:
Space weather, magnetometer, UV aurora, radiation detector, Mars, Earth

INTRODUCTION:
The Earth and Mars have different viewing sides of the Sun during most of the year, and this changes with solar longitude throughout their orbit around the star. Moreover, the Sun has a synodic rotation period of 26.24 days. Depending on the elongation angle of Mars, an instrument operating on its surface can, for instance, observe space weather perturbations caused by the face of the Sun that will spin to Earth in 8–13 days, and the other way around. We propose to establish a network of a set of long-term space weather monitoring instruments operating on the surface and orbit of Mars to provide a complementary view of space weather effects on Mars.

These coordinated studies may help to elucidate the impacts of space weather on different planets and the interactions with their magnetosphere and atmospheres. This network will allow delivering early warnings to either Earth or Mars during the onset of solar storms. Having a reliable space-weather warning procedure will be critical to facilitate the safe and sustained future human exploration of Mars.

FEASIBILITY STUDY:
In this work, we analyze the existing observations of three sensors that are already operating on Mars and compare them with some measurements of space weather activity on Earth. In particular, to perform a feasibility analysis, we take the measurements of the UV sensor of REMS at night [1], searching for UV excitation bands of the atmospheric molecules, and the measurements of the RAD sensor [2], both operating on the Curiosity Rover at Crater Gale (4.59° S, 137.44° E) since August 2012; and the magnetic field measurements of the InSight lander [3], at Elysium Planitia (3.0° N, 154.7° E). These data are publicly available at the Planetary Data System [4]. This kind of studies may be continued in the future by instruments on the ExoMars 2022 surface platform and rover, such as the UV-sensors (in HABIT instrument) [5], the magnetometer AMR (part of the METEO instrument), MAIGRET, and the dosimeters of ADRON-EM and ADRON-RM and FREND on the Exomars Trace Gas Orbiter, on-orbit around Mars [6, 7].

The following figures provide two comparisons of space weather signatures as sensed by instruments based on Earth and Mars. In the case of magnetometer responses, we have applied a 9-day delay shift to the Martian magnetometer to account for the synodic rotation and elongation angle of Mars at the moment of observation and compare with the measured Earth Ap index for those dates. This allows to compare delayed signals that serve as precursors and prepare the procedures for early warning systems. In the case of night-time sky aurora glow we can compare the UV measurements of different channels with the simultaneously measured particle doses that reach the surface, this can be used to model particle cascades and excitation profiles through the atmosphere. This kind of analysis will be trained with the currently existing observations to allow for its systematic real-time imple

mentation with the future ExoMars observations and other Mars operating missions.

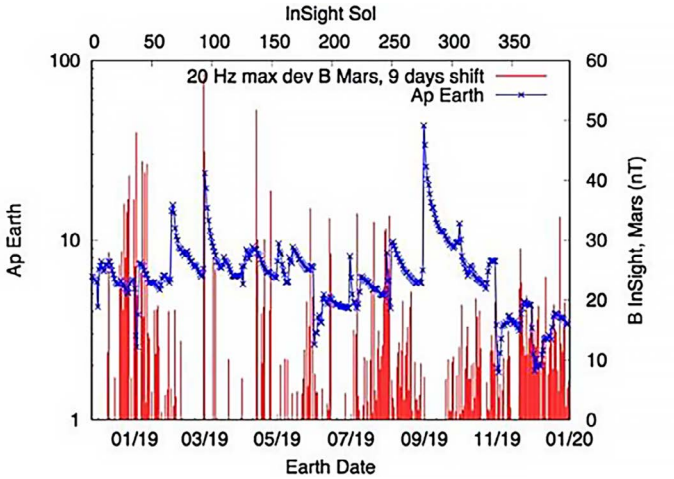

Fig. 1. Comparison of the Ap-index as measured on Earth with the magnetic perturbations detected by InSight on Mars

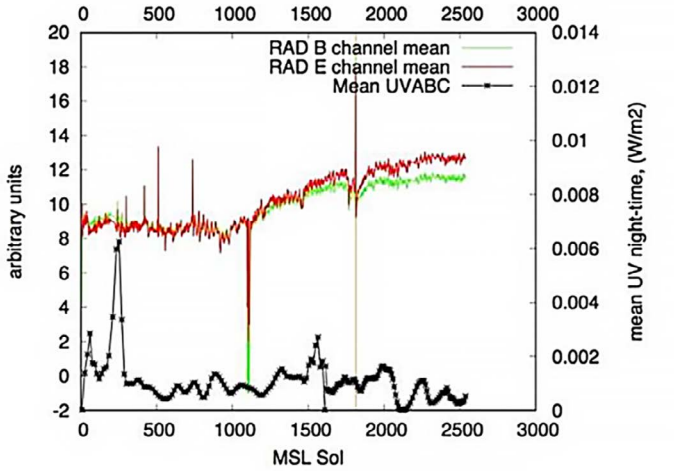

Fig. 2. Comparison of the average radiation values measured by channels B and E of RAD with the night-time UV signals detected by the UV sensor of REMS. Both measurements have been acquired by the Curiosity Rover on Mars

REFERENCES:

[1] Gómez-Elvira J. et al. REMS: The Environmental Sensor Suite for the Mars Science Laboratory Rover // Space Science Reviews. 2012. V. 170. No. 1–4. P. 583–640. doi: 10.1007/s11214-012-9921-1.
[2] Hassler D. M. et al. The radiation assessment detector (RAD) investigation // Space Sciences Rev. 2012. V. 170. P. 503–512.
[3] Johnson C. L. et al. Crustal and Time-Varying Magnetic Fields at the InSight Landing Site on Mars // Nature. Geoscience. 2020. V. 13. No. 3. P. 199–204. doi: 10.1038/s41561-020-0537-x.
[4] NASA Planetary Data System. Geoscience Node. https://pds.nasa.gov.
[5] Martin-Torres J. et al. The HABIT (HabitAbility: Brine Irradiation and Temperature) Environmental Instrument for the ExoMars 2022 Surface Platform // Planetary and Space Science. 2020. P. 104968. doi: 10.1016/j.pss.2020.104968.
[6] https://exploration.esa.int/web/mars/-/56933-exomars-2020-surface-platform
[7] Vago J. L., Westall F., Pasteur Instrument Teams, Landing Site Selection Working Group, and Other Contributors. Habitability on early Mars and the search for biosignatures with the ExoMars Rover // Astrobiology. 2017. V. 17. P. 471–510.

MARS EXPRESS SCIENCE HIGHLIGHTS AND FUTURE PLANS

D. V. TITOV[1], J.-P. BIBRING[2], A. CARDESIN[3], T. DUXBURY[4], F. FORGET[5], M. GIURANNA[6], F. GONZÁLEZ-GALINDO[7], M. HOLMSTRÖM[8], R. JAUMANN[9], A. MÄÄTTÄNEN[10], P. MARTIN[3], F. MONTMESSIN[10], R. OROSEI[11], M. PÄTZOLD[12], J. PLAUT[13], AND MEX SGS TEAM[3]

[1] *ESA-ESTEC, 2200 AG Noordwijk, The Netherlands* (*dmitri.titov@esa.int*)
[2] *IAS-CNRS, Orsay, France*
[3] *ESA-ESAC, Madrid, Spain*
[4] *George Mason University, Fairfax, VA, USA*
[5] *LMD, Paris, France*
[6] *IAPS-INAF, Rome, Italy*
[7] *IAA, Granada, Spain*
[8] *IRF, Kiruna, Sweden*
[9] *IPF-DLR, Berlin, Germany*
[10] *LATMOS/IPSL, CNRS, Guyancourt, France*
[11] *IRA-INAF, Bologna, Italy*
[12] *RIU-Uni Cologne, Cologne, Germany*
[13] *JPL, Pasadena, CA, USA*

KEYWORDS:
Mars, geology, climate, aeronomy, escape, history

After 16 years in orbit Mars Express remains one of ESA's most scientifically productive Solar System missions which publication record now approaches 1300 papers. Characterization of the geological processes on a local-to-regional scale by HRSC, OMEGA and partner experiments on NASA spacecraft has allowed constraining land-forming processes in space and time. Recent studies suggest geological evidence of a planet-wide groundwater system on Mars and surface clay formation during short-term warmer and wetter conditions on a largely cold ancient Mars. HRSC team released the Digital Elevation Model (DEM) of the MC-11 quadrangle and the Southern polar cap at 50 m/px resolution. Mars Express provided essential contribution to the selection of the Mars-2020 landing sites and supporting characterization of potential landing sites for Chinese Tianwen-1 mission.

One-and-one-half decade of monitoring of atmospheric parameters such as temperature, dust loading, water vapor and ozone abundance, water ice and CO2 clouds distribution, collected by SPICAM, PFS, OMEGA, HRSC and VMC together with subsequent modeling have provided key contributions to our understanding of the Martian climate. In 2019 PFS confirmed observations of a methane abundance "spike" in the Gale crater observed *in-situ* by the Curiosity Rover. Recent similar quasi-simultaneous observations were in disagreement, thus indicating that the methane "enigma" continues. This poses a significant challenge to both observers and modelers. The radio-science experiment MaRS revealed fine structure of the boundary layer which depth varies from 2 km in topographic lows to ~10 km over highlands.

Observations of the ion escape during a complete solar cycle revealed that ion escape can be responsible for removal of about 10 mbar of the atmosphere over Mars' history. This implies existence of other, more effective, escape channels. The structure of the ionosphere derived from MARSIS and MaRS sounding was found to be significantly affected by the solar activity, dust loading in the lower atmosphere, and crustal magnetic field. The observations suggest that the sunlit ionosphere over the regions with strong crustal fields is denser and extends to higher altitudes as compared to the regions with no crustal anomalies. Ionospheric models aim at creating user-friendly data base of plasma parameters that would be of great service to the planetary community. Focused exploration of the Martian moons continues.

The mission is notionally extended till the end of 2022. A science case for the mission extension till the end of 2025 has been submitted. The talk will give the Mars Express status, review the recent science highlights, and outline future plans including synergistic science with TGO.

SOLAR WIND AT MARS AND MAGNETIC FIELD INTERACTIONS

S. Jimenez[1], M. Ramírez-Nicolás[2], D. Usero[2], P. J. Pascual[3], M. P. Velasco[1], L. Vázquez[2]

[1] *Universidad Politécnica de Madrid*, *Spain*

[2] *Universidad Complutense de Madrid*, *Spain*

[3] *Universidad Autónoma de Madrid* *Spain*

(*s.jimenez@upm.es*)

KEYWORDS:
Mars, magnetic field, Ionosphere, crustal magnetic field, solar wind, MARSIS

INTRODUCTION:

Using data from the Mars Advanced Radar for Subsurface and Ionospheric Sounding (MARSIS) onboard Mars Express [1], we retrieve the magnetic field in Mars ionosphere [2]. We consider the effect due to the crustal fields and to the Solar wind. This is relevant in the context of the observed aurorae in Mars under Solar storms, either localized above crustal fields [3] or diffuse above both the nocturnal and the diurnal zones of the planet [4]. We aim at retrieving the three dimensional map of the magnetic filed and to discriminate the effects due to the planet and those due to the Solar wind. In this way, we reconstruct the magnetic field due to the Solar Wind for a specific region of space and time, based on a multipole expansion.

REFERENCES:

[1] Orosei R. , Jordan R. L. , Morgan D. D. , Cartacci M., Cicchetti A., Duru F., Gurnett D. A., Heggy E., Kirchner D. L., Noschese R., Kofman W., Masdea A., Plaut J. J., Seu R., Watters T. R., Picardi G.. Mars Advanced Radar for Subsurface and Ionospheric Sounding (MARSIS) after nine years of operation: a summary // Planetary and Space Science. 2015. V. 112. P. 9–114.

[2] Ramírez-Nicolás M., Sánchez-Cano B., Witasse O., P.-Blelly L., Vázquez L. The effect of the induced magnetic field on the electron density vertical profile of the Mars' ionosphere: A Mars Express MARSIS radar data analysis and interpretation, a case study // Planetary and Space Science. 2016. V.1 26. P. 49–62.

[3] Bertaux J-.L., Leblanc F., Witasse O., Quemerais E., Lilensten J., Stern S. A., Sandel B., Korablev O. Discovery of an aurora on Mars // Nature. 2005. V. 435. P. 790–794.

[4] Deighan J., Jain S. K., Chaffin S., Fang X., Halekas J. S., Clarke J. T., Schneider N. M., Stewart A. I. F., J.-Chaufray Y., Evans J. S., Stevens M. H., Mayyasi M., Stiepen A., Crismani M., McClintock W. E., Holsclaw G. M., Lo D. Y., Montmessin F., Lefèvre and B F.. Jakosky M.. Discovery of a proton aurora at Mars // Nature. Astronomy. 2018 V. 2. P. 802–807.

FROM SPACE AND RADIATION TO NEW MATERIALS

L. Vázquez
Departamento de Análisis Matemático y Matemática Aplicada,
Facultad de Informática,
IMI y Universidad Complutense de Madrid,
28040 Madrid, *Spain*
(*lvazquez@fdi.ucm.es*)

KEYWORDS:
Mars, electromagnetic radiation, dielectrics, new materials

INTRODUCTION:
The analysis of the different codes related to simulate the radiation on different scenarios on Mars surface, show they have basic common features. On the other hand, they differ on different aspects as the energy range, characteristics of the particles integrating the radiation and the local environments where we can have dust. This issue is closely related to the use of suitable materials for the associated payloads. In this framework, we have to remark that the last 10–15 years had witnessed a rapid growth of interest in the phenomena of resonant electromagnetic inductance in all-dielectric structures irradiated by electromagnetic waves. The use of dielectric materials with a high value of permittivity makes it possible to create subwavelength elements whose dimensions are significantly smaller than the wavelength of the incident radiation in the microwave range, and move to higher frequencies, including THz and IR bands, and even up to visible frequencies. Structures based on such dielectric elements make it possible to control not only the electric, but also the magnetic component of the electromagnetic field. In this context, we can have an invisibility effect which is useful for creating highly transparent or cloaking effect materials in the optical, terahertz, and microwave ranges.

REFERENCES:
[1] *Overview of Main Radiation Transport Codes.* Nikolaos Schetakis, Rodrigo Crespo, José Luis Vázquez-Poletti, Mariano Sastre, Luis Vázquez, Alessio Di Iorio. Geoscientific Instrumentation Methods and Data Systems https://doi.org/10.5194/gi-2020-7. In press.
[2] *The Wave Equation: From Eikonal to Anti-Eikonal Approximation*. Luis Vázquez, Salvador Jiménez, Alexander B. Shvartsburg. Modern Electronic Materials 2 (2016) 51–53.
[3] *About Some Possible Implementations of the Fractional Calculus*. María Pilar Velasco, David Usero, Salvador Jiménez, Luis Vázquez, José Luis Vázquez-Poletti and Mina Mortazavi. Mathematics 2020, 8, 893; doi:10.3390/math8060893.
[4] *Resonant Phenomena in All-Dielectric Rectangular Circuit Induced by a Plane Microwave*. A. B. Shvartsburg, V. Ya. Pecherkin, S. Jiménez, L. M. Vasilyak, L. Vázquez and S. P. Vetchinin. Submitted to Journal of Physics D: Applied Physics.

DRONE MAGNETOMETRY: A NEW APPROACH TO STUDY PRESENT AND PAST CONDITIONS IN THE PLANETARY BODIES

M. DÍAZ MICHELENA[1], S. FERNANDEZ ROMERO[1], M. A. RIVERO RODRÍGUEZ[2], P. MORATA BARRADO[3], E. DE DIEGO CUSTODIO[1]

[1] *Space Magnetism Area, Payloads and Space Sciences Dept. INTA, Ctra. Torrejón — Ajalvir km 4, 28850 Torrejón de Ardoz, Spain* (*diazma@inta.es*)

[2] *ISDEFE as external consultant for INTA, Ctra. Torrejón — Ajalvir km 4, 28850 Torrejón de Ardoz, Spain*

[3] *Structures and Mechanisms Area, Materials and Structures Dept. INTA, Ctra. Torrejón — Ajalvir km 4, 28850 Torrejón de Ardoz, Spain* (*diazma@inta.es*)

KEYWORDS:
magnetic surveys, drones, crustal magnetism

INTRODUCTION:

The magnetic minerals record the environmental magnetic field during their formation. For example, the different flows erupted by a volcano present a magnetic signature [1], which depends on factors like the cooling process and the atmosphere. The magnetic signature of rocks can be erased during an impact of a meteorite and the minerals will be re-magnetized if there is an environmental magnetic field during the solidification of melted areas [2]. Therefore, large-scale magnetic measurements can provide important information about the present and past conditions of the surfaces, their atmospheres and shaping processes.

The satellites bound to planetary bodies often carry magnetometers. These instruments can be useful to determine their magnetic moment and the magnetic characteristics of their large-scale magnetic environment i. e. if they present a magnetosphere or an ionosphere and in which shape they drape the bodies. However, the satellites often orbit or fly by their targets at high distances compared to the dimensions of most geological features.

The measuring distance to be able to discern the contrast in magnetic intensity provided by geological features needs to be comparable with its dimensions and the lower the distance the higher the spatial resolution achieved.

This would lead to the development of on ground magnetic measurements to travel along the history of the planets through the magnetized rocks. However, this would cover small areas due to the rover autonomies and would have an important impact on the rover design, which is in general discarded.

An approach via magnetometers on board drones is much more appealing always that the bodies have atmospheres, which allow lift enough to fly.

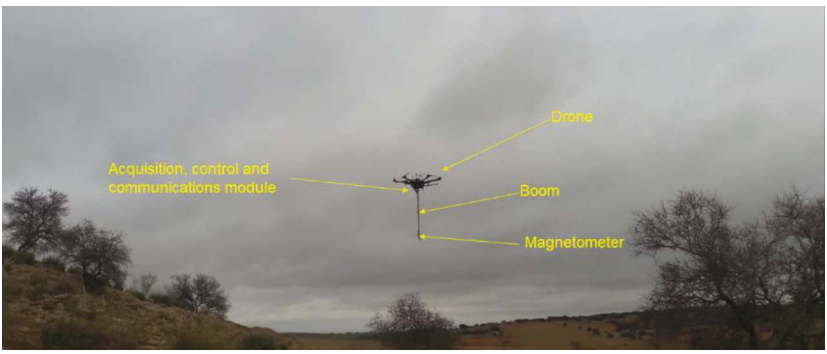

Fig. 1. Implementation of the system: vector magnetometer with a foldable boom, acquisition, control and communications module, in a hexacopter during the field campaign in Cerro Gordo volcano at Campos de Calatrava volcanic field in Spain

There are attempts to survey planets with aerial platforms like the Dragonfly of NASA to Titan.

In this work we introduce a low weight system to perform magnetic surveys on board different aerial platforms with good performance to register the magnetic field vector sourced by crustal features. We describe its implementation in an hexacopter and the whole system validation through a field campaign in Cerro Gordo volcano at Campos de Calatrava volcanic field in Spain.

The validated system has been selected to perform a magnetic survey in Deception Island caldera of the South Shetland Islands close to the Antarctic Peninsula, which represents a harsher environment. A similar system implemented in different aerial platforms could be used to characterize the surfaces of the Moon highly cratered or Mars with the strong magnetic signature associated to its crust.

REFERENCES:

[1] Lillis R. J., Frey H. V., Manga M., Mitchell D. L., Lin R. P., Acuña M. H., Bougher S. W. An improved crustal magnetic field map of Mars from electron reflectometry: Highland volcano magmatic history and the end of the Martian dynamo // Icarus. 2008. V. 194. P. 575–596.

[2] Langlais B., Thébault E., Quesnel Y. Magnetic signature of demagnetized impact craters: tools to time the shutdown of the dynamo on Mars? // Proc. Lunar and Planetary Science XXXVIII. 2007. Art. 1573. 2 p.

COMBINATION OF METHANE SPONTANEOUS EMISSION AND ION-MOLECULAR REACTIONS AS A POSSIBLE WAY TO EXPLAIN THE VARIATIONS OF METHANE CONCENTRATION IN MARTIAN ATMOSPHERE

A. K. Pavlov[1], D. A. Tsurkov[1,2], A. A. Pavlov[3]
[1] *Ioffe Physical-Technical Institute, Russian Academy of Sciences, 26 Politekhnicheskaya str., St. Petersburg, 194021, Russia* (*anatoli.pavlov@mail.ioffe.ru*)
[2] *Peter the Great St. Petersburg State Polytechnic University, 29 Politekhnicheskaya str., St. Petersburg, 195251, Russia*
[3] *Planetary Environments Laboratory, NASA Goddard Space Flight Center, Greenbelt, MD 20771, USA*

KEYWORDS:
Mars, atmosphere, methane destruction, cosmic rays, ionization

Variations of methane abundance in the Martian atmosphere is one of the most intriguing problems in Mars exploration. The SAM instrument on the Curiosity rover detected both seasonal (0.2–0.6 ppb) and abrupt sporadic variations of methane (up to 20 ppb) over several years of observations near the surface in the Gale crater. On the other side, measurements of ExoMars mission discovered an extremely low methane concentration (<50 ppt) in the atmosphere above 4–8 km from the ground. However, a short spike of methane on 15 June 2013 detected by MSL has been also observed independently by Mars Express near the Gale crater. The photochemical lifetime of methane is 300–500 years while the global atmospheric mixing time is about one Martian year. Therefore, we consider cosmic rays ionization of the Martian atmosphere and subsequent atmospheric ion-molecular reactions as a possible process of rapid methane destruction (ion methane destruction — IMD). We show that the atmospheric lifetime of methane can be as short as one Martian year for methane concentrations of ~1 ppb. We further demonstrate that IMD is capable of decreasing the global average methane abundance from ~10 ppb levels down to ~1 ppb over the last 10–15 years. Also, we discuss a destruction of “gas traps” in Martian subsurface regolith as a possible source of seasonal methane releases. The combination of such short spikes of methane emission and IMD process might help to reconcile methane observations by MSL and TGO (ExoMars mission).

ATMOSPHERIC ESCAPE OF ATOMIC OXYGEN DURING THE AURORAL EVENTS AT MARS

V. I. Shematovich, E. S. Kalinicheva
Institute of Astronomy of the Russian Academy of Sciences, Moscow, Russia (*shematov@inasan.ru*)

KEYWORDS:
Mars, solar wind, high-energy proton and hydrogen atom precipitation, auroral phenomena, atmospheric escape, kinetic Monte Carlo model

INTRODUCTION:
It is known that sputtering of atmospheric gas during proton auroral events is accompanied by the formation of the suprathermal hydrogen and oxygen atom flux escaping from the atmosphere [1]. The formation rate of suprathermal oxygen atoms can be estimated with the Monte Carlo kinetic model [2], which describes the precipitation of high-energy particles from the solar wind plasma and/or planetary magnetosphere into the planet's atmosphere. Under conditions of extreme solar events such as solar flares and coronal mass ejections, this phenomenon should be carefully studied since the magnitude of the escaping hot O flux induced by precipitation may become prevailing over photochemical sources, as follows from the estimates obtained from recent observations of the Mars Atmosphere and Volatile Evolution (MAVEN) spacecraft (SC) [3].

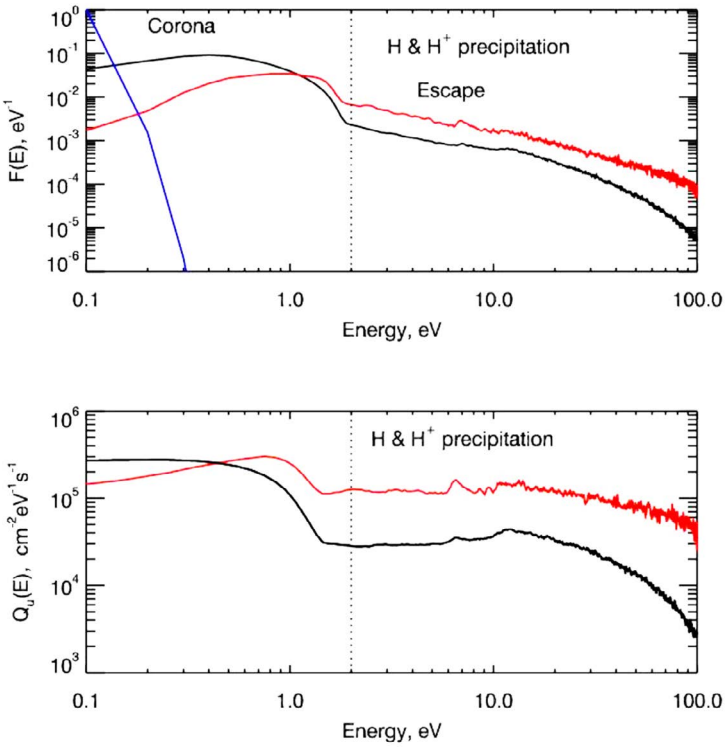

Fig. 1. (upper panel) The normalized distribution functions *F*(*E*) by the kinetic energy of upward moving thermal (blue line) and suprathermal oxygen atoms at an altitude of 500 km of the Mars exosphere are shown. The vertical dashed line shows the escape energy (~2 eV) of oxygen atoms from the Martian atmosphere. (bottom panel) The energy spectra of an upward flux of oxygen atoms at an altitude of 500 km are shown, which are responsible for both thecpopulation of the hot corona (region to the left of the dashed line) and formation of the escape flux from the Martian atmosphere due to the precipitation of high-energy hydrogen atoms (red lines) and protons (black lines) from the solar wind plasma

We present the model calculation results of the atomic oxygen loss rate from the Martian atmosphere induced by precipitation of high-energy protons and hydrogen atoms (H/H+) from the solar wind plasma. Penetration of energetic protons and hydrogen atoms from the solar wind plasma to the upper atmosphere of Mars at altitudes of 100–250 km is accompanied by the momentum and energy transfer in collisions with the main component in the transition (between thermosphere and exosphere) region, atomic oxygen. This process is considered as atmospheric sputtering during proton auroral events, which is accompanied by formation of the suprathermal hydrogen and oxygen atom fluxes escaping from the atmosphere.

Processes of kinetics and transport of hot oxygen atoms in the transition region of Mars' upper atmosphere were investigated. The kinetic energy distribution functions for suprathermal oxygen atoms were calculated (see Figure 1). It has been shown that, during proton auroral events on Mars, the exosphere is populated with a significant amount of suprathermal oxygen atoms, kinetic energy of which reach the escape energy, 2 eV. In addition to photochemical sources, a hot fraction is formed in the oxygen corona; and a non-thermal flux of atomic oxygen escaping from the Martian atmosphere is produced during proton aurora events [4]. Proton aurorae are sporadic auroral events. Consequently, according to the estimates obtained from the recent MAVEN observations the magnitude of the precipitation-induced escaping flux of hot oxygen atoms may become prevailing over the photochemical sources under conditions of the extreme solar events such as solar flares and coronal mass ejections [3].

ACKNOWLEDGEMENTS:
This study was supported by the Russian Foundation for Basic Research, project No. 18-02-00721a.

REFERENCES:

[1] Shematovich V. I., Marov M. Ya. Escape of planetary atmospheres: physical processes and numerical models // Physics–Uspekhi. 2018. V. 61. P. 217.
[2] Bisikalo D. V., Shematovich V. I., Gérard J.-C., Hubert B. Monte Carlo simulations of the interaction of fast proton and hydrogen atoms with the Martian atmosphere and comparison with *in-situ* measurements // J. Geophysical Research. 2018. V. 123. P. 58.
[3] Jakosky B. M., Brain D., Chaffin M., and 129 more. Loss of the Martian atmosphere to space: Present-day loss rates determined from MAVEN observations and integrated loss through time // Icarus. 2018. V. 315. P. 146.
[4] Shematovich V. I., Kalinicheva E. S. Atmospheric escape of oxygen atoms during the proton aurorae at Mars // Astron. Reports. 2020. V. 64. P. 628.

MARTIAN DUST ACTIVATION DUE TO AIR SHOCK WAVES FROM SMALL IMPACTS

B. A. Ivanov
Institute for Dynamics of Geospheres, *Russian Academy of Science*, *Leninsky Prospect 38-1*, *Moscow*, *Russia*, *119334*(*baivanov@idg.chph.ras.ru*)

KEYWORDS:
Mars, impact craters, atmospheric shock waves, dust, HiRise.

INTRODUCTION:
HiRise images and CTX repeating images confirmed Malin's et al. observation [1] that just-formed small impact craters on Mars in dusty terrains activate near-surface fine dust, creating prominent albedo features around craters [2, 3]. In some cases, these albedo features could be explained with air-shock waves generated by impact [3, 4]. Here we test an idea how the geometry of impact-related albedo features may be converted to the efficiency of air-shock generation for small meteoroid impacts in Martian conditions.

AIR SHOCK WAVES (ASW):
The meteoroid passage through the atmosphere generates so-called "ballistic shock wave" (BSW), well known, for example, from the recent Chelyabinsk meteorite fall [5]. The impact into a solid surface generates also a quazi-hemispherical air shock wave. This shock wave may be treated approximately in terms of the well-known spherical shock wave (SSW) [6, 7, 8]. Our working hypothesis is that ASW, interacting with the surface, could make characteristic traces in zone of wave collisions – SSW from neighbor simultaneous impacts could produce "parabolas", while BSW/SSW collision at the surface could produce "scimitars" [8]. The well-known properties of explosion ASWs allow us estimate main energetic parameters of ASW, generated by impacts on Mars.

In the presented work we discuss length and width of selected parabolic albedo strips and compare measured width with a theoretical model.

SPHERICAL AIR WAVE:
Properties of explosion SAW are well known from experiments and numerical modeling [9, 10]. The energy scaling of pressure, positive and negative phases duration could be expressed through the single parameter – the characteristic length:

$$\Lambda_s = (E_s/p_a)^{1/3} \quad (1)$$

where E_s is the effective source energy and p_a is the ambient atmospheric pressure. In SI units $[E_s]$ = J, $[p_a]$ = Pa, and Λ_s is measured in meters.

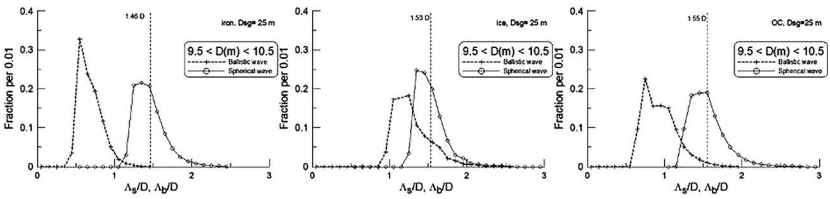

Fig. 1. Frequency distribution of characteristic length values for BSW and ASW for Martian craters for all possible entry angles and velocities for a crater of 10 m indiameter assuming the target with 20 % porosity and strength/gravity transition same as terrestrial alluvium

The reasonable first order guess is to assume that the effective source energy for the SAW is proportional to the kinetic energy of a crater-forming projectile *KE*. Previously published estimates [8] give the lower limit of the E_s/KE ratio (which may be defined as the "impact SAW efficiency") as ~ 10^{-3} (0.1 %). Experiments show a possibility of much larger efficiencies of 1 % to 10 % [6, 7]. To estimate Es and Ls we need to relate values of *KE* and the observed crater diameter. Hopefully the reliable numerical modeling has

been published recently [11] for a wide range of soil cohesion, friction, and porosity.

We assume the entry velocity distribution for small projectiles similar to observed Mars-crossers [12] and use Monte-Carlo method to model frequency distribution of all possible combinations of the entry velocity, and entry angle. The model produce frequency of KE values for selected crater diameters D (Figure 1). We find that for iron, ice, and ordinary chondrite projectiles the value of the characteristic length (Eq. 1) only slightly vary near the ratio $\Lambda_s/D \sim 1.5$ for the assumed $E_s/KE \sim 0.1$ %.

MEASURED PARABOLA WIDTH:

We study about 1000 HiRise images of "new" craters and find ~20 parabolas near pairs of craters formed by fragments of a single "parent" projectile. The working hypothesis is that two weak ASWs make a strip of enhanced negative pressures where "rings" of negative pressures are overlapped. If so, the minimum width W of a "parabola" should be of the order of Λ_s. (as for terrestrial explosion airblast [10]) and growing up with the distance (Figs. 2 and 3).

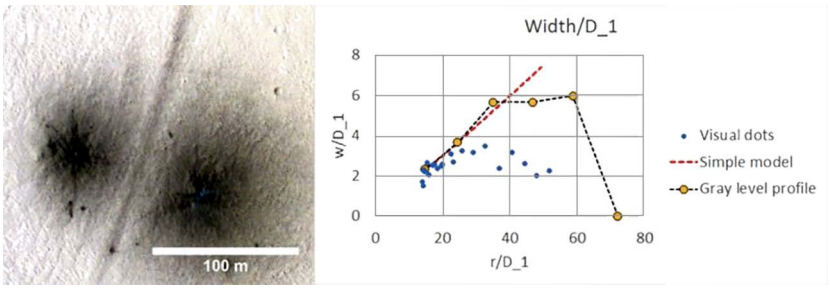

Fig. 2. The "parabola" (here — near vertical dark strip) in ESP_011618_1885 HiRise image. Two craters of ~3 m in dimeter produces ASW with the minimal width of ~6 m indicating that $\Lambda_s/D \sim 2$.

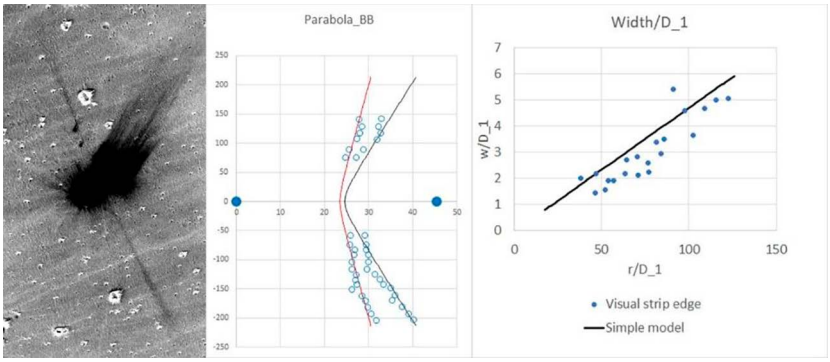

Fig. 3. The "parabola" in PSP_007496_1735 HiRise image. Left — highly stretched image where dark haloes cover two main craters of ~1.7 m in diameter. Middle — exaggerated horizontally parabola boundaries (dots) in comparison with the wave crossing model. Right — measured W vs. distance from the larger crater in comparison with the model. The observed width corresponds to $\Lambda_s/D \sim 0.65$

CONCLUSIONS:

The first physical comparison between models and observations demonstrates that the measured width of albedo strips near new impact craters on Mars may be explained with the assumptions of two (hemi-) spherical air shock wave interaction. The model of crossing negative pressure zones give a reasonable explanation to the observed parabola geometry. The strip width W increase with a distance allow us estimate the ASW characteristic length Λ_s (Eq. 1) in a range of 0.2 to 2 crater diameter D, close to expected values for the ASW generating efficiency of 0.1 %.

The further advance of the proposed model promises the quantitative estimate of air shock positive and negative pressures and impulses. Knowledge

of these absolute values open the way to understand the location of “darker” (finer?) dust, lifted to the surface during the crater formation, and observed now as “dark haloes”, “parabolas” and “scimitars”.

ACKNOWLEDGEMENTS:
The work is supported within the Russian Academy of Science project “Origin and evolution of Space studied with telescopic observations and space missions” (the former Program 28 and Program 12).

REFERENCES:

[1] Malin M.C., Edgett K.S., Posiolova L.V., McColley S.M., and Dobrea E. Z. N. Present-day impact cratering rate and contemporary gully activity on Mars // Science. 2006. V. 314 (5805). P. 1573–1577.
[2] McEwen A. S., Grant J. A., Tornabene L. L., Byrne S., Herkenhoff K. E., Bridges N. T., and HiRISE Team. HiRISE Observations of Small Impact Craters on Mars. // 36st Lunar and Planetary Science Conference. 2007. abs. #2009.
[3] Bart G. D., Daubar I., Ivanov B. A., Dundas C. M., McEwen A. S. Dark halos produced by current impact cratering on Mars // Icarus. 2019. P. 45–57.
[4] Ivanov B. A., Melosh H. J., McEwen A. S. New Small Craters in High Resolution HiRISE Images – IV // 45th Lunar and Planetary Science Conference. 2014. abs. #1812.
[5] Popova O. P., Jenniskens P. Emel’yanenko V. and 52 others. Chelyabinsk Airburst, Damage Assessment, Meteorite Recovery, and Characterization // Science. 2013. V. 342(6162). P. 1069–1073.
[6] Schultz P. H. Effect of impact angle on vaporization // J. Geophysical Research. 1996. V. 101. P. 21 117–21 136.
[7] Gee D. J., Reinecke W. G., Levinson S. J. Blast phenomena associated with high-speed impact // Intern. J. Impact Engineering. 2007. V. 34. P. 178–188.
[8] Ivanov B. A. Air shock wave traces on Mars // Abstr. 10th Moscow Solar System Symp. 10M-S3. Space Research Institute, Moscow, Oct. 7–11, 2019. V. 1. P. 17–19. Abs. #10MS3-MS-12.
[9] Brode H.L. Blast wave from a spherical charge // Phys. Fluids. 1959. V. 2. P. 217–229.
[10] Krauthammer T., and Altenberg A. Negative phase blast effects on glass panels // Intern. J. Impact Engineering. 2000. V. 24(1). P. 1–17.
[11] Prieur N.C., Rolf T., Luther R., Wünnemann K., Xiao Z., and Werner S.C. The effect of target properties on transient crater scaling for simple craters // J. Geophysical Research: Planets. 2017. V. 122(8). P. 2017JE005283. doi:10.1002/2017JE005283.
[12] JeongAhn Y., and Malhotra R. The current impact flux on Mars and its seasonal variation // Icarus. 2015. V. 262. P. 140–153.

DIURNAL AND SEASONAL EVOLUTION OF MARTIAN ATMOSPHERIC THERMAL STRUCTURE FROM ACS-TIRVIM EXPERIMENT ONBOARD TGO EXOMARS

P. Vlasov[1], N. Ignatiev[1], S. Guerlet[2], D. Grassi[3], A. Grigoriev[1,4], A. Shakun[1], D. Patsaev[1], I., Maslov[1], M. Luginin[1], E. Millour[2], F. Forget[2], G. Arnold[5], A. Trokhimovskiy[1], O. Korablev[1], F. Montmessin[6]

[1] *Space Research Institute* (*IKI*), *Moscow*, *Russia* (*pavel.vlasov@phystech.edu*)
[2] *Laboratoire de Météorologie Dynamique* (*LMD*), *Paris*, *France*
[3] *Istituto di Astrofisica e Planetologia Spaziali — Istituto Nazionale di Astrofisica*, *Rome*, *Italy*
[4] *Australian National University*, *Canberra*, *Australia*
[5] *DLR*, *Berlin*, *Germany*
[6] *LATMOS*, *Guyancourt*, *France*

KEYWORDS:
Martian atmosphere, ExoMars, ACS-TIRVIM, nadir observations, dust storm, thermal structure, dust and water ice opacities, diurnal cycle

The ExoMars Trace Gas Orbiter (TGO) is a mission by ESA and Roscosmos, which started its operational scientific phase in March 2018. The Atmospheric Chemistry Suite (ACS) is a set of three spectrometers (NIR, MIR, and TIRVIM) designed to observe the Martian atmosphere in solar occultation, nadir and limb geometry [1]. The thermal infrared channel — TIRVIM is a Fourier-transform spectrometer capable of operating in nadir and occultation modes in the spectral range of 1.7–17 μm. In nadir mode it covers the range of 5–17 μm with the spectral resolution 1 cm^{-1}. The TGO orbit and ACS observation strategy provides unique opportunity to study diurnal variations of temperature field by thermal sounding in nadir mode with dense coverage of local times compared to previous similar experiments (TES/MGS, PFS/Mars Express, MCS/MRO).

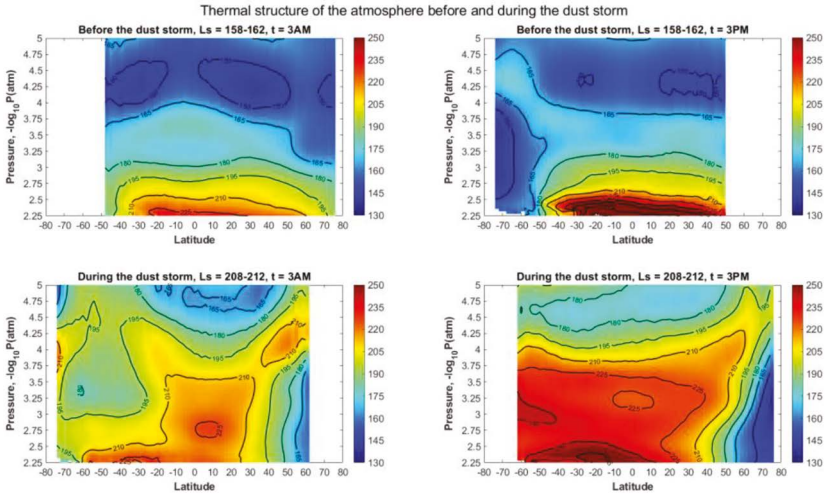

Fig. 1. Thermal structure of the Martian atmosphere before (L_S ~160° of MY 34, April 2018) and during (L_S ~210°, July 2018) the dust storm at 3AM and 3PM

We present an overview of observations and main results obtained in nadir mode of measurements of TIRVIM instrument in a period from 13 March 2018 (L_S = 144° of MY 34) to 15 July 2018 (L_S = 212°) with the latest calibrations of TIRVIM data. This period includes the beginning and the peak of the dust storm which is the event of particular interest. The self-consistent retrievals of vertical temperature profiles in unison with aerosol (dust and water ice) opacities and surface temperature were performed by solving the inverse problem of radiative transfer and realized by the method of optimum estimation or statistical regularization [2, 3]. The results of this overview include thermal structure of Martian atmosphere from the surface up to 60–70 km, dust and water ice column opacity (taken at 1075 cm^{-1} and 825 cm^{-1} respectively) distributions maps. It also includes investigation of diurnal cycle and diurnal variations of temperature field of the atmosphere before and during the dust storm with dense coverage of local times.

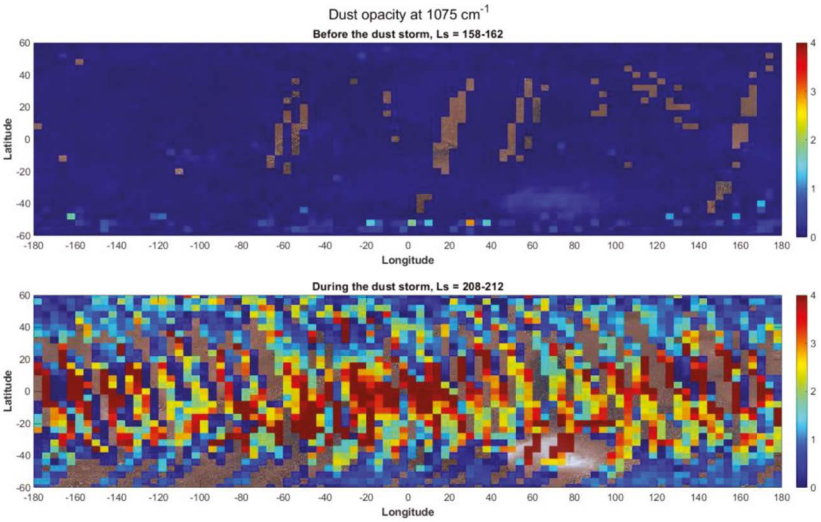

Fig. 2. Dust opacity at 1075 cm^{-1} before (L_S ~160° of MY 34, April 2018) and during (L_S ~210°, July 2018) the dust storm

ACKNOWLEDGEMENTS:
ACS TIRVIM data analysis is supported by the RSF grant No. 20-42-09035.

REFERENCES:

[1] Korablev O., Montmessin F. et al. The Atmospheric Chemistry Suite (ACS) of three spectrometers for the ExoMars 2016 Trace Gas Orbiter // Space Sciences Rev. 2018. V. 214. Art. 7. 62 p. doi:10.1007/s11214-017-0437-6.
[2] Rodgers C. D. Inverse Methods for Atmospheric Sounding: Theory and Practice. World Scientific Publishing, 2000. 239 p.
[3] Conrath B. J. et al. Mars Global Surveyor Thermal Emission Spectrometer (TES) observations: Atmospheric temperatures during aerobraking and science phasing // J. Geophysical Research. 2000. V. 105. No. E4. P. 9509–9519.

UPPER MESOSPHERIC WATER ON MARS AS MEASURED BY ACS TGO SOLAR OCCULTATIONS

D.A. Belyaev[1], A.A. Fedorova[1], J. Alday[3], F. Lefevre[2], O.I. Korablev[1], F. Montmessin[2], A.Yu. Trokhimovskiy[1], A. Patrakeev[1], and ACS team

[1] *Space Research Institute (IKI), Moscow, Russia, (bdenya.iki@gmail.com);*

[2] *LATMOS/CNRS, Paris, France;*

[3] *AOPP, Department of Physics, University of Oxford, UK*

KEYWORDS:
water vapor, martian atmosphere, mesosphere, thermosphere, IR spectroscopy, water escape

INTRODUCTION:

In this paper, we present results from sensitive solar occultation measurements in the 2.65 – 2.7 μm spectral range with detection of episodic water enrichment in the upper mesosphere of Mars, up to 120 km of altitude. The dataset is based on the middle infrared channel of Atmospheric Chemistry Suite (ACS – MIR) operating onboard ExoMars Trace Gas Orbiter (TGO) since April 2018, which corresponds to Ls 163 of the 34th Martian Year (MY34). In the mentioned spectral range the instrument allows tropospheric, mesospheric and thermospheric retrievals of temperature and CO_2 density in parallel with the mesospheric water abundance. We report the most humid mesosphere occurred in the dusty and perihelion seasons of the MY34, where the H_2O enrichment was established about 20-40 ppbv at altitudes of 110 – 120 km. This phenomenon increases a capability of water escape from Mars through the direct photo dissociation of the molecule in the upper mesosphere.

The retrievals of density/temperature profiles in IKI are funded by the RSF grant #20-42-09035.

FIRST DETECTION OF HCL IN THE ATMOSPHERE OF MARS BY ACS TGO

A. Trokhimovskiy[1], K. S. Olsen[2], O. Korablev[1], F. Lefèvre[3], F. Montmessin[3], A. Fedorova[1]

[1] *Space Research Institute (IKI), Moscow, Russia, (a.trokh@gmail.com);*

[2] *Department of Physics, University of Oxford, Oxford, UK;*

[3] *Laboratoire Atmosphères, Milieux, Observations Spatiales (LATMOS/CNRS), Paris, France*

Keywords:

Mars, atmosphere, hydrogen chloride, ACS.

INTRODUCTION:

A major quest in Mars' exploration has been the hunt for atmospheric gases potentially unveiling ongoing activity of geophysical or biological origin [1]. Here we report the first detection of a halogen gas, HCl, which could in theory originate from contemporary volcanic degassing or chlorine released from gas-solid reactions. Our detections made with the ACS instrument within ~3.2−3.8 μm [2], onboard the ExoMars Trace Gas Orbiter, reveal widely distributed HCl in the 1−4 ppbv range, 20 times greater than previously reported upper limits. HCl increased during the 2018 global dust storm and declined soon after its end, pointing to the exchange between the dust and the atmosphere. Considering chlorine's role in terrestrial atmospheres, Martian HCl introduces a new paradigm and may contribute to understanding the origin of oxychlorines on Mars' surface.

The peak HCl concentrations on Mars ~1–4 ppbv are comparable to those in Earth's upper stratosphere and mesosphere. On Mars, the destructive ozone cycle, including odd-oxygen, well-known in the Earth's stratosphere, would be ~20 times more efficient than assumed with previous upper limits on HCl. On the other hand, the transient nature of the HCl enhancement detected by ACS suggests the existence of a strong and unexpected loss process of that species, likely heterogeneous and efficient in the lower atmosphere or at the surface of Mars. Such a pathway may be photochemical, related to the advection pattern of other gases, such as H_2O, or to the absorption by dust itself. Combined with the hypothesized HCl production from the airborne dust, our discovery suggests that the Martian photochemistry should be revised.

REFERENCES:

[1] Vago J., Witasse O., Svedhem H., et al. ESA ExoMars program: The next step in exploring Mars. Sol. Syst. Res., 2005, 49, P. 518–528.

[2] Korablev O., Montmessin F., Trokhimovskiy A., et. al., The Atmospheric Chemistry Suite (ACS) of Three Spectrometers for the ExoMars 2016 Trace Gas Orbiter. Space. Sci. Rev., 2018, 214, 7.

PHOTOCHEMISTRY OF HCL IN THE MARTIAN ATMOSPHERE

V. A. Krasnopolsky
Moscow Institute of Physics and Technology (*PhysTech*)
(*vlad.krasn@verizon.net*)

KEYWORDS:
Mars, chemical composition, photochemistry, heterogeneous chemistry, chlorine species

The recent discovery of HCl on Mars using ACS and NOMAD spectrographs at the ExoMars Trace Gas Orbiter and the observed correlation with seasonal dust activity indicate dust as a source of HCl on Mars. Chlorine was observed in Martian rocks and dust using gamma-ray, infrared, and alpha-particle X-ray spectroscopy and sample analyses at the landing probes. Chlorine can exist in the rocks and dust as chlorides and perchlorates, e. g. $Ca(ClO_4)_2$. The Martian chlorides discussed in the literature are NaCl (4.25 eV), $MgCl_2$ (4.87 eV), $CaCl_2$ (5.06 eV), $FeCl_2$, and $FeCl_3$ (1.85 eV). Values in parentheses are dissociation energies. The most promising heterogeneous reactions of atmospheric chlorine formation are

$FeCl_3 + H \rightarrow FeCl_2 + HCl + 2.63$ eV, (R1)

$FeCl_3 + O \rightarrow FeCl_2 + ClO + 0.9$ eV. (R2)

Heterogeneous loss of atmospheric chlorine is expected via

$HCl + H_2O_{ice}$ (uptake), (R3)

$FeCl_2 + Cl \rightarrow FeCl_3$. (R4)

The reversible uptake (R3) close to one is the only measured value for these reactions, and the reaction probability required for our problem is unknown.

To reproduce the HCl observations, two models of local photochemistry are developed for midlatitudes at aphelion ($L_S \approx 70°$, 40° N) and perihelion ($L_S \approx 250°$, 40° S). Input data include temperature profiles, dust, ice, and H_2O vapor column abundances, eddy diffusion, dust vertical profiles and ice particle sizes. Vertical profiles of water vapor and ice aerosol are calculated using these data (Figure 1). The next phase is incorporation of traditional photochemistry into the models. Finally, the HCl photochemistry is involved based on our model for Venus. Rate coefficients of the heterogeneous reactions (R1)–(R4) are adjusted to fit the observations, and the results are discussed.

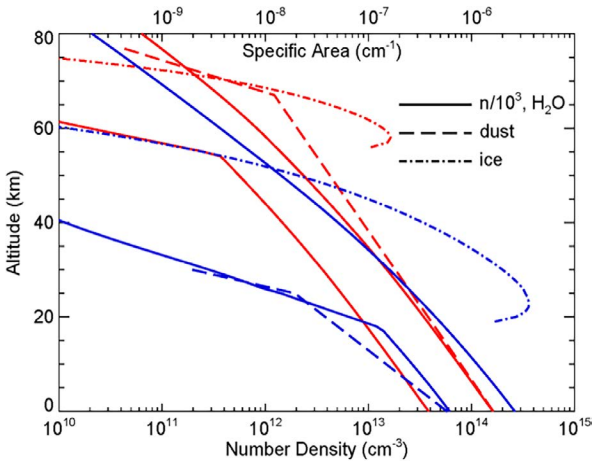

Fig. 1. CO_2 and H_2O densities and dust and ice specific area at aphelion (40° N, blue) and perihelion (40° S, red)

TOPOGRAPHIC CHARACTERISTICS AND CHRONOLOGY OF THE UZBOI-LADON FLUVIAL SYSTEM ON MARS

M. A. Ivanov[1], H. Hiesinger[2]
[1] *Vernadsky Institute*, *RAS* (*mikhail_ivanov@brown.edu*)
[2] *Muenster University*,
Muenster, *Germany*

KEYWORDS:
Mars, Argyre, Uzboi, outflow channels, chronology, topography

INTRODUCTION:
Uzboi and Ladon Valles are usually considered as specific parts of a single system of outflow channels (Uzboi-Ladon-Morava, ULM) that extends northward from the main rim of Argyre basin for ~2000 km and disappears within Margaritifer Chaos [1–4]. It was proposed that the ULM system formed by massive water flows from a giant lake in Argyre [5, 6], although evidence was presented suggesting that the overflow from Argyre is inconsistent with the actual topographic configuration of the region [7]. Because of this controversy, we investigated the upper portion of the ULM system that includes: (1) Bond crater, (2) Uzboi Vallis, (3) Holden crater, and (4) the upper stretches of Ladon Vallis in order to assess their topographic characteristics and to establish the general sequence of events during formation of the system. Our study was based on the topographic data (MOLA topographic map, 1/128 degree resolution) and images provided by the THEMIS spectrometer (100 m/px resolution) and the mosaic of the CTX images (6 M/px resolution).

TOPOGRAPHIC CONFIGURATION OF COMPONENTS OF THE UZBOI-LADON SYSTEM:

1) Bond crater (~120 km diameter): its flat floor is at elevation of ~–1.5 km and the mean elevation of the rim is ~0.68 km (±0.39 km, 1σ); thus, the mean depth of the crater is ~2.2 km and its volume is estimated to be ~(20–25)·10^3 km^3. The northern half of the Bond rim, which is directed toward Uzboi Vallis, is slightly lower than the southern half but show no evidence for either single or multiple breaches that could connect Bond with the upper portions of Uzboi.
2) Uzboi Vallis: The topographic map shows that the uppermost portion of Uzboi Vallis represents a circular topographic depression (~65 km diameter and ~0.9 km deep), which is adjacent to the northern rim of the Bond crater. The southern wall of the depression cuts the northern rim of the crater and represents a cliff-like feature ~0.6 km high. Thus, the Uzboi head depression postdates formation of the Bond crater.

A topographic profile along the thalweg of Uzboi Vallis shows five distinct topographic features. (1) The upper reach of Uzboi Vallis begins at the breach of the head depression and extends for ~36 km northward at relatively steady general slope of ~0.28 degrees. (2) A mound-like feature [8] occupies the middle portion of the Uzboi moat and extends for ~120 km. The highest portion of the mound occurs exactly against the mouth of Nirgal Vallis. (3) The lower reach of Uzboi begins after the mound, extends for ~130 km and is about horizontal (mean slope is ~0.03 degrees northward). The northmost edge of the lower reach closely approaches the rim of Holden crater (~10–15 km) and represents a trough that is~35 km wide and ~1.5–2 km deep. These characteristics of the trough indicate that it postdates the Holden crater, otherwise it was completely or partly filled by the Holden ejecta. (4) A terminal narrow channel incises the floor of the northmost part of the lower reach of Uzboi and represent a narrow, ~2 km wide, channel with steep walls and depth of ~0.1–0.2 km. The length of the channel is ~30 km and its mean slope is ~0.09 degrees. (5) A breach of the Holden crater rim represents a short, ~22 km long, V-shaped narrow channel with the highest mean slope of ~1.5 degrees.

The total volume of the Uzboi Vallis topographic moat (including its head depression) is estimated to be ~$4.5 \cdot 10^3$ km^3. An important characteristic of Uzboi Vallis is that features indicative of a catastrophic flooding (e. g., tear-drop islands, cataracts, overflow channels) are absent along the entire length of Uzboi.

3) Holden crater (~150 km diameter): it has a flat floor the main portion of which is at ~–2 km elevation. The rim of the crater is heavily dissected and show large topographic variations; its mean elevation is ~–0.12 km (±0.58 km, 1σ). The rim of the crater shows two distinct lower parts: the first is the Uzboi breach and the second occupies the eastern portion of the rim where its mean elevation is ~-0.75 km (±0.25 km, 1σ). This lower portion of the rim is directed toward the large topographic depression of the ancient impact Holden basin [9, 4]. The total volume of the Holden crater (below the eastern lowering) is estimated to be ~$18.5 \cdot 10^3$ km^3.
4) Ladon Vallis: The main channel of Ladon Vallis begins as a full-sized feature (~10–12 km wide) near the deepest, central, potion of the Holden basin [4] that represents a broad (~65–70 km across) and shallow (0.2–0.3 km deep) topographic depression with knobby surface. The valley networks channels are converging toward the central depression of the Holden basin [4] which, thus, likely represent the water source area of Ladon Vallis. On the left side of the uppermost stretch of the Ladon main channel, there are several large (15-20 km long) tear-drop islands and broad (6–7 km wide) overflow channels that suggest a catastrophic release of water from the Ladon source area. The islands are on a plateau that is ~0.4 km higher than the floor of the main channel. Neither morphological nor topographical evidence exists for a trough-like feature that could represent remnants of the proposed ULM fluvial system southward of the Ladon source area.

CHRONOLOGY:

In order to reconstruct the general sequence of events of the Uzboi-Ladon system, we have performed the crater size-frequency distribution (CSFD) measurements in four key areas: (1) in the Bond crater (its northern portion unaffected by ejecta from the Hale crater), (2) on the floor of Uzboi Vallis (its lower stretch), (3) in the central massif of the Holden crater, and (4) on the floor of Ladon Vallis. The CSFD measurements show the following absolute model ages (AMA): (1) Bond, two AMAs, 3.74+0.04/-0.06 Ga and 3.58±0.02 Ga; (2) Uzboi, 3.48+0.03/-0.04 Ga, (3) Holden, two AMAs, 3.87+0.03/-0.04 Ga and 3.63±0.02 Ga, (4) Ladon, two AMAs, 3.71+0.07/-0.13 Ga and 3.31±0.04 Ga. These AMA estimates suggest the following general sequence of events in the study region. (1) Formation of the Bond and Holden craters (Late Noachian), (2) formation of Ladon Vallis (transition from Late Noachian to Early Hesperian), (3) formation of Uzboi Vallis and resurfacing events in the Bond and Holden craters (Late Hesperian and transition to Early Amazonian), (4) resurfacing events at Ladon Vallis (Early Amazonian).

CONCLUSIONS:

The topographic characteristics and the AMAs of the major parts of the Uzboi-Ladon fluvial system allow drawing of the following conclusions.

1) Uzboi and Ladon Valles are not pieces of a larger, single outflow system (ULM) but represent individual fluvial features with independent histories.
2) Modes of formation of Uzboi and Ladon Valles were strongly different. Complete lack of features indicative of a catastrophic flooding in association with Uzboi Vallis suggests that its topographic depression has been carved by multiple low-power flows that gradually removed material from the Uzboi moat and re-deposited it on the floor of the Holden crater. The total volume of the Holden crater is able to accommodate all materials removed from Uzboi Vallis. In contrast, Large tear-shaped islands and overflow channels at the upper stretches of Ladon Vallis suggest that this system was related to a sudden and powerful release of large amount of water from the source area near the center of the Holden basin.

3) The Holden crater did not segment the originally contiguous system (ULM) but the rim of the crater represented a major dam on the way of flows during formation of Uzboi Vallis.
4) The head depression of Uzboi Vallis postdates the Bond crater whose northern rim in not breached. Thus, even if the crater could be full of water, it did not serve as a primary source for the formation of either the Uzboi head depression or Uzboi Vallis itself.
5) The Uzboi head depression is ~250 km northward of the main rim of Argyre basin and was formed by flows from the local sources that were not connected directly with the basin. Thus, there is no evidence suggesting existence of a major outflow from Argyre [5, 6].

REFERENCES:

[1] Grant J. A., Parker T. J. Drainage evolution in the Margaritifer Sinus region // Mars, J. Geophysical Research. 2002. V. 107. No. E9. 5066. doi:10.1029/2001JE001678.
[2] Grant J. A., Irwin R. P., Grotzinger J. P. et al. HiRISE imaging of impact megabreccia and sub-meter aqueous strata in Holden Crater, Mars // Geology. 2008. V. 36. No. 3. P. 195-198. doi:10.1130/G24340A.
[3] Grant J. A., Irwin R. P., Wilson S. A., Buczkowski D., Siebach K. A lake in Uzboi Vallis and implications for Late Noachian-Early Hesperian climate on Mars // Icarus. 2011. V. 212. P. 110–122.
[4] Irwin R. P., Grant J. A. Geologic Map of MTM-15027, -20027, -25027, and -25032 Quadrangles, Margaritifer Terra Region of Mars: Scientific Investigations Map 3209. Scale 1:1,000,000. US Geological Survey, 2013.
[5] Parker T. J. Geomorphology and geology of the southwestern Margaritifer Sinus-northern Argyre region of Mars: M. S. thesis. Geol. Dept., Calif. State Univ., Los Angeles, 1985. 165 p.
[6] Parker T. J., Grant J. A., Anderson F. S., Banerdt W. B. From the South Pole to the Northern Plains: The Argyre Planitia story. // 6th Intern. Conf. Mars. LPI Contrib. 1164, Lunar and Planet. Inst., Houston, Tex. 2003. Abstract 3274.
[7] Hiesinger H., Head J. W. Topography and morphology of the Argyre Basin, Mars: implications for its geologic and hydrologic history // Planet. Space Sci. 2002. V. 50. No. 10–11. P. 939–981.
[8] Wilson S. A., Grant J. A., Howard A. D., Buczkowski D. L. The nature and origin of deposits in Uzboi Vallis on Mars. Journal of Geophysical Research // J. Geophysical Research. 2018. V. 23. P. 1842-1862. https://doi.org/ 10.1029/2017JE005508.
[9] Pondrelli M., Baliva M. A., Lorenzo Di., Marinangeli L., Rossi A. P. Complex evolution of paleolacustrine systems on Mars: An example from the Holden crater // J. Geophysical Research. 2005. V. 110. E04016. doi:10.1029/2004JE002335.

IDENTIFICATION AND CHARACTERIZATION OF NEW FELDSPAR-BEARING ROCKS IN THE WALLS OF VALLES MARINERIS, MARS

J. Flahaut[1], M. Barthez[1], V. Payet[1], F. Fueten[2], M. Guitreau[3], G. Ito[1], P. Allemand[4], C. Quantin-Nataf[4]

[1] *CRPG, CNRS UMR7358/Université de Lorraine, 15 rue Notre-Dame des Pauvres, 54500 Vandœuvre-lès-Nancy, France, (flahaut@crpg.cnrs-nancy.fr)*

[2] *Department of Earth Sciences, Brock University, St. Catharines, Ontario, Canada L2S 3A1*

[3] *LMV, Université Clermont-Auvergne/CNRS, 63178 Aubière, France*

[4] *LGL, TPE, Université Lyon 1/CNRS, 69622 Villeurbanne Cedex, France*

KEYWORDS:
Mars, Valles Marineris, VNIR spectroscopy, CRISM, feldspar minerals

INTRODUCTION:
Visible Near infrared (VNIR) spectroscopy has previously led to many discoveries pertaining to Mars geologic history (e. g., the discovery of hydrated minerals associated with ancient terrains with the Observatoire pour la Minéralogie, l'Eau, les Glaces et l'Activité, OMEGA [1]). Plagioclase feldspar minerals can also be identified with spectroscopic techniques thanks to a 1.3 µm absorption in the VNIR domain (e. g., [2]). Previous lunar analog studies show, however, that when mixing powders of Ca plagioclase with a mafic component (olivine or pyroxene), the feldspar absorption band is quickly masked [3]. This study further demonstrates that the 1.3 µm feature is only detectable if the plagioclase abundance is >90 %. Based on these observations, previous feldspar absorptions on Mars have been tentatively interpreted as evidence for nearly pure anorthositic rocks [4]. A recent study led by [5], however, suggests that rocks with less than 90 % plagioclase could reproduce the 1.3 µm feature if large feldspar crystals are involved, although no rock measurements were made. In the present study, we describe new feldspar signatures detected with the Compact Reconnaissance Imaging Spectrometer for Mars (CRISM) VNIR spectral-imager on the walls of the Valles Marineris canyon system on Mars, and discuss possible interpretations.

METHODS:
CRISM data available at the walls of eastern Valles Marineris, and at surrounding impact crater central peaks, where [6, 7] previously identified light-toned cumulate rocks, were downloaded from the Planetary Data System. CRISM is a visible near-infrared spectral imager using 2 detectors between 0.4 and 3.9 µm, with a spectral resolution of 6.55 nm and spatial resolution up to 18 m/px. CRISM data were processed (photometric correction, atmospheric correction, map-projection) with the dedicated ENVI CRISM Analysis Toolkit (CAT) [8]. Data were further cleaned from residual noise using a custom-made routine known as Mineral Recognizer [9]. Spectral parameters [10] were then computed on cleaned data.

Associated rock textures and elevations were assessed from the Context Camera (CTX) and the High Resolution Imaging Science Experiment (HiRISE) images and Digital Terrain Models (DTMs). In parallel, we collected VNIR spectra for various (uncrushed) terrestrial rocks containing a large range of feldspar abundances and grain sizes to establish a reference library [11].

RESULTS:
Eight CRISM observations at the walls of eastern Coprates Chasma show positive values of the BD1300 spectral parameter. Associated spectra show a broad absorption feature centered at 1.3 µm similar to previous Mars detections made by [4] and terrestrial anorthite spectra (Figure 1).

The detections are often limited to a few CRISM pixels, making it difficult to identify a specific outcrop/texture associated with the feldspar signature. One CRISM observation shows positive BD1300 values associated with a 200 m thick sub-horizontal layer. Detections are made at various elevations on the walls, and they are often associated with hydrated minerals, suggesting that the feldspar-bearing rocks are either weathered or spatially mixed with the clay-rich layer of the middle walls [6].

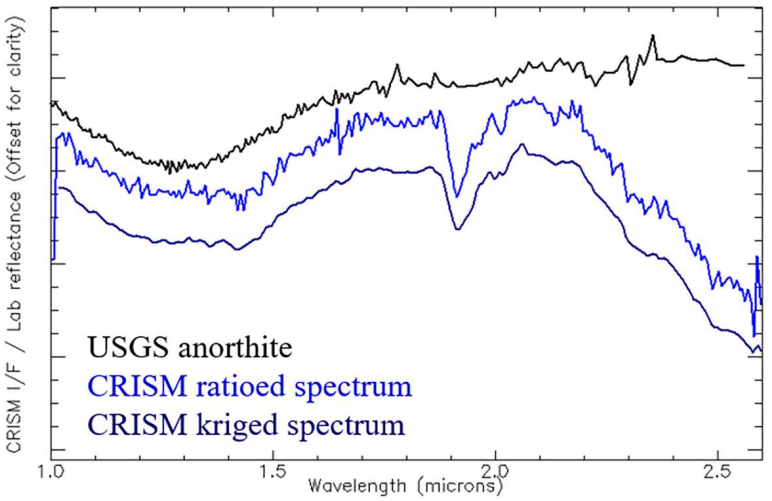

Fig. 1. Putative Mars CRISM feldspar signatures are compared with terrestrial anorthite HS201.3B from the USGS reference library [12]

DISCUSSION AND PERSPECTIVES:

The observed detections are consistent with the signature of plagioclase feldspar mineral, indicating the presence of feldspathic or even possibly felsic rocks. The distribution of the signatures, which are limited to eastern Coprates Chasma where hundreds of dikes were previously identified [13–14], and the association with a layer suggest the presence of effusive eruptive products. a recent work by [11] shows that feldspar signatures can be seen on phenocryst basalts, for instance. Further work is needed to establish and compare the observed signature with a newly developed whole rock reference library, but our results suggest that the Valles Marineris signatures may not represent an (primary) anorthositic crust [4] or a (tertiary) continental crust [15].

REFERENCES:

[1] Bibring, J. P. et al. (2006). Science, 312(5772).
[2] Adams, J. B., and Goullaud, L. H. (1978). LPSC Proc. 9, 2901–2909.
[3] Cheek L. C. et al. (2014). American Min., 99(10), 1871–1892.
[4] Carter J. and F. Poulet (2013). Nature. Geoscience, 6, 1008–1012.
[5] Rogers, A. D., and Nekvasil, H. (2015). GRL, 42(8), 2619–2626.
[6] Flahaut J. et al. (2013). Icarus, 221(1), 420–435.
[7] Quantin C. et al. (2013). Icarus, 221 (1), 436–452.
[8] Murchie S. et al. (2007). JGR, 112, E5.
[9] Flahaut et al. (2020) EGU meeting.
[10] Viviano-Beck C. E. et al. (2014). JGR, 119, 1403–1431.
[11] Barthez M. et al. (2020), this meeting.
[12] Clark R. N. et al. (2017). USGS Data Series 231.
[13] Flahaut J. et al. (2011). GRL, 38, L15202.
[14] Brustel C. et al. (2017). JGR, 122, 1353–1371.
[15] Sautter V. et al. (2016). Lithos, 254-255, p.36–52.

SULFATES ON MARS: A PYROCLASTIC AIRFALL MODEL FOR ORIGIN, EMPLACEMENT, AND INITIAL ALTERATION OF VALLES MARINERIS INTERIOR LAYERED DEPOSITS

J. W. Head[1], L. Wilson[1,2]
[1] *Dept. Earth, Environ. and Planet. Sci., Brown Univ., Providence RI 02912 USA*
[2] *Lancaster Environ. Centre, Lancaster Univ., Lancaster LA1 4YQ UK*
(*James_Head@brown.edu, l.wilson@lancaster.ac.uk*)

KEYWORDS:
Mars climate, sulfur, volcanic eruptions, interior layered deposits

INTRODUCTION:
Sulfur is both ubiquitous and locally concentrated on the surface of Mars and the Martian sulfur cycle [1] is of intense interest due to the information it provides about: 1) mantle composition, source regions and differentiation processes, 2) magmatic eruptive processes, environments of sulfur exsolution and retention in effusive and explosive eruptions, sulfur speciation during eruptions and interaction with the atmosphere and surface, 3) atmospheric evolution and effects and constraints on climate, 4) surface sedimentary deposition, aqueous and eolian transport, concentration and diagenesis, implications for climate evolution, 5) groundwater processes (solution, leaching from bedrock, transport, evaporative concentration and deposition, 6) post-depositional diagenesis and implications for the hydrological cycle, 7) host rock characteristics, sources, environments of emplacement, and 8) the role of sulfur in environmental conditions, liquid water acidity/alkalinity, and creation and maintenance of environments conducive or restrictive to formation and evolution of life.

The past several decades of Mars exploration have shown that sulfur-related surface deposits are concentrated in time and space on Mars. Pioneering orbital remote sensing data [2] demonstrated that a period favoring non-acidic aqueous alteration and formation of phyllosilicates was followed by an acidic aqueous alteration environment in the Late Noachian-Early Hesperian which resulted in the emplacement of sulfate deposits, and was coincident with a period of significant volcanism. This acidic aqueous alteration environment was followed by the "atmospheric aqueous-free alteration" period of anhydrous ferric oxide formation during the Amazonian [2]. Subsequent and complementary orbital remote sensing data [3] provided insight into the locations of the sulfate-rich environments and the stratigraphic relationships between phyllosilicates and sulfates. Sulfates were concentrated in several distinctive environments (e. g., Meridiani-type and Valles Marineris-type layered deposits, intracrater clay-sulfates, polar gypsum deposits) and were often interbedded with phyllosilicates (particularly in Valles-type interior layered deposits, ILDs [3–6]) showing that the change in surface environments from non-acidic to acidic [3] may have been transitional.

What are the necessary requirements for the formation, evolution and preservation of sulfates? These conditions are highly specific due to high sulfate solubility and the environmental sensitivity of sulfates to phase transitions (temperature and humidity) [1] and include: 1) sources of S, 2) sources of liquid water and climates conducive to the derivation (leaching) and/or transport of S, 3) acidic environments resulting from S concentration in aqueous solutions, 4) sufficiently warm conditions to collect S-rich waters, and then to evaporate water and concentrate and deposit sulfates, 5) oscillating climate conditions to permit the interbedding of phyllosilicates and sulfates, 6) environments to explain their concentration in certain locations/settings, and 7) subsequent dry/cold climates necessary to preserve ancient sulfate deposits to the present.

Surface exploration of the *Meridiani-type layered deposits* by *Opportunity* showed that the Burns formation consisted of 18–25 wt % S, mixtures of Mg and Ca sulfates, and about 10 % jarosite [7]. Together with sedimentary structures and stratigraphic relationships, these data were interpreted to indicate that it was emplaced in an eolian environment in which the sulfates formed in a groundwater upwelling low-pH aqueous evaporative environment, and underwent subsequent diagenesis. The process was envisioned to involve repeated upwellings of groundwater, periodically recharging local subaqueous depositional settings, and evaporating to concentrate the S and create the sulfate-rich deposits [7]. Pioneering theoretical and laboratory work [8–9] has shown that surface water and groundwater interactions with basalts can leach and concentrate S in solution, a primary prerequisite for further evaporative concentration and sulfate deposition. Modelling of the Martian hydrological cycle [10] showed that an episodic evaporative environment at Meridiani could be formed by rainfall and infiltration in equatorial regions, lateral groundwater migration and leaching of sulfur during transport, upwelling and evaporation at Meridiani, a general interpretation adopted to account for *Opportunity* data [11].

Remote sensing characterization of the Valles Marineris ILDs [3–6] showed that: 1) sulfate deposits were distinctly layered, 2) monohydrated sulfates were overlain by polyhydrated sulfates, 3) phyllosilicate and sulfate layers were interbedded, and 4) ILDs occur in kms-thick deposits exposed in eroded plateaus on the floors of Valles Marineris. While the origin and age of the ILDs are controversial [12], the formation of the sulfates is generally attributed to the same groundwater upwelling and evaporative deposition model as invoked at Meridiani [10]. Sulfur was concentrated by groundwater leaching from basaltic rocks, and further concentrated and deposited in sulfates by evaporative processes [3, 10].

While the groundwater concentration and evaporation scenario successfully accounts for a large number of requirements imposed by observations, it may not account for all documented environments of sulfate emplacement and preservation [3] on Mars. It also requires stringent sulfur mass-balance relations [12] and long-duration global warm and wet environmental conditions at the time of formation, conditions that have been difficult to reconcile with climate models [13]. We explore the role of magmatic processes [14] as an additional model for formation, evolution and preservation of sulfates on Mars.

GENERATION, ASCENT AND ERUPTION OF MAGMA ON MARS:
As a basis for understanding the character and nature of volcanic eruptions in the Martian environment (e. g., low gravity, currently low and historically evolving atmospheric pressure, presence of groundwater and ground ice) we have developed a theoretical and predictive framework for the generation, ascent and eruption of magma on Mars [14]. We have shown that basaltic plinian eruptions are highly favored (relative to Earth) [14–15] and explored the characteristics and dispersal of tephra [16] and gases from such eruptions in different locations and under different P_{atm} conditions, and how this might lead to the observed distribution of fine-grained deposits [16]. The potential behavior and fate of S species during volcanic eruptions has also been investigated [17], including the role of H_2SO_4 precipitates in surface melting and creation of aqueous acidic environments [18].

DISCUSSION:
On the basis of these considerations, we address the question: Can volcanic eruptions under Martian conditions account for the characteristics of units in the Valles Marineris Interior Layered Deposits? Observations consistent with such an hypothesis include: 1) The Tharsis region is the most significant focus of volcanism on Mars, beginning in the Noachian and continuing through the Amazonian, with peak regional resurfacing in the Late Noachian-Early Hesperian [19]. 2) Explosive plinian basaltic volcanism is favored on Mars in general, and with increasing altitude (Tharsis) and decreasing P_{atm}. 3) Any interaction of rising magma and groundwater/ground ice can contribute to explosivity [14]. 4) The Martian environment favors the pro-

duction of finer ash relative to Earth (~22 μm geometric mean for Mars), enhancing dispersal. 5) The presence and dominance of fine ash creates a profusion of readily available nucleation sites for condensation of co-erupted H_2O and S species. 6) Airfall products are predicted to consist of tephra coated with condensed H_2O and S species, producing extensive layered and graded deposits, and possible lapilli beds [15]. 7) The distribution of eruptive products is predicted to be focused latitudinally (equatorial in the case of Tharsis sources), with decreasing grainsize as a function of distance from the vent [16]. 8) Rapid formation of aerosols is predicted to occur, with global warming due to erupted S species being very short-lived, and global cooling ensuing until ambient conditions return [17]. 9) On the basis of calculated tephra dispersal and cooling times, temperatures of deposited tephra will decrease with distance from the vent, with the majority of deposit temperatures being close to that of the ambient atmosphere. 10) Magmatic exsolution of sulfur is favored by lower P_{atm} and enhanced by higher altitude eruption sites (Tharsis). 11) Petrogenetic relations favor the co-exsolution of H_2O and S species under these conditions. 12) Sulfur speciation and atmospheric chemistry predictions favor H_2SO_4 formation and widespread dispersal during and immediately following eruptions [18]. 13) Condensation and ensuing precipitation of H_2SO_4 is predicted to melt any existing surface snow and ice, and to provide acidic aqueous surface environments favoring sulfate precipitation [18]. 14) Estimates of eruption duration and continuity readily predict deposit accumulations in excess of hundreds of meters to kilometers. 15) Oscillation of eruption conditions and S speciation may lead to alternate water-rich and sulfur-rich depositional conditions and phyllosilicate/sulfate Interbedding.

CONCLUSIONS:

The characteristics of Martian volcanism in the Tharsis region appear to meet the necessary requirements for the formation, evolution and preservation of sulfates in the ILD, including: 1) sources of sulfur (*magmatic exsolution and precipitation*), 2) sources of liquid water (*co-precipitated and surface H_2O melted by H_2SO_4*) and climates conducive to the derivation and/or transport of sulfur (*operates in a cold and icy climate; concentration by groundwater leaching of basaltic bedrock is not required*), 3) acidic environments resulting from sulfur concentration in aqueous solutions (*provided by H_2SO_4 precipitation and melting*), 4) sufficiently warm conditions to collect S-rich waters (*ponding of acidic meltwater created by H_2SO_4 precipitation*), and then to evaporate water and concentrate and deposit sulfates (*dry evaporative environments following eruptive phases*), 5) oscillating climate conditions to permit the interbedding of phyllosilicates and sulfates (*oscillatory conditions very plausible in the transition to lower P_{atm}*), 6) environments to explain their concentration in certain locations and settings on Mars (*adjacent to long-lived Tharsis volcanic sources*), and 7) subsequent dry and cold climatic conditions necessary to preserve the ancient sulfate deposits to the present (*cold and icy conditions remain as P_{atm} evolves to present conditions*).

In order to test this hypothesis further, we are currently developing predictive eruption and tephra/volatile dispersal models that can serve as an interpretative framework to compare to the detailed characteristics and trends observed in the Valles Marineris ILDs [e. g. 3–6].

REFERENCES:

[1] King and McLennan (2010) Elements 6, 107.
[2] Bibring et al. (2006) Science 312, 400.
[3] Murchie et al. (2009) JGR 114, E00D06.
[4] Roach et al. (2010) Icarus 206, 253; 207, 659.
[5] Bishop et al. (2009) JGR 114, E00D09.
[6] Wendt et al. (2011) Icarus 213, 86.
[7] McLennan and Grotzinger (2008) The Martian Surface, Cambridge, 541.
[8] Tosca and McLennan (2006) EPSL 241, 21.
[9] Tosca et al. (2005) EPSL 240, 122.
[10] Andrews-Hanna et al. (2007) Nature. 446, 163; ibid (2010) JGR 115, E06002; Andrews-Hanna and Lewis (2011) JGR 116, E02007.
[11] Arvidson et al. (2016) JGR 121, 1602.
[12] Michalski and Niles (2012) Geology 40, 419.

[13] Wordsworth et al. (2013) Icarus 222, 1.
[14] Wilson and Head (1994) RG 32, 221; ibid, LPSC 51 1391.
[15] Wilson and Head (2007) JVGR 163, 83.
[16] Kerber et al. (2011) Icarus 216, 212; (2012) Icarus 219, 358; (2013) 223, 149.
[17] Kerber et al. (2015) Icarus 261, 133.
[18] Kreslavsky and Head (2020) LPSC 51 1828.
[19] Carr and Head (2010) EPSL 294, 185.

GEOLOGIC AND CLIMATOLOGIC HISTORY OF EARLY MARS: RECENT DEVELOPMENTS, UNKNOWNS AND DIRECTIONS FOR THE NEXT DECADE

J. W. Head[1], R. D. Wordsworth[2], L. Wilson[3], M. A. Kreslavsky[4], A. M. Palumbo[1], H. Y. McSween[5]
[1] *Brown Univ., Providence, RI*
[2] *Harvard Univ.,Cambridge, MA*
[3] *Lancaster Univ., Lancaster UK*
[4] *UCSC, Santa Cruz, CA*
[5] *Univ. Tenn., Knoxville, TN*

KEYWORDS:
Mars early climate, warm and wet, cold and icy, valley networks

INTRODUCTION:
Mars is extremely fascinating due to its many similarities to Earth, its potential for life, and as a human exploration goal. For these and related reasons, Mars has been the destination for more than 40 robotic missions since 1960. Guided by a theme of "Follow the Water", the results of these missions and related research have transformed our perception of Mars. Emerging as a critical area of focus in understanding the evolution of Mars has been the Late Noachian (LN)-Hesperian (H) era [1], due to compelling evidence for fundamental changes in geodynamics, atmosphere, climate, geomorphology, volcanology, and the water and sulfur cycles. Here we assess the state of understanding at the end of the 1st decade of the 21st century, highlight findings of the 2nd decade, and raise important questions to address in the 3rd decade.

KNOWLEDGE CIRCA 2010:
This period marked the end of two decades of data gathering and global characterization (summarized in [2–9]): improved dynamical models of terrestrial planet formation showed that Mars was anomalously small; lunar magma ocean scenarios were applied to Mars to address the origin and evolution of the primary crust; ancient crustal magnetic fields were discovered; global gravity data provided crustal thickness; global topography ushered in an era of quantitative geomorphology; orbital remote sensing data showed that Mars is a dynamic planet with time-dependent mineralogical alteration (N-phyllosilicates, H-sulfates and A-anhydrous iron oxides) and local distinctive mineralogical and weathering environments; high resolution images revealed stratigraphic relationships and details of geologic processes (including evidence for N and H oceans); geomorphological, mineralogical, and isotopic ratio data suggested a significant N water inventory, widespread pluvial, fluvial and lacustrine activity, enhanced degradation, and warm and wet climate conditions in the LN-H; detailed models were developed for a vertically integrated N hydrological cycle and a colder horizontally stratified LH-A hydrological cycle; outflow channels were interpreted as catastrophic outbursts of huge volumes of pressurized groundwater (GW) beneath a thickening global cryosphere; the origin of the hemispheric dichotomy was attributed to a huge oblique impact; geological and geophysical data suggested that the Tharsis volcanic and tectonic province had largely formed by the MN, stabilizing Mars against further TPW; the role of spin-axis/orbital evolution in climate change became clear (leading to improved understanding of the global distribution of ice and the significance of non-polar glaciation); new findings from Martian meteorites led to maturation of the field of astrobiology.

Syntheses near the end of these decades [2–9] raised fundamental questions about the: initial volatile inventory of a 'too-small' Mars; duration of the magnetic field; role of crater and basin formation in geological and climatalogical evolution; nature of a warm and wet early Mars and how it transitioned to its current state; location of the missing carbonates inferred from the loss of the early atmosphere; causes and implications of time-correlated mineralogical and geological evolution; rates and implications of atmospheric loss

to space; meaning of the SNC meteorites in terms of mantle characteristics and processes, initial and changing fO_2, petrogenetic evolution, and volatile presence and abundance.

2010–2019:

What did we learn in the last decade [e. g., 10–14] and how did this change the fundamental questions? Planetary accretion and dynamics models underlined the unusual nature of Mars and its bombardment history; newly developed global data sets enabled compilations, comparisons, and age dating of valley networks (VN), open and closed-basin lakes (OBL/CBL), deltas and fans, impact craters of all scales, outflow channels and buried ice deposits; improved crater statistics refined geological history and era boundaries; a global geologic map of Mars was published; new models linking interior evolution and surface geology/chronology emerged; the age of the demise of the magnetic field (and thus its shielding effect on atmospheric loss) was identified as prior to the formation of the last large basins; multidisciplinary modeling brought increased clarity to the effects of crater and basin formation on atmospheric blow-off, retention, volatile cycling, and climate; Mars meteorites provided new clues about ancient non-volcanic processes, atmospheric history and water budget; new and improved general circulation models (GCMs) of early Mars (with a water cycle) found that the climate was likely to have been characterized by an ambient mean annual temperature (MAT) of ~225 K, liquid water was not stable, precipitation was in the form of snow, not rain, and if atmospheric pressure exceeded a few 10s of millibars, an adiabatic cooling effect resulted in surface H_2O being transported to the southern uplands and the south polar regions (the 'cold and icy highlands' model); among the implications of these GCMs are that a global cryosphere existed, the hydrological system/cycle was horizontally stratified, glacial accumulation in the uplands would have been cold-based, transient warming events of some type were needed to temporarily raise MAT to well in excess of 273 K to produce VN/OBL/CBL; the duration of focused fluvial and lacustrine activity shortened to a phase in the LN-EH; the environment of surface phyllosilicate formation supporting an early warm and wet climate became less clear and increasingly removed in time from VN/OBL/CBL; alternative candidate environments of phyllosilicate formation associated with initial high-temperature accretional stages, subsurface GW hydrothermal circulation, and impact basin-related climate alterations emerged with more clarity; evidence for additional carbonates was found, but not in abundances thought necessary to account for 'missing' atmospheric CO_2; tracing of the surface-near surface water inventory back in time revealed much lower predictions for the Noachian water budget than thought previously; plausible sources of GW and recharge to pressurize the GW system, crack the cryosphere, and produce significant volumes of water to form the outflow channels remained elusive; climate modeling of the fate of water outbursts in outflow channels showed little influence on climate and no substantial ponding to form seas or oceans; Antarctic analog investigations showed that the "high" weathering rates typical of LN Mars still correspond to the lowest on Earth, being similar to those in terrestrial icy polar deserts with MAT << 273 K; phyllosilicate and sulfate occurrences are interbedded and overlap in time, blurring the initial separation into eras; new insights into mantle state, evolution and petrogenesis underlined the close relationship of atmospheric pressure and release of H_2O and S species; improved volcanological models helped track the interaction and distribution of tephra and exsolved gases as a function of atmospheric pressure; the origin of sulfates and their detailed nature at several Mars rover sites and other sulfate occurrences was attributed to a vertically integrated hydrological system; recent data on atmospheric loss rates to space suggest that N atmospheric pressure did not exceed ~1 bar.

FUNDAMENTAL QUESTIONS AND RESEARCH THEMES FOR THE 2020S AND BEYOND:

How do these results frame future questions? Ten themes and related sub-questions are emerging. The first four broadly address 'inheritance': *What were the initial conditions and events and how did they set the stage for the evolution of Mars?*

1. Origin: Size, location and growth rates; budget of volatiles; earliest bombardment history?
2. Solar State and Evolution: Solar state, radiance and temporal variability?
3. Crustal Formation and Evolution: Nature of magma ocean and its aftermath; primary and secondary crust formation; associated outgassing history and implications for the atmosphere?
4. Geodynamic Evolution and Petrogenetic History: Core formation, ensuring mantle convection patterns and changes with time; redox state(s) and petrogenetic evolution; timing and role of basins; changes in magmatic sources/styles/compositions with time; primary or fractionated magmas; timing of Tharsis, relation to TPW and tectonic activity?

The following six themes broadly address the question: *What was the nature and evolution of the early climate?*

1. Nature of Ancient Atmosphere and Climate: What were N "ambient conditions", 'warm and wet' or 'cold and icy'? How did species and quantities change with time; nature of primary and secondary atmospheres, their transition and evolution; nature and evolution of volcanic degassing and relationship to evolving atmospheric pressure; nature, scale and duration of ambient climate perturbations and influence on MAT?
2. Candidate Climate Perturbations: What events perturbed the ambient atmosphere? Role of seasonal, spin axis/orbital variations, impacts, greenhouse gas input, hydrolysis, clouds, and solar variability?
3. Water Cycle: What was the initial water budget, how did it change with time; Was the hydrological cycle ever vertically integrated; how was water partitioned (sources, sinks, D/H, rates of loss to space)?
4. Sulfur Cycle: What was the total S budget, how did it partition with time; nature of volcanic S exsolution as a function of evolving atmospheric pressure; S cycle (sources, sinks, evolution, relative roles of direct volcanic deposition and groundwater basalt leaching and evaporative deposition); origin of Valles Marineris ILDs?
5. Mineralogical and Geomorphological Evolution and Implications: What do detailed geological, mineralogical and temporal data tell us about the diversity of occurrences of phyllosilicates and sulfates? What is the distribution and origin of salts, carbonates and silica-rich deposits? What do these data tell us about LN-H climate and weathering processes and rates; how are crater degradation and VN/CBL/OBL origin linked to LN-H mineralogy, climate and GW/volcanic processes?
6. Environments for the Formation and Evolution of Life: New insights, terrestrial perspectives and evolving paradigms are leading away from a sustained 'warm and wet' early Mars, toward an ambient 'cold and icy' climate. What strategies/proxies are needed to explore potential biotic environments in Antarctic-like surfaces and a warmer, wetter and geochemically active 'Mars underground'?

SYNTHESIS:

Future exploration, guided by these questions and a focus on *Mars System Science*, will continue to revolutionize our thinking as we explore Mars with an additional triad of rovers, work toward sample return and pave the way for human exploration.

REFERENCES:

[1] Tanaka et al. (2014) USGS SIM 3292.
[2] McSween (1994) Meteoritics 29, 757.
[3] Haberle (1998) JGR 103, 28467.
[4] Solomon et al. (2005) Science 307, 1214.
[5] Nimmo and Tanaka (2005) Ann. Rev. EPS 33, 133.
[6] Bibring et al. (2006) Science 312, 400.
[7] Murchie et al. (2009) JGR 114, E00D06.
[8] Carr and Head (2010) EPSL 294, 185.
[9] Fassett and Head (2011) Icarus 211, 1204.
[10] Grott et al. (2013) SSR 174, 49.
[11] Ehlmann and Edwards (2014) Ann. Rev. EPS 42, 291.
[12] Kite (2019) SSR 25, 10.
[13] Haberle et al. (2017) *The Atmosphere and Climate of Mars*, Cambridge.
[14] Wordsworth (2016) Ann. Rev. EPS, 44, 381.

THE FORMATION OF YOUNG GULLIES ON MARS BY THE MELTING AND BOILING OF WATER AT HIGH OBLIQUITY

J. L. Dickson[1,2], A. M. Palumbo[2], J. W. Head[2], L. A. Kerber[3], C. I. Fassett[4], M. A. Kreslavsky[5]

[1] *Division of Geological and Planetary Sciences, California Institute of Technology, Pasadena, CA, USA (jdickson@caltech.edu)*

[2] *Department of Earth, Environmental and Planetary Sciences, Brown University, Providence, RI, USA*

[3] *Jet Propulsion Laboratory, Pasadena, CA, USA*

[4] *Marshall Space Flight Center, Huntsville, AL, USA*

[5] *Earth and Planetary Sciences, University of California, Santa Cruz, CA, USA*

KEYWORDS:
Mars, water, gullies, Amazonian, hydrology, climate

INTRODUCTION:

Gullies on Mars exhibit morphologies that resemble H_2O-carved channels on Earth [1]. The distribution of gullies is well-constrained in latitude and slope orientation [2], suggesting a relation to climate; however, they are found at high elevations where pressure is below 612 Pa, and, as a result, liquid H_2O is not possible at these locations in the current climate [2, 3]. Modification of existing gullies is temporally associated with seasonal CO_2 activity [4, 5], suggesting that gullies could form from: CO_2-ice superposing ice-cement on steep slopes is pressurized, causing sediment-entraining gas flows [6]. Deepening of gullies would be achieved through the sublimation of previously buried H_2O-ice [6].

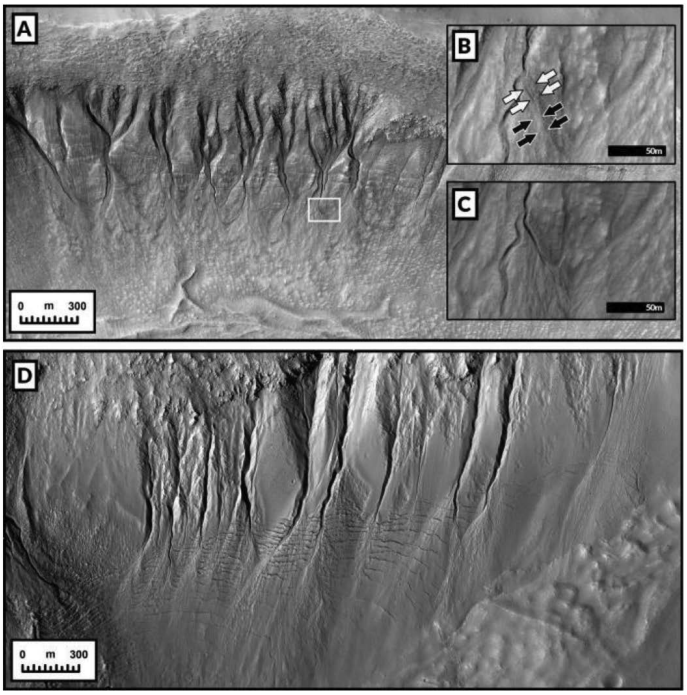

Fig. 1. (A) HiRISE image ESP_032011_1425 in Terra Sirenum, showing changes within a gully fan (4). New channel marked in red to show scale relative to entire gully systems. (B) Pre-activity showing buried channel (white arrows) and fan material (black arrows), as noted in (4). HiRISE image ESP_013115_1420. (C) Post-activity inset showing exhumed channel and fan material, with newly defined channel bend upslope. (D) HiRISE image PSP_007592_1425 (176.52° E, 37.40° S) showing cross-cutting fractures on gully fans

Mapping of >2000 gullies in Sysyphi Cavi with repeat imagery over 6 Mars years shows that ~98.3 % of gullies show no activity and no gullies experienced mappable channel erosion [7], despite occurring within a latitude band where CO_2 processes are common [8]. Thus, current activity appears capable of mobilizing loose sediment on steep slopes but its capacity for eroding through ice-cement has not been observed.

If modification within gullies today is inadequate to explain the formation of gullies, did they form in another climate? At 35° obliquity the mid-latitudes experience net accumulation of H_2O in the form of the latitude-dependent mantle [9–11], a draping unit composed of H_2O-ice and dust that manifests on steep slopes as pasted-on terrain, an ice-cemented substrate for deeply incised gullies (Figure 1) and a potential source for the fluid that carved them [12]. This unit has undergone tens of meters of depletion [13]. Was this depletion due entirely to sublimation or was any of the ice lost via melting, with gullies as the morphologic signature of this process [14, 15]? At 35° obliquity, massive CO_2 slabs currently within the South Polar Residual Cap would sublimate [16] and double the current atmospheric density [17]. We used the 3D Laboratoire Météórologie Dynamique (LMD) GCM [18] to simulate three obliquity values that Mars has experienced in the last 1 million years to test whether conditions above the triple point of H_2O were achieved at gully locations.

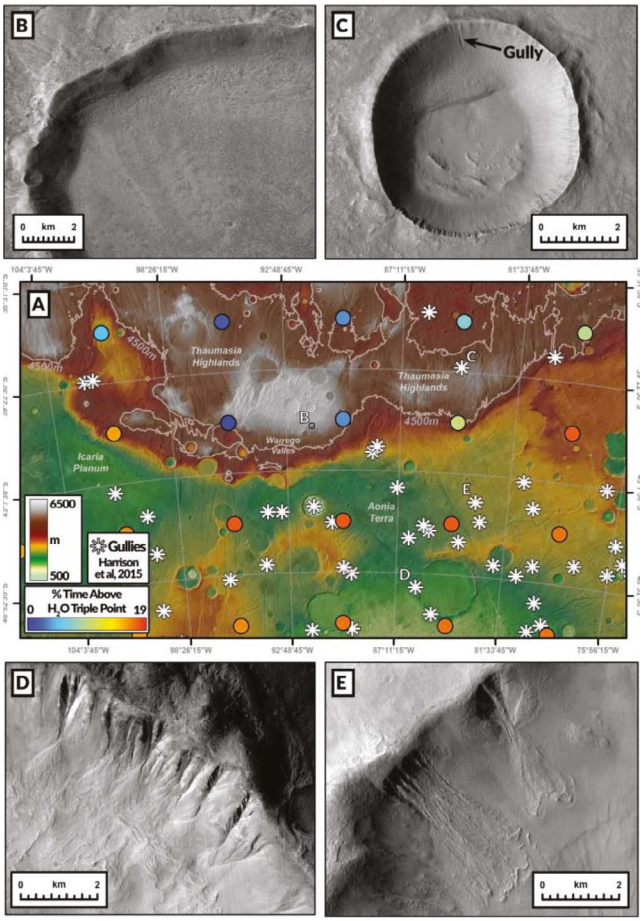

Fig. 2. The uppermost vertical extent of gullies on Mars. (A) GCM results (colored dots) show percentage time spent above the triple point for H2O, with a rapid decline from Icaria Planum and Aonia Terra to Warrego Valles. (B) Steep, pole-facing slope hosting pasted-on terrain with no gullies visible at CTX resolution (5 m/px). (C) The highest elevation gully on Mars. (D) Deeply incised gullies in Aonia Terra. (E) Well-incised gullies in Aonia Terra

RESULTS:

At 35° obliquity, (630K years ago) [19] minimum conditions for melting are achieved at nearly all gully sites in each hemisphere. Each hemisphere experiences increased H_2O-ice accumulation in the mid- and high-latitudes that are recorded in our model, and the margins of this surface unit are moved poleward by the 273 K contour through the course of spring and summer. Unlike in lower-obliquity simulations, this surpassing of 273 K occurs at >612 Pa, such that some component of the ice loss could potentially be due to melting.

More than 3/4 of gullied landforms on Mars (78.4 %) occur between 25° S and 50° S [20], and all of these locations achieve potential melting conditions with 98.2 % of them surpassing the triple point for >10 % of the year when perihelion occurs during southern summer at 35° obliquity. This latitude range also hosts the highest elevation gullies on Mars, along the southern margin of the Thaumasia Highlands, and these all experience conditions above the triple point. Spatially, our model predicts a rapid increase in potential melting conditions when descending across the ~4500 m contour (Figure 2). The summit of the Warrego Valles watershed experiences potential melting conditions for ~0.6 % of the year in our simulations, while the adjacent lower plains to the south experience melting conditions for ~13.6 % of the year, among the highest values for gullied terrain in the southern mid-latitudes (see Figure 2).

This steep gradient between conditions above and below the triple point, defined by the ~4500 m contour, can be traced around the southern extent of the Thaumasia Highlands for ~1700 km and corresponds directly with the upper elevation extent of gullies on Mars [20] (see Figure 2). Gully channels are well-incised through pasted-on terrain with large bedrock alcoves and are densely concentrated on crater walls within plains to the south of Thaumasia, Icaria Planum and Aonia Terra (see Figure 2). The abrupt termination of gullies at the ~4500 m contour (Fig. 2) is challenging to explain by CO_2 processes alone. The cutoff of gullies at ~4500 m is well explained by the metastability of H_2O at high-obliquity.

Our results reveal a correlation between the upper elevation limit of gullies on Mars and the upper elevation limit of where triple point conditions are predicted to have been achieved at 35° obliquity. This argues for a model of gully formation due to liquid water activity at high obliquity followed by modification by CO_2 processes during low obliquity regimes like today.

REFERENCES:

1. Malin M. C., Edgett K. S. Evidence for Recent Groundwater Seepage and Surface Runoff on Mars // Science. 2000. V. 288. P. 2330–2335.
2. Heldmann J. L., Mellon M. T. Observations of martian gullies and constraints on potential formation mechanisms // Icarus. 2004. V. 168. P. 285–304.
3. Haberle R. M., McKay C. P., Schaeffer J., Cabrol N. A., Grin E. A., Zent A. P., Quinn R. On the possibility of liquid water on present-day Mars // J. Geophysical Research: Planets. 2001. V. 106. P. 23317–23326.
4. Dundas C. M., Diniega S., McEwen A. S. Long-term monitoring of martian gully formation and evolution with MRO/HiRISE // Icarus. 2015. V. 251. P. 244–263.
5. Dundas C. M., McEwen A. S., Diniega S., Hansen C. J., Byrne S., McElwaine J. N., The formation of gullies on Mars today / Geological Society, London. Special Publications. 2019. V. 467. P. 67–94.
6. Pilorget C., Forget F. Formation of gullies on Mars by debris flows triggered by CO 2 sublimation // Nature. Geoscience. 2016. V. 9. P. 65–69.
7. Raack J., Conway S. J., Heyer T., Bickel V. T., Philippe M., Hiesinger H., Johnsson A., Massé M. Present-day gully activity in Sisyphi Cavi, Mars — Flow-like features and block movements // Icarus. 2020. Art. 113899.
8. Portyankina G., Hansen C. J., Aye K.-M. Present-day erosion of Martian polar terrain by the seasonal CO_2 jets // Icarus. 2017. V. 282. P. 93–103.
9. Head J. W., Mustard J. F., Kreslavsky M. A., Milliken R. E., Marchant D. R. Recent ice ages on Mars // Nature. 2003. V. 426. P. 797–802.
10. Mischna M. A. , Richardson M. I., Wilson R. J., McCleese D. J. On the orbital forcing of Martian water and CO_2 cycles: A general circulation model study with simplified volatile schemes // J. Geophysical Research: Planets. 2003. V. 108. Iss. E6. doi:10.1029/2003JE002051.
11. Madeleine J.-B., Head J. W., Forget F., Navarro T., Millour E., Spiga A., Colaïtis A., Määttänen A., Montmessin F., Dickson J. L. Recent Ice Ages on Mars: The role

of radiatively active clouds and cloud microphysics // Geophysical Research Letters. 2014. V. 41. P. 4873–4879.
12. Christensen P. R. Formation of recent martian gullies through melting of extensive water-rich snow deposits // Nature. 2003. V. 422. P. 45–48.
13. Dickson J. L., Head J. W., Goudge T. A., Barbieri L. Recent climate cycles on Mars: Stratigraphic relationships between multiple generations of gullies and the latitude dependent mantle // Icarus. 2015. V. 252. P. 83–94.
14. Dickson J. L., Head J. W. The formation and evolution of youthful gullies on Mars: Gullies as the late-stage phase of Mars' most recent ice age // Icarus. 2009. V. 204. P. 63–86.
15. Costard F., Forget F., Mangold N., Peulvast J. P. Formation of Recent Martian Debris Flows by Melting of Near-Surface Ground Ice at High Obliquity // Science. 2002. V. 295. P. 110–113.
16. Phillips R. J., Davis B. J., Tanaka K. L., Byrne S., Mellon M. T., Putzig N. E., Haberle R. M., Kahre M. A., Campbell B. A., Carter L. M., Smith I. B., Holt J. W., Smrekar S. E., Nunes D. C., Plaut J. J., Egan A. F., Titus T. N., Seu R. Massive CO_2 Ice Deposits Sequestered in the South Polar Layered Deposits of Mars // Science. 2011. V. 332. P. 838–841.
17. Bierson C. J., Phillips R. J., SmithI. B., Wood S. E., Putzig N. E., Nunes D., Byrne S. Stratigraphy and evolution of the buried CO_2 deposit in the Martian south polar cap // Geophysical Research Letters. 2016. V. 43. P. 4172–4179.
18. Forget F., Hourdin F., Fournier R., Hourdin C., Talagrand O., Collins M., Lewis S. R., Read P. L., Huot J.-P. Improved general circulation models of the Martian atmosphere from the surface to above 80 km // J. Geophysical Research: Planets. 1999. V. 104. P. 24155–24175.
19. Laskar J., Levrard B., Mustard J. F. Orbital forcing of the martian polar layered deposits // Nature. 2002. V. 419. P. 375–377.
20. Harrison T. N., Osinski G. R., Tornabene L. L., Jones E. Global documentation of gullies with the Mars Reconnaissance Orbiter Context Camera and implications for their formation // Icarus. 2015. V. 252. P. 236–254.

MARS CRATER MODIFICATION IN THE LATE NOACHIAN: EVIDENCE FOR COLD-BASED CRATER WALL GLACIATION AND ENDORHEIC BASIN FORMATION

D. B. Boatwright, J. W. Head
Dept. of Earth, Environmental and Planetary Sciences, Brown University, Providence, RI 02912 USA (*benjamin_boatwright@brown.edu; james_head@brown.edu*)

KEYWORDS:
Mars climate, fluvial processes, glaciation, crater modification, Noachian

INTRODUCTION:
Mars is currently characterized by a hypothermal, hyperarid climate that is thought to have persisted throughout the Amazonian [1]. The distribution of water ice on Mars has changed over time due to periodic variations in spin axis obliquity [2]. During periods of relatively higher obliquity than present, water ice is mobilized from the poles and deposited as snow and ice in the mid-latitudes, producing cold-based glacial landforms (Figure 1 A–B) [3–6].

Geologic evidence suggests that the ambient climate in the Noachian was significantly different. Fluvial and lacustrine features have been interpreted to indicate the presence of a warm and wet climate with rainfall and runoff that persisted over tens of millions of years [7–8]. However, global climate models predict Noachian temperatures well below those required to sustain liquid water at the surface [9–10]. These models also predict that the distribution of water ice will mostly be controlled by altitude rather than latitude. Supporting geomorphic evidence for this hypothesis has been elusive because glaciation in such an environment is predicted to be cold-based and, as in the Amazonian, melting is limited to top-down (supraglacial) sources [11]. We search for characteristic cold-based glacial morphologies preserved in high-altitude terrains in order to better assess the character of potential cold-based glacial processes in the Noachian [12].

GEOLOGY OF CRATER B:
We report on the geology of an unnamed 54-km diameter Noachian-aged crater in the southern highlands that displays evidence for cold-based glaciation (Figure 2). The crater is located in ~800 km northwest of the Hellas basin rim in Terra Sabaea. In a study of eroded crater floors in the same region, Irwin et al. [13] noted that the interior of this crater, which they designated "B", contains a dark-over-light stratigraphy characterized by a more resistant lower unit covered by a more erodible upper unit outcropping as knobs and mesas. Sinuous ridges preserved in the dark-toned upper unit were interpreted as inverted paleochannels.

On the basis of this previous work, we mapped the interior of the crater in detail using 5 m/pix CTX and 0.25 m/pix HiRISE visible imagery, 25 m/pix CTX stereo topography, and 100 m/pix THEMIS quantitative thermal inertia data. We also conducted crater counts down to 100 m in diameter on the crater B floor using 5 m/pix CTX visible images to determine an Early Hesperian (~3.43 Ga) resurfacing age using the Hartmann chronology (Hartmann, 2005). These data reveal an ensemble of additional features (Figure 1C, 2) not previously described in Noachian-aged craters that we interpret to indicate a history of cold-based glaciation and top-down melting.

Subdued alcoves are seen in the steepest sections of the crater wall with average slopes of ~15˚ (Figure 1C). A series of lobate, upslope-facing scarps occurs near the base of the wall, often between the alcoves and the inverted ridge heads. A narrow debris apron occurs along the base of the crater wall, often superposing the upslope-facing scarps and inverted ridges.

Inverted tributary ridges are distributed throughout the crater floor, but two tributary networks are particularly well preserved in the east and south

(Figure 2). They follow the same general morphologic trend extending radially from the crater wall, along the gently sloping floor to the lowest points of the crater, where they terminate in depositional basins. The proximal morphology is characterized by highly bifurcated clusters of narrow, subparallel ridges that emerge from beneath the debris apron at the base of the crater wall. The proximal ridge network in the east merges into a wider, flat-topped medial morphology downslope; approximately a dozen medial ridges then coalesce into four larger trunk ridges. The smaller network in the south maintains a mostly medial morphology before thinning into smaller ridges near the base.

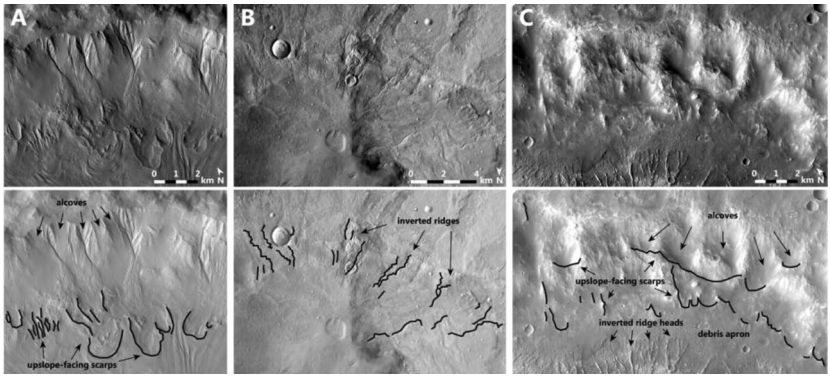

Fig. 1. (A) Amazonian cold-based glacial morphologies in an unnamed crater in Terra Sirenum. Moraine scarps mark former locations of glacial lobes. (B) Amazonian glaciofluvial valleys in the crater Greg have been inverted into ridges on the crater floor. (C) Degraded remnants of alcoves and scarps are still preserved in crater B. The scarps are closely associated with the position of the debris apron and inverted ridge heads. CTX visible mosaic

Two depositional basins are located in the lowest parts of the crater floor (Figure 2). Most of the inverted ridges originating from below the upslope-facing scarps on the eastern crater wall terminate in the larger northern basin. A second, smaller basin to the south of the first is readily identified by its distinct texture and bright margin. It is positioned ~30 m higher than the larger basin and is covered in closely spaced eolian dunes. Multiple inverted ridges originating from the southern crater wall can be observed terminating directly at the southwestern margin of the smaller second basin.

DISCUSSION AND CONCLUSIONS:

We interpret the alcove-scarp-ridge system (Figure 1C, 2) as the result of top-down melting of a cold-based crater wall glacier, leading to proglacial outwash in the form of fluvial channels that transported glacially derived sediment into multiple low-lying basins in the crater floor. Thermal inertia data indicate coarse to very coarse sand grain sizes in the inverted ridges, which is consistent with an origin as sedimentary lag deposits that became armored against erosion and were topographically inverted [13]. The depositional basins generally have a higher thermal inertia than the ridges or debris apron, which is the opposite of what might be expected of fine-grained channel effluent or lacustrine deposits. However, the depressed topography in these basins is likely a result of eolian deflation which first removed any fine-grained channel-derived sediments and subsequently revealed the underlying light-toned unit, which has high thermal inertia due to its greater resistance to erosion than the dark-toned upper layer that contains the inverted ridges.

The endorheic crater B basin, with completely internal drainage, lies in contrast to the similarly-aged open- and closed-basin lakes on Mars [14–15]. The lack of significant exterior drainage into crater B argues against an origin for the inverted ridges as the depositional remnants of fluvial valley networks derived from areally distributed rainfall and runoff. Likewise, groundwater sapping is unlikely to produce the dense, high stream-order ridges we observe. We hypothesize that a brief period of atmospheric warming caused

top-down melting of cold-based crater wall glaciers during the transition from Noachian climate conditions to conditions more typical of the Hesperian and Amazonian. Recognition and documentation of these features provides specific criteria to search for other examples of past glaciation in the southern highlands in order to further test hypotheses of Mars climate evolution.

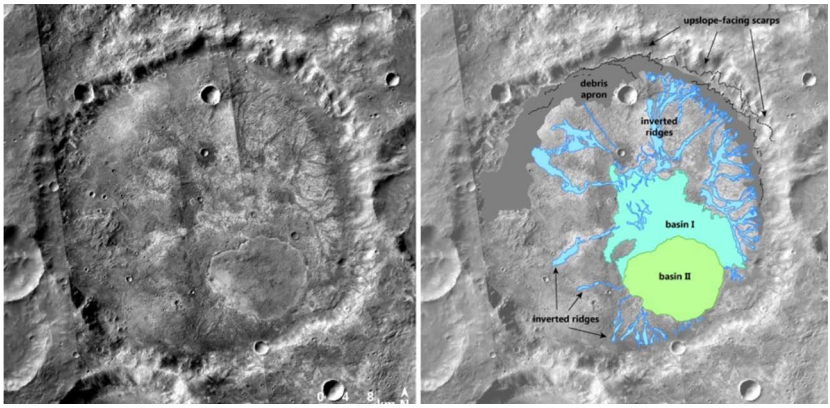

Fig. 2. Crater B and sketch map overlay showing major geologic features. Inverted tributary ridges begin near the crater wall base in association with upslope-facing scarps and debris apron and terminate in two depositional basins. CTX visible mosaic

REFERENCES:

[1] Carr M. H., Head J. W. (2010) EPSL 294.
[2] Laskar J. et al. (2004) Icarus 170.
[3] Berman D. C. et al. (2005) Icarus 178.
[4 Jawin E. R. et al. (2018) Icarus 309.
[5] Berman D. C. et al. (2009) Icarus 200.
[6] Fassett C. I. et al. (2010) Icarus 208.
[7] Craddock R. A., Howard A. D. (2002) JGR 107.
[8] Ramirez R. M., Craddock R. A. (2018) Nature. Geo. 11.
[9] Forget F. et al. (2013) Icarus 222.
[10] Wordsworth R. et al. (2013) Icarus 222.
[11] Fastook J. L., Head J. W. (2015) PSS 106.
[12] Marchant D. R., Head J. W. (2007) Icarus 192.
[13] Irwin R. P. et al. (2018) JGR 123.
[14] Fassett C. I., Head J. W. (2008) Icarus 198.
[15] Goudge T. A. et al. (2015) Icarus 260.

LARGE IMPACT BASIN-RELATED CLIMATIC AND SURFACE EFFECTS ON MARS: ARGYRE BASIN AS A CASE STUDY

A. M. Palumbo, J. W. Head
Department of Earth, Environmental and Planetary Sciences,
Brown University,
Providence RI 02912 USA
(*Ashley_Palumbo@Brown.edu*)

KEYWORDS:
climate, basin, Mars, Noachian

INTRODUCTION:
The collision of large bolides with planets with substantial atmospheres, such as Earth and early Mars, results in significant climatic and surface effects [e. g. 1]. For impacts forming basins >~500 km diameter, these post-impact effects would be global and include [e. g. 2]: (1) transient high atmospheric and surface temperatures, (2) deposition of material that was vaporized by the impact event and subsequently condensed (i. e. terrestrial spherule layer), (3) a transient phase of intense, hot rainfall and (4) surface aqueous alteration, made possible by the hot rainfall and high temperatures. On Mars, the formation of such large basins, including the Hellas, Isidis, and Argyre basins, occurred in the Early to Middle Noachian [3]; such intense, global effects would have occurred only during the earliest parts of Mars history. Additionally, in comparison to similarly aged lunar basins, the Martian basins are significantly more degraded and eroded, possibly due to the more erosive background climate and post-basin formation effects on Mars.

Previous studies have qualitatively [2] and quantitatively [4–9] estimated the effects from large basin-scale impact events on early Mars but lack detailed application to any specific event. We expand upon previous analyses by exploring the climate and surface effects from the formation of the youngest of the large Martian basins, the Argyre basin. We choose to study the youngest of the large basins because the signature would be best preserved and closest to the present-day surface.

ASSESSMENT:
Although the initial 1D studies of basin-scale post-impact effects made critical estimates on the thickness and influence of the spherule layer and induced rainfall rates, durations, and abundances [4], the modeled processes are better treated in 3D and, thus, we rely of the results of 3D analyses [8–9] in our assessment. Specifically, using 3D Global Climate Models (GCMs), Steakley et al. [8] and Turbet et al. [9] revisited post-impact effects for moderate (30, 50, and 100 km diameter bolides) and large (>100 km diameter bolide) impact events, respectively. We utilize the findings of Turbet et al. [9] as a guide because the size of impactors explored by Turbet et al. [9] are the best representation of Argyre-scale effects.

Next, we discuss each of the key post-impact effects, including qualitative and quantitative estimates for the Argyre post-impact effects.

Transient high atmospheric and surface temperatures. The collision of a very large impactor with the surface causes a large energy transfer [10]; substrate and impactor material are ejected, melted, and vaporized. The vaporized component will contain water and silicate-rich material [5]. The presence of this vapor in the atmosphere and associated formation of global clouds would cause atmospheric and surface temperatures to dramatically increase.

Deposition of material that was vaporized by the impact event and subsequently condensed. As the atmosphere begins cooling from the initial very hot state, it will reach the condensation temperature of the silicate-rich material. The material will condense, traverse through the atmosphere, possibly quench during travel, and be deposited onto the surface. On Earth, these deposits are referred to as spherule layers [e. g. 11–13]. The spherule layer from

the Argyre event would have been ~34 m thick [7] and silicate-rich, possibly retaining an olivine signature due to early quenching during traverse through the atmosphere [2]. As on Earth, the texture of this unit would be easily differentiated from surrounding units at the rover scale due to the quenched spherules and welded solid nature.

Initially, the unit is expected to be so hot (possibly >1000 K) [5] that it could cause surface temperatures to remain above freezing for millennia [5] and the thermal interaction with the underlying unit could lead to partial alteration of the underlying unit.

A transient phase of intense, hot rainfall. As the atmosphere continues cooling, it will reach the condensation temperature for water vapor. Impact-induced rainfall from basin-scale impact events could dramatically change the landscape on a relatively short timescale. When considering a reasonable surface water inventory and bolide composition, rainfall rates of up to ~2.6 m/yr could persist continuously for decades [9]; such continuous, high rate rainfall is unprecedented on Earth for such durations [e. g. 14, 15]. Additionally, due to the very high temperatures and atmospheric water vapor concentration, post-impact rainfalls could be characterized by temperatures near the vaporization point [9].

The induced rainfalls have characteristics of a hot, long-lived deluge [2] implying that impact-induced rainfall may have contributed to abundant morphologic and mineralogic alteration of the surface. The morphologic alteration would include smoothing of plains and degradation of crater rims and the mineralogic alteration is discussed next.

Surface aqueous alteration, made possible by the hot rainfall and high surface temperatures. Efficiency of surface aqueous alteration is a balance of (1) interaction with liquid water, (2) temperature, and (3) duration [16]. Although post-impact rainfall and above-freezing temperatures may only persist for decades, the rainfall and atmosphere temperatures would be very high above ambient conditions and, thus, significant aqueous alteration could occur.

IMPLICATIONS:

There are four key implications from this assessment, including: (1) distinguishing the role of impact-induced aqueous alteration from that associated with normal climate conditions, (2) predictions of areas where the spherule layer and alteration products may be observed, (3) the transition from a basin-scale impact-dominated regime to a basin-free regime in Martian climate evolution, and (4) guidelines for exploration and recognition of these impact-related units at rover and sample return scale. In this section, we discuss each of these implications.

Distinguishing the role of impact-induced aqueous alteration from that associated with normal climate conditions. Impact-induced aqueous alteration is predicted to have (1) alteration products in a top-down leaching profile and (2) partial or full alteration of the olivine-rich spherule layer, possibly to Mg-carbonates, located stratigraphically above the basaltic substrate. By identifying locations where these characteristics are observed, we can identify areas that may contain an aqueous alteration signature from post-impact conditions, as opposed to ambient climate conditions.

Predictions of areas where the spherule layer and alteration products may be observed. Because the Argyre basin is the youngest of the large basins, the spherule layer and aqueous alteration products that were produced from impact-induced rainfall are preserved closest to the surface. Further, because the post-impact effects from the formation of Argyre were global, the spherule layer and alteration products should be observable on Noachian-aged terrains that have not experienced abundant subsequent morphologic and mineralogic alteration.

An olivine-rich signature can be used to guide identification of possible spherule units [2] and subsequent analyses of these areas to determine if they are in fact spherule units should include (1) assessment of thermal inertia to determine if the unit is welded solid, which we expect for a spherule

unit, or, for example, more consistent with a loose, unconsolidated volcanic ash layer (as has been proposed to be a source of olivine-rich units on Mars [17]), (2) determination of whether aqueous alteration of the unit is consistent with overland flow, and (3) a relatively consistent thickness, as is expected for a spherule unit. If these criteria are met, we may conclude that an identified unit is in fact formed from post-impact effects and evidence for aqueous alteration in the area, both of the olivine-rich unit and underlying substrate, may be attributed to impact-induced rainfall, not ambient background climate conditions. One such area that may satisfy the above criteria includes the olivine-rich unit in NE Syrtis, which may be explored by the NASA Mars 2020 Perseverance rover and *in-situ* observations can further test this hypothesis.

The transition from a basin-scale impact-dominated regime to a basin-free regime in Martian climate evolution. Post-impact effects, specifically impact-induced rainfall, offer an explanation for smoothing of plains, degradation of crater rims, and surface aqueous alteration in the Early to Middle Noachian; these observations may not be evidence for a long-lived "warm and wet" Noachian climate. Additionally, the erosive capability of these effects could be responsible for much of the enhanced erosion of Martian basins in comparison to lunar basins.

Guidelines for exploration and recognition of these impact-related units at rover and sample return scale. While orbital observations can provide important first-order characterization of relevant units, *in-situ* observations at the rover and sample return scale will provide critical information to determine if a candidate spherule layer (identified in orbital data) is in fact a spherule unit. For example, *in-situ* and laboratory measurements of morphology at the grain scale and precise ages would determine whether the unit is consistent with a unit formed from one of the large Martian basins. For these reasons, we look forward to the Mars 2020 mission and the possibilities that a spherule unit may be observed *in-situ* and a sample may ultimately be returned to Earth.

CONCLUSIONS:

Our investigation of the post-impact effects from the formation of the Argyre basin suggest that these effects, including the spherule layer and aqueous alteration products, should be preserved at or very near the surface and, as a result, are an interesting topic for future study and exploration.

ACKNOWLEDGEMENTS:

This work was supported by NASA Headquarters under the NASA Earth and Space Science Fellowship Program for AMP; Grant 90NSSC17K0487.

REFERENCES:

[1] Collins et al. (2005), MAPS 40, p817.
[2] Palumbo and Head (2018), MAPS 53, p687.
[3] Fassett and Head (2011), Icarus 211, p1204.
[4] Segura et al. (2002), Science 298, p1977.
[5] Segura et al. (2008), JGR 113, E11007.
[6] Segura et al. (2012), Icarus 220, p144.
[7] Toon et al. (2010), AREPS 28, p303.
[8] Steakley et al. (2019), Icarus 330, p169.
[9] Turbet et al. (2020), Icarus 335, p113419.
[10] Melosh (1989), Oxford Univ Press.
[11] Glass and Simonson (2012), Elements 8, p43.
[12] Johnson et al. (2016), Icarus 271, p350.
[13] Johnson and Melosh (2012), Icarus 217, p416.
[14] Jennings (1950), Monthly Weather Review.
[15] Zhang et al. (2013), J Hydrometeor 14, p1952.
[16] Bishop et al. (2017), LPSC 2018, abs1804.
[17] Kremer et al. (2019), Geology 47, p677.

ANALYSIS OF H_2O TRANSMISSION SPECTRA IN THE MARTIAN ATMOSPHERE AS MEASURED BY THE ACS-TIRVIM SOLAR OCCULTATIONS

E. Fedorova[1,2], D. Belyaev[1,2], N. Ignatiev[1], A. Shakun[1], O. Korablev[1,2], A. Fedorova[1,2], F. Montmessin[3], A. Trokhimovskiy[1]

[1] *Space Research Institute* (*IKI*), *Moscow*, *Russia*

[2] *Moscow Institute of Physics and Technology* (*MIPT*), *Dolgoprudny*, *Russia*

[3] *LATMOS/CNRS*, *Guyancourt*, *France*

KEYWORDS:
Martian atmosphere, water vapor, solar occultation, ACS, ExoMars, spectroscopy

INTRODUCTION:

Study of the hydrological cycle on Mars is of fundamental importance, and nowadays there is a number of sensitive experiments concerning the water distribution on the planet. Measurements of H_2O vertical profiles depending on temperature and dusty seasons allow to research mechanisms of the water vapor transport into the upper atmosphere (mesosphere and thermosphere). Recently, such an analysis discovered a rise of water content up to altitudes of 70–100 km and even its saturation during the global dust storm in 2018 [1]. This phenomenon increases a potential for H_2O escape from Mars.

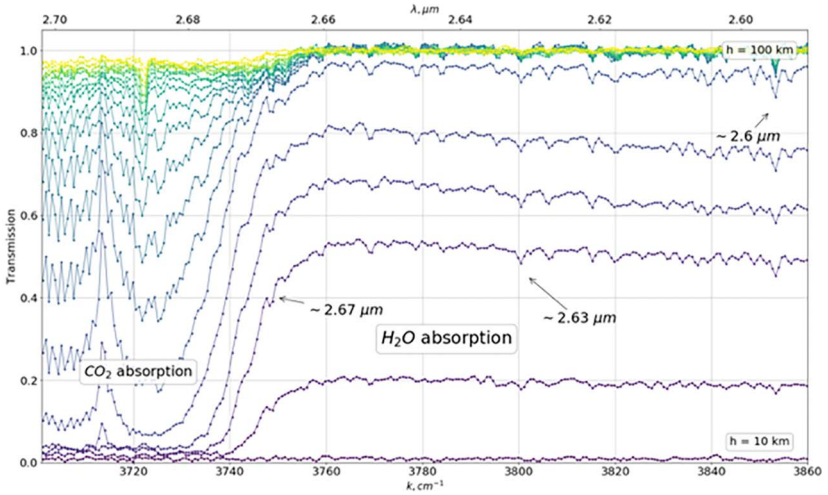

Fig. 1. Transmission spectra obtained from ACS-TIRVIM observations (orbit 09FC01, altitude range 10-100 km)

In this work, we present an analysis of the water transmission spectra obtained from the ACS-TIRVIM solar occultation observations. TIRVIM is the thermal infrared channel (2–17 μm spectral range) of the Atmospheric Chemistry Suite (ACS), which has been operating onboard the ExoMars Trace Gas Orbiter (TGO) since April 2018 [2]. While the solar radiance is occulted by the atmosphere in the instrument field of view the H_2O absorption around the strong 2.65 μm band can be measured by TIRVIM. Analysis of the transmission with a spectral resolution of ~0.1 cm^{-1} makes it possible to determine the water vapor vertical distribution at the altitude range from 10 to 100 km. Calculation of spectra was made on a basis of HITRAN 2016 database [3] taking into account H_2O lines broadening in the CO_2-atmosphere [4]. In parallel, calibration of the measured transmission spectra by wavelength was performed with the help of the solar spectrum. We present preliminary re-

sults of the retrieved H_2O concentrations by a fitting of the modeled spectra to the measured ones in the spectral range of 2.65–2.7 μm.

The H_2O spectral analysis is supported by the RSF grant #20-42-09035.

REFERENCES:

[1] Fedorova A. A. et al. Stormy water on Mars: The distribution and saturation of atmospheric water during the dusty season // Science. 2020. eaay9522.
[2] Korablev O. I. et al. The Atmospheric Chemistry Suite (ACS) of three spectrometers for the ExoMars 2016 Trace Gas Orbiter // Space Sciences Rev. 2018. V. 214. P. 7.
[3] Gordon I. E. et al. The HITRAN2016 molecular spectroscopic database // J. Quantitative Spectroscopy and Radiative Transfer. 2017. V. 203. P. 3–69.
[4] Gamache R. R. et al. A spectral line list for water isotopologues in the 1100–4100 cm^{-1} region for application to CO2-rich planetary atmospheres. // J. Molecular Spectroscopy. 2016. V. 326. P. 144–150.

GRAVITY WAVE ACTIVITY IN THE MARTIAN ATMOSPHERE AT ALTITUDES 10–160 km FROM ACS/TGO SOLAR OCCULTATIONS

E. D. Starichenko[1,2], D. A. Belyaev[1,2], A. S. Medvedev[3], A. A. Fedorova[1], O. I. Korablev[1], F. Montmessin[4], A. Trokhimovskiy[1]

[1] *Space Research Institute of the Russian Academy of Sciences, Moscow, Russia*

[2] *Moscow Institute of Physics and Technology, Dolgoprudniy, Russia*

[3] *Max Planck Institute for Solar System Research, Göttingen, Germany*

[4] *LATMOS/IPSL, UVSQ Université Paris-Saclay, UPMC Univ. Paris 06, CNRS, Guyancourt, France*

KEYWORDS:
Gravity waves, potential energy, Martian atmosphere, Atmospheric Chemistry Suite, Trace Gas Orbiter, solar occultation

INTRODUCTION:
Atmospheric gravity waves (GW) are periodic oscillations of air masses that manifest themselves as fluctuations of density, temperature, pressure and other fields. We derive such characteristics of GW as Brunt-Väisälä frequency, potential energy, amplitude of perturbations and fluxes from vertical distributions of density and temperature.

We report on the first results of GW retrievals in the Martian atmosphere from the solar occultation experiment performed by the Atmospheric Chemistry Suite (ACS) onboard the ExoMars Trace Gas Orbiter TGO [1]. This is the first time when temperature and density profiles were measured simultaneously in almost the entire atmosphere. The ACS is a set of infrared spectrometers operating on the orbit of Mars since April 2018. The mid-infrared channel (ACS-MIR) is a cross-dispersion spectrometer covering the 2.3–4.2 μm spectral range with the resolving power reaching ~30 000. In the solar occultation mode, the spectrometer can observe thin layers of the Martian thermosphere and lower atmosphere in strong (e. g. 2.7 and 4.3 μm) and weak (about 3 μm) CO_2 absorption bands with vertical resolution ~1 km. The near-infrared channel (ACS-NIR) is another echelle spectrometer working in the 0.73–1.6 μm spectral range with the resolving power ~25 000 [2]. Due to the high resolution, these instruments (operating simultaneously) allow for resolving the temperature, pressure and density fluctuations at the unprecedented altitude range from 10 to 160 km. The dataset we present consists of more than 100 vertical profiles derived at seasons from the second half of MY34 to the first half of MY35 in the both Martian hemispheres. The data analysis in IKI is supported by the RSF grant No, 20-42-09035.

REFERENCES:
[1] Korablev O., Montmessin F. et al. The Atmospheric Chemistry Suite (ACS) of three spectrometers for the ExoMars 2016 Trace Gas Orbiter // Space Sciences Rev. 2018. V. 214. Art. 7. 62 p. doi:10.1007/s11214-017-0437-6.

[2] Fedorova A., Montmessin F. et al. Stormy water on Mars: The distribution and saturation of atmospheric water during the dusty season // Science. 2020. V. 367. Iss. 6475. P. 297–300. doi:10.1126/science.aay9522.

ANALYSIS OF THE MAGNETIC FIELD DATA OF MARS

A. M. Salnikov[1], A. V. Batov[1,2,3], T. V. Gudkova[2], I. E. Stepanova[2,3]
[1] *V. A. Trapeznikov Institute of Control Sciences RAS, 65 Profsoyuznaya street, Moscow, Russia* (*salnikov@ipu.ru*)
[2] *Schmidt Institute Physics of the Earth RAS, B.Gruzinskaya, 10, Moscow, Russia*
[3] *Sirius University of Science and Technology, 1 Olympic Ave, Sochi, Russia*

KEYWORDS:
Mars, magnetic field, regularization, approximation, inverse problem

INTRODUCTION:
Mars has no active magnetic dynamo field today, but it possesses a remanent magnetic field that may reach several thousand nanoteslas locally. There is a wealth of maps and models of the magnetic field [1–4]. Recently InSight (Interior Exploration using Seismic Investigations, Geodesy, and Heat Transport) lander has provided new magnetic field strength and direction measurements. It turned out that the InSight landing site's magnetic field is ten times stronger than predicted by satellite-based models [5]. This knowledge indicates that the magnetic field of the planet needs further study and analysis.

THE METHOD:
When reproducing an estimated magnetic field, physical source models usually contain a set of simple entities (dipoles, prisms, icosahedrons, or spherical caps) spatially distributed in the Martian crust. For example, we can represent magnetic spectra using a spherical shell of randomly oriented point dipoles [6]. Notice that the majority of the works use equivalent source dipoles (e. g. [1, 2, 8]).

We use one of the variants of the linear integral representations method named S-approximations method to look at the magnetic field sources, positioned beneath the surface of the planet at different depths. It is one of the effective methods for interpreting gravimagnetic exploration data, based on the fundamental formula of the theory of harmonic functions [7]. The essence of the method is that if the components of the magnetic field are known (in our case, we know the values of magnetic potential on a given relief), then the field potential can be represented as the sum of single and double layers created by a combination of carriers located below a given relief. In the general case, the carriers of the single and double layers can be surfaces (or their pieces), curves (or their parts), or three-dimensional bodies. We have examined the approximation construction of the method for the case when the carriers of both the single and double layers are horizontal planes. As a small region can be considered a horizontal surface, Mars' ellipticity is not taken into account. Specifically, when processing the interpretation data, we use carriers located on two horizontal planes. We also construct the magnetic field's analytic continuations upward and downward for a small selected region of the planet. The features of magnetic anomalies are smoothed when we continue them upward and are increased when we continue them downward, as the theory suggests.

RESULTS:
For calculations in the present work, we use the model developed by Langlais with colleagues [8], which has a spatial resolution of ~160 km at the surface, corresponding to spherical harmonic degree 134. It shows small scales and distinct features, which can be associated with geological signatures [8].

We calculate the depths of the magnetic field sources that give the best match with the observed values for our method, given that the result mainly depends on the selected region and the thickness of the crust in this region [9].

For the entire planet, we use a regional version of the S-approximation method, where the carriers of both the single and double layers are spheres of specific radii instead of planes.

ACKNOWLEDGEMENTS:
The study was performed under a government contract of the Schmidt Institute of Physics of the Earth of the Russian Academy of Sciences. The reported study was funded by RFBR, project number 19-35-51014.

REFERENCES:
[1] Purucker M. E., Ravat D., Frey H., Voorhies C., Sabaka T., Acuña M. H. An altitude-normalized magnetic map of Mars and its interpretation // Geophysical Research Letters. 2000, V. 27. P. 2449–2452. https://doi.org/10.1029/2000GL000072.
[2] Langlais B., Purucker M. E., Mandea M. Crustal magnetic field of Mars // J. Geophysical Research. 2004. V. 109. Art. E02008. https://doi.org/10.1029/2003JE002048.
[3] Arkani-Hamed J. Magnetization of Martian lower crust: Revisited // J. Geophysical Research. 2007. V. 112. Art. E05008. https://doi.org/10.1029/2006JE002824.
[4] Morschhauser A., Lesur V., Grott M. A spherical harmonic model of the lithospheric magnetic field of Mars // J. Geophysical Research: Planets. 2014. V. 119. P. 1162–1188. https://doi.org/10.1002/2013JE004555.
[5] Johnson C. L., Mittelholz A., Langlais B. et al. Crustal and time-varying magnetic fields at the InSight landing site on Mars // Nature. Geoscience. 2020. V. 13. P. 199–204. https://doi.org/10.1038/s41561-020-0537-x.
[6] Lewis K. W., Simons F. J. Local spectral variability and the origin of the Martian crustal magnetic field // Geophysical Research Letters. 2012. V. 39. Art. L18201. https://doi.org/10.1029/2012GL052708.
[7] Stepanova I. E., Gudkova T. V., Batov A. V. Application of the modified method S- and F-approximations for the study of density anomalies under Hellas Planitia // 12th Intern. Conf. Management of large-scale system development (MLSD). Moscow, Russia, 2019. https://doi.org/10.1109/MLSD.2019.8911100.
[8] Langlais B., Thébault E., Houliez A., Purucker M. E., Lillis R. J. A new model of the crustal magnetic field of Mars using MGS and MAVEN // J. Geophysical Research: Planets. 2019. V. 124. P. 1542–1569. https://doi.org/10.1029/2018JE005854.
[9] Wieczorek M. A. et al. Global Crustal Thickness Modeling of Mars Using InSight Seismic Constraints // 51st Lunar and Planetary Science Conf. Woodlands, Texas. LPI Contribution. 2020. No. 2326. id. 1393.

EFFECT OF THIRD- AND HIGHER-ORDER TIDE ON THE ESTIMATE OF DISSIPATIVE FACTOR FOR MARS

T. V. Gudkova[1], V. N. Zharkov[1], A. V. Batov[1,2]
[1] *Schmidt Institute Physics of the Earth RAS, B. Gruzinskaya, 10, Russia* (*gudkova@ifz.ru*)
[2] *Institute of Control Sciences of RAS, 65 Profsoyuznaya street, Moscow, Russia*

KEYWORDS:
dissipative factor, attenuation, seismic waves, interior structure, Mars

INTRODUCTION:
The seismic experiment is going on Mars [1, 2].The seismic experiment is to insert some corrections to the model distribution of the dissipative function. At present the knowledge of the model dissipative factor of Martian interiors is of importance for the interpretation of seismic recordings. The values of the dissipative factor of Martian interiors were discussed from physical point of view in [3], where the distribution Q_μ in PREM was taken as a trial one. In [4] assuming that on the P–T plane, the areotherms and the geotherm are rather close, we took the four-layers piecewise constant distribution $Q_\mu(l)$ from QLM9 model [5] up to the depth of $l = 670$ km as a trial zero approximation, and adapted it to the conditions of Martian interiors. In the present study we calculate the correction, which the third- and higher-order tide introduce into the estimate of Q factor for Mars.

INTERIOR STRUCTURE MODEL:
The trial model of interior structure of Mars is based on the cosmochemical WD-model [6] and the laboratory high pressure-temperature experiments along a trial areothern and WD composition [7, 8]. The moment of inertia and Love numbers of model M_50 (crust 50 km, core radius 1821 km) [4], which is taken for calculations, is in agreement with the recent data [9, 10] ($I = 0.3639$, k_2^e (elastic) $= 0.162$). Higher orders elastic Love numbers for this model are: $k_3^e = 0.051$ ($i = 3$), $k_4^e = 0.023$ ($i = 4$), $k_5^e = 0.014$ ($i = 5$).

TRIAL DISTRIBUTION OF THE DISSIPATIVE FACTOR IN THE INTERIORS OF MARS:
For Mars there is the only constraint on the distribution of the dissipative factor of the interiors $Q_\mu(l)$, obtained from observations, this is the secular acceleration of its satellite Phobos. The secular acceleration is directly linked to the tidal dissipation [11, 12]

$$\frac{1}{n}\cdot\frac{\mathrm{d}n}{\mathrm{d}t} = -3n\alpha\left[-3\frac{k_2}{2Q_2}\left(\frac{R}{\alpha}\right)^5 - 6\frac{k_3}{3Q_3}\left(\frac{R}{\alpha}\right)^7 - 10\frac{k_4}{4Q_4}\left(\frac{R}{\alpha}\right)^9 - 15\frac{k_5}{2Q_5}\left(\frac{R}{\alpha}\right)^{11} + \ldots\right],$$

where α is mass ratio of Phobos and Mars, R is the mean radius of Mars, α is the orbital radius of Phobos.

Love numbers are functional of the shear modulus $\mu_0(r)$, the bulk modulus $K_0(r)$ and the density $\rho_0(r)$. The variation of tidal Love numbers k and h, and the tidal lag from Phobos ε_2 [13]

$$\delta h = \int_0^1 \left\{\frac{h_\mu \mu_0}{Q_\mu} + \frac{h_K K_0}{Q_K}\,\mathrm{d}x\right\}, \quad \delta k = \int_0^1 \left\{\frac{k_\mu \mu_0}{Q_\mu} + \frac{k_K K_0}{Q_K}\,\mathrm{d}x\right\},$$

where $x = r/R$, xc is the core radius, h_μ, h_K, k_μ и k_K — functional derivatives of k and h over m and K. Let us denote $\alpha_1 = k_\mu\mu_0$, $\beta_1 = k_K K_0$, $\alpha_2 = h_\mu\mu_0$, $\beta_2 = h_K K_0$.

$$\varepsilon_2 = \frac{1}{2\overline{Q}_{t_2}} = \frac{1}{k_2}\int_{x_c}^1 k_\mu(x)\frac{\mu_0(x)}{Q_\mu(x,\sigma_t)}\,\mathrm{d}x,$$

These functions for the second- and higher-orders are calculated for M_50 model and drawn in the Figure 1. They show fraction of Q_μ of the each layer

to $\overline{Q}_{t_2}$. As seen from the Figure 1, the higher the degree, the more important the upper layers are.

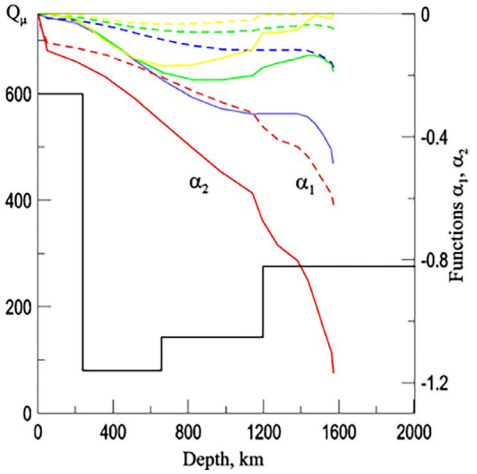

Fig. 1. The distribution of the dissipative factor $Q_\mu(l)$ in the crust and the upper mantle of the Earth in the QLM9 model [5]adapted to the depths of Mars (solid black line) and contribution of each layer to the final value of Q: functions $\alpha_1 = k_\mu\mu_0$, $\alpha_2 = h_\mu\mu_0$ for M_50 model as a function of depth for different orders i: red — $i = 2$. blue — $i = 3$. green — $i = 4$. yellow — $i = 5$.

The dissipative factor $Q_m(l)$, the shear modulusm (l) and tidal Love number of the planet k_2 depend on frequency (the period of Phobos rotation around Mars, $T_{2Ph} = 5.55\ h = 2{\cdot}10^4$ s, the period of the solar semidiurnal tidal wave$T_{2S} = 12$ h 19 min $\approx 4.434{\cdot}10^4$ s). Let σ_0, σ_1 and σ_2 be the frequencies at the periodof1s, 1 h = $3.6{\cdot}10^3$ s and the basic Phobos tidal wave of period ~$2{\cdot}10^4$ s, respectively. The models of Q and shear modulus dependence on frequency are listed in the Table. The index n in the power dependence of $Q_\mu(l)$ is in the range of ~0.1–0.3.

Table 1. The dependence of Q and shear modulus μ on frequency [14–16]

T	1s	1h=3.6x10³ s	5.5h=2x10⁴s	12.19h=44340s
	σ_0	σ_1	σ_2	σ_3
			Phobos period	Solar tide

1. Q does not depend on frequency,

Lomnitz model

$$\frac{\mu_0(\sigma_1)}{\mu_0(\sigma_0)} = 1 - \frac{2}{\pi Q_\mu}\ln\frac{\sigma_0}{\sigma_1}$$

2 and 3 Weak dependence of Q on frequency, n~0.1-0.2

$$Q_\mu(\sigma_2) = Q_\mu(\sigma_1)\left(\frac{\sigma_2}{\sigma_1}\right)^n$$

$$\frac{\mu_0(\sigma_2)}{\mu_0(\sigma_1)} = 1 - \frac{1}{Q_\mu(\sigma_1)}\left[\left(\frac{\sigma_1}{\sigma_2}\right)^n - 1\right]ctg\frac{n\pi}{2}$$

The calculations at the transformation of a primary distribution of $Q_\mu(l)$ in the seismic range of periods to the Phobos period of 5.55 h were performed for the values of index n between 0.1 and 0.3.

In [4] it was shown that the values of $\overline{Q}_{t_1}$ for interior structure model of Mars M_50 — 96.2 — is rather close to the observed value 91.9±3.3 for n = 0.1.

The increasing of n leads to smaller value of the dissipative factor, while the correction for the third- and higher-orders tide leads the increase of the obtained result. Taking into account the uncertainty in values of n, the effect of third- and higher-orders tide allows to accept the estimate of the dissipative factor, calculated for the second-order tide.

ACKNOWLEDGEMENTS:
The study was performed under a government contract of the Schmidt Institute of Physics of the Earth of the Russian Academy of Sciences

REFERENCES:

[1] Lognonne P., Banerdt W. B., Giardini D. et al. SEIS: Insight's Seismic Experiment for internal structure of Mars // Space Sciences Rev. 2019. V. 215(1). P. 12.
[2] Giardini D., Lognonné P., Banerdt W. B. et al. The seismicity of Mars // Nature. Geoscience. 2020. https://doi.org/10.1038/s41561-020-0539-8.
[3] Lognonné Ph., Mosser B. Planetary seismology // Surv. Geophys. 1993. V. 14. P. 239–302.
[4] Zharkov V. N., Gudkova T. V., Batov A. V. On estimating the dissipative factor of the Martian interior // Solar System Research. 2017. V. 51. P. 479–490.
[5] Lawrence J. F., Wysession M. E. QLM9: A new radial quality factor (Q_μ) model for the lowermantle // Earth and Planetary Science Letters. 2006. V. 241. P. 962–971.
[6] Wänke H., Dreibus G. Chemistry and accretion history of Mars // Philosophical transactions of the Royal Society of London. 1994. V. 349. P. 285–293.
[7] Bertka C. M., Fei Y. Mineralogy of the Martian interior up to core-mantle boundary pressures // J. Geophysical Research. 1997. V. 102. No. 3. P. 5251–5264.
[8] Bertka C. M., Fei Y. Density profile of an SNC model Martian interior and the moment-of-inertia factor of Mars // Earth and Planetary Science Letters. 1998. V. 157. P. 79–88.
[9] Konopliv A. S., Park R. S., Folkner W. M. An improved JPL Mars gravity field and orientation from Mars orbiter and lander tracking data // Icarus. 2016. V. 274. P. 253–260.
[10] Genova A., Goossens S., Lemoine F. G. et al. Seasonal and static gravity field of Mars from MGS, Mars Odyssey and MRO radio science // Icarus. 2016. V. 272. P. 228–245.
[11] Smith J. C., Born G. H. Secular acceleration of Phobos and Q of Mari // Icarus, 1976. V. 27 (1). P. 51–53.
[12] Jacobson R. A., Lainey V. Martian satellite and ephemerides // Planetary and Space Science. 2014. V. 102. P. 35–44.
[13] Zharkov V. N., Gudkova T. V. Construction of Martian Interior Model // Solar System Research. 2005. V. 39. No. 5. P. 343–373.
[14] Zharkov V. N., Gudkova T. V., Molodensky S. M. On models of Mars' interior and amplitudes of forced nutations. 1. The effects of deviation of Mars from its equilibrium state on the flattening of the core-mantle boundary // Physics of the Earth and Planetary Interiors. 2009. V. 172. P. 324–334.
[15] Akopyan S. Ts., Zharkov V. N., Lubimov V. M. Theory of attenuation of torsional oscillations of the Earth // Phys. Solid Earth. 1977. V. 8. P. 3–11.
[16] Molodensky S. M., Zharkov V. N. On Chandler wobble and frequency dependence Qmof Earth' mantle // Izv. AN SSS. Fizika Zemli. 1982. No. 4. P. 3–16. (in Russian).

FRESH MARTIAN IMPACT CLUSTERS

E. Podobnaya, O. Popova, D. Glazachev
Institute for Dynamics of Geospheres RAS,
Moscow, *Russia*

KEYWORDS:
Meteoroids, Mars, craters, impacts, cluster, fragmentation, strewn fields

INTRODUCTION:
In recent years, about 700 fresh dated meteoroid impact sites have been discovered on Mars [1–3]. Meteoroid impacts resulted in the formation of single craters and crater fields, with crater sizes up to 50 m. Meteoroids, which produced the craters, are of meters-scale, similar objects are observed on the Earth as superbolides [4]. Due to the more rarefied Mars atmosphere (in comparison with the Earth) falling meteoroids are less destroyed. Nevertheless, near 50 % of meteoroids are fragmented in the Martian atmosphere and are forming crater clusters. The comparison of Martian and terrestrial fireballs allows to suggest 40–50 % of terrestrial meteoroids would lead to the formation of crater fields on Mars [4]. The study of craters on Mars allows us to study the fragmentation details that cannot be detected in terrestrial conditions.

CRATER CLUSTERS AND THEIR DESCRIPTION:
The paper is dealing with craters strewn fields. Strewn fields are often described by an ellipse, the direction of the main axis of the ellipse coincides with the direction of meteoroid flight. This description allows to estimate roughly trajectory azimuth and entry angle based on the ellipse parameters. The study of these strewn fields permits to determine the details of meteoroids destruction in the atmosphere and the meteoroid properties [5]. In this paper we used different methods for searching minimal square ellipse, describing crater strewn field. The first method is statistical ellipse covering 90 % of points, made with function in Wolfram Mathematica. Next one is an average from 400 ellipses covering 90 % of randomly selected data points from cluster, obtained using the covariance matrix. Finally, third is also average from set of 400 ellipses, which are evaluated by method from [6]. All methods were aimed to find ellipses covering 90 % of craters of the cluster, as it is suggested that observed crater cluster may be incomplete. Obtained estimates were compared with previous results [3].

In general, all considered methods results in approximately the same value of the meteoroid trajectory azimuth, the difference is no more than 15° in most cases. Meteoroid entry angle depends on the ratio of scattering ellipse radiuses, its estimations for different methods in most cases do not differ more than on 15° from initial estimation [3]. Comparison of scattering ellipses (by the number of craters covered and by area) obtained by various methods showed that considering methods give a scattering ellipse with an area of 1.5–2 times larger than the area obtained from initial estimates [3].

REFERENCES:
[1] Malin M. C., Edgett K. S., Posiolova L. V., McColley S. M., Noe Dobrea E. Z. Catalog of New Impact Sites on Mars Formed May 1999–March 2006. Malin Space Science Systems / Inc., San Diego, California. 2006.
[2] Daubar I. J., McEwen A. S., Byrne S., Kennedy M. R., Ivanov B. The current Martian cratering rate // Icarus. 2013. V. 225. No. 1. P. 506–516.
[3] Daubar I. J., Banks M. E., Schmerr N. C., Golombek M. P. Recently Formed Crater Clusters on Mars // J. Geophysical Research: Planets. 2019. V. 124. No. 4. P. 958–969.
[4] Hartmann W. K., Daubar I. J., Popova O., Joseph E. C. Martian cratering 12. Utilizing primary crater clusters to study crater populations and meteoroid properties // Meteoritics and Planetary Science. 2018. V. 53. No. 4. P. 672–686.
[5] Ivanov B., Melosh H. J., McEwen A. New impact craters and meteoroid densities on Mars // Proc. EPSC-DPS Joint Meeting. Nantes, France. 2011. P. 786.
[6] Oliker N., Ostfeld A. Minimum volume ellipsoid classification model for contamination event detection in water distribution systems // Environmental modelling and software. 2014. V. 57. P. 1–12.

AUTOMATED DENOISING FOR MINERAL IDENTIFICATION ON HYPERSPECTRAL DATA

V. Payet, J. Flahaut, G. Ito, M. Barthez, S. Breton
Centre de Recherches Pétrographiques et Géochimiques (*CRPG*),
CNRS UMR7358/*Université de Lorraine*,
15 rue Notre-Dame des Pauvres, *54500 Vandoeuvre-lès-Nancy*,
France (*payet.diaz.vincent@outlook.com*)

KEYWORDS:
denoising, hyperspectral imagery, mineralogy, data processing, algorithm

INTRODUCTION:
Mineral identification with VNIR (visible-near infrared) hyperspectral image cubes often relies on the calculation of spectral criteria (e. g., band depths), which can be biased by noise. Noise can mask shallow mineral absorption bands such as the 1.3 µm absorption band, typical of feldspar minerals [1], tentatively identified recently on Mars CRISM (the Compact Reconnaissance Imaging Spectrometer for Mars) hyperspectral data. The present study aims to develop a user-friendly Python tool called *Mineral Recognizer* to denoise hyperspectral signal and compute spectral criteria on large multispectral or hyperspectral data. *Mineral Recognizer* can dynamically implement customized denoising and spectral criteria methods for multiple datasets and planets, making it more flexible than generic tools.

DATA:
Mineral Recognizer has been developed to read and write ENVI files and ASCII single spectra files. As of today, the routine can process Mars CRISM, Earth Hyperion and Moon Mineralogy Mapper (M3) datasets, as well as single spectrum acquired with laboratory instruments such as the ASD Fieldspec4 point spectrometer [e. g., 2, 3, 4].

DENOISING METHODS:
Five denoising methods have been implemented in the *Mineral Recognizer* program, using statistical or signal processing technologies. In a graphical interface, the user is prompted the wavelength range to be used, the denoising method to be applied (and related parameters) and the output directory. The user may also decide to remove the spectral continuum (which is commonly done for lunar data as they are strongly affected by space weathering [5]) using the upper convex hull approach.

Ordinary kriging
Ordinary kriging is a geostatistical interpolation method giving the best-unbiased estimation of intermediate values. A statistical process, defined by the chosen variogram, models the interpolated values. Linear (non-stationary) and Hole-effect (stationary) variogram models were selected after several phases of testing on both CRISM and M3 spectra. Denoising 1D-spectra with kriging does not need to assume the domain stationarity hypothesis but it does require an estimation of the noise range in spectral domain. Kriging is the most precise denoising method implemented in *Mineral Recognizer*. It is however less adapted to batch processing of various data because of the process's slowness and high sensitivity to the noise characteristics.

Wiener filter
Wiener filter is a linear signal filter used to estimate a random process by linear-time invariant filtering. The Wiener filter minimizes the mean square error between the random process and the desired process. The desired process is chosen as based on the assumed signal-to-noise ratio provided by the user. Wiener filter is a precise method with a moderate processing time.

Natural spline
Natural spline is a piecewise polynomial interpolation. The number of nodes, the number of divisions, and a polynomial degree need to be defined. This denoising method is mildly precise but it runs fast.

Sliding median

Sliding median consists of calculating a median for each point within a fixed size-sliding window. This method is the fastest method available on the *Mineral Recognizer* but it is also generally the least accurate.

APPLICATION ON CRISM HYPERSPECTRAL DATA FOR FELDSPAR BEARING ROCKS IDENTIFICATION:

Mineral Recognizer has been developed aiming to facilitate feldspar detections on Mars and to better constrain Mars geological history [2]. Denoising directly impacts spectra geometry, and thus, it impacts the result of mineral criteria calculation. Figure 1 represents denoising results for different methods on a CRISM feldspar bearing spectrum.

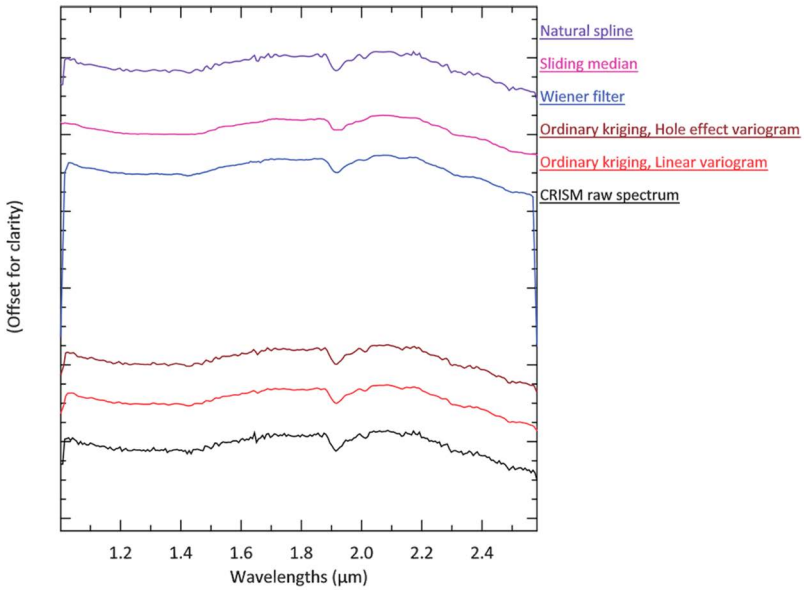

Fig. 1. CRISM reflectance spectrum with a 1.3 µm absorption band. Comparison between raw spectrum and denoised spectra

LIMITATIONS AND FURTHER APPLICATIONS:

Mineral Recognizer allows denoising and criteria on large datasets, improving mineral detection. However, denoising a large dataset can induce biases and requires a manual check of detections. The *Mineral Recognizer* workflow must be applied after atmospheric, photometric and geometric corrections. *Mineral Recognizer* could be further improved by implementing the capability to read and write new data types, new denoising methods and more complex criteria algorithms. Additionally, data learning could be developed to collect data and improve mineral identification using methods other than the spectral criteria method.

REFERENCES:

[1] Carter J., Poulet F. (2013). Nature. Geoscience, 6, 1008–1012.
[2] Flahaut J. et al. (2020), this meeting.
[3] Ito G. et al. (2020), this meeting.
[4] Barthez M. et al. (2020), this meeting.
[5] Adams ., McCord T. (1970), Geochimica et Cosmochimica. Acta Suppl., 3, 1937–1945.

VNIR SPECTROSCOPIC ANALYSIS OF ANALOGUE FELDSPATHIC ROCKS AS A REFERENCE FOR THE INTERPRETATION OF MARS DATA

M. Barthez[1,2], J. Flahaut[1,2], G. Ito[1,2], M. Guitreau[3,4], V. Payet[1,2], R. Pik[1,2]
[1] *CRPG, CNRS UMR 7358*
[2] *Université de Lorraine, 54500 Vndoeuvre-lès-Nancy, France* (*marie.barthez5@etu.univ-lorraine.fr*)
[3] *LMV, CNRS UMR 6524*
[4] *Université Clermont Auvergne, 63178 Aubière, France*

KEYWORDS:
Mars, feldspar minerals, feldspathic rocks, VNIR spectroscopy, spectral libraries, CRISM

INTRODUCTION:
New feldspar detections made with visible-near infrared (VNIR) spectroscopy on Mars [1], raise questions on the nature of the rocks involved and the magmatic processes responsible for their formation. These detections show a 1.3-micron absorption band which has been so far interpreted as anorthosites containing more than 90 % plagioclase based on lunar studies [2]. However, these studies are based on VNIR spectra acquired in the laboratory, on binary mixtures of powders, containing Ca-plagioclase feldspar mixed with a mafic mineral such as olivine or pyroxene [3]. Similar laboratory spectra of 'pure' mineral powders are gathered in the USGS spectral library [4].

This contribution presents our laboratory results regarding VNIR spectra measurements of several (uncrushed) terrestrial rocks containing feldspars of various compositions, in various amounts, and with different grain sizes. In order to select possible analogue rock candidates, we study how all these factors influence the spectral response and in which cases the 1.3-micron band can be reproduced. Finally, the sparse detections that have been recently made in the Valles Marineris region of Mars are compared with our library results and discussed.

METHODS:
The objective of our study is to use VNIR reflectance spectroscopy to create a new reference spectral library containing reflectance spectra acquired on uncrushed terrestrial feldspathic rocks. Over 40 rocks of various types (volcanic, plutonic and metamorphic) were analyzed for this purpose.

Reflectance spectra of this rock collection was measured with an ASD Fieldspec4 spectrometer in our laboratory. This instrument operates in three different wavelength ranges (VNIR, SWIR 1 and SWIR 2), from 0.35 µm to 2.5 µm, with a spectral resolution between 3 and 8 nm. The optical fiber allows to collect spectra with or without accessories such as contact probe, or Muglight ASD, provided an artificial halogen light source.

In parallel, we analyzed Mars VNIR hyperspectral remote sensing data from the CRISM instrument (Compact Reconnaissance Imaging Spectrometer for Mars) onboard MRO (Mars Reconnaissance Orbiter) where feldspar signatures were recently reported [1]. Raw data were downloaded from the PDS (Planetary Data System), corrected with the ENVI CAT (CRISM Analysis Toolkit) following the method described in [5] and then denoised using a custom-made routine known as Mineral Recognizer [6]. Spectral criteria [7] are then computed to investigate whether or not an absorption band for a given wavelength was present. The BD1300 criteria was used in this study to highlight pixels which might contain a feldspar absorption band at 1.3 µm.

RESULTS
Out of 42 measured analogue rocks, 18 rocks display absorption features around 1.3 µm. The rocks with positive 1.3 µm signatures include dacite,

basalt, granodiorite, granite and diabase. Several spectra were measured on these rocks, resulting in a total of 82 positive spectra in our new spectral library. The feldspar-bearing rocks have absorption band centers varying from 1.15 to 1.4 μm. One of these positive spectra is plotted in Figure 1 and compared with a terrestrial anorthite spectrum from the USGS spectral library [4].

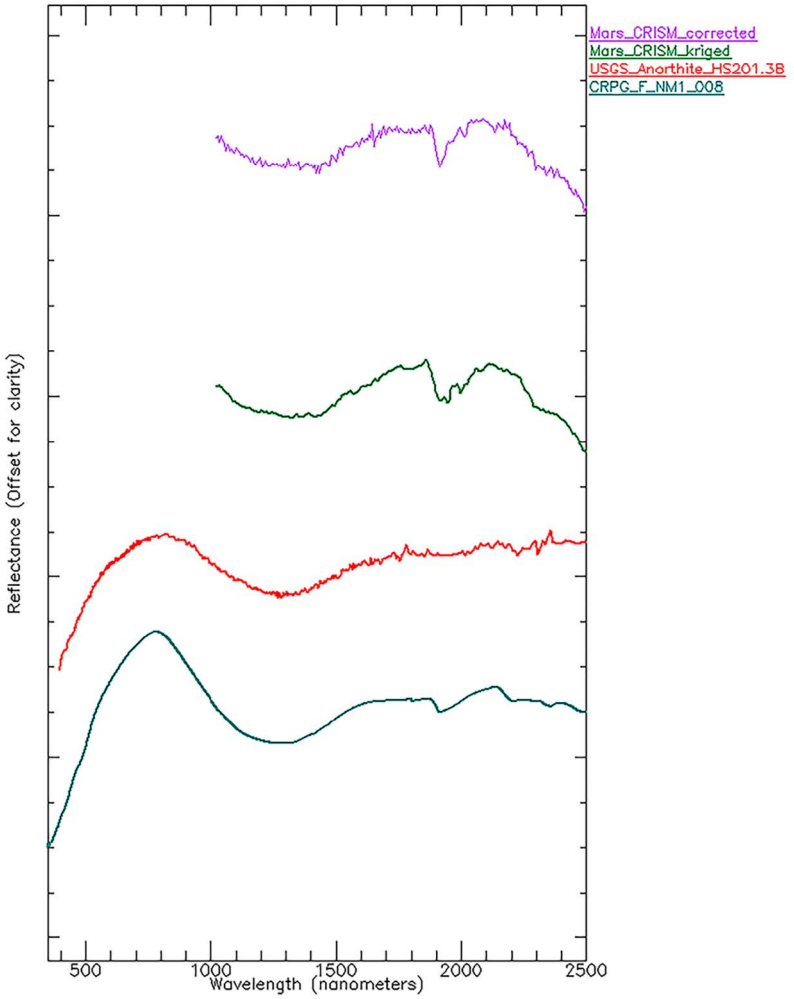

Fig. 1. A CRISM feldspar ratioed spectrum (raw and denoised by kriging [6]) is shown in comparison with terrestrial anorthite (USGS) [4] and a spectrum from our new spectral library (CRPG) collected on a diabase. The dotted line indicates the position of the 1.3-micron absorption band

A similar absorption is observed on eight analyzed CRISM cubes (see example on Figure 1). The position of the center of the absorption band in the CRISM data is around 1.25 μm. If we compare the CRISM data to the spectra of our library, the right and left shoulders of the absorption band are very often equidistant from the center of the band, although the CRISM spectra here are limited to wavelengths >1 μm, making the left shoulder difficult to examine.

DISCUSSION AND PERSPECTIVES:

VNIR spectra collected on terrestrial feldspathic whole rocks show diagnostic plagioclase signatures which are similar to the ~1.3 μm absorption feature observed on Mars and on the USGS reference spectral library. Other candidate minerals, however, could show broad absorption bands centered

between 1.1 and 1.3 μm, such as garnet, micas, or volcanic glass. Still, spectral characteristics of both our library spectra and Mars CRISM spectra are more consistent with plagioclase.

Our future work includes a detailed petrographic characterization of the analyzed samples. It is already shown, however, that some of our samples do not contain more than 40 % plagioclase crystals and still display a similar absorption band centered at 1.3 μm on the reflectance spectrum, as can be observed on the USGS spectra. These results are therefore in contradiction with previous analysis of powder mixtures [8] which determined that the presence of 90 % of calcic plagioclase is necessary in a rock for its band to be observable in a reflectance spectrum [3]. We argue that presence of an absorption band is also influenced by the grain size factor: the larger the grain size, the deeper the absorption band, and most of our studied rocks do contain feldspar phenocrysts.

We conclude, from the comparison of our library spectra with the Mars CRISM spectra, that a range of effusive and plutonic rocks could correspond to the observed signatures. Previous studies suggested that these spectral signatures correspond to anorthositic primary crust [2], or felsic tertiary crust [9]. Although these hypotheses are plausible, our results illustrate that it is virtually impossible to infer the presence of a primary or tertiary crust solely on the basis of feldspar detection. Further constraints are required to unambiguously conclude on the true nature of the rocks and the exact geological context of these peculiar signatures.

REFERENCES:

[1] Flahaut J. et al. (2019). Goldschmidt Abstracts, 2019, 1010 (and this meeting).
[2] Carter J. et al. (2013). Nature. Geoscience, 6, 1008–1012.
[3] Cheek L. C. et al. (2014). American Mineralogist, 99(10), 1871–1892.
[4] USGS spectral library: https://www.usgs.gov/labs/spec-lab.
[5] Murchie S. et al. (2007). J. Geophy. Res, 112, E5.
[6] Payet V. et al. (2020). This meeting.
[7] Viviano-Beck C. E. et al. (2014). Journal of Geophysical Research: Planets, 119, 1403–1431.
[8] Crown D. A., Pieter C. M. (1987). Icarus, 72(3), 492–506.
[9] Sautter V. et al. (2016). Lithos, 254-255, p. 36–52.

MINERAL MAPPING IN ALTIPLANO-PUNA VOLCANIC COMPLEX FOR MARS ANALOG STUDY

G. Ito[1], J. Flahaut[1], M. Barthez[1], O. González-Maurel[2], B. Godoy[3], M. Martinot[4], V. Payet[1]

[1] *Centre de Recherche Pétrographiques et Géochimiques* (*CRPG*), *CNRS/Université de Lorraine*, *15 Rue Notre Dame des Pauvres*, *54500*, *Vandoeuvre-lès-Nancy*, *France* (*gen.ito@univ-lorraine.fr*)

[2] *Department of Geological Sciences*, *University of Cape Town*, *Rondebosch*, *7700*, *South Africa*

[3] *CEGA and Departamento de Geología*, *Universidad de Chile*, *Plaza Ercilla 803*, *Santiago*, *Chile*

[4] *LGLTPE*, *CNRS/Université de Lyon*, *69622 Villeurbanne*, *France*

KEYWORDS:
Remote sensing, VNIR spectroscopy, Hyperion, Landsat, Atacama desert, Mars analog

INTRODUCTION:
Within the central Andean region at 21–24° S, the Altiplano-Puna volcanic complex is a province characterized by stratovolcanoes, ignimbrites, domes, and other volcanic features with composition ranging from basaltic andesite to dacite [1]. This region, along with its vicinity, possesses unique environments comparable to some planetary bodies due to its arid climate, volcanic terrain, and hydrothermal activities, and it has particularly been used as analog sites to study the geology and mineralogy of Mars [2].

We carried out geological and mineralogical mapping of the Altiplano-Puna volcanic complex and its vicinity using orbital remote sensing data, namely Hyperion hyperspectral imager onboard the Earth Observing One (EO-1) satellite and Operational Land Imager (OLI) onboard the Landsat 8 satellite. This is done in order to accomplish three goals: 1) Understand the regional context of the samples collected from this area in previous field expeditions; 2) Improve interpretations of similar datasets of Mars; and 3) Utilize the advantage of remote sensing to better understand the geology and mineralogy of Altiplano-Puna volcanic province. Here, we present spectral characterizations of the study area at different spatial scales using various methods, and we attempt to interpret the mineralogy with a guidance from samples collected at the study site.

REMOTE SENSING DATA:
EO-1 Hyperion is NASA's spaceborne hyperspectral imaging instrument that operated from 2000 to 2017. It contained 220 spectral bands in the 0.4–2.5 μm wavelength range, and it had a spatial resolution of 30 m/pixel. Hyperion products are usually long, narrow strips of hyperspectral cube with 7.7 km swath width.

Landsat 8 OLI is a multispectral imaging instrument operated jointly by NASA and US Geological Survey (USGS). OLI possesses nine bands in the 0.43–2.29 μm range with a spatial resolution of 30 m/pixel, except for the panchromatic band 8 (15 m/pixel). Swath width of OLI is 185 km. Landsat 8 also has two bands in the thermal infrared (10.6–12.5 μm; 100 m/pixel) mainly used for atmospheric and cloud corrections.

METHODS:
Landsat 1T level 2 GeoTiff reflectance products for the study area were downloaded from USGS Earth Explorer data portal. To show the general spectral variabilities that exist in the study area, decorrelation stretch (DCS; 2.20, 1.61, and 0.65 μm as red, green, and blue) was applied.

Hyperion L1T GeoTiff radiance products were also downloaded from USGS Earth Explorer and converted to reflectance using ENVI FLAASH atmospheric correction tool. The selection of Hyperion images and the subsetting within each image was guided by the Landsat DCS image and sampling

locations. Reflectance image cubes, which contained noticeable amounts of noise and occasional unrealistically large/small values, were first despiked and then smoothed with a sliding median method using a custom made program for processing spectral data known as Mineral Recognizer [3].

Selected subsets of Hyperion image cubes were first reduced in dimensionality using the minimum noise fraction method. Then, candidates of spectrally pure pixels were identified using pixel purity index and n-dimensional visualizer tools in ENVI. Using the spectra of identified pure pixels as endmembers, mineral distribution was computed using the spectral angle mapper algorithm.

RESULTS AND DISCUSSION:

Landsat DCS image showed considerable spectral variabilities (Figure 1) where broad units correlated well with the regional geological maps [4]: fresh salt crusts in cyan, ignimbrite sheets in yellow, silicic domes in pink, and more mafic flows in dark purple. This allowed both a first order characterization of the field site and strategic selections of Hyperion imageries for further in-depth investigations. An advantage of Landsat imageries is the large spatial coverage in comparison to Hyperion which, combined with the computationally light DCS technique, is appropriate for broad-scale analysis spanning the entire study area. This contributes to the first step of our automated multispectral or hyperspectral data processing procedure (in development) that benefits from fast turnout time and maximum spatial extent suited for survey-type analysis.

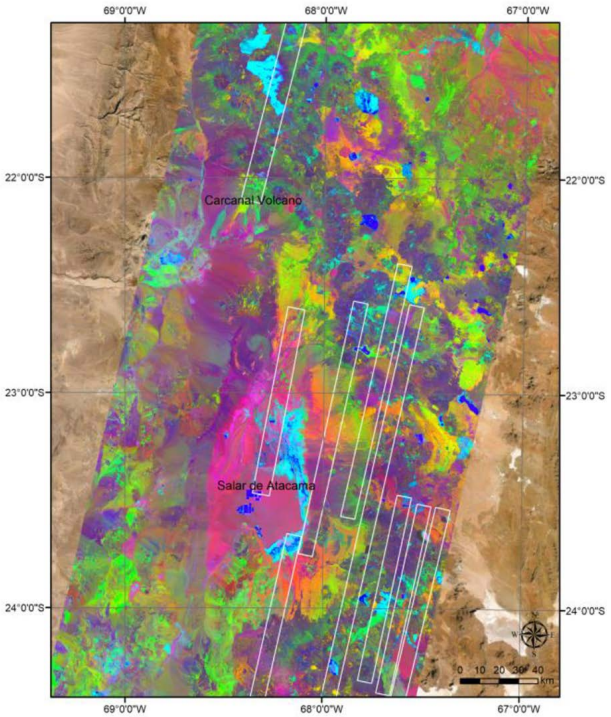

Fig. 1. Landsat DCS image overlaid on a Digital Globe satellite image. Gamma stretch was applied to blue to better use color scale. Selected Hyperion footprints are shown as white rectangles. The central part of the image is occupied by the well-known Salar de Atacama, which marks the limitation of the volcanic centers to the West

A preliminary mineral classification using the approach described in the Methods was conducted near Carcanal volcano (68° 21’ W, 22° 3’ S) (Figure 1). Iron oxides (hematite) and iron-bearing phyllosilicate minerals were identified as potential candidates of end-members. A spectrum of a sample (recognized as red scoria from visual observation) that coincided with the location

of the identified area matched the spectrum of the "hematite" end-member. Furthermore, the mineralogy and spatial distribution of the identified pixels were consistent with a previous study that used a combination of different satellite-based spectral datasets [5].

In the Landsat DCS image, the areas that were identified as "hematite" in the Hyperion analysis corresponded to yellow areas which could indicate that the mineralogy of other yellow areas in Landsat DCS image is the same. If mineralogical information gained from detailed analysis of Hyperion imagery, which was on the order of 5–10 km spatial scale, can be scaled up to Landsat scales (10's to 100 km), it would be an important link to have in efficiently characterizing the whole study area. We are in the process of examining this scalability and optimal ways of using various remote sensing spectral data for mineralogical/geological analysis of planetary surfaces.

ACKNOWLEDGMENT:
This work was funded by CNRS Momentum and LUE future leader programs.

REFERENCES:

[1] de Silva S. L. Altiplano-Puna volcanic complex of the central Andes // Geology. 1989. V. 17, P. 1102–1106.
[2] Flahaut J., Martinot M., Bishop J. L., Davies G. R., and Potts N. J. Remote sensing and *in-situ* mineralogic survey of the Chilean salars: An analog to Mars evaporate deposits? // Icarus. 2017. V. 282. P. 152–173.
[3] Payet V., Flahaut J., Ito G., Barthez M., Breton S. Automated denoising for mineral identification on hyperspectral data // 11th Moscow Intern. Symp. 5–9 Oct. 2020, Moscow, 2020.
[4] Sélles M. D., Gardeweg M. P. Geología del Área Ascotán-Cerro Inacaliri Región de Antofagasta: Carta Geológica de Chile. Serie Geología Básica. No. 190. 2017.
[5] Hubbard B. E., Crowley J. K. Mineral mapping on the Chilean – Bolivian Altiplano using co-orbital ALI, ASTER and Hyperion imagery: Data dimensionality issues and solutions // Remote Sensing of the Environment. 2005. V. 99. P. 173–186.

ADVANCES IN CLOUD COMPUTING FOR MARS DATA PROCESSING

J. L. Vázquez-Poletti[1], N. Schetakis[2], M. Sastre[1,2], R. Crespo[1], I. M. Llorente[1], L. Vázquez[1], A.Di Iorio[2]
[1] *Universidad Complutense de Madrid, Spain*
[2] *ALMA SISTEMI SRL, Italy*

KEYWORDS:
radiative transport codes, cloud computing, serverless computing, Mars, radiation

INTRODUCTION:
This contribution focuses on computing strategies for radiation transport codes, which often provide accurate predictions of expected Martian radiation dose levels, after being adapted to space conditions.

Several space agencies and institutions use to work with self-developed codes, generating a vast common library where aspects such as energy range and projectile types are to be considered in order to choose.

In the context of our work in the IN-TIME (In-Situ Instrument for MARS and EARTH dating applications) European Research Project [1], these codes have been reviewed and compared. The result is a list of 8 main codes that fall within two main classifications according to their methods: deterministic (HZETRN) and Monte-Carlo (SHIELD, GEANT4, FLUKA, PHITS, HETC-HEDS) [2].

CODE SELECTION AND EXECUTION:
One of the main objectives of our work is to produce a system that would choose the optimal radiative transport code based on the user requirements and starting conditions. The system would then deploy a complete computing solution where the selected code would be executed with provided input files.

As this computing solution needs to be optimal by means of execution time (these codes demand a high processing capacity) and budget cost, we have turned to cloud computing.

The Cloud is based on the use of different computing resources that can be used together to execute different tasks and be scaled on demand [3]. Its dynamism and elasticity allows a defined infrastructure to the needs of a specific application, resulting in an efficiency boost [4].

As an evolution of cloud computing, serverless comes as model where infrastructure management is completely managed by the providers, having the user just to upload the source code or atomic task to be executed [5].

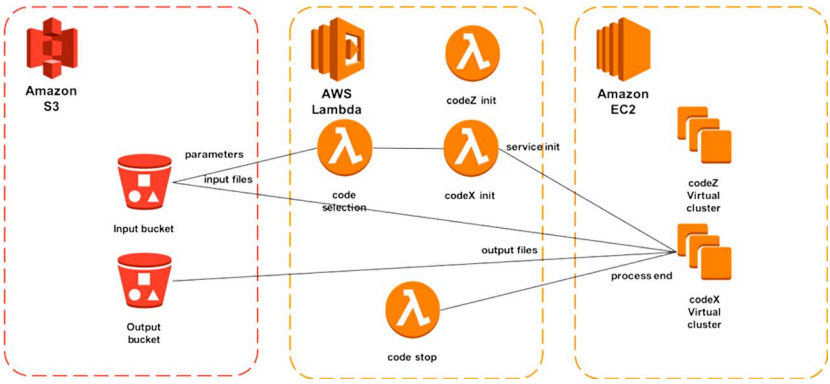

Fig. 1. Combined serverless architecture using Amazon Web Services Lambda (code selection and task control) and Elastic Compute Cloud (code execution). Simple Storage Service is used for input and output files

From serverless computing other cloud services can be orchestrated, being this particular model our basis for the radiative transport code selection

layer (see Figure 1). In a first stage, the codes themselves can be provided in the form of virtual machine images that would be booted up and replicated, based on the user input data and execution/cost optimization rules.

In the future, it's our intention to perform a complete study on porting these codes to a pure serverless computing environment. The objective would be to optimize the efficiency at the same level we obtained with the Mars Express MARSIS data process [6].

ACKNOWLEDGEMENTS:
This research has been carried out in the framework of the IN-TIME project, which is funded by the European Commission under the Horizon 2020 Marie Skłodowska-Curie actions Research and Innovation Staff Exchange (RISE) (Grant Agreement 823934), and the EDGECLOUD project, funded by the Spanish Ministry of Science, Innovation and Universities (RTI2018-096465-B-I00).

REFERENCES:

[1] INTIME Project. https://intime-project.eu/
[2] Schetakis N., Crespo R., Vázquez-Poletti J. L., Sastre M., Vázquez L., and Di Iorio A. Overview of Main Radiation Transport Codes, Geosci. Instrum. Method. Data Syst. Discuss., https://doi.org/10.5194/gi-2020-7, in press, 2020.
[3] Armbrust M., Fox A., Griffith R., Joseph A. D., Katz R., Konwinski A., Zaharia M.: A view of cloud computing // Communications of the ACM. 2010. V. 53(4). P. 50–58.
[4] Dillon T., Wu C., Chang E. Cloud computing: issues and challenges // 24th IEEE Intern. Conf. advanced information networking and applications. 2010. P. 27–33.
[5] Baldini I., Castro P., Chang K., Cheng P., Fink S., Ishakian V., Suter P. Serverless computing: Current trends and open problems // Research Advances in Cloud Computing. Singapore: Springer, 2010. 20 p.
[6] Vazquez-Polett J. L., Llorente I. M., Hinsen K., Turk M. Serverless computing: from planet mars to the cloud // Computing in Science and Engineering. 2018. V. 20(6). P. 73–79.

MATHEMATICAL ADVANCES IN FRACTIONAL MODELS FOR THE MARTIAN ATMOSPHERIC DUST DYNAMICS

M. P. Velasco[1], D. Usero[2], S. Jiménez[1], J. L. Vázquez-Poletti[2], L. Vázquez[2]
[1] *Universidad Politécnica de Madrid*
(*mp.velasco@upm.es*; *s.jimenez@upm.es*)
[2] *Universidad Complutense de Madrid*
(*umdavid@mat.ucm.es*; *jlvazquez@fdi.ucm.es*; *lvazquez@fdi.ucm.es*)

KEYWORDS:
dust, solar radiation, fractional calculus, Mittag-Leffler functions, fractional ordinary and partial differential equations, cloud computing

INTRODUCTION:
Aerosols are minute particles suspended in the atmosphere which can scatter and absorb sunlight if they are sufficiently large. Thus, the aerosols interact both directly and indirectly with the radiation budget and climate. a direct effect of the interaction of the aerosols with the Sun radiation and climate is that the aerosols scatter sunlight directly back into space. By other hand, the aerosols in the lower atmosphere can modify indirectly the size of cloud particles, changing how the clouds reflect and absorb sunlight, thereby affecting the energy budget of the planet.

The dust particles are a type of aerosol with a significant effect on climate, because the dust is composed of particles of minerals that absorb sunlight as well as scatter it. By absorbing sunlight, the dust particles warm the layer of the atmosphere where they reside and this could inhibit the formation of storm clouds and expand the desert scenario.

In the particular case of the Martian atmosphere, the dust aerosols have an important effect on the solar radiation and both surface and atmospheric heating rates, which are also basic drivers of atmospheric dynamics. The importance of the dust in the Martian exploration was recognized early in 1972 and since then dust is a target of atmospheric studies. Principally, the dust aerosols cause an attenuation of the solar radiation traversing the atmosphere. This attenuation is modeled by the Lambert-Beer-Bouguer law, where the aerosol optical thickness plays an important role and, through Angstrom law, the aerosol optical thickness can be approximated [1–3].

However, the classical model often does not fit to the reality since the propagation of the solar radiation in the atmosphere is a complex process, whose dynamic is governed by different time/space scales. Thus, it is natural to think about integro-differential equations to describe a better modeling. In this point, the Fractional Calculus offers new scenarios of modeling, since the fractional derivatives and integrals are non-local and they involve convolution kernels which act as memory factors. These properties make that the Fractional Calculus offers more suitable models to describe many physical phenomena, for instance, the dynamic of the Martian atmosphere. Specifically, the attenuation of the solar radiation traversing the atmosphere can be modeled more accurately by a fractional diffusion equation, which provides a generalization of the classical Angstrom law [4–6].

Continuing the work started in [7–10], we show the mathematical, numerical and computational advances in fractional diffusion models to obtain a more accurate model of the attenuation of the solar radiation traversing the atmosphere. We discuss some questions of the model: interpretation of variables, statement of initial and boundary conditions, analytic and numerical solutions in one and three space dimensions, and computational simulations vs observational data. Furthermore, our objective is to apply these models in the context of the development of the sensors of Universidad Carlos III de Madrid, and to deal possible experiments in the Planetary Atmosphere and Surface Chamber of the Astrobiology Center.

ACKNOWLEDGEMENTS:
The authors thank to the support of MINECO of Spain, through the projects ESP2016-79135-R, TIN2015-65469-P.

REFERENCES:

[1] Cachorro V. E., de Frutos A. M., Casanova J. L. Determination of the Angstrom turbidity parameters // Applied Optics. 1987. V. 26. No. 15. P. 3069–3076.
[2] Córdoba C., Vázquez L. Characterization of atmospheric aerosols by an *in-situ* photometric technique in planetary environments // First Jet Propulsion Laboratory In Situ Instruments Workshop: Proc. SPIE / Eds. Bearman G. H., Beauchamp P. M. 2003. V. 4878. P. 54–58.
[3] Angstrom A. On the atmospheric transmission of sun radiation and on dust in the air // Geografiska Annaler. 1929. V. 11. P. 156–166.
[4] Diethelm K. The analysis of fractional differential equations. Springer, 2010.
[5] Kilbas A. A., Srivastava H. M., Trujillo J. J. Theory and Applications of Fractional Differential Equations. Elsevier, 2006.
[6] Zaslavsky G. M., Baleanu D., Tenreiro J. A. Fractional Differentiation and its Applications. Physica Scripta, 2009.
[7] Velasco M. P., Usero D., Jiménez S., Aguirre C., Vázquez L. Mathematics and Mars Exploration // Pure and Applied Geophysics. 2015. V. 172. No. 1. P. 33–47.
[8] Velasco M. P., Usero D., Jiménez S., Vázquez-Poletti J. L., Vázquez L. Modeling and simulation of the atmospheric dust dynamic: Fractional Calculus and Cloud Computing // Intern. J. Numerical Analysis and Modeling. 2018. V. 15. No. 1–2. P. 74–85.
[9] Velasco M. P., Usero D., Jiménez S., Vázquez-Poletti J. L., Vázquez L. Fractional diffusion models for the atmosphere of Mars // Fractal and Fractional. 2018. V. 2. No. 1.
[10] Velasco M. P., Usero D., Jiménez S., Vázquez L., Vázquez-Poletti J. L., Mortazavi M. About some possible implementations of the Fractional Calculus // Mathematics 2020. V. 8. No. 6. P. 893.

MARTIAN MULTICHANNEL DIODE LASER SPECTROMETER EXPERIMENT FOR THE EXOMARS-2022 LANDER MISSION: M-DLS INSTRUMENT FABRICATION AND LABORATORY CALIBRATION RESULTS

I. Vinogradov[1], V. Barke[1], A. Budovaya[2], I. Gazizov[2], I. Golovnin[4], V. Kazakov[1], T. Kozlova[1], Yu. Lebedev[1], S. Malashevich[2], V. Meshcherinov[2], A. Nosov[1], A. Rodin[2], O. Roste[1], M. Spiridonov[3], E. Tepteeva[2], A. Venkstern[1], S. Zenevich[2], M. Ghysels-Dubois[5], G. Durry[5], L. Bizien[6]

[1] *Space Research Institute IKI of the Russian Academy of Sciences, Moscow, Russia* (*imant@iki.rssi.ru*)

[2] *Moscow Institute of Physics and Technology MIPT, Moscow Region, Russia* (*alexander.rodin@phystech.edu*)

[3] *Prokhorov General Physics Institute GPI, Russian Academy of Sciences, Moscow, Russia*

[4] *Lomonosov Moscow State University, Faculty of Physics, Moscow, Russia*

[5] *GSMA, UMR CNRS 7331, Université de Reims, BP 1039, 51687 Reims, Cedex 2, France*

[6] *Institut Supérieur de l'Aéronautique et de l'Espace, 10, av. Edouard Belin, BP 54032, 31055 Toulouse, Cedex 4, France*

KEYWORDS:
ExoMars-2022, martian atmosphere; chemical and isotopic composition variations, tunable diode laser absorption spectroscopy, integrated cavity output spectroscopy

INTRODUCTION:

Martian multichannel diode laser spectrometer (M-DLS) experiment for the ExoMars-2022 mission is aimed in continuous study of atmosphere near the Martian surface at the location of the EM-2022 stationery landing platform during one Martian year. Compact and lightweight M-DLS instrument was fabricated and has been successively delivered on-board of the EM-2022 landing platform. M-DLS laboratory calibrations confirmed advantage of tunable diode laser absorption spectroscopy (TDLAS) combination with integrated cavity output spectroscopy (ICOS) for fine measurement of weak absorption lines of a gas sample, to be taken from the low-pressure ambient Martian atmosphere. H_2O and CO_2 molecular content and isotopic ratio variations of D/H, $^{18}O/^{17}O/^{16}O$, $^{13}C/^{12}C$ will be retrieved from recorded and sent back to Earth absorption data. M-DLS experimental results would help for further understanding of physics and chemistry of interactions between surface and atmosphere of Mars.

Current activity of the research team is concentrated on proper telemetrical control of the M-DLS instrument operation and of its on-board interfacing; on correct use of M-DLS instrumental functions, including ICOS-specific ones, for accurate treatment of high-resolution optical transmission spectra for monochromatic light passing through the gas-filled analytical cell sensor; and on spectral database accurate experimental verification at the M-DLS work ranges of 2656 nm (H_2O isotopologues) and 2808 nm (CO_2 isotopologues) for adequate fitting of recorded absorption spectra, and for resulting sub-percent accuracy for retrieving values of D/H, $^{18}O/^{17}O/^{16}O$, $^{13}C/^{12}C$ ratios and H_2O, CO_2 content.

DIAMOND DETECTORS OF SPACE RADIATION: THE WAYS TO COUNTER THE POLARIZATION EFFECT

K. V. Zakharchenko[1], A. A. Altukhov[1], R. F. Ibragimov[2], V. A. Kolyubin[1], S. A. Lvov [1], E. M. Tyurin[2]

[1] *Industrial Technological Center "UralAlmazInvest", Ltd. 121108, 4, Ivana Franko str., Moscow, Russia*

[2] *National Research Nuclear University "MEPhI". 115409, 31, Kashirskoe sh., Moscow, Russia*

KEYWORDS:
Space radiation, electrons, protons, diamond, detector, polarization

INTRODUCTION:

Diamond has ultimately high radiation and temperature hardness. This determines the prospects of diamond-based radiation detectors for long-term space missions [1, 2]. The stability of charge collection efficiency of the detectors is very important to provide correct measurement of radiation characteristics. Polarization of diamonds under action of ionizing particles is one of main factors affecting their stability [3, 4]. The main mechanism of polarization is the filling of the traps in the diamond by charge carriers leading to appearance of polarization electric field counteracting the drift of charge carriers.

The use of electronic grade diamond plates makes polarization effects negligible under action of beta-radiation [5]. Nevertheless the particles with high linear energy transfer (heavy charged particles) or low track length (alpha-particles) still give rise to polarization of high quality diamonds [4, 5]. So polarization of diamond detectors is still the problem to be resolved.

Previous investigations [5] have shown that the exposure of detectors under radiation with bias voltage switched off is an effective way to depolarize diamond detectors.

The aim of this work is the experimental investigation of polarization in diamond detectors under action of different ionizing particles and determination of the ways to counter its influence on the characteristics of the detectors.

EXPERIMENTAL METHODS AND RESULTS:

Diamond detectors have been fabricated of electronic grade diamond plates with thin metal electrodes deposited on interfacial layer. The bias voltage has been applied to the electrodes. The output signals of the detectors have been registered using Greenstar digital processor.

Polarization of diamond detectors has been investigated under action of beta, alpha, neutron radiation and heavy charged particles (Ar, Cr, Xe nuclei). The neutron radiation as been used to simulate the action of protons [6].

Evolution of the spectra of detectors output under action of ionizing particles has been observed. The value of charge collection efficiency was determined by peak position of the spectrum of detector output signal. Polarization of the detectors appeared as decrease of peak position and increase in peak width (FWHM). The criterion of depolarization was the restoration of peak position and FWHM to the values of depolarized detector.

The action of beta particles and neutrons hasn't lead to notable polarization effects in diamond detectors. On the contrary the action of alpha particles polarized the diamond strongly. The rate of polarization increased when the bias voltage increased. The action of heavy charged particles has led to quick polarization of diamond detectors followed by stabilization of peak position.

These results are well explained by polarization caused by internal field of charged traps. Depolarization occurs when the traps are deactivated either under action of ionizing particles or by capturing charge carriers having opposite charge. Weak polarization caused by beta and neutron radiation is explained in terms of large track length of these particles.

Depolarization of diamond detectors has been conducted by two ways. The first one was to maintain the detector under action of ionizing particles at zero bias voltage. In the second way the visible light was used to discharge the filled traps. The advantage of depolarization by visible light is the control capabilities because the rate of depolarization depends on light intensity. The time of depolarization by visible light was about tens second compared to minutes when the detector was simply maintained at zero bias voltage.

To estimate the polarization parameters we checked the spectra of polarized detectors at increased bias voltage. When the bias voltage increased the peak position and spectrum FWHM were restored. Estimated value of polarization field corresponding to strong polarization was about 10^3 V/cm. The filled traps concentration and light intensity necessary to depolarize the diamond have been estimated.

CONCLUSIONS:

Polarization of radiation detectors based on electronic grade diamond plates has been investigated. The parameters of polarization and depolarization have been estimated. Depolarization by visible light is shown to be very effective compared to maintaining the detector at zero bias voltage. This way is perspective to be used in radiation monitoring instrumentation based on diamond detectors.

Acknowledgments:

The work has been partially supported by Federal State Budgetary Institution "Fund for Promoting the Development of Small Forms of Enterprises in the Scientific and Technical Sphere" (Innovation Assistance Fund), Project №61893"

REFERENCES:

[1] Kania D. R., Landstrass M. I., Plano M. A., Pan L. S., Han S. Diamond radiation detectors // Diamond and Related Materials. 1993. V. 2. P. 1012–1019.

[2] Gladchenkov E. V.,Zakharchenko K. V.,Ibragimovich R. F.,Kaperko A. F.,Kolyubin V. A., Kulagin V. P., Nedosekin P. G., Tyurin E. M. Experimental Investigations and Mathematical Simulation of the Operation of Ionizing-Radiation Diamond Detectors // Instruments and Experimental Techniques. 2017. V. 60. No. 3. P. 339–344.

[3] Zhang M., Y. Xia, Wang L., Gu B. CVD diamond photoconductive devices for detection of X-rays // J. Physics D: Applied Physics. 2004. V. 37. P. 3198.

[4] Kassel F., Guthoff M., Dabrowski A., De Boer W. Severe signal loss in high particle rate enviroments by charge trapping in radiation induced defects // Physica status solidi (a). 2016. V. 213. P. 2641–2649.

[5] Ibragimov R. F., Tyurin E. M., Kadilin V. V., Kolyubin V. A., Zaharchenko K. V., Nedosekin P. G. Research of work stability of diamond detectors used in SCR DDIR // J. Physics: Conference Series. 2016. V. 675. P. 042013.

[6] Zakharchenko K. V., Altukhov A. A., Ibragimov R. F., Kolyubin V. A., Lvov S. A., Tyurin E. M. Characterization of space radiation monitor based on diamond sensitive elements for future interplanetary missions // Proc. 10th Moscow Solar System Symp. 10M-S3. P. 285–287.

LIFE IN ICE: IMPLICATIONS TO LIFE ON THE MOON AND SMALL SOLAR SYSTEM BODIES

R. B. Hoover
United States Space and Rocket Center, *One Tranquility Base*, *Huntsville*, *Alabama*, *35805*, *USA* (*RichardBHoover@Icloud.com*)

KEYWORDS:
ice, Moon, comets, Vostok, bacteria, cyanobacteria, diatoms, tardigrades, cryosphere

INTRODUCTION:
Half a century ago the Apollo-11 Astronauts landed on the Moon. Although it was the general consensus of the scientific community that life could not exist on the Moon, the Apollo-11 crew and support staff were placed in absolute quarantine or 3 weeks in a specially configured Air Stream Trailer. On 20 November 1969, the Apollo-12 astronauts walked from the lunar module to inspect the Surveyor III spacecraft that had landed on 20 April 1967 near the eastern shore of Oceanus Procellarum.

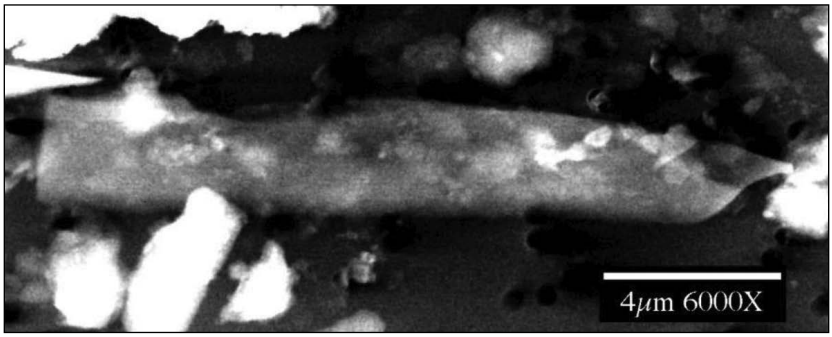

a

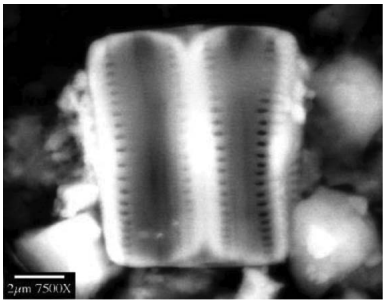

b

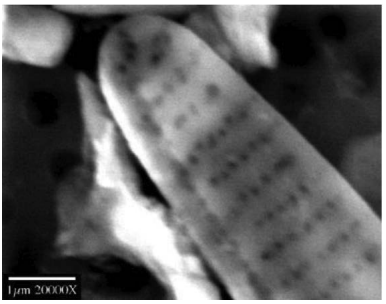

c

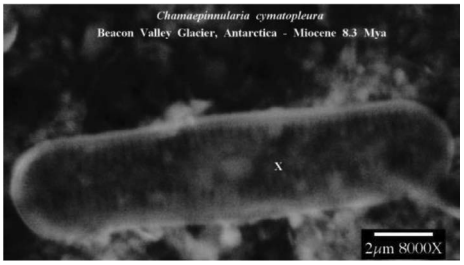

d

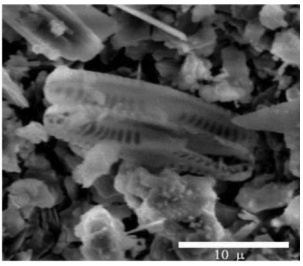

e

Figure 1. SEM images of diatoms in Vostok ice cores from : *a* — 1002M 6kx; *b* — 2827M 7.5kx; *c* — 3025M 20kx; *d* — Miocene Ice from the Beacon Valley of Antarctica; *e* — Orgueil CI1 carbonaceous meteorite

They carefully removed the Surveyor III TV camera and returned it to Earth for disassembly and detailed microbiological analysis to search for aerobic and anerobic bacteria [1]. They obtained growth from an interior piece of foam of a single bacterium identified as *Streptrococcus mitis* by scientists at the Center for Disease Control in Atlanta. For a variety of reasons, they concluded this microbe was merely a harmless pre-launch terrestrial contaminant that had survived on the lunar surface for 2.5 years. It became the consensus of the scientific community that the waterless and heavily irradiated surface of Moon was devoid of life and the contamination program for returning astronauts was terminated.

Plans are now underway to return Astronauts to the South Pole of the Moon by 2024. It has now become widely accepted that there exist significant quantities of water ice in permanently shaded regions of deep caters at the lunar poles. The Moon Mineralogy Mapper detected signatures of water ice at the optical surface (depth < few millimeters) within 20° latitude of both poles [2]. Some of the lunar polar ice may have been delivered to these craters by the accretion of comets, carbonaceous meteorites, water-bearing asteroids and ices eject from the rings, icy moons, and polar caps of planetary bodies.

At the time of the Apollo missions it was widely believed that life could not exist in ice. Sabit Abyzov [3, 4] and David Gilichinsky [5] carried out pioneering studies that established that ancient Vostok and Beacon Valley, Antarctica ice and Siberian permafrost. Other researchers have confirmed their discoveries regarding cryopreserved viable ancient microorganisms in glaciers and permafrost [7–10]. Microorganisms have been found living in thin films of meltwater surrounding tiny black rocks and cryoconite dust in polar glaciers and wind created ice sculptures of Antarctica [11]. Figure 1 shows Scanning Electron Microscope images of diatoms and cyanobacterial sheath from the deep ice layers above Lake Vostok and the Miocene ice of the Beacon Valley Glacier. It is now well established that a wide variety of prokaryotes (bacteria and cyanobacteria) and eukaryotes (diatoms, algae, tardigrades and ice worms) populate the cryosphere of Earth.

It is submitted that the ice in the deep craters at the South Pole of the Moon provide the most readily accessible and scientifically important target for Astrobiology. The discovery of cryopreserved microorganisms (living or dead), would answer the most significant questions of Astrobiology:

Does Extraterrestrial Life employ the same suite of chiral proteinogenic Amino Acids, *Nucleobases and other life critical biomolecules as Earth organisms?* and *Is Life Restricted to Planet Earth or a Cosmic Imperative?*

REFERENCES:

[1] Mitchell F. J., Ellis W. L. Surveyor III: Bacterium isolated from lunar-retrieved TV camera // Proc. Second Lunar Science Conference. 1971. V. 3. P. 2721–2733.
[2] Li et al. Direct evidence of surface exposed water ice in the lunar polar regions // Proc. National Academy of Sciences. 2018. V. 115. P. 8907–8912.
[3] Abyzov S. S., Bobin N. E. Koudryashov B. B. Microbiological flora as a function of ice depth in central Antarctica // Life Sciences and Space Research. Oxford, 1979. P. 99–103.
[4] Abyzov S. S. Microorganisms in the Antarctic Ice // Antarctic Microbiology / ed. E. I. Friedmann. N. Y.: Willey-Liss Inc., 1993. P. 265–295.
[5] Gilichinsky D. A., Vorobyova E. A., Erokhina L. G., Fyordorov-Davydov D. G., Chaikovskaya N. R., Fyordorov-Dayvdov D. G. Long-term preservation of microbial ecosystems in permafrost //Advances in Space Research: the official journal of the Committee on Space Research (COSPAR). 1992. V. 12. P. 255–263.
[6] Hoover R. B., Abyzov S. S. Ivanov M. V. Environmental Scanning Electron Microscopy Investigations of Ancient Microorganisms from Deep Ice above Lake Vostok // Proc. Society of Photo-Optical Instrumentation Engineers. 1999. V. 3755. P. 187–198.
[7] Bulat S. A., Alekhina I. A., Blot M., Petit J. R., de Angelis M., Wagenbach D., Lipenkov V. Ya., Vasilyeva L. P., Wloch D., Raynaud D., Lukin V. V. DNA Signature of Thermophilic Bacteria from the Aged Accretion Ice of Lake Vostok, Antarctica: Implications for Searching for Life in Extreme Icy Environments // Intern. J. Astrobiology. 2004. V. 3. P. 1–7.
[8] Bulat S. A., Alekhina I. A., Lipenkov V.Ya., Lukin V. V., Marie D., Petit J. R. Cell Concentrations of Microorganisms in Glacial and Lake Ice of the Vostok Ice Core, East Antarctica // Microbiology. 2009. V. 78. P. 808–810.

[9] Christner B. C., Mosley-Thompson E., Thompson L. G., Reeve J. N. Isolation of bacteria and 16S rDNAs from Lake Vostok accretion ice // Environmental Microbiology. 2001. V. 3. P. 570–577.
[10] Hoover R. B. Life in Ice: Implications to Astrobiology // Proc. Society of Photo-Optical Instrumentation Engineers. 2009. V. 7441. Art. 74410P. 12 p.
[11] Pikuta E. V., Williams M. D., Liu Z. Patel N. B., Liu Y., Bruce A. M., Liu Yuchen, Hoover R. B., Busse H.-J., Lawson P. A., Whitman W. B. *Sanguibacter gelidistatuariae* sp. nov., a novel psychrotolerant anaerobe from an ice sculpture in Antarctica, and emendation of descriptions of the family *Sanguibacteraceae*, the genus *Sanguibacter* and species *S. antarcticus*, *S. inulinus*, *S. kedieii*, *S. marinus*, *S. soli* and *S. suarezii* // Intern. J. Systematic and Evolutionary. 2017. V. 67. P. 1442–1450.

ON THE FORMATION AND TRANSFORMATION OF ORGANIC MATTER IN THE SOLAR SYSTEM

M. A. Zaitsev, M. V. Gerasimov
Space Research Institute, Russian Academy of Sciences, Moscow 117997, Russia (mzaitsev@iki.rssi.ru)

KEYWORDS:
organic matter, Solar System, meteorites, carbonaceous chondrites, macromolecular embeddings, hypervelocity impacts, volatile organic compounds, impact-initiated synthesis, impact-shock type of metamorphism

INTRODUCTION:
There were many possible sources of organic matter (OM), essential chemical elements, and inorganic compounds for OM formation in the nebula and the early Solar System: interstellar medium, dust particles etc. [1–3]. The initial ("relict") organic matter has been subjected to the complex transformation with the Solar System evolution under the UV irradiation, shocks, thermal and aqueous processing etc. As the result, we can observe very complex OM in meteorites — which give us a clear insight into the composition of extraterrestrial matter [3]. OM is an inherent part of meteorites and especially of carbonaceous chondrites (CCs). The main form of OM in CCs is submicron, macromolecular embeddings. The nature of OM is still not established. It is important to be able to correlate structural peculiarities of the CCs OM with possible mechanisms of its formation. According to the similarity of the macromolecular embeddings observed in CCs [4] and structures obtained in laboratory hypervelocity impacts simulations by pulse laser [5] the impact-initiated pathway of the embeddings formation should also be considered. Moreover, it was assumed on the aspect of the prebiotic synthesis of organic compounds (OC) on the early Earth – the impact-initiated synthesis of OM was highly competitive in performance with other main abiotic sources of organics, such as delivery by accreted bodies, photochemical synthesis, synthesis under the action of lightning discharges, etc. [6].

RESULTS AND THEIR DISCUSSION:
During the pulse laser vaporization experiments (simulating high temperature vapor conditions forming during hypervelocity impacts) performed with CCs of different types [7] we observed that the pattern of hydrocarbons from volatile organic compounds (VOCs) in starting meteorites and in their recondensates were rather similar in presence of initial inert (helium) gas medium. The circumstance that VOCs, being rather sensitive to redox conditions can be re-synthesized with about the same pattern of hydrocarbons, speaks for about the same way of origin. That means that the origin of VOCs in CCs could be a result of synthesis during impacts in space or on parent bodies in inert vacuum-like conditions but not in dense hydrogen cloud, as the CCs laser vaporization in presence of reducing (hydrogen) gas medium gives drastically different pattern of hydrocarbons.

Despite an impact-generated vapor cloud itself provides extreme conditions (high temperature and pressure, free oxygen presence, etc.), which are incompatible with any significant abundances of any complex OC [5], the OC formation takes place even under such conditions due to: heterogeneous catalytic reactions (in particular, Fischer-Tropsch type reactions) proceeding on the extremely developed surface of condensing silicate particles, and the formation of the mantle, composed of high-molecular-weight (soot-like) OM and molecular carbon, on the surface of these silicate particles. This carbonaceous matter preserves the low-molecular OC, forming simultaneously, against thermal destruction and oxidation. Moreover, if there is only a source of C, H, N and other chemical elements, essential for the OC formation, whatever in the impactors, or surrounding gas medium, complex OC can be formed by impact-initiated synthesis [8–9], including biologically significant ones – amino acids, urea, carboxylic acids etc. [9].

CONCLUSION:

An impact-shock type of metamorphism, accompanying hypervelocity impacts, plays an important role for the OM transformation (with significant part of resynthesizing OM) in the Solar System as it was shown particularly on example of CCs OM. Despite the full initial decomposition of OM during the hypervelocity impacts the subsequent impact-initiated synthesis in vapor plume gives the same pattern of, for example, certain VOCs. Thus, this type of metamorphism can favors the reproducing and keeping the OC pattern throughout the Solar System history.

ACKNOWLEDGEMENTS:

This work was supported in part by I.17P Program of the RAS.

REFERENCES:

[1] Chemistry in Space / eds. Greenberg J. M., Pironello V. Kluwer Academic Publishers, 1991. 470 p.

[2] Solid State Astrochemistry / eds. Pironello V., Krelowski J., Manicò G. Kluwer Academic Publishers, 2003. 464 p.

[3] Ehrenfreund P., Sephton M. A. Carbon molecules in space: from astrochemistry to astrobiology // Faraday Discussions. 2006. V. 133. P. 277–288.

[4] Changela H. G., Cody G. D., Alexander C. M.O'D., Nittler L. R., Peeters Z., De Gregorio B. T., Stroud R. M. TEM study of insoluble organic matter in primitive chondrites: unusual textures associated with organic nanoglobules // 44th Lunar and Planetary Science Conference. The Woodlands, Texas. USA. 18–22 March 2013. Abs. No. 3101.

[5] Gerasimov M. V., Ivanov B. A., Yakovlev O. I., Dikov Yu. P. Physics and chemistry of impacts // Earth. Moon. Planets. 1998. V. 80. P. 205–259.

[6] Chyba C., Sagan C. Endogenous production, exogenous delivery and impact-shock synthesis of organic molecules: an inventory for the origins of life // Nature. 1992. V. 355. No. 6356. P. 125–132.

[7] Zaitsev M. A., Gerasimov M. V., Vasiljeva A. S., Korochantsev A. V., Ivanova M. A., Lorenz C. A. On the similarity of volatile organics patterns in meteorites and in impact induced vapor plume // 81st Annual Meeting Meteoritical Society. Moscow, Russia, 22–27 July 2018. Abs. No. 6208.

[8] Zaitsev M. A., Gerasimov M. V., Safonova E. N., Vasiljeva A. S. Peculiarities in the formation of complex organic compounds in a nitrogen – methane atmosphere during hypervelocity impacts // Solar System Research. 2016. V. 50. P. 113–129.

[9] Zaitsev M. A., Gerasimov M. V., Vasiljeva A. S. Impact-initiated synthesis as a source of organic matter on the early Earth: Amino acids formation from the components of a nitrogen-methane atmosphere in the case of volatile-poor stony impactors // 81st Annual Meeting Meteoritical Society. Moscow, Russia, 22–27 July 2018. Abs. No. 6142.

A NOVEL AND COMPACT LASER DESORPTION — MASS SPECTROMETRY SYSTEM FOR SENSITIVE IN SITU DETECTION OF AMINO ACIDS ON EXTRATERRESTRIAL SURFACES

P. Wurz[1], N. F. W. Ligterink[2], V. Grimaudo[1], P. Moreno-García[3], R. Lukmanov[1], M. Tulej[1], I. Leya[1], R Lindner[4], C. S. Cockell[5], P. Ehrenfreund[6,7], A. Riedo[1]

[1] *Space Research and Planetary Sciences, Physics Institute, University of Bern, Switzerland* (*peter.wurz@space.unibe.ch*)
[2] *Center for Space and Habitability, University of Bern, Switzerland*
[3] *Interfacial Electrochemistry Group, Department of Chemistry and Biochemistry, University of Bern, Switzerland*
[4] *Life Support and Physical Sciences Instrumentation Section, European Space Agency, ESTEC, The Netherlands*
[5] *School of Physics and Astronomy, UK Centre for Astrobiology, University of Edinburgh, United Kingdom*
[6] *Laboratory for Astrophysics, Leiden Observatory, Leiden University, The Netherlands*
[7] *Space Policy Institute, George Washington University, 20052 Washington DC, USA*

KEYWORDS:
Bio-molecule detection, icy moons, Europa lander, laser mass spectrometer

INTRODUCTION:

For more than four decades space exploration missions have searched for molecular signatures of life on planetary surfaces beyond Earth. Often pyrolysis gas chromatography mass spectrometry has been used as the technique of choice on such space exploration missions. These instruments have relatively low detection sensitivity and their measurements often suffer from the simultaneous presence of chloride salts and minerals. The ocean worlds in the outer Solar System, such as the icy moons Europa and Enceladus, represent potentially habitable environments and therefore are prime targets for the current search for biosignatures and even life. For future space exploration missions, novel measurement concepts, capable of detecting low concentration of biomolecules with significantly improved sensitivity and specificity are required. Here we report on a novel analytical technique for the detection of extremely low concentrations of amino acids using ORIGIN, a compact and lightweight laser desorption ionisation mass spectrometer designed and developed for *in-situ* space exploration missions. The identified unique mass fragmentation pattern of amino acids coupled to a multi-position laser scan, allows for a robust identification and quantification of amino acids. With a detection limit of a few fmol·mm^{-2}, and the possibility for sub-fmol detection sensitivity, this measurement technique improves over current space exploration systems by three orders of magnitude. Moreover, our detection method is not affected by chemical alterations through surface minerals and/or salts, such as NaCl, that are expected to be present at the percent level on the surfaces of ocean worlds. Our results demonstrate that ORIGIN is a promising instrument for the detection of signatures of life and ready for upcoming space missions, such as the Europa Lander mission of NASA.

INSTRUMENT:

The ORIGIN system consists of a miniature reflectron time-of-flight mass spectrometer (160 mm×Ø60 mm, $m/\Delta m \approx 1'000$) [1] that has a nanosecond pulsed laser system as an ion source. The mass analyser is axis symmetric with a central hole at the entrance and exit. The nanosecond laser pulses ($\tau \approx 3$ ns, $\lambda = 266$ nm) are guided through a beam expander and via various mirrors to the focusing lens. The laser pulses are guided through the mass

analyser to the sample surface, which is positioned just below. Importantly, the sample is positioned slightly out of focus, i. e. the focal point is about a millimeter below the exit. Below the exit, i. e., below the mass analyser, a steel sample holder on a sample translation stage is placed, where the laser desorbs and ionises the sample material. Only cations can enter the ion optical system of the mass analyser and are guided to the micro channel plate (MCP) detector system. For every laser pulse a full ToF spectrum is recorded, which is converted to a mass spectrum. The sample, i. e., desiccated organic films of amino acids, are prepared in polished cavities of Ø3 mm by dropcasting 1 µL amino acid solution of 100–1 µM, resulting in average surface concentrations of 14–0.14 pmol·mm^{-2}. Each of these filled cavities is sampled at 40 positions, linearly spaced by ~50 µm, with 100 laser shots at each position. The resulting mass spectra are filtered based on peak signal-to-noise ratios (SNRs) to remove spectra without signal. For the data handling and data analysis we use in-house developed software.

RESULTS:

To test the performance of the ORIGIN instrument [2] on complex samples of biologically relevant species, measurements were performed using mixtures containing all twenty amino acids (0.7 pmol·mm^{-2} each) with and without added NaCl (~0.7 µg·mm^{-2}). NaCl is added to simulate measurement conditions on icy moons, which are known to have large amounts of salt embedded in the ice. Figure 1 shows the mass spectra for scans at two laser pulse energies at 1.4 and 2.6 µJ. The amino acid signals are clearly visible and the signal size increases with increasing pulse energy. Except for lysine, mass fragments of all amino acids are clearly identified in the 2.6 µJ measurement. However, not all signals can be unequivocally assigned to a single amino acid, since some of the mass fragments overlap. For example, this hinders the unambiguous identification of alanine just based on the m/z = 44 signal.

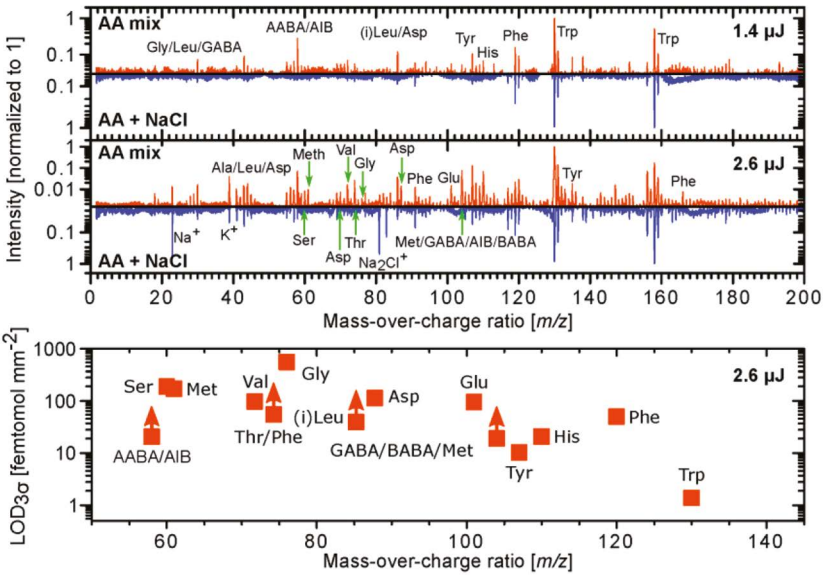

Fig. 1. Top: Measured mass spectra of a mixture of 20 amino acids (0.7 pmol·mm^{-2} per amino acid, red) and the same mixture with added NaCl (~0.7 µg·mm^{-2}, blue). The mixtures were measured with pulse energies of 1.4 (upper panel) and 2.6 µJ (middle panel). Out of the 20 amino acids, eleven can directly be identified from their unique mass features. Bottom panel: 3σ limits of detection ($LOD_{3\sigma}$) calculated from the 2.6 µJ measurement. Lower limits are given for signals that are clearly detected but have contributions from multiple amino acids

When NaCl is added, the amino acids still can be identified via their unique mass fragmentation signature, however at somewhat lower signal intensities. Sodium chloride is mostly UV transparent and thus the laser pulse will still interact with the amino acids. Therefore, it is likely that the salt crust

reduces desorption and/or ionisation of the amino acids and higher laser pulse energies may be required. The bottom panel of Figure 1 shows for the amino acids detected in the 2.6 μJ pulse campaign the 3σ limit of detection. The high SNR of the mass fragments makes it possible to detect many of the amino acids at surface concentrations below 100 fmol·mm^{-2}, and in the case of tryptophan even down to 1 fmol·mm^{-2}.

For a meaningful comparison with the Level-of-Detection (LOD) requirements given in the Europa Lander Science definition report [3] (1 nM material in a 1 g, or 1 ml, sample, which corresponds to 1 pmol of material), these numbers need to be converted to average surface coverage. Sublimating the water of this sample and distributing the remaining molecules over the same area as the sample holder cavities, i. e., 7.1 mm^2, results in a surface concentration of 141 fmol·mm^{-2}.

It remains important to stress that the sensitivity of the ORIGIN system can easily be improved, i. e., the LOD lowered. For example, sampling 400 positions, instead of 40, of the same surface results in a tenfold increase in signal and would already push the $LOD_{3\sigma}$ of the system into the sub-fmol·mm^{-2} regime. In addition, the gain of the MCP detector can still be increased by a factor of 32.

REFERENCES:

[1] Rohner U., Whitby J. A., Wurz P. A miniature laser ablation time-of-flight mass spectrometer for *in-situ* planetary exploration // Measurement Science and Technology. 2003. V. 14. Art. 2159.

[2] Ligterink N., Riedo A., Wurz P., Ehrenfreund P., Cockell C., Tulej M., Grimaudo V., Lindner R. ORIGIN: a novel and compact Laser Desorption — Mass Spectrometry system for sensitive *in-situ* detection of amino acids on extraterrestrial surfaces // Nature Science Reports. 2020. V. 10. Art. 9641. 10 p.

[3] Hand K. P. et al. Report of the European Lander Science Defintion Team / NASAS. 2017. JPL D-97667.

NEW MICROBIAL FINDS IN THE SUBGLACIAL ANTARCTIC LAKE VOSTOK

S. Bulat, M. Doronin, D. Sumbatyan
NRC 'Kurchatov Institute', *Petersburg Nuclear Physics Institute*,
St. Petersburg-Gatchina, *Russia* (*bulat@omrb.pnpi.spb.ru*)

KEYWORDS:
Antarctica, subglacial Lake Vostok, lake unsealing, ice cores, life, extremophiles, bacteria, 16S rRNA genes, contamination, astrobiology

The objective was to search for microbial life in the subglacial Antarctic Lake Vostok by analyzing the uppermost water layer entered the borehole and shortly got frozen within following three unsealing of the lake (February 5, 2012; January 25, 2015, and February 3, 2015). The new sample to study was 3721m deep re-cored borehole-frozen water ice obtained following second lake unsealing.

The ice segment was thoroughly decontaminated in the cold and cleanroom facilities. The kerosene smell was still present upon ice melting indicating for contamination by kerosene-based drill fluid. The genomic DNA isolated following meltwater concentrating was amplified with v3-v4 16S rRNA bacterial gene region-specific primers. As a preliminary trial, the amplicons generated were cloned and sequenced by the standard Sanger method.

The DNA analyses came up with a total of 16 bacterial phylotypes at the low gene library cover — 55.2 % indicating significant biodiversity. Of them, only one phylotype 3721v34-24 successfully passed all contamination criteria, including own Contaminant library consisting of 329 16S rRNA gene entries (as for July 2020). It proved to be unique in distinguishing from previously discovered highly likely lake-water inhabiting three phylotypes [1]. Amongst them, are hitherto-unknown and phylogenetically unclassified phylotype w123-10 likely belonging to *Parcubacteria* Candidatus *Adlerbacteria*, 3429v3-4 showing below genus-level similarity with *Herminiimonas glaciei* of *Oxalobacteraceae* (*Beta-Proteobacteria*) and 3698v46-27 being conspecific with several species of *Marinilactobacillus* of *Carnobacteriaceae* (*Firmicutes*).

The phylotype 3721v34-24 dominated comprising 41.4 % clones with three allelic variants. It remained taxonomically unidentified — 87.7 % (below family-level) similarity with *Mucilaginibacter daejeonensis* NR_041505 of *Bacteroidetes* (Sphingobacteriaceae). A few identical in a sequence DNA clones were retrieved from GenBank — e. g., uncultured unidentified *Bacteroidetes* DQ316809 from uranium-contaminated sediment (USA). With a single mismatch, more sediment clones were found out — e. g., KC431957 and DQ404664, both unidentified. Consequently, the new lake-water phylotype proved to be an unidentified and unclassified 'sediment-loving' bacterium assigning to the new for the lake inhabitants *Bacteroidetes* phylum. The implementation of NGS Illumina MiSeq and Oxford Nanopore sequencing technologies are in further plans to clarify the biodiversity issue of the given lake-water frozen sample. Thus, newly discovered bacterial phylotype, along with three previously recorded, might represent ingenious cell populations in the subglacial Lake Vostok.

REFERENCES:

[1] Bulat S. A. Microbiology of the subglacial Lake Vostok: first results of borehole-frozen lake water analysis and prospects for searching for lake inhabitants // Philosophical Transactions of The Royal Society A. Mathematical Physical and Engineering Sciences. 2016. V. 374(2059). Art. 20140292.

SOURCES OF MATERIALS FOR THE WESTERN DELTA OF JEZERO CRATER (MARS), ASTROBIOLOGICAL IMPLICATION

N. E. Demidov[1], M. A. Ivanov[2], A. T. Basilevsky[2]
[1] *Arctic and Antarctic research institute, St. Petersburg, Russia* (*nikdemidov@mail.ru*)
[2] *Vernadsky Institute of Geochemistry and Analytical Chemistry RAS, Moscow, Russia*

KEYWORDS:
Mars, Jezero crater, Jezero delta, glaciation, astrobiology

INTRODUCTION:
One of the strategic tasks of the Mars studies is "Seek signs of life". On July 30, 2020, the NASA Mars 2020 mission was launched. The Perseverance rover of the Mars 2020 will investigate Jezero crater on the western rim of Isidis basin, scientific tasks include search of potential signs of life. Jezero is interpreted as once containing an open basin paleolake [1], that has two inflow and one outflow channels. The well-preserved deltas are attached to the mouths of the inlets [2, 3]. The western delta is the most prominent deposition body on the Jezero floor and will be a primary target of the Perseverance rover. Fluvial activity in the watershed of the western delta is inferred to have ceased together with majority of valley networks around 3.8 Ga [4]. The floor of the crater shows a diversity of spectral signatures suggesting a wide range of mineral compositions including clays and carbonates [5–7], minerals that may have a biological potential [e. g., 8]. In our study, we investigated the morphology and topographic configuration of the western inflow channel [9] in order to constrain sources and astrobiolgical potential of different lithologies that are associated with the western delta.

MORPHOLOGIC ANALYSIS OF WESTERN INFLOW CHANNEL:
The morphology of the western channel is significantly changed when the channel crosses graben of Nili Fossae. Eastward of Nili (the cis-Nili part), the channel is ~90 km long and represents a narrow (mostly 0.5-1 km wide along entire extent) structure that often changes its direction and meanders near Jezero crater. Depth of the channel is a few tens of meters (estimates from the MOLA data). In places, the channel bifurcates and then its branches coalesce again, but the channel lacks tributaries. Edges of the channel are smooth without prominent indentations.

Westward of Nili (the trans-Nili part), the channel is a distinctly broader structure whose width varies from ~2 to ~6 km and depth varies from many tens of meters up to a few hundred meters. Edges of the channel are rough, jagged and sometimes represent cliff-like structures. Within the widenings, the channel usually has single or multiple islands of irregular shape with the rough, cliff-like edges. The most important difference of the trans-Nili channel from its cis-Nili counterpart is the presence of abundant tributaries. The tributaries occur on both sides of the central channel and represent relatively short (a few kilometers long, up to 15 km) and broad (first kilometers) valleys with jagged edges. The valleys appear as shallow (a few tens of meters deep) structures with a U-shaped transverse profile. The tributaries often begin in circs (e. g., impact craters) at a relatively high elevation within the surrounding uplands and elevation of the valley floors is gradually lowering toward the central channel.

The topographic configuration of the regional background of both parts of the western channel is also different. For the cis-Nili channel, the background represents a broad plain-like surface with numerous short-wavelength (hundred meters across) variations. The plain is slightly tilted to East (mean gradient is ~0.38°) and South (mean gradient is ~0.16°). Although the cis-Nili part of the channel is on regional slope to South, the channel extends eastward and its path is controlled by the local topographic variations.

The entire trans-Nili part of the western channel (~130 km long) is in the thalweg of a broad regional trough that is ~60 km wide and ~100-200 m deep at its western end (~74° E) and ~20–30 km wide and ~500 m deep at its eastern end near graben of Nili Fossae. The tributaries are extending along the general slope of the trough sides. Thus, in contrast to the cis-Nili part, the upper portion of the western channel was mostly controlled by the regional topography.

Clear differences in morphology and topography of the cis- and trans-Nili parts of the western channel indicate different modes of their formation. We interpret the cis-Nili part as a true fluvial feature and the trans-Nili part as a feature of glacial origin. This part is topographically higher, have been formed earlier, and, thus, formation of the western channel began by accumulation and movement of glaciers within the broad topographic trough on the western rim of Isidis. The glaciers removed material from the surface, relocated it within the central valley, and ultimately, brought it to the Nili Fossae structural zone. The graben of Nili could potentially serve as traps for masses of ice and meltwater at the glaciers bed. These traps obviously have been breached either by ice, or meltwater, or both. The morphology of the cis-Nili part of the channel, however, suggests that this feature has a fluvial nature and, thus, had been formed by meltwater released from the glacier base.

DISCUSSION/ASTROBIOLOGICAL IMPLICATION:

Our interpretation of the possible modes of formation of the upper and lower parts of the western channel may have important implications to the climatic history of Mars and to the inventory of materials that can be discovered and analyzed in Jezero crater.

The climatologic aspect of our study is that an extensive, warm-based glacier (or glaciers) existed on the western rim of Isidis basin in the yearly Hesperian times [10]. This portion of the rim is in the subequatorial (15–20° N) zone and, in contrast to the tropical glaciers elsewhere on Mars [e. g. 11] is at relatively low elevations, below ~1.5 km. Presence of glaciers and liquid water within the channel and the lake provides evidence that paleotemperatures at the Noachian-Hesperian transition in the Jezero region were, at least locally, in the terrestrial range (±0 °C) and thus favourable for life.

Unraveling the history of development of the western channel helps to constrain source areas of materials that accumulated in Jezero crater. If the main inflow of sedimentary materials was provided by the fluvial channels then the deposits were first removed by glaciers from the surface of the western Isidis rim and then redeposited by fluvial systems within Jezero. The lack of tributaries to the western channel suggests that the area eastward of Nili Fossae had minor influence on the composition of deposits in the crater and the sedimentary deposits in Jezero represent a mixture of materials removed from the cis-Nili part of the western channel and materials brought by the glacier(s) to the Nili Fossae zone. Both areas show no spectral signatures of carbonates and minor signatures of clays [5–7, 12].

Phyllosilicates or clays particles, if not originated due to subsurface hydrothermal alteration, are probably products of surface weathering in a warm and wet climate prior to a cold epoch when the Jezero region was fully or partly glaciated. As the spectral signatures of clays are relatively widespread in Jezero watershed [6], glaciohydrologic activity was responsible for transportation and concentration of clay minerals in the sedimental trap of Jezero delta. Clay sedimentation in a habitable environment could preserve a wide range of sedimentary microbialites, morphological fossils and organic biosignatures as it happens on Earth. The *in-situ* origin of clay minerals in the paleolake (as it is known to happen with deposition of the red clays in distinct part of oceans on Earth) is unlikely as this very slow process contradicts with the high depositional rates in the delta environments.

Vice-versa, due to absence of carbonates in the Jezero watershed it is reasonable to state that marginal carbonates detected in Jezero were originated *in-situ* as chemical sediments. They represent paleorecord of physical-chem-

ical environments in Jezero paleolake. Unlike clays, carbonates are not the best environments for prolonged preservation of organic materials and microfossils, because carbonates are subjected to recrystallization over the geological time. At the same time, carbonates as we know on Earth may contain macroscopic biochemical growth structures like stromatolites, which serve as a model for alternative/additional to clays target for biosignature detection.

REFERENCES:

[1] Fassett C. I., Head J. W. Fluvial sedimentary deposits on Mars: Ancient deltasin a crater lake in the Nili Fossae region // Geophysical Research Letters. 2005. V. 32. Art. L14201.
[2] Goudge T. A. et al. Assessing the mineralogy of the watershed and fan deposits of the Jezero crater paleolake system, Mars // J. Geophysical Research Planets. 2015. V. 120(4). P. 775–808.
[3] Goudge T. A. et al. Stratigraphy and paleohydrology of delta channel deposits, Jezero crater, Mars // Icarus. 2018. V. 301. P. 58–75.
[4] Fassett C. I., Head J. W. The timing of martian valley network activity: Constraints from buffered crater counting // Icarus. 2008. V. 195. P. 61–89.
[5] Mustard J. F. et al. Mineralogy of the Nili Fossae region with OMEGA/MarsExpress Data: 1. Ancient impact melt in the Isidis basin and implications for the transition from the Noachian to Hesperian // J. Geophysical Research. 2007. V. 112. Art. E08S03.
[6] Elhmann et al. Clay minerals in delta deposits and organic preservation potential on Mars // Nature geoscience. 2008. V. 1. P. 355–358.
[7] Ehlmann B. L. et al. Identification of hydratedsilicate minerals on Mars using MRO-CRISM: Geologic context near Nili Fossaeand implications for aqueous alteration // J. Geophysical Research. 2009. V. 114. Art. E00D08.
[8] Horgan B. H. N. et al. The mineral diversity of Jezero crater: Evidence for possible lacustrine carbonates on Mars // Icarus. 2020. V. 339. Art. 113526.
[9] Goudge T. A. et al. A transported origin for alteration minerals within the Jezero crater, Mars paleolake basin: evidence from catchment and delta mineralogy // Proc. 45th Lunar and Planetary Science Conf. 2014. Abstr. 1164.
[10] Ivanov M. A. et al. Major episodes of geologic history of Isidis Planitia on Mars // Icarus. 2012. V. 218. P. 24–46.
[11] Fastook J. L. et al. Tropical mountain glaciers on Mars: Altitude-dependence of ice accumulation, accumulation conditions, formation times, glacier dynamics, and implications for planetary spin-axis/orbital history // Icarus. 2008. V. 198. P. 305–317.
[12] Mangold N. et al., Mineralogy of the Nili Fossae region with OMEGA/Mars Express data: 2. Aqueous alteration of the crust // J. Geophysical Research. 2007. V. 112. Art. E08S04.

THE EFFECT OF COSMIC RAYS ON THE HUMAN HIPPOCAMPUS

Z. Ashrafzadeh[1,2], J. Fatemi[1], P. Davoudi[1]
[1] *Bahonar University of Kerman*
[2] *The International Occultation Timing Association-Middle East section*
(*info@iota-me.com*)

KEYWORDS:
cosmic ray, HZE, hippocampus, simulation, neural network

INTRODUCTION:
The cosmic rays above the atmosphere are made up of different particles and HZE, which are heavy and energetic particles. These particles can have a devastating effect on astronauts 'brains, including the astronauts' hippocampus during space missions, as well as a long-distance trip to Mars, which reduces IQ in astronauts (https://www.ncbi.nlm.nih.gov/). And in recent years, these issues have been explored.

In this paper, the simulation of the collision of cosmic particles with the neural network and finally the data obtained from this simulation of the extent of possible damage in astronauts are also examined (https://www.nature.com/articles/srep34774). And the simulated particles include protons, carbon, and alpha, which can be used to detect potential hazards and ultimately provide solutions to prevent damage.

ANALYSIS AND CONCLUSION:
As mentioned, particles with more than one proton are known as HZE particles above the atmosphere. The properties of these particles are such that the heavier the particle, the greater the damage from this particle. For example, carbon, which is heavier than alpha, does more damage because the LET (Linear energy transfer) of carbon particles is higher than Alpha, so heavier particles, higher LET they have, and ultimately the more damage they do to the neurons in the hippocampus. The results are shown in Table 1.

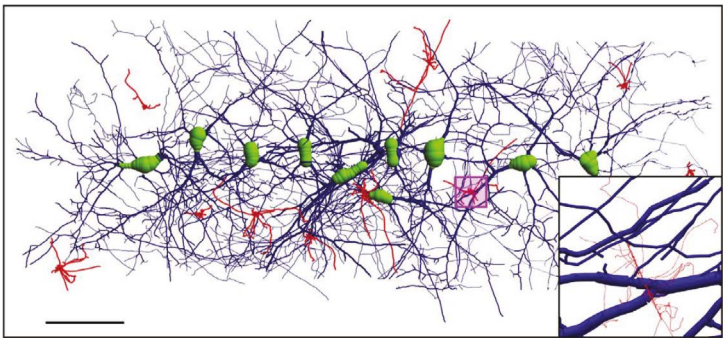

Figure 1. A sample three-dimensional representation of the neural network composed of 10 cells. The main panel shows an XY projection of the full 640_280_25-lm simulation volume

Table 1. The physical parameters of ionizing radiations and the coincidence statistics

Particle name	Energy (MeV)	Numbers of trials	LET (KeV/um)
Proton	100	100	0.72
Alpha			8.59
Carbon			188.95

REFERENCES:
[1] Belov O. V., Batmunkh M., Incerti S., Lkhagva O. Radiation damage to neuronal cells: Simulating the energy deposition and water radiolysis in a small neural network // Physica Medica.2016. V. 32. No. 1. P. 1510–1520.

THE STABILITY OF ENZYMES TO THE EFFECT OF IONIZING RADIATION UNDER SIMULATED EXTRATERRESTRIAL CONDITIONS

V. Cheptsov[1,2], A. Belov[1], A. Pavlov[3], D. Tsurkov[3], E. Vorobyova[1], D. Frolov[3,4], V. Lomasov[4]

[1] *Department of Soil Biology, Lomonosov Moscow State University, Moscow 119991, Russia* (*cheptcov.vladimir@gmail.com*)

[2] *Space Research Institute, Russian Academy of Sciences, Moscow 117997, Russia*

[3] *Ioffe Physical-Technical Institute, Russian Academy of Sciences, St. Petersburg 194021, Russia*

[4] *Peter the Great St. Petersburg State Polytechnic University, St. Petersburg 194021, Russia*

KEYWORDS:
biomarkers, proteins, accelerated electrons, Mars, astrobiology

INTRODUCTION:

Studies on the resistance of various biomolecules (biomarkers) to the effects of extraterrestrial factors are necessary to identify the types of molecules that are most stable in space conditions, to assess the duration of their preservation, to detect the transformations that they undergo after the certain influences. This contributes to the identification of promising space bodies, landing sites, geological structures and types of deposits for study, the development of the necessary tools and the adaptation of analytical techniques, as well as the correct interpretation of data obtained during space missions.

Ionizing radiation is considered as the main factor destroying biomolecules in extraterrestrial conditions [1–3].

At the studies of the biomolecules resistance to radiation, the pure chemicals are usually studied after irradiation under conditions of normal atmospheric pressure and temperatures close to room temperature [1, 4–6]. At the same time, it is known that the mobility of free radicals, which are the main cause of radiation damage, significantly depends on the temperature under irradiation [7]. The stability of biomolecules can also be influenced by the chemical composition of the environment, since, gaseous oxygen, water, salts, and minerals are the sources of free radicals [8], as well as by an interactions of biomolecules (or their residues) with any environmental substances [8, 9]. Consequently, for a correct assessment of the biomarkers stability on any space objects, the reproduction of the most complete set of factors is required.

We irradiated soddy-podzolic soil with accelerated electrons under low temperature (–130 °C) and low pressure (0.01 Torr) and estimated changes in the activity of soil enzymes *in-situ* after irradiation.

MATERIALS AND METHODS:

A sample of soddy-podzolic soil, collected from the Moscow region of Russia from a depth of 5–10 cm (horizon A) was used for the study. The sample is described in [11]. The sample was dried to air-dry moisture (2.9 %), cleared of roots, and passed through a sterile sieve with apertures of 1 mm diameter.

For irradiation, the soil was packaged in polyethilene bags; the thickness of the samples was about 0.7–0.8 mm. Then the samples were placed in a climatic chamber, which allows maintaining a low temperature (–130 °C) and low pressure (0.01 Torr) during irradiation [12]. Further, the samples were irradiated by accelerated electrons (~1 MeV) with 10 kGy and 100 kGy doses. To control the effect of pressure and temperature, some of the samples were exposed at –130 °C and 0.01 Torr for 10 minutes (without irradiation).

Further, the activity of catalase was determined by the gasometrical method and the activity of dehydrogenases by the triphenyltetrazolium approach was measured in the control and irradiated samples [13].

RESULTS AND CONCLUSION:

Catalase activity remained at the control level both after exposure to low pressure and low temperature and after irradiation with doses of 10 kGy and 100 kGy. Dehydrogenase activity was unchanged after low pressure and low temperature exposure as well as after 10 kGy irradiation, but decreased by 5 times after 100 kGy irradiation. It is known that the dehydrogenase activity of soils is mainly caused by the activity of intracellular dehydrogenases of actively metabolizing soil microorganisms, and correlates well with fluctuations in the number of culturable bacteria. A sharp decrease in dehydrogenase activity after exposure to a dose of 100 kGy is consistent with a decrease in reproductive activity and the transition of a significant part of the bacterial microbial communities to a hypometabolic/dormant state after impact of the factors above [12]. The enzyme catalase in soil retains its activity well outside microbial cells, entering into physicochemical interactions with mineral, colloidal and organic soil components. Due to immobilization in a heterophase environment, active catalase is resistant to physical factors and can be accumulated in significant concentrations, carrying out a specific reaction of peroxide decomposition.

It has been established that biologically active macromolecules, in particular, extracellular enzymes (catalase) immobilized in the soil (regolith), are stable and retain activity when exposed to high-energy electrons in high doses, at least up to 100 kGy.

The data obtained substantiate the possibility of a long-term preservation of enzymes (proteins) under low-temperature extraterrestrial conditions, e.g. in regolith of Mars or inside meteorites.

The study was partially supported by RFBR, grant No. 20-02-00470.

REFERENCES:

[1] Blanco Y. et al. Effects of gamma and electron radiation on the structural integrity of organic molecules and macromolecular biomarkers measured by microarray immunoassays and their astrobiological implications // Astrobiology. 2018. V. 18. No. 12. P. 1497–1516.
[2] Pavlov A. K., Blinov A. V., Konstantinov A. N. Sterilization of Martian surface by cosmic radiation // Planetary and Space Science. 2002. V. 50. No. 7–8. P. 669–673.
[3] Pavlov A. A. et al. Degradation of the organic molecules in the shallow subsurface of Mars due to irradiation by cosmic rays // Geophysical Research Letters. 2012. V. 39. No. 13.
[4] Cherubini C., Ursini O. Amino acids chemical stability submitted to solid state irradiation: the case study of leucine, isoleucine and valine // SpringerPlus. 2015. V. 4. No. 1. P. 541.
[5] Iglesias-Groth S. et al. Amino acids in comets and meteorites: stability under gamma radiation and preservation of the enantiomeric excess // Monthly Notices of the Royal Astronomical Society. 2011. V. 410. No. 3. P. 1447-1453.
[6] López-Islas A., Colín-García M., Negrón-Mendoza A. Stability of aqueous formaldehyde under γ irradiation: prebiotic relevance // Intern. J. Astrobiology. 2019. V. 18. No. 5. P. 420–425.
[7] Dartnell L. R. et al. Low-temperature ionizing radiation resistance of Deinococcus radiodurans and Antarctic Dry Valley bacteria // Astrobiology. 2010. V. 10. No. 7. P. 717–732.
[8] Baumstark-Khan C., Facius R. Life under conditions of ionizing radiation // Astrobiology. Berlin, Heidelberg: Springer, 2002. P. 261–284.
[9] Bonner W. A. et al. The radiolysis and radioracemization of amino acids on clays // Origins of life and evolution of the biosphere. 1985. V. 15. No. 2. P. 103–114.
[10] Materese C. K., Gerakines P. A., Hudson R. L. The Radiation Stability of Thymine in Solid H_2O // Astrobiology. 2020. V. 20. Iss. 8. P. 956–963.
[11] Cheptsov V. et al. Viability of the soddy-podzolic soil microbial community after 148–1250 kGy gamma irradiation // Planetary and Space Science. 2019. V. 172. P. 8–13.
[12] Cheptsov V. et al. Survivability of soil and permafrost microbial communities after irradiation with accelerated electrons under simulated Martian and open space conditions // Geosciences. 2018. V. 8. No. 8. P. 298.
[13] Tabatabai M. A. Soil enzymes // Methods of Soil Analysis: Part 2 Microbiological and Biochemical Properties. 1994. V. 5. P. 775–833.

RESISTANCE OF DT57C BACTERIOPHAGE TO IRRADIATION BY HIGH-ENERGY ELECTRONS

E. I. Sukhova[1], E. A. Vorobyova[1], V. S. Cheptsov[1,2], A. A. Belov[1], D. A. Skladnev[3], A. K. Pavlov[4]

[1] *Lomonosov Moscow State University, Soil Science Faculty, 119234, Russian Federation, Moscow, Leninskie Gory, 1 (nuachto@gmail.com)*

[2] *Space Research Institute of RAS, 117997, Russian Federation, Moscow, 84/32 Profsoyuznaya Street*

[3] *Winogradsky Institute of Microbiology of RAS, Russian Federation, Moscow, 119991, Leninsky Prospekt, 14*

[4] *Ioffe Physical-Technical Institute of RAS, St. Petersburg, 194021, Polytekhnicheskaya Street, 26*

KEYWORDS:
astrobiology; biomarkers; extreme factors; irradiation; viruses; resistance

INTRODUCTION:

Aiming to assess the limits of terrestrial life forms' viability the microorganisms (bacteria, archaea, or fungi) are usually studied. However, the most numerous biological objects on the Earth are viruses, the number of which exceeds the total number of all organisms. The total number of viruses is estimated as ~10^{30} in the oceans and ~10^{31} on the entire planet [1], while the majority of viruses are bacteriophages [2]. Viruses are characterized by a complete absence of metabolism and translation apparatus, and therefore their existence is possible only in the presence of host organisms. For this reason, they are considered like biomarkers in astrobiological studies. Nevertheless, studies of the resistance of viruses to the effects of extreme factors of extraterrestrial space are rare to date. Ionizing radiation is considered as the main factor limiting the preservation of organisms and biomolecules outside the Earth. The conditions (temperature, pressure, composition of the atmosphere, concentration of water, etc.) under which irradiation takes place significantly affect the radiation effects. Taking into account all the above we studied DT57C bacteriophage resistance to accelerated electrons irradiation under low pressure and low temperatures conditions.

MATERIALS AND METHODS:

Bacteriophage DT57C obtained from Winogradsky Institute of Microbiology RAS, was irradiated with accelerated electrons (~1 MeV) at 5 kGy and 10 kGy doses under low pressure (~0.01 Torr) and low temperatures (from –50 °C to –165 °C) conditions in order to assess the possible lifetime of viruses in outer space and on various space objects. Bacteriophage samples (in liquid LB-media and in montmorillonite) were placed in a climatic chamber, which was developed for modeling of the extraterrestrial conditions, and which allows to maintain low temperatures and low pressure during irradiation. Temperature and pressure effects were controlled by placing one of the samples in the chamber for 10 minutes at 0.01 Torr pressure and –150 °C temperature.

For immobilization, 1 ml of phage suspension in LB-media was added to 2 g of sterile (calcined at 600 °C) montmorillonite. Then montmorillonite with phages introduced into it was thoroughly mixed with a sterile glass rod, dried at 28 °C, rubbed with a sterile pestle and divided into several portions for subsequent irradiation at different temperatures and a pressure of 0.01 Torr.

The number of phages active after irradiation was counted using the double-layer method (Gratia method). The *Escherichia coli* HS 3-104 strain (host of the DT57C bacteriophage) was used for the study. The total number of phages was determined using epifluorescence microscopy (EFM) with acridine orange dye.

RESULTS AND DISCUSSION:

The virulence index of phages was calculated as the percentage of the abundance found by the double-layer method to the total abundance determined using EFM (Figure 1). After 5 kGy irradiation under the temperature gradient from –50 °C to –165 °C the numbers of virulent phages in liquid culture con-

stituted 125-69 % of the total ones. That is, the ability of phages to infect host cells decreased both depending on the irradiation dose and depending on the decrease in the irradiation temperature. For the samples irradiated with 10 kGy dose this figure was 2–5 % of the total numbers for temperatures of –50 °C and –165 °C. It indicates that with an increase in the dose, there was not only a decrease in the total number of phage particles, but also a loss of virulence of the phages that had preserved their native DNA; however, a decrease in the irradiation temperature below –50 °C at a dose of 10 kGy didn't matter from the point of view of phage virulence.

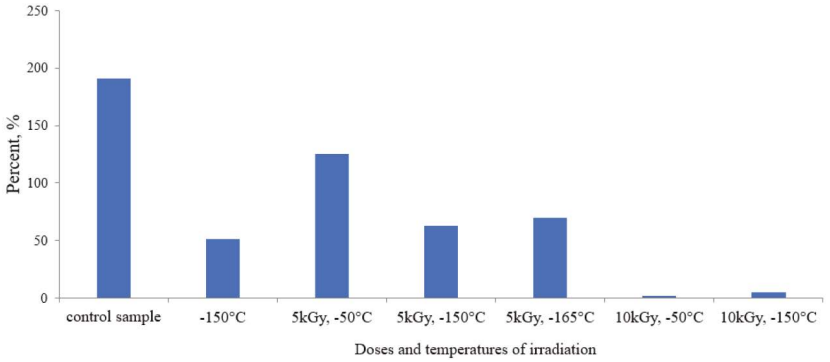

Fig. 1. Phage virulence index in liquid LB-media

In montmorillonite the virulence was lower than in liquid LB-media (Figure 2). In the control samples the number of virulent phages was 9–12 % of the total number, which is 5 times lower than in the liquid medium. After 5 kGy irradiation at –50 °C and –165 °C temperatures the numbers of virulent phages were 10 and 4 % of the total numbers of viral particles. This is an order of magnitude less than in a liquid media, but differs little from the control sample. It is suggested that the phage particles fixed in the mineral matrix, while maintaining a sufficiently high number, had a reduced virulence, which was practically unchanged after high-dose irradiation with accelerated electrons under decreasing temperature.

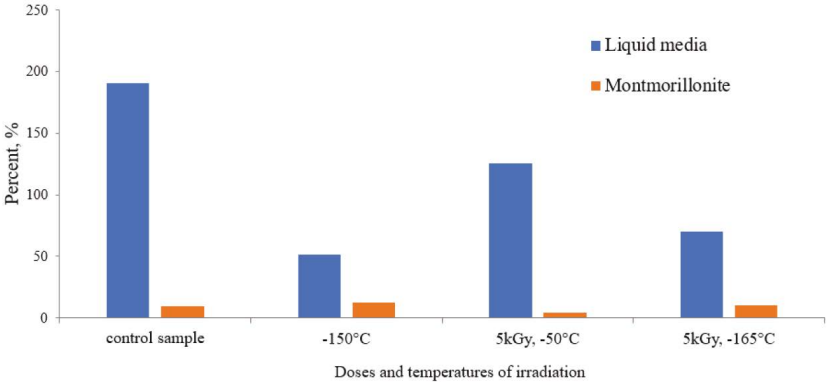

Fig. 2. Comparison of phage virulence indicators after irradiation in different media

The data obtained allow to estimate how long the phage could retain virulence in the regolith of Mars or in the ice of Europa with a constant accumulation of radiation damage. The intensity of ionizing radiation on the surface of modern Mars is about 0.076 Gy/year [3]. A radiation dose of 10 kGy can be accumulated in the surface layer of the regolith for about 130,000 years. This means that at least for such period of time in the present cold conditions of Mars the phages could retain virulence. At a depth of 5 m, the radiation intensity is not higher than 5 mGy/year, and 10 kGy dose can be accumulated over 2 million years. Reasoning in a similar way, it can be assumed that phage

particles can persist in the ice of Europe for at least 30 years at a depth of 10 cm and at least 1000 years at a depth of 1 m [4].

It is estimated that most Martian meteorites reach Earth after thousands and millions of years in outer space. Based on the calculated data on the intensity of dose accumulation inside meteorites, which is no more than 0.25 Gy/year in interplanetary space (depending on the size and composition of meteorite) [5], the results of the study suggest the potential preservation of virulence by phages for at least 40 thousand years in open space (i. e., accumulation of 10 kGy dose for this period).

CONCLUSION:

DT57C phage is resistant to irradiation by high-energy electrons in high doses at low temperatures and low pressure. The phage retained a high number of viral particles and virulence after irradiation. The resistance of the DT57C phage to irradiation at low temperatures exceeds the known limits of the viruses radioresistance.

The phage immobilized in montmorillonite exhibited the increased resistance to radiation comparing the one irradiated in liquid medium. In a mineral environment the virulence of the phage was reduced, but it was still present regardless of the mode of irradiation with accelerated electrons (within the studied range).

Theoretical calculations suggest the possibility of long-term preservation of virulence by phages in extraterrestrial conditions.

The study was partially supported by RFBR, grant No. 20-02-00470.

REFERENCES:

[1] Breitbart M., Rohwer F. Here a virus, there a virus, everywhere the same virus? // Trends in Microbiology. 2005. V. 13. No. 6. P. 278–284.
[2] Hatfull G. F., Hendrix R. W. Bacteriophages and their genomes // Current Opinion in Virology. 2011. V. 1. No. 4. P. 298–303.
[3] Hassler D. M. et al. Mars' surface radiation environment measured with the Mars Science Laboratory's Curiosity rover // Science. 2014. V. 343. No. 6169. Art. 1244797. 35 p.
[4] Pavlov A. et al. Survival of radioresistant bacteria on Europa's surface after pulse ejection of subsurface ocean water // Geosciences. 2019. V. 9. No. 1. 8 p.
[5] Homeck G. et al. Viable transfer of microorganisms in the Solar System and beyond // Astrobiology: The Quest for the Conditions of Life // eds. Horneck G., Baumstark-Khan C. Berlin, Germany: Springer, 2002. P. 57–76.

MICROBIAL COMMUNITIES OF NOVAYA ZEMLYA PERMAFROST: PHYSIOLOGICAL PROPERTIES AND ASTROBIOLOGICAL IMPLICATION

A. A. Belov[1,2], V. S. Cheptsov[1,2,3], N. A. Manucharova[1], Z. S. Ezhelev
[1] *Lomonosov Moscow State University*, *Soil Science Faculty*, *119991 Moscow*, *Russia*
[2] *Network of Researchers on Chemical Evolution of Life* (*NoR CEL*), *Leeds 01924*, *UK*
[3] *Space Research Institute*, *Russian Academy of Sciences*, *119991 Moscow*, *Russia*

KEYWORDS:
culturable bacterial communities, physiological profiling, metabolic activity, 16S rRNA sequencing, stress tolerance, antibiotic resistance

INTRODUCTION:
The study of microorganisms associated with extreme ecological niches of the biosphere is one of the most important tasks of modern microbial ecology. Such investigations have both fundamental and applied importance; they provide new data on microbial biodiversity, functioning of ecosystems, global biogeochemical substances cycles, evolutionary paths of microorganisms, resistance mechanisms (including drug-resistance), new metabolic processes and genetic systems, previously undescribed biologically active compounds, and so forth. Simultaneously, many of modern extreme ecotopes are considered as analogs of some Solar System space bodies because of their list of characteristics and, for this reason, attract researchers' attention as model objects in different astrobiological investigations.

The analysis was performed for the samples collected in the northern part of the Severniy Island (Figure 1) of Novaya Zemlya archipelago (76.896389° N, 67.561389° E).

Fig. 1. Sampling region map. Red circle indicates sampling site location

Proteobacteria were identified as dominant group (45.5 %) in the community *in situ*, subdominant positions in the community were represented by *Actinobacteria*, *Bacteroidetes*, and *Acidobacteria* phyla (39.8 % in total), and representatives of *Gemmatimonadetes*, *Chloroflexi*, and *Verrucomicrobia* phyla were the minor components of the community (11.9 % in total). The percentage of other bacterial phyla representatives was less than 1 %.

The revealed total numbers of prokaryotic cells at the level of ~10^8 cells per gram of sediment or ice and numbers of culturable bacteria about 10^6–10^8 CFU/g are well consistent with the data of previously performed studies on the microbial communities of cold environments [1–3]. The dominant phyla found both using 16S rRNA genes Illumina sequencing and by culturing, were typical for frozen soil and ice samples. Many representatives of isolated taxa are well-known for their ability to survive the effects of low

temperatures [4]. High functional activity of the studied communities was indicated by the results of multisubstrate testing: Relatively higher indices of the community's metabolic activity on different substrates at low temperature (10 °C) are probably caused by the climate of the studied region — temperatures close to 10 °C are much more regular during the year, compared to higher temperatures. However, higher numbers of culturable bacteria and an increase of their morphological and taxonomic diversity were detected at mesophilic temperatures.

The results of physiological assays of the strains revealed the ability of investigated strains to reproduce on the nutrient media right up to the temperature of 2 °C, regardless of the temperature conditions of primary isolation from the native sample. Apart from the ability to reproduce at low temperatures, many of the isolated strains were able to reproduce in high temperature conditions (45–50 °C), which allows to assume the thermotolerant, predominantly mesophilic properties of culturable communities. In regard to the pH of the media, the investigated communities demonstrated neutrophilic moderate acido and high alkalitolerant properties, which were previously shown for the culturable bacterial communities of extreme ecosystems [5–8]. 40 % and more of the strains in the communities studied were able to reproduce at the pH of native sample (close to pH 5). It was previously suggested that cold and freeze tolerance could be associated with salt tolerance [9]. Investigated strains' resistance to the presence of different salts in the media could be explained by the linkage of physiological mechanisms responsible to cold- and salt-tolerance. However, explicit correlations between the resistance to low temperature and high salt concentrations, based on the data obtained, were not observed. Furthermore, high resistance to high concentrations of soluble salts in the media could be caused by studied strains' adaptations to low water activity (a_w) conditions, which originates both at lower temperatures and high concentration of soluble substances. Inhibitory effect rising in the following sequence: $MgSO_4$, KCl, NaCl, $Mg(ClO_4)_2$, $NaHCO_3$ was observed previously for the culturable bacterial communities associated with hot arid desert soils [6, 8].

Antibiotic-resistant strains were isolated from all samples studied. Antibiotic-resistant strains were predominantly resistant to chloramphenicol and tetracycline. Among the investigated strains (134 strains of aerobic heterotrophic bacteria) isolated from the Novaya Zemlya archipelago samples, the six isolates were resistant to five out of seven studied antibiotics — *Ochrobactrum* sp. KBP.AS.113, *Bacillus* sp. KBP.AS.262, *Microbacterium paraoxydans* KBP.AS.275, *Stenotrophomonas maltophilia* KBP.AS.402, *Brachybacterium* sp. KBP.AS.478, *Brevibacillus brevis* KBP.AS.483. More than a half of the isolated strains (66 %) were antibiotic resistant—besides aforementioned high-resistant strains, 18 % of all isolated bacteria were resistant to 4 different antibiotics, 13 % were resistant to 3 antibiotics, 11 % were resistant to two investigated antibiotics, and 20 % were characterised as being resistant to one antibiotic.

The obtained results allow to suggest that the bacterial communities of the investigated samples are able to retain metabolic activity in a wide range of external influences and thereby to contribute to global biospheric processes. The results obtained indicate a high adaptive potential of the studied microbial communities to temperature fluctuations, different pH and different concentrations of soluble compounds. It could testify on the retention of functional activity of the communities in conditions that are changing and non-typical for the Arctic ecosystem.

REFERENCES:

[1] Jansson J. K., Taş N. The microbial ecology of permafrost // Nature Reviews Microbiology. 2014. V. 12. Art. 414. doi:10.1038/nrmicro3262.

[2] Gilichinsky D., Vishnivetskaya T., Petrova M., Spirina E., Mamykin V., Rivkina E. Bacteria in permafrost // Psychrophiles: From Biodiversity to Biotechnology / eds. Margesin R., Schinner F., Marx J. C. Berlin, Heidelberg: Springer, 2008. P. 83–102.

[3] Vorobyova E., Soina V., Gorlenko M., Minkovskaya N., Zalinova N., Mamukelashvili A., Gilichinsky D., Rivkina E., Vishnivetskaya T. The deep cold biosphere: Facts

and hypothesis // FEMS Microbiology Reviews. 1997. V. 20. Iss. 3–4. P. 277–290. doi:10.1111/j.1574-6976.1997.tb00314.x.

[4] Miteva V. Bacteria in snow and glacier ice. In Psychrophiles: From Biodiversity to Biotechnology // eds. Margesin R., Schinner F., Marx J. C. Berlin, Germany: Springer, 2008. P. 31–50.

[5] Makhalanyane T. P., Valverde A., Gunnigle E., Frossard A., Ramond J. B., Cowan D. A. Microbial ecology of hot desert edaphic systems // FEMS Microbiology Reviews. 2015. V. 39. P. 203–221. doi:10.1093/femsre/fuu011.

[6] Belov A. A., Cheptsov, V. S., Vorobyova E. A., Manucharova N. A., Ezhelev Z. S. Stress-Tolerance and Taxonomy of Culturable Bacterial Communities Isolated from a Central Mojave Desert Soil Sample // Geosciences. 2019. V. 9. Iss. 4. Art. 166. 1 p. doi:10.3390/geosciences9040166.

[7] Rampelotto P. Extremophiles and extreme environments // Life. 2013. V. 3. P. 482–485. doi:10.3390/life3030482.

[8] Belov A. A., Cheptsov V. S., Vorobyova E. A. Soil bacterial communities of Sahara and Gibson deserts: Physiological and taxonomical characteristics // AIMS Microbiology. 2018. V. 4. Iss. 4. P. 685–710. doi:10.3934/microbiol.2018.4.685.

[9] Vishnivetskaya T., Kathariou S., McGrath J., Gilichinsky D., Tiedje J. M. Low-temperature recovery strategies for the isolation of bacteria from ancient permafrost sediments // Extremophiles. 2000. V. 4. P. 165–173. doi:10.3390/su2061602.

EFFICIENCY OF CHARGE EXCHANGE BETWEEN SOLAR WIND PROTONS AND THE EXTENDED HYDROGEN CORONA OF MARS

V. I. Shematovich, D. V. Bisikalo
Institute of Astronomy of the Russian Academy of Sciences, *Moscow*, *Russia*
(*shematov@inasan.ru*)

KEYWORDS:
Mars, solar wind, high-energy proton and hydrogen atom precipitation, auroral phenomena, atmospheric ultraviolet emissions, kinetic Monte Carlo model

INTRODUCTION:
Recently discovered proton auroras [1] are the ones of a few observed phenomena on Mars that arise as a result of direct interaction of solar wind protons with an extended hydrogen corona.

The results of model calculations [2] of the efficiency of charge exchange between protons of the solar wind and hydrogen atoms in the extended corona of Mars are presented. It is shown that the energy spectrum of hydrogen atoms penetrating the Martian atmosphere is identical to the spectrum of protons of the unperturbed solar wind. The charge exchange efficiency varies in the range of 2–4 % depending on the position of the boundary of the induced Mars magnetosphere (Figure 1).

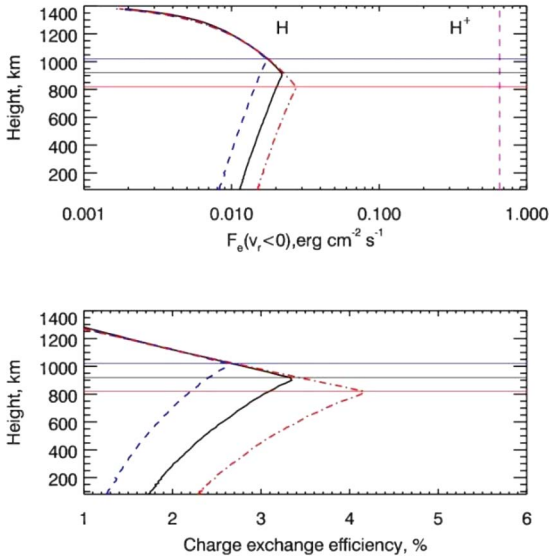

Figure 1. Height profiles of the downward energy flux of atomic hydrogen generated due to the charge exchange between protons of the unperturbed solar wind with thermal hydrogen atoms in the extended corona of Mars, depending on the position of the induced magnetosphere boundary (*upper panel*). Height profiles of the charge exchange efficiency are shown in dependence on the position of the induced magnetosphere boundary (*bottom panel*)

The calculated fluxes and energy spectra of high-energy hydrogen atoms penetrating through the induced magnetosphere boundary are an external boundary condition for the previously developed kinetic Monte Carlo model of the high-energy proton and hydrogen atom precipitation into the Martian atmosphere [3, 4]. This coupled numerical model is designed to study the auroral phenomena on Mars and, in particular, will be used for detailed calculations of the characteristics of the atomic hydrogen emission in the Ly-α line and for comparison with observations of the recently discovered proton aurora [1, 5] on Mars.

ACKNOWLEDGEMENT:
This study was supported by the Russian Science Foundation (project No. 19-12-00370).

REFERENCES:

[1] Deighan J., Jain S. K., Chaffin M. S. et al. Discovery of proton aurora at Mars // Nature Astronomy. 2018. V. 2. P. 802–807.
[2] Shematovich V. I., Bisikalo D. V. Kinetic calculations of the charge exchange efficiency between solar wind protons and extended hydrogen corona of Mars // Astronomy Reports. 2020. V. 64. No. 11 (in press).
[3] Bisikalo D. V., Shematovich V. I., Gérard J.-C., Hubert B. Monte Carlo simulations of the interaction of fast proton and hydrogen atoms with the Martian atmosphere and comparison with in situ measurements // J. Geophysical Research. 2018. V. 123. P. 58.
[4] Shematovich V. I., Bisikalo D. V., Gérard J.-C., Hubert B. Kinetic Monte Carlo model of the precipitation of high-energy proton and hydrogen atoms into the Martian atmosphere with taking into account the measured magnetic field // Astronomy Reports. 2019. V. 63. No. 10. P. 835.
[5] Hughes A., Chaffin M., Mierkiewicz J. et al. Proton Aurora on Mars: A Dayside Phenomenon Pervasive in Southern Summer // J. Geophysical Research: Space Physics. 2019. V. 124. Iss. 12. P. 10,533–10,548.

SOLAR WIND INTERACTION WITH THE EARTH'S HIGH-LATITUDE IONOSPHERE DURING GEOMAGNETIC STORM IN JUNE 2015 BY THE RADIO OCCULTATION DATA

V. N. Gubenko, I. A. Kirillovich
Kotel'nikov Institute of Radio Engineering and Electronics RAS, Fryazino branch, Vvedensky square 1, Fryazino 141190, Moscow region, Russia (*vngubenko@gmail.com; gubenko@fireras.su*)

KEYWORDS:
earth's high-latitude ionosphere, solar wind, geomagnetic storm, radio occultation, refractive attenuation and absorption of signals

INTRODUCTION:
In June 22–23, 2015 coronal mass ejections (CMEs) toward the Earth took place on the Sun. This event was recorded by many spacecrafts and ionospheric stations. The most powerful ejection was identified by a magnetometer as a jump of interplanetary magnetic field (IMF) from ~10 to ~40 nT, and it was also noted by SWEPAM (Solar Wind Electron, Proton, and Alpha Monitor) instrument as a sudden increase in solar wind density from ~20 to ~45 particles/cm^3 with a corresponding increase in pressure to values above 50 nPa. The impact of the CME with the bow shock was expected on June 22, 2015 at ~18:36 UT, after a smaller shock at ~05:40 UT. The Boyle index, associated with the strong southward component of the IMF vector, sent a "yellow alert" signal at 06:04 UT and a "red alert" at 18:34 UT before the CME was impacted the bow shock. Coronal mass ejections were accompanied by powerful X-ray fluxes which were detected by the geostationary GOES-13 and -15 spacecrafts. These ejections provoked a strong magnetic storm of class G4 on Earth (G4 = *Kp* – 4). A detailed description of geomagnetic conditions on June 22–23, 2015 during the storm (density, speed and pressure of the solar wind; components *Bx*, *By*, *Bz* of the interplanetary magnetic field) can be found at the work [1].

The aim of this work is to analyze the L1-band radio signals (carrier frequency f_1 = 1575.42 MHz), emitted by transmitters from GPS satellites and recorded by receivers onboard low orbital Formosat-3/COSMIC satellites, in order to determine the small-scale structure of the Earth's high-latitude ionosphere at altitudes from 50 to 110 km during the storm in June 2015.

REFRACTIVE ATTENUATION AND ABSORPTION OF THE L1-BAND RADIO WAVES IN THE EARTH'S LOWER IONOSPHERE:
To obtain parameter estimates of the small-scale structure in the Earth's lower ionosphere during the abovementioned geomagnetic storm, we selected from the large Formosat-3/COSMIC database about 100 radio occultation (RO) measurements carried out from June 22 to 23, 2015. The selected RO data sessions were performed at latitudes from 65° N to 88° N and they covered an altitude interval from 50 to 110 km.

It is hardly to detect the beginning of geomagnetic storm from the RO data, but we have found that fluctuations of the $P(h)$ and $X(h)$ values in the interval 80–100 km of the Earth's high-latitude ionosphere increase from the moment of passage of the powerful X-ray flux. Note that the electron density N_e increases at night, becoming more than 10^5 cm^{-3} (Figure 1). From a comparison of graphs in Figure 1*a* (panels a and c), it can be seen that the altitude position of electron density maximum in the ionospheric layer practically coincides with the position of refractive attenuation minimum of the signal. This corresponds to results of the works [2–4], where it was shown that, when the propagation vector is parallel to the ionization plane of sporadic E-layer during the RO sounding of the Earth's ionosphere, the radio wave propagation through its central part (electron density peak) is leading to strong defocusing of the rays, and when passing through the edges — to their focusing.

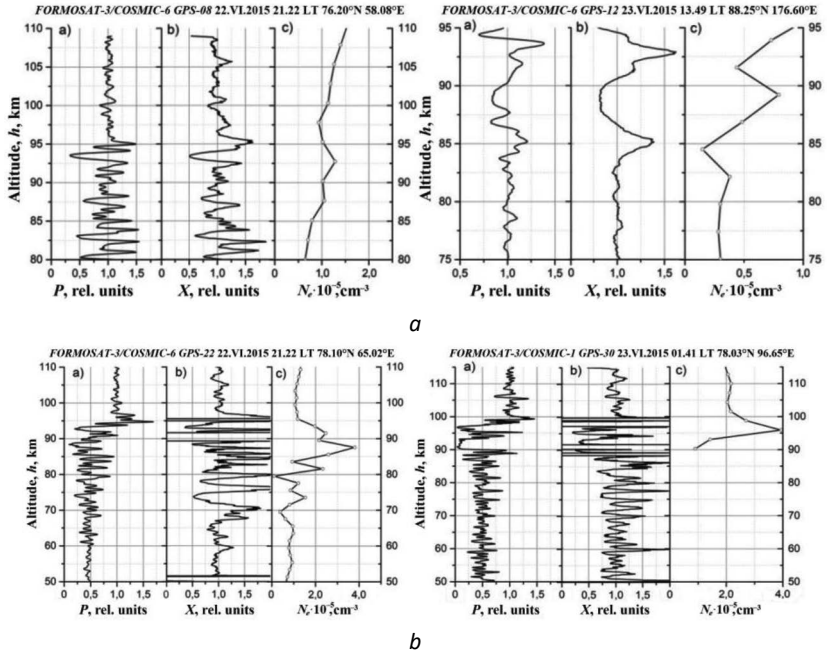

Fig. 1. Altitude profiles of the normalized power — $P(h)$, the refractive attenuation — $X(h)$ and electron density — $N_e(h)$ obtained from the RO data of Formosat-3/COSMIC-6 satellite: *a* — 22.06.2015 at 21:22 LT in the ionospheric region with coordinates 76.2° N, 58.08° E (*left*) and 23.06.2015 at 13:49 LT in the region with coordinates 88.25° N, 176.6° E (*right*); *b* — 22.06.2015 at 21.22 LT in the ionospheric region with coordinates 78.1° N, 65:02° E (*left*) and 23.06.2015 at 01:41 LT in the region with coordinates 78.03° N, 96.65° E (*right*)

As seen from data presented in Figure 1*b*, when radio sounding of the region of the Earth's polar cap (78.03° N, 96.65° E) at altitudes from 101.5 to 90.3 km (the ray descends from top to bottom) is ongoing, the power of decimeter radio waves decreases on average to 0.1 (–10 dB), then returns to 0.5 (–3 dB) and further remains at the same level. Radio sounding of the other region of the polar cap (78.1° N, 65.02° E) showed that the average signal level drops to 0.5 (–3 dB) at an altitude of 89.5 km and then remains at that level (see Figure 1*b*). Analysis of profiles $X(h)$ in Figure 2 shows that the average value $\langle X \rangle$ is $\langle X \rangle = 1$ (0 dB), i. e. refractive attenuation in altitude ranging from 50 to 90 km is practically absent. Therefore, we believe that the aforementioned attenuation of signal power $P(h)$ observed in the analyzed altitude range can be associated with the radio wave absorption in the Earth's lower ionosphere during geomagnetic storm.

A small radio wave absorption (up to –1 dB), which can be seen in the RO data at GPS-frequencies, was mentioned in the work [5]. The most characteristic features of the high-latitude ionosphere (*D*-region) are the special radio wave absorption in the polar cap, caused by the proton invasion with energies of tens MeV, and anomalous auroral absorption associated with electron precipitations. During periods of solar flares directed toward the Earth, due to a sharp increase in solar ionizing X-ray radiation, the sudden ionospheric disturbances occur to manifest themselves as ionization increases, mainly in the *D*- and *E*-ionospheric regions. Auroral radio wave absorption, observed often in the aurora zone during periods of magnetospheric storms and substorms, is associated with precipitations of charged particles (mainly electrons with energies of 20–100 keV) from the magnetosphere to the Earth's lower ionosphere [6].

The absorption of L1-band signals was observed very clearly for the two RO sessions of Formosat-3/COSMIC measurements in the Earth's ionosphere (see Figure1*b*). For one of them, the radio wave power attenuation reached –10 dB with a return to the level of –3 dB. For other RO measurement ses-

sion, it was –3 dB (Figure 1*b*, panels a). Using these data and solving the inverse problem, one can determine the vertical profile of radio wave absorption coefficient in the Earth's lower ionosphere.

CONCLUSION:

The data of about 100 RO sessions of probing the high-latitude (>65° N) ionosphere of the Earth's northern hemisphere have been analyzed. These Formosat-3/COSMIC measurements were carried out on June 22–24, 2015 at the carrier GPS-frequency 1545.42 MHz (band L1). It was found that the altitude location of electron density maximum in the ionospheric layer practically coincides with the altitude position of the refractive signal attenuation minimum, which corresponds to early RO sounding results of sporadic E-layers in the Earth's ionosphere.

Based on the analysis of Formosat-3/COSMIC RO measurements carried out during strong geomagnetic storm on June 22–23, 2015 (class G4), the absorption of decimeter radio waves (L1-band) in the Earth's high-latitude lower ionosphere was detected. The absolute value of absorption is ~3 dB in the interval of 60–90 km, and in some cases it reaches ~10 dB at altitudes from 90 to 95 km. It is shown that from the obtained data one can find altitude profiles of the radio wave absorption coefficient in the Earth's lower ionosphere.

ACKNOWLEDGEMENTS:

This study was partially supported by the Russian Foundation for Basic Research (RFBR project No. 19-02-00083 A) and program No. 12 of the Presidium of the Russian Academy of Sciences.

REFERENCES:

[1] Reiff P. H., Daou A. G., Sazykin S. Y., Nakamura R., Hairston M. R., Coffey V., Chandler M. O., Anderson B. J., Russell C. T., Welling D., Fuselier S. A., Genestreti K. J. Multispacecraft observations and modeling of the 22/23 June 2015 geomagnetic storm // Geophysical Research Letters. 2016. V. 43. P. 7311–7318. doi:10.1002/2016GL069154.

[2] Gubenko V. N., Pavelyev A. G., Kirillovich I. A., Liou Y.-A. Case study of inclined sporadic E layers in the Earth's ionosphere observed by CHAMP/GPS radio occultations: Coupling between the tilted plasma layers and internal waves // Advances Space Research. 2018. V. 61. No. 7. P. 1702–1716, doi:10.1016/j.asr.2017.10.001.

[3] Gubenko V. N., Kirillovich I. A. Modulation of sporadic E layers by small-scale atmospheric waves in Earth's high-latitude ionosphere // Solar-Terrestrial Physics. 2019. V. 5. No. 3. P. 98–108. doi:10.12737/stp-53201912.

[4] Zeng Z., Sokolovskiy S. Effect of sporadic E cloud on GPS radio occultation signal // Geophysical Research Letters. 2010. V. 37. Art. L18817. doi:10.1029/2010GL044561.

[5] Gorbunov M. E. Radio occultation sounding the atmosphere. In: Dynamics of wave and exchange processes in the atmosphere. M.: GEOS, 2017. Ch. 4. P. 407–457 [in Russian].

[6] Brunelli B. E., Namgaladze A. A. Physics of ionosphere. M.: Nauka, 1988. 528 p. [in Russian].

ON THE MOVEMENT OF ENSEMBLES OF OBJECTS BY THE SPATIO-TEMPORAL TECHNOLOGY

N. P. Bulatova
Schmidt Institute of Physics of the Earth of the Russian Academy of Sciences, Moscow, Russia (*n.p.bulatova@mail.ru*)

KEYWORDS:
space-time technology, universal navigation system, Sun, solar neutrinos, elementary particles, vector-angles

The question of movement of ensembles of objects (particles, planets, physical fields, plate lithospheric) have been developed in space-time technology [1, 2]. For a long time, scientists observing the motion of stars and planets thought about the structure of the world. Different systems were proposed,, representing in different ways the motion of the planets in the solar system: if around the Earth - geocentric Ptolemaic system (Ptolomaeus, 100–170 years), if around the Sun — the heliocentric Keplerian system (Johann Kepler, 1571–1630), etc. For a long time, scientists have been completely satisfied with Kepler's System consisting of three laws until they have begun researches of mutual influence of celestial bodies and the interplanetary environment through physical fields. At present the known systems allow us to consider the movement of each planet or their satellites in astrometric terms only individually, without liaison with other planets and the Sun. The research results are often fragmentary due to the high cost of systematic observations and observation devices.

Using the example of studying the movement of solar neutrinos between the Earth and the Sun, the author proposed an original system for describing the movement of objects of various scales (from suns to elementary particles) in a 3-dimensional model of the Earth [3]. This system includes universal navigation to describe, for example, the movement of celestial bodies relative to the Earth as a change in the direction of the vector linking them to the Earth, and usually changes depending on their position in space [4]. This vector can be represented as a pair: "source" (Sun, planets) — "detector" (Earth). The system is based on the use of two spherical and one Cartesian coordinate systems. The centers of the spherical and Cartesian systems coincide with the center of the "detector" (point 0 of the Earth), the center of the other coincides with the Central point of the "source".

Thus, after placing the observer (detector) in the center of the Earth and connecting the observed objects by radius vectors, we can get a simple system that allows us to simultaneously track the change in the direction of movement of an ensemble of objects. Distance from the center of the Earth can be various. So, the study of movement of planets of the Solar system was a new system in which the position of each object can be described by two angles of vector of the classical spherical coordinate system (math.). First angle with the OZ axis directed to the celestial pole, we shell name the Polar Zenith angle (astron.); the second angle with the axis — *OX*, "the hour angle" — *t*, correspondingly, which coincides with the reference terrestrial solar day. The ecliptic plane, while transformed into an open conical surface, seems to consist of vectors with parameters *T*, *t* corresponding to the earth's seasonal and diurnal solar time.

As a result of investigation following are proposed: 1) the new universal navigation system [5] and 2) the kinematic theory of motion [6]. Their allow us to study movement objects of different-scale (as ensembles) and processes inside the sphere, on the surface and outside it (in near-earth space and interplanetary space) in a single coherent system, combining all this information into one common system [3, 7].

REFERENCES:

[1] Bulatova N. P. On the movement of ensembles of objects (planets, tectonic of the plates) by the spatio-temporal technology // Abstract European Planetary Science Congress. 2014.
[2] Bulatova N. P. Spatio-Temporal Technology. M.: LENAND, 2016. 120 p.
[3] Bulatova N. P. On the Solar Neutrino Tomography of the Earth: scanning geometry // Izv. Physics Solid Earth. 1999. V. 35. No. 2. P. 150–160.
[4] Bulatova N. P. The method of moving source and its application to the study of the Earth // OGGGGN Bull. Russian Academy of Sciences. 2000. No. 2(12). V. 1. P. 110–125.
[5] Bulatova N. P. On the universal space-time coordinate system for astrophysical and geophysical research // The planet Earth System. M.: LENAND, 2009. P. 64–68.
[6] Bulatova N. P. On vector flow through the sphere // Geoinformatics. 1998. No. 4. P. 21–23.
[7] Bulatova N. P. Three-dimensional spatio-temporal modeling of geophysical events and the movement of celestial bodies // Complex Systems. 2012, V. 20. No. 3. P. 215–227.

THE INFLUENCE OF THE PARENT STAR Ly-α RADIATION ON ABSORPTION IN THE H-α LINE OF THE HOT ATMOSPHERES HD 189733B AND HD 209458B

I. B. Miroshnichenko[1,2], I. F. Shaikhislamov[1,2], A. G. Berezutsky[1], E. S. Vetrova[1,2]

[1] *Institute of Laser Physics SB RAS, 630132, Russia, Novosibirsk, Acad. Lavrentyeva, 15b* (*mib383@gmail.com*)

[2] *Novosibirsk State Technical University, Russia, Novosibirsk, Prospekt K. Marksa, 20*

KEYWORDS:
exoplanet, planetary wind, stellar wind, multi-fluid model, Monte Carlo radiation transport

INTRODUCTION:
The results of computer simulation of resonance scattering of stellar Ly-α photons by hydrogen atoms in the atmospheres of hot Jupiters HD 189733b and HD 209458b are presented. The simulation was carried out using the Monte Carlo method (Monte Carlo radiation transport) in three-dimensional geometry, while the problem was considered in dynamics. As the initial data, we considered the distribution of temperature and bulk density of hydrogen atoms in the atmospheres of the planets, obtained by hydrodynamic modeling [1]. The emission spectrum of Lyα was specified using profiles from [3].

RESULTS:
Based on the developed model, we obtained the distribution of the bulk density of hydrogen atoms excited to the second level for the atmospheres of exoplanets HD 189733b and HD 209458b. Using the obtained distributions, the Hα absorption / transmission spectra were calculated, which are shown in Figure 1.

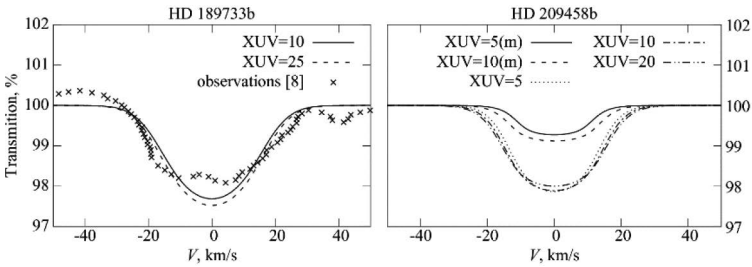

Fig. 1. H-α transmission spectrum of planets HD 189733b and HD 209458b

The results obtained for the planet HD 189733b were compared with observational data, as well as with the calculations of other authors, and good agreement was obtained.

ACKNOWLEDGEMENTS:
This work was carried out as part of the RSF (project No. 18-12-00080) and RFBR (No. 20-02-00520). Parallel computer modeling was performed using the supercomputer center of Moscow State University, the Interdepartmental Supercomputer Center of the RAS Siberian Supercomputer Center of the SB RAS and the supercomputer center of Novosibirsk State University.

REFERENCES:
[1] Shaikhislamov I. F., Khodachenko M. L., Lammer H., Berezutsky A. G., Miroshnichenko I. B., Rumenskikh M. S. Three-dimensional modelling of absorption by various species for hot Jupiter HD 209458b // Monthly Notices of the Royal Astronomical Society. 2020. V. 491. No. 3. P. 3435–3447.

[2] Bourrier V., des Etangs A. L. 3D model of hydrogen atmospheric escape from HD 209458b and HD 189733b: radiative blow-out and stellar wind interactions // Astronomy and Astrophysics. 2013. V. 557. P. A124.

[3] Cauley P. W., Redfield S., Jensen A. G., Barman T. Variation in the pre-transit Balmer line signal around the hot Jupiter HD 189733b // The Astronomical J. 2016. V. 152. No. 1. P. 20.
[4] Huang C., Arras P., Christie D., Li Z. Y. A model of the Hα and Na transmission spectrum of HD 189733b // The Astrophysical J. 2017. V. 851. No. 2. P. 150.

DUSTY PLASMA PROCESSES ASSOCIATED WITH METEOR SHOWERS IN THE EARTH'S ATMOSPHERE

T. I. Morozova, S. I. Popel
Space Research Institute, *Russian Academy of Sciences*, *Moscow*, *Russia*
(*timoroz@yandex.ru*)

KEYWORDS:
meteors, meteor showers, meteoroids, tail of meteoroid, dusty plasmas, charging of dust particles, dust acoustic waves, electrophonic sounds, dust particles in the Earth's atmosphere, modulational instability

INTRODUCTION:
Passages of meteors are independent of man natural phenomena which are difficult to predict. One need to study these phenomena in detail to understand the processes caused by them and the consequences that passages of meteors bear for nature and man. A special place in meteor physics is occupied by the study of the occurrence of sound phenomena accompanying the passage of meteors. It can be sounds heard simultaneously with the passage of bright fireballs, and after their passage and during meteor showers. Signals from meteoroids cover a wide range of frequencies: from 0 Hz to several kHz [1–3]. Anomalous sounds, heard simultaneously with the passage of meteors and called electrophonic, are obviously associated with electromagnetic phenomena. When a meteor reaches a certain height in the atmosphere at which it is crushed and burned, observers on Earth can hear various sounds, such as whistling, crackling, hissing, hum [4]. It is assumed that they can be described not by one, but by several physical mechanisms and can be connected to the charged dust in the tail of meteoroid. Dusty plasmas in meteor tails occurs due to meteor body fragmentation and further charging of dust fragments under the action of different currents: ion current, electron current, mechanoemission current, reverse current of mechanoelectrons and thermoelectron current. It leads to positive particle charges for typical parameters of dusty plasmas of the meteor tail mainly due to emission currents.

It was proposed that modulation of the electromagnetic waves from the meteoroids in the Earth's atmosphere in the low frequency range can be connected with sound phenomena from the passage of a meteoroids [5]. The appearance of low-frequency noise in the ionosphere as a result of the development of modulational interaction of electromagnetic waves associated with the dust acoustic perturbations was considered in [6–8].

DISCUSSION:
The study discusses dusty plasma processes in the Earth's ionosphere associated with the passage of meteor bodies and the spread of the tail of meteoroid. The research covers both the processes occurring in the tail of meteoroid itself and the processes that occur in the Earth's atmosphere during the passage of a meteoroid, as well as their response and influence on observers and the operation of various technical systems. In particular, mechanisms are proposed to explain the occurrence of sound phenomena accompanying the passage of meteors during meteor showers. The mechanism of the formation of dusty plasmas in the tail of meteoroid is described. It is shown that as a result of charging dust particles of a meteor matter, there are created conditions for the appearance of dust acoustic waves. Dust acoustic disturbances are excited as a result of the development of modulational instability of electromagnetic waves from a meteor and have frequencies characteristic of dust sound (0.003–60 Hz). Eyewitness data showed that observers on the Earth can hear low-frequency sounds that occur during meteor showers. It is assumed that sound waves can reach the Earth's surface as a result of the transfer of dust particle perturbations to the oscillations of neutrals, whose concentration is high in the atmosphere. Here are described mechanisms of crushing of meteorites and the charging of the meteor dust. The characteristic charges of dust fragments for particles of nano- and micro-sizes are

estimated. Dust particles of various shapes are considered. The increments at which the modulational excitation of low-frequency dust acoustic pertirbations occur are calculated. The conditions for the development of modulational instability are given.

ACKNOWLEDGEMENTS:
The work was supported by Grant of Russian Science Foundation (project No. 19-72-00005).

REFERENCES:

[1] Spalding R., Tencer J., Sweatt W., Conley B., Hogan R., Boslough M., Gonzales G., Spurný P. // Scientific Reports. 2017. V. 7. P. 41251. doi:10.1038/srep41251.
[2] Verveer P., Bland A., Bevan A. W. R. // 63rd Ann. Meteoritical Soc. Meeting. 2000. P. A163–A164.
[3] Zgrablić G., Vinković D., Gradečak S., Kovačić D., Biliskov N., Grbac N., Andreić Ž., Garaj S. // J. Geophysical Research. 2002. V. 107. P. SIA11-1. doi:10.1029/2001JA000310.
[4] Keay C. S. L. // J. Scientific Exploration. 1993. V. 7. P. 337.
[5] Spalding R., Tencer J., Sweatt W., Conley B., Hogan R., Boslough M., Gonzales G., Spurný P. // Scientific Reports. 2017. V. 7. P. 41251. doi:10.1038/srep41251.
[6] Kopnin S. I., Popel S. I., Yu M. Y. // Plasma Physics Reports. 2007. V. 33. P. 323–329.
[7] Kopnin S. I., Morozova T. I., Popel S. I. // Plasma Physics Reports. 2015. V. 41. No. 2. P. 171–177.
[8] Borisov N. D., Kopnin S. I., Morozova T. I., Popel S. I. // Plasma Physics Reports. 2019. V. 45. No. 4. P. 355–360.

CHESS — CONSTELLATION OF CUBESATS: ANALYZING THE DRIVERS OF THE EARTH'S EXOSPHERE WITH MS AND GNSS

R. Fausch[1], P. Wurz[1], M. Rothacher[2], N. Martinod[3], T. Trébaol[3], A. Villegas[3], F. Corthay[4], M. Joss[5], J. Kneib[6], N. Pazos[7], and the CHESS team[1–7]

[1] *Physics Institute, University of Bern, Sidlerstrasse 5, 3012 Bern, Switzerland* (*rico.fausch@space.unibe.ch*)

[2] *Institute of Geodesy and Photogrammetry, ETH Zürich, Robert-Gnehm-Weg 15, 8093 Zürich, Switzerland*

[3] *Ecole Polytechnique Fédérale de Lausanne EPFL, ENT-R ESC PPH 335 Station 13, 1015 Lausanne, Switzerland*

[4] *Institute of Systems Engineering, University of Applied Sciences Western Switzerland HES-SO Valais, Route du Rawil 47, 1950 Sion, Switzerland*

[5] *Competence Center for Electronics, Lucerne University of Applied Sciences and Arts HSLU, Technikumstrasse 21, 6048 Horw, Switzerland*

[6] *Laboratory of Astrophysics, Ecole Polytechnique Fédérale de Lausanne EPFL, Chemin des Maillettes 51, 1290 Versoix, Switzerland*

[7] *Haute Ecole Arc HES-SO, Rue de la Serre 7, 2610 St-Imier, Switzerland*

KEYWORDS:
terrestrial exosphere, exospheric temperature, exospheric density, atmospheric escape, night-side transport, composition variation at the day-night-side terminator

Chemical composition and density measurements of the upper atmosphere provide key insights into the origin and evolution of celestial objects. The density and the chemical composition of planet's atmosphere may evolve from a hostile, dense primary atmosphere to a life-harbouring tertiary atmosphere as present on Earth by losing atmospheric species to space upon formation of the object. The present-day atmospheric escape rates can be measured or inferred from exospheric temperatures and density profiles, for many species of the upper atmosphere. By modelling, these escape rates can be adapted to conditions in the past to study the evolution of the atmospheric composition.

The terrestrial exosphere and upper ionosphere are complex dynamic regions that adapt to several endogenous and exogenous drivers. The Sun as such a driver forces the upper atmosphere to respond to the solar UV/EUV flux and solar energetic particles. These external influences cause a variation of both the density, extent, and the chemical composition of the upper atmosphere on several time scales ranging from minutes to the age of the Solar System leading to various phenomena including atmospheric evolution and night-side transport of species. Although these interactions have been extensively studied over the past decades, the scientific community still lacks some basic measurements in the terrestrial upper atmosphere to derive the exospheric temperatures and its variation as a function of the corresponding drivers.

Thus, we designed the CHESS mission consisting of two 3U CubeSat-type satellites on different orbits. The science payload of each spacecraft consists of a new generation of dual-frequency GNSS receivers [1] for total air density measurements from drag and total electron content above the satellites and a compact time-of-flight mass spectrometer [2] for in situ measurements of both the chemical composition and density in the upper atmosphere. Enabled by these two novel scientific instruments, the primary goal of the CHESS mission is to record an inventory of the neutral species and ions present at various heights in the exosphere. From these measurements, we will derive numerous atmospheric properties including exospheric temperature profiles, compositional variations of the exosphere, atmospheric escape rates, as function of the external drivers.

ACKNOWLEDGEMENT:
The support of the whole CHESS team is acknowledged.

REFERENCES:

[1] Chen K., Meindl M., Rothacher M., Kreiliger F., Styger E., Joss M., De Florio S., Gilabert L. A GNSS Payload with Commercial Off-The-Shelf Receivers for CubeSat Precise Orbit Determination // 4th COSPAR Symposium — Small Satellites for Sustainable Science and Development. Nov. 4–8, 2019, Herzliya, Israel. 2019.

[2] Fausch R., Wurz P., Tulej M., Rohner U. CubeSatTOF: Planetary Atmospheres Analyzed with a 1U High-Performance Time-Of-Flight Mass Spectrometer // Proc. Small Satellite Conf. 2020.

INEUTRINO TELESCOPE AND THE SUN

I. M. Minaev[2], O. B. Khavroshkin[1], V. V. Tsyplakov[1]
[1] *Institute Common Physics*
[2] *Institute Physics of the Earth*, *RAS*, Moscow, Russia (khavole@ifz.ru)

KEYWORDS:
Sun, neutrino flux, radiation pattern, neutrino telescope, cavitation model of neutrino radiation

In this study, an attempt is made to study the Sun on the basis of modern equipment and the latest advances in the study of solar neutrino fluxes. In particular, a neutrino telescope based on the ANRI effect is used. This made it possible to start the problem of the internal structure of the Sun within the framework of the model of a neutrino source of the central zone. The first results obtained from the flow pattern are in good agreement with the cavitation radiation neutrino model.

SCIENCE GOALS AND MISSION OBJECTIVES FOR THE FUTURE EXPLORATION OF ICE GIANTS SYSTEMS — A HORIZON 2061 PERSPECTIVE

M. Blanc[1,2], K. Mandt[3], O. Mousis[2], N. André[1], A. Bouquet[2], S. Charnoz[4], K. Craft[3], M. Deleuil[2], L. Griton[1], R. Helled[5], R. Hueso[6], L. Lamy[7], J. Lunine[8], Th. Ronnet[9], J. Schmidt[10], K. Soderlund[11], D. Turrini[12], E. Turtle[3], P. Vernazza[2], O. Witasse[13]

[1] *IRAP, CNRS-Université Toulouse III, France* (*michel.blanc@irap.omp.eu*)
[2] *LAM, CNRS-Aix-Marseille Université, Marseille, France*
[3] *JHU-APL, Laurel, MD, USA*
[4] *Institut de Physique du Globe de Paris*
[5] *University of Zurich, Switzerland*
[6] *Universidad del País Vasco* (*UPV/EHU*)
[7] *LESIA, CNRS-Observatoire de Paris, Meudon, France*
[8] *Cornell University, Ithaca, NY, USA*
[9] *Lund University, Sweden*
[10] *University of Oulu, Finland*
[11] *Institute for Geophysics, Jackson School of Geosciences, University of Texas at Austin, Austin, TX, USA*
[12] *Institute for Space Astrophysics and Planetology INAF-IAPS, Italy*
[13] *ESA-ESTEC, The Netherlands*

KEYWORDS:
ice giants, giant planets, outer solar system, planetary systems, origins, diversity, workings, habitability

The comparative study of the different planetary systems accessible to our observations is a unique source of new scientific insight: it can reveal to us the diversity of these systems and of the objects within them, help us better understand their origins and how they work, find and characterize habitable worlds, and ultimately, search for alien life in our galactic neighborhood. But, in the solar system itself, two of its secondary planetary systems, the ice giant systems, as well as their two main objects, Uranus and Neptune, remain poorly explored. We will present an analysis of our current limited knowledge of these systems in the light of six key science questions about planetary systems formulated in the "Planetary Exploration, Horizon 2061" long-term foresight exercise: (Q1) What is the diversity of planetary systems objects? (Q2) What is the diversity of their architectures? (Q3) What do we know of their origins and formation scenarios? (Q4) How do they work? (Q5) Do they host potential habitats? (Q6) Where and how to search for life?

We will show that a long-term plan for the space exploration of ice giants and their systems, complemented by the combination of Earth and space-based observations, will provide major contributions to answers to these six questions. In order to do so, we identify the measurements that must be performed in priority to address each of these questions, the destinations to choose (Uranus, Neptune, Triton or a subset of them), and the combinations of space platform(s) (orbiter, atmospheric entry probe(s), lander…) and of flight sequences needed.

Based on this analysis, we look at the different launch windows available until 2061, using a Jupiter fly-by, to send a mission to Uranus or Neptune.

We find that:

(1) a single mission to one of the Ice giants, combining an atmospheric entry probe and an orbiter tour starting on a high-inclination, low-periapse orbit, followed by a sequence of lower- inclination orbits, at least at one of the planets, will make it possible to address a broad range of these key questions;

(2) a combination of two well-designed missions to each of the ice giant systems, to be flown in parallel or in sequence, will make it possible to address five out of the six key questions, and to establish the prerequisites for addressing the sixth one. The 2032 Jupiter fly-by window offers a unique opportunity to achieve this goal;

(3) if this window cannot be met, using the 2036 Jupiter fly-by window to send a mission to Uranus first, and then the 2045 window for a mission to Neptune, will achieve the same goals. As a back-up option, the feasibility of sending an orbiter + probe mission to one of the planets and using the opportunity of a mission on its way to the interstellar medium to execute a close fly-by of the other planet and deliver a probe into its atmosphere should be studied carefully;

(4) based on the expected science return of the first two missions, a third mission focusing on the search for life at a promising moon, namely Triton based on our current knowledge, or perhaps one of the active moons of Uranus after due characterization, can be properly designed.

By the 2061 horizon, the first two missions of this plan can be implemented and the design of a third mission focusing on the search for life can be consolidated. Given the likelihood that such a plan may be out of reach of a single national agency, international collaboration is the most promising way to implement it.

A PRELIMINARY STUDY OF MIT COUPLING AT JUPITER BASED ON JUNO OBSERVATIONS AND MODELLING TOOLS

M. Blanc[1], Y. Wang[1], N. André[1], P.-L. Blelly[1], Ph. Louarn[1], C. Louis[1], A. Marchaudon[1], J.-C. Gérard[2], B. Bonfond[2], D. Grodent[2], B. M. Dinelli[3], A. Adriani[4], A. Mura[4], B. Mauk[5], G. Clark[5], F. Allegrini[6], S. Bolton[6], R. Gladstone[6], J. Connerney[7], S. Kotsiaros[8], W. Kurth[9]

[1] *IRAP, Toulouse, France* (*michel.blanc@irap.omp.eu*)
[2] *University of Liège, Belgium*
[3] *ISAC-CNR, Roma, Italy*
[4] *INAF, Frascati, Italy*
[5] *JHU-APL, Laurel, MD, USA*
[6] *SwRI, San Antonio, TX, USA*
[7] *NASA-Goddard Space Flight Center, Greenbelt, MD, USA*
[8] *University of Maryland, MD, USA*
[9] *University of Iowa, USA*

KEYWORDS:
planetary magnetospheres, giant planets, space exploration, MIT coupling, Jovian ionosphere

The dynamics of the Jovian magnetosphere is controlled by the complex interplay of the planet's fast rotation, its solar-wind interaction and its main plasma source at the Io torus. Juno observations have amply demonstrated that the Magnetosphere-Ionosphere-Thermosphere (MIT) coupling processes and regimes which control this interplay are significantly different from their Earth and Saturn counterparts. At the ionospheric level, these MIT coupling processes can be characterized by a set of key parameters which include ionospheric electrodynamic parameters (conductances, currents and electric fields), exchanges of particles along field lines and auroral emissions. Knowledge of these key parameters in turn makes it possible to estimate the net deposition/extraction of momentum and energy into/out of the Jovian upper atmosphere. We will present a method combining Juno multi-instrument data (MAG, JADE, JEDI, UVS, JIRAM and WAVES), adequate modelling tools (the TRANSPLANET ionospheric dynamics model and a simplified set of ionospheric current closure equations) and the AMDA data handling tools to provide preliminary estimates of these key parameters and their variation along the ionospheric footprint of Juno's magnetic field line and across the auroral ovals for three of the first perijoves of the mission. We will discuss how this synergistic use of data and models can also contribute to provide a better determination of poorly known parameters such as the vertical structure of the auroral and polar Jovian neutral atmosphere.

COMPARISON OF THE DEEP ATMOSPHERIC DYNAMICS OF JUPITER AND SATURN IN LIGHT OF THE JUNO AND CASSINI GRAVITY MEASUREMENTS

Y. Kaspi[1], E. Galanti[1], A. P. Showman[2], D. J. Stevenson[3], T. Guillot[4], L. Iess[5], S. J. Bolton[6]

[1] *Dept. of Earth and Planetary Sciences, Weizmann Institute of Science, Rehovot, 76100, Israel* (*yohai.kaspi@weizmann.ac.il*)

[2] *Lunar and Planetary Laboratory, University of Arizona, Tucson, AZ 85721-0092, USA*

[3] *Division of Geological and Planetary Sciences, California Institute of Technology, Pasadena, CA, 91125, USA*

[4] *Université Côte d'Azur, OCA, Lagrange CNRS, 06304 Nice, France*

[5] *Sapienza Universitá di Roma, 00184, Rome, Italy*

[6] *Southwest Research Institute, San Antonio, TX 78238, USA*

KEYWORDS:
Jupiter, Saturn, Juno, Cassini, planetary atmospheres, zonal jets, gravity science

ABSTRACT:
The nature and structure of the observed east-west flows on Jupiter and Saturn have been a long-standing mystery in planetary science. This mystery has been recently unraveled by the accurate gravity measurements provided by the Juno mission to Jupiter and the Grand Finale of the Cassini mission to Saturn. These two experiments, which coincidentally happened around the same time, allowed the determination of the overall vertical and meridional profiles of the zonal flows on both planets [1–3]. Here we will discuss what has been learned about the zonal jets on the gas giants in light of the new data from these two experiments. The gravity measurements not only allow the depth of the jets to be constrained, yielding the inference that the jets extend to roughly 3000 and 9000 km below the observed clouds on Jupiter and Saturn, respectively, but also provide insights into the mechanisms controlling these zonal flows [4]. Specifically, for both planets this depth corresponds to the depth where electrical conductivity is within an order of magnitude of 1 S/m, implying that the magnetic field likely plays a key role in damping the zonal flows [5, 6]. An intrinsic characteristic of any gravity inversion, as discussed here, is that the solutions might not be unique. In this talk, we will analyze the robustness of the solutions and present several independent lines of evidence supporting the results presented here.

REFERENCES:

[1] Kaspi Y., Galanti E., Hubbard W. B. et al., Jupiter's atmospheric jet streams extend thousands of kilometres deep // Nature. 2018. V. 555. P. 223–226.

[2] Iess L., Militzer B., Kaspi Y. et al. Measurement and implications of Saturn's gravity field and ring mass // Science. 2019. V. 364. Art. 1052.

[3] Galanti E., Kaspi Y., Miguel Y. et al. Saturn's deep atmospheric flows revealed by the Cassini grand finale gravity measurements // Geophysical Research Letters. 2019. V. 46(2). P. 616–624.

[4] Kaspi Y., Galanti E., Showman A. P., Stevenson D. J., Guillot T., Iess L., Bolton S. J. Comparison of the deep atmospheric dynamics of Jupiter and Saturn in light of the Juno and Cassini gravity measurements // Space Science Reviews. 2020. V. 216. Art. 86.

[5] Liu J., Goldreich P. M., Stevenson D. J. Constraints on deep-seated zonal winds inside Jupiter and Saturn // Icarus. 2008. V. 196. P. 653–664.

[6] Cao H., Stevenson D. J. Zonal flow magnetic field interaction in the semi-conducting region of giant planets // Icarus. 2017. V. 296. P. 59–72.

INFRARED OBSERVATIONS OF JUPITER'S AURORAE AND ATMOSPHERE

A. Mura, A. Adriani, the JIRAM Team
INAF-IAPS Rome Italy (*alessandro.mura@inaf.it*)

KEYWORDS:
Jupiter, aurorae, atmosphere

ABSTRACT:
NASA's Juno mission has been observing the Jovian aurorae since 2016 from a polar, highly elliptical orbit [1–3]. From this very favorable position above the poles, Juno obtained unprecedented in-situ measurements of Jupiter magnetosphere, and unique, remote-sensing views of the polar regions, for the investigation of both atmosphere and aurorae. For the atmosphere, unprecedented full views of the polar atmospheric structures have been acquired for the first time during orbit 4 [4] by the Jovian InfraRed Auroral Mapper (JIRAM) [5]. Other observations permit to study the baroclinic waves extending for significant longitudinal span in the Northern Equatorial Belt [6] and over the polar structures. Spectral measurements provided the opportunity to measure abundances of water, ammonia, phosphine, germane and arsine at all latitudes down to pressures of 4–5 bars. Limb observations at the low latitudes permit to profile abundances of methane and trihydrogen cation in the stratosphere and the thermosphere of the planet. Infrared Aurora comes from electron precipitation, which produces, indirectly, H3+ thermal emission. Images of aurorae in this range are collected by JIRAM at each Juno perijove pass. In the main oval, the field aligned electric currents have very low densities, less than what was previously assumed to explain the intense auroral emissions. Juno observed the high energy (>100 keV) auroral electron, but also a lower energy component (~1 keV), which plays a substantial role. Inside the main oval, persistent upward broadband high-energy (~1 MeV) electron are observed. Also, intense auroral emissions are observed in regions where little or no precipitating electron flux is detected, possibly indicating excitation from strong ionospheric electric currents. Juno also revealed a puzzling structure in the electromagnetic interactions between Jupiter and its moons [7], whose signature is the presence of auroral footprints. These are a peculiar series of emission features extending downstream of the leading one and look like a repeating pattern of swirling vortices. These multiple features have a very small scale (~100 km), which is not compatible with the simple paradigm of multiple Alfven wave reflections. Other puzzling structures are observed, such as the splitting of Io's footprint tail well downstream of the leading feature, or Ganymede's footprints (main and secondary), which appear as a pair of emission features instead of one. Here we present results from the most significant observations performed by the instrument since the start of the mission.

REFERENCES:
[1] Connerney J. E. P. et al. Jupiter's magnetosphere and aurorae observed by the Juno spacecraft during its first polar orbits // Science. 2017. V. 356. Iss. 6340. P. 826–832. doi:10.1126/science.aam5928.
[2] Bolton S. et al. Jupiter's interior and deep atmosphere: The initial pole-to-pole passes with the Juno spacecraft // Science. 2016. V. 356. Iss. 6340. P. 821–825.
[3] Bagenal F. et al. Magnetospheric Science Objectives of the Juno Mission // Space Science Reviews. 2017. V. 213. Iss. 1–4. P. 219–287. doi:10.1007/s11214-014-0036-8.
[4] Adriani A. et al. Clusters of Cyclones Encircling Jupiter's Poles // Nature. 2018. V. 555. P. 216–219.
[5] Adriani A. et al. JIRAM, the Jovian Infrared Auroral Mapper // Space Science Reviews. 2014. V. 213. P. 393–446. doi:10.1007/s11214-014-0094-y, 2014.
[6] Adriani A. et al., Characterization of Mesoscale Waves in the Jupiter NEB by Jupiter InfraRed Auroral Mapper on board Juno // The Astromical J. 2018. V. 156. P. 246.
[7] Mura et al. Juno observations of spot structures and a split tail in Io-induced aurorae on Jupiter // Science. 2018. V. 361. P. 774–777.

JUPITER'S TEMPERATE BELT/ZONE CONTRASTS AT DEPTH REVEALED BY JUNO

L. N. Fletcher[1], F. Oyafuso[2], M. Allison[3], A. Ingersoll[4], L. Li[5], Y. Kaspi[6], E. Galanti[6], M. Wong[7], G. Orton[2], Zh. Zhang[4], Ch. Li[8], St. Levin[2], S. Bolton[9]

[1] *University of Leicester, School of Physics and Astronomy, Leicester, United Kingdom (leigh.fletcher@leicester.ac.uk)*

[2] *Jet Propulsion Laboratory, California Institute of Technology, 4800 Oak Grove Drive, Pasadena, CA 91109, USA*

[3] *Goddard Institute for Space Studies, New York, NY, USA*

[4] *California Institute of Technology, Pasadena, CA, USA*

[5] *University of Houston, Houston, TX, USA*

[6] *Department of Earth and Planetary Sciences, Weizmann Institute of Science, Rehovot 76100, Israel*

[7] *SETI Institute, Mountain View, CA, 94043-5139*

[8] *Department of Astronomy, University of California Berkeley, Berkeley, CA 94720-3411, USA*

[9] *Southwest Research Institute, San Antonio, Texas, TX, USA*

KEYWORDS:
giant planets, atmospheric dynamics, Juno, Jupiter

INTRODUCTION:
The locations of Jupiter's cloud-top east-west jets are relatively constant over time and define the cyclonic belts and their neighbouring anticyclonic zones. Thermal-infrared observations of the upper troposphere reveal cool temperatures, elevated abundances of condensate and disequilibrium gases, and enhanced cloud opacity over the zones, and the opposite over the belts [1]. This distribution implies upwelling motions in zones and subsidence in belts. This picture has been called into question by the observed eddy-momentum flux convergence into the eastward jets (and divergence from the westward jets [2]), which suggests a compensating flow in the opposite direction, from belts into zones, which is partially supported by the distribution of lightning at low- and mid-latitudes [3]. It is possible that two different atmospheric regimes exist: a deep regime where eddies are able to drive the zonal flows, and a higher-altitude regime where those zonal flows decay with altitude (e.g., [4]). Reconciling this apparent inconsistency remains a key challenge for the understanding of Jupiter's atmosphere, and Juno observations of the deeper atmosphere shed important light on this issue.

METHODOLOGY:
Juno's Microwave Radiometer (MWR) examines the vertical structure of Jupiter's belts and zones below the clouds by sounding in six channels from 1.4 to 50 cm, sensing from the cloud-tops at ~0.7 bar to pressures greater than 300 bar. Initial results [5] revealed contrasts at depth that bore a potential resemblance to the belt/zone structure in the upper troposphere. We report on progress in our analysis of averaged nadir microwave brightness and its emission-angle dependence from the first two years of Juno's mission. We investigate the correlation between the meridional gradient of the brightness temperature at all emission angles and the cloud-top zonal winds. These brightness temperature gradients reflect changes in gaseous opacity (e.g., ammonia and water), kinetic temperature, or both. We explore the implications of the contrasts observed between belts and zones as a function of depth sounded by MWR.

PRELIMINARY RESULTS:
Meridional brightness temperature gradients above the clouds (p < 1 bar) were measured by the VLT/VISIR mid-infrared instrument in 2016, alongside the 1.37-cm MWR channel sensing temperatures and ammonia at p ~ 0.7 bar. The gradients show a strong negative correlation with the cloud-tracked zonal winds and suggest a combination of zonal jet decay with altitude in the upper troposphere (e.g., [4]), along with depletion of volatiles (ammonia) within cyclonic belts (e.g., as noted by Ingersoll et al., [6]). MWR observations

suggest that this negative correlation persists as deep as ~1.5–3.5 bar for both the tropical and temperate jets. For the strong eastward jet at 6° N, this is broadly consistent with results from both the Galileo Probe [7] and Cassini cloud-tracking [8], which suggested that the jet decayed with height from the ~5-bar level to the 0.5-bar level by more than 90 m/s. We will report on our initial exploration of how these correlations change at deeper pressure levels by looking at MWR wavelengths beyond 10 cm, probing well below the expected condensation level of Jupiter's water clouds.

ACKNOWLEDGEMENTS:
Fletcher was supported by a Royal Society Research Fellowship and European Research Council Consolidator Grant (under the European Union's Horizon 2020 research and innovation programme, grant agreement No. 723890) at the University of Leicester. Levin, Orton, and Oyafuso were supported by the National Aeronautics and Space Administration through funds distributed to the Jet Propulsion Laboratory, California Institute of Technology.

REFERENCES:
[1] Gierasch et al., 1986, doi:10.1016/0019-1035(86)90125-9.
[2] Ingersoll et al., 1981, doi:10.1029/JA086iA10p08733.
[3] Little et al., 1999, doi:10.1006/icar.1999.6195.
[4] Pirraglia et al., 1981, doi:10.1038/292677a0.
[5] Li et al. 2017, doi:10.1002/2017GL073159.
[6] Ingersoll et al., 2017, doi:10.1002/2017GL074277.
[7] Atkinson et al., 1998, doi:10.1029/98JE00060.
[8] Li et al., 2006, doi:10.1029/2005JE002556.

PECULIAR MOVEMENT OF A PAIR OF SATURN SATELLITES

T. V. Salnikova[1], S. Ya. Stepanov[2]
[1] *Lomonosov Moscow State University, GSP-1, Leninskie Gory, Moscow, 119991, Russian Federation* (*tatiana.salnikova@gmail.com*)
[2] *Dorodnicyn Computing Center, Federal Research Center "Computer Science and Control" of Russian Academy of Sciences, Vavilova str., 40, Moscow, 119991, Russian Federation* (*stepsj@ya.ru*)

KEYWORDS:
Saturn satellites, pair Janus — epimetheus dynamics, orbits rearrangement, horseshoe-shaped orbits

INTRODUCTION:
The peculiar movement, mentioned in the title, takes place for the satellites pair Janus — Epimetheus of Saturn. Initially astronomers take these two satellites for one satellite Janus, but in October 1978 S. Larson and J. Fountain open that in reality there are two objects moving along very close orbits [1]. Later this observation was confirmed by the space probe Voyager-1. In the rotating frame these trajectories have a horseshoe shape. It was surprising astronomical discovery, and the attention of astronomers and mathematicians to explain this phenomenon has not yet diminished [2, 3]. This phenomenon was investigated numerically and analytically by means of KAM-theory, but some questions remain. For instance bifurcation and stability issue for this type of motion are not fully investigated.

PROBLEM SETTING:
In this paper we give a numerical parametric investigation of this phenomenon in frame of the planar restricted three-body problem. The results are presented in form of the Poincare bifurcation and the stability diagrams for dependencies of initial conditions for periodic rearrangements on the parameters of problem.

REFERENCES:
[1] Fountain J. W., Larson S. M. Saturn's ring and nearby faint satellites // Icarus. 1978. V 36(1). P. 92–106.
[2] P.ousse A., Niedermann L., Robutel P. On the co-orbital motion in the three-body problem: existence of quasi-periodic horseshoe-shaped orbits: arXiv:1806.07262 [math.DS], 2018.
[3] Niedermann L., P.ousse A., Robutel P. La stabilité des lunes de Saturne, Janus et Épiméthée: de l'observation astronomique à la théorie KAM : arXiv:1807.10220v1 [math.HO], 2018.

OVERVIEW OF JUNO RESULTS AT JUPITER

S. J. Bolton, and the Juno Science Team
Southwest Research Institute, *San Antonio*, *TX 78257 USA*
(*sbolton@swriu.edu*)

KEYWORDS:
Juno, Jupiter, interior, atmosphere, magnetosphere

INTRODUCTION:
NASA's Juno mission to Jupiter launched in 2011 and arrived at Jupiter on July 4, 2016. Juno's scientific objectives include the study of Jupiter's interior, atmosphere and magnetosphere with the goal of understanding Jupiter's origin, formation and evolution. An extensive campaign of Earth based observations of Jupiter and the solar wind were orchestrated to complement Juno measurements during Juno's approach to Jupiter and during its orbital mission around Jupiter. This presentation provides an overview of results from the Juno measurements and the collaborative campaign during the early phases of Juno's prime mission. Scientific results include Jupiter's interior structure, magnetic field, deep atmospheric dynamics and composition, and the first in-situ exploration of Jupiter's polar magnetosphere and aurorae.

Fig. 1

THE DEPTH OF JUPITER'S STORMS

S. J. Bolton, and the Juno MWR Team
Southwest Research Institute, *San Antonio*, *TX 78257 USA*
(*sbolton@swriu.edu*)

KEYWORDS:
Juno, Jupiter, cyclones, atmosphere

INTRODUCTION:
For over 100 years, Jupiter has been observed and its atmosphere characterized by a well-organized system of zones and belts disrupted by storms and vortices such as the Great Red Spot (GRS). How these features change with depth has been an outstanding question for decades [1, 2]. The Galileo probe in 1995 challenged our understanding by finding that water was not well mixed even at a depth of ~22 bars [3, 4], which is substantially below its expected condensation level. Results from Juno extended the puzzle by showing that both ammonia and water vary across most of the planet at much greater depths than their expected saturation levels [5–8] and the gravitational signatures of the atmospheric zonal flows are present at depths approaching 10^5 bar [9, 10]. We present 3D radio maps from the Juno Microwave Radiometer (MWR) [11] that are effectively horizontal slices of Jupiter's atmosphere at depths ranging from 1 bar to hundreds of bar pressure. The maps show the vertical extent of Jovian storm vortices, some of which reach well below the condensation levels of water and ammonia. The results are surprising because they demonstrate that contrary to expectations, Jupiter's weather extends hundreds of kilometers deeper than the condensation levels of its volatiles.

REFERENCES:
[1] Dowling T. E. Dynamics of Jovian atmospheres // Annual Review of Fluid Mechanics. 1995. V. 27. P. 293–334.
[2] Vasavada A. R., Showman A. P. Jovian atmospheric dynamics: an update after Galileo and Cassini // Reports on Progress in Physics. 2005. V. 68. P. 1935–1996.
[3] Niemann H. B. et al. The composition of the Jovian atmosphere as determined by the Galileo probe mass spectrometer // J. Geophysical Research: Planets. 1998. V. 103. P. 22,831–22,845.
[4] Wong M. H., Mahaffy P. R., Atreya S. K., Niemann H. B., Owen T. C. Updated Galileo probe mass spectrometer measurements of carbon, oxygen, nitrogen, and sulfur on Jupiter // Icarus. 2004. V. 171. P. 153–170.
[5] Folkner W. M., Woo R., Nandi S. Ammonia abundance in Jupiter's atmosphere derived from the attenuation of the Galileo probe's radio signal // J. Geophysical Research: Planets. 1998. V. 103. P. 22,847–22,855.
[6] Bolton S. J. et al. Jupiter's interior and deep atmosphere: The initial pole-to-pole passes with the Juno spacecraft // Science. 2017. V. 356. P. 821–825.
[7] Li C. et al. The distribution of ammonia on Jupiter from a preliminary inversion of Juno microwave radiometer data // Geophysical Research Letters. 2017. V. 44. P. 5317–5325.
[8] Ingersoll A. P. et al. Implications of the ammonia distribution on Jupiter from 1 to 100 bar as measured by the Juno microwave radiometer // Geophysical Research Letters. 2017. V. 44. P. 7676–7685.
[9] Kaspi Y. et al. Jupiter's atmospheric jet streams extend thousands of kilometers deep // Nature. 2018. V. 555. P. 223–226.
[10] Guillot T. et al. A suppression of differential rotation in Jupiter's deep interior // Nature. 2018. V. 555. P. 227–230.
[11] Janssen M. A. et al. MWR: Microwave radiometer for the Juno mission to Jupiter // Space Science Reviews. 2017. V. 213. P. 138–185.

JUNO'S EXPLORATION OF JUPITER'S MAGNETIC FIELD AND MAGNETOSPHERE

J. E. P. Connerney[1,2], D. J. Gershman[2], S. Kotsiaros[3], Y. Martos[2,4], J. L. Joergensen[3], P. S. Joergensen[3], J. M.G. Merayo[3], M. Herceg[3], M. Benn[3], T. Denver[3], J. Bloxham[5], K. M. Moore[6], S. J. Bolton[7], S. M. Levin[8]

[1] *Space Research Corporation, Annapolis, MD, United States (jack.connerney@nasa.gov)*
[2] *NASA Goddard Space Flight Center, Greenbelt, MD, United States*
[3] *Technical University of Denmark (DTU), Lyngby, Denmark*
[4] *University of Maryland College Park, College Park, Maryland, United States*
[4] *Technical University of Denmark (DTU), Lyngby, Denmark*
[5] *Harvard University, Cambridge, MA, United States*
[6] *Caltech, Pasadena, CA, United States*
[7] *Southwest Research Institute, San Antonio, TX, United States*
[8] *Jet Propulsion Laboratory (JPL), Pasadena, CA, United States*

KEYWORDS:
Jupiter's magnetic field, magnetosphere, magnetodisc

INTRODUCTION:

The Juno spacecraft, in polar orbit about Jupiter since July 4, 2016, maps Jupiter's magnetic and gravitational potential fields and probes its deep atmosphere in search of clues to the planet's formation and evolution [1]. Juno executes close periJove passes (to ~1.05R_j radial distance at peri Jove; one R_j = 71,492 km, Jupiter's equatorial radius) every 53 days. By the end of its prime mission, Juno will have circled the planet 34 times, uniformly sampling longitudes separated by less than 12° at the equator. At present, Juno nears the end of its prime mission (having completed PJ29), and with an increasing number of orbits comes increased spatial resolution of the planetary magnetic field.

Juno's magnetometer investigation (MAG) is equipped with two magnetometer sensor suites [2], located 10 and 12 m from the center of the spacecraft at the end of one of Juno's three solar panel wings. Each contains an accurate (100 ppm absolute vector accuracy) fluxgate magnetometer (FGM) sensor and a pair of co-located non-magnetic star tracker camera heads. The star cameras monitor the attitude of the magnetometer sensors continuously, correcting for the slight (~0.1°) thermoelastic deformation of the spacecraft solar array experienced during off-sun maneuvers and perijove passes (close proximity to Jupiter warms the array by a few degrees C). Such deformations, if not measured and corrected, would otherwise compromise measurement vector accuracy.

Early in Juno's prime mission, very detailed 10 degree and order spherical harmonic model (JRM09, for Juno Reference Model after 9 orbits) was extracted from a partial solution to a 20 degree/order model representation, providing the first new information about Jupiter's magnetic field in decades [3, 4]. As we near the end of Juno's prime (baseline) mapping mission, now with orbits more densely spaced, a model (JRM24) with increased spatial resolution of the main field is obtained. This model is a partial solution to a degree 30 spherical harmonic representation, with terms to degree and order 18 reasonably well resolved. The field and evidences a more compact source geometry, as one might expect with increasing spatial resolution, and exposes tantalizing hints of the effects of deep zonal fluid flow on the magnetic field. Comparison with earlier magnetic field models is suggestive of secular variation [5, 6] but inconsistencies among prior analyses call for caution in interpretation. A thorough retrospective analysis [7] of Voyager, Pioneer, and Ulysses observations, combined with Juno's detailed field model (JRM09) provides the first unambiguous evidence of Jovimagnetic secular variation and relates the variation to the penetration of zonal winds into the electrically conducting interior, as anticipated by Cao and Stevenson [8].

This presentation will explore the implications of the field as evidenced in the most recent model and discuss prospects for what can be learnt in Extended Mission, which will continue Juno's mission through orbit 77, in October 2025. The mapping mission will include a detailed magnetic survey above Great Blue Spot (GBS), an intense patch of reverse magnetic flux near the equator, as well as a global mapping grid with orbit separation of <6° at the equator.

REFERENCES:

[1] Bolton S. J., and the Juno Science Team. The Juno mission // Proc. Intern. Astronomical Union Symp. 2010. No. 269. P. 92–100.
[2] Connerney J. E.P., Benn M., Bjarno J. B. et al. The Juno Magnetic Field Investigation // Space Science Reviews. 2017. doi:10.1007/s11214-017-0334-z.
[3] Connerney J. E.P., Kotsiaros S., Oliversen R. J., Espley J. R., Joergensen J. L., Joergensen P. S. et al. A new model of Jupiter's magnetic field from Juno's first nine orbits // Geophysical Research Letters. 2018. V. 45. doi:10.1002/2018GL077312.
[4] Moore K., Rakesh Y., Kulowski L. et al. A complex dynamo inferred from the hemispheric dichotomy of Jupiter's magnetic field // Nature. 2018. V. 561. P. 76–78. doi:10.1038/s41586-018-0468-5.
[5] Connerney J. E.P., Açuna M. H. Jovimagnetic secular variation // Nature. 1982. V. 297. P. 313–315.
[6] Ridley V. A., Holme R. Modeling the Jovian magnetic field and its secular variation using all available magnetic field observations // J. Geophysical Research: Planets. 2016. V. 121. doi:10.1002/2015JE004951.
[7] Moore K. M., Cao H., Bloxham J., Stevenson D. J., Connerney J. E.P., Bolton S. J. Time-variation of Jupiter's internal magnetic field consistent with zonal wind advection // Nature Astronomy. 2019. doi:10.1038/s41550-019-0772-5.
[8] Cao H., Stevenson D. J. Zonal flow magnetic field interaction in the semi-conducting region of giant planets // Icarus. 2017. V. 296. P. 59–72.

IN SITU OBSERVATIONS ABOVE THE JOVIAN IONOSPHERE BY JUNO JADE-I

P. W. Valek[1], F. Allegrini[1,2], F. Bagenal[3], J. Connerney[4,5], R. W. Ebert[1,2], W. S. Kurth[6], D. J. McComas[7], J. R. Szalay[7], R. J. Wilson[3]

[1] *Southwest Research Institute, San Antonio, Texas, USA* (*pvalek@swri.edu*)
[2] *Department of Physics and Astronomy, University of Texas at San Antonio, San Antonio, Texas, USA*
[3] *Laboratory for Atmospheric and Space Physics, University of Colorado Boulder, Boulder, Colorado, USA*
[4] *Space Research Corporation, Annapolis, Maryland, USA*
[5] *Goddard Space Flight Center, Greenbelt, Maryland, USA*
[6] *Department of Physics and Astronomy, University of Iowa, Iowa City, Iowa, USA,*
[7] *Department of Astrophysical Sciences, Princeton University, Princeton, New Jersey, USA*

KEYWORDS:
Jupiter, ionosphere, Juno, JADE, in situ, equatorial, high latitude ions

INTRODUCTION:

The low altitude, high-velocity trajectory of the Juno spacecraft enables the Jovian Auroral Distributions Experiment (JADE) [1] to make in situ observations of Jovian ionospheric plasma. Ions are observed to energies below 1 eV. The character of the ionosphere is observed to change as the spacecraft crosses magnetic field lines that connect to Io. At latitudes poleward of the Io field lines, ionospheric ions consist primarily of protons and are seen at higher altitudes, ~0.5R_J (~36,000 km) [2]. JADE-I also observes ions of magnetospheric origin at high latitudes. The source of the magnetospheric ions is tied to the Io torus and plasma sheet, indicated by the cut off seen in both the magnetospheric and ionospheric plasma at Io M-shells. The high latitude ionospheric protons are observed simultaneously with a loss cone in the magnetospheric ions. This suggests precipitating magnetospheric ions contribute to the heating of the upper ionosphere, raising the scale height, and pushing ionospheric protons to higher altitudes. At equatorial latitudes cold heavy ions of O and S are seen with the protons [3]. The equatorial ionospheric ions are confined to lower altitudes (< ~7000 km) than those seen at higher latitudes. Here we present in situ observations from the Juno JADE-I instrument of both the high latitude and equatorial ionosphere of Jupiter.

REFERENCES:

[1] McComas D. J. et al. The Jovian Auroral Distributions Experiment (JADE) on the Juno mission to Jupiter // Space Science Reviews. 2017. P. 1–97, doi: 10.1007/s11214-013-9990-9.
[2] Valek P. W. et al. Jovian high-latitude ionospheric ions: Juno in situ observations // Geophysical Research Letters. 2019. V. 46(15). P. 8663–8670. doi:10.1029/2019GL084146.
[3] Valek P. W., Bagenal F., Ebert R. W., Allegrini F., McComas D. J., Szalay J. R., Wilson R. J., Bolton S. J., Connerney J. E.P. Juno in situ observations above the Jovian equatorial ionosphere // Geophysical Research Letters. 2020. V. 47(12). e2020GL087,623. doi:10.1029/2020GL087623, e2020GL087623 2020GL087623.

LATEST RESULTS FROM THE JUNO MICROWAVE RADIOMETER AT JUPITER

S. M. Levin, and the Juno MWR Team
Jet Propulsion Laboratory, *California Institute of Technology*, *Pasadena CA*, *USA*, *91108* (*steven.levin@jpl.nasa.gov*)

KEYWORDS:
Jupiter, microwave, atmosphere, atmospheric dynamics, composition, Juno, MWR

The Microwave Radiometer (MWR) instrument on the Juno spacecraft has been collecting data at Jupiter since 2016, in a series of close (~5000 km) perijove passes every 53 days. Enabled by Juno's polar orbit and close perijoves, MWR measures the Jovian atmosphere over a wide range of latitudes, longitudes, and emission angles, resulting in numerous discoveries, puzzles, and fresh insights related to atmospheric composition, dynamics, lightning, and other features at depths as deep as 100 bars or more. In addition, the MWR data set includes unique observations of the synchrotron emission from Jupiter's inner radiation belts. We will present an overview of the most recent MWR results, incorporating data from the 28 perijove passes expected to be complete by October of 2020.

THE GLOBAL ABUNDANCE OF WATER IN JUPITER'S ATMOSPHERE: A PROGRESS REPORT

S. M. Levin, and the Juno MWR Team
Jet Propulsion Laboratory, *California Institute of Technology*, *Pasadena CA*, *USA*, *91108* (*steven.levin@jpl.nasa.gov*)

KEYWORDS:
Jupiter, microwave, atmosphere, water, composition, Juno, MWR

The most important scientific goal for the Microwave Radiometer (MWR) instrument on the Juno spacecraft is determination of the global abundance of water in Jupiter's atmosphere. Enabled by Juno's polar orbit and close perijoves every 53 days, MWR measures the Jovian atmosphere at 0.6, 1.25, 2.6, 5.2, 10 and 22 GHz, over a wide range of latitudes, longitudes, and emission angles. From the initial data set in 2016, it was clear that Jupiter's deep atmosphere is more complex and less homogenous than originally expected [1, 2]. Despite this complexity, MWR data have been used to determine the water abundance near the Jovian equator [3]. Here we will present progress in extending that determination to other latitudes, in pursuit of the global water abundance.

REFERENCES:

[1] Bolton S. J. et al. Jupiter's interior and deep atmosphere: The initial pole-to-pole passes with the Juno spacecraft // Science. 2017. V. 356. No. 6340. P. 821–825.
[2] Li C. et al. The distribution of ammonia on Jupiter from a preliminary inversion of Juno microwave radiometer data // Geophysical Research Letters. 2017. V. 44. No. 11. P. 5317–5325.
[3] Li C. et al. The water abundance in Jupiter's equatorial zone // Nature Astronomy. 2020. V. 4. P. 609-616.

OBSERVATIONS OF JUPITER'S ATMOSPHERE BY JUNO'S STELLAR REFERENCE UNIT

H. N. Becker[1], J. W. Alexander[1], S. K. Atreya[2], S. J. Bolton[3], M. J. Brennan[1], S. Brown[1], M. Florence[1], A. Guillaume[1], T. Guillot[4], A. Ingersoll[5], S. M. Levin[1], J. I. Lunine[6], P. G. Steffes[7], Y. S. Aglyamov[6]

[1] *Jet Propulsion Laboratory, California Institute of Technology, 4800 Oak Grove Drive, Pasadena, CA, 91109, USA* (*heidi.n.becker@jpl.nasa.gov*)
[2] *Climate and Space Sciences and Engineering, University of Michigan, Ann Arbor, MI, USA*
[3] *Southwest Research Institute, San Antonio, TX, USA*
[4] *Université Côte d'Azur, OCA, Lagrange CNRS, Nice, France*
[5] *California Institute of Technology, Pasadena, CA USA*
[6] *Cornell University, Ithaca, NY USA*
[7] *School of Electrical and Computer Engineering, Georgia Institute of Technology, Atlanta, GA, USA*

KEYWORDS:
Juno, Jupiter, atmosphere, lightning, aurorae, rings, moons

Juno's Stellar Reference Unit (SRU) star camera is a highly sensitive broadband (450–1100 nm) imager with the primary engineering task of supporting onboard attitude determination. Juno's Radiation Monitoring Investigation [1] has utilized the SRU as a "part time" science imager, exploiting the engineering features of the camera to acquire unprecedented high resolution observations of Jupiter's lighting and aurorae during the spacecraft's low altitude flybys of Jupiter's dark side. Unique images of Jupiter's ring system and moons have also been returned [2], as well as *in situ* particle data providing insights into Jupiter's innermost radiation belts [3]. We will present highlights of the low light phenomena uniquely captured by Juno's SRU at Jupiter and discuss the atmospheric dynamics implied by the SRU lightning observations.

REFERENCES:

[1] Becker H. N., Alexander J. W., Adriani A. et al. The Juno Radiation Monitoring (RM) Investigation // Space Sciences Reviews. 2017. V. 213. P. 507–545.
[2] Becker H. N. et al. Highlights of scientific imagery from Juno's Stellar Reference Unit // EPSC-DPS Joint Meeting. Geneva, Switzerland, 2019. id. EPSC-DPS2019-107. Bibcode: 2019EPSC...13..107B.
[3] Becker H. N. et al. Observations of MeV electrons in Jupiter's innermost radiation belts and polar regions by the Juno radiation monitoring investigation: Perijoves 1 and 3 // Geophysical Research Letters. 2017. V. 44. P. 4481–4488.

CARBON DIOXIDE CLATHRATES IN THE TITAN INTERIORS

A. N. Dunaeva, V. A. Kronrod, O. L. Kuskov
Vernadsky Institute of Geochemistry and Analytical Chemistry RAS, Moscow (*dunaeva.an@gmail.com*)

KEYWORDS:
Titan, carbon dioxide clathrates, CO_2-H_2O system, love numbers

INTRODUCTION:

Carbon dioxide clathrates are thought to be one of the main components of rock/ice planetesimals, which are considered as building blocks of gas giant planets and their icy satellites, including Titan. CO_2 content in the ice component of planetesimals reaches 8–10 % [1], where CO_2 can either be trapped as a guest molecule in structure I clathrate (CO_2-sI) or can condense as pure CO_2-ice. During the Titan accretion and its further differentiation, CO_2-compounds can be included in the satellite's water-ice shell (outer ice Ih-crust, water ocean and underlying high-pressure ices), and also can remain in the rocky-ice mantle, if its formation is modeled (Figure 1).

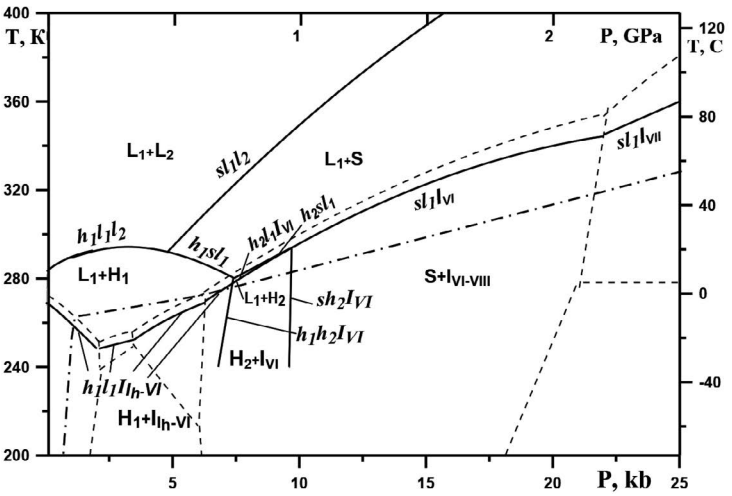

Fig. 1 Phase equilibria in the CO_2-H_2O system in excess of H_2O. Thin broken lines — H_2O system; heavy solid lines — CO_2-H_2O system (reconstructed from [2]); L_1 — H_2O-rich liquid; L_2 — CO_2-rich fluid; S — solid-CO_2 (dry CO_2-ice); H_1 — CO_2-sI hydrate; H_2 — high-pressure CO_2-hydrate; I — water ice polymorphs (indicated by subscripts). Lowercase italics — three-phase equilibrium lines; capital letters — stable phases in the binary CO_2-H_2O system. Dash-dotted curve — Titan thermal profile in water-ice shell and rock-ice mantle at the satellite's heat flux of 5.8 mW/m^2.

Carbon dioxide content in the rock-ice mantle is probably consistent with the initial composition of accreted ices, while in the outer icy crust and internal ocean the content, distribution and forms of CO_2 existence depend on the certain conditions at the later stages of satellite accretion. In particular, under conditions of surface warm ocean (T ~ 300 K) and at high temperatures of accretion, the dissociation of icy CO_2-compounds seems likely. In this case, part of the gaseous CO_2 enters the primary atmosphere and part of the CO_2 remains in the aqueous solution, and as the ocean cools down, it is distributed between the dissolved and clathrate forms. In accordance with the temperature-composition diagrams of the CO_2-H_2O system [2, 3], when diluted CO_2-H_2O solution freezes, CO_2-sI clathrates are formed first, resulting in lower salinity of initial solution and subsequent co-crystallization of clathrates and ice-Ih at the eutectic point. Thus, the clathrates can be captured by the growing ice crust of Titan with partial sinking to the ocean floor due to their higher density.

The accumulation of clathrates within the Titan icy crust may also be associated with the condensation of atmospheric CO_2 at the satellite surface during the post-accretion cooling of the primary atmosphere. In addition, the formation of clathrate structures in the icy crust can occur due to release of free CO_2 from planetesimals's organic matter owing to local heating of the outer parts of Titan by high-velocity impactors during the late stage of accretion and/or the LHB [4]. Tectonic or impact dislocations of the outer ice shell can lead to the formation of vertical cracks that fosters degassing of the inner ocean, formation of clathrate dikes, and, as a consequence, additional saturation of the outer icy crust with clathrates.

The presence of clathrates in Titan's icy crust affects its rheological properties, which is reflected in the tidal Love number k_2 — a relevant parameter for constructing models of the satellite internal structure. In this work, the k_2 values are calculated for the Titan models both with a purely ice crust and assuming 5 wt.% CO_2-sI clathrates. The calculations took into account different compositions and densities of the satellite's internal ocean. The obtained values of k_2 are compared with the experimental results [5, 6].

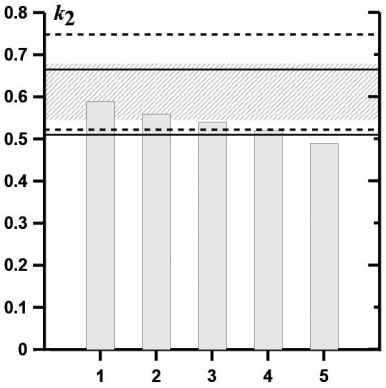

Fig. 2 Titan Love number, k_2, for different compositions of the satellite outer ice crust and internal ocean. 1 — Ice crust composition: Ih + 5 % CO_2-sI, ocean composition: 5 % NH_3 + dissolved salts [7]; 2, 3, 4, 5 — Titan models with a pure icy Ih-crust and an internal ocean of follow composition: seawater, pure water, methanol aqueous solution (10 % CH_3OH), ammonia aqueous solution (15 % NH_3), respectively. Shaded area is the region of experimental k_2 values [6]. Solid and dashed lines are $k_2 \pm 1\sigma$: 0.589±0.075 and 0.637±0.112 [5]. Thickness of the outer ice crust (93–97 km) corresponds to the satellite's heat flow of 5.8 mW/m^2.

RESULTS:

To estimate the Titan Love numbers k_2, the coupled system of the equations of elasticity theory and the equations of the theory of gravitational potential was used [8]. The input data are the density and rheological properties of the satellite's interior. The elastic moduli (K_T and μ) of CO_2 clathrates were determined by the molecular dynamics method in [9] at the pressure and temperature range close to the Titan Ih-crust conditions: 233–278 K and 0.2–1.1 kb. It is shown that, at given T–P interval, shear modulus μ of CO_2 clathrate increases with temperature, decreases with pressure and varies in the interval of 1.58–1.74 GPa, which is much lower than μ of pure Ih-ice (4 GPa). The density of the CO_2 clathrates mainly depends on T–P conditions of their formation and the degree of filling the clathrate cavities with gas molecules and varies within 1054–1112 kg/m^3 [10].

The calculation results in comparison with k_2 data obtained from space observations are presented in Figure 2. It is shown, that the measured k_2 values respond the best to the Titan model with an ocean of ammonia-salt composition and with icy Ih-crust containing 5 wt.% of CO_2 clathrates. The model including sea water also gives a good matching. Titan model with a purely water ocean is within the error $k_2 \pm 1\sigma$. Calculations with water-ammonia and water-methanol oceans fall into the interval $k_2 \pm 1\sigma$ only in case of relatively low (<5 %) concentrations of dissolved NH_3 and CH_3OH.

ACKNOWLEDGEMENTS:
This research was supported by the RFBR (grant No. 18-05-00685).

REFERENCES:

[1] Marboeuf U., Thiabaud A., Alibert Y., Cabral N., Benz W. From stellar nebula to planetesimals // Astronomy and Astrophysics. 2014. V. 570. Art. A35.
[2] Bollengier O., Choukroun M., Grasset O., Le Menn E., Bellino G., Morizet Y., …, and Tobie G. Phase equilibria in the H_2O-CO_2 system between 250–330 K and 0–1.7 GPa: Stability of the CO_2 hydrates and H_2O-ice VI at CO_2 saturation // Geochimica et Cosmochimica Actâ. 2013. V. 119. P. 322–339.
[3] Longhi J. Phase equilibria in the system CO_2-H_2O I: New equilibrium relations at low temperatures // Geochimica et Cosmochimica Acta. 2005. V. 69(3). P. 529–539.
[4] Tobie G., Gautier D., Hersant F. Titan's bulk composition constrained by Cassini-Huygens: implication for internal outgassing // The Astrophysical J. 2012. V. 752(2). P. 125.
[5] Iess L., Jacobson R. A., Ducci M., Stevenson D. J., Lunine J. I., Armstrong J. W., Asmar S. W., Racioppa P., Rappaport N. J., Tortora P. The tides of Titan // Science. 2012. V. 337(6093). P. 457–459.
[6] Durante D., Hemingway D. J., Racioppa P., Iess L., Stevenson D. J. Titan's gravity field and interior structure after Cassini // Icarus. 2019. V. 326. P. 123–132.
[7] Leitner M. A., Lunine J. I. Modeling early Titan's ocean composition // Icarus. 2019. V. 333. P. 61–70.
[8] Raevskiy S. N., Gudkova T. V., Kuskov O. L., Kronrod V. A. On reconciling the models of the interior structure of the Moon with gravity data // Izvestiya, Physics of the Solid Earth. 2015. V. 51(1). P. 134–142.
[9] Jia J., Liang Y., Tsuji T., Murata S., Matsuoka T. Elasticity and stability of clathrate hydrate: role of guest molecule motions // Scientific reports. 2017. V. 7(1). P. 1–11.
[10] Uchida T., Hondoh T., Mae S., Kawabata J. Physical data of CO_2 hydrate // Direct Ocean Disposal of Carbon Dioxide. 1995. P. 45–61.

THERMAL EVOLUTION OF ROCKY CORES OF THE ICY GIANT SATELLITES

V. A. Kronrod, E. V. Kronrod, O. L. Kuskov
Vernadsky Institute of Geochemistry and Analytical Chemistry RAS, *Moscow*, *Russia* (*va_kronrod@mail.ru*)

KEYWORDS:
icy giant satellites, core, temperature, convection, chondrites

INTRODUCTION:

As a result of space-research missions to Jupiter and Saturn (Galileo, Cassini-Huygens) carried out in recent decades, fundamentally new information was obtained about the ice giant satellites Ganymede, Callisto and Titan, which made it possible to build models of the internal structure of the satellites. The main existing satellite models include a water-ice shell (± undifferentiated rock-ice mantle), an iron-silicate (hydrosilicate) core (± internal Fe – FeS core) [1, 2]. Questions about the composition, state of aggregation, size and physical properties of satellite cores, their thermal evolution, as well as the mechanisms of formation are still the subject of much discussion. Models of the internal structure of large ice satellites [1–3] impose restrictions on the composition of satellite cores in accordance with the substance of ordinary (L/LL) or carbonaceous (CI) chondrites or their mixtures. The temperature distributions in the satellite cores largely determine the degree of hydration of their silicate component, the presence or absence of internal metal cores. In this paper, we present the results of estimates of non-stationary temperature regimes in cores taking into account convective transfer processes.

DESCRIPTION OF THE MODEL AND RESULTS:

During the last stages of accretion of satellites, as a result of impactors action, the temperature of the near-surface regions increased sufficiently to initiate the ice melting. This leads to the separation of the rock-iron component and its migration to the satellite center accompanied by formation of inner rock-iron (silicate-iron) core. The process of heating of the proto-core with the energy of radioactive decay to a temperature above the melting temperature of ice (~500 K), the redistribution of ice, water and rock materials with the formation of a homogeneous rocky core takes about 500 million years [4]. Further, the thermal evolution of the cores goes on due to radioactive energy sources.

It is assumed that the cores consist of a mixture of L/LL and CI – chondritic matter, hereinafter with the indices *Sil*, *HS*, respectively. Mass concentrations of CI chondrites (C_{HS}) and L/LL chondrites ($C_{Sil} = 1 - C_{HS}$) are specified. The cores of ice satellites after formation are heated due to the decay energy of radioactive isotopes. The approximation of the radiogenic heat release of chondritic matter by the equation of radioactive decay in the range of 500– 4,500 Ma from CAI leads to the initial value of the power of radiogenic sources $H_{0\,Sil} = 3.1334 \cdot 10^{-11}$ W/kg и $H_{0\,HS} = 2.1336 \cdot 10^{-11}$ W/kg, and also makes it possible to determine the constants of the radioactive decay of L/LL chondritic and CI-chondritic substances: $\lambda_{Sil} = -1.4457 \cdot 10^{-17}$, $\lambda_{HS} = -1.4553 \cdot 10^{-17}$. The temperature distributions in the core are calculated from numerical solution of the one-dimensional unsteady heat equation with initial (500 K) and boundary conditions (360 K). Two heat transfer mechanisms are considered: conductive (diffuse mechanism) and convective (transfer of volumes of liquid with different temperatures). The transition to convection is estimated by the Rayleigh number (*Ra*) for the case of internal energy sources uniformly distributed in the volume [5, 6]:

$$Ra(t) = \frac{\rho_m^2 \alpha_m g_m R_C^5 Q(t)}{k_m \kappa_m \eta_m},$$

where subscript *m* denotes that given parameter is mean in the convection zone; *g* is the average gravity in the considered layer; α is the coefficient of

thermal volume expansion; κ is value of coefficient of temperature diffusion; k is the thermal conductivity; η — composite viscosity' $Q(t)$ — heat release per unit mass of the core matter at a given point in time; R_C — convection zone radius ($R_C = R_{core} - h_{TBL}$); R_{core} — core radius. Thermal boundary layer thickness h_{TBL} is constrained from conditions $Ra_{cr\,TBL} \approx 100$ [5]. The heat transport in the convection zone is modeled simply by multiplying the coefficient of the heat conduction in the convection zone: $K = Nuk_{conduct}$, [6]. Nu is dimensionless Nusselt number; $Nu = 1.04(Ra/Ra_{crit})^{1/3}$, $Ra_{crit} \approx 1000$ [7]. Under calculations the following values of required parameters were used for silicate and hydrous silicate material respectively: ρ = 3800 and 2600 kg/m^3, heat capacity c_p = 920 and 1360 J·kg^{-1}·K^{-1}. Thermal conductivity coefficient k was 4.2 and 2.95 W·m^{-1}·K^{-1}, representing pure silicate and antigorite minerals. The viscosity of silicates + hydrosilicates is calculated using the isostress model for a composite [8], and the viscosity of silicates is determined as a function of temperature and pressure [9], the viscosity of hydrosilicates is assumed to be $4 \cdot 10^{19}$ Pa s over the entire temperature and pressure range [10]. Possible phase transitions of hydrosilicate ↔ silicates in the temperature range 900 K are not considered.

The results of calculations of the number Ra, the heat flux from the surface Q_S, and the temperature distribution T as a function of radius and time for R_{core} = 1500 km are shown in Figure 1, 2.

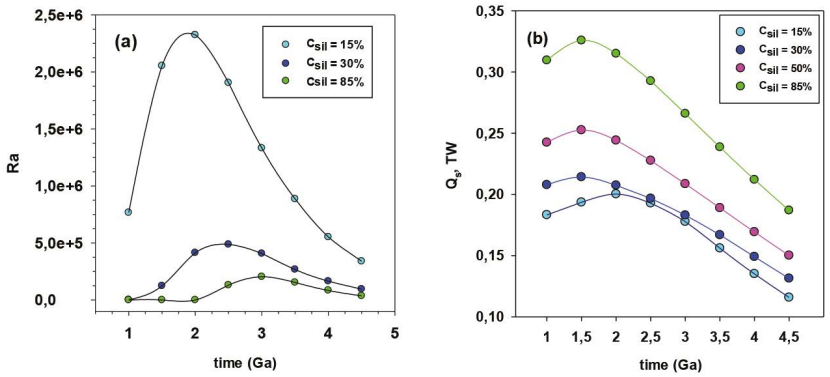

Fig. 1 Dependence of the number Ra (a) and the heat flux from the surface Q_S (b) on time (time) and the content of silicates (C_{sil}) for the core R_{core} = 1500 km in the interval 500–4.500 Ma.

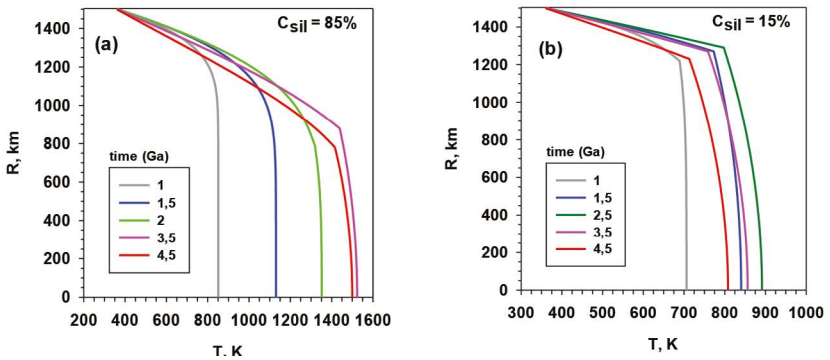

Fig. 2 Temperature distributions (T) in the core (R_{core} = 1.500 km) as a function of radius (R) and time with a silicate content of 15 % (a) and 85 % (b)

According to the calculation results, it can be concluded that in the presence of convection, the composition of the core rocks largely determines the thermal evolution of the core. For example, in the transition from a silicate composition to the predominance of hydrosilicates, the temperature difference can reach ≈600 K.

ACKNOWLEDGEMENTS:
The work was performed as part of the state assignment of Vernadsky Institute of Geochemistry and Analytical Chemistry № 0137-2020-0004 with partial financial support from RFBR grant under project No. 18-05-00685.

REFERENCES:

[1] Fortes A. D. Titan's internal structure and the evolutionary consequences // Planetary and Space Science. 2012. V. 60. P. 10–17. doi:10.1016/j.pss.2011.04.010.
[2] Dunaeva A. N., Kronrod V. A., Kuskov O. L. Physico-chemical models of the internal structure of partially differentiated Titan // Geochemistry Intern. 2016. V. 54. No. 1. P. 27–47.
[3] Kronrod V. A., Kuskov O. L. Chemical differentiation of the Galilean satellites of Jupiter: 4. Isochemical models for the compositions of Io, Europa, and Ganymede // Geochemistry Intern. 2006. V. 44. P. 529-546. doi:10.1134/S0016702906060012.
[4] Castillo-Rogez J. C., Lunine J. I. Evolution of Titan's rocky core constrained by Cassini observations // Geophysical Research Letters. 2010. V. 37. Art. L20205.
[5] Grasset O., Sotin C., Deschamps F. On the internal structure and dynamics of Titan // Planetary and Space Science. 2000. V. 48. P. 617–636. doi:10.1016/S0032-0633(00)00039-8.
[6] Czechowski L., Witek P. Comparison of early evolutions of mimas and enceladus// Acta Geophysica. 2015. V. 63. No. 3. P. 900–921.
[7] Turcotte D. L., Schubert G. Geodynamics. 2nd ed. Cambridge: Cambridge University Press, 2002. 465 p.
[8] Ji S., Zhao P. Flow laws of multiphase rocks calculated from experimental data on the constituent phases // Earth and Planetary Science Letters. 1993. V. 117. P. 181–187.
[9] Kimura J., Nakagawa T., Kurita K. Size and compositional constraints of Ganymede's metallic core for driving an active dynamo // Icarus. 2009. V. 202. P. 216–224.
[10] Hilairet N., Reynard B., Wang Y., Daniel I., Merkel S., Nishiyama N., Petitgirard S. High-Pressure Creep of Serpentine, Interseismic Deformation, and Initiation of Subduction // Science. 2007. V. 318. P. 1910–1913.

SOME INTERESTING FEATURES OF THE METHANE AND AMMONIA ABSORPTION BANDS BEHAVIOR ON JUPITER

P. G. Lysenko, V. G. Teifel, V. D. Vdovichenko, A. M. Karimov, G. A. Kirienko, V. A. Filippov, G. A. Kharitonova, A. P. Khozhenets
Fesenkov Astrophysical Institute (*FAI*) *NSA RK*, *Almaty*, *Kazakhstanl* (*lyssenko_petr@mail.ru*)

KEYWORDS:
Jupiter, atmosphere, clouds, great red spot, ammonia, methane, molecular absorption bands, spectrophotometry

INTRODUCTION:

A comparison of the variations of weak and moderate molecular absorption bands of ammonia and methane in the wavelength range of 0.60–0.90 μm on the Jupiter disk with data on latitudinal variations in brightness temperatures in the microwave range of radio emission of Jupiter is made. The existence of noticeable latitudinal differences in the position of extrema at different absorption bands is noted.

The weak absorption bands of methane and ammonia, which are present in the visible region of the spectrum of Jupiter, are of interest for studies of the structural properties of the cloud cover of Jupiter and the deeper region of its troposphere. The study of their behavior in the form of spatio-temporal variations in their intensity is the traditional direction of many years of research conducted by the Laboratory of the Moon and Planets Physics of the Astrophysical Institute. In recent decades, since 2004, a large amount of material that is homogeneous by the method of spectral observations of Jupiter has been accumulated. This material covers more than one period of the revolution of Jupiter around the Sun. In recent years, a number of interesting features that deserve attention and further study have been discovered.

One of the interesting facts was the discovery of a pronounced depression of ammonia absorption in the latitudinal belt near 15 degrees of the Northern Hemisphere, that is, in the southern outskirts of the Northern Equatorial Belt (NEB). This depression was turned out to coincide with the region of abnormally high brightness temperature in the microwave range of thermal radiation of Jupiter, and it was described in a number of works carried out under the guidance of I. De Pater (for example, [1]. Another well-defined depression of ammonia absorption was found in the Great Red Spot (GRS) [2], and it indicates an increased cloud density in GRS.

The second feature that we noticed when comparing the latitudinal variations of different absorption bands is the mismatch in the latitude of the positions of the extrema (maxima and minima) of the equivalent widths for different absorption bands (Figure 1).

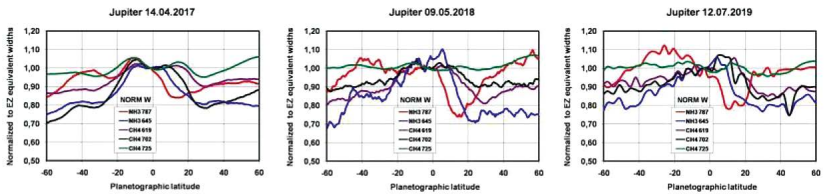

Fig. 1. Relative latitudinal changes in the equivalent widths of the absorption bands of ammonia and methane according to observations in 2017–2019

These differences are systematic, and earlier, in 1999, we discovered the same feature when studying latitudinal variations in methane absorption bands from observations at all longitudes of Jupiter [3].

The depression of ammonia absorption that we found in the NH_3 785 nm band coincided in latitudinal location with the anomalously high brightness

temperature observed in the microwave (millimeter) radio range at frequencies of 12–14 GHz.

In Figure 2, we compare the latitudinal absorption course measured in 2017 for the methane and ammonia bands in the visible spectral region with the latitudinal microwave brightness temperature variations also related to 2017 [4].

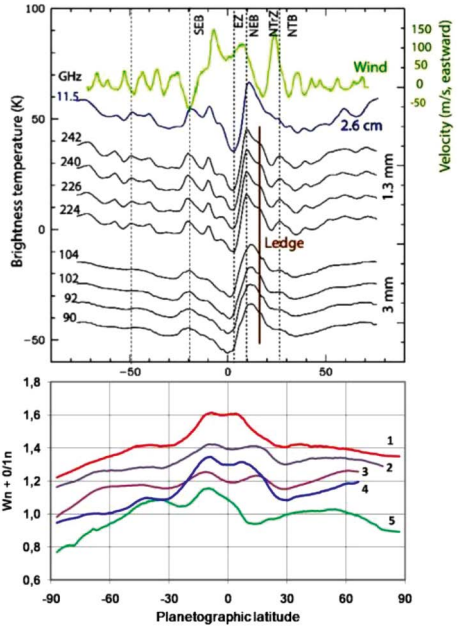

Fig. 2. Comparison of latitudinal variations in brightness temperatures in a number of microwave radio emission ranges [4] and equivalent bandwidths of methane and ammonia absorption bands normalized to equator in the visible spectrum: 1 – NH_3 645 nm; 2 — CH_4 619 nm; 3 — CH_4 702 nm; 4 — CH_4 725 nm: 5 — NH_3 787 nm

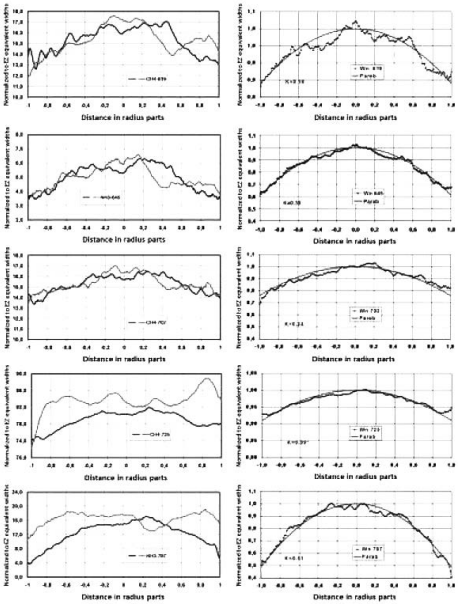

Fig. 3. On the left is a comparison of the equivalent widths of the absorption bands of methane and ammonia along the central meridian and equator of Jupiter in 2018. On the right is a parabolic representation of the course of normalized values of equivalent widths along the equator in 2019

One can see that a well-marked depression of ammonia absorption occurs at the same latitude (about 15 degrees' north latitude) as the sharp maximum of the brightness radio temperature at all frequencies shown on the upper graph. In addition, a characteristic tendency of brightness radio temperatures to a slight increase towards high latitudes is noticeable, while the tendency of molecular absorption bands is noticeably inverse.

All studied absorption bands exhibit noticeable latitudinal variations in intensity, to a certain extent, correlating with the zonal structure of the cloud cover. However, the latitudinal course of absorption differs significantly from the course of absorption along the equator and other latitudinal zones of Jupiter. Despite some longitudinal variations, the zonal absorption course is well approximated by parabolas ($y = 1 - kx^2$), where y is the equivalent bandwidth normalized to the center of the disk, x is the relative distance in fractions of the radius, and k is the parabola curvature coefficient). A significant decrease in absorption to the edges of the disk is observed (Figure 3), and it is more pronounced in the weak bands.

Any analysis of the above observational data in various models of the atmosphere of Jupiter indicates a number of variable factors affecting the reflected and intrinsic radiation of Jupiter that are observed.

ACKNOWLEDGEMENTS:
This work was carried out in the framework of grant financing of the Ministry of Education and Science of the Republic of Kazakhstan 0073/GF4 and AP05131266.

REFERENCES:

[1] de Pater I., Sault R. J., Butler B., DeBoer D., M. H. Wong. Peering through Jupiter's clouds with radio spectral imaging // Science. 2016. V. 352. Iss. 6290. P. 1290–1294.
[2] Tejfel' V. G., Vdovichenko V. D., Lysenko P. G., Karimov A. M., Kirienko G. A., Filippov V. A., Kharitonova G. A., Khozhenets A. P. The Great Red Spot on Jupiter: some features of the ammonia absorption // Izvestija NAN RK. Ser. fiz.-mat. 2018. No. 3. P. 23–31.
[3] Tejfel' V. G. Kharitonova G. A., Glushkova E. A., Sinyaeva N. V. Variations of the methane absorptions on Jupiter's disk from zonal CCD spectrophotometry data // Solar System Research. 2001. V. 35. No. 4. P. 261–277.
[4] de Pater I., Sault R. J., Moeckel C., Moullet A., Wong M. H., Goullaud C., Cosentino R. First ALMA Millimeter-wavelength Maps of Jupiter, with a Multiwavelength Study of Convection //The Astronomical J. 2019. V. 158. No. 4. P. 139–145.

UPDATE ON BEPICOLOMBO AND FIRST RESULTS FROM MEASUREMENTS DURING CRUISE

J. Benkhoff
ESA/ESTEC, SCI-SC, Keplerlaan 1, 2200AG Noordwijk, Netherlands
(*johannes.benkhoff@esa.int*)

KEYWORDS:
Mercury Exploration, BepiColombo, dual spacecraft mission

INTRODUCTION:
BepiColombo was launched on 20 October 2018 from the European spaceport in French Guyana and is now on route to Mercury to unveil Mercury's secrets. BepiColombo, a two-orbiter mission, with its state of the art and very comprehensive payload will perform measurements to increase our knowledge on the fundamental questions about Mercury's evolution, composition, interior, magnetosphere, and exosphere. The mission has been named in honor of Giuseppe (Bepi) Colombo (1920–1984), who was a brilliant Italian mathematician, who made many significant contributions to planetary research and celestial mechanics.

The BepiColombo spacecraft is during its 7-year long journey to the innermost terrestrial planet in a so-called 'stacked' configuration: The two spacecraft, Mio (Magnetospheric Orbiter to study the environment) and the MPO (Mercury Planetary Orbiter to study the planet and its interior), are connected to each other, and stacked on-top of the Mercury Transfer Module (MTM). Only in late 2025, the 'stack' configuration is abandoned and the individual elements spacecraft are brought in to their final Mercury orbit: 480×1500 km for MPO, and 590×11640 km for Mio.

On its way BepiColombo has several opportunities for scientific observations — during the cruise into the inner solar system and during nine flybys (one at Earth, two at Venus and six at Mercury). However, since the spacecraft is in a stacked configuration during the flybys only some of the instruments on both spacecraft will perform scientific observations. In April 2020 BepiColombo has passed Earth. The next planetary flyby will be on 15 October 2020 at Venus.

A status of the mission and instruments and a summary of first results from measurements taken during the Earth flyby and during the first two years in cruise will be given.

FIRST RESULTS OF THE MONITORING OF COSMIC GAMMA-RAY BURSTS BY THE MGNS INSTRUMENT ONBOARD ESA BEPICOLOMBO MISSION TO MERCURY

A. S. Kozyrev, M. L. Litvak, N. Lukyanov, A. A. Malakhov, I. G. Mitrofanov, A. B. Sanin
Institute for Space Research, Profsojuznaja 84/32, 117997 Moscow, Russian Federation

KEYWORDS:
Nuclear-planetology, gamma-ray spectroscopy, cosmic gamma-ray burst

INTRODUCTION:

The Mercury Gamma-ray and Neutron Spectrometer (MGNS) is a scientific instrument developed to study the elementary composition of the Mercury's sub-surface by measurements of neutron and gamma-ray emission of the planet. MGNS measures neutron fluxes in a wide energy range from thermal energy up to 10 MeV and gamma-rays in the energy range of 300 keV up to 10 MeV with the energy resolution of 5 % FWHM at 662 keV and of 2 % at 8 MeV. The innovative crystal of $CeBr_3$ is used for getting such a good energy resolution for a scintillation detector of gamma-rays.

During the BC long cruise and mapping stages, it is planned that the MGNS instrument will operate practically continuously to perform measurements of neutrons and gamma-ray fluxes for achieving two main goals of investigations: global mapping of Mercury elemental composition of the subsurface layer and detection of cosmic gamma-ray burst.

The second goal of MGNS operations is the participation in the Inter Planetary Network (IPN) program for the localization of sources of Gamma–Ray Bursts in the sky. In fact, the localization accuracy by the interplanetary triangulation technique is inversely proportional to the distance between the spacecrafts that jointly detected a GRB. Before the launch of BepiColombo, the IPN network included a group of spacecrafts in the near-to-Earth orbit (e. g. Konus-Wind, Fermi-GBM, INTEGRAL, Insight-HXMT) and the Mars Odyssey spacecraft on the orbit around Mars. Now, MGNS provides another interplanetary location, potentially increasing the accuracy of GRBs localization. Pre-set value of time resolution for continuous measurements of profiles of GRBs is 20 seconds. Since of November 14, 2019, the BC Mission Operation Centre has allocated downlink resources to run MGNS continuously in a 1 s time resolution for GRB measurements. The GRB detection rate, based on data with a time resolution of 1 sec is about 2–3 GRB's per month.

This report will present the current status of MGNS instrument at the cruise stage to Mercury and status of cosmic gamma–ray bursts registration by the instrument onboard the ESA BepiColombo mission.

COMPILATION OF A NEW GLOBAL CATALOG OF MERCURY'S CRATERS

E. A. Feoktistova[1], A. Yu. Zharkova[1,2], A. A. Kokhanov[2], Zh. F. Rodionova[1], V. A. Rotaru[2]

[1] *Sternberg Astronomical Institute Moscow University, Universiteytskiy pr. 13, Moscow, Russia, 119234* (*jeanna@sai.msu.ru*)

[2] *Moscow State University of Geodesy and Cartography, Gorokhovskiy per. 4, Moscow, Russia, 105064* (*a_zharkova@miigaik.ru*)

KEYWORDS:
Mercury, catalog, craters, morphology, morphometric parameters, statistical analysis

INTRODUCTION:
Creation of a new global catalog of Mercury's craters based on Mariner-10 [1] and the latest MESSENGER data is a complex task performed jointly by the Sternberg State Astronomical Institute (SAI) and MIIGAiK. Currently, there are not so many catalogs of Mercury craters; before we started our work we analyzed one of such examples — global GIS-catalog of Mercury's craters created by the Braun University, USA [2]. It is based on data gathered by MESSENGER and includes coordinates and diameters of craters more than 20 km in diameter. At the same time, it doesn't provide any morphological information. Our catalog on the other hand consists of two subdirectories: 1) the morphological catalog of craters with a size of 10 km and larger; 2) the morphometric catalog of all digitized craters.

DATA AND METHODS:
In addition to the required elements of any catalog (coordinates of craters and their diameters), we included morphological description of craters. Morphometric characteristics, such as: 1) the diameter of the interior feature (flat floor, central peak, or inner ring); 2) depth and relative depth of each crater; 3) max and min slopes; 4) the average level of inclination of the external surface; 5) internal slopes of crater; 6) the ratio of volume of the crater rim to the volume of the bowl will be added to the catalog later.

Morphometric parameters listed above can be measured using the DEM processing method as well as morphological features can be identified and described by visual image analysis. We use MESSENGER MDIS global mosaic of Mercury with resolution ~166 m/pixel and several MESSENGER DEMs — the first global Mercury DEM with resolution 665 m/pixel [3] and four DEMs on Mercury quadrants with resolution ~222 m/pixel [4]. ArcGIS was used as main software.

MAIN RESULTS:
More than 3600 craters that have not been digitized before were included to the catalog. In total, morphological features of thirteen main parameters for 11 909 craters of Mercury are added to our catalog at the time this abstract was written (Table 1).

Digitization of craters was carried out gradually by sectors — quadrangles. The number of craters varies from quadrangle to quadrangle, due to the varying degrees of surface roughness. For example, more than 390 craters were digitized on the territory of the H-9 quadrangle, while on H-2 quadrangle were digitized about 210. As a result, the gaps in the catalog of Braun University were significantly filled especially for the range of crater diameters from 10 to 20 km. Coordinates of added craters were defined with the accuracy ±0.1°.

Morphological analysis of craters was performed. As result statistical data were obtained, which are presented in the tables below. Table 1 shows the comparison with the Moon, carried out according to [5].

CONCLUSIONS:
A new global digital GIS catalog of Mercury's craters, containing the morphometric and morphological information, not only summarizes and systematiz-

es existing data. Catalog will simplify creation of thematic maps and facilitate the solution of fundamental problems such as study and estimation of deposits of volatile compounds in the polar regions of Mercury.

Table 1. Quantity of craters with different morphological features on Mercury and the Moon in %

Morphological features		Mercury	Moon
Rim degradation	1	2,4	19
	2	15,6	27
	3	38,6	27
	4	31,3	21
	5	12,1	6
Terrace		52	6
Faults		18,3	1,5
Hills		26,8	12,9
Central peaks		11,4	5,5
Ridges		1,8	3
Chains		40,5	12
Fissures		0,5	2
Flat floor		25,9	7
Rough floor		62,9	71,5
Dark material on a part of floor		37,1	11
Dark material on total floor		11,5	0,1
Local terrain	Highland	35,6	94
	Plains	18,3	3
	Transitional zone	46,1	3

Table 2. Number and percentage of craters by classes of preservation degree

Class of preservation degree	Number	%
1	289	2,4
2	1854	15,6
3	4598	38,6
4	3730	31,3
5	1438	12,1

Table 3. Number and percentage of craters with/without terraces

Terraces	Number	%
with	6192	52
without	5717	48
With faults without terraces	1681	14,1

Table 4. Number and percentage of craters with/without peaks and hills

Peaks and hills	Number	%
With	4540	38,1
Without	7369	61,9

ACKNOWLEDGEMENTS:
E. A. Feoktistova, A. Yu. Zharkova, A. A. Kokhanov and Zh. F. Rodionova were supported by Russian Foundation for Basic Research (RFBR), project No. 20-35-70019.

REFERENCES:

[1] Pike R. J. Geomorphology of impact craters on Mercury // Mercury / eds F. Vilas, C. R. Chapman, M. Matthews. Tucson: Univ. Arizona Press, 1988, P. 165–273.
[2] Fassett C. I., Kadish S. J., Head J. W., Solomon S. C., Strom R. G. The global population of large craters on Mercury and comparison with the Moon // Geophysical Research Letters. 2011. V. 38. Art. L10202. doi:10.1029/2011GL047294.
[3] Becker K. J.; Robinson M. S.; Becker T. L.; Weller L. A.; Edmundson K. L.; Neumann G. A.; Perry, M. E.; Solomon, S. C. First Global Digital Elevation Model of Mercury // 47th Lunar and Planetary Science Conference, 2016, LPI Contribution No. 1903, P. 2959.
[4] Preusker F. Oberst J., Stark A., Matz K-D., Gwinner K., Roatsch T. High-Resolution Topography from MESSENGER Orbital Stereo Imaging — The Southern hemisphere // European Planetary Science Congress: Abstracts. 2017. V. 11. EPSC2017–591.
[5] Kozlova E. A., Sitnikov B. D., Rodionova J. F., Shevchenko V. V. Analysis of Mercurian Craters by Means of Cartographic Method // Proc. 22nd Intern. Cartographic Conference (ICC). A Coruña, Spain, 9–16 July, 2005. “Mapping Approaches into a Changing World”.

HUMAN AND ROBOTIC LUNAR EXPLORATION

I. G. Mitrofanov
Space Research Institute of the Russian Academy of Sciences (*IKI*), *Moscow 117997*, *Russia* (*mlitvak.iki@gmail.com*)

KEYWORDS:
Moon, lunar program, robotic and manned missions, lunar station

INTRODUCTION:
The 21st century is the centenary of the beginning of Lunar exploration. This world-historical process will be ensured by the integration of robotic and manned space systems, which will be evolved in three successive initial stages. This report will discuss challenges and expected results of these stages of the formation of national lunar cosmonautics.

MOON EXPLORATION STAGES:
At the very first preparatory stage (2021–2030) only projects using robotic Lunar missions will be carried out. Exploration and selection of the most favorable polar region of the Moon for dislocation on it of a Russian polar lunar station in the future will be performed, physical and chemical properties of polar regolith will be studied, an engineering model of lunar natural environment will be built in the vicinity of south and north poles. The final project of this stage will be delivery to Earth and detailed study of the composition of Lunar polar regolith in the laboratories on Earth to determine its isotopic composition and presence of complex molecular organic compounds of cosmic origin.

The second stage (2030–2035) will begin after the creation of a manned complex for expeditions to lunar orbits. At this stage, the implementation of the integrated program of studying the Moon with the use of orbital manned systems and landing automatic vehicles will begin. For this stage of the Lunar exploration, manned lunar orbiting ships based on the “Eagle” Space Complex and automatic space shuttle complexes based on the “Corvette” space complex will be created, which will perform multiple landings in Lunar regions for their study, followed by docking with manned lunar orbiters. Crews of cosmonauts in lunar orbit will ensure the functioning of scientific equipment complexes on the Lunar surface, handling with shuttle-delivered samples of lunar soil, refill shuttles with fuel and replace their payloads for delivery to the lunar surface. In fact, the second stage will begin the creation of the first elements of lunar infrastructure on the Moon surface in the area selected for the Russian lunar station to prepare first polar manned expedition.

At the third stage, approximately after 2035, manned expeditions to the lunar surface will begin to the selected and pre-prepared area of the future Russian polar lunar station. At this stage, robotic and manned systems will be integrated directly on the lunar surface to build up space infrastructure and initiate research programs. Specific objectives of this activity will be identified during the preceding first and second stages, but generally it will be aimed for creating life support conditions for cosmonauts, deploying lunar observatory equipment and research laboratories, repairing and upgrading lunar equipment.

It is at this third stage the exploration and in situ utilization of lunar resources will begin. Resources such as water and their components hydrogen and oxygen will be used to provide manned expeditions to the lunar surface. Lunar mineral resources could become a raw material for mining operations. The possibility of such mining in the long term may become a condition of involvement of private business in lunar cosmonautics. Space activities at this stage will initiate astronomy and space physics researches and programs. Their main element will be development of perspective space tools and technologies for a manned expedition to Mars in the middle of this century.

THE RECONNAISSANCE OF LUNAR RESOURCES

M. L. Litvak, I. G. Mitrofanov
Space Research Institute of the Russian Academy of Sciences (*IKI*),
Moscow 117997, Russia

KEYWORDS:
Moon, lunar resources, lunokhod

INTRODUCTION:
Today space agencies in different countries are discussing and developing comprehensive lunar programs combining scientific researches, preparation of the extended stay of astronauts on the lunar surface and in situ resource utilization (ISRU) plans [1]. The Russian lunar program also assumes that the most attractive areas on the Moon with high resource potentials should be selected and explored to create future Russian lunar base. The implementation of this approach begins with robotic missions gradually solving declared tasks and passing from science challenges to industrial and technological ones to prepare a launch pad for the manned missions. The medium and heavy size moon rovers capable to traverse long distances and to conduct a geological survey of the lunar polar regions are required in near future to complete first step of lunar program. They should find local areas that meet certain conditions including available mining/extraction of hydrogen, oxygen, various metals and their compounds required for providing astronauts with air, water, rocket fuel and materials for creation of lunar base. In our work we suggest to discuss methods that could be effective for initial geological exploration from board of lunar rovers.

METHODS:
In our approach we consider possibilities of a nuclear spectroscopy (neutron and gamma spectrometers, see [2]) combined with IR, radar, deep drilling and sampling analysis technologies for a remote sensing from board a lunar rover of water ice deposits, various chemical elements or chemical compounds distributed at different depths in a lunar soil, which are important for exploration of lunar resources and creation of a permanent lunar base. Following the results of this research, a prototype of a science payload oriented for ISRU tasks could be offered for the installation onboard a medium size lunar rover and a geological survey technique are developed to provide quick identification of water ice deposits, metals and their compounds in the underlying layer during rover traverse. This will allow to survey large territories and to choose the most interesting and promising locations for the next missions.

REFERENCES:
[1] Crawford I. A. (2015), Progress in Physical Geography (2015), 39, 137–167.
[2] Litvak et al., (2020),Solar System Research, 54, 275–287.

DUST AND DUSTY PLASMAS AT THE MOON. CHALLENGES OF MODELING AND MEASUREMENTS

L. M. Zelenyi, S. I. Popel, A. V. Zakharov
Space Research Institute of the Russian Academy of Sciences (*IKI*), *Moscow 117997*, *Russia* (*lzelenyi@iki.rssi.ru*)

KEYWORDS:
Moon, dusty plasmas, photoelectric effect, future space missions, modeling

INTRODUCTION:

The lunar dust represents a substantial risk factor for both manned lunar missions and functioning of the future lunar station. In particular, due to adhesion, the lunar dust sticks to the space suites, the surfaces of spacecraft, instruments, etc., which can threaten the proper functioning of the systems. In particular, the absorption of solar radiation sharply increases on dust-covered surfaces of the instruments, causing them to overheat. Dust also represents a health hazard for the astronauts. For example, dust stuck to the space suits can penetrate the lunar module after the astronauts return into it. During the entire return flight to Earth or during their stay on the lunar station, the astronauts can inhale the lunar dust in the atmosphere of the module in a weightlessness condition.

It is assumed that the illuminated surface of the Moon becomes charged as a result of the action of the solar radiation, solar wind plasma, and plasma of the Earth's magnetotail. The surface of the Moon emits electrons upon interaction with the solar wind due to the photoelectric effect, which leads to the formation of a layer of photoelectrons above the surface. Photoelectrons are also emitted from the dust particles soaring above the surface of the Moon due to the interaction of the latter with the electromagnetic radiation of the Sun. Dust particles on the surface of the Moon or in the near-surface layer absorb photoelectrons, photons of solar radiation, and electrons and ions of the solar wind, as well as electrons and ions of the magnetospheric plasma when the Moon enters the Earth's magnetotail. All these processes lead to the charging of the dust particles, their interaction with the charged surface of the Moon, their liftoff, and their motion [1, 2].

The electrostatic processes described above are an important factor leading to the formation of the dusty plasma system above the lunar surface. In addition, meteoroid impacts also contribute to the formation of the dusty plasma system above the surface of the Moon [3–5]. Micron-sized dust particles formed as a result of meteoroid impacts must be taken into account when describing the scattering of solar light from the dust particles above the lunar terminator region in order to explain the glow observed by the Surveyor spacecrafts above this area. High velocities (exceeding 10 m/s) and micron-scale size are characteristic features of the particles appearing in the dusty plasma system above the surface of the Moon as a result of meteoroid impacts.

The purpose of this work is to give a brief review of the dusty plasmas near the surface of the Moon. Problems related to theoretical and numerical modeling of the dusty plasma system near the Moon, its experimental investigation, and interpretation of data on near-lunar dusty plasmas are formulated.

PARTICLES OF LUNAR REGOLITH:

Particles of lunar regolith lifted either as a result of electrostatic processes (see, e.g., [1, 2]) or meteoroid impacts [325] are usually considered to represent the dust component of plasma above the surface of the Moon. The size distribution of particles present on the lunar surface plays an important role in the description of the rise of dust particles above the Moon. Despite the variability in the shape of the particles composing the regolith, their distribution on the surface of the Moon obeys the lognormal law (the Kolmogorov distribution), which is typical for the case of multiple fragmentation. The va-

lidity of the lognormal size distribution (the Kolmogorov distribution) of the lunar-regolith particles is corroborated by the experimental data.

DUST DISTRIBUTION ABOVE THE ILLUMINATED PART OF THE MOON: The distribution of dust and electrons in the near-surface layer of the illuminated part of the Moon can be calculated based on the theoretical model [6] that describes the dynamics of noninteracting dust particles. Photoelectrons emitted from both the lunar surface and the dust particles soaring above the Moon are taken into consideration. Analysis of the photoelectrons emitted from the dust particles requires a self-consistent description because photoelectrons influence the dust-particle distribution, while the latter determines the number of photoelectrons. Due to self-consistent character of the problem, it can be solved only by applying numerical methods using iterations. In the zero-order approximation, we neglect the effect of photoelectrons emitted from the surface of the dust particles. This allows determining the dust distributions above the surface of the Moon. After that, the distributions of photoelectrons emitted from the surfaces of the dust particles are calculated for the dust-particle distributions obtained at the previous step. Dust distributions with new distributions of photoelectrons above the surface of the Moon are calculated at the next step. After that, the photoelectron distributions are determined for the calculated dust-particle distributions, etc.

To determine the altitude and size distributions of the dust particles above the surface of the Moon, the probability of the particles' presence at a certain altitude (inversely proportional to the time of particle presence at this altitude) is calculated. The probability given above is multiplied by a normalization factor that is calculated in such a way as to obtain an adequate description of the size distribution of the lunar dust on the surface of the Moon. The data from [7] on the size of particles on the surface of the Moon were used for determining the normalization factor. The results of the calculation of the dust-particle distribution for several relatively large values of subsolar angle θ (exceeding 70°) are presented in Figure 1. The region with the corresponding latitude is of interest because the Luna-25 and Luna-27 spacecraft are expected to land near the polar regions of the Moon.

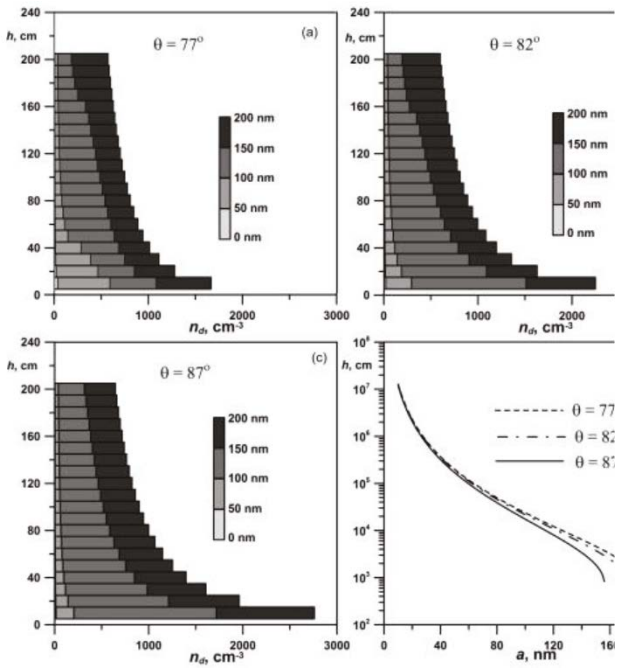

Fig. 1. Dust-particle distributions above the surface of the Moon for θ = 77° (a); 82° (b); 87° (c). Also shown are maximum possible altitudes that can be reached by the dust particles (d) for the following near-surface photoelectron parameters: the number density N_0 = 130 cm^{23} and the temperature T_e = 1.3 eV

THE INFLUENCE OF A SPACECRAFT:

One of the directions of the investigation of the Moon in the course of the Luna-25 and Luna-27 missions that is being developed currently and is expected to be implemented in the first half of the 2020s is the analysis of the dynamics of the dust particles and dusty plasma environment near the surface of the Moon. The Lunar Dust Monitor (LDM) experiment is being prepared for this purpose. The design of the instrument for the detection of dust particles implies using a method that has not yet been used in lunar studies. The plasma parameters will be measured in the LDM experiment by sensors located in the zone of the environment perturbed by the lander. Therefore, the results of the measurements obtained by this instrument must be corrected taking into account the influence of the lander on the environment. An improved version of the LDM instrument will be mounted on the Russian Luna-27 lander. This lander will be equipped with a rod on which the sensors of the plasma parameters will be mounted.

SUMMARY:

The lunar dust, and especially its finely dispersed component with the particle size varying from tens of nanometers to hundreds of micrometers, represents a highly dynamic component of the lunar regolith. To a significant extent, the lunar-dust's behavior is determined by the solar radiation and the intensity of the UV radiation in particular. Charged particles of the lunar regolith are capable of rising above the surface of the Moon as a result of electrostatic processes. These particles become an important part of the dusty plasma exosphere of the Moon. Theoretical and numerical modeling clarifies some of the specificities of the dusty plasma system above the Moon. However, there are problems related to its parameters and manifestations that should be addressed in the future. Below, we list some of the important directions of investigations for a detailed research of the dusty plasma above the Moon:

- the quantum yield and the work function of the lunar regolith;
- the influence of the implanted hydrogen on the photoemission properties of the lunar regolith;
- waves in the plasma above the surface of the Moon;
- the influence of the lander on lunar dusty plasma environment.

REFERENCES:

[1] Popel S. I., Golub' A. P., Zelenyi L. M., Dubinskii A. Yu. Lunar dust and dusty plasmas: Recent developments, advances, and unsolved problems // Planetary and Space Science. 2018. V. 156. P. 71284.
[2] Zelenyi L. M., Popel S. I., Zakharov A. V. Dusty plasma at the Moon. Challenges of modeling and measurements // Plasma Physics Reports. 2020. V. 46. No. 5. P. 527–540.
[3] Popel S. I., Golub' A. P., Lisin E. A., et al. Impacts of fast meteoroids and the separation of dust particles from the surface of the Moon // J. Experimental and Theoretical Physics Letters. 2016. V. 103. No. 9. P. 563–567.
[4] Popel S. I., Golub' A. P., Zelenyi L. M., Horányi M. Impacts of fast meteoroids and a plasma-dust cloud over the lunar surface // J. Experimental and Theoretical Physics Letters. 2017. V. 105. No. 10. P. 635–640.
[5] Popel S. I., Golub' A. P., Zakharov A. V. et al. Formation of dusty plasma clouds at meteoroid impact on the surface of the Moon // J. Experimental and Theoretical Physics Letters. 2018. V. 108. No. 6. P. 356–363.
[6] Popel S. I., Kopnin S. I., Golub' A. P. et al. Dusty plasma at the surface of the Moon // Solar System Research. 2013. V. 47. No. 6. P. 419–429.
[7] Colwell J. E., Batiste S., Horányi M. et al. Lunar surface: Dust dynamics and regolith mechanics // Reviews of Geophysics. 2007. V. 45. Art. RG2006.

50 YEARS OF LUNOKHOD-1: PAST, PRESENT AND FUTURE OF PLANETARY ROVERS

A. T. Basilevsky[1], M. I. Malenkov[2], J. W. Head[3]
[1] *Vernadsky Institute of Geochemistry and Analytical Chemistry RAS, Kosygin str., Moscow, 119991 Russia (atbas@geokhi.ru)*
[2] *Space Research Institute, Moscow, 117997 Russia*
[3] *Department of Earth, Environmental and Planetary Sciences, Brown University, Providence, RI, 02912 USA*

KEYWORDS:
Lunokhod, rover, trafficability, mass, chassis, wheel, scientific instrument, spectrometer, sensor, camera, radar

INTRODUCTION:
50 years ago, on November 17, 1970, the first planetary rover landed on the Moon (Figure 1). It traveled 9,93 km along the plains of Mare Imbrium and using 7 instruments studied the characteristics of the lunar surface and more distant space environment [e. g., 1, 2]. On August 7, 1971, the first piloted Lunar Roving Vehicle (LRV1) arrived on the Moon as part of the Apollo 15 mission [e. g. 3]. Since that time, several robotic rovers have studied the lunar and Martian surface and two LRVs were used in the Apollo 16 and 17 missions. In this talk we will report on the technical characteristics of the robotic and piloted rovers as well as the instruments on the robotic rovers and will suggest requirements for future missions involving planetary rovers.

Fig 1. The Crew of Lunokhod-1 (standing, from right to the left): V. G. Samal', G. G. Latypov, V. I. Chubuklin, A. V. Chvikov, I. L. Fedorov, N. M. Kozlitin, L. Ya. Mosenzov, K. K. Davidovsky, N. M. Eremenko, V. M. Sapranov, A. E. Kozhevnikov, V. G. Dovgan' and members of the State Commission (sitting, from right to the left): G. N. Babakin, G. A. Tyulin, A. I. Bolshoy, V. P. Panteleev, A. P. Romanov, N. I. Bugaev. November 22, 1970 — 5 days after landing. Control point Shkol'naya, Crimea. Photo of V. G. Dovgan'

KEY FEATURES OF REAL PLANETARY ROVERS:
General characteristics of all self-propelled chassis: type of propeller — wheel; type of drive: all-wheel drive; type of supporting structure; single-section frame or container; type of drive of wheels - individual electromechanical built-in (motor wheels), type of material of wheels: metals. Features of the specifications for planetary rovers are given below (mass, kg; dimensions, m) based on [1, 4–8].

SCIENTIFIC INSTRUMENTS ON PLANETARY ROVERS:
Below are listed scientific instruments of the planetary rovers considered. Sources of this information are: Lunokhod-1 — [1], Lunokhod-2 — [4], Yutu-1/2 — [10], Spirit/Opportunity — [11], Curiosity — [12].

Objects/Specif.	Lun.-1/ Lun.-2	LRV1,2,3	Sojou.	Spirit/ Oppor.	Curiosity	Yutu-1/ Yutu-2
study	Moon	Moon	Mars	Mars	Mars	Moon
Total mass	756/840	716 (max)	15,6	185	899	120
Mass s-p chassis,	105	211	–	–	–	–
Speed, km/h	0,8; 2,0 discrete	0–16,0 smooth	0,036	0,18	0,144	0,2
Wheel formula: USA/RF	8 (4×2)/ 8×8	4 (2×2) /4×4×4	6 (3x2)/ 6×6×4	6 (3×2)/ 6×6×4	6 (3×2)/ 6×6×4	6 (3×2)/ 6×6×4
Wheel base	1,705	2,29	≈0,5	≈1,51	≈2,4	1,25
Track	1,6	1,83	≈0,22	≈1,42	≈2,3	0,85
Type of rim or tire	rigid mesh rim	elastic braided tire	rigid sheet rim	rigid sheet rim	rigid sheet rim	rigid sheet rim
Wheel diameter	0,51	0,82	0,13	0,26	0,508	0,3
Type of suspension	Elastic, indepen.	Elastic, indepen.	Rock. Bogie	Rock. Bogie	Rock. Bogie	Rock. Bogie
Clearance	0,38	0,35	0,18	≈0,29	0,75	≥0,2
St. angle: Long./ tran.	43°/45°	45°/45°	45°/–	≈45°/–	–	
Type of ch. battery	Silver – Cadm.	Silver – Zinc	lithium thionyl chlor.	lithium ion	radioisotope power	
Resource of work, years old	0,82/ 0,29	0,008	0,25	6,1/ 14,37	8,9 (works)	0,027/ >1,5 works
Distance travel. km.	9,93/ 39,16	29,7 (LRV1)	0,1	7,703/ 45,16	more than 22	0,114/ > 0,448

Lunokhod-1: 17.11.1970–14.09.1971	***Lunokhod-2: 15.01.1973–10.05.1973***
Two navigation TV cameras Four panoramic TV cameras X-ray fluor. spectrometer RIFMA Soil mechanics sensor PROP Laser retroreflector X-ray telescope PT-1 Radiation detector PB-2H	Two navigation TV cameras Four panoramic TV cameras X-ray fluor. spectrometer RIFMA Soil mechanics sensor PROP Laser retroreflector X-ray telescope PT-1 Radiation detector PB-2H Magnetometer UV/Visible Astrophotometer Photodetector

Yutu-1: 14.12.2013 – 31.07.2016 ***Yutu-2: 03.01.2019 – still works***	***Spirit: 04.01.2004 – 22.03.2010*** ***Opportunity: 25.01.2004 – 10.06.2018***
Two navigation TV cameras Two panoramic TV cameras Two hazard avoidance cameras Alpha X-ray spectrometer APXS Infrared spectrometer Ground-penetrating radar GPR	Two navigation TV cameras Two panoramic stereo TV cameras Two hazard avoidance cameras Min. Thermal Emission Spectrometer Mössbauer spectrometer Alpha X-ray spectrometer APXS Microscopic Imager Magnets Rock abrasion tool

Curiosity: 06.08.2012–10.06.2018	
Two pairs of navigation TV cameras APXSMast camera system (Medium and Narrow Angle Cameras) 4 pairs of hazard avoidance cameras Chemistry and Camera complex	Alpha X-ray spectrometer Chemistry and Mineralogy Sample Analysis at Mars Dust Removal Tool

Rover Environmental Monitoring Station Mars Hand Lens Imager	Radiation assessment detector Dynamic Albedo of Neutrons Mars Descent imager Robotic arm

SUGGESTIONS FOR FUTURE MISSIONS WITH PLANETARY ROVERS:
From consideration of the past and ongoing rover-involved missions, the following requirements are suggested:

- High-resolution imaging for selection of landing site and detailed planning of the rover route.
- Hazard avoided landing — so as not to land on local steep slopes, tall rocks.
- Presence of robotic arm providing the possibility of direct contact of the instrument sensors with studied objects, including vertical sides of rocks.
- Possibility to clean the studied surface to remove the weathered material.
- Possibility to collect the samples for subsequent delivery to Earth or to the spacecraft or base equipped with analytical instruments.
- Possibility to replace the samples collected earlier with new ones.

In designing lunar and planetary rovers for future missions, it is necessary to take into account the need to visit both short-term stations and permanent bases. Their major required attribute of the rover will be the ability to explore a wide variety of terrain and to operate well in each. The unified components of these capabilities, for example, self-propelled chassis, should be available for mass production and provide a long-term resource. They should have increased cross-country trafficability to move towards targets, usually along the shortest routes, including in the shadowed zones of lunar craters, and at lunar night.

REFERENCES:
[1] Movable Laboratory on the Moon Lunokhod-1 / ed. Vinogradov A. P. M.: Nauka, 1971. 128 p.
[2] Karachevtseva I. P. et al. Cartography of the Lunokhod-1 landing site and traverse from LRO image and stereo-topographic data // Planetary and Space Science. 2013. V. 85. P. 175–187.
[3] Malenkov M. I. et al. They are Ahead of time: The Influence of the Soviet and American Lunar Rovers on modern Planetary Research.
[4] Marov M. Ya., Hantress U. T. Soviet Works in the Sun System. Tekhnologies and openings. 2nd ed. M.: Fizmatlit, 2017. 610 p.
[5] Kemurjdian A. L. Planetokhody. M.: Mashinostroenie, 1993.
[6] https://spaceflight101.com/change/change-3/.
[7] https://mars.nasa.gov/mer/.
[8] https://mars.nasa.gov/msl.
[9] Li C. et al. The Chang'e 3 Mission Overview // Space Science Reviews. V. 190. Iss. 1–4. P. 85–101.
[10] Jia et al. The scientific objectives and payloads of Chang'E-4 mission // Planetary and Space Science. 2018. V. 162. P. 207–215.
[11] Squyres S. et al. Athena Mars rover science investigation // J. Geophysical Research. 2003. V. 108. No. E12. 8062.
[12] Vasavada A. R. et al. Overview of the Mars Science Laboratory mission: Bradbury Landing to Yellowknife Bay and beyond // J. Geophysical Research Planets. 2014. V. 119. P. 1134–1161.

CANDIDATE LANDING SITES AND POSSIBLE CANDIDATE LANDING SITES AND POSSIBLE TRAVERSES AT THE SOUTH POLE OF THE MOON FOR THE LUVMI-X ROVER

M. Joulaud[1,2,3], J. Flahaut[2], D. Urbina[3], H. K. Madakashira[3], G. Ito[2], J. Biswas[4], S. Sheridan[5]

[1] *Ecole Nationale Supérieure de Géologie, Université de Lorraine, 54500 Vandœuvre-lès-Nancy, France (marine.jld21@gmail.com)*

[2] *CRPG, CNRS/Université de Lorraine, 54500 Vandœuvre-lès-Nancy, France*

[3] *Space Applications Services NV/SA, 1932 St-Stevens-Woluwe, Belgium*

[4] *Institute of Astronautics, Technische Universität München, 85748 Garching, Germany*

[5] *Faculty of Science, Technology, Engineering and Mathematics, The Open University, Milton Keynes, UK*

KEYWORDS:
Lunar poles, volatiles, LUVMI-X, ISRU, water ice, landing sites, GIS

INTRODUCTION:

Lunar volatiles, such as water, are considered to be a crucial resource for future exploration, enabling the use of the Moon as a platform for even more remote destinations. As water is most likely to be found in the form of ice at the lunar poles (where surface temperatures can be as low as 40 K, i. e. below the water temperature of sublimation in vacuum, 110 K [1]), multiple upcoming missions target the South Pole cold traps [2]. PSRs (Permanently Shadowed Regions) in particular are cold enough to capture and retain volatiles but present challenging conditions (rough topography, low illumination, low temperatures, and limited Earth visibility; [3] and references within). Funded by the EU program Horizon 2020, Space Applications Services developed the LUVMI-X rover (LUnar Volatiles Mobile Instrument) [4], aimed at sampling and analyzing lunar volatiles in the polar regions, including in a PSR. The LUVMI-X nominal payload includes a Volatiles Sampler and a Volatiles Analyser for volatiles investigation, along with a LIBS and a radiation detector. A mass spectrometer is also included; droppable and propellable payload versions are in development for inaccessible sites (such as PSRs). This solar-powered rover has an autonomy of one or two Earth nights and can drill down to 20 cm in the lunar regolith. The goal of this paper is to find suitable landing sites for this rover that are both scientifically interesting and technically reachable.

SELECTION OF CRITERIA AND DATA:

Table 1. Rover specifications and related data, with associated weight

Specifications	Data (Source, resolution)	Weight
Slopes < 10°	Digital Elevation Model of the South Pole (LRO[A] LOLA[B], 20m/px)	Compulsory
PSRs < 5 km	WAC[C] mosaic of the South Pole (100m/px) + map of PSRs [6] (LRO[A] Camera, 100m/px)	Compulsory
H signatures > 100 ppm	Hydrogen signatures in ppm (LPNS[D], 15km/px)	Compulsory 10/100
Maximum illumination	Average Sun visibility (LRO[A] LOLA[B], 240m/px) from [6]	50/100
Depth of water ice needs to be < 20 cm	Predictive ice stability depth (LRO[A] Diviner, 200m/px) from [1]	25/100
Maximum Earth visibility	Average Earth visibility (LRO[A] LOLA[B], 240m/px) from [6]	15/100

[A]Lunar Reconnaissance Orbiter. [B]Lunar Orbiter Laser Altimeter. [C]Wide Angle Camera. [D]Lunar Prospector Neutron Spectrometer.

Available remote sensing imagery for the lunar South Pole (Table 1) was downloaded from the Planetary Data Service or corresponding instruments'

websites and added into a Geographic Information System (GIS). LUVMI-X scientific objectives and technical specifications were then translated into a list of criteria and computed in our GIS using reclassifications, buffers, and intersections [3, 4]. Using ArcGIS, reclassified data were overlaid with different weights to define and rank compliant areas (= which meet the compulsory criteria) (Table 1). Regions Of Interest (ROI) were finally identified by mapping out compliant areas >453 km² (i. e., areas allegedly large enough to hold a 24×6 km landing ellipse). This ellipse size is based on the technical abilities of current commercial landers proposed by CLPS [5]).

LANDING SITES RANKING AND SELECTION:
Global results and comparison to literature

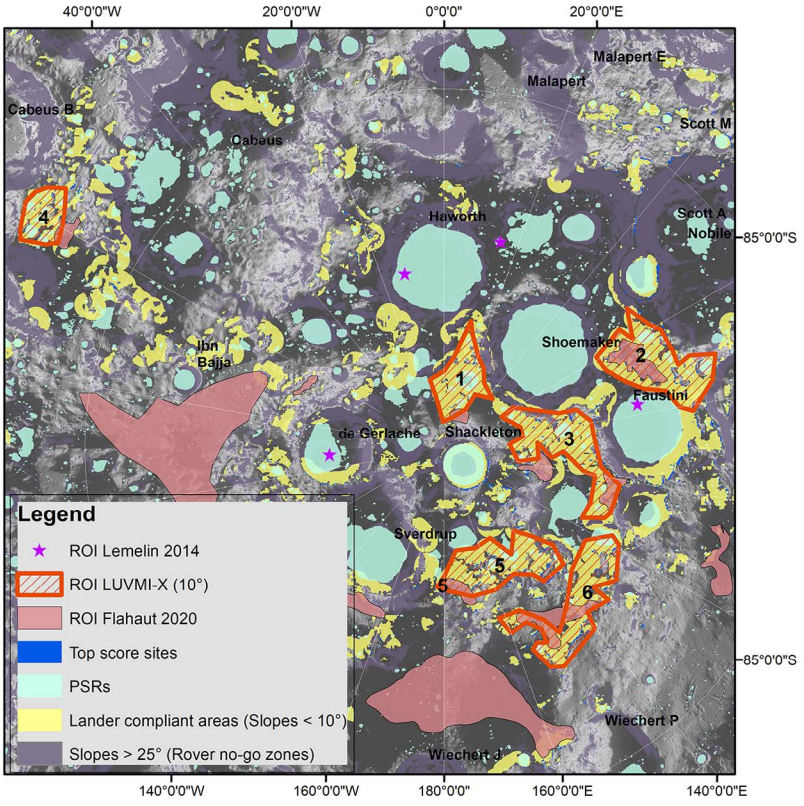

Fig. 1. ROI for the LUVMI-X rover (orange, this study) are compared to ROI from Lemelin et al. (2014, stars) and Flahaut et al. (2020, pink). Background is the LROC WAC image, all data are presented in South Pole stereographic projection.

Our GIS analysis (Figure 1) allowed us to identify six ROI (orange hatched areas) for the LUVMI-X mission, which were compared with previous South pole ROI from the literature (Lemelin et al., 2014, stars [7]; Flahaut et al., 2019, pink [3]). First, none of the LUVMI-X ROI intersects with Lemelin's landing sites because the latter are only located within PSR; Lemelin's sites do not meet the technical specifications of the LUVMI-X rover which is solar-powered. However, parts of Flahaut's ROI overlap with the LUVMI-X sites of this study. Flahaut's largest ROI (Wiechert, Ibn Bajja) do not overlay with LUVMI-X ROI as Flahaut's study only considers surface water ice. On the contrary, our study is intended for a rover able to drill down to 20 cm. In addition, Wiechert and Ibn Bajja are two far sides sites; their Earth visibility is highly restricted in comparison to near side sites. Slopes under 25° are also displayed because of LUVMI-X's technical limitations concerning slope egress after landing.

ROI final ranking

The identified ROI are further ranked based on areas and statistics on Sun and Earth visibilities, Diviner average surface temperatures, and H signatures (Table 2). H signatures from Lunar Exploration Neutron Detector (LEND) and water ice signatures from Moon Mineralogy Mapper (M^3) [8] are also used to compare each ROI.

ROI 4 presents the lowest average H signatures from LEND and does not comprise any evidence for surface ice from M^3. Even if it has the highest average Sun visibility, it presents a complex shape, which is not sufficient to hold a 24×6 km landing ellipse. ROI 6 has the highest Sun visibility, yet the lowest Earth visibility and *H* signatures from LPNS; it also presents too many non-compliant pixels along with a restrictive shape for the landing ellipse. ROI 5 could be discarded as it presents too many non-compliant pixels. Although ROI 1 has the lowest temperature and lowest percentage of non-compliant pixels, it also has one of the smallest areas and the lowest Sun visibility. Therefore, ROI 2 and 3 seem to be the best candidates for LUVMI–X. While ROI 3 has high *H* signatures from LPNS and LEND, ROI 2 presents the highest *H* signatures (LPNS) along with more evidence for water ice from M^3. ROI 2, located on a topographic high between Shoemaker and Faustini, comprises the best site from Flahaut et al. (2020).

Table 2. Average zonal statistics on previously defined ROI. Red = low suitability, yellow = intermediate suitability, green = high suitability (NB: Int = intermediate)

ROI	1	2	3	4	5	6
Area (km²)	493.73	1007.42	897.32	375.94	815.67	931.76
% of non compliant pixels	13.87	21.22	16.18	19.67	24.83	25.15
Sun visibility	0.115	0.169	0.141	0.133	0.184	0.225
Earth Visibility	0.308	0.292	0.354	0.409	0.312	0.288
H from LPNS (ppm)	141.3	157.2	154.3	143.1	142.5	126.3
H from LEND	Int.	Int.	High	Low	Int.	Int.
Temperature (K)	70.16	78.78	74.56	80.48	83.65	83.67

PERSPECTIVES FOR LUVMI-X:

Future work includes a higher resolution analysis of the selected ROI using LROC Narrow Angle Camera images (at 1 m/px) and LOLA DEM (at *x* m/px) in order to map potential hazards and check PSR accessibility. A landing ellipse will then be proposed inside the selected ROI. Finally, traverses will be established based on LUVMI-X concept of operations and scientific objectives. Waypoints will be defined and then linked either by minimizing the used energy or maximizing the varying Sun and/or Earth visibilities during the mission and will be used as an input to parametric and thermal models of the rover.

REFERENCES:

[1] Paige D., Siegler M., Zhang J-A., Hayne P., Foote E., Bennett K., Vasavada A., Greenhagen B., Schofield J., McCleese D., Foote M., DeJong E., Bills B., Hartford W., Murray B., Allen C., Snook K., Soderblom L., Calcutt S., Taylor F., Bowles N., Bandfield J., Elphic R., Ghent R., Glotch T., Wyatt M., Lucey P. Diviner lunar radiometer observations of cold traps in the Moon's south polar region // Science. 2010. V. 330. P. 479–482.

[2] Crawford I. A., Anand M., Barber S., Cowley A., Crites S., Fa W., Flahaut J., Gaddis L., Greenhagen B., Haruyama J., Hurley D., McLeod C., Morse A., Neal C., Sargeant H., Sefton-Nash E., Tartèse R. Lunar Resources. 2020.

[3] Flahaut J., Carpenter J., Williams J–P., Anand M., Crawford I. A., van Westrenen W., Füri E., Xiao L., Zhao S. Regions of Interest (ROI) for Future Exploration Missions to the Lunar South Pole // Planetary and Space Science. 2020. V. 80. Art. 104750.

[4] Gancet J., Urbina D., Biswas J., Losekamm M., Sheridan S., Evagora A., Richter L. LUVMI and LUVMI-X: Lunar Volatiles Mobile Instrumentation Concept and Extension // Proc. ESA ASTRA Symp. 2019.

[5] Astrobotic. Peregrine Lunar Lander, Payload User's Guide. 2020.

[6] Mazarico E., Neumann G. A., Smith D. E., Zuber M. T., Torrence M. H. Illumination conditions of the lunar polar regions using LOLA topography // Icarus. 2011. V. 211. P. 1066–1081.
[7] Lemelin M., Blair D. M., Roberts C. E., Runyon K. D., Nowka D., Kring D. A. High priority lunar landing sites for *in-situ* and sample return studies of polar volatiles // Planetary and Space Science. 2014. V. 101. P. 149–161.
[8] Li S., Lucey P. G., Milliken R. E., Hayne P. O., Fisher E., Williams J.-P., Hurley D. M., Elphic R. C. Direct evidence of surface exposed water ice in the lunar polar regions // Proc. National Academy of Sciences. 2018. V. 115(36). P. 8907–8912.

RUSSIAN LUNA-26 ORBITER MISSION: SCIENCE AND IMPLEMENTATION

A. A. Petrukovich, L. M. Zelenyi, K. V. Anufreichik, I. G. Mitrofanov, O. V. Korablev
Space Research Institute, *Russian Academy of Sciences* (*IKI*), *Moscow 117997*, *Russia*

KEYWORDS:
Moon, Luna-26, orbital mapping

Russian Lunar orbiter mission Luna-26 is targeted to probe lunar surface and subsurface composition, as well as neutral, dust and plasma exosphere. It includes 13 scientific instruments from four countries. We present the mission profile and discuss the role of the mission in the Russian lunar program.

OVERVIEW OF LUNA-27 SCIENCE INSTRUMENTS

V. I. TRETYAKOV, L. M. ZELENYI, I. G. MITROFANOV
Space Research Institute of the Russian Academy of Sciences (*IKI*),
Moscow 117997, *Russia* (*vladtr@mx.iki.rssi.ru*)

KEYWORDS:
Moon, Polar Regions, Landers, spacecraft, robotic missions

Scientific goals, current status and plans of nearest activities for Russian Lander missions with SC Luna-27 of project Luna-Resource-1(PA) will be presented. Mission aimed on search for volatiles and water ice in upper layer of regolith, study structure and content of regolith and investigate of moon's near-surface dust and plasma exosphere at lunar polar regions.

The scientific experiments including Lunar Drill that were selected in accordance to the main goals of these missions, will be described. Preliminary landing sites for Luna-27 will be presented selected on the base both of engineering suitability (flatness and roughness of surface, radio visibility, solar irradiation and so on) and of scientific motivation. The detailed plan of surface operations during the first lunar days will be presented and discussed.

The content of international cooperation for Luna-25 and Luna-27 missions will be described.

ESA'S PROSPECT PAYLOAD ON LUNA-27: DEVELOPMENT STATUS

D. J. Heather[1], E. Sefton-Nash[1], R. Fisackerly[1], R. Trautner[1], D. J. P. Martin[2], J. D. Carpenter[1], B. Houdou[1], P. Reiss[1], S. Barber[3], the ESA Lunar Exploration Team, the PROSPECT Science Team and the PROSPECT Industrial Team

[1] *ESTEC, European Space Agency, Noordwijk, The Netherlands* (*dheather@cosmos.esa.int*)
[2] *ECSAT, European Space Agency, Harwell, Didcot, UK*
[3] *The Open University, Milton Keynes, UK*

KEYWORDS:
Moon, volatiles, polar, Luna Resource, PROSPECT

INTRODUCTION:
The Package for Resource Observation and in-Situ Prospecting for Exploration, Commercial exploitation and Transportation (PROSPECT) is a payload in development by ESA for use at the lunar surface. Current development is for flight on the Russian-led Luna-Resource Lander (Luna-27) mission, which will target the south polar region of the Moon. PROSPECT will perform an assessment of volatile inventory in near surface regolith (down to ~1 m), and elemental and isotopic analyses to determine the abundance and origin of any volatiles discovered. Lunar polar volatiles present compelling science and exploration objectives for PROSPECT, but solar wind-implanted volatiles and oxygen in lunar minerals (extracted via ISRU techniques) constitute potential science return anywhere on the Moon, independently of a polar landing site. PROSPECT is comprised of the ProSEED drill module and the ProSPA analytical laboratory, plus the Solids Inlet System (SIS), a carousel of sealable ovens (for evolving volatiles from regolith) [1] (Figure 1).

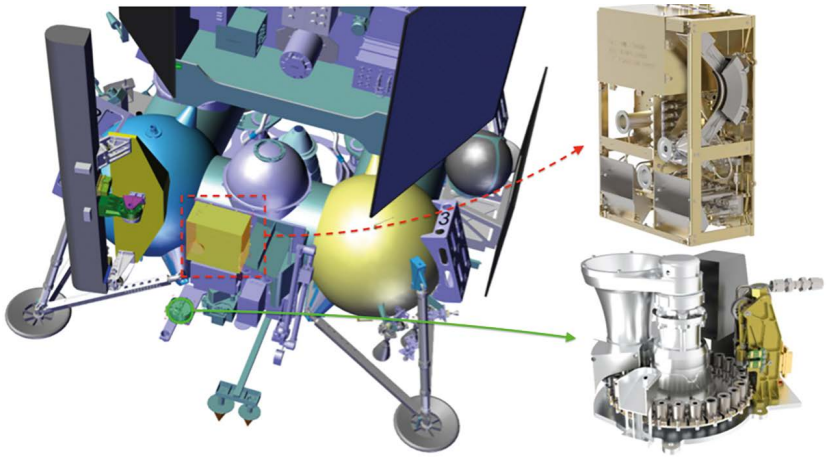

Fig. 1. Renderings. Left: PROSPECT mounted on Luna 27, including ProSEED drill module (left), Solids Inlet System [SIS] (green circle), and analytical laboratory drawer (yellow box) containing ProSPA gas processing system and instruments

Upper right: ProSPA analysis package containing magnetic sector and ion-trap mass spectrometers.

Lower right: Solids Inlet System to receive samples from drill sampling mechanism, with sample camera assembly (Sam-Cam) and carousel of ovens for volatile extraction from regolith samples.

In ensemble, PROSPECT has a number of sensors and instruments (including ion-trap and magnetic sector mass spectrometers, imagers, and sensors for temperature, pressure, and permittivity) that form the basis for a range of science investigations [2] that are (almost all) led by the PROSPECT Science Team:

- Imaging, Surface Modelling and Spectral Analysis,
- Drilling, Geotechnics and Sample Handling,
- ProSPA ISRU Precursor Experiments,
- ProSPA ISRU Prospecting,
- ProSPA Light Elements and Isotopes,
- ProSPA Noble Gases,
- Thermal Environment and Volatile Preservation,
- Permittivity (ESA-led).

DEVELOPMENT STATUS AND CURRENT ACTIVITIES:
PROSPECT Phase C, 'detailed definition', began in December 2019. A plan of research activities is in progress to gain from and guide on-going development, build strategic scientific knowledge, and to prepare for operation of the payload.

Recent developments include the construction of an EM of the p-sensor and of the ProSeed imaging system, and their successful testing in representative environments. Details of further activities are described below.

Drill Testing
Testing of the ProSEED Development Model was carried out in December 2019 as part of the final Phase B activities. Test procedures were formulated to demonstrate drilling and sampling functionality in ambient, cold and thermal vacuum (TV) laboratory conditions (at CISAS, University of Padova). Tests included drilling into, and sampling from, well-characterized NU-LHT-2M simulant mixed with anorthosite inclusions of various sizes, according to a layered scheme that describe depth-density profile and distribution of inclusions and a range of plausible water ice contents.

ProSPA Bench Development Model (BDM)
The BDM of the ProSPA analytical lab at the Open University has been tested to demonstrate science performance against measurement requirements. Dedicated efforts in 2019 focused on verification of evolved gas analysis (EGA) via measurement of meteorite standards, constraint of oxygen yield via demonstration of ISRU capabilities, improving understanding of sensitivity of science requirements to regolith volatile abundance and possible contamination, and understanding the performance of oven seal materials.

VOLATILE PRESERVATION:
Particular efforts since 2018 have focused on understanding the capability of PROSPECT to sufficiently preserve volatile content in regolith throughout the sampling-analysis chain: from drilling to sealing of the ovens, until measurement of evolved gases in ProSPA's ion-trap and magnetic sector mass spectrometers. PROSPECT's ability to meet science requirements must persist for the range of possible volatile contents expected in near-surface regolith at landing sites in the lunar south-polar region.

ACKNOWLEDGEMENTS:
The PROSPECT Industrial Consortium and development of ProSEED is led by Leonardo (Italy). The development of ProSPA is led by the Open University (UK).

REFERENCES:
[1] Barber S. et al., (2018), Euro. Lunar Symp. Abstract 099.
[2] Sefton-Nash E. et al., (2018), Euro. Lunar Symp., Abstract 114.

LUNAR ROVER AND SOIL INTAKE SYSTEM FOR LUNA-28

A. Nosov, T. Kozlova, M. Litvak, V. Yakovlev, A. Perhov, A. Feofanov, V. Mikhalsky
Space Research Institute, *Russian Academy of Sciences* (*IKI*), *Moscow 117997*, *Russia* (*el.vb0247@gmail.com*)

KEYWORDS:
Moon, polar, Luna-28, lunar rover, robotic arm, drill system

INTRODUCTION:

The main goal of the Russian Luna-28 mission (Luna-GRUNT project) is to ensure the successful delivery of the maximum possible amount of polar lunar regolith taken from different depths with preservation of volatiles and water ice.

At present, a technical proposal has been completed regarding mission requirements, concept and a list of the possible science payload.

The largest and most significant components of science payload are the soil intake system and the small lunar rover. They will be developed to study and to sample lunar regolith at various depths around lander before launch of return module and along a rover path after the launch of return module.

In this study, we considered conceptual versions of the soil-intake system and lunar rover.

The soil sampling system (Figure 1) provides soil acquisition from the lunar subsurface down to two meters depth, delivery of soil samples to scientific analytical instruments for onboard study, hermetical encapsulation of soil samples taken from the various depths to ensure the preservation of water and volatile substances and loading them into the receiving container of the return module (to return samples to the Earth).

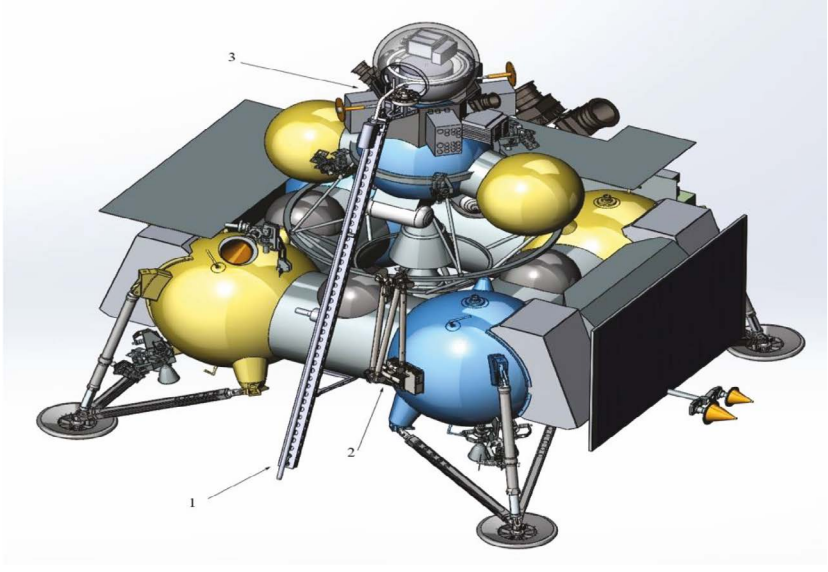

Fig. 1. Soil intake complex, which consists: of manipulator complex (1); drilling device (2); encapsulation device (3)

The sampling of lunar soil from the shallow depths (10–20 cm) is carried out by robotic arm, and from 0.5–2 m depths — by a deep depth drill. The distribution of samples between analytical scientific instruments and return module will be provided by robotic arm, transportation and encapsulation devices combined in one suit.

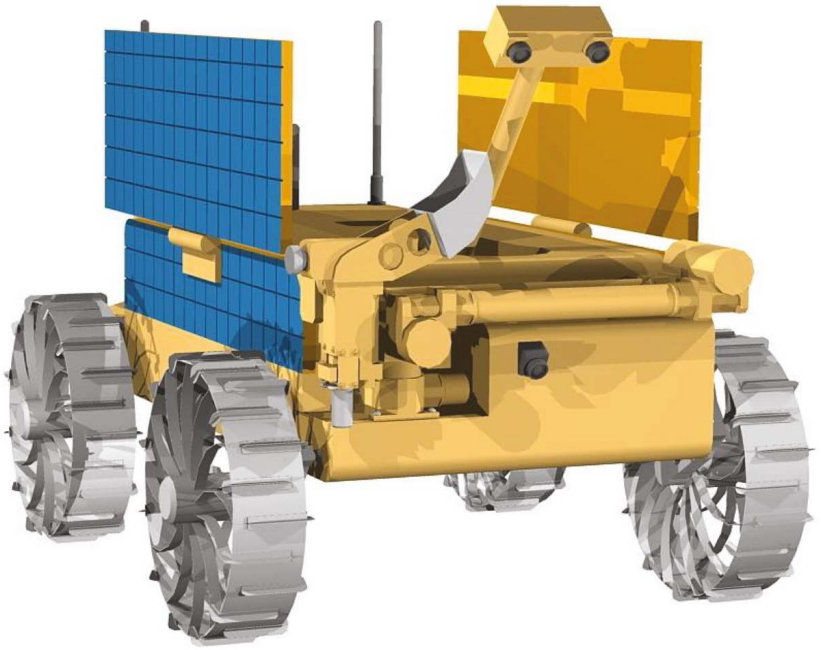

Fig. 2. Conceptual view of the lunar rover model

In addition to the sample return to Earth, another priority goal of the mission is a long-term exploration of the lunar surface at the remote vicinity of the landing site (100–1000 m). To implement this goal Luna-28 lander should deliver to the lunar surface a small or middle class autonomous lunar rover equipped with corresponding science instrumentation (applicable for the geological survey) and multifunctional robotic arm for the sample collection. The rover surface operations shall be conducted both under direct telecontrol from the Earth and in the auto navigation modes. The rover shall survive during lunar nights to extend mission up to 1 year. The rover design and its science instrumentation should be studied in detail to select the optimal concept within allocated mass of the rover (~100 kg). The conceptual view of the lunar rover model is shown in Figure 2.

TECHNOLOGY OF 3D PRINTING ON THE MOON

T. M. Tomilina, A. A. Kim, S. N. Ponomareva
Blagonravov Institute for Mechanical Engineering Research of Russian Academy of Science, Nizhny Novgorod, Russia (*mlitvak.iki@gmail.com*)

KEYWORDS:
Moon, lunar regolith, 3-D printer

The exploration of the Moon in the coming decades will require the creation of a space infrastructure on its surface. It is advisable to manufacture structural elements for such an infrastructure directly from the lunar regolith using 3D printing technologies — this will eliminate the need to transport such elements from the Earth to the Moon. In the longer term, based on 3D printing technologies mechanical units and parts will most likely be manufactured for assembling interplanetary spacecrafts on the Moon. Therefore, many space centers have now begun to develop such technologies. This report will provide a brief overview of the achieved results and planned researches in this area.

In particular, the report will outline the concept of the Russian space experiment “Lunar Printer0, which was proposed at IMASH RAS for implementation within the framework of the promising lunar project “Luna-Grunt”. In this experiment on the lunar surface, it is planned to conduct full-scale tests of options of 3D printing from the lunar regolith of typical samples of mechanical parts and perform their primary sorting. The most successful samples will be delivered to the Earth for detailed studies of their physical and mechanical properties and characteristics. Based on the results obtained, the first initial data will be worked out for creating 3D printer of mechanical structure elements from the lunar regolith and variants for their practical application will be proposed.

CONCEPT OF GAMMA-RAY SPECTROMETER WITH TAGGED CHARGED PARTICLES OF GALACTIC COSMIC RAY FOR LUNAR RESOURCE INVESTIGATIONS

A. B. Sanin, I. G. Mitrofanov, A. A. Anikin, M. L. Litvak, D. V. Golovin, A. S. Kozyrev
Space Research Institute of the Russian Academy of Sciences (*IKI*), *Moscow 117997*, *Russia* (*sanin@np.cosmos.ru*)

KEYWORDS:
Moon, soil composition, gamma-spectrometer, resource investigation, future missions

INTRODUCTION:
Planetary bodies with little or no atmosphere may emit gamma-rays generated in the subsurface due to the bombardment of high-energy charged particles of Galactic Cosmic Rays (GCRs). GCR particles have high energies and produce hadronic and electro-magnetic showers to depths up to several meters. Neutrons and charged particles produced in the hadronic shower have energies of ~0.5 MeV and higher. Most of the charged particles have energy too low to induce nuclear reactions, however, neutrons can produce radionuclides via inelastic scattering and thermal neutron capture reactions. High-energy GCR particles may also produce gamma rays in the subsurface soil by spallation. Each radionuclide or excited nucleus emits gamma-rays with well-defined energy (so-called characteristic emission lines). Thus, identifying such lines and their intensity in the measured gamma-ray spectra makes it possible to estimate the mass fractions of the corresponding elements in a planetary surface (see, for example, [1]).

Gamma-spectroscopy has been used for decades to study the Moon, Mars, Mercury, Venus and some asteroids [2-8] and is actually the main method for remotely determining the chemical composition of the surface soil layer of celestial bodies. Due to the fact that gamma-spectrometers are installed on board spacecraft, which are constantly bombarded by GCRs, the measured gamma-spectra can be contaminated with the inevitable contribution of gamma-rays from the spacecraft carrying the instrument. This significantly reduces the accuracy or completely prevents the determination of the content in the soil of those chemical elements that are present in the structural elements of the spacecraft (hydrogen, carbon, oxygen, silicon, magnesium, aluminum, titanium, etc.).

At present, long-term programs for the exploration of the Moon and Mars are being discussed. The purpose of these programs is not only to study the celestial bodies' formation and evolution, but also to find ways to practically use the natural resources available on the surface to maintain the long-term stay of cosmonauts on the surface in habitable bases. Gamma-spectroscopy will undoubtedly play a key role in such research. However, for its successful application, it is necessary to exclude the background of gamma-radiation from the spacecraft. How this problem is solved will determine the choice of scientific payload, the design of the spacecraft and the program for determining planetary resources.

CONCEPT OF COSMIC GAMMA-RAY SPECTROMETER WITH TAGGED CHARGED PARTICLES:
The concept of a cosmic gamma-ray spectrometer with tagged charged particles (CGS-TCP) is accomplished by the addition of a plane detector of charged particles over a spot on the surface, which is selected for study. Counts in the charged particle detector (ChPD) tag GCR particles that fall into the volume of surface below the spot. Such volume can be defined as the "volume of tagged charged particles": its depth corresponds to the free path of incoming cosmic particles and outgoing gamma rays, while the boundaries correspond to the geometric factor of the ChPD (see Figure 1).

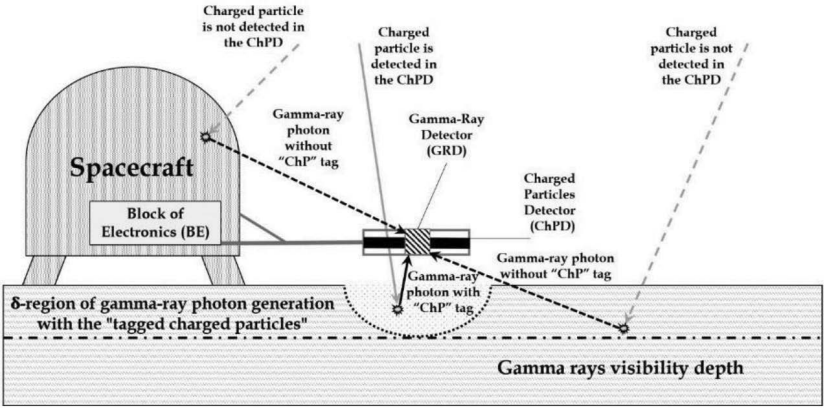

Fig. 1. The concept of CGS-TCP instrument for gamma-ray spectroscopy of a planetary surface composition

Gamma-rays from the subsurface are detected by the gamma-ray detector (GRD), and for each event, the instrument measures the time between gamma-ray detection and tagged GCR particle to the accuracy of nanoseconds. Like the tagged neutron method, the measurement of counts from particles in the ChPD and photons in the GRD can apply coincidence criterion between detections. This criterion can be defined as, for example, time interval between detection counts in ChPD and in GRD is less than several tens of nanoseconds. When this condition is met, the "ChP" logical label is assigned to the detected gamma-ray photon in the GRD. The logical unit of the instrument might implement the coincident procedure onboard, or, if the downloading data rate allows, it may be implemented during the data processing on the Earth. The overwhelming majority of such tagged counts correspond to photons that were emitted from the "volume of tagged charged particles" by GCR particles that were recorded by the ChPD. The energy spectrum of tagged counts in the GRD is the useful "signal" — the spectral lines in the energy spectrum characterize the elemental composition of the material inside the "volume of tagged charged particles".

The development and laboratory modelling of the cosmic gamma-spectrometer with "tagged charged particles" (CGS-TCP) is carried out within the framework of the project No. 18-12-004848 of the Russian Science Foundation [9]. A laboratory prototype of CGS-TCP instrument has been created and the technique of gamma-spectroscopy with "charged particle tags" was tested using the phazotron facility of the Joint Institute for Nuclear Research. A significant increase in the sensitivity for the main rock-forming elements of celestial bodies was achieved in case of selecting spectrometer signals according to the criterion of coincidence with protons, which cause secondary gamma-radiation in a thick target as an analogue of planetary matter.

REFERENCES:

[1] Masarik J., Reedy R. Gamma ray production and transport in Mars // J. Geophysical Research. 1996. V. 101. P. 18,891–18,912.
[2] Lawrence D. J., Feldman W. C., Barraclough B. L., Elphic R. C., Thomsen D. R. Global elemental maps of the Moon: The Lunar Prospector Gamma-Ray Spectrometer // Science. 1998. V. 281 P. 1484–1489.
[3] Kobayashi S. et al. Determining the Absolute Abundances of Natural Radioactive Elements on the Lunar Surface by the Kaguya Gamma-ray Spectrometer // Space Science Reviews. 2010 V. 154 P. 193–218.
[4] Evans L. G., Reedy R. C., Starr R. D., Kerry K. E., Boynton W. V. Analysis of gamma ray spectra measured by Mars Odyssey // J. Geophysical Research: Planets. 2006. V. 111 Art. E03S04.
[5] Wang X., Zhang X., Wu K. Thorium distribution on the lunar surface observed by Chang'E-2 gamma-ray spectrometer // Astrophysical Space Sciences. 2016. V. 361 P. 234.
[6] Evans L. G., Peplowski P. N., Rhodes E. A., Lawrence D. J., McCoy T. J., Nittler L. R., Solomon S. C., Sprague A. L., Stockstill-Cahill K. R., Starr R. D., Weider S. Z., Boynton W. V., Hamara D. K., Goldsten J. O. Major-element abundances on the surface

of Mercury: Results from the MESSENGER Gamma-Ray Spectrometer // J. Geophysical Research: Space Physics. 2012 V. 117 Art. E00L07.
[7] Surkov I. A. Geochemical studies of Venus by Venera 9 and 10 automatic interplanetary stations // Proc. 8th Lunar Science Conf. Houston, Tex., March 14–18, 1977. V. 3. P. 2665–2689.
[8] Prettyman T. H., Feldman W. C., McSween H. Y. et al. Dawn's Gamma Ray and Neutron Detector // Space Sciences Reviews. 2011. V. 163. P. 371–459.
[9] Mitrofanov I. G., Sanin A. B., Nikiforov S. Y. Cosmic gamma-ray spectrometer with tagged charged particles of Galactic Cosmic Rays // Nuclear Instruments and Methods in Physics Research. 2020 V. 953. Art. 163148.

VOLCANICALLY-INDUCED TRANSIENT ATMOSPHERES ON THE MOON: ASSESSMENT OF DURATION, SIGNIFICANCE AND CONTRIBUTIONS TO POLAR VOLATILE TRAPS

J. W. Head[1], L. Wilson[1,2], A. N. Deutsch[1], M. J. Rutherford[1], A. E. Saal[1]
[1] *Department of Earth, Environmental and Planetary Sciences, Brown University, Providence, RI 02912 USA* (*james_head@brown.edu*)
[2] *Lancaster Environment Centre, Lancaster University, Lancaster LA1 4YQ UK*

KEYWORDS:
Lunar atmosphere, degassing, volcanism, volatiles, poles, ice

SUMMARY:
A transient lunar atmosphere formed during a peak period of volcanic outgassing and lasting up to about ~70 Ma was recently proposed [1]. We utilize forward-modeling of individual lunar basaltic eruptions and the observed geologic record to predict eruption frequency, magma volumes, and rates of volcanic volatile release. Typical lunar mare basalt eruptions have volumes of ~10^2–10^3 km^3, last less than a year, and have a rapidly decreasing volatile release rate. The total volume of lunar mare basalts erupted is small and the repose period between individual eruptions is predicted to range from 20,000-60,000 years. Only under very exceptional circumstances could sufficient volatiles be released in a single eruption to create even a tenuous atmosphere. The frequency of eruptions was likely too low to sustain even a tenuous atmosphere for more than a few thousand years. We find that transient, volcanically-induced atmospheres were inefficient sources for volatile delivery to permanently shadowed lunar polar regions.

INTRODUCTION:
We use improved models of the generation, ascent and eruption of lunar basaltic magma [2], to predict flow volumes, eruption frequencies [3], and temporal magmatic volatile release patterns in individual eruptions [4, 5]. Key components of this analysis are 1) the range (and mean value) of magma volumes erupted in individual eruptions, 2) the masses, and hence volumes, of the various gases released in any one eruption, 3) the duration of the eruption and the gas release rate (varying significantly as the eruption progresses), 4) the typical time intervals between eruptions (repose periods) as a function of geologic time and 5) the timescale for the dissipation of an atmosphere once one is emplaced. We review the geological basis for the first four components, examine the potential time-dependence and variability of gas release in an individual typical eruption, and finally address the question: *Are these gas-release values sufficient to form a transient atmosphere and, if so, for what duration?* We then compare our findings with the broad-scale, time-averaged peak flux estimates of Needham and Kring [1], and address similarities and differences and their causes, and how estimates might be refined in the future. We conclude by assessing whether the forward-modeling predictions of gas-release rates are sufficient to: 1) act as a significant supply of volatiles to the permanently shadowed lunar polar cold-trap regions and 2) form a transient lunar atmosphere for a period sufficient to favor astrobiological activity [6].

DISCUSSION:
What effect does the non-linear release of gas during the four phases of a typical volcanic eruption (Figure 1a) have on the peak loss of volatiles during an eruption? To address this question, we first look at the magma volume eruption rate as a function of time for an eruption releasing 250 km^3 of magma (a medium-scale volume in the ~100–300 km^3 average eruption volume range described above) and lasting 46 days (about average for the 1–3 month range discussed above) (Figure 1b). Magma volume flux is clearly highest in the first ten days (Phase 1 and 2), decreasing two orders of magnitude from an initial peak flux of 10^6 $m^3 \cdot s^{-1}$, to 10^4 $m^3 \cdot s^{-1}$ after ~10 days.

Eruption Phase	PHASE 1 Dike penetrates to surface, transient gas release phase	PHASE 2 Dike base still rising, high flux hawaiian eruptive phase	PHASE 3 Dike equilibration, lower flux hawaiian to strombolian transition phase	PHASE 4 Dike closing, strombolian vesicular flow phase
Dike Configuration	Crust Mantle			
Surface Eruption Style	Transparent gas Pyroclasts	Opaque pyroclastic fountain Sinuous rille Lava lake	Fountain declines toward strombolian	a) Proximal foam flow b) Distal flow inflation
Magma Rise Speed	30 to 20 m/s	20 to 10 m/s	5 to <1 m/s	< 1 m/s
Magma Volume Flux	~10^6 m^3/s	10^6 to 10^5 m^3/s	10^5 to ~10^4 m^3/s	~10^4 m^3/s
Percent Dike Volume Erupted	<5%	~80%	~5%	~10%
Phase Duration	~3 minutes	~4 days	~6 days	~30 days

(a)

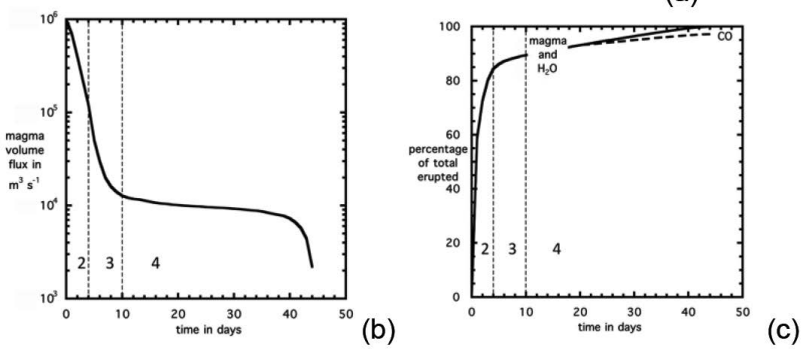

Figure 1. Forward modeling results for a 250 km^3 lunar volcanic eruption: a) The characteristics of four eruptive phases during the eruption with diagrams and parameters representing typical values. The relative duration of individual phases depends on the total dike volume and vertical extent. b) Magma volume flux for the typical eruption in (a) as a function of time. c) Percentage of total magma and gas released as a function of time. Vertical broken lines in parts (b) and (c) separate labeled phases; Phase 1 is too brief to be visible

Magma volume flux remains at this low value for the next 30 days (Phases 3–4) before falling to zero in the last 4 days at the end of the eruption. Thus, ~90 % of the total volume of magma erupted is emplaced in Phase 2, the hawaiian phase characterized by maximum magma degassing and volatile loss. Using the magma volatile species proposed by [4], the percentages of the magma, water, and CO released as a function of time in the same eruption are shown in Figure 1c. Released water closely mimics the erupted magma, unless a significant amount is left trapped in late-stage magma (Phase 4) intruded into earlier flow lobes during flow inflation. If significant inflation occurs, and the inflating gas does not escape, about 95% of the water would be released instead of 100 % as shown in Figure 1c. The CO in the magma, preferentially released at very great depth, does not all escape: CO released in Phase 4 does not have time to reach the surface before the conduit freezes, even allowing for bubble coalescence and rise. However, this only represents a few percent of the total CO and so almost all of the total is released. In summary, the implied intervals between typical lunar eruptions, ~13,000 to 40,000 years, are 6-7 times greater than the likely durations of the vast majority of individual transient atmospheres, between ~2,000 and 6,000 years. Only for the single, extreme example of Schröter's Valley are the time scales comparable. Otherwise, only if all of the Moon's ~10^7 km^3 of basaltic volcanism were to have taken place within a 300 Ma interval would the time scales generally be comparable. The non-linear release of gas during the four phases of a single

eruption do not alter this conclusion; even though volatile release is concentrated in the first 25–35 % of the eruption, the long repose periods between eruptions preclude sufficient buildup to create an enduring atmosphere. The same is true of leakage of gas from magma reservoirs between eruptions: if half of a typical magma volatile inventory is released uniformly over the ~40 ka average interval between eruptions, the leakage rate is somewhat less than 1 $kg \cdot s^{-1}$, an order of magnitude less than the atmospheric loss rate.

CONCLUSIONS:

On the basis of our analysis of the generation, ascent and eruption of lunar mare basalt magmas and forward-modeling individual eruptions, we conclude that it is very unlikely that the Moon had a semi-permanent (as long as ~70 Ma) volcanically-driven atmosphere as proposed by [1], even during a period of peak volcanic flux in early lunar history. We attribute the differences between our estimates and those of [1] to their use of maximum impact basin depths as average depths, and assignment of all excess volumes below datable units to one age (e. g., $5.9 \cdot 10^6$ km^3 assigned to 3.5 Ga in the case of Imbrium).

We also conclude that these low volatile release volumes and rates are not conducive to optimizing the transport of released volatiles from the eruption site to the poles to enhance the accumulation of volatiles in polar cold traps, nor of creating temporary environments that might favor astrobiological activity [6]. Our results suggest that the vast majority of volatiles in lunar polar cold traps were more likely to have originated from volatile-rich impacts, rather than volatile release from volcanic eruptions, similar to findings about polar cold-trap volatile deposits on Mercury [e. g., 7–9]. In order to refine these estimates, future lunar exploration goals should include further analysis of detailed lava flow thicknesses, ages, volumes, volatile contents and repose periods, as well as better determination of the interior structure of mare deposits in large impact basins.

REFERENCES:

[1] Needham & Kring (2017). Earth and Planetary Science Letters, 478, 175–178.
[2] Wilson & Head (2017). Icarus, 283, 146–175.
[3] Head & Wilson (2017). Icarus, 283, 176–223.
[4] Rutherford, Head, Saal, Hauri, & Wilson (2017) American Mineralogist, 102, 2045–2053.
[5] Wilson & Head (2018) Geophysical Research Letters, 45, 5852–5859.
[6] Schulze-Makuch & Crawford (2018) Astrobiology, 18(8), 985–988.
[7] Ernst, Chabot, & Barnouin, O. S. (2018) Journal of Geophysical Research, 123(10), 2628–2646.
[8] Deutsch, Head, & Neumann (2019) Earth and Planetary Science Letters, 520, 26–33.
[9] Deutsch, Head III, Parman, Wilson, Neumann & Lowden (2020) Lunar and Planetary Science Conference, LI, abstract 2259.

UNVEILING THE MINERALOGICAL COMPOSITION OF LUNAR FAR SIDE MARE BASALTS

N. Bott[1], J. Flahaut[1], M. Martinot[2], G. Ito[1]
[1] *CRPG, CNRS/ Université de Lorraine, 54500 Vandœuvre-lès-Nancy, France* (*nicolas.Bott@obspm.fr*)
[2] *LGL, TPE, CNRS/ Université de Lyon, 69622 Villeurbanne Cedex, France*

KEYWORDS:
Moon, surface, spectroscopy, mineralogy, volcanism

INTRODUCTION:
One of the Moon's most surprising characteristics is its crustal asymmetry; the farside hemisphere, dominated by ancient highlands and covered with a few mare deposits, has a different volcanic history than the (sampled) nearside [1]. Surface dating of the lunar mare basalts revealed that the volcanism on the Moon lasted between ~3.9–4.0 and ~1.2 Ga, with a peak in the volcanic activity ~3.6-3.8 Ga ago [2]. A recent study further demonstrated that the mineralogy of the nearside mare basalts reveals a late stage volcanism with high titanium content and olivine contribution [3]. More recent spectroscopic analyses focused on the farside's crustal rocks composition (e. g. [4] for South Pole-Aitken [SPA] basin), but no comprehensive study of the farside mare compositions has been conducted up to now.

DATA AND METHODS:
In this work, we used spectroscopic data of the Moon Mineralogy Mapper (M3) onboard Chandrayaan-1 to survey the mineralogy of all mare deposits in the VNIR domain (0.4–3 µm). Each mare unit was mosaicked separately and processed using the method of [5]; an IDL routine automatically computes and removes the continuum of each spectrum, and determines its spectral parameters (e. g. band centers, band areas, band depths, spectral slope). To compare with the mineralogy of the nearside [3], we also mosaicked three selected mare regions, each representative of one spectral unit. Finally, we applied statistics on spectral parameters of interest to survey the variation in mineral signatures and compositions of farside maria.

PRELIMINARY RESULTS:

We found that spectra of mare basalts are dominated by pyroxene signatures (Figure 1). However, some mare units (e. g. Al-Biruni, see Figure 2) showed considerable differences in band characteristics in which cases we computed statistics on each mare subunits.

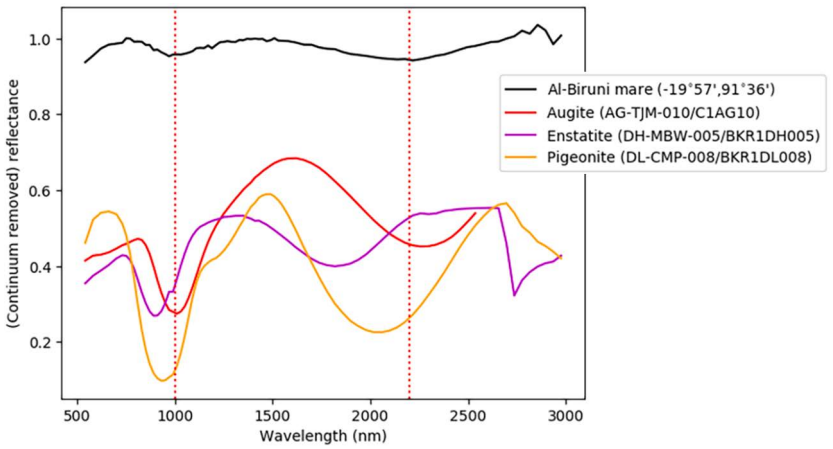

Fig. 1. Continuum removed spectrum of Al-Biruni mare deposit (19° 57', 91° 36') with RELAB reference spectra of augite, enstatite and pigeonite for comparison

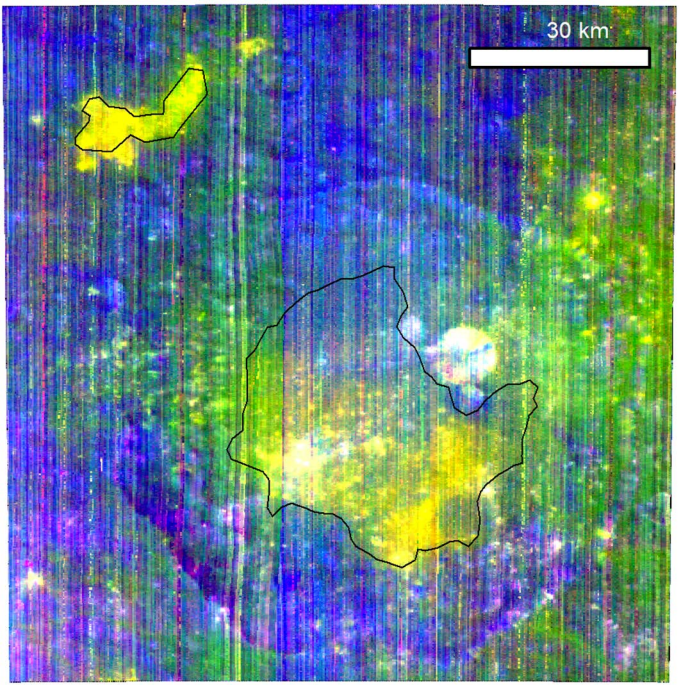

Fig 2. RGB (R = Band Area 1; G = Band Area 2; B = Reflectance at 1489 nm) image of the two Al-Biruni mare deposits (yellow tones)

Major differences were also observed in SPA mare units when they were compared to Mare Australe deposits and other maria outside of the SPA basin (Figure 3).

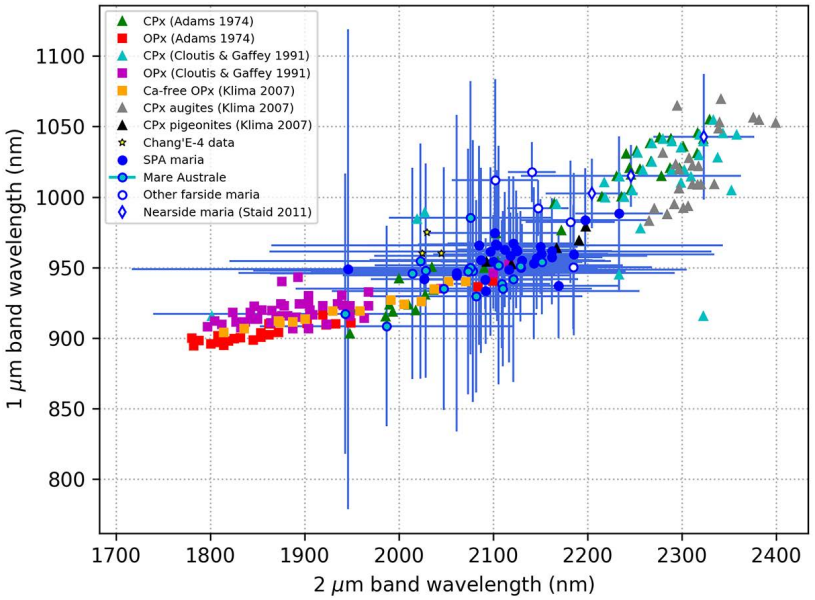

Fig 3. Variations in pyroxene band 1 and band 2 absorptions within the farside maria. Synthetic pyroxenes from [6, 7] and nearside mare units from [3] are shown for comparison

This suggests that different pyroxene compositions within SPA. Moreover, the nearside mare units we defined based on [3] are clearly distinct from all farside mare deposits since they are the richest in clinopyroxenes (see Figure 3).

CONCLUSION AND PERSPECTIVES:
The results we have so far indicate slightly different mineralogies of mare basalts between the nearside and the farside of the Moon and, if confirmed by looking at the other spectral parameters, could mirror its crustal dichotomy. We plan to investigate possible evidence of olivine and possible correlations with age and location, as well as intra-SPA diversity with our spectral parameters set.

ACKNOWLEDGEMENTS:
The authors want to thank Jan Hendrik Pasckert and Harald Hiesinger for having kindly shared with us their shapefiles of SPA mare deposits [8]. Fundings from the CNRS Momentum, LUE Future Leader and CNES APR are much appreciated.

REFERENCES:
[1] Head III J. W., Wilson L. Lunar mare volcanism: Stratigraphy, eruption conditions, and the evolution of secondary crusts // Geochimica et Cosmochimica Acta. 1992. V. 56.
[2] Hiesinger H. et al. Ages of mare basalts on the lunar nearside // J. Geophysical Research. 2000. V. 105.
[3] Staid M. I. et al. The mineralogy of late stage lunar volcanism as observed by the Moon Mineralogy Mapper on Chandrayaan-1 // J. Geophysical Research. 2011. V. 116.
[4] Moriarty D. P., Pieters C. M. The Character of South Pole-Aitken Basin: Patterns of Surface and Subsurface Composition // J. Geophysical Research. 2018. V. 123.
[5] Martinot M. et al. Mineralogical Diversity and Geology of Humboldt Crater Derived Using Moon Mineralogy Mapper Data // J. Geophysical Research. 2018. V. 123.
[6] Klima R. L. et al. Spectroscopy of synthetic Mg-Fe pyroxenes I: Spin-allowed and spin-forbidden crystal field bands in the visible and near-infrared // Meteoritics and Planetary Science. 2007. V. 42.
[7] Adams J. B. Visible and near-infrared diffuse reflectance spectra of pyroxenes as applied to remote sensing of solid objects in the solar system // J. Geophysical Research. 1974. V. 79.
[8] Pasckert J. H., Hiesinger H., Van der Bogert C. H. Lunar farside volcanism in and around the South Pole-Aitken basin // Icarus. 2018. V. 299.

YOUNG MARE BASALTS IN THE CHANG'E-5 LANDING REGION, NORTHERN OCEANUS PROCELLARUM

Y. Qian[1,2], L. Xiao[1], J. W. Head[2], H. Hiesinger[3], C. van der Bogert[3], L. Wilson[4]
[1] *School of Earth Sciences, China University of Geosciences, Wuhan, China (yuqi_qian@cug.edu.cn)*
[2] *Departmental of Earth, Environmental, and Planetary Sciences, Brown University, Providence, USA*
[3] *Institut für Planetologie, Westfälische Wilhelms-Universität Münster, Münster, Germany*
[4] *Lancaster Environment Centre, Lancaster University, Lancaster, UK*

KEYWORDS:
Chang'e-5, Moon, Lunar Landing Site, Young Mare Basalts, Chronology

INTRODUCTION:
Chang'e-5 (CE-5) is China's first lunar sample return mission. Northern Oceanus Procellarum has been selected as the landing region (41–45° N, 49–69° W, Figure 1). CE-5 scheduled to launch at the end of 2020, and plans to collect ~2 kg of lunar samples [1]. The CE-5 landing region is in the northwest of Procellarum KREEP Terrain (PKT) [2] on the near side of the Moon. Mons Rümker is a huge volcanic complex in the south of this region, with a diameter of ~70 km. Therefore, this region is also named as "the Rümker region".

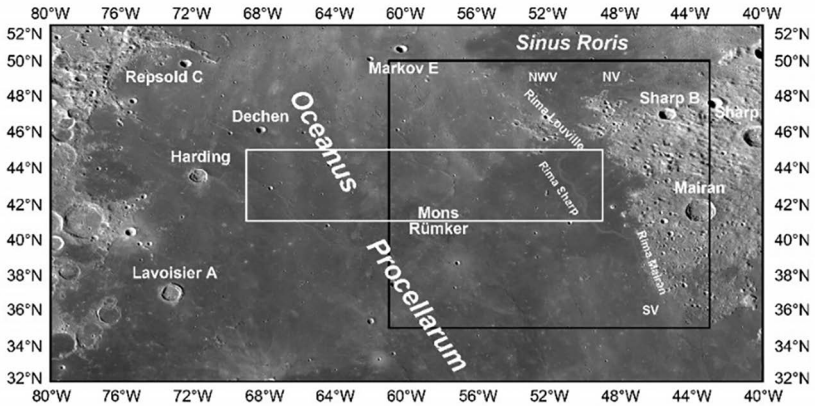

Fig. 1. CE-5 landing region (white box) and the current study area (black box)

Northern Oceanus Procellarum was chosen with some of the youngest mare basalts on the Moon, which have not yet been sampled [1, 3]. [4] described the geological characteristics and scientific significance of the CE-5 landing region in detail, which divided the young mare basalts into Em3 and Em4 (Figure 2). Sampling these young mare basalts could profoundly improve our understandings of lunar mantle properties, impact history, and late thermal history.

A complete understanding of the geological backgrounds of the landing site is crucial to properly interpret the laboratory analysis of the returned samples. Thus, we undertake the present research to study the young mare basalts in the CE-5 landing region. We focus on Em4 in this research.

GEOMORPHOLOGY:
Em4 is a large lava plain, covering an area of ~37 000 km^2. Em4 has a mean elevation of –2530 m and a mean slope of 0.9° (baseline length, ~180 m). The elevation is controlled by the occurrence of wrinkle ridges, which may reflect the underlying features [5]. Kipukas and Mairan domes (silica-rich) are embayed by these young basalts.

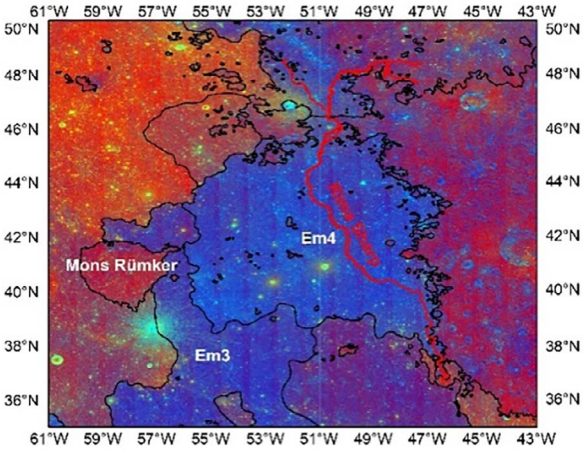

Fig. 2. Kaguya MI color composite map of young mare units (Em3, Em4) in the CE-5 landing region

Rima Sharp extends across the area, and three source vents closely associated with the rille are identified. Rima Sharp is described as the longest sinuous rille on the Moon [6]. [6] interpreted Rima Sharp originates from the north and the main branch length is 566 km. We find evidence that Rima Sharp is composed of two independent sinuous rilles; their channels are combined by rille capture.

COMPOSITION:

Em4 is a kind of special mare basalts on the Moon, with high TiO_2 (6 wt. %, mean content) and FeO (1 wt. %, mean content). The Modified Gaussian Model has been used to quantify the mineral abundance using Moon Mineralogy Mapper OP2C data. The Em4 basalts are richest in CPX (47 wt. %), followed by OPX (32 wt. %) and OLV (21 wt. %), assuming CPX + OPX + OLV = 100 wt. %. The Em4 mare basalts, one of the Erasthenian-aged basalts in PKT, is not as rich in olivine as previous think [7].

STRATIGRAPHY:

Em4 is the youngest unit in the region. It covers all preexisting units, including Em3, and Imbrian-aged low-Ti mare basalts; and embays preexisting hills, domes, and crater rims. Large craters can penetrate through the overlaying Em4 basalts and excavate low-Ti basalts. Based on the crater excavation technique [8], the average thickness of Em4 is estimated to be 39 ~63 m. Furthermore, its total volume is constrained between 1450 ~2350 km^3. This value is within the value (30–60 m) set by CSFD measurements of the single flow unit in PKT [9].

A systematic chronology study of Em4 has been accomplished and compared with other studies [3, 10–11]. The Em4 young mare basalts have an average age of 1.46 Ga. Crater dating results reveal some age variations. The locations of possible youngest basalts have been determined.

MAGMA SOURCE:

The source vents or fissures of Em4 basalts are not exposed. We are investigating three possible options [11]: 1) eruption occurred through a dike(s), with the source vent buried by later erupting parts of the flow unit; 2) eruption occurred through sinuous rilles; 3) The young flow unit is composed of more than one flow, sourced from different vents. We are currently utilizing all the datasets available to constrain the magma sources, which is significant to the sample analysis.

REFERENCES:

[1] Li C., Wang C., Wei Y., Lin Y. China's present and future lunar exploration program // Science. 2019. V. 365. P. 238–239.
[2] Jolliff B. L., Gillis J. J., Haskin L. A. et al. Major lunar crustal terranes: Surface expressions and crust-mantle origins // J. Geophysical Research: Planets. 2000. V. 105. P. 4197–4216.

[3] Hiesinger H., Head J. W., Wolf U. et al. Ages and stratigraphy of lunar mare basalts: A synthesis // Special Paper of the Geological Society of America. 2011. V. 477. P. 1–51.
[4] Qian Y. Q., Xiao L., Zhao S. Y. et al. Geology and Scientific Significance of the Rümker Region in Northern Oceanus Procellarum: China's Chang'E-5 Landing Region // J. Geophysical Research: Planets. V. 123. P. 1407–1430.
[5] Sharpton V. L., Head J. W. Lunar mare ridges: Analysis of ridge-crater intersections and implications for the tectonic origin of mare ridges // 18th Lunar and Planetary Science Conference. Houston, TX, Mar. 16–20 1987: Proc. 1988. V. 18. P. 307–317. P. 307–317.
[6] Hurwitz D. M., Head J. W., Hiesinger H. Lunar sinuous rilles: Distribution, characteristics, and implications for their origin // Planetary and Space Science. 2013. V. 79–80. P. 1–38.
[7] Staid M. I., Pieters C. M., Besse S. et al. The mineralogy of late stage lunar volcanism as observed by the Moon Mineralogy Mapper on Chandrayaan-1 // J. Geophysical Research: Planets. 2011. V. 116. Art. E00G10. 16 p.
[8] Budney C. J., Lucey P. G. Basalt thickness in Mare Humorum: The crater excavation method // J. Geophysical Research: Planets. 1998. V. 103. P. 16855–16870.
[9] Hiesinger H, Head J. W., Wolf U. et al. Lunar mare basalt flow units: Thicknesses determined from crater size-frequency distributions // Geophysical Research Letters. V. 29. P. 84–89.
[10] Wu B., Huang J., Li Y. et al. 2018. Rock Abundance and Crater Density in the Candidate Chang'E-5 Landing Region on the Moon // J. Geophysical Research: Planets. V. 123. P. 3256–3272.
[11] Jia M., Yue Z., Di K. et al. A catalogue of impact craters larger than 200 m and surface age analysis in the Chang'e-5 landing area // Earth and Planetary Science Letters. 2020. V. 541. Art. 116272.
[12] Head J. W., Wilson L. Generation, ascent and eruption of magma on the Moon: New insights into source depths, magma supply, intrusions and effusive/explosive eruptions (Part 2: Predicted emplacement processes and observations) // Icarus. 2017. V. 283. P. 176–223.

THE ORIGIN OF THE LUNAR PROCELLARUM KREEP TERRANE (PKT): STRATIGRAPHIC EVIDENCE AND IMPLICATIONS FOR LUNAR GEOLOGICAL AND THERMAL EVOLUTION

J. Zhang[1,2], J. W. Head[2], J. Liu[1], R. W. K. Potter[2,3]
[1] *Center for Lunar and Planetary Science, Institute of Geochemistry, Chinese Academy of Sciences, Guiyang 550081, China (zhangjiangyi@mail.gyig.ac.cn)*
[2] *Department of Earth, Environmental and Planetary Sciences, Brown University, Providence, RI 02912 USA*
[3] *Clarivate Analytics, London, UK*

KEYWORDS:
KREEP, Procellarum KREEP terrane, thorium, SPA basin

INTRODUCTION:
Most lunar evolution models predict that fractional crystallization of a lunar magma ocean will produce a layer of melt enriched in incompatible elements such as K, REE, and P (i. e., KREEP) [1]. Some workers [2] have proposed that the surficial distribution of Th, which has been measured on a global-scale [3–5], can be used as a proxy for determining the global distribution of KREEP. The Th and FeO distributions are also used to divide the lunar surface into three main Terranes: Procellarum KREEP (PKT), Feldspathic Highland (FHT) and South Pole-Aitken (SPAT) [2]. Here, we use the boundary of PKT in [6].

There are obvious high-Th abundance locations in the PKT, but almost none in FHT, and only medium-Th concentrations in parts of SPAT (Figure 1). The lateral extent and distribution of the residual magma ocean "KREEP" layer is currently a matter of debate. On the basis of the asymmetry of the Th distribution, some workers suggested that the Procellarum region is the oldest lunar impact basin, the formation of which may have caused the accumulation of KREEP-rich residual liquid on the nearside; in contrast, the lunar farside generally lacks the same high abundances of Th and other KREEPy elements [7, 8]. Other mechanisms have been proposed to explain the asymmetry of KREEP materials, including inhomogeneous differentiation of the magma ocean [9], and antipodal effects of impact [10].

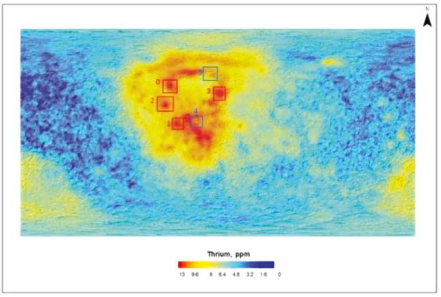

Fig. 1. Thorium abundance from Lunar Prospector gamma-ray spectrometer overlain on LOLA hillshade map. Red and blue square boxes show high-Th and low-Th concentrations, respectively. 0 is crater Mairan; 1 —Kepler; 2 — Aristarchus; 3 — Aristillus; 4 — Copernicus; 5 — Plato

In this analysis, we use impact craters and basins superposed on the ancient lunar crust to document the 3-D (lateral and vertical) extent of Th in PKT and SPA in order to establish the geometry and potential evolution of the KREEP layer. We use the relations between transient cavity depth or diameter and crater excavation depth given by Potter [11] and Melosh [12] to obtain sampling depth data. We then assess the three-dimensional geometry of Th concentrations in the PKT and compare the relations between PKT and SPA as a basis for a hypothesis to explain Th distribution and characteristics.

DATA:
We use a synthesis of data from remote sensing, geomorphologic mapping, and comparative analysis. Thorium abundance from the Lunar Prospector mission [13] are merged with an altimetric shaded relief map [14] and crater depth/diameter from the LPI Lunar Impact Crater Database [19].

RESULTS:
The Th abundance map shows that the high-Th areas are 1) mainly related to Imbrium ejecta (Fra Mauro Formation-FMF) and/or post-Imbrium KREEP volcanism/impact melt in the PKT, and 2) concentrated at the location of young impact craters in mare and highlands regions (Figures 1, 2) [15]. We studied several such craters located on highlands and mare regions (see Figure 1; Table 1), including Mairan, Kepler, Aristarchus, Aristillus, Copernicus and Plato. In particular, the high-Th concentration regions are near Mairan, Kepler, Aristarchus, and Aristillus. However, not all craters on Imbrium ejecta show high-Th concentrations. Copernicus and Plato, which are located on the FMF and the Imbrium rim respectively, show relatively low Th values, suggesting that the high-Th terrain does not occur directly below the surficial FMF in these areas.

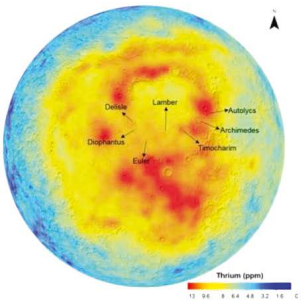

Figure 2. Craters analyzed within Imbrium

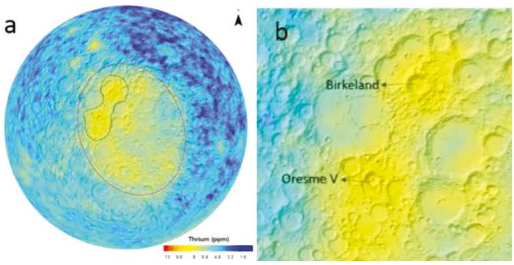

Figure 3. Thorium abundance from Lunar Prospector gamma-ray spectrometer overlay the LOLA hillshade map: (a) — Red dashed oval represents approximate contour of SPA which shows relatively higher Th concentration than the around FHT. Green dashed polygon represents the highest Th value region in SPA, centered on two impact craters; (b) — Birkeland and Oresme V crater in SPA with peak Th abundances

Table 1. Craters studied

Name	Diameter (km)	Apparent depth (km)	Trainsent crater depth(km)	Excavation depth (km)
Diophantus	17.57	2.801	5.72	1.91
Delisle	24.83	1.897	7.67	2.56
Euler	26.03	1.924	7.99	2.66
Kepler	**31**	**1.999**	**8.88**	**2.96**
Lambert	30.12	2.012	9.04	3.01
Timocharis	**34.14**	**2.09**	**10.06**	**3.53**
Autolycus	**38.8**	**2.174**	**11.23**	**3.74**
Aristarchus	**42**	**2.193**	**11.51**	**3.84**
Mairan	**34.49**	**2.184**	**11.83**	**3.94**
Aristillus	**54.37**	**2.407**	**14.94**	**4.98**
Archimedes	81.04	2.798	20.97	6.99
Copernicus	96	2.846	24.24	8.08
Plato	100.68	2.859	25.22	8.41

* Craters highlighted in **red** represent high-Th craters in PKT.

Craters within Mare Imbrium generally show lower Th abundance than those on the highlands (suggesting that they are excavating maria, not Th-rich FMF or crust), with two exceptions — Timocharis and Autolycus. These two craters appear to excavate through Th-poor maria and into Th-rich Imbrium basin deposits (FMF etc., Table 1). A second concentration of Th is within Mare Ingenii in SPA (Figure 3a). This concentration shows peaks at two impact craters, Brikeland (81.4 km diameter) and Oresme V (56.1 km diameter) (Figure 3b) [20].

DISCUSSION:

There exists a higher Th abundance in PKT than its surrounding areas, which suggests that KREEP materials are mainly concentrated in the subsurface of the PKT [2, 6, 16, 17], perhaps throughout the crust. In the PKT, combining these high-Th craters and their excavation depths (Table 1), we found that craters on the highlands (mostly FMF) show the highest Th abundances, except Copernicus and Plato, the excavation depths of which are deeper than other high-Th locations. We thus interpret the Th concentration to have been excavated by the Imbrium impact and distributed only onto the very shallow surface of the highlands (FMF) and thus much less abundant at deeper depth. There are two craters that show relatively high Th abundance in Imbrium (see Figure 2). The high-Th values of Aristillus impact ejecta (Autolycus values may due to Aristillus ejecta) and Timocharis crater ejecta, both located in the maria, show high Th even though the mare is many hundreds of meters thick. We therefore suggest that both penetrated through the mare basalts of the Imbrium basin and excavated underlying Th-rich material. This lends support to the model of the Th rich material being concentrated primarily in Imbrium basin ejecta deposits and related impact melt and KREEP volcanism, independent of the lunar mare fill. In SPA, observed Th anomalies occur on the central, more mafic floor of the basin (see Figure 3) suggesting that their formation is related to basin formation and is likely indigenous [18, 20].

INTERPRETATION:

Based on these stratigraphic and geometric relationships, we interpret the high Th distribution in PKT and SPA to be related to sequential oblique and near-vertical impacts. First, an oblique impact formed a Procellarum basin, removing much of the upper and middle crust in the area and bringing the residual KREEP-rich layer close to the surface. This was followed by formation of the SPA basin by oblique impact [10, 18], similarly removing much of the upper and middle crust and exposing the KREEP-rich lower crust covered by SPA impact melt. Subsequently, the more-vertical, but still oblique, Imbrium impact penetrated into the shallow KREEP layer, brought closer to the surface by the Procellarum impact, ejecting it to form the FMF and related Th-rich ejecta and impact melt deposits. Later mare volcanism buried the KREEP-rich deposits under hundreds of m to km of lava. In the SPA basin, similar vertical impacts Brikeland and Oresme V excavated Th-rich material from below the melt sheet to create the locally high Th anomalies. In summary, this interpretive scenario attributes the origin of the PKT and SPA Th anomalies to sequential impact processes, requiring no additional processes to concentrate KREEP in the SPA or PKT terrain at depth, in agreement with [21]. Analysis of the young Procellarum mare basalt samples [22] to be returned by Chang'E 5 will provide a test of this hypothesis.

ACKNOWLEDGEMENTS:

This work was supported by the National Natural Science Foundation of China (Grant No. 41773065 and 41941003).

REFERENCES:

[1] Warren & Wasson (1979) RGSP 17, 73.
[2] Jolliff et al. (2000) JGR 105, 4197.
[3] Lawrence et al. (1998) Science 281, 1484.
[4] Lawrence et al. (2003) JGR 108, 5102.
[5] Lawrence et al. (2007) GRL L03201.
[6] Haskin et al. (2000) JGR 205.
[7] Warren & Kallemeyn (1998) LPI 6048.
[8] Zhu et al. (2019) JGR 124, 2117.
[9] Loper et al. (2002) JGR 107, 5046.

[10] Schultz et al. (2011) GSA SP 477.
[11] Potter et al. (2015) GSA SP 518, 99.
[12] Melosh (1989) 74.
[13] Binder (1998) Science 281. 5382.
[14] Smith et al. (2010) Space Sci Rev, 150, 209.
[15] Lawrence et al. (2000) JGR 105, 20307.
[16] Wieczorek et al. (2000) JGR 105, 20417.
[17] Haskin (1998) JGR 103, 1679.
[18] Garrick-Bethell et al. (2005) GRL 32, L13203.
[19] http://www.lpi.usra.edu/lunar/surface/.
[20] Moriarty et al. (2019) LPSC 50, #2874.
[21] Evans (2019) LPSC 50 #2733.
[22] Qian et al. (2018) JGR 123, 1407.

WHY GO FORWARD TO THE MOON? BECAUSE IT IS AN INTEGRAL PART OF THE EARTH — MOON SYSTEM

C. M. Pieters[1], J. W. Head[1], C. R. Neal[2]
[1] *Dept. Earth, Environmental, and Planetary Sciences, Brown University, Providence, RI 02912 USA* (*Carle_Pieters@brown.edu*)
[2] *University of Notre Dame, Notre Dame, IN 46556 USA*

KEYWORDS:
Earth-Moon environment, transformative science, international cooperation, commercial interests, long-term planning

INTRODUCTION:
Space exploration (with both humans and robots) continues to inspire the world while simultaneously expanding technology and strengthening the global economy that is increasingly technology linked. Goals and achievements have evolved considerably from the historic accomplishments of Luna and Apollo, and over the last 50 years exploration of destinations across the entire Solar System have been achieved at least at a reconnaissance level. Space-based technology has now become essential to (and dramatically enhances) life on planet Earth. The expanding international space-faring community is poised to actively participate in a long-term Earth-Moon venture during the next 50 years.

FORWARD TO THE MOON:
There are several fundamental reasons why the Moon is central to long-term space exploration activities:

Science. The Moon presents a window into the history of early Earth-Moon environment. We now recognize the intimate co-evolution of these two planetary bodies over the last 4.5 Ga. The early history of Earth is lost, but discoveries from the Moon yet to be made (timing of Solar System events, water, constraints on the origin of life) are transformative in nature [1].

International Cooperation. The pervasively international nature of space exploration provides unparalleled opportunities for building trust and partnerships with allies as well as creating new alliances around the world.

Opportunities in the Earth-Moon Environment. As space-faring nations progress beyond low-Earth orbit, the Moon is a most accessible stable planetary platform. It is often viewed as the 8th continent of Earth with as yet unknown resources for the future, encouraging growth of a commercial space sector into the future.

Rational Progression During the Next 50 Years. The next steps for human exploration begin with the Moon by establishing systems, technology, and experience essential for sustaining humans on a planetary body that is accessible and close to home, enabling a safe expansion of the horizon to Mars and beyond.

REFERENCES:
[1] Pieters C. M., Canup R. M., Kring D. A., Head III J. W., Scott D. R. (2018). Transformative Lunar Science, White Paper, 1-8. https://sservi.nasa.gov/wp-content/uploads/2018/02/TransformativeLunarScience.pdf.

GEOLOGICAL EXPLORATION OF THE MOON: STRATEGIES, CONCEPTS, APPROACHES

A. Gusev[1], H. Hanada[2], A. Kosov[3], Zh. Meng[4], J. Ping[5]
[1] *Kazan Federal University*, *Kazan*, *Russia*
[2] *National Astronomical observatory of Japan*, *Oshu*, *Japan*
[3] *Space Research Institute RAS*, *Moscow*, *Russia*
[4] *College of Geoexploration Science and Technology*, *Jilin University*, *Changchun*, *China*
[5] *National Astronomical Observatory of China CAS*, *Beijing*, *China*
(*agusev33@gmail.com*)

KEYWORDS:
Moon, internal structure, surface layer, regolith, water, lunar rare minerals.

INTRODUCTION:
In the new millennium, the successfully implemented lunar projects SMART-1 (2004–2006), Kaguya (2007–2009), Chang'E-1/2, 3/4 (2007–2019+), Chandrayaan (2008–2009), LRO (2009–2019+), GRAIL (2011–2012), LADEE (2013–2014) increased the flow of highly accurate and multi-parameter information from spacecraft and caused an unprecedented a boom of public and professional interest, research enthusiasm and ambitious state plans of the world's leading powers for robotic and geologic exploration of the Moon by 2025yr. Implementation of modern long-term programs of scientific research and industrial exploration of the Moon the SELENE-2, ILOM (JAXA, Japan), Artemis (NASA, USA), Chang'E-4–8 (China), Chandrayaan-2 (India), Luna-25–28 (RCA, Russia) is aimed both at creating long-term lunar bases and geological exploration of the lunar interior, as well as at obtaining a wide range of scientific information about the internal structure, dynamic and topographic shape of the Moon, its internal geological structure, including a multilayer liquid-solid lunar core and regolith [1–3]. With the development of modern manned cosmonautics and the flight cost reduction, the Moon becomes an important and attractive celestial object for creating long-term scientific and experimental bases on its visible side. The lunar base will be a unique place for scientific research in the field of planetology, cosmology, radio astronomy, radiation biology, gravity and human space safety during long-distance flights in the solar system (Mars).

FUNDAMENTAL ISSUES:
What would we like to know about the Moon? Why is the visible and reverse side of the Moon so different in relief, tectonic formations, gravitational, geochemical, mineralogical and magnetic distributions and anomalies? Is there water ice in the polar regions of the Moon and is it possible for it to be developed and used for lunar bases? What is the nature and origin of the largest crater (more than 2500 km in diameter, up to 12 km deep) in the Solar System located at the south pole of the Moon? What are the sizes and geochemical composition of the liquid core, viscoelastic mantle and solid crust of the thin marine and thick continental parts of the Moon? What is the source of the paleomagnetic field of the Moon found in the investigation of lunar samples? What is the future of the Moon-Earth system?

STRATEGIES:
1. **ESA** strategy for science at the Moon [4]: 1. Analysis of new and diverse samples from the Moon; 2. Detection and characterization of polar water ice and other lunar volatiles; 3. Deployment of geophysical instruments and the build up a global geophysical network; 4. Identification and characterization of potential resources for future exploration; 5. Deployment long wavelength radio astronomy receivers on the lunar far side; 6. Characterisation of the dynamic dust, charge and plasma environment; 7. Characterisation of biological sensitivity to the lunar environment.
2. **ESA** space resources strategy [9]: The utilization of space resources for exploration may be within reach for the first time; made possible by recent advances in our knowledge and understanding of the Moon and asteroids,

increased international and private sector engagement in space activities and the emergence of new technologies. Key sectors of interest include mining, metallurgy, materials, energy, robotics and autonomy. The first utilization of space resources will be on the Moon; a source of water, oxygen, metals and other materials.

CONCEPTS:

1. The study of the surface of the Moon, whether it be a robot, a human or a human robot, is based on educational practices that can be tested lunar analogs on Earth [5]. Teaching the basics of geoscience and the use of specialized geophysical equipment has been successful for NASA's Apollon program. The recent expansion of the ESA PANGEA-X cosmonaut training campaign made it possible to use and verify several geological and geophysical experiments and protocols on the volcanic lunar analog territories of Lanzarote, as well as their integration. The concept of augmented field geology and geophysics for planetary analogs (AGPA) [6] includes a flexible set of experiments - the practices deployed during the ESA PANGEA-X field campaign. Activities performed included remote sensing (stereo grammetry, LIDAR) and geophysical (geoelectrics, active and passive seismic) studies. The goal of the AGPA is to integrate the collection of training data and analogue field geology procedures with *in-situ* geophysical methods and remote sensing to maximize and increase the impact of science and work efficiency both at the stages of data analysis and at the planning stage for exploration.

2. **Space resources** [9] will be a major topic of activity internationally over the next decade and may become a major motivation for investments in space exploration in the future. Europe has extensive expertise and capabilities to bring to this new field of investigation, from both space and Earth industries. Europe needs to engage now in order to have a role, to influence the way forward and benefit from the endeavor. This will require a multidisciplinary approach; bringing together space and non-space, science and industry, public and private. The resources of space are vast and their potential enormous. Realizing their potential will require innovation and invention, initiative and risk taking, vision and careful planning, but equally a common understanding on the applicable international legal framework.

Approaches: 1. This new lunar space technology [7] shows the fluorination process *in-situ* for the production of oxygen and silicon from 1 kg lunar regolith can be produced 0.21 kg of silicon and 0.32 kg of oxygen with a total cooling load of 17 MJ/kg regolith and an electric load of 29 MJ/kg regolith. **2.** Water ice has been detected at the lunar poles, but existing and near-future orbital datasets do not have the capabilities to determine its horizontal and vertical distribution at meter to hundred-meter scales relevant for mining operations. **Highlights:** Geologic system model [8] describes lunar ice deposits as potential economic resources. Ice Favorability Index maps developed based on ice sources, capture, and retention. 3D cratering simulations show ice mixed into regolith column by gardening. Ice should not end up in concentrated subsurface orebodies. **3.** Key products for exploration are propellant, water, oxygen, consumables for life support and materials including metals. Propellants can be manufactured from locally sourced water (e. g. in ice at the lunar poles), hydrogen and oxygen from water and lunar minerals. Building materials can be produced from the dust, soil (regolith) and rocks found on planetary surfaces. Metals and materials can be produced from the metal oxides and silicates found in local rocks.

Final remarks [4, 9]: Activities implemented during the period 2020–2030 should deliver as a minimum the below listed outcomes to address the above priorities. These outcomes are to be achieved utilizing European instrumentation, ideally as part of internationally coordinated activities accompanied by new orbital data to optimize the overall science return.

- New lunar samples returned from a minimum of two unexplored locations with subsequent analysis in European laboratories.
- *In-situ* measurements conducted on polar water ice and other polar volatiles.

- A suite of measurements obtained from at least one geophysical package, ideally as part of a global lunar network.
- Geochemical, mineralogical, and geophysical measurements conducted on a non-polar resource deposit.
- *In-situ* measurement attained of the dust, plasma and exosphere environment at the lunar surface.
- At least one new laser retroreflector and radio/light beacons deployed at the lunar surface.
- Measurement of the impact of the lunar surface environment on a representative biological model.

REFERENCES:

[1] Gusev A., Hanada H., Petrova N., Kosov A., Kuskov O., Kronrod V., Kronrod E., Rotation, physical librations and interior structure of the active and multi-layer Moon: Monograph. Kazan: Kazan University Publishing Co., 2015 328 p. (Russian + English)
[2] Hanada H., Gusev A. et al. Development of a Small Telescope like PZT and Results of Experiments on the Ground // Gyroscopy and Navigation. 2017. V. 8(4). Iss. 4. P. 304–319.
[3] Li J., Meng Z., Gusev A. Recent Advances in Lunar Exploration Using Radar and Microwave Techniques // Advances in Astronomy. 2019. Special Issue. Art. id. 4794258.
[4] https://exploration.esa.int/web/moon/-/61371-esa-strategy-for-science-at-the-moon.
[5] Analogs for Planetary Exploration / eds. Garry W., Bleacher J. No. 483 in GSA Special Paper. The Geological Society of America, Boulder, USA, 2011. 567 p.
[6] AGPA Team: http://www.agpa-project.eu accessed January 2018
[7] Turan E. M. et al. A flow sheet for the conversion of lunar regolith using fluorine gas // Advances in Space Research. 2020. V. 65. Iss. 7. P. 1852–1862.
[8] Cannon K. M., Britt D. T. A geologic model for lunar ice deposits at mining scales // Icarus. 2020. V. 347. https://doi.org/10.1016/j.icarus.2020.113778.
[9] https://exploration.esa.int/web/moon/-/61369-esa-space-resources-strategy.

CALCULATION OF INTERNAL STRUCTURE AND PHYSICAL PROPERTIES OF THE LOWERMOST LUNAR MANTLE FROM GEOPHYSICAL AND GEOCHEMICAL DATA

E. V. Kronrod[1], K. Matsumoto[2], O. L. Kuskov[1], V. A. Kronrod[1]
[1] *Vernadsky Institute of Geochemistry and Analytical Chemistry RAS, Moscow* (*e.kronrod@gmail.com*)
[2] *RISE Project, National Astronomical Observatory of Japan*

KEYWORDS:
Moon, numerical simulation, inversion, internal structure, seismic, thermodynamic properties, low velocity zone.

INTRODUCTION:
Studying the internal structure of the lunar interior is important for understanding of its thermal regime, the history of the lunar dynamo, the origin and evolution of the Moon. A special issue is the study of the lunar core and the layer at the boundary between the solid mantle and the liquid or partially molten core (low-velocity/low-viscosity zone — LVZ).

The evidence of existence of a partially molten layer follows from seismic [1, 2] and selenodetic [3, 4] data. The existence of LVZ is consistent with the moment of inertia, tidal Love number, and quality factor Q [5–7], although models without LVZ are also possible [8].

In this study using Markov chain Monte Carlo method (MCMC) for inversion of selenodetic and seismic data together with thermodynamic approach we constructed internal structure models including LVZ properties. Distinctive feature of these models is that they are consistent with geochemical and geophysical constraints.

THE MODEL AND APPROACH:
We consider a viscoelastic spherically symmetric model of the Moon with nine layers (megaregolith, crust, four-layer mantle, LVZ, outer liquid core, and solid inner core). Seismic and selenodetic information was used as observed data (seismic travel times, mean radius (R), mass (M), normalized moment of inertia (MOI), second-order Love numbers (k_2), and monthly Q_m and annual Q_a quality factors). We also used geochemical constraints on the composition and properties of the crust, mantle, and core. Bulk Al_2O_3 and FeO concentrations are included as observed data as well. For inversion we used Markov chain Monte Carlo method. Thermodynamic modeling of phase relations and physical properties in the multicomponent mineral system CFMAS was used for mantle physical properties calculation [9]. Properties of LVZ (thickness, seismic velocities, viscosity) were obtained during the calculations.

RESULTS AND DISCUSSION:

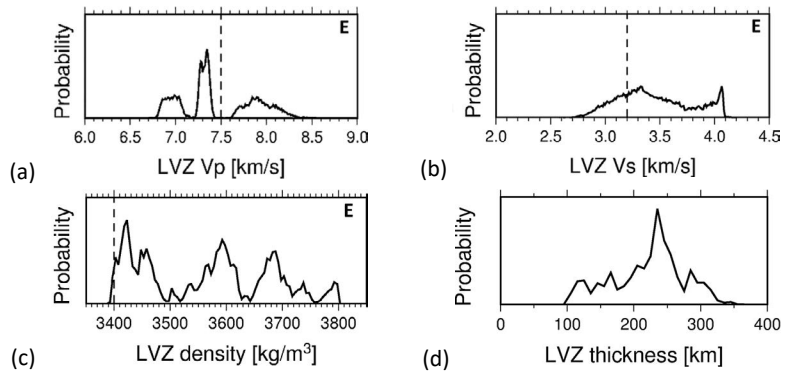

Fig. 1. Inversion results for LVZ *P*-, *S*-wave velocities (a, b), density (c) and thickness (d) for geochemical models E. Dashed vertical lines indicate values from [2]

The calculations were performed for two types of geochemical models of the lunar composition: 1 — with bulk Al_2O_3 content close to Earth's value (model E), 2 — bulk Al_2O_3 concentration higher than 4,5 wt % (model M) [2]. For model E bulk Al_2O_3 = 4,05±0,36 wt % and for model M bulk Al_2O_3 = 5,91±0,39 wt %. Bulk FeO = 12,25±1,33 wt % for both geochemical models. To obtain internal structure models consistent with geochemical constraints we used seismic travel times (TT) dataset from [10] with errors in TT increased three times [11]. The resulting LVZ parameters for model E and model M are shown in Figure 1 and Figure 2.

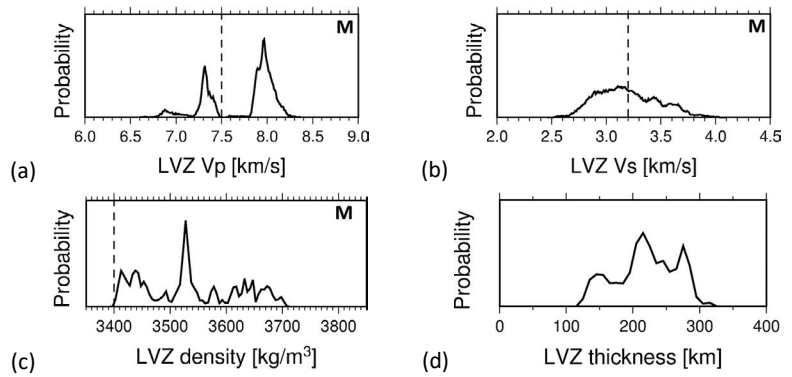

Fig. 2. Inversion results for LVZ P-, S-wave velocities (a, b), density (c) and thickness (d) for geochemical models M. Dashed vertical lines indicate values from [2]

For both types of geochemical models (E and M) we have obtained quite similar results. Differences in mantle composition and density have little effect on the LVZ parameters. For both types sof models calculated seismic velocities are in the range of 7.3–8 km/s for V_P and 3–3.5 km/s for V_S, and are in good agreement with [2] and [5]. LVZ density is 3450 kg/m^3 — higher those from [2] and [7]. The LVZ thickness is in the range of 100–300 km with the most probable values of 240–250 km for model E and 200–300 km for model M.

ACKNOWLEDGEMENTS:
The work was performed as part of the state assignment of Vernadsky Institute of Geochemistry and Analytical Chemistry No. 0137-2020-0004 with partial financial support from JSPS KAKENHI grant 17K05643, RFBR grant under project No. 18-05-00225 and program No. 17 of the Presidium of the Russian Academy of Sciences.

REFERENCES:

[1] Garcia R. F., Gagnepain-Beyneix J., Chevrot S., Lognonné P. Very preliminary reference Moon model // Physics of the Earth and Planetary Interiors. 2011. V. 188. P. 96–113.
[2] Weber R. C., Lin P., Garnero E. J., Williams Q., Lognonné P. Seismic detection of the lunar core // Science. 2011. V. 331. P. 309–312. doi:10.1126/science.1199375.
[3] Williams J. G., Konopliv A. S., Boggs D. H., Park R. S., Yuan D-N., Lemoine F. G., Goossens S., Mazarico E., Nimmo F., Weber R. C., Asmar S. W., Melosh H. J., Neumann G. A., Phillips R. J., Smith D. E., Solomon S. C., Watkins M. M., Wieczorek M. A., Andrews-Hanna J. C., Head J. W., Kiefe W. S., Matsuyama I., McGovern P. J., Taylo G. J., Zuber M. T. Lunar interior properties from the GRAIL mission // J. Geophysical Research: Planets. 2014. V. 119 No. 7. P. 1546–1578. doi:10.1002/2013JE004559.
[4] Konopliv A. S., Park R. S., Yuan D., Asmar S. W., Watkins M. M., Williams J. G., Fahnestock E., Kruizinga G., Paik M., Strekalov D., Harvey N., Smith D. E., Zuber M. T. The JPL lunar gravity field to spherical harmonic degree 660 from the GRAIL Primary Mission // J. Geophysical Research. 2013. V. 118. P. 1415–1434. doi:10.1002/jgre.20097.
[5] Matsumoto K., Yamada R., Kikuchi F., Kamata S., Ishihara Y., Iwata T., Hanada H., Sasaki S. Internal structure of the Moon inferred from Apollo seismic data and selenodetic data from GRAIL and LLR // Geophysical Research Letters. 2015. V. 42. No. 18. P. 7351–7358. doi:10.1002/2015GL065335.

[6] Harada Y., Goossens S., Matsumoto K., Yan J., Ping J., Noda H., Haruyama J. Strong tidal heating in an ultralow-viscosity zone at the core-mantle boundary of the Moon // Nature Geoscience. 2014 V. 7. P. 569–572. doi:10.1038/NGEO2211.
[7] Khan A., Connolly J. A. D., Maclennan J., Mosegaard K. Joint inversion of seismic and gravity data for lunar composition and thermal state // Geophysical J. International. 2007. V. 168. P. 243–258.
[8] Matsuyama I., Nimmo F., Keane J. T., Chan N. H., Taylor G. J., Wieczorek M. A., Kiefer W. S., Williams J. G. GRAIL, LLR, and LOLA constraints on the interior structure of the Moon. // Geophysical Research Letters. 2016. V. 43. P. 8365–8375. doi:10.1002/2016GL069952.
[9] Kuskov O. L., Kronrod E. V., Kronrod V. A. Thermo-chemical constraints on the lunar bulk composition and the structure of a three-layer mantle // Physics of the Earth and Planetary Interiors. 2019. V. 286. P. 1–12. https://doi.org/10.1016/j.pepi.2018.10.011
[10] Lognonné P., Gagnepain-Beyneix J., Chenet H. A new seismic model of the Moon: implications for structure, thermal evolution and formation of the Moon // Earth and Planetary Science Letters. 2003. V. 211. P. 27–44.
[11] Kronrod E. V., Matsumoto K., Kuskov O. L., Kronrod V. A., Yamada R., Kamata S. Adjustment of geophysical and geochemical models of the Moon // 49th Lunar and Planetary Science Conf. 2018. LPI Contrib. No. 2083. 1667.pdf.

CHRONOLOGY OF VOLCANISM IN THE MOSCOVIENSE BASIN

J. Chu [1], M. A. Ivanov[2], A. M. Nikishin[1]
[1] *Lomonosov Moscow State University*, *Faculty of Geology*, *Moscow*, *Russia* (*vladimirchujun@yandex.ru*)
[2] *Vernadsky Institute of Geochemistry and Analytical Chemistry*, *Russian Academy of Science*, *Moscow*, *Russia* (*mikhail_Ivanov@brown.edu*)

KEYWORDS:
Impact basin, crater size-frequency distribution, absolute model age, volcanism, concentration

INTRODUCTION:
Moscoviense basin is one of fewer impact basins with lava filling on the far side of the Moon and located within the area of the thickest crust [1]. Yet, the floor of the basin itself is considered as a region with the thinnest crust on the Moon [2]. This strong contrast may imply that the style of lava filling in Moscoviense probably differs from the other basins on the Moon and efforts of many researchers have been focused on the Moscoviense basin. Based on the spectral data combined with the crater size-frequency distributions (CSFD) measurements, the floor of basin was divided into at least three units indicating three episodes of volcanism: (1) ancient mare unit with the lowest Ti content and the absolute model age (AMA) of 3.9 Ga (Im), located in the southern part of basin [3]; (2) low-Ti basalt mare unit with the AMA of ~3.5–3.7 Ga in the western part of the basin (IItm) [3, 4]; (3) the youngest hight-Ti basalt mare unit in the eastern part of the basin with the AMA ~2.6 Ga (Ehtm) [5]. In our study, we performed a photogeological analysis of the basin floor to outline specific morphological units that represent distinct geological bodies corresponding to different phases of volcanic activity. When the units have been defined and mapped, we performed the CSFD measurements in order to determine the AMAs of the volcanic phases in the Moscoviense basin [6].

DATA AND METHODS:
We used the Wide-Angle Camera (WAC) images from LRO spacecraft to perform both the photogeological analysis of the surface and the CSFD measurements within defined units [7]. The SELENE (Kaguya) images were used to distinguish ejecta from craters of different ages and identify chains and clusters of secondary craters [8]. We have applied the Clementine data to characterize the units by their model concentrations of FeO and TiO_2 [9]. The compositional characteristics of volcanic units of different ages allow tracing of the compositional evolution of volcanism within mare Moscoviense.

RESULTS:
Photogeological analysis
We divided the floor of the Moscoviense basin into two type of units according to their surface characteristics: albedo, apparent roughness, and visible abundance of impact craters.

(1) *Cratered floor unit*, distinguished by rough, strongly cratered surface. This unit is exposed in the southern and central parts of the floor and near its northern and eastern edges. (2) *Complex of plains*, defined by a smooth surface with both less frequent and smaller impact craters compared with the cratered floor units. The complex of plains further subdivided into *dark* and *light plains* by the albedo variations.

The geological map of the floor of the Moscoviense basin is shown in Figure 1.

AMAs of the Moscoviense basin and individual floor units
Within the entire Moscoviense basin (outlined topographically), we have counted all craters greater than 500 m to determine the age of the basin itself. The result is ~4.0 Ga.

We have divided the floor of the basin into 36 counting areas and performed CSFD measurements in each of them to determine AMAs of the photogeo-

logically defined units. The results are as follows. (1) The AMAs of the cratered floor ranges from 4.0 to 3.6 Ga. (2) There are four small patches of plains on the surface of cratered floor unit; the AMAs of these patches are ~1.2 Ga. (3) The AMAs of the light plains show two groups: the older group is 4.0–3.4 Ga old, and the younger group is 1.7–1.2 Ga old. (4) The AMAs of the dark plains also show two groups: the older group is 4.0–3.5 Ga old, and the younger group is 1.3–0.68 Ga old. The youngest plains occur in the southern part of the dark plains with the AMA of 0.68 Ga.

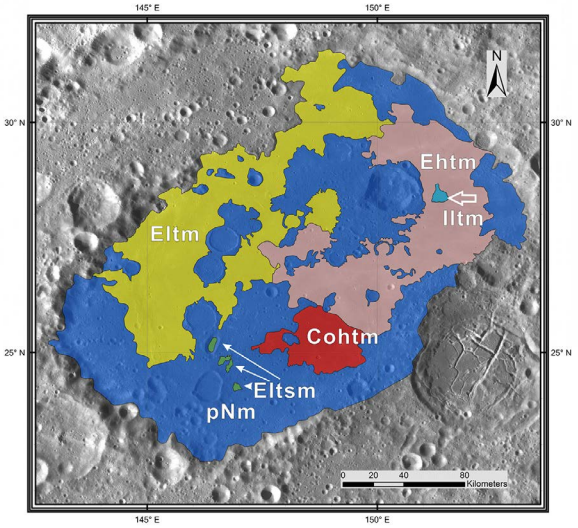

Fig 1. Geological map of the Moscovience basin floor. (pNm: Ancient mare unit of pre-Nectarian system; Iltm: low-Ti mare unit of Imbrian system; Eltm: low-Ti mare unit of Eratosthenian system; Ehtm: High-Ti mare unit of Eratosthenian system; Cohtm: High-Ti mare unit of Copernican system

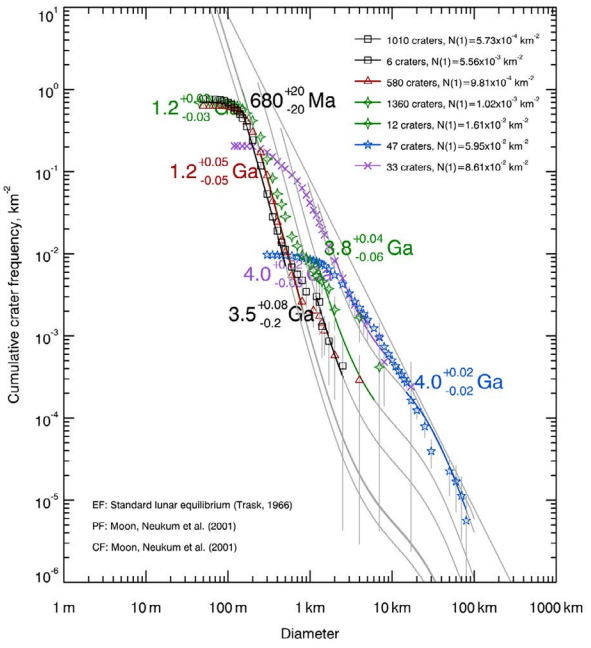

Fig 2. Cumulative size-frequency distribution of craters of morphological units on the floor of the Moscoviense basin: complex of plains (black plots: southern part of dark plains, green plots: eastern part of dark plains, red plots: western part, light plains); cratered floor unit (violet plots: southern part); the whole basin (blue plots).

The summary of our AMA determinations is shown in Figure 2 that clearly shows two age clusters for the volcanic units on the floor of the Moscoviense basin.

Concentrations of FeO and TiO_2 as a function of time.

The frequency of the AMAs and the concentration of TiO_2 and FeO are shown in Figure 3.

The histogram shows that morphological units in the Moscoviense basin were formed mainly during two episodes: the first episode continued from 4.0 to 3.5 Ga (pre-Nectarian-Imbrian times); During this episode, the cratered floor unit was formed. The second episode continued from 2.0 to 0.68 Ga (Eratosthenian and Copernican times). During this episode, the complex of plains, both light and dark, was formed. In our study, we determined that the peak of volcanism during the second episode occurred ~1.2 Ga ago in the eastern and western parts of the Moscoviense basin, and the youngest volcanism, which was located in the southern part of basin, shows the AMA of 0.68 Ga. This volcanic activity is much younger than the other volcanic plains on the far side of the Moon [10].

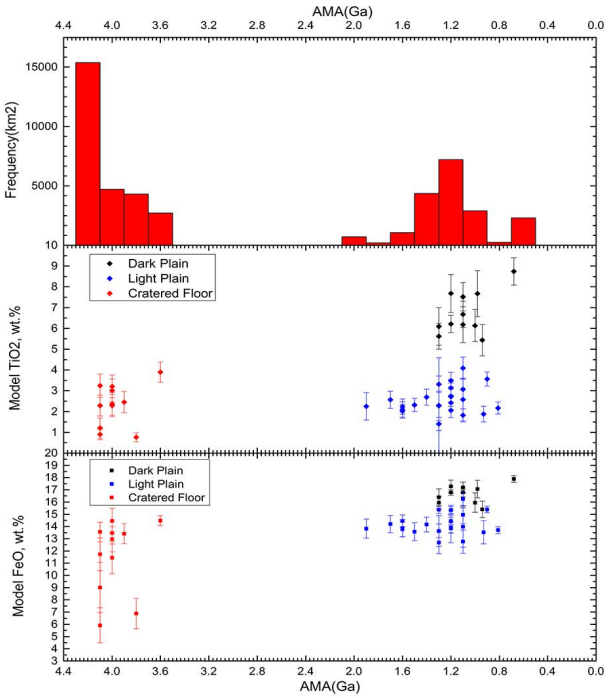

Fig 3. Histogram of the AMAs (top) and FeO and TiO2 contents vs. AMAs for all counting areas on the floor of the Moscoviense basin

The plots showing the distribution of TiO2 and FeO contents as a function of the AMAs reveal following features. (1) There is no obvious difference for the TiO2 content between the cratered floor and the light plains. (2) The cratered floor shows exceptionally large variations of FeO content. (3) The FeO contents of the light and the dark plains are close to each other with the dark plains being more enriched in TiO2. (4) The FeO and TiO_2 contents do not show correlation with AMAs, which is consistent with the result of [11].

REFERENCES:

[1] Gillis-Davis J. J., Lucey P. G., Hawke B. R. Mare Moscoviense a window into the interior of the Moon// Lunar and Planetary Science XXXVII. 2006.
[2] Wieczorek M. A. et al. The crust of the Moon as seen by GRAIL// Science. 2012. V. 339. P. 671–675.
[3] Morota T. et al. Ages and thicknesses of mare basalts in mare Moscoviense: Results from SELENE(Kaguya) terrain camera data// 40th Lunar and Planetary Science Conference. 2009.

[4] Bhattacharya S. et al. Lithological mapping of central part of Mare Moscoviense using Chandrayaan-1 Hyperspectral Imager (HySI) data // Icarus. 2011. V. 212. P. 470–479.
[5] Haruyama J. et al. Long-lived volcanism on the lunar farside revealed by SELENE Terrain Camera// Science. 2009. V. 323. P. 905–908.
[6] Michael G. G., Neukum G. Planetary surface dating from crater size-frequency distribution measurements: partial resurfacing events and statistical age uncertainty// Earth and Planetary Science Letters. 2010. V. 294. P. 223–229.
[7] Robinson M. S. et al. Lunar Reconnaissance Orbiter Camera (LORC) instrument overview// Space Science Review. 2010. V. 150. P. 81–124.
[8] Haruyama J. et al. Global lunar-surface mapping experiment using the Lunar Imager/Spectrometer on SELENE// Earth Planets Space. 2008. V. 60. P. 243–255.
[9] Lucey P. G. et al. Lunar iron and titanium abundance algorithms based on final processing of Clementine ultraviolet-visible images// J. Geophysical Research. 2000. V. 105. No. E8. P. 20297-20305.
[10] Pasckert J. H. et al. Small-scale lunar farside volcanism// Icarus. 2015. V. 257. P. 336–354.
[11] Hiesinger H. et al. Lunar mare basalts: Mineralogical variations with time// Lunar and Planetary Science XXXII. 2001.

SWIRLS AS INTERGROWTHS OF LIGHT MAGNESIAN SILICATES (PREDOMINANT ENSTATITE) AND NATIVE IRON

G. G. Kochemasov
IGEM of the Russian Academy of Sciences, 35 Staromonetny, 119017 Moscow, Russia (*kochem.36@mail.ru*)

KEYWORDS:
Moon, wave structures, swirls, Native Fe, enstatite, magnetism, SPA Basin, plagioclase-rich areas

INTRODUCTION:
Several enigmatic structural and petrologic features of the Moon are widely discussed: origin and global spreading of the high-Ti lunar basalts, Fe concentrations (Figure 1) not pronounced in the deepest Basin, mascons, swirls.

The Moon moves away from Earth. Loosing its angular momentum due to slowing rotation a necessary compensation is fulfilled by sending dense materials into the crust. Varying density basalt flows (high, low, very low-Ti) reflect various stages of the slowing rotation process. Various contents of dense mineral component — ilmenite in basalts means various densities of the rock. Iron in basalts can be in less dense dark minerals and denser ilmenite thus influencing overall basalt densities corresponding to requirements of "healing" diminishing angular momentum.

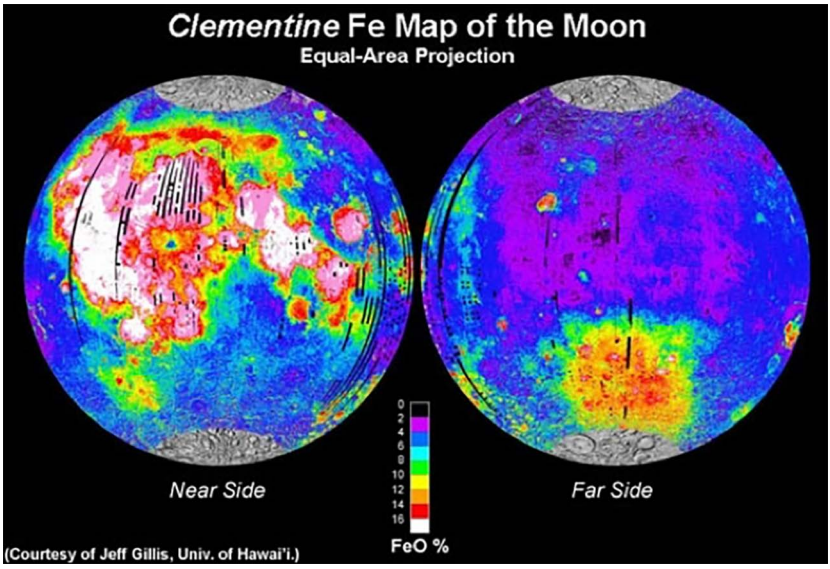

Fig. 1. Fe map of the Moon

Spectral mapping of basalt types [6] indicates that for large parts of Oceanus Procellarum younger basalts are more titanium rich than the older basalts, thus somewhat reversing the trend found in the returned samples [5]. In some smaller basins spectral mapping also shows titanium richer basalts being older than titanium pure ones [4]. Thus, one may conclude that decreasing rotation rate of the Moon was not smooth but rather uneven.

The deepest SPA Basin must be filled with denser rocks than the shallower Procellarum Ocean filled with basalts and Ti-basalts. The Clementine spectral data show presence of orthopyroxene and absence of plagioclase [7] favoring some dense ultrabasic rocks. An obvious tendency to approach this type of rock would be to observe it in the Luna 24 samples from also very deep (up to 4.5 km) Mare Crisium. In fragments there prevail pyroxene and VLT-ferrobasalts (Mg-poor). Unusual melt matrix breccia with globules and crystals of

Fe metal were also found [1]. Among glass droplets there 40–54 % are irons. Nearly half of the black and brown droplets have either vesicles or iron droplet trains or both [1, 2]. A significant portion of Mg enriched fragments in the Luna-24 soil is also observed.

The lunar global magnetic map (Figure 2) favors a conclusion about some important Fe metal admixture increasing not only magnetism but also overall rock density of the deepest Basins and Mares. An association of Mg-pyroxene enstatite with Fe-Ni metal is well known in cosmic materials (for an example, E-chondrites). On the Moon enigmatic but characteristic swirls with high albedo, elevated magnetism and diffused boundaries could be presented by this type of high-Mg (light in color) with Fe metal rock. The SPA Basin is one of the enriched with swirls relatively magnetic areas (Figure 2) [3]. Another deep in relief and relatively magnetic is the Mare Crisium area. In the Reiner Gamma swirl area some small rifts are detectable.

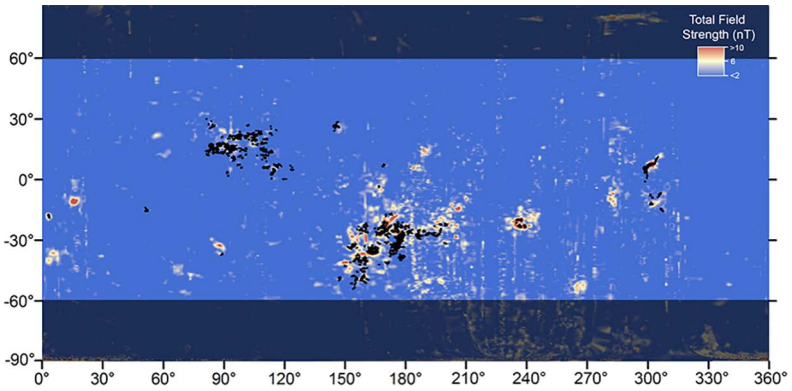

Fig. 2. Lunar magnetism and swirls (black) [3]

The SPA Basin as a part of the lunar tectonic triad having the largest geoid anomaly in some places shows spectral geochemical signs of the highland rocks [8, 9]. They are exposed “windows” of these rocks revealing a real basement of the deeply subsided SPA Basin. An important role of a plagioclase-rich litologies there is stressed by a plagioclase-rich rock fragment (60–80 vol.% plagioclase) found in Von Kármán crater by Yutu-2 rover [13]. This fragment could be brought to the surface after regolith layering as a diminished density rock.

A significant part of the basic-UB infilling of the SPA Basin could be presented by the above mixture (Mg-silicate + native Fe)-swirls [12]. Harder, denser and lighter in color, they could “protrude” through surrounding darker regolith. and appear quite visible for remote mapping. Metal iron is an important component of the constructive materials for the Moon and Cosmos investigations. The Chang’E-4 will bring new facts for the lunar sciences [10, 11].

Finally, one could build an imaginary “basaltic ladder” having in mind connection between basic rocks and elevations. On the top of it are placed KREEPs-relatively light less dense basalts occupying relatively elevated terrains (Procellarum KREEP Terrain-PKT) in the central part of the Procellarum Oceanus. In the middle are various basalts with various titanium contents. In the basal part are swirls-native iron-magnesian silicates intergrowths relatively dense and less dark but magnetic (Figure 2).

REFERENCES:

[1] Basu A.et al.(1977) Conference on Luna-24, Houston, LPI Contribution 304, P. 14–17.
[2] Basu A. et al. (1977) the same, P. 18–21.
[3] Denevi B. W. et al (2016) Icarus, V. 273, 15 July 2016, P. 53–67. doi:10.1016/j.icarus.2016.01.017.
[4] Hiesinger H. et al. (2000) J.Geoph.Res., 2000, V. 185, #E12, 29239–275.
[5] Hiesinger H. and J. W. Head III. (2016) Workshop on New Views of the Moon II, abs.8030.

[6] Pieters C. M. (1978) Proc. Lunar Planet. Sci. Conf., 9th, 1978, 2825–2849.
[7] Pieters C. M. (1997) Annales Geophysicae, Suppl. III to V. 15, P. 792.
[8] Pieters C. M. et al. The Moon Mineralogy Mapper (M3) on Chandrayaan-1 // Current Science. 2009. V. 96. No. 4, P. 500–505.
[9] Romme D., Wohler C., Grumpe A.,Hiesinger H. South Pole-Aitken Basin: anorthosite rich material as indicator for a complex layering of the Basin crust structure // 8th Moscow Solar System Symp. 2017. Abstr. 8MS3-PG-05, P. 42–43.
[10] Kochemasov G. G. New planetology and geology: tectonic identity and principal difference of terrestrial oceans and lunar basins // New Concepts in Global Tectonics (NCGT). 2017. V .5. No. 1. P. 131–133.
[11] Kochemasov G. G. Regular wave tectonics of the Moon // Encyclopedia of Lunar Science / ed. B. Cudnik. Springer International Publishing AG, part of Springer Nature, 2018. https:// doi.org/10.1007/978-3-319-05546-6_121-1
[12] Kochemasov G. G. Possible Fe-metal enriched areas in the SPA Basin // Developing a New Space Economy. 2019. 5024pdf.
[13] Ma P., Sun Y., Zhu M-H. et al. A plagioclase-rich rock measured by Yutu–2 Rover in Von Kármán crater on the far site of the Moon // Icarus. 2020. doi:org/10.1016/j.icarus.2020.113901.

HYGINUS CRATER AND GRABEN: DIKE EMPLACEMENT AND EVOLUTION, MAGMATIC FOAM EXTRUSIONS, AND IRREGULAR MARE PATCHES

L. Qiao[1], J. W. Head[2], L. Wilson[3], Z. Ling[1]
[1] *Inst. Space Sci., Shandong Univ., Weihai, Shandong, 264209, China* (*LeQiao.GEO@Gmail.com*)
[2] *Dep. Earth, Env. and Planet. Sci., Brown Univ., Providence, RI, 02912, USA*
[3] *Lancaster Env. Centre, Lancaster Univ., Lancaster LA1 4YQ, UK*

KEYWORDS:
Rima Hyginus, Hyginus Crater, Irregular Mare Patches, Dike Emplacement, Magmatic Foam, Mare Volcanism, Moon/Lunar

INTRODUCTION:
Rimae Hyginus and Ariadaeus, two linear rilles trending ~N75°W in southern Mare Vaporum, are typical ~2–3 km wide graben, each ~210–220 km long, 200–400 m deep, and often broken into right-lateral, *en echelon* segments (Figure 1).

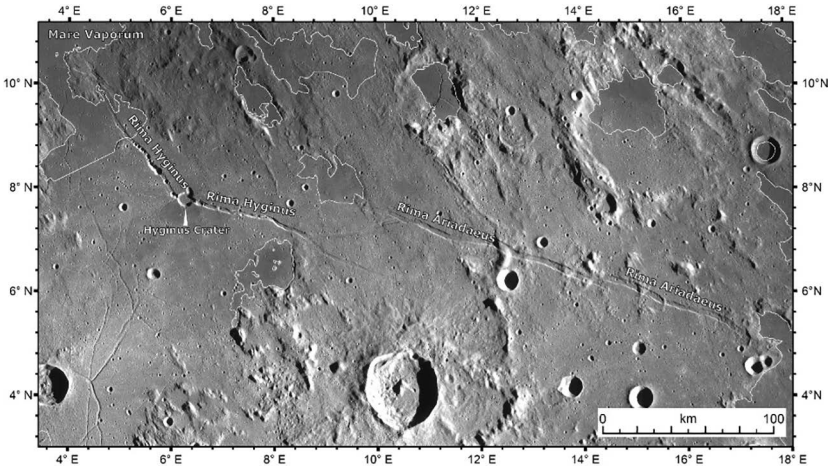

Fig. 1. Regional WAC image of Rima Hyginus and Ariadaeus. Mare boundaries are delineated by white lines

Hyginus, the westernmost, ~215 km long rille, is notable for its ~10 km diameter pit crater and its N°45W-oriented ~70 km long segment of the graben, together forming a distinctive elbow in the Hyginus graben structure (Figure 2). The eastern segment of Rima Hyginus broadly proceeds parallel with the Ariadaeus rille system to the east, and shows multiple re-directions. This rille takes shape in some smooth basin ejecta terrain ~45 km north of the Agrippa crater, extends ~37 km in an ~N°75W trend. It is then re-directed into a direction of N°45W and proceeds a short distance of ~15 km. Afterwards, Rima Hyginus rotate anticlockwise twice: firstly to a N°67W direction over a distance of 24 km, and finally back to the initial trend of N75°W and proceed 48 km until it approaches the 9-km Hyginus crater. At the second turning point, a graben branch, typically 2.5 km wide, emerges from Rima Hyginus, which extends westward over a distance of 38 km and connects with another small branch (18 km long) from the western terminal portion of Rima Ariadaeus. At Hyginus crater, this rille is characterized by a distinctive reorientation, into a direction of N35°W, radial to the Imbrium basin center (see Figure 2). It then extends ~100 km in a very slightly wavy manner, until dissipating in the hummocky terrains at the south margin of Mare Vaporum, where it is intersected by another N70°W-trending, 3 km wide graben. Dozens of pit craters are identified along the two branches of Rima Hyginus.

In addition, a series of distinctive left-lateral *en echelon* graben occurs on the western ~70 km side of Hyginus crater [1].

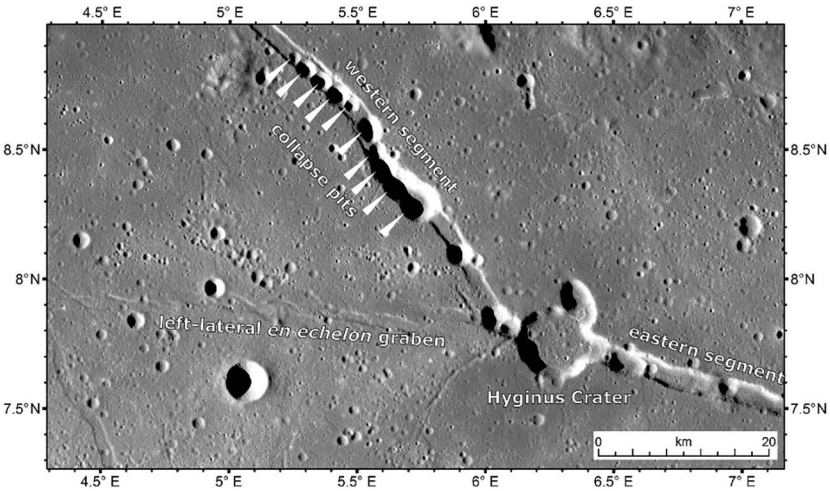

Fig. 2. Local Kaguya TC map of Hyginus graben and crater

Dozens of small, pit-type IMPs are identified on the of Hyginus Crater floor [2, 3]. This suite of re-directed grabens, abundant associated interior pit and IMP features have made Rima Hyginus distinctive from other lunar rilles.

FORMATION AND EVOLUTION STAGES OF RIMA HYGINUS GRABEN:
We interpret Rimae Hyginus and Ariadaeus to be the surface manifestations of separate dike emplacement events [4–8]: magma-filled cracks propagated from source regions at great depths to the shallow subsurface and stalled, creating near-surface extensional stress fields above the stalled dike, resulting in the observed graben. Rille width-depth relationships suggest a dike width of ~100–200 m and a depth of ~500–1000 m to the top of the dikes. In contrast to some lunar linear rilles (e. g., Rima Parry V), no evidence for extrusive or explosive volcanic activity is seen along Rima Ariadaeus, but Rima Hyginus is characterized by more than 20 pit craters located along the graben, the most prominent one being the ~10 km Hyginus crater, which also hosts numerous Irregular Mare Patches (IMPs).

We outline evidence for the following sequence of events in the emplacement of the Hyginus graben and its associated structures: 1) the Hyginus dike propagated vertically from depth with an initial orientation of ~N80W; 2) as it approached the surface, dike propagation was significantly influenced by the near-surface stress field, dominantly radial to the Imbrium impact basin, about 15 degrees NE of its strike at depth; 3) in the latter stages of its vertical propagation, responding to the Imbrium-radial stress field, the dike underwent rotation, creating distinctive left-lateral *en echelon* graben on the western ~70 km side of Hyginus crater, and causing reorientation of the western segment of the dike to N45 W; 4) as the dike reached its shallowest depth and stalled, the two major continuous graben features formed, diverging away from the elbow; 5) near-coincident with graben formation, the uppermost part of the convex-upward dike penetrated the surface at the elbow, and vented Phase 1 gas, migrating laterally from along the convex-upward dike, and small amounts of vesicular magma (magmatic foam), that had accumulated in the dike tip during its upward propagation; 6) venting of the laterally migrating gas from along the top of the dike at the elbow created void space below the vent and caused the collapse of the elbow area, forming Hyginus crater; 7) near-simultaneously, the pit craters along the arms of Hyginus rille formed by collapse of the graben floor to accommodate the void space created by the vented gas (the total volume of the pit craters, 45 km^3, is similar to the total volume of Hyginus crater, 59 km^3); 8) immediately following the collapse and formation of Hyginus crater, very vesicular magmatic foams that formed just below the gas at the top

of the dike were extruded into the interior of Hyginus crater; 9) these magmatic foams formed mounds and coated the interior of Hyginus, to produce irregular mare patches (IMPs); 10) solidification of the Hyginus crater interior extrusive deposits occurred rapidly and dike solidification was complete in a few thousand years. The Rima Hyginus elbow-like configuration is the first documented example of regional near-surface stress field reorientation of a magmatic dike from the deeper lunar mantle. Finally, large irregular mare patch (IMP) occurrences have been found in several volcanic environments: 1) Ina, a pit crater atop a small shield volcano; 2) Cauchy 5, a pit crater and flanking flows on a small shield volcano; and 3) Sosigenes, a linear graben with a central collapse crater [3]. The Hyginus Crater irregular mare patch occurrence provides an additional IMP environment that is most similar to the Sosigenes occurrence, a collapse crater located on a dike-related graben.

REFERENCES:

[1] Wilson L., Hawke B. R., Giguere T. A., Petrycki E. R. An igneous origin for Rima Hyginus and Hyginus crater on the Moon // Icarus. 2011. V. 215. P. 584–595.
[2] Braden S. E., Stopar J. D., Robinson M. S., Lawrence S. J., van der Bogert C. H., Hiesinger H. Evidence for basaltic volcanism on the Moon within the past 100 million years // Nature. Geoscience. 2014. V. 7. P. 787–791.
[3] Qiao L., Head J. W., Ling Z., Wilson L. Lunar irregular mare patches: Classification, characteristics, geologic settings, updated catalog, origin, and outstanding questions // J. Geophysical Research: Planets. 2020. V. 125. e2019JE006362.
[4] Head J. W., Wilson L. Lunar graben formation due to near-surface deformation accompanying dike emplacement // Planetary and Space Science. 1993. V. 41. P. 719–727.
[5] Wilson L., Head J. W. Generation, ascent and eruption of magma on the Moon: New insights into source depths, magma supply, intrusions and effusive/explosive eruptions (Part 1: Theory) // Icarus. 2017. V. 283. P. 146–175.
[6] Head J. W., Wilson L. Generation, ascent and eruption of magma on the Moon: New insights into source depths, magma supply, intrusions and effusive/explosive eruptions (Part 2: Predicted emplacement processes and observations) // Icarus. 2017. V. 283. P. 176–223.
[7] Wilson L., Head J. W. Eruption of magmatic foams on the Moon: Formation in the waning stages of dike emplacement events as an explanation of “irregular mare patches” // J. Volcanology and Geothermal Research. 2017. V. 335, P. 113–127.
[8] Wilson L., Head J. W. Controls on Lunar Basaltic Volcanic Eruption Structure and Morphology: Gas Release Patterns in Sequential Eruption Phases // Geophysical Research Letters. 2018. V. 45. P. 5852–5859.

ESTIMATES OF THE NUMBER OF NEAR-EARTH OBJECTS BASED ON THE NUMBER OF LUNAR CRATERS FORMED DURING THE LAST BILLION YEARS

S. I. Ipatov[1], E. A.Feoktistova[2], V. V. Svetsov[3]
[1] *Vernadsky Institute of Geochemistry and Analytical Chemistry of RAS, Moscow, Russia* (*siipatov@hotmail.com*)
[2] *Sternberg Astronomical Institute, Lomonosov Moscow State University, Moscow, Russia*
[3] *Institute of Dynamics of Geospheres of RAS, Moscow, Russia*

KEYWORDS:
Lunar craters, diameters, impactors, near-Earth objects, lunar seas

INTRODUCTION:

Mazrouei et al. [1] concluded that the number of collisions of near-Earth objects (NEOs) with the Moon per unit time increased by a factor of 2.6 about 290 Myr ago. Their conclusions were based on analysis of the ages of Copernican craters (i.e. craters with an age $T \le 1.1$ Gyr). Earlier, based on the studies of bright rays in craters, McEwen et al. [2] supposed that the number of new craters increased by a factor of 2 during the last 300 Myr.

Probabilities of collisions of near-Earth objects with the Moon: Estimates of the characteristic time T_E elapsed before the collision of an Earth-crossing object (ECO) with the Earth could vary by a factor of several in different papers. In [3] based on our approach of calculation of T_E, we obtained T_E = 67 Myr. Using the Opik's approach, Bottke et al. [4] obtained T_E = 134 Myr for a smaller number of ECOs. At T_E = 100 Myr the probability p_E of a collision of an ECO with the Earth during a year is equal to 10^{-8}. In [5–7] considered values of p_E were close to $3 \cdot 10^{-8}$, and $T_E \approx 300$ Myr. In our estimates the ratio of the probabilities of collisions of ECOs with the Earth to the probabilities of their collisions with the Moon was considered to be equal to 22 [8]. Probably, one of the reasons of the differences in the values of T_E and p_E in [3] and [5–7] can be caused by that estimates were made for different time intervals. Our calculations of T_E and p_E were made for the model with various orientations of orbits (not only those at the present time). Therefore, our estimates correspond to probabilities of collisions of ECOs with the Earth during large time intervals. Estimates of some other authors can correspond to probabilities of collisions of 1 km NEOs with present orientations of their orbits during a shorter time interval. For example, in [6] considered time interval equaled to ±300 yr. It was noted in [6] that the effect of gravitational focusing for NEOs with absolute magnitude $H < 27$ was greater by a factor of 1.85 than the effect for NEOs with $H < 18$. The greater effect of gravitational focusing for smaller objects can be caused by the possibility of their encounters with the Earth with smaller velocities than for larger NEOs, because there can be more various orbital orientations for a larger number of NEOs. We suppose that, though the number of NEOs and the mean values of their orbital elements during millions of years can be about the same as those at the present time, during evolution of the disk of NEOs, orbital elements of some NEOs could get such values, at which probabilities of their collisions with the Earth and the Moon can be greater than those based on the present orbits of 1-km NEOs.

On Fig. 26 in [7] for 1-km ECOs, the curve of the number of impacts with the Earth of objects brighter than a given absolute magnitude H vs. H corresponds to $p_E = 4 \cdot 10^{-9}$. If we extrapolate this curve from the region of $17 \le H \le 25$ to $H \ge 26$, then the values of the curve at $H \ge 26$ fits the old data on bolides [9], but are smaller by a factor of several than the new data on bolides from [10]. Therefore, we suppose that in our estimates of the number of collisions of NEOs with the Earth during 1 Gyr we can also use T_E = 100 Myr and $p_E = 10^{-8}$. At $p_E = 10^{-8}$ for the present number of NEOs, and for the considered time interval equaled to 1.1 billion years, we obtained $N_{est} \approx 267$ collisions of 1 km

NEOs with the full surface of the Moon and $N_{est} \approx 41$ collisions of 1 km NEOs with the region of the Ocean of Storms (Oceanus Procellarum) and other seas of the visible side of the Moon. The ratio of this region to all surface of the Moon is 0.155.

THE NUMBER OF KNOWN CRATERS WITH AN AGE LESS THAN 1.1 BILLION YEARS:

The characteristic diameter of a crater formed after a collision of an ECO with a diameter of 1 km with the Moon was estimated in [11–12] to be about 15–17 km. The number of known craters with an age less than 1.1 Gyr was estimated in [11–12] on the basis of the database [13]. In our new estimates of the number of craters, we did not consider such craters, but we used the catalog of lunar craters [14], as well as the data from [1]. For the data from [14], 53 lunar craters with a diameter $D \geq 15$ km belong to the Copernican period, and 29 of them are located in the region of the seas of the visible side of the Moon. For the data from the accompanying materials to [1], the number of such craters for almost full lunar surface and for the region of the seas is 44 and 12, respectively. If we suppose that the number of craters per unit area for the entire surface of the Moon is the same as for the region of the Ocean of Storms and the seas of the visible side, then the above estimates of the number of craters on the seas equaled to 29 and 12, correspond to the number N_{obs} of the observed craters equaled to 187 and 77 for a whole lunar surface. These numbers of N_{obs} show that in the regions of the seas of the visible side of the Moon there are more Copernican craters with $D \geq 15$ km per unit area than on the entire surface of the Moon. For a whole surface of the Moon, the number of Copernican craters with $D \geq 15$ km is 44 and 53 for data from [1] and [14], respectively. These numbers are smaller by factors of 6.1 and 5.0 than $N_{est} \approx 267$ obtained at $T_E = 100$ Myr. As N_{est} is proportional to $1/T_E$, then $N_{est} \approx 89$ at $T_E = 300$ Myr. $N_{est} \approx 267$ also exceeds estimates of the number of craters on the Moon (77 and 187 for [1] and [14], respectively) if their number per unit area is the same as that for the considered region of the seas.

Mazrouei et al. [1] supposed that the probability of collisions of NEOs with the Moon increased by a factor of 2.6 about 290 Myr ago. For the model in which the probability of a collision of a NEO with the Moon was equal to the current value for the last 290 Myr, and before that within 810 Myr it was 2.6 times less than the current value, the number of craters formed would be 0.6 from the estimate obtained on the basis of the current number of NEOs. Our above estimates of N_{est} and N_{obs} allow an increase in the probability of collisions of NEOs with the Moon by a factor of 2.6 about 290 Myr ago. With this conclusion, the paper [1] agrees better with the estimates based on the craters from the region of the seas. Therefore, we can assume that the number of craters with an age of not more than 1.1 Gyr per unit area for the entire surface of the Moon could be approximately the same as that for the region of seas, that is, be more than the current estimate for the entire surface of the Moon. More detailed results presented in this abstract can be found in [15].

CONCLUSIONS:

The characteristic diameter of the lunar crater, formed as a result of a collision of 1-km near-Earth object (NEO) with the Moon, was estimated to be about 15 km. The number of known Copernican craters with a diameter $D \geq 15$ km per unit area on the seas, according to various authors, exceeds the same number for the rest of the Moon by a factor not less than two. Our estimates do not contradict to the increase in the number of NEOs after a possible catastrophic destruction of large main belt asteroids, which could have occurred over the past 300 Myr, but they do not prove this increase. The number of Copernican craters with $D \geq 15$ km can be greater than the number of the craters presented in [1]. The probability of a collision with the Earth during a year of an Earth-crossing object (ECO) could be 10^{-8} if we consider large time intervals. For such probability, our estimates of the number of craters correspond to the model in which the number of 15-km Copernican craters per unit area for the entire surface of the Moon would be

the same as for the region of the seas, if the data [14] for $D < 30$ km would be as complete as for $D > 30$ km. For such a model, the rate of crater formation over the last 1.1 Gyr could be permanent.

ACKNOWLEDGEMENTS:
The work was carried out as a part of the state assignments of the Vernadsky Institute of RAS No. 0137-2020-0004, the Sternberg Astronomical Institute of MSU, and the Institute of Dynamics of Geospheres of RAS. Studies of the probabilities of collisions of asteroids with the Earth were supported by the grant No. 13.1902.21.0039 “Theoretical and experimental studies of the formation and evolution of extrasolar planetary systems and characteristics of exoplanets” of the Russian Ministry of Education and Science.

References:

[1] Mazrouei S., Ghent R. R., Bottke W. F. et al. // Science. 2019. V. 363. P. 253–255.
[2] McEwen A. S., Moore J. M., Shoemaker E. M. // JGR: Planets. 1997. V. 102. No. E4. P. 9231–9242.
[3] Ipatov S. I., Mather J. C. // Annals of the New York Academy of Sciences. 2004. V. 1017. P. 46–65. http://arXiv.org/format/astro-ph/0308448.
[4] Bottke W. F., Nolan M. C., Greenberg R., Kolvoord R. A. // Hazards due to comets and asteroids / ed. T. Gehrels. The University of Arizona press. 1994. P. 337–357.
[5] Werner S. C., Ivanov B. A. // Treatise on Geophysics. 2nd ed. 2015. V. 10. P. 327–365.
[6] Emel’yanenko V. V., Naroenkov S. A. // Astrophysical Bull. 2015. V. 70. P. 342–348.
[7] Granvik M., Morbidelli A., Jedicke R. et al. // Icarus. 2018. V. 312. P. 181–207.
[8] Le Feuvre M., Wieczorek M. A. // Icarus. 2011. V. 214. P. 1–20.
[9] Brown P. G. Spalding R. E., ReVelle D. O. et al. // Nature. 2002. V. 420. P. 294–296.
[10] Brown P. G., Assink J. D., Astiz L. et al. // Nature. 2013. V. 503. P. 238–241.
[11] Ipatov S. I., Feoktistova E. A., Svetsov V. V. // 10th Moscow Solar System Symposium 9M-S3 2018: abstracts. M.: IKI, 2018. 9MS3-PS-77. P. 349–351.
[12] Ipatov S. I., Feoktistova E. A., Svetsov V. V. // Proc. IAU. 2020. V. 14. Symp. S345, Cambridge University Press, 2020. P. 299-300. doi:10.1017/S1743921319001467.
[13] Losiak A., Kohout T., O’Sullivan K. et al. Lunar Impact Crater Database. Lunar and Planetary Institute, Lunar exploration Intern Program. 2009. Updated by Ohman T. 2011.
[14] Losiak A., Kohout T., O’Sullivan K. et al. Lunar Impact Crater Database // Lunar and Planetary Institute. Lunar exploration Intern Program. 2009. Updated by Ohman T. 2015.
[15] Ipatov S. I., Feoktistova E. A., Svetsov V. V. Number of Near-Earth Objects and Formation of Lunar Craters for the Last Billion Years // Solar System Research. 2020. V. 54. No. 5. P. 384–404.

MORPHOLOGY AND AGE OF LUNAR CRATER INA

A. T. Basilevsky[1], G. G. Michael[2]
[1] *Vernadsky Institute of Geochemistry and Analytical Chemistry RAS, Kosygin str., 119991 Moscow, Russia* (*atbas@geokhi.ru*)
[2] *Freie Universitaet Berlin, Malteserstr., 74-100, Haus D, 12249 Berlin, Germany*

KEYWORDS:
Basaltic volcanism, irregular mare patch, impact crater, hill, morphologic freshness

INTRODUCTION:
Ina is a 2.9×1.9 km planimetrically D-shaped crater of ~60 m deep located near the center of lunar nearside (Figure 1). It was identified in the photos taken from the Apollo-15 and -17 orbital modules [1, 2], but the best images of it were taken by the LROC NAC camera [3] and thus the most detailed studies of Ina were done using these images [4–7]. These studies showed that crater Ina is on the top of gentle-sloped shield basaltic volcano. Inside Ina there are low (5–25 m) flat-topped hills with steep slopes, separated by rough terrain with meter-scale relief. Ina and the landforms inside it are considered by all mentioned teams as resulting from basaltic volcanism.

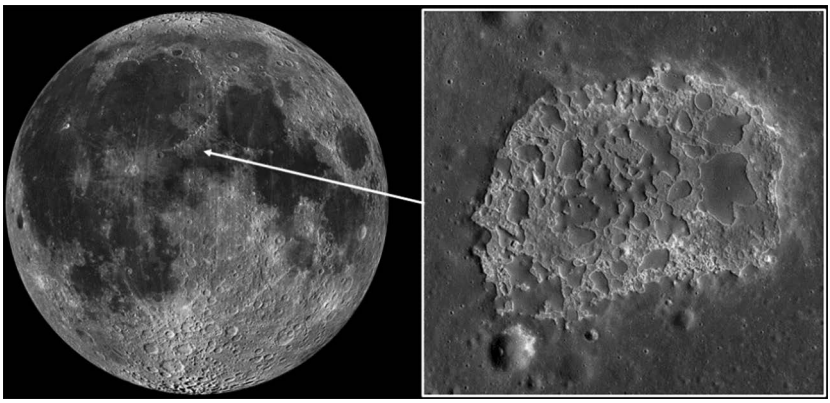

Fig 1. Location of crater Ina on the lunar nearside. Left is LROC WAC mosaic of lunar nearside, right is part of LROC NAC image M119815703

However, further interpretations are very different. On the shield volcano slopes the spatial density of small craters was measured which corresponded to an absolute age of ~3,5 Ga [7]. But on the intra-Ina hills the crater density was found to be much lower corresponding to an age < 100 Ma [6]. Similar low crater densities were found on so-called 'irregular mare patches (IMP)' [6] so that crater Ina as well as IMPs are considered to be cases of very young lunar volcanism.

There is a different interpretation of the same observations: According to [7, 8], hills inside Ina are composed not of 'normal' basalts but of 'magmatic foam': massive pumice with porosity >75 %. Based on some experiments [9] and model calculations [10] these authors suggested that meteorites impacting magmatic foam should produce craters of larger depth but smaller diameter, thus leading to significantly lower apparent ages. So [7, 8] concluded that crater Ina is contemporaneous to the shield volcano on which Ina occurs.

In the present talk we consider the morphologic freshness of intra-Ina landforms trying to conclude whether the crater is young or old, and compare morphologies of small craters superposed on intra-Ina hills and on the slopes of the mentioned shield volcano, trying to understand if they are similar/

different and thus to conclude if the hills are composed of magmatic foam or 'normal' basalts.

MORPHOLOGIC FRESHNESS OF INTRA-INA LANDFORMS:

The eastern third of Ina crater and the adjacent surface of the shield volcano of very gentle slope are seen in Figure 2. The volcano slopes look like normal mare: smooth plain peppered with small craters. The lunar surface bombarded by meteorites is a place of lateral material exchange: in any location ejecta from newly-forming craters are dispersed in all directions while ejecta from the neighboring and distant craters arrive in at this location. On subhorizontal surfaces, which dominate in the lunar maria, the balance of incoming and outgoing materials is close to neutral. Depressions are zones of positive balance, receiving more material from outside than they return. Adjacent to depressions are zones of negative balance, which lose more ejecta than they receive from the adjacent depression [11, 12]. Observations made by the Apollo-15 and Lunokhod-2 teams showed that the effective distance of the lateral material exchange on the Moon varies from tens to hundreds meters and a layer of regolith of decimeters to a few meters is involved [13, 14]. So one could expect that crater Ina in its near-boundary part should receive a surplus of up to a few meters depth of crater ejecta from the adjacent mare-like terrain. This material is expected to be present at the foot of Ina inner slopes and should soften the relief of the inter-Ina rough terrain and diffuse boundaries of the inter-Ina hills.

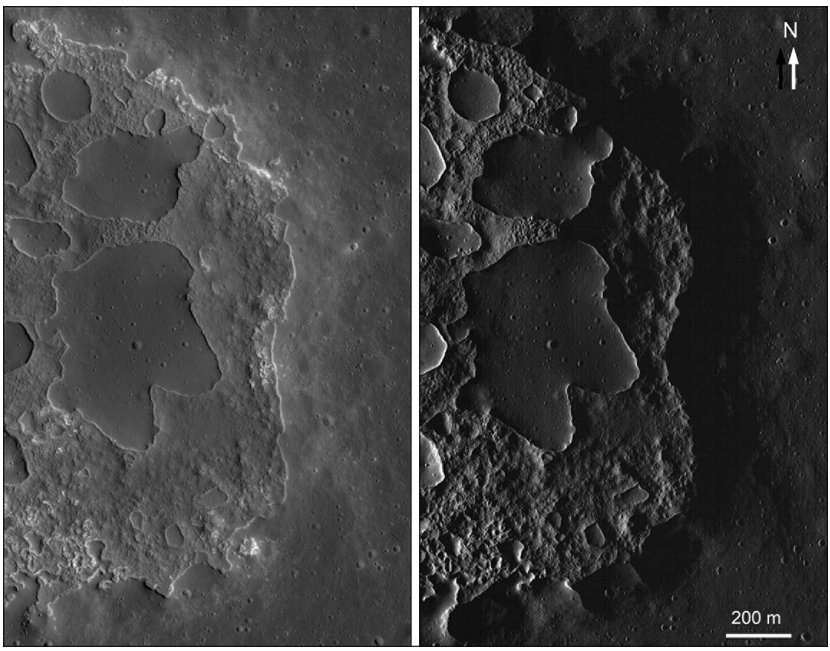

Fig. 2. Eastern part of crater Ina as it is seen in LROC NAC images M119815703 — left and M116282876— right. Sun elevation above the horizon is 36° and 6,5°, correspondingly, original resolution 0,55 m

As can be seen in Figure 2, this is not the case and no ejecta accumulation nor softening/diffusing of intra-Ina landforms is observed. This is certain evidence that crater Ina and landforms in it are young (<100 Ma).

COMPARING MORPHOLOGIES OF CRATERS ON INTRA-INA HILLS AND ADJACENT MARE:

Images of small morphologically fresh craters located on intra-Ina hills and on the adjacent mare-like shield volcano slopes are shown in Figure 3. For comparison, we selected only morphologically fresh craters because it is logical to expect that in the process of the crater destruction/evolution the potential

differences between craters formed on magmatic foam and on 'normal' basalts should disappear.

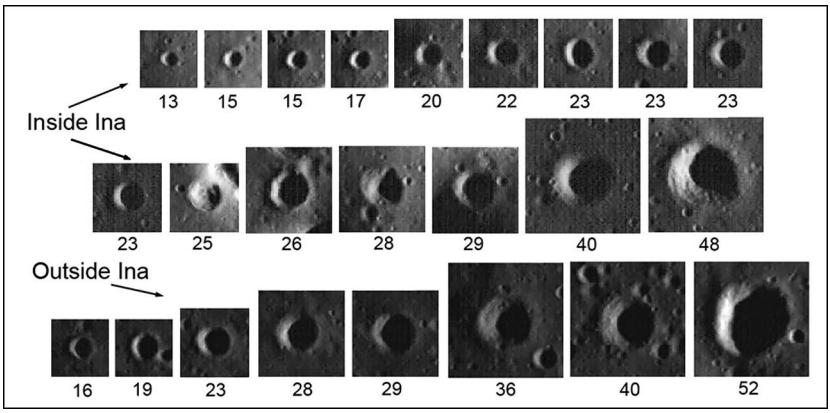

Fig. 3. LROC NAC images of craters formed on the intra-Ina hills and on adjacent mare-like surface. Numbers below images are the crater diameters in meters

It is seen in Figure 3, that craters, formed on these two different terrains, are morphologically very similar. They have an elevated rim that, possibly, should not be present for craters formed in magmatic foam.

REGOLITH ACCUMULATION MODEL:

We simulated the regolith accumulation that should occur over 3.5 Ga from ejecta of craters forming in a) typical mare material, and b) magmatic foam, where craters are hypothesized to occur 3x smaller, finding a) 10–20 m b) ~1 m, using methods of [15]. That the morphology of craters of similar size within and outside Ina does not differ observably suggests that the post-compression crater formation is similar, so we assume that the volume of excavation remains proportional to the final crater volume. The reduction in regolith thickness is less than estimated from scaling the excavated volume, because of the reduction of ejecta recycling over an equivalent area.

CONCLUSIONS:

It follows from the above consideration that the crater Ina boundaries and intra-Ina landforms are morphologically very fresh suggesting that Ina is a product of very young (< 100 Ma) lunar volcanism. Morphologies of small impact craters superposed on mare-like surface and on intra-Ina hills are very similar suggesting that the latter are not composed from the magmatic foam. This latter conclusion, however, is preliminary and demands additional studies.

REFERENCES:

[1] Whitaker E. F. An unusual mare feature. NASA Spec. Publ. V. 289. 1972. P. 25-84–25-85.
[2] Evans R. E., El-Baz F. Geological observations from lunar orbit // Apollo-17 Prelim. Sci. Rep. NASA SP 330. 1973. P. 28-1–28-32.
[3] Robinson M. S. et al. Lunar Reconnaissance Orbiter Camera (LROC) instrument overview // Space Science Review. 2010. V. 150. Iss. 1–4. P. 81–124.
[4] Robinson M. S. et al. High resolution imaging of Ina // Lunar and Planetary Science Conference XLI. 2010. Abs. 2592.
[5] Garry W. B. et al. The origin of Ina: Evidence for inflated lava flows on the Moon // J. Geophysical Research. 2012. V. 117. E00H31.
[6] Braden S. E. et al. Evidence for basaltic volcanism on the Moon within the past 100 million years // Nature. Geoscience. 2014. V. 7. P. 787-791.
[7] Qiao Le et al. Ina pit crater on the Moon // Geology. 2017. V. 45. No. 5. P. 455–458.
[8] Wilson L., Head J. W. Eruption of magmatic foams on the Moon // J. Volcanology and Geothermal Research. 2017. V. 335. P. 113–127.
[9] Schultz P. H. et al. Impact crater size and evolution: Expectations for Deep Impact // 33rd Lunar and Planetary Science Conference. 2002. Abs. 1875.

[10] Wünnemann K. et al. A strain-based porosity model for use in hydrocode simulations of impacts and implications for transient crater growth in porous targets // Icarus. 2006. V. 180. P. 514–527.
[11] Arvidson R. et al. Horizontal transport of the regolith, modification of features, and erosion rates on the lunar surface // The Moon. 1975. V. 13. P. 61–79.
[12] Basilevsky A. T. et al. Mechanisms of destructions of small craters of the Moon // Solar System Research. 2020. V. 54. No. 4. P. 1–11.
[13] Swann G. A. et al. 3. Preliminary geologic investigations of the Apollo-14 landing site // Apollo-14 Prelim. Sci. Report. NASA SP-272. 1971. P. 39–85.
[14] Basilevsky A. T. et al. A possible lunar outcrop: A study of Lunokhod-2 data // The Moon. 1977. V. 17. P. 19–28.
[15] Michael G. et al. On the history of the early meteoritic bombardment of the Moon: Was there a terminal lunar cataclysm? // Icarus 2018. V. 302 P. 80–103.

ROCK ABUNDANCE IN THE PLASKETT LUNAR CRATER

E. A. Grishakina, M. A. Ivanov
Vernadsky Institute of Geochemistry and Analytical Chemistry, RAS, 119991, Kosygin St. 19, Moscow, Russia (*grishakina@geokhi.ru*)

KEYWORDS:
Plaskett crater, rockiness, rock abundance, boulders

Based on new high-precision data, the rockiness in the lunar crater Plaskett was estimated, the correlation of rockiness and surface slopes is analyzed: 1) on the inner slope, 2) on the central hill, and 3) in the bottom. To construct a mosaic of images, images of a narrow-angle camera LROC NAC were used. The resolution of the images, according to which the boulders were deciphered by visual inspection, is 1 meter for the 1st section, 2.5 meters for the 2^{nd} and 3^{rd} sections. When creating a slope map, a digital elevation model was taken from the data of the LOLA laser altimeter on the LRO orbiter. Within the first test site on the inner slope in the western part of the crater, whose area is about 9 km^2, a unimodal distribution of more than 2300 stones was found, the average stone diameter was 2.54 m, the standard deviation was 1.04 m. Within the second site, on the central hill of the crater with the same area, a unimodal distribution of more than 1300 stones was found, the average stone diameter was 5.42 m, the standard deviation was 2.51 m. Within the third section, a unimodal distribution of more than 400 stones was found in the bottom of a crater with a similar area, the average stone diameter was 4.22 m, standard deviation — 1.26 m. In the first and second sections, the presence of traces of rolling stones was noted, both sections being investigated are inclined surfaces. The different resolution of the original decrypted images does not allow to correctly compare the results for the detection of stones less than 3.5 m. The normal distribution of stones in the study areas is an indicator of the predominance of one random process that forms the current state of rockiness, — impact processing of surface material. The different nature of the curves of the frequency-dimensional distribution of boulders, shown in the graphs, demonstrates the distinct influence of slope processes on rockiness to varying degrees on steep and gently sloping surfaces, on the inner slope and on the central hill of the crater

DEPTHS OF THE COPERNICANS CRATERS LOCATED ON LUNAR MARIA AND HIGHLANDS

E. A. Feoktistova[1], S. I. Ipatov[2]
[1] *Sternberg Astronomical Institute*, *Lomonosov Moscow State University*, *Moscow*, *Russia* (*Hrulis@yandex.ru*)
[2] *Vernadsky Institute of Geochemistry and Analytical Chemistry*, *Russian Academy of Sciences*, *Moscow*, *Russia*

KEYWORDS:
Moon, craters, lunar mare and highlands

INTRODUCTION:
Copernican craters are the lunar craters formed over the past 1.1 billion year. Differences in the depths of older (with an age less than 3.2 billion years) craters located on the lunar maria from the depths of craters located on the highlands were studied in [1–4]. It was concluded that large highland craters usually are deeper than large maria craters. This difference was explained by the properties of the underlying crater surface. In [5] no differences have been found between the depths of the craters on the maria and on the highlands. Below we study the dependence of depths of lunar Copernican craters on their diameters for two types of underlying surface (maria or highlands).

RELATIONSHIP OF THE RATIO OF THE DEPTH OF A CRATER TO ITS DIAMETER WITH THE DIAMETER:
In our work, we used the database of lunar craters [6] and data from [7]. 111 Copernican craters (33 are on the maria and 86 are on the highlands) with diameters from 10 to 100 km and located between 80° N and 80° S were identified in [7]. Young craters were found to have high rock abundance in their ejecta, whereas rock abundance decreases with increasing crater age, eventually becoming indistinguishable from the background for craters older than ~1 Gyr. Only 66 lunar craters with a diameter of more than 10 km are Copernican according to the data [6]. 38 of them are located on the maria and 28 on the highland. The largest number of Copernican craters considered in [7] have a diameter of $10 \le D < 20$ km and are located on the highlands.

Formulas (1)–(2) and (3)–(4) for the depth/diameter distribution of complex Copernican craters earlier were obtained by Kalynn et al. [2] and Pike [1], respectively:

$h = 1.558D^{0.254}$ for highlands, (1)

$h = 0.870D^{0.352}$ for mare, (2)

$h = 1.028D^{0.317}$ for highlands, (3)

$h = 0.819D^{0.341}$ for mare. (4)

Only three craters with D not more than about 30 km (two mare craters with D close to 30 km and one highland crater with $D \approx 25$ km) were among complex craters considered in [7].

To analyze the dependence of h/D on the diameter for Copernican craters population, we calculated diameters and depths of the craters based on the data from Lunar Orbiter Laser Altimeter (LOLA) elevation profiles with the use of Digital Elevation Model (DEM) [8]. The average values of h/D obtained for craters from [6] and [7] are presented in Table 1. As in [9], the ratio of the area of the considered region of the maria to the area of the whole surface of the Moon is 0.155. The table shows that for diameters $D > 30$ km the depths of craters on the highlands are not smaller than those on the maria. At $10 < D < 30$ km mare craters are usually deeper than highland craters.

We used the software from https://planetcalc.ru/5992/ to obtain the formulas for approximation of the dependences of the ratio h/D of the depth of a crater to its diameter on the diameter for Copernican craters on the highlands and the maria. We formally separate craters into two groups based only on the dependence of h/D on D. It was supposed that “simple” craters mainly have $D < 15$ km, and “complex” craters mainly have $D > 19$ km.

Table 1 The mean values of *h*/*D* over intervals of *D* for Copernican craters on the lunar maria and the highlands. The number of craters in the considered interval is presented in parentheses. The craters were selected based on the data from [6] and [7]

Interval of *D,* km	Losiak et al. + Mazrouei et al., highland	Losiak et al. + Mazrouei et al., mare
10.0–12.5	0.16346 (37) <	**0.2036** (21)
12.6–15	0.1657 (23) <	**0.1742** (4)
15.1–17.5	0.1374 (6) <	**0.1646** (4)
17.6–18.4	**0.1576** (3) ≥	0.1522 (1)
18.5–20	0.0903 (3) <	**0.1329** (3**)**
20.1–25	0.0847 (6) <	**0.1231** (6)
25.1–30	0.0999 (2) <	**0.1266** (2)
30.1–40	**0.0955** (6) ≥	0.0946 (7)
40.1–50	**0.0670** (5) >	0.0654 (2)
50.1–60	**0.0832** (2) >	0.601 (4)
60.1–70	**0.0628** (2) >	0.0598 (2)
70.1–80	**0.0573** (2) **>**	0.0534 (2)
80.1–100	**0.0519** (3) **>**	0.0392 (1)

We used the power and linear approximations for the ratio *h*/*D* of the depth of a crater to its diameter on the diameter in forms $h/D = kD^{\alpha}$ and $h/D = bD + c$, respectively. For simple craters from [6] and [7] we have $b = -0.00298$ and $c = 0.2037$ for linear approximation for highland craters, and $b = -0.01056$ and $c = 0.3198$ for linear approximation for mare craters. We have $k = 0.334$ and $\alpha = -0.281$ for simple highland craters, and $k = 1.124$ and $\alpha = -0.715$ are for simple mare craters in power approximation.

For complex craters we found linear approximations in forms:

$h/D = -0.000580D + 0.1042$ for the highland craters,

and $h/D = -0.001679D + 0.165$ for the mare craters, respectively.

Our formulas for power approximations of the *h*/*D* ratio for complex craters are presented below:

$h/D = 0.277\ D^{-0.353}$ for the highland craters,

and $h/D = 1.589\ D^{-0.81}$ for the mare craters.

Based on analysis of intersections of the above fit lines, we can conclude that the value of the diameter for which *h*/*D* is greater for mare craters than for highland craters is probably between 45 and 55 km. We suppose that the estimate (about 30–40 km) of such transition diameter between depths of mare and highland craters made based on Table 1 is more accurate. In our opinion, different relative depths of craters on the highlands and on the maria can be due not only to various properties of the underlying surface, as it was suggested in [2–4], but also to some differences in the mechanism of formation of craters on the highlands and on the maria.

ACKNOWLEDGEMENTS:
The work was carried out as a part of the state assignments of the Vernadsky Institute of RAS No. 0137-2020-0004 and state assignments of the Sternberg State Astronomical Institute of MSU No. AAAA-A20-120012990068-0.

REFERENCES:

[1] Pike R. J. Target-dependence of crater depth on the Moon // Proc. Lunar and Planetary Science Conference XII. 1981. P. 845–847.
[2] Kalynn J., Johnson C. L., Osinski G. R., Barnouin O. Topographic characterization of lunar complex craters // Geophysical Research Letters. 2013. V. 40. P. 38–42.
[3] Chandnani M., Herrick R. R., Kramer G. Y. Geologic analyses of the causes of morphological variations in lunar craters within the simple-to-complex transition // J. Geophysical Research. 2019. V. 124. P. 1238–1265.
[4] Osinsky G. R., Silber E. A., Clayton J., Grieve R. A. F., Hansen K., Johnson C. L., Kalynn J., Tornabene L. L. Transitional impact craters on the Moon Insight into

the effect of target lithology on the impact cratering process // Meteoritics and Planetary Science. 2019. V. 54. P. 573–591.
[5] Pike R. J. Size-dependence in the shape of fresh impact craters on the moon // Impact and Explosion Cratering: Planetary and Terrestrial Implications / eds. D. J. Roddy, R. O. Pepin, R. B. Merrill. Tucson University of Arizona Press, 1977. P. 489–509.
[6] Losiak A., Kohout T., O'Sullivan K., Thaisen K., Weider S. Lunar Impact Crater Database. Lunar and Planetary Institute, Lunar exploration Intern Program. 2009 Updated by T. Ohman. 2015. https://www.lpi.usra.edu/scientific-databases/; https://www.lpi.usra.edu/lunar/surface/Lunar_Impact_Crater_Database_v08Sep2015.xl.
[7] Mazrouei S., Ghent R. R., Bottke W. F., Parker A. H., Gerno T. M. Earth and Moon impact flux increased at the end of the Paleozoic // Science. 2019. V. 363. P. 253–255.
[8] https://ode.rsl.wustl.edu/moon/.
[9] Ipatov S. I., Feoktistova E. A., Svetsov V. V. The number of near-Earth objects and formation of lunar craters during the last billion years // Solar System Research. 2020. V. 54. No. 5. P. 384–404.

ESTIMATES OF THE MODEL THICKNESS OF THE CRATER EJECTA IN THE SOUTH POLAR REGION OF THE MOON

A. S. Krasilnikov, S. S. Krasilnikov, M. A. Ivanov
Vernadsky Institute of Geochemistry and Analytical Chemistry RAS, *Moscow*, *Russia* (*grossular13@gmail.com*)

KEYWORDS:
Moon, South Pole, ejecta thickness, secondary craters, ejecta

INTRODUCTION:
The South polar region of the Moon is considered by the "Roskosmos" corporation as the primary target for the Russian program of study and exploration of the Moon. The high interest for this area is related to the enhanced concentrations of hydrogen in its regolith [1] and to the diversity of geological processes that acted in the lunar sub-polar regions [2]. Resurfacing in the South polar region was largely linked to the formation of the oldest known, pre-Nectarian, SPA basin and the other basins of the Nectarian and Imbrian ages. The SPA ejecta deposits have a high scientific value because they may contain materials excavated from the lunar mantle and, in any case, represent the oldest materials that can be found on the surface of the Moon. The younger craters that were able to penetrate beneath the SPA deposits are also of a great interest because their ejecta could deliver the pre-SPA materials to the surface.

One of the major tasks during photogeological analysis of areas selected for the landing missions is the determination of the sources of materials that accumulated at the landing spot. For the Moon, the principal re-distributors of materials are impact craters that form contiguous ejecta, fields of the secondary craters, and rays. In our work, we estimated thickness of the basin and crater ejecta blankets using several proposed model approaches and the geological map of the South polar region of the Moon.

THE THICKNESS ESTIMATES:
As the base, we used the geological map that portrays variety of morphologies and their stratigraphic ages. The most important features in the study area are impact craters. The dimensions of the larger craters (>20 km) were taken from the lunar crater database [3] and the diameters of the smaller craters were calculated from the data reported in [4]. Five models can be used to estimate the thickness of ejecta of craters of different diameters: McGetchin [5], Pike [6], Housen [7], Fassett [8] and Sharpton [9].

The model by McGetchin [5] was based on the data related to the small-scale impact craters and craters formed during the nuclear explosion tests and extrapolated to the impact structures of larger diameters. McGetchin [5] have proposed the following formula for the ejecta thickness (T): $T = 0.14\ R\ 0.74\ (r/R)^{-3}$. Here and thereafter, R is the crater radius, r is the distance from the crater center; all values are in meters. In his paper, Pike [6] severely critiqued the McGetchin's approach and proposed his own formula: $T = 0.033\ R\ (r/R)^{-3}$. A model by Housen [7] was developed based on a theoretical modelling of an impact of a projectile with specific velocity, diameter, and density. Their resulting formula is: $T = 0.0078\ R\ (r/R)^{-2.61}$. Using new topographic data collected by the LOLA instrument [10], Fassett [8] developed a model that describes changes of the ejecta thickness for the Orientale basin. Their formula is: $T = 2900(\pm300)\cdot(r/R)^{-2.8(\pm0.5)}$, where R is the radius of the Cordillera rim. Finally, in his work, Sharpton [9] used the new topographic data to describe the topology of relatively small craters (2–45 km diameter) and proposed the following formula for the ejecta thickness: $T = 3.95(\pm1.19)\ R^{0.399}(r/R)^{-3}$.

In our work we used formulae by Housen [7] and Sharpton [9], because the approaches by McGetchin [5] and Pike [6] appear to either underestimate or overestimate the thickness and the approach by Fassett [8] seems

to be applicable to the basin-like structures. We applied the formula by Housen to craters larger than 45 km, for all smaller craters we used the formula by Sharpton. With the help of these formulae, we estimated the ejecta thickness of the Nectarian and younger craters that show recognizable zone of contiguous ejecta. Our results are presented in the map (Figure 1) that shows variations of the ejecta in zones centered at 2500, 5000, 10000 and 20000 meters from the center of the studied craters.

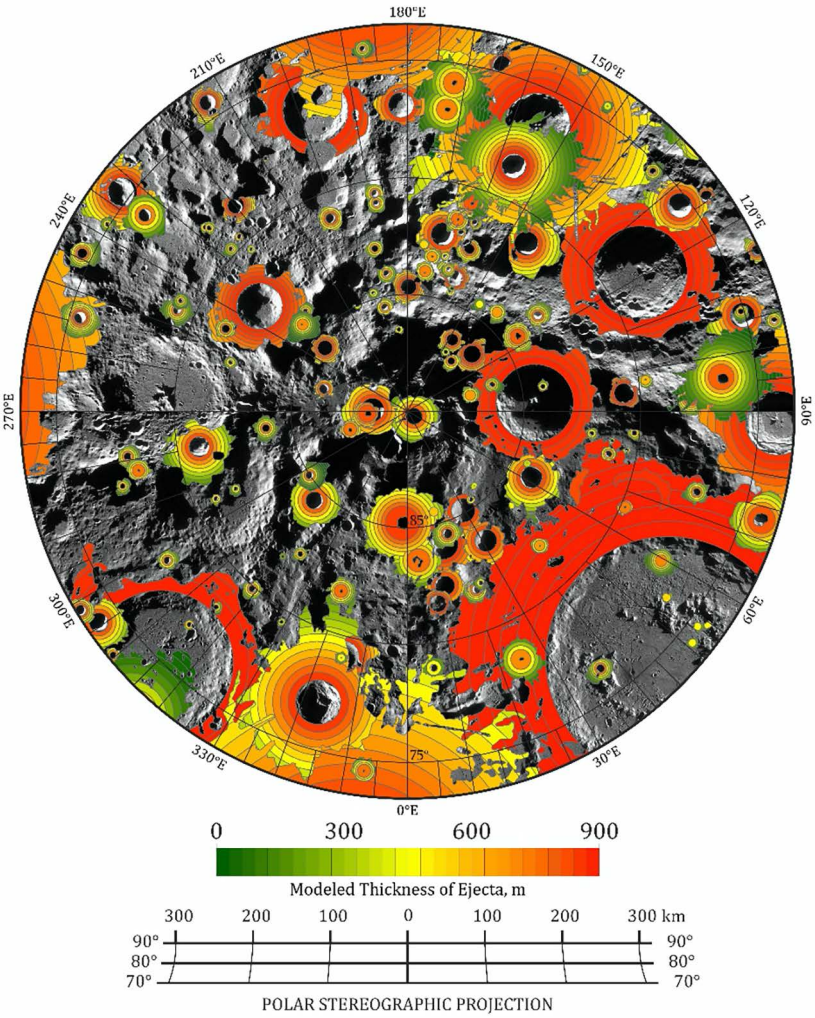

Fig. 1. The model thickness of ejecta blankets for craters of the Nectarian – Copernican ages in the South polar region of the Moon

REFERENCES:

[1] Sanin A. B., Mitrofanov I. G., Litvak M. L. et al. Hydrogen distribution in the lunar polar regions // Icarus. 2017. V. 283. P. 20-30.
[2] Ivanov M. A., Abdrakhimov A. M., Basilevsky A. T. et al. Geological characterization of the three high-priority landing sites for the Luna-Glob mission // Planetary and Space Science. 2018. V. 162. P. 190–206.
[3] Head J. W., Fassett C. I., Kadish S. J. et al. Global distribution of large lunar craters: Implications for resurfacing and impactor populations // Science. 2010. V. 329(5998). P. 1504–1507.
[4] Krasilnikov S. S., Ivanov M. A. Geological mapping of the south pole of Moon // 9M-S3. 2018. Art. PS-71, P. 358.
[5] McGetchin T. R., Settle M., Head J. W. Radial thickness variation in impact crater ejecta: implications for lunar basin deposits // Earth and Planetary Science Letters. 1973. V. 20(2). P. 226–236.

[6] Pike R. J. et al. Ejecta from large craters on the Moon: Comments on the geometric model of McGetchin // Earth and Planetary Science Letters. 1974. V. 23(3). P. 265–271.
[7] Fassett C. I., Head J. W., Smith D. E. et al. Thickness of proximal ejecta from the Orientale Basin from Lunar Orbiter Laser Altimeter (LOLA) data: Implications for multi-ring basin formation // Geophysical Research Letters. 2011. V. 38(17). Art. L17201.
[8] Housen K. R., Schmidt R. E., Holsapple K. A. Crater ejecta scaling laws: fundamental forms based on dimensional analysis // J. Geophysical Research. 1983. V. 88(B3). P. 2485–2499.
[9] Sharpton V. L. Outcrops on lunar crater rims: Implications for rim construction mechanisms, ejecta volumes and excavation depths // J. Geophysical Research: Planets. 2014. V. 119(1). P. 154–168.
[10] Smith D. E., Zuber M. T., Jackson G. B. et al. The lunar orbiter laser altimeter investigation on the lunar reconnaissance orbiter mission // Space Science Reviews. 2010. V. 150(1–4). P. 209–241.

MORPHOMETRIC FEATURES OF CRATERS IN THE SOUTHERN POLAR REGION OF THE MOON

N. A. Slodarzh[1], Zh. F. Rodionova[2], T. I. Levitskaya[1]
[1] *Ural Federal University, Mira street 19, Ekaterinburg, Russia* (*nikolai.slodarzh@yandex.ru*)
[2] *Sternberg Astronomical Institute Moscow State University, Universitetskiy pr. 13, Moscow, Russia* (*jeanna@sai.msu.ru*)

KEYWORDS:
Moon, craters, morphometry, measurements, coordinates, diameters, statistical analysis, DEM

INTRODUCTION:
In this work, we studied about 1320 Lunar craters located in latitude from 60° to 90° S with diameters larger than 10 km (Figure 1). Based on measurements made with the ArcGIS Desktop software package, a catalog was compiled. The source data was a DEM with a resolution of 120 meters per pixel by LRO LOLA [1]. An additional CraterTools [2] module for ArcMap was used to digitize the craters.

METHODS:
In this study were calculated and compiled into catalog various parameters [3] for each crater in workspace, including coordinates of its center, diameter, depth, rim height, angles of internal and external slopes. For measurements of heights and depth buffer zones were created: one with diameter equal to 50 % of the crater diameter to cover its floor (blue zones in Figure 2), and two rings inside and outside the rim, each with a thickness equal to 2 % of the crater's diameter (pink and yellow areas in Figure 2), in which was calculated DEM's statistics. Similar method with buffer rings was used for angular measurements, which are made not only for the whole crater, but for each of its cardinal directions too.

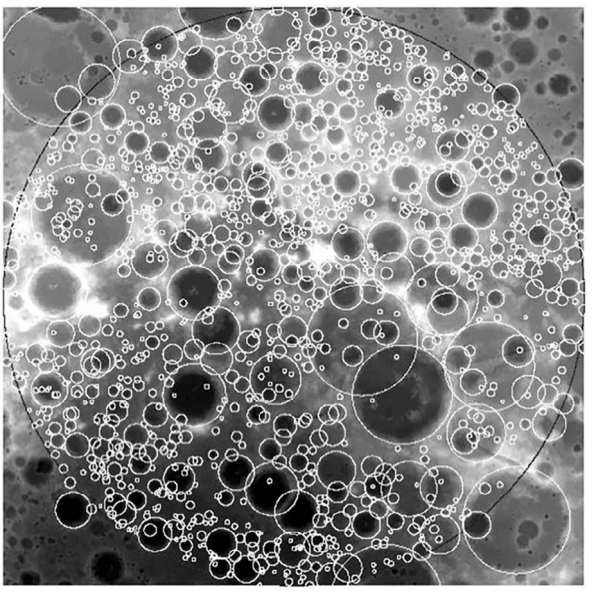

Fig. 1. DEM of study area (60° to 90° S). Height values range from –9127.5 to 7025.5 m. 1,320 craters larger than 10 kilometers in diameter were digitized and measured in the workspace

For each crater 8 3D profiles were created for later study and comparison, example of their usage shown below. Depth to diameter (d/D) ratio was calculated. Craterstats 2 [4] program was used to calculate workspace area's age based on crater size-frequency distribution (CSFD) [5].

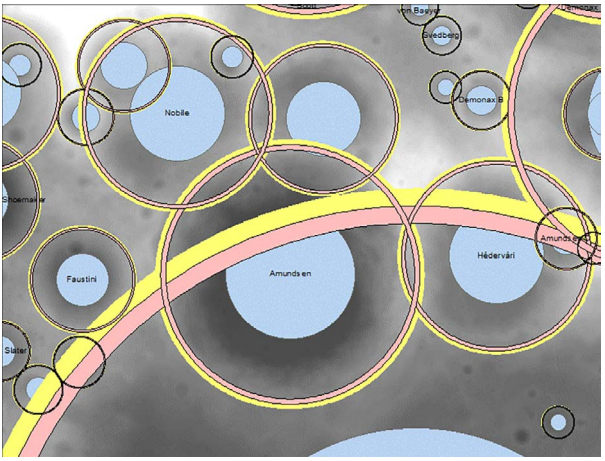

Fig. 2. Buffer zones for depth and height measurements

DISCUSSION AND CONCLUSION:

Figure 3 shows profiles of the Amundsen crater (latitude –84.46°, longitude 86.89°, diameter 104.5 km).

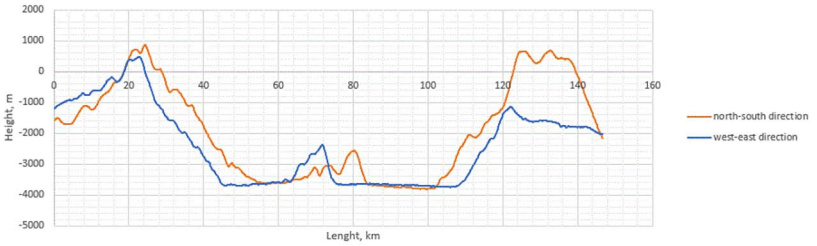

Fig. 3. Profiles of Amundsen crater

On North-South direction: the difference in the heights of the crest of the rim 0.3 km, the height of the central peak 1.1 km. On West-East direction: the western ridge of the rim is 1.5 km higher than the eastern one. The height of the central peak equals 1.2 km.

The Figure 4 shows graph of crater depth to diameter ratio (d/D) [6]. The graph adds lines corresponding to $d/D = 0.1$, $d/D = 0.2$ and third order polynomial trend line.

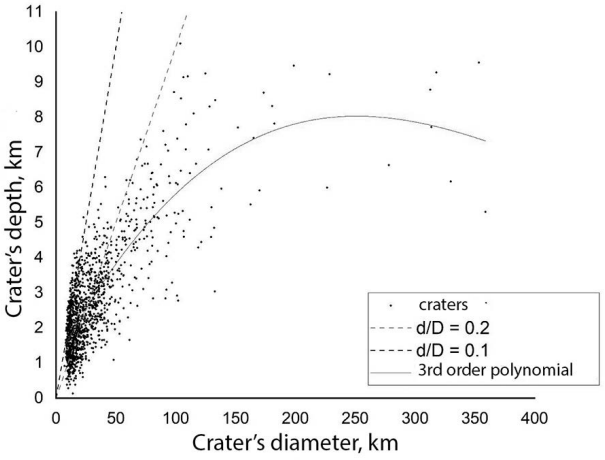

Fig. 4. Graph of crater depth to diameter ratio (d/D)

The Figure 5 shows results of Craterstats 2 work. Estimated age of surface containing craters is (4,100±0,004) billion years, it's underlying surface's age is (4,200±0,020) billion years.

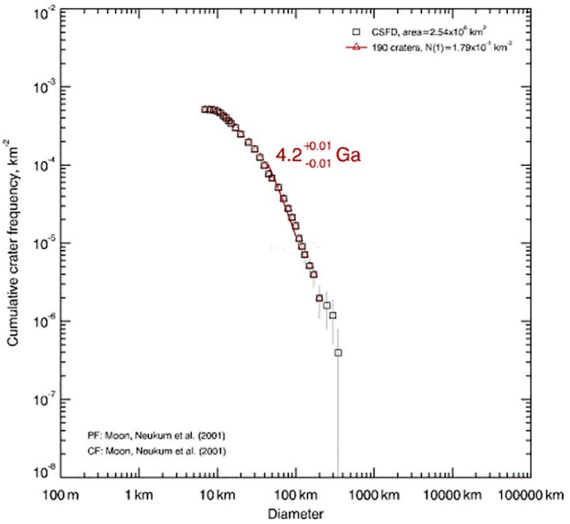

Fig. 4. Cumulative distribution of the craters and surface age determination using Craterstats 2

ACKNOWLEDGEMENTS:
The authors thank G. G. Michael and A. A. Kokhanov for their help.

REFERENCES:

[1] LOLA PDS Data Node. http://imbrium.mit.edu/.
[2] Head III J. W. et al. Global Distribution of Large Lunar Craters: Implications for Resurfacing and Impactor Populations // Science. 2010. V. 329. Art. 1504.
[3] Rodionova Zh. F., Dekhtyareva K. I. Main morphometric characteristics of lunar craters // Trudy GAISh. 1988. V. 60. P. 179–192.
[4] Michael G. G., Platz T., Kneissl T. et al. Planetary surface dating from crater size-frequency distribution measurements: Spatial randomness and clustering // Icarus. 2012. N0. 218. P. 169–177.
[5] Platz T., Michael G. Planetary surface dating from crater statistics // PGM Meeting, USGS Flagstaff, 19 June 2012.
[6] Kokhanov A. A., Karachevtseva I. P., Zubarev A.E et al. Mapping of potential lunar landing areas using LRO and SELENE data // Planetary and Space Science. 2018. No. 162. P. 179–189.

PROBLEM OF "SOUTH POLE-AITKEN" BASIN FORMATION

A. A. Barenbaum[1], M. I. Shpekin[2]
[1] *Oil and Gas Research Institute RAS, Gubkin str. 3, Moscow,119333, Russia* (*azary@mail.ru*)
[2] *Kazan Federal University, Kremlyovskaya 18. Kazan, Tatarstan, 420008, Russia* (*michaels1@yandex.ru*)

KEYWORDS:
South Pole-Aitken basin on Moon, galactic comets, cumulative mechanism of crater formation

ANNOTATION
The hypothesis is proposed that the unique South Pole-Aitken basin (SPA) on the Moon could arise as a result of the last four cometary bombardments of the Moon by galactic comets as a result of the cumulative mechanism of crater formation.

GENERAL INFORMATION ABOUT SPA BASIN

The South Pole-Aitken basin is one of largest impact structures not only on the Moon, but throughout the Solar System. It was discovered half a century ago [1, 2] by the Soviet space stations Zond-6 (1968) and Zond-8 (1970). But even today its origin remains obscure.

The SPA basin is elliptical in shape and is located in the southern hemisphere on the far side of the Moon (Figure 1). It got its name from the names of two objects on its opposite sides: the Moon south pole and the Aitken crater. The basin has young craters and smaller sea basins, and under its bottom there is an excess of dense rocks that do not give the Bouguer gravity anomaly, as in ordinary mascones [3].

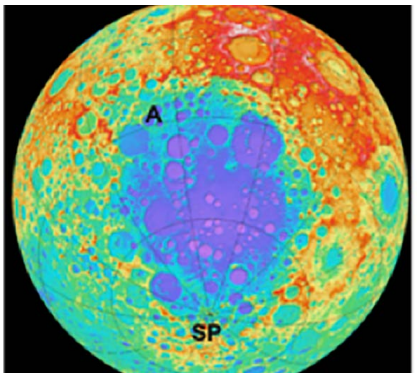

Fig 1. Map of heights of the Moon. South Pole-Aitken basin on the far side of the Moon. Designated: SP is South Pole, A is Aitken crater

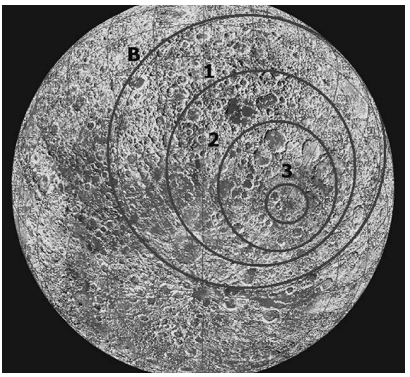

Fig 2. Rings in multi-ring structure of SPA basin, plotted on the Moon image with a central meridian of 160° west longitude [4]

Several misaligned rings (Figure 2) are distinguished in the structure of the basin [4] at different topographic heights. Rings differ in diameters and composition of rock. Ring "B" denotes a shaft with a diameter of 3500 km that surrounds the SPA basin and which can be traced along the ridge system in the northwestern, northern, northeastern, and eastern parts of the basin [4]. At a number of points, the shaft reaches a height of H = 8 km. The substance of its rocks, as well as the elevated area located behind it, has anorthosite composition typical of the rocks of the upper part of the Moon's crust.

The ellipse "1" with a major semi-axis of 970 km corresponds to a profile with H = 0 km, which corresponds to the spherical surface of the Moon with a radius of 1738 km. This ellipse determines the actual size of the SPA basin. Its center has coordinates 53° south latitude and 169° west longitude.

The ellipse "2" corresponds to a profile with the mark of $H = -4$ km. Its semi-major axis is ≈640 km, and the center is even more shifted south relative to the "B" ring. The rocks of the basin to depth of ≈4 km contain more Fe and Th, which indicates the presence of material of the middle and lower crust of the Moon.

Ring "3" with a radius of ≈200 km separates the deepest part of the basin, starting from $H = -6$ km. The center of this ring is displaced from the center of the ring "B" in a southeast direction by already ≈730 km. Moreover, the composition of the rocks up to depths of $H = -8$ km differs little from the rocks of the overlying layer.

HYPOTHESES OF SPA BASIN ORIGIN

There is no generally accepted explanation of the origin of the SPA basin. It is believed that the basin could have formed 4.2–4.3 billion years ago as result of the fall of a very large asteroid onto the Moon [5]. In this case, one could expect the presence in the basin of a large amount of mantle material from depths of ~200 km. Such material, however, is absent both in the pool itself and on the surface around the pool. Therefore, it is believed that the fall occurred at a small angle (≈30°) to the lunar surface [6]. An argument in favor of this assumption is also the presence of an elevated area above all in the northeast, as well as in the northwest of the basin (see Figure 1).

At the same time, judging by the displacement of the rings, the authors of the work [3] found that the impactor could move almost perpendicular to the plane of the ecliptic. The angle of its fall to the Moon was ~75°. This displacement is interpreted as a trace of the trajectory of the impactor immediately before contact with lunar surface. The authors also concluded that the impactor was most likely not an asteroid, but a comet type body.

The question of the nature of the fallen body that formed the SPA basin, however, has not been resolved. According to [7], the impactor could relate to a different population of cosmic bodies than bodies, as result of which all other basins on the Moon were formed.

A NEW APPROACH TO SOLVING THE PROBLEM

In the works [8–11] we showed that large craters and sea basins on the Moon, as well as Mars and Mercury, were created did not by the falls of interplanetary asteroids, as today is believed [12], but at the result of bombardments by high-speed comets of galactic origin. The bombardments are in the nature of intense cometary showers lasting ≈1–5 million years, which occur during the periods of the sun's stay in the jet streams and spiral arms of the Galaxy and are repeated after ≈20-37 million years. At this, after 150 million years, galactic comets alternately bombard the southern and northern hemispheres of the planets [13].

As a result, most craters ≈10–180 km in diameter and basins larger than 180 km in size on the Moon, Mars and Mercury arose during the last one and to a lesser extent during the two or three previous cometary bombardments, when comets mostly fell in the southern hemisphere of the planets.

The last bombardment took place of ≈5–1 mln years ago, when the Solar System was in the stream of galactic comets near the Sun — in the branch of Orion-Cygnus. According to our estimates [14], the flux density of these comets was $\Phi \approx 5 \cdot 10^{-10}$ year^{-1}·km^{-2}, and their density of incidence on Moon, Earth and other planets was $\approx 2 \cdot 10^{-3}$ km^{-2}.

Given the density of comets falling on the south pole of the Moon and Mercury, which have no atmosphere, as well as Mars, which has a very rarefied gas shell, craters from the fall of many comets overlapped each other, which led to an increase in depth and size of resulting impact structure. We called this mechanism of the formation of the largest craters and sea basins "cumulative" [9]. We believe [14] that such a "cumulative mechanism" can also explain the origin of the SPA basin on the Moon.

HYPOTHESIS RATIONALE

We will perform the following elementary calculation. Let us estimate the number of galactic comets that fell in the SPA basin in accordance with their flux density in the Orion-Cygnus branch $\Phi \approx 5 \cdot 10^{-10}$ year^{-1}·km^{-2},

and find their kinetic energy. Let us take the basin radius R = 2000 km, the average energy of comets $E_k \approx 5 \cdot 10^{21}$ J and the duration of their bombardment $\Delta t = 4$ mln years. Then, during this time, number $N = \pi R^2 \Phi \Delta t \approx 6 \cdot 10^3$ comets with full energy $E_\Sigma = NE_k = 3 \cdot 10^{25}$ J can fall into the basin.

This energy could well go to the formation of the SPA basin. To answer the question whether this energy is enough for this or not, we compare the value of E_Σ with the energy of the ejection of rocks from the pool during the formation of its bowl. Let us consider the most extreme case, when all substance ejected from a basin bowl acquires a second cosmic velocity equal to $v = 2.4$ km/s on the Moon and leaves the Moon. The energy required for this will be $E = Mv^2/2$, where M is the mass of the ejected substance. Assuming the basin depth $H = 6$ km, its area $S = 3 \cdot 10^6$ km^2, and assuming that the rocks consisted of anorthosite with a density $\rho = 3.3$ g·cm^{-3}, we obtain the rock volume $V = SN = 1.9 \cdot 10^7$ km^3, their mass $M = \rho V = 6.2 \cdot 10^{19}$ kg and the energy required to eject rocks from the SPA basin, $E = 1.8 \cdot 10^{26}$ J.

According to [15], when impact craters are forming, only a small amount of material from the near-surface region of craters ejects at a speed exceeding the first cosmic velocity on the planet. The bulk of the rocks have a significantly lower ejection rate, which prevents rock fragments from moving far from the crater.

These discarded rock fragments may explain the existence of the rampart surrounding the SPA basin, as well as the origin of the higher terrain in the northeast of the basin. Therefore, if we assume that the bulk of the matter was ejected from the SPA basin at a speed an order of magnitude lower than the second cosmic one for the Moon, then the energy required for the formation of the basin will decrease by 2 orders of magnitude and become equal to ≈5 % of the total energy of galactic comets $E_\Sigma = 3 \cdot 10^{25}$ J.

Even taking into account the fact that each of 6,000 galactic comets that fell down into the SPA basin, was able to vaporize, melt, and heat rock mass in several times higher than mass of the comet [15]. The energy intensity of these processes cannot exceed the several first percent of energy E spent on the formation of the SPA basin bowl as a whole.

This calculation shows that the galactic comets could well have formed the SPA basin. Earlier [17], we found that many large craters and marine basins of the Southern hemisphere on far side of the Moon could have arisen during last cometary bombardment 5–1 mln years ago. In particular, these include Aitken and Tsiolkovsky craters, as well as the Orientale mare.

Figure 1 is clearly seen that these structures are located within the vast highlands surrounding the SPA basin from the north-east, north, and north-west, which, we believe, partly consists of rocks ejected during formation of the basin [16]. Therefore, the SPA basin age is older than 5 Myr, and it could forming during the three previous cometary bombardments, which took place in the ≈23, ≈40 and ≈65 mln years ago [13].

In connection with this, a weighty argument in favor of our hypothesis is displacement of the basin rings in a south-eastern direction [4]. When the Sun moves in a galactic orbit, the angle between the ecliptic plane and the direction toward the Galaxy center, from where the galactic comets come, changes. At this the angle between the lunar equator and direction of comets incidence on Moon also changes. According to calculations [13], for the last bombardment this angle was close to 58°, while for the previous three bombardments it was 54°, 45°, and 35°, respectively.

This calculation is consistent with the nature of displacement of the ring centers in the SPA basin (Figure 2) according to [4]. Thus, it can be assumed that the SPA basin was formed as a result of the last four bombardments of the Moon by galactic comets. The reason for its occurrence was a powerful cometary bombardment, which occurred on the border of the Mesozoic and Cenozoic 65 mln years ago. The maximum density of comets incidence was in the region of latitudes close to the center of the ring “B”, where at that time the axis of rotation of Moon passed. During the next three bombardments, the axis Moon rotation and, as a consequence, its South pole moved step by

step to their current position, occupying positions that coincided with the centers of the rings “1”, “2” and “3”.

CONCLUSION

A hypothesis is proposed according to which the South Pole-Aitken basin on the Moon arose under the influence of galactic comets falls. This hypothesis differs from other known hypotheses in that:

1. The SPA basin on the Moon was created not by the impact of one large cosmic body that fell, but as result of the multiple bombardments the Moon by high-speed galactic comets on during periods of the Solar System being in the jet streams of the Galaxy.
2. The physical mechanism of the formation of the SPA basin under impact of bombardments by galactic comets is similar to the “cumulative mechanism” [13] of the creation by these comets marine basins larger than 180 km on the Moon, as well as on Mars and Mercury. The main difference is that the SPA basin was formed as a result of not one, but last four comet bombardments.
3. The elliptical shape and specific ring-shaped structure of the basin is caused not only by the oblique incidence of galactic comets, but also by an increase in the angle of their incidence relative to the modern plane of the Moon equator during of each subsequent bombardment.
4. The formation time of the SPA basin should be considered Cenozoic, which is the age of the basin is 65 mln years.

REFERENCES:

[1] Rodionov B. N., Isavnina I. V. et al. Cosmic. Res. 1971, V.9, 410–417.
[2] Shpekin M. I. Proceeding of Astronomy Institute RAS, M., 2020 v.5 (in print)
[3] James P. B., Smith D. E. et al. Geophys. Research Let. 2019, V.10, 5100–5106.
[4] Shevchenko V. V., Chikmachev V. I., Pugacheva S. G. Astron. Vestnik, 2007, V. 41, No. 6, 447–462.
[5] Hiesinger H. et al. 2012, id. EPSC2012-832: journal, P. 56.
[6] Wieczorek M.A, Weiss B.P, Stewart S. T. Science. 2012, V. 335 (6073), P. 1212–1215.
[7] Byrne C. J. Lunar and Planet Sci. Conf. XXXVI. 2005. 1260.
[8] Barenbaum A. A., Shpekin M. I. J. of Physics: Conf. Ser. 2018. 946. 012079.
[9] Barenbaum A. A., Shpekin M. I. Ninth Moscow Solar System Symp., 2018, 9MS3-PS-85, P. 368–370.
[10] Barenbaum A. A., Shpekin M. I. J. of Physics: Conf. Ser. 1147, 2019, 012057.
[11] Barenbaum A. A., Shpekin M. I. Tenth Moscow Solar System Symp. 2019, 10MS3-PS-50. P. 112–114.
[12] Melosh H. J., Freed A. M. et al. Science. 2013, V.340, Issue 6140, 1552–1555.
[13] Barenbaum A. A. Galaxycentric Paradigm in Geology and Astronomy, 2010, (PH: Librokom, Moscow). P. 567.
[14] Barenbaum A. A., Shpekin M. I. 35 Intern. Conf. on Equations of State for Matter. Book of Abstracts. Moscow and Chernogolovka and Nalchik, 2020, 158.
[15] Melosh H. J. Impact Cratering. A Geological Process, 1989, New York: Oxford University Press Inc.
[16] Barenbaum A. A., Shpekin M. I. Vestnik ONZ RAN, 2011, No. 3, NZ6011.
[17] Taylor G. J. PSR Discoveries: Hot Idea: South Pole-Aitken (SPA) basin 2020.
[18] Pieters C. M. , J. W. Head III J. et al. JGR: Planets, 2001 V. 106, 28,001–28,022.

THE PROPOSED LANDING SITE FOR THE LUNA-25 MISSION IN THE SOUTH POLAR REGION OF THE MOON

S. G. Pugacheva, E. A. Feoktistova, V. V. Shevchenko
Sternberg State Astronomical Institute Moscow University
(*hrulis@yandex.ru*)

KEYWORDS:
Moon, landing sites, lunar mission

INTRODUCTION:

We investigated the area of the proposed landing site of the Luna-Glob mission. Currently, the area located near the Boguslawsky crater (72°54′ S, 43°16′ E) in the south polar region of the Moon was selected as the possible landing site of the Luna–Globe mission, which is planned for 2020. The area centered at the point (69°30′ S, 43°18′ E) is located to the north of Boguslavsky crater, between the Bussengo crater (70° 13′ S, 53° 44′ E) and Bussengo E crater(67° 05′ S, 46° 38′ E) [1].

We used data from the Lunar Orbiter Laser Altimeter (LOLA) Digital Elevation Model (DEM) [2] to calculate the morphometric parameters of this area, such as slope, aspect and altitude of the each surface element. The altitude difference in this area is 2–2.5 km: from –1.2 in small craters to 1.5 km on the slopes of large carters. According to our calculations, the surface slopes in the central part of the region on average do not exceed 5°, which corresponds to the criterion for selecting landing sites for future lunar missions [3]. The maximum slopes are observed on the slopes of neighboring craters and reach 20 or more degrees.

The neutron spectrometer LEND onboard LRO [4] probe has detected a decrease in the epithermal neutron flux in this area, which has been interpreted as the presence of increased hydrogen content in the soil [4]. There are several sources of hydrogen-containing compounds in the polar regions of the Moon: 1) solar wind, protons of which, interacting with regolith of the Moon, can be implanted into regolith particles or can form molecules of water, some of which migrating may subsequently accumulate in “cold traps” near the poles; 2) collisions of asteroids, comets or micrometeorites with the surface of the Moon and 3) degassing of the Moon’s interior. The lifetime of such deposits is determined by the rate of their vaporization, which is a function of temperature. Information obtained by the LEND neutron spectrometer refers to the soil layer with a thickness of 1–1.5 m. Thus, it can be assumed that the deposits of water ice, if they exist in these areas, can be under a layer of regolith with a thickness to 1.5 m.

We calculated the temperature regime and investigated the possibility of the existence of water ice in this area. The maximum temperatures in the central part of this region are in the range of 300–340 K. On some slopes these values increase to 360 K. Night temperatures drop to 90–111 K. There are no permanently shaded areas in this area. Under such conditions, water ice deposits can exist for a long time only under a layer of soil in this area. According to our calculations, the minimum soil thickness required for the existence of water ice deposits over a long period of time (1 billion years) is 0.3 m.

REFERENCES:

[1] http://wms.lroc.asu.edu/lroc/view_rdr_product/WAC_GLOBAL_P900N0000_064P
[2] https://ode.rsl.wustl.edu/moon/
[3] Flahaut J., Wöhler C., Berezhnoy A. A., Rommel D., Grumpe A., Feoktistova E. A. et al. Candidate landing sites for the Luna-25 mission // Proc. 7th Lunar Exploration Symp. 10–14 Oct. 2016, Moscow. 2016. P. 235–245.
[4] Mitrofanov I. G. et al. Testing polar spots of water-rich permafrost on the Moon: LEND observations onboard LRO // J. Geophysical Research. 2012. V. P.117.

EVOLUTION OF THE MOON AND POSSIBLE DYNAMICS OF ITS INTERIOR

N. A. Chujkova, L. P. Nasonova, T. G. Maksimova
Sternberg Astronomical Institute Moscow University, *Moscow*, *Russia*,
(*chujkova@sai.msu.ru*, *nason@sai.msu.ru*)

KEYWORDS:
Moon, evolution, internal structure, internal gravity field, convection

Introduction:

For the early stage of the Moon's development**,** a possible lunar topography and internal density distribution were determined. The distribution of anomalies of the attractive force and gravitational potential in various layers of the upper mantle is found, due to the gravity influence of the anomalous structures of the crust and mantle. An analysis of the results leads to the conclusion about the possibility of convective movements in molten electrically conductive layers of the mantle, enriched in Fe, which could generate an ancient magnetic field.

For the current state of the density structure of the Moon [1] (Chuikova et al., 2020), gravitational anomalies in various layers have also been determined, which can lead to solid-state convection in some hardened regions of the Moon.

REFERENCES:

[1] Chuikova N. A., Nasonova L. P., Maksimova T. G. Determination of Global Density Inhomogeneities and Stresses Inside the Moon // Solar System Research. 2020. V. 54. No 4. P. 1–12.

THE OPTIMAL ARRANGEMENT OF SEISMIC STATIONS ON THE MOON FOR RECORDING MOONQUAKES

V. Yu. Burmin
Schmidt Institute of Physics of the Earth, *Russian Academy of Sciences*, *Bolshaya Gruzinskaya 10*, *Moscow 123995*, *Russia* (*burmin@ifz.ru*)

KEYWORDS:
Moon, seismic stations, optimal observation system

INTRODUCTION:
The moon is the only object, except for the Earth, where seismic methods have been successfully applied, giving the most complete and objective information in the study of its internal structure.

The first lunar seismometer was installed on July 20, 1969 in the Sea of Tranquility on the visible side of the moon during the Apollo 11 expedition. He fed on solar panels and kept seismic recording only during the day. In the period from November 1969 to December 1972, on the visible side of the moon, a network of four homogeneous automatic seismic stations was created that feed on isotopic power plants designed for 10 years of continuous operation. Apollo seismometers continued to operate for eight years, during which they transmitted information on the natural seismic activity of the moon, and the structure of the lunar crust and upper mantle [Goins et al., 1981; Lognonne, 2005]. However, the deep bowels of the moon remained not accessible to the Apollo seismic network.

Since seismic stations were located within a small area on the lunar surface, such a network was not able to effectively record moonquakes occurring at arbitrary points in the bowels of the moon. Here, optimal configurations of seismic station networks are considered, which make it possible to effectively register moonquakes, which should be implemented in future seismic experiments on the Moon and other planets of the earth group.

RESULTS:
According to a study conducted by the author earlier, the optimal geometry of a network of seismological observations on a ball is a network whose observation points are located at the vertices of a regular polyhedron, having: a) triangles as faces; b) the length of the side of the face close to the specified one, in accordance with the minimum magnitude of the moonquake, so that it is recorded by at least four stations [3].

Fig. 1. A model of a network of observation points on the surface of the moon that coincides with the vertices of the tetrahedron inscribed in the lunar sphere

If any moonquake were recorded at any point on the lunar surface, then it is sufficient to place seismic stations of the optimal network at points that coincide with the vertices of one of the regular tetrahedra inscribed in the lunar ball (Figure 1). The tetrahedron has a minimum number of vertices from all regular polyhedra with triangular faces. The length of the side of the face of the tetrahedron inscribed in the lunar sphere is >>2836.67 km (Figure 1).

But since moonquakes with different magnitudes are recorded at different distances from the hypocenter, the distances between stations in the observation network must be selected in accordance with the minimum strength of the moonquakes to be recorded.

To build an optimal network, one of the regular polyhedra with triangular faces (true polyhedra) can be taken as a basis: a tetrahedron, octahedron or icosahedron inscribed in the lunar sphere. As know, the tetrahedron has 4 faces, 4 vertices and 6 edges, the octahedron has 8 faces, 6 vertices and 12 edges, and the icosahedron has 20 faces, 12 vertices and 30 edges (Figure 2). We project each of the three polyhedra from the center of the ball to the lunar surface. Then we obtain regular spherical polyhedra, the faces of which are the same equilateral spherical triangles.

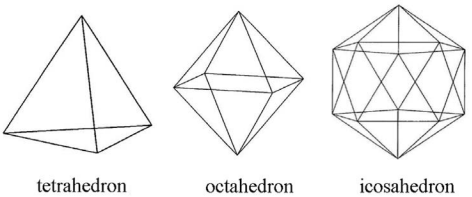

Fig. 2. True polyhedrons

Take the icosahedron as the basis. The icosahedron has the maximum number of vertices from all regular polyhedra with triangular faces. The length of the side of the face of the icosahedron inscribed in the lunar sphere is >>1826.60 km.

To obtain a system with smaller minimal bases, we divide the spherical triangles into four parts as follows. In each triangle, we interconnect along the arc of a large circle of the mid-center of its sides. As a result, we obtain a partition of each triangle into four triangles. Continuing the indicated partitioning procedure, we obtain an observation system with even smaller bases. In the general case, for an n-fold partition of the spherical polyhedron generated by the icosahedron, we have $f_n = 20 \cdot 4^n$ faces, $k^n = 30 \times 4^n$ edges and $e_n = 10 \cdot 4^n + 2$ vertices.

CONCLUSIONS:

Thus, optimal systems of teleseismic observations are covering the surface of the ball with triangles, at the vertices of which there are observation points.

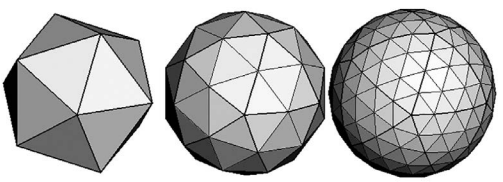

Fig. 3. An example of a multiple splitting of the surface of an icosahedron

These triangles form hexagons on almost the entire surface of the ball, at the vertices and centers of which there are observation points, and in 12 regions they form pentagons whose centers coincide with the vertices of the original icosahedron. At the same time, the optimal seismological network on the plane is also covering the plane with hexagons with observation points at their centers. It should be noted that the optimal systems of seismological observations on the ball and on the plane coincide for almost the entire surface of the ball, except for 12 regions. The sizes of these regions depend on the multiplicity of the partition of the initial icosahedron. The greater the multiplicity of the partition, the smaller these areas (Figure 3). If we take an octahedron or tetrahedron as the initial regular polyhedron, then there will be 6 and 4 such regions, but in them the triangles will form quadrangles and triangles, respectively.

The optimal system is determined not uniquely, but up to an arbitrary rotation around any of the three arbitrarily selected mutually perpendicular axes passing through the center of the ball.

REFERENCES:

[1] Goins N. R., Dainty A. M., Toksoz M. N. Lunar seismology — the internal structure of the Moon // J. Geophysical Research. 1981. V. 86. P. 5061–5074.
[2] Lognonné P., Gagnepain-Beyneix J., Chenet H. A new seismic model of the Moon: implications for structure, thermal evolution and formation of the Moon // Earth and Planetary Science Letters. 2003. V. 211. P. 27–44.
[3] Burmin V. Yu. Optimal geometry of a network of teleseismic observations // Doklady Akademii nauk. 1994. V. 344. No. 3. P. 364–367.
[4] Burmin V. Yu. Optimal location of seismic stations on the surface of the globe // Izv. RAS. Physics of the Earth. 1994. No. 12. P. 1–9.

STUDY OF THE DYNAMIC STRUCTURE OF THE NEAR–LUNAR ORBITAL SPACE

N. A. Popandopulo, T. V. Bordovitsyna, A. G. Aleksandrova, V. A. Avdyushev, I. V. Tomilova
National Research Tomsk State University, Tomsk, Russia
(*nikas.popandopulos@gmail.com*)

KEYWORDS:
Near–Lunar orbital space, dynamic structure, numerical modeling, lunar satellite lifetime

INTRODUCTION:
The knowledge of the dynamic features of the near-lunar space is necessary for its optimal mastering. This work is devoted to a study of the special features of the dynamics of the artificial Moon satellites (AMS) with intermediate and high orbits in the range of semimajor axes from 2500 to 26000 km.

RESULTS:
The AMS motion was predicted for a 10-year period using the program "Numerical Simulation of AMS Motion" developed by the authors of the report. In the process of research, the following perturbing factors were taken into account: the influence of the selenopotential up to harmonics of the 50^{th} order and degree and the attraction of the Sun and the Earth.

The results shown in Figure 1 illustrate the main feature of the dynamics of near-lunar objects in the intermediate and high orbits. The dependences of the AMS eccentricity and lifetime increase on the semimajor axis and the inclination of the orbits are well traced. These features of the dynamics of near-lunar satellites were also emphasized by other authors [1–4]. As can be seen, the increase in the eccentricity is accompanied by the drastically reduced lifetimes of satellites in the orbits.

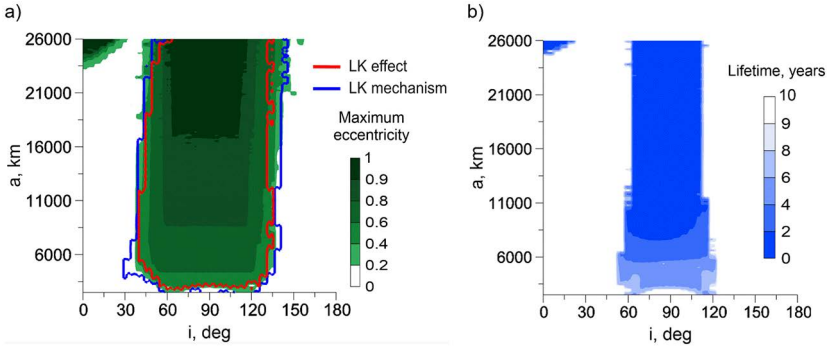

Fig. 1. Estimates of the satellite eccentricity (a) and lifetime in the orbit (b) depending on the initial values of the inclination and semimajor axis of the objects

Such increase in the eccentricity in the near-polar orbits, as a rule, is a consequence of the action of the Lidov – Kozai mechanism [5–8]; therefore, we studied this problem in more detail. This mechanism is manifested in the Lidov–Kozai resonance and effect.

The analytical method of revealing the action of secular resonances on the orbital dynamics of objects was described in detail in our work [9]. The Lidov–Kozai effect was estimated by the presence of the energy transfer between the eccentricity and the inclination while maintaining the integral $c_1 = \sqrt{1-e^2}\cdot\cos i$, and the presence of the sharp Lidov – Kozai resonance was judged by the proximity to zero of the Lidov – Kozai integral for a negative value of the Lidov integral $c_2 = \left(2/5 - \sin^2\omega\cdot\sin^2 i\right)e^2$.

Figure 1a shows contours of regions affected by the Lidov – Kozai mechanism (in dark blue color) and effect (in red color) according to our estimates.

An analysis of the results shown in Figure 1a demonstrates that the main source of the eccentricity growth in the intermediate and high orbits is the influence of the Lidov – Kozai mechanism on the AMS dynamics.

It can be clearly seen that the region of manifestation of the Lidov – Kozai effect covers the most part of the region in which the Lidov – Kozai mechanism acts on the orbital evolution of objects.

Our investigations showed that in the dynamics of objects with intermediate orbits, the Lidov – Kozai effect will be manifested through its overlap with the field action. Moreover, from our analysis of the results obtained it follows that the gravitational field of the Moon accelerates the manifestation of the Lidov – Kozai effect. The given effect is illustrated by Figure 2. Our studies showed that the higher the orbit, the smaller the manifestation of the field-induced Lidov – Kozai effect. Moreover, for objects in high orbits, the effect will be manifested practically in its pure form.

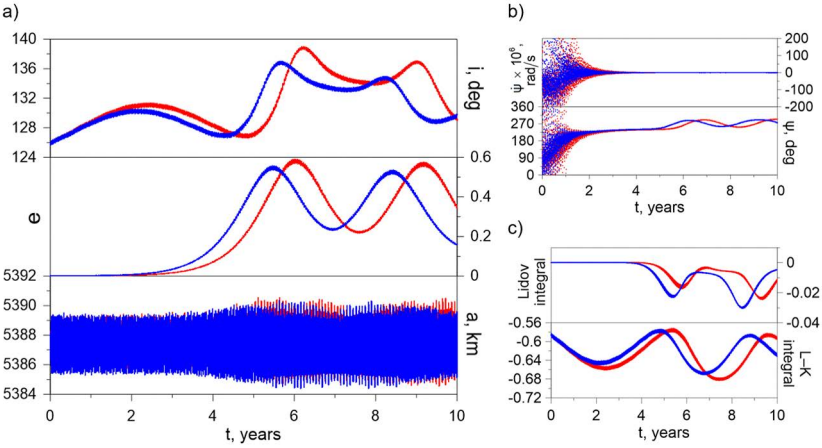

Fig. 2. Manifestation of the Lidov – Kozai effect for the object with semimajor axis less than 8500 km with allowance for perturbations from the total gravitational field of the Moon and the attraction of the Earth and the Sun (in dark blue color) and only from the Earth and the Sun (in red color): a) evolution of the orbit elements: b) resonant characteristics: c) time variations of the Lidov integral and the Lidov – Kozai integral

As to the growth of the orbit eccentricities for near-equatorial objects with semimajor axes in the vicinity of 26000 km, it is caused by the direct effect of the Earth.

CONCLUSIONS

Thus, our studies have shown that a part of the near-lunar objects has a short lifetime in the orbit, which is explained by the growth of the eccentricities of their orbits. Analyzing the results obtained, we can state that for the near-polar objects this phenomenon is caused by the influence of the Lidov – Kozai mechanism, and for the near-equatorial objects, it is caused by the direct influence of the Earth.

ACKNOWLEDGEMENTS

This work was supported by the Russian Science Foundation (Scientific Project No. 19-72-10022).

REFERENCES:

[1] Ramanan R. V., Adimurthy V. An analysis of near-circular lunar mapping orbits // J. Earth System Science. 2005. V. 114. No. 6. P. 619–626.
[2] Song Y. J., Park S. Y., Kim H. D., Sim E. S. Development of precise lunar orbit propagator and lunar polar orbiter's lifetime analysis// J. Astronomy and Space Sciences. 2010. V. 27(2). P. 97–106.
[3] Gupta S., Sharma R. Effect of Altitude, Right Ascension of Ascending Node and Inclination on Lifetime of Circular Lunar Orbits // Intern. J. Astronomy and Astrophysics. 2011. V. 1. No. 3. P. 155–163. doi:10.4236/ijaa.2011.13020.
[4] Tzirti S., Noullez A., Tsiganis K. Secular dynamics of a lunar orbiter: a global exploration using Prony's frequency analysis// Celestial Mechanics and Dynamical Astronomy. 2014. V. 118. P. 379–397.

[5] Lidov M. L. The evolution of orbits of artificial satellites of planets under the action of gravitational perturbations of external bodies// Planetary and Space Science. 1962. V. 9. Iss. 10. P. 719–759.
[6] Kozai Y. Secular perturbations of asteroids with high inclination and eccentricity // Astronomical J. 1962. V. 67. P. 591–598.
[7] Shevchenko I. The Lidov – Kozai effect — Applications in exoplanet research and dynamical astronomy. 2017. doi:10.1007/978-3-319-43522-0.
[8] Ito T., Ohtsuka K. The Lidov – Kozai Oscillation and Hugo von Zeipel // Monographs on Environment, Earth and Planets. 2019. V. 7. No. 1. P. 1–113.
[9] Aleksandrova A. G., Bordovitsyna T. V., Popandopulo N. A. et al. A New Approach to Calculation of Secular Frequencies in the Dynamics of Near-Earth Objects in Orbits with Large Eccentricities// Russian Physics J. 2020. V. 63, No. 1. P. 64–70.

DIODE LASER SPECTROSCOPY SENSOR DLS-L OF THE GC-L INSTRUMENT FOR THE LUNA-RESOURCE (LUNA-27) MISSION: SCIENTIFIC TARGETS, DESIGN OPTIONS AND FUTURE PERSPECTIVES

I. Vinogradov[1], V. Barke[1], I. Gazizov[2], V. Kazakov[1], T. Kozlova[1], Yu. Lebedev[1], V. Meshcherinov[2], A. Nosov[1], A. Rodin[2], O. Roste[1], M. Spiridonov[3], A. Stepanov[4], E. Tepteeva[2], A. Venkstern[1], S. Zenevich[2], M. Ghysels-Dubois[5], G. Durry[5], L. Bizien[6]

[1] *Space Research Institute*, *Russian Academy of Sciences* (*IKI*), *Moscow 117997*, *Russia* (*imant@iki.rssi.ru*)

[2] *Moscow Institute of Physics and Technology MIPT*, *Dolgoprudnyi*, *Moscow Region*, *Russia*

[3] *Prokhorov General Physics Institute* (*GPI*), *Russian Academy of Sciences*, *Moscow*, *Russia*

[4] *Lomonosov Moscow State University*, *Faculty of Physics*, *Moscow*, *Russia*

[5] *GSMA*, *UMR CNRS 7331*, *Université de Reims*, *BP 1039*, *51687 Reims*, *Cedex 2*, *France*

[6] *Institut Supérieur de l'Aéronautique et de l'Espace*, *10*, *avenue Edouard Belin — BP 54032*, *31055 Toulouse*, *Cedex 4*, *France.*

KEYWORDS:
Luna-Resource, lunar soil, chemical composition, isotopic ratios, tunable diode laser absorption spectroscopy

INTRODUCTION:
Lunar soil studies are planned on-board of the Luna-27 polar landing probe of the scheduled Luna-Recourse mission. A sensor, which is called DLS-L, was designed as an additional analytical unit, integrated into a Gas Chromatography (GC-L) instrument of a Gas Analytical Package, targeted to study products, pyrolytically evolved from soil samples of a close location near the Lunar probe landing point. The DLS-L aims in an independent measurement of pyrolytical output dynamics and integral content of H_2O, CO_2, and in retrieving of isotopic ratios D/H, $^{18}O/^{17}O/^{16}O$, $^{13}C/^{12}C$ for isotopologues of H_2O and CO_2. The DLS-L sensor data would help for further understanding of physics and chemistry of the Lunar body, as original data of polar Lunar soil first-ever direct study.

METHOD OF MEASUREMENT:
Advantages of tunable diode laser absorption spectroscopy (TDLAS) will provide for fine and rapid measurement of each target molecule of gas species, delivered by carrier gas He from a miniature pyrolytical cell of the GC-L instrument into the DLS-L analytical volume — a small capillary tube with edge optical windows. Gas sample will be sounded by a set of monochromatic distributed feed back (DFB) lasers, operated sequentially. The DLS-L output data will be sent back to Earth as series of instant high resolution optical transmission spectra of the sampled gas, measured at near-IR regions of 2.64 μm (for H_2O isotopologue absorption lines), 2.68 μm (H_2O and CO_2 main molecules), 2.78 μm (CO_2 isotopologues), and a set of corresponding service data (local *P*, *T* values, etc.). Actual molecular content values and isotopic ratios will be retrieved with sub-percent accuracy from absorption spectral line shapes and other recorded data.

FUTURE PERSPECTIVES:
Further and yet simple improvement of the DLS-L sensor can be done by extending of the molecular targets list, for carrying out additional measurements at near-IR ranges of 1.53 μm for H_2C_2, NH_3, HCN main molecules and of 2.44 μm for OCS molecule. Available for these ranges DFB-laser modules are completely compatible with the current DLS-L sensor configuration. Isotopic ratio for these molecules could be measured, keeping similar instrument's layout, at wavelength ranges beyond 3 μm, where molecular absorption be-

comes much stronger. DFB-lasers, emitting at those longer wavelengths, are known as interband cascade lasers (ICL) or quantum cascade lasers (QCL), and are still noticeably more demanding sources of monochromatic light. Future laser absorption spectrometer, efficiently operating at longer wavelength, both in near-IR and medium-IR ranges, could become next generation instrument for scientific payload on-board of future landing probes.

MEASUREMENTS OF THE ELECTRIC AND MAGNETIC FIELDS ONBOARD THE LUNA-26 SPACECRAFT

S. V. Kulikov[1], S. I. Klimov[1], S. P. Savin[1], V. A. Styazhkin[2], A. A. Skalsky[1], O. Santolik[3], I. Kolvasova[3]

[1] *Space Research Institute of Russian Academy of Sciences* (*IKI*), *84/32 Profsouznaya*, *Moscow*, *Russia* (*kulikov@rx24.ru*)

[2] *Pushkov Institute of Terrestrial Magnetism*, *Ionosphere and Radio Wave Propagation Russian Academy of Sciences*, *Troitsk*, *Russia*

[3] *International Accreditation Forum*, *Prague*, *Czechia*

KEYWORDS:
Moon, solar wind, Lunar magnetic field, magnetic anomalies, mini-magnetosphere, plasma waves, Luna-26

INTRODUCTION:

The Moon does not possess an intrinsic global magnetic field, but the regions of strong crustal magnetic fields have been detected on its surface [1]. Moreover, the Moon has no significant atmosphere that can protect it from solar wind protons bombardment. The interaction of the solar wind with the lunar surface and magnetic anomalies reveals a variety of interesting phenomena for an electromagnetic survey, such as backscattering of solar wind protons from the lunar surface, the formation of magnetosphere-like obstacles around lunar magnetic anomalies (mini-magnetospheres), transport of the dayside protons accelerated by the solar wind convective electric field to the lunar wake region, presence of significant wave activities at the lunar plasma environment and more [2].

The LPMS-LG (tri-axial fluxgate magnetometers) and LEMRA-L (Long-wavelength electromagnetic radiation analyzer) devices onboard the Luna-26 spacecraft reveals the possibility of the electromagnetics monitoring of the plasma environment on the low-altitude orbit (50 km) around the Moon.

REFERENCES:

[1] Coleman P. J., Schubert G., Russel C. T., Sharp L. R. Satellite measurement of the moon's magnetic field: A preliminary report // The Moon. 1972. V. 4. P. 419–429.

[2] Bhardwaj A., Dhanya M. B., Alok A., Barabash S. A new view on the solar wind interaction with the Moon // Geoscience Letters. 2015.

MAIN FEATURES OF MOON'S RADIO BEACON AND ORBITER KA-BAND RECEIVER, INCLUDED INTO LUNA-RESOURCE-1 PROJECT

A. Kosov[1], J. Ping[2], A. Gusev[3], V. Gromov[1], V. Dehant[4], S. Le Maistre[4], M. Vasilev[5]

[1] *Space Research Institute of Russian Academy of Sciences*, *84/32 Profsouznaya*, *Moscow*, *Russia*, *117997* (*akosov@iki.rssi.ru*)
[2] *National Astronomical Observatories of CAS*, *Beijing*, *China*
[3] *Kazan University*, *Kazan*, *Russia*
[4] *Royal Observatory of Belgium*, (*ROB*), *Brussels*, *Belgium*
[5] *Institute of Applied Astronomy* (*IAA RAS*), *St-Petersburg*, *Russia*

KEYWORDS:
radio science, Doppler effect, Moon, interior structure, core properties, gravity field, general relativity

INTRODUCTION:
The Russian Lunar space exploration program up to 2025 includes: the Luna-Resource orbiter and the Luna-Resource lander. Currently two different radio science (RS) instruments have been included into the projects: the radio beacon, deployed on the lander and the Ka-band receiver, deployed on the orbiter. By means of the radio beacon and the Ka-band receiver it will be possible to conduct a lot of valuable investigations and celestial mechanics experiments. Moreover, the instruments will be very useful for service tasks such as a navigation and a low rate telemetry transfer to Earth.

THE RADIO BEACON DEPLOYED ON THE LANDER:
Lander radio beacon have one *X* band receiver and two transmitters: *X* band and Ka-band. The radio beacon has three main modes of operation: autonomic mode of operation, mode of coherent transponder and mode of scientific data transmitter. In autonomic mode the frequency stability of irradiated signal will be determined by the stability of internal reference source. In coherent transponder mode, the transmitter signals will be locked on a reference signal sent from Earth. In scientific data transmitter mode the radio beacon can transmit data to Earth's antenna with speed up to 0.1 Mbps depending of performance of Earth ground station. This feature is very useful as it does not need a relay orbiter and it can be used immediately when the lander will be powered and the main radio link will not be operational yet.

The Radio Beacon instrument is a single box with mass of about 2 kg and volume of about 2 liters. There are three antennas: a patch receiver antenna at frequency 7.2 GHz (X-band up-link), a patch transmitter antenna at frequency 8.4 GHz (X-band down-link) and waveguide transmitter antenna at frequency 32 GHz (Ka-band). The main beams of the *X* band antennas are directed to the Earth, the main beam of the *Ka* band antenna is directed to zenith. The received reference signal at 7.2 GHz is converted to transmitted signals at 8.4 GHz and 32 GHz without loss of coherency. Such type of conversion is possible by means of PLL circuits with 749/880 and 749/3344 ratios for X-band and Ka-band frequency translation respectively. The instrument is capable to irradiate up to 0.1 W in each channel. The antennas gain is 4.5 dBi. The polarization of all antennas is circular right.

The instrument could be powered from lander battery or from nuclear power source. The maximum consumption power is less than 7 W.

THE KA-BAND RECEIVER, DEPLOYED ON ORBITER:
The Ka-band receiver has been included into scientific payload of the Luna-Resource-1 orbiter. The receiver is intended to obtain the signal from Lunar radio beacon or from Earth's transmitter. It will allow precise measurements of Doppler shift and, therefore, of the relative velocity and acceleration.

The reference signal at 32 GHz is radiated by Radio beacon via waveguide antenna to the zenith. By measuring the signal frequency with the orbiter receiver it is possible to measure the acceleration of the receiver with respect

to radio beacon. As a result, it will be possible to retrieve the parameters of the global gravitational field as well as the local gravitational field, which will allow to create the gravitation field map in vicinity of the Radio beacon [1].

The main parameters of the Lunar Orbiter Receiver

Central frequency	32 GHz (Ka-band)
Bandwidth	0.5 MHz
Noise temperature	150 K
Accuracy of the d*V*/d*t* measurements	$3 \cdot 10^{-3}$ cm/s^2

The receiver has two switched antennas: nadir antenna to receive signal from radio beacon and zenith antenna to receive signal from Earth transmitter.

DISCUSSION:

Scientific outcome of the RS experiments using the lander radio beacons

The list of scientific objectives for Lunar investigation by RS methods was discussed by Dehant et al. [2] and Kosov et al. [3]. The objectives includes improvement of the reference frames for the Earth, better understanding of the Moon's interior, and better determination of the parameters of General Relativity. Improvement of the gravity field near the landing site can also be added in that list.

The capabilities of scientific experiments are determined to a large degree by measurement accuracy. RS experiments in Same Beam Interferometer (SBI) mode allow to measure 3D displacements with accuracy about 0.1 mm [4]. The Radio beacon is adapted for precise ranging based on Pseudo-Noise phase modulation in agreement with recommendation for high accuracy spacecraft position measurement provided by standard of the Consultative Committee for Space Data Systems CCSDS 414.1-B-2. The ranging possibility do also allow to consider the beacon in the VLBI (Very Long Baseline Interferometry) observation, therewith making the link with the inertial frame. The Radio beacon working in coherent transponder mode could compete with Lunar Laser Ranging (LLR) [5].

Improvements on the LLR alone is already a very nice advance in Moon science. The models that sustain the geophysical interpretation of the data will have to be advanced in parallel as detailed by Kopeikin [6].

The current LLR data yield the strongest limits to date on variability of the gravitational constant [7]. The resulting RS ranging tests of gravitational physics would improve the limit by an order of magnitude. Williams et al. [8] report a test of the geodetic precession, which is a relative deviation from general relativity. As stated in Turyshev and Williams [7], the accurate RS ranging and LLR data has been able to quickly eliminate several suggested alterations of physical laws.

The Orbiter receiver is capable to measure Doppler shift with high accuracy corresponding to $3 \cdot 10^{-3}$ cm/s^2 accuracy of acceleration measurement, which is competitive with NASA GRAIL project.

CONCLUSIONS:

Together with information from radial laser ranging, the RS experiment will allow determining the position and velocity of the Moon with respect to the Earth at a never-reached precision of the millimeter level and a few hundredths of mm/s. The tangential component from VLBI together with the accurate Doppler measurements will push the insight into the Moon's orbital and rotational (librations) behaviors to as yet unknown frontiers and there with obtain information on the core of the Moon. This conclusion is further strengthened by the recent reprocessing of lunar seismic data and the findings related to a liquid core, a partial melting boundary layer, and a solid inner core inside the Moon [9, 10].

Constraining the detailed structure of the lunar core is necessary to improve our understanding of the present-day thermal structure of the interior and the history of a lunar dynamo, as well as the origin and thermal and compositional evolution of the Moon.

More knowledge of Lunar gravitational field will allows as well better understanding of Lunar internal structure.

REFERENCES:

[1] Gromov V. D., Kosov A. S. The Objectives of the Radioscience Experiment in Luna-Resource and Luna-Glob Space Projects // 6M-S3 Symp. Abstract Book. Moscow, Russia. 2015. P. 43–44 (6MS3-MN-20).
[2] Dehant V. et al. Geodesy instrument package on the Moon for improving our knowledge of the Moon and the realization of reference frames // Planetary and Space Science. 2012. V. 68. P. 94–104.
[3] Kosov A. S. et al. Radioscience experiments for Martian and Lunar missions // 8MS3 Symp. Abstract Book. Moscow, Russia. 2017. 8MS3-IM-17.
[4] Gregnanin M. et al. Same beam interferometry as a tool for the investigation of the lunar interior // Planetary and Space Science. 2012. V. 74. P. 194–201.
[5] Gromov V. D., Kosov A. S. The Ranging Accuracy of the Radioscience Experiment with the Radio-Beacon Transponder in Comparison with Laser Ranging // 7M-S3 Symp. Abstract Book. Moscow, Russia. 2016. 7MS3-PS-65.
[6] Kopeikin S. M. Millimeter Laser Ranging to the Moon: a comprehensive theoretical model for advanced data analysis // Proc. 16th Intern. Workshop on Laser Ranging Entitled 'SLR – the Next Generation'. 2008. Poznan, Poland. 2009. V. 1. P. 54–263.
[7] Turyshev S. G., Williams J. G. Space-based tests of gravity with laser ranging // Intern. J. Modern Physics. 2007. V. D16. P. 2165–2179.
[8] Williams J. G. et al. Improving LLR tests of gravitational theory // Intern. J. Modern Physics. 2004. V. D13. No. 3. P. 567–582.
[9] Weber R. C., Lin P. Y., Garnero E., Williams Q., Lognonné P. Seismic detection of the lunar core // Science. 2011. V. 331. No. 6015. P. 309–312.
[10] Garcia R. F., Gagnepain-Beyneix J., Chevrot S., Lognonné P. Very preliminary reference Moon model // Physics of the Earth and Planetary Interiors. 2011. V. 188. P. 96–113.

SUNRISE, SUNSET AND CULMINATION OF STARS AND BODIES OF THE SOLAR SYSTEM ON THE LUNAR SKY

B. A. Epishin, M. I. Shpekin
Kazan Federal University, Kazan
(*epishin.boris@yandex.ru; MichaelS1@yandex.ru*)

KEYWORDS:
Astrometric observatory, ephemeris, coordinates in lunar sky, Solar System bodies, computer program, physical libration

This report is a continuation of the cycle of the author papers related to the development of the project of the "on-lunar" astrometric observatory [4–7].

The report presents a new computer program for calculating the rising and setting, as well as the culmination of Solar System objects in the lunar sky for a given topocenter on the lunar surface. The results of calculations for the star, the Sun and the Earth are presented in two versions: in the first, the topocenter is located in the circumpolar region of the northern hemisphere, in the second — near the center of the western hemisphere in the region of the Orientale Mare.

For these calculations, we have developed C+ program using WPF technology. Figure 1 shows the program interface. The initial data is the choice of a celestial object: Sun, Earth, Mercury, Venus, Mars, Jupiter, Saturn, Uranus, Neptune, Pluto and star. If star is selected, we take the star coordinate from the list of the catalog of bright stars (about 800) [1] included in the program. Next, we enter the selenographic latitude and longitude of the observation topocenter. We also indicate the period: the beginning and end of the ephemeris and enter the difference in seconds between ephemeris and universal time.

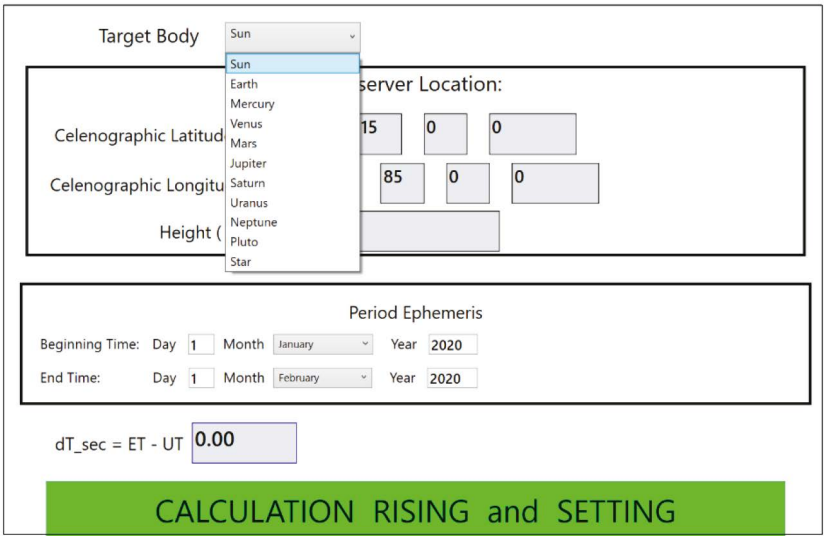

Fig. 1. View of the calculation program interface of rises, sets and culminations of celestial objects in the lunar sky for a given topocenter on the lunar surface

The calculations were carried out on the basis of barycentric coordinates of celestial objects of the DE 430 JPL theory [2]. The physical libration of the Moon when calculating the topocentric coordinates of celestial objects was taken into account according to the algorithm of the Russian Yearbook [3].

For example, the Polar star, the Sun and the Earth were taken. It should be noted right away that the north pole of rotation of the lunar celestial sphere

will be in the Draco constellation, while on Earth it is located in the Ursa Minor constellation. From Table 1 it can be seen that the Polar star in the upper culmination approaches almost to the zenith, and in the lower one — rather high above the northern part of the horizon. The Sun on the Moon will rise or set in about an earth month (Table 2). The time from sunrise to upper culmination is approximately one week, from upper culmination to sunset — also a week. And this means from sunrise to sunset a lunar day lasts two weeks. The Earth on the Moon always moves in a limited area of he sky in the form of an ellipse with a semi-major axis of about 15 degrees. The location of the Earth in the lunar sky depends on the location of the observer on the lunar surface. For example, in the central region of the visible hemisphere of the Moon, the Earth will be visible near the zenith and never goes beyond the horizon. From the territory of the lunar marginal zone, the Earth will be visible near the lunar horizon. From here one can observe the rising and setting of the Earth, due to the libration of the Moon (Table 3, as well as our analysis, published earlier [4]).

Table 1. The culmination of the Polar star (№11767 HIP) on the Moon during one and half months for a topocenter with selenographic latitude of 75° N and longitude of 85° W

Culmination	Date (UTC)	Altitude
Lower	3 May 2020 08:03:55	+50° 58′ 42″
Upper	16 May 2020 23:29:12	+81° 00′ 50″
Lower	30 May 2020 15:46:23	+51° 00′ 50″
Upper	13 June 2020 07:12:39	+81° 03′ 08″

Table 2. Sunrises and sets and culminations of the Sun on the Moon during the month for the topocenter with selenographic latitude of 15° S and longitude of 85° W (Spring Lake)

Phenomenon	Date (UTC)	Coordinates
Sunrise	7 May 2020 05:38:18	Azimuth = –88° 55′ 42″
Upper culm.	14 May 2020 15:23:47	Height = +75° 53′ 52″
Sunset	22 May 2020 00:24:40	Azimuth = +89° 10′ 13″
Lower culm.	29 May 2020 08:29:37	Height = –74° 24′ 15″
Sunrise	5 June 2020 17:22:51	Azimuth = –89° 39′ 16″

Table 3. Earth rises and sets on the Moon during two months for the topocenter with selenographic latitude of 15 S and longitude of 85 W (Spring Lake)

Phenomenon	Date (UTC)	Azimuth
Lower	9 May 2020 03:00:50^{s}	–87° 58′ 15″
Upper	16 May 2020 20:12:45	–97° 01′ 23″
Lower	6 June 2020 11:19:24	–89° 36′ 50″
Upper	13 June 2020 06:23:30	–97° 08′ 35″

It is important to note that all calculations in the developed program are autonomous and independent from yearbooks. This can help in organizing and conducting astrometric observations at the lunar observatory. Knowing the exact movement of celestial objects in the lunar sky, it is possible to determine with high accuracy the selenocentric coordinates of the observatory on the Moon. And knowing the exact location of the observer, conduct high-precision astrometric observations from the surface of the Moon. On the basis of such observations, it is possible to determine the parameters of the physical libration of the Moon with high accuracy. This will make it possible to build a high-precision model of the Moon's physical libration.

REFERENCES:

[1] Astronomical Yearbook for 2011. SPb.: IAA RAS, 2011. 732 p.
[2] JPL planetary and lunar ephemerides. ftp://ssd.jpl.nasa.gov/pub/eph/planets/.
[3] Brumberg V. A., Glebova N. I., Lukasheva M. V., Malkov A. A., Pit'eva E. V., Rumyantseva L. I., Sveshnikov L. L., Fursenko M. A. Rasshirennoe ob"yasnenie k "Astrono-

micheskomu ezhegodniku" [Expanded explanation to the "Astronomical Yearbook"]: Trudy IPA RAN. 2004. No. 10. P. 62–67.

[4] Epishin B. A., Shpekin M. I. Analysis of apparent motion of Sun, Earth and stars on the lunar sky // 8th Moscow Intern. Solar System Symp. (8M-S3) 2017. IKI RAN, Moscow: book of abstr. 2017. P. 361–363. https://ms2017.cosmos.ru/docs/8ms3-abstract_book.pdf.

[5] Epishin B. A., Shpekin M. I. Analysis of occultations of stars by the Earth on the lunar sky // 9th Moscow Intern. Solar System Symp. (9M-S3) 2018. IKI RAN, Moscow: book of abstr. P. 381–383. https://ms2018.cosmos.ru/docs/9m-s3-abstract-book.pdf.

[6] Epishin B. A., Shpekin M. I. The development ephemeris software for astrometric observations from the surface of the Moon // Intern. Symp. "AstroKazan-2016" Lunar Exploration and Space Technology Heritage, KFU. Kazan, 2016. 4 p. http://kpfu.ru/portal/docs/F431945769/MAKET_FINAL.pdf.

[7] Shpekin M. I. Some principles of creating astrometric observatory on the Moon territory // 5th Moscow Intern. Solar System Symp. (5M-S3) 2014. IKI RAN, Moscow: book of abstr. 2014. P. 207ab–208ab. http://ms2014.cosmos.ru/sites/ms2014.cosmos.ru/files/5m-s3_abstract_book.pdf.

TREMBLING MOON CAUSING REPLENISHMENT OF ITS ATMOSPHERE AND REGOLITH LAYERING

G. G. Kochemasov
IGEM of the Russian Academy of Sciences, 35 Staromonetny, 119017 Moscow, Russia (*kochem.36@mail.ru*)

KEYWORDS:
Moon, wave structures, fine microwave warping, sparse atmosphere, regolith layering.

Intersecting ripples of certain wavelengths and produced them tectonic granules are inversely proportional to the satellite main orbital frequencies (1/1 month — πR/4 and 1/1 year — πR/60 for the Moon) and calculated side frequencies (division and multiplication of the higher frequency by the lower one- πR/15 and πR/240) [6]. The granules can be observed on the lunar surface more or less pronounced. Often they are confused with impact craters but their even sizes and regular shoulder-to-shoulder disposition in lines and grids normally solve the problem.

Rare chances present the landings of the Chinese probes Chang'E 3and4 on the Mare Imbrium and SPA areas. Landing surface possibly cleaned by thruster jets of landing device revealed clear crossing lineation of a few centimeters spacing and produced them granules. This very fine granulation fortunately can be calculated comparing it with a track of the Yutu' rover weel. (about 10 cm wide) (Figure 2, 3). An explanation of the granule size should be done with the above modulation procedure using two frequencies as was done for some celestial bodies earlier [6–9]. The Moon main frequencies are 1/1 year and 1/1 month, the modulating Galaxy frequency is about 1/200 000 000 years. A scale is the Earth's orbiting period 1 year with the corresponding tectonic granule size πR/4 [7–9].

CALCULATIONS FOR THE MOON:
(1y. : 200 000 000y)πR = (1:200 000 000) 3.14×1738 km = 5.46 cm wave length for the circumsolar orbiting (or 0.46 cm wavelength for the around Earth orbiting). By the same galactic frequency modulation one obtains enigmatic metric radio waves for the Sun and decametric waves for Jupiter [7–9]. Radio emission of the Moon at 2.5 cm wavelength was described in Berezhnoi et al., 2001 [1].

The Chinese Chang'E-1 orbiter was equipped with a passive microwave radiometer (MRM) to measure the natural microwave emission from the lunar surface. The microwave emission, characterized by a frequency-dependent brightness temperature (TB), is related to the physical temperature and dielectric properties of the lunar surface. The new features revealed and their possible connections with the lunar geology were discussed. Daytime brightness temperatures are found to correlate well with TiO_2 abundance by numerical analysis [12].

In an earlier publication Chan et al. [2] indicated that resulting maps from the high frequency microwave channel show lunar topographic signatures with close similarity to those seen in Clementine's lunar topographic maps, while the low frequency channels reveal intriguing lunar surface properties not previously observed.

Thus, some relationship between lunar microwave emission and the geological background was discussed earlier [1, 2, 12]. In the present work we show existence of the fine crossing rippling of the lunar surface at the microwave lengths and its origin indicating at galactic structuring trace.

Similar fine cm-size crossing rippling is clear in images of the Apollo-11 (Figure 1). Thus, this modulation process, involving orbital frequencies of the Moon and Galaxy, is observed at the northern and southern lunar hemispheres as well as in the near and far lunar sides. Now, one might speak

about the whole Moon modulation event. It is worth to note that the same approach is applied to calculating frequencies of the Martian global dust storms (joint consideration of the rotation and orbiting of Mars-spin-orbit coupling) [10, 13].

Fig. 1. Ouldrin on the Moon

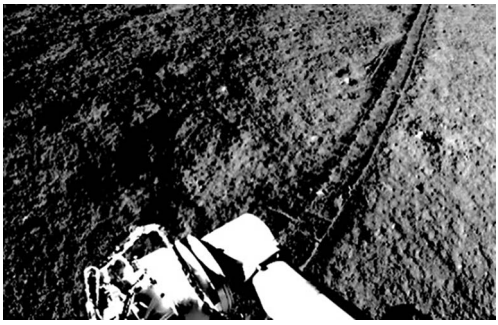

Fig. 2. Yutu-1 rover weel track on Mare Imbrium surface clearly showing fine intercrossing lineation (centimeters spacing). A portion of Chang'E 3 image 00

Fig. 3. Yutu-2-wheel-tracks-350x350-jpg.

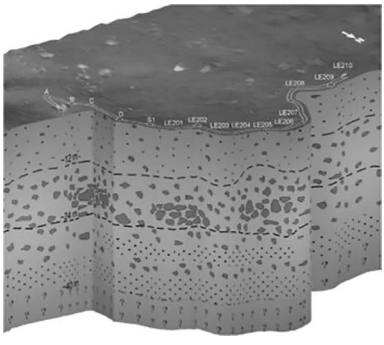

Fig. 4. Regolith layering. F3.large_-350x307.jpg. Data of Chang'4.

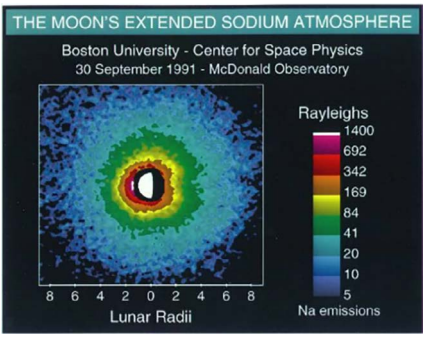

Fig. 5.The moon's sodium atmosphere

It is commonly accepted that in formation of the very thin lunar atmosphere [Figure 5] participate the solar wind, the UV radiation, steady bombardment of micrometeoroids. As a result, the whole spectra of elements and compounds were reported: alkali, rare gases, hydrogen, carbon, methane [3–5, 14, 15]. We suppose that to the listed agents should be added constant during billions of years trembling the satellite in the microwave diapason due to modulation of around Earth frequency by orbiting in Galaxy (sweeping out elements and compounds from the lunar lithosphere).

Not less important result of the fine microwave trembling the Moon is in regolith layering. The recent data of the Chang-4 show that in the SPA Basin along track of the rover the regolith cover is layered: the upper about 12 m are composed of finer fragments than the full of larger fragments underlying layer (24 m, Figure 4) This might be explained by that the upper finer fragments are predominantly less dense that the lower larger ones composed of intergrowths silicates with native iron [11].

REFERENCES:

[1] Berezhnoi A. A., Bervalds E., Khavroshkin O. B., Ozolins G., Shevchenko V. V., Tsyplakov V. V. Radio emission of seismic origin from the Moon at 25 mm during the Leonid 2000 meteor shower // 1st Convention of Lunar Explorers. 8–10 March, 2001: Programme and Contributed Abstracts. Palais de la Découverte, Paris, France. 2001. P. 2.

[2] Chan K. L., Tsang K. T., Kong B., Zheng Y-C. Lunar regolith thermal behavior revealed by Chang'E-1 microwave brightness temperature data // Earth and Planetary Science Letters. 2010. V. 295.(1–2). P. 287–291.

[3] Cook J. J. C., Stern S. A., Feldman P. D., Gladstone G. R., Retherford K. D., Tsang C. C. C. New upper limits on numerous atmospheric species in the native lunar atmosphere// Icarus. 2013. V. 225. P. 681–687.

[4] Hodges R. R. Jr. Methane in the lunar exosphere: Implications for solar wind carbon excape // Geophysical Research Letters. 2016. V. 43. P. 6742–6748.

[5] Killen R. M., Ip W.-H., The surface-bounded atmospheres of Mercury and the Moon // Reviews Geophysics. 1999. V. 37. P. 361–406.

[6] Kochemasov G. G. On one condition of further progress in lunar studies // 1st Convention of Lunar Explorers. 8–10 March, 2001: Programme and Contributed Abstracts. Palais de la Découverte, Paris, France. 2001. P. 26.

[7] Kochemasov G. G. Universe of oscillations: sound-radiowaves-gamma-rays-ether // Geophysical Research Abstracts. 2003. V. 5. Atr. 02159.

[8] Kochemasov G. G. () Wave modulations in the Solar system bodies and their radio emissions // Geophysical Research Abstracts. 2008. V. 10. Art. EGU2008-A-01272. SRef-ID: 1607-7962/gra/EGU2008-A-01272, EGU General Assembly 2008.

[9] Kochemasov G. G. Radiowaves and tectonic dichotomy: two sides of one coin // Geophysical Research Abstracts. 2002. V. 4. European Gepphysical Society XXVII General Assembly. Nice, France, 21–26 April 2002.

[10] Kochemasov G. G. Modulated wave frequencies in the Solar system and Universe // Universal J. Physics and Application. 2018. V. 12(4). P. 68–75. doi:10.13189/ujpa.2018.120402.

[11] Kochemasov G. G. Possible Fe-metal enriched areas in the SPA Basin // Developing a New Space Economy. 2019. 5024.pdf.

[12] Zheng Y. C., Tsang K. T., Chan K. L., Zou Y. L., Zhang F., Ouyang Z. Y. First microwave map of the Moon with Chang'E-1 data: the role of local time in global imaging // Icarus. 2012. V. 219. Iss. 1. P. 194–210.

[13] Shirley J. H. Orbit-spin coupling and the circulation of the Marian atmosphere // Planetary and Space Science. 2017. V. 141. P. 1–16. doi:10.1016/j.pss.2017.04.006.

[14] Yokota Sh., Terada K., Saito Y. et al. KAGUYA observations of indigenous carbon ions from the Moon // Science Advances. 2020. V. 6. No. 19. eaba 1050. doi:10.1126/sciadv.aba1050.

[15] Zhang A., Wieser M., Wang C. et al. Emission of energetic neutral atoms measured on the lunar surface by Chang'E-4 // Planetary and Space Science. 2020. V. 189. doi:org/10.1016/j.pss.2020.104970.

THE 10 MICRON SILICATE FEATURE IN THE AGGLOMERATED DEBRIS PARTICLES

E. Chornaya[1,2], E. Zubko[3], G. Videen[3,4]
[1] *Far Eastern Federal University, 8 Sukhanova St., Vladivostok 690950, Russia (ekaterina.d.chornaya@gmail.com);*
[2] *Institute of Applied Astronomy of RAS, 10 Kutuzova Emb., Saint-Petersburg, 191187, Russia;*
[3] *Humanitas College, Kyung Hee University, 1732 Deogyeong-daero, Yongin-si, Gyeonggi-do 17104, Republic of Korea*
[4] *Space Science Institute, 4750 Walnut Street, Boulder Suite 205, CO 80301, USA*

KEYWORDS:
Comets; dust; thermal emission; mid-IR spectrometry; 10-μm silicate feature; modeling; agglomerated debris particles; discrete dipole approximation.

INTRODUCTION:
Mid-IR observations of various comets reveal the so-called *10-μm silicate feature*, a series of peaks arising in their spectra between 8 and 13 μm (e.g., [1, 2]). These peaks result from stretching vibrations in Si–O bonds in the silicate species of comets [2]. It has long been thought that the silicate feature places a strict constraint on size and/or morphology of dust in comets. Namely, if dust particles are compact, their radius should not exceed 1 μm; otherwise, particles must have a very fluffy morphology with their constituents being smaller than 1 μm [2]. Such a constraint, however, was inferred with an oversimplified spherical model of cometary dust particles [3]. Recent laboratory measurements of irregularly shaped olivine particles demonstrated this constraint being overrestrictive; even millimeter-sized particles are capable of producing the 10-μm silicate feature [4]. In this work we study the 10-μm silicate feature in the agglomerated debris particles. These are highly realistic model particles (see ten exemplars on top of Fig. 1), whose irregular shape mimics what was found in cometary dust *in situ* (e.g., [5]). Furthermore, agglomerated debris particles have proven capability of fitting astronomical observations of comets in the visible (e.g., [6] for review). In particular, they satisfactorily reproduce polarimetric observations of various comets over a wide range of phase angle [7]. It is of high practical interest, therefore, to investigate the applicability of the agglomerated debris particles also to mid-IR observations of comets.

MODELING THERMAL EMISSIVITY:
Thermal emissivity of a target $E(\lambda,T)$ is immediately interrelated to its absorptivity $A(\lambda,T)$ via the *Kirchhoff's law of thermal radiation*: $E(\lambda,T) = A(\lambda,T)\,BB(\lambda,T)$ (e.g., [8]). Here, λ and T stand for wavelength and temperature, respectively, and $BB(\lambda,T)$ denotes the function of the Black-body thermal radiation. Therefore, investigation of the emissivity of a given object implies studying its absorptivity.

We study absorption cross section C_{abs} (e.g., [8]) of agglomerated debris particles using the discrete dipole approximation (DDA). We refer to reference [6] for more details on the algorithm of generation of the agglomerated debris particles and on DDA computation of their light-scattering response. The absorption cross section depends on the complex refractive index of their material m and by ratio of the radius r to λ of the incident radiation. We adapt m for Mg-rich pyroxene glass ($MgSiO_3$) from [9] and investigate particle radii r = 1, 5, 10, and 20 μm over the wavelength range λ = 8–13.5 μm. In each pair of m and r, we consider a minimum 500 randomly generated samples for statistical reliability.

RESULTS AND DISCUSSION:
The four lower panels in Fig. 1 show spectra of C_{abs} of agglomerated debris particles of different size. In all cases, one can see a noticeable excess of absorptivity compared to the bottom end of spectrum, λ = 8 μm. This is consistent with finding of 10-μm silicate feature in [4] in olivine particles whose size significantly exceeds the 1-μm constraint drawn in [3].

Another interesting phenomenon is the shift of maximum of C_{abs} with increasing particle size. Indeed, while the smallest agglomerated debris particles with r = 1 μm reveal a maximum of C_{abs} at λ = 9.4 μm, the particles with r = 5 μm show it at λ = 10.2 μm, r = 10 μm – at λ = 10.8 μm, and r = 20 μm – at λ = 11.4 μm. Therefore, the series of peaks in the mid-IR spectra of comets around λ ~ 10 μm might be indicative of a non-monotonic size distribution of dust particles.

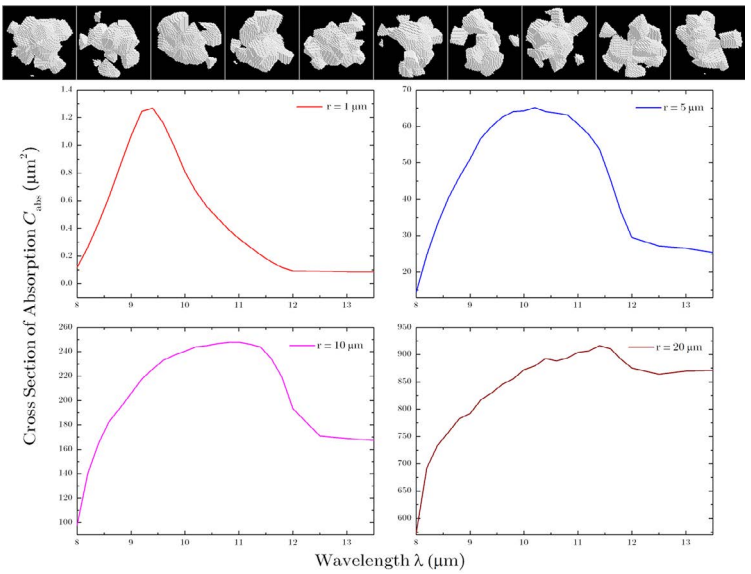

Fig. 1. Ten samples of the agglomerated debris particles (top) and mid-IR spectra of their cross section of absorption C_{abs} (middle and bottom) at four different sizes (see the legend and text).

It is finally worth noting that the polarimetric response from comets in the visible is dominated by dust particles whose radii do not exceed 3 μm [6]. On the other hand, as it appears from Fig. 1, the 10-μm silicate feature may be produced by larger particles. Such particles produce a minor effect on polarization. This may explain the lack of significant correlation between polarization and the 10-μm silicate feature that was noticed in some comets (e.g., [10]).

REFERENCES:

[1] Gehrz, R. D., Ney, E. P. 0.7- to 23-μm photometric observations of P/Halley 1986 III and six recent bright comets // Icarus. 1992. V. 100. P. 162-186.
[2] Hanner M. S., Bradley J. P. in Comets II, eds. M. C. Festou, H. U. Keller, H. A. Weaver. University of Arizona Press, 2004. 555 p.
[3] Hanner M. S., Veeder G. J., Tokunaga A. T., The dust coma of comet P/Giacobini-Zinner in the infrared // Astron. J. 1992. V. 104. P. 386-393.
[4] Chornaya E., et al. Revisiting the particle-size constraint of the 10-μm silicate feature // Icarus. 2020. V. 350. Article ID: 113907.
[5] Chornaya E., et al. Imaging polarimetry and photometry of comet 21P/Giacobini-Zinner // Icarus. 2020. V. 337. Article ID: 113471.
[6] Zubko E., Videen G., Arnold J. A., MacCall B., Weinberger A. J., Kim S. S. On the small contribution of supermicron dust particles to light scattering by comets // Astrophys. J. 2020. V. 895. Article ID: 110.
[7] Zubko E., Videen G., Hines D. C., Shkuratov Yu. The positive-polarization of cometary comae // Planet. Space Sci. 2016. V. 123. P. 63–76.
[8] Bohren C.F., Huffman D.R. Absorption and scattering of light by small particles. Wiley, New York, 1983. p.
[9] Dorschner J., et al. Steps toward interstellar silicate mineralogy. II. Study of Mg-Fe-silicate glasses of variable composition // Astron. Astroph. 1995. V. 300. P. 503–520.
[10] Manset N., Bastien P. Polarimetric Observations of Comets C/1995 O1 Hale-Bopp and C/1996 B2 Hyakutake // Icarus. 2000. V. 145. P. 203–219.

BLUE COLOR OF DISINTEGRATING COMET C/2019 Y4 (ATLAS)

A. Kochergin[1,2], O. Ivanova[3], E. Zubko[4], M. Zheltobryukhov[2], E. Chornaya[1,2], M. Husarik[3], G. Videen[4,5], I. Luk'yanyk[6], G. Kornienko[2], S. S. Kim[4,7], D. V. Glamazda[8], A. M. Sobolev[8]

[1] *Far Eastern Federal University, 8 Sukhanova St., Vladivostok 690950, Russia, (kochergin.av@outlook.com)*

[2] *Institute of Applied Astronomy of RAS, 10 Kutuzova Emb., Saint-Petersburg, 191187, Russia*

[3] *Astronomical Institute of the Slovak Academy of Sciences, SK-05960 Tatransk´a Lomnica, Slovak Republic*

[4] *Humanitas College, Kyung Hee University, 1732 Deogyeong-daero, Yongin-si, Gyeonggi-do 17104, Republic of Korea*

[5] *Space Science Institute, 4750 Walnut Street, Boulder Suite 205, CO 80301, USA*

[6] *Taras Shevchenko National University of Kyiv, Astronomical Observatory, 3 Observatorna Str., 04053 Kyiv, Ukraine*

[7] *Department of Astronomy and Space Science, Kyung Hee University, 1732 Deogyeong-daero, Yongin-si, Gyeonggi-do 17104, Republic of Korea*

[8] *Kourovka Astronomical Observatory, Ural Federal University, 19 Mira St., Ekaterinburg 620003, Russia*

KEYWORDS:
comet C/2019 Y4 (ATLAS), photometry, dust, color

INTRODUCTION:
Comets preserve the least processed materials of the time of Solar System formation. Studying such materials can provide clues for better understanding the circumstances of Solar-System formation and, hence, planetary systems around other stars. This causes great interest in investigation of comets by means of ground-based astronomical techniques and *in situ* space probes. Over their five-billion-year life comets may also experience multiple close encounters with the Sun, whose radiation along with meteoroid bombardment could significantly alter the uppermost layer of their nucleus. Such a layer would not necessarily be representative of the pristine materials. On the other hand, this layer also feeds activity of a comet upon its approach to the Sun, contaminating the coma with processed dust. It is significant that these processed dust particles may appear at higher volume concentration in the vicinity of the nucleus, where space probes are aimed at collecting samples. This may somewhat distort the conclusions on the microphysics of pristine dust particles (e. g., [1]). However, such contamination is expected to be lower in disintegrating comets as their nuclei disrupt, emanating an enormous amount of pristine dust particles preserved beneath the outermost layer. In this short paper, we report results of the *VR* photometry of disintegrating Comet ATLAS (C/2019 Y4) that was observed in late April through the beginning of May, 2020.

OBSERVATIONS:
The color of light scattered by comets is determined by the microphysical and chemical properties of its dust. While it was long thought that the dust in comets is red in appearance [2], recent studies reveal it is not always the case [3, 4]. What is even more important it is that a single photometric observation may hardly characterize the color of a given comet as it can be the subject of fast and dramatic variations. We, therefore, repeated photometric observations of disintegrating Comet ATLAS on five epochs, April 18, 26, 29, and May 4 and 13 of 2020.

Four observations were conducted at the Ussuriysk Astrophysical Observatory, a division of the Institute of Applied Astronomy of RAS (code C15; Russia), using a 0.25–m telescope (F = 0.753 m). This telescope is equipped with a commercially available CCD detector *FLI ProLine PL9000* (resolution — 3056×3056, size of pixel — 12 μm) and the broadband V, R, and I filters of the

standard *Johnson – Cousins* photometric system. Their efficient wavelengths are $\lambda_V = 0.55$ μm, $\lambda_R = 0.64$ μm, and $\lambda_I = 0.79$ μm, respectively. Each night we repeated measurements some 10 to 16 times. All images were processed using the Image Reduction and Analysis Facility (IRAF) software system for reduction and analysis of astronomical data. The data reduction includes dark-frame subtraction, removal of cosmic-ray events, and flat-field correction.

On April 18 and May 13, 2020, a *Satelliten Beobachtung Gerät* telescope (Schmidt optical system, $D = 0.5$ m, $F = 0.788$ m) of the Kourovka Astronomical Observatory (KAO), Ural Federal University, Russia, was used to observe the comet in the Johnson – Cousins *V* and *R* filters. Images were obtained with an *Alta U32* CCD camera (*Apogee*, USA), resolution 2184×1472 pixels and 6.8–μm pixel. More details on this instrument can be found elsewhere [5]. Measurements of the comet were repeated 2–4 times in each filter, and images were processed in the same way as described above.

RESULTS AND DISCUSSION:

Figure 1 shows the photometric image of Comet ATLAS obtained through the *I* filter on April 29 of 2020. The yellow circle marking the photometric center has projected radius of 20,000 km. Within this aperture we integrate the signal in all photometric filters. As one can see, it embraces a considerable part of the apparent coma.

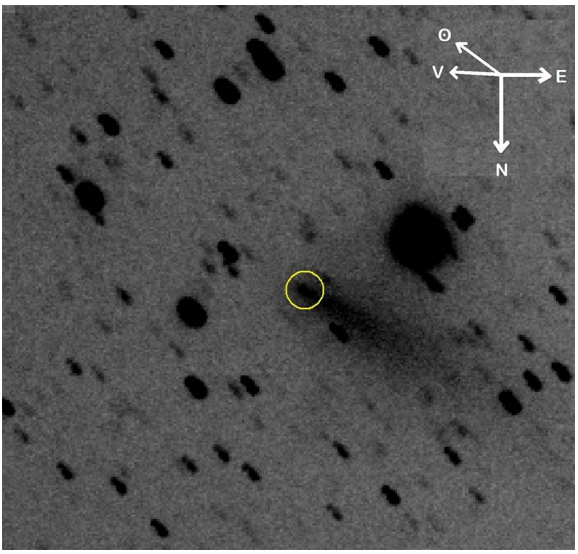

Fig. 1. Photometric image of disintegrating Comet ATLAS obtained on April 29 of 2020 with the *I* filter

Using these observations we compute the true color index of the comet that is already compensated for the color of the solar radiation adapted from [6]. The results for the pair of *V* and *R* filters are summarized in Table 1. Sequentially, the columns show the date, average color index, standard deviation describing scattering of results of individual measurements, and standard deviation of the average color index. The color of comets is characterized with the color slope *S* (e. g., Eq. 1 of [4]), shown in the sixth column, with its uncertainty in the seventh column.

Negative values of the color slope *S* in Table 1 suggest blue color of Comet ATLAS. As one can see, there is reasonable quantitative agreement between the results obtained at the two observatories in nearby epochs. For instance, on the first epoch, they suggest moderately negative values of the color slope in Comet ATLAS, which are consistent with what was previously detected in other comets [3, 4]. Interestingly, in mid-April, polarimetric observations of Comet ATLAS have revealed its similarity to Comet C/1995 O1 (Hale-Bopp) [7]. It is significant that the dust population in Comet Hale-Bopp was also found to be blue in appearance on some epochs [8].

Table 1. the *V*–*R* color of disintegrating Comet ATLAS

Date	*V*–*R*, mag	σ, mag	σ_{av}, mag	S, % per 0.1 μm	σ_S, % per 0.1 μm	Observatory
18.04	−0.190	0.090	0.032	−19.4	3.3	C15
18.04	−0.134	0.081	0.022	−13.7	2.3	KAO
26.04	−0.465	0.080	0.022	−46.9	2.2	C15
29.04	−1.034	0.068	0.026	−98.5	2.1	C15
04.05	−0.879	0.101	0.030	−85.3	2.6	C15
13.05	−0.664	0.234	0.058	−65.9	5.4	KAO

However, the strength of the blue color in Comet ATLAS became truly outstanding in late April through the beginning of May. One could suggest, therefore, a significant contribution of gaseous emissions into the signal measured with the broadband *V* filter. On the other hand, such an explanation would not be consistent with the high positive polarization measured in Comet ATLAS with the *V* filter during similar epochs [7]. This implies the blue color of Comet ATLAS would be attributed to its dust particles. While strongly blue color of disintegrating Comet ATLAS is confirmed by at least two independent observational campaigns, the mechanism(s) governing this phenomenon is poorly understood and is a subject for further investigation.

REFERENCES:

[1] Zubko E. et al. Evaluating the carbon depletion found by the Stardust mission in Comet 81P / Wild 2 // Astron. Astrophys. 2012. V. 544. Article ID: L8.
[2] Jewitt D., Meech K. J. Cometary grain scattering versus wavelength, or, “What color Is comet dust?” // Astrophysical J. 1986. V. 310. P. 937–952.
[3] Ivanova O. et al. Colour variations of Comet C / 2013 UQ4 (Catalina) // Mon. Not. Roy. Astron. Soc. 2017. V. 469. P. 2695–2703.
[4] Luk’yanyk I. et al. Rapid variations of dust colour in comet 41P/Tuttle251 – Giacobini – Kresák // Mon. Not. Roy. Astron. Soc. 2019. V. 485. P. 4013–4023.
[5] Glamazda D. V. SBG camera of Kourovskaya astronomical observatory // Astrophys. Bull. 2012. V. 67. P. 242–248.
[6] Willmer C. N. A. The absolute magnitude of the Sun in several filters // Astrophys. J. Supp. Ser. 2018. V. 236. Art. ID: 47.
[7] Zubko E. et al. Polarization of disintegrating Comet C/2019 Y4 (ATLAS) // Mon. Not. Roy. Astron. Soc. 2020. V. 497. P. 1536–1542.
[8] Weiler M. et al. The dust activity of comet C/1995 O1 (Hale-Bopp) between 3 AU and 13 AU from the Sun // Astron. Astrophys. 2003. V. 403. P. 313–322.

CHARACTERIZING PRIMORDIAL DUST IN COMETS: IMPLICATION TO C/2019 Y4 (ATLAS)

E. Zubko[1], M. Zheltobryukhov[2], E. Chornaya[3,2], A. Kochergin[3,2], G. Videen[1,4], G. Kornienko[2], S. S. Kim[1,5]

[1] *Humanitas College, Kyung Hee University, 1732 Deogyeong-daero, Yongin-si, Gyeonggi-do 17104, Republic of Korea* (*evgenij.s.zubko@gmail.com*)

[2] *Institute of Applied Astronomy of RAS, 10 Kutuzova Emb., Saint-Petersburg, 191187, Russia*

[3] *Far Eastern Federal University, 8 Sukhanova St., Vladivostok 690950, Russia*

[4] *Space Science Institute, 4750 Walnut Street, Boulder Suite 205, CO 80301, USA*

[5] *Department of Astronomy and Space Science, Kyung Hee University, 1732 Deogyeong-daero, Yongin-si, Gyeonggi-do 17104, Republic of Korea*

KEYWORDS:
comet C/2019 Y4 (ATLAS), polarimetry, disintegration, dust, carbonaceous materials, silicates

INTRODUCTION:

Comets are believed to be remnants of planetesimals from the time of Solar System formation. Therefore, they are considered as reservoirs of material of Solar–System formation in its least processed form. On the other hand, during their subsequent evolution, comets may also experience numerous close approaches to the Sun that allow the development of a refractory surface layer under repeated exposure to the solar radiation, solar wind, and meteoroid bombardment. Such a crust resembles the regolith surface of asteroids morphologically. It is significant that the crust particles being emanated into a cometary coma along with the pristine dust may put a bias on our retrievals of dust microphysics in the early Solar System. However, the relative contribution of the crust particles gets reduced in disintegrating comets because a disruption causes a nearly instant release of significant quantity of pristine material from the inner part of the nucleus. In this work we report polarimetric observations of Comet ATLAS (C/2019 Y4) whose disintegration started in early April of 2020 [1].

OBSERVATIONS:

Interaction of unpolarized solar radiation with randomly oriented cometary dust particles produces linearly polarized scattered radiation, whose electric field vector lies perpendicular to or coincident with the scattering plane defined by the locations of the Sun, the comet, and the observer [2]. The degree of polarization of this scattered field is defined by $P = (F_{\perp} - F_{||})/(F_{\perp} + F_{||})$, where $F_{\perp}$ and $F_{||}$ are the fluxes of the scattered light whose electric fields vibrate perpendicular or within the scattering plane, respectively. P is often expressed in percent. It is significant that P is dependent on the geometry of observation / illumination and, hence, it is a function of phase angle α.

We started polarimetric observations of Comet ATLAS on March 15 of 2020, several weeks before disintegration, with the goal of measuring its polarimetric response over an extremely wide range of phase angle. Such a response provides clues for understanding the microphysical properties of dust within the coma (see, e. g. [3]). We were lucky, therefore, to measure the polarization prior and after Comet ATLAS's disintegration, which allows us to compare the materials of the processed crust with the pristine interior materials released by its subsequent disintegration. The observations continued until May 6. Over this time period, we gathered polarization in Comet ATLAS on 17 epochs.

We measured the degree of linear polarization of Comet ATLAS using a 0.5–m telescope (F = 1.62 m) of the Ussuriysk Astrophysical Observatory, a division of the Institute of Applied Astronomy of RAS (code C15; Russia). This telescope is equipped with a commercially available CCD detector SBIG

STX–16803 (resolutio — 4096×4096, size of pixel — 9 μm), the *V* filter of standard Johnson photometric system (efficient wavelength λ_{eff} = 0.551 μm and bandpass Δλ = 0.088 μm), and a dichroic polarization filter (analyzer). The analyzer is rotated through three fixed position angles 0°, +60°, and +120°, which allows for the complete characterization of its linear polarization. At each position of the analyzer, we took a short-exposure image of the comet, repeating measurements for 15 full rotations of the analyzer, 45 images in total. On one epoch, the number of full rotations was limited to 7 due to quickly changing weather conditions. All images were processed using the Image Reduction and Analysis Facility (IRAF) software system for reduction and analysis of astronomical data. The data reduction includes dark frame subtraction, removal of cosmic-ray events, flat-field correction, and compensation of instrumental polarization. We refer to [4] for more detailed description of the data reduction.

RESULTS AND DISCUSSION:

Figure 1 shows the polarimetric response of Comet ATLAS measured through a circular aperture with radius of 6000 km versus polarization measured with the blue and green continuum filters in five other comets [5–7]. Prior to disintegration (blue points), the polarization of Comet ATLAS closely matches what was found in Comet Hale – Bopp (C/1995 O1). It is worth noting that the latter comet is recognized in the literature as a comet with the highest value of polarization maximum P_{max} [8]. However, within the error bars, Comet ATLAS appears also consistent with Comet Hyakutake (C/1996 B2).

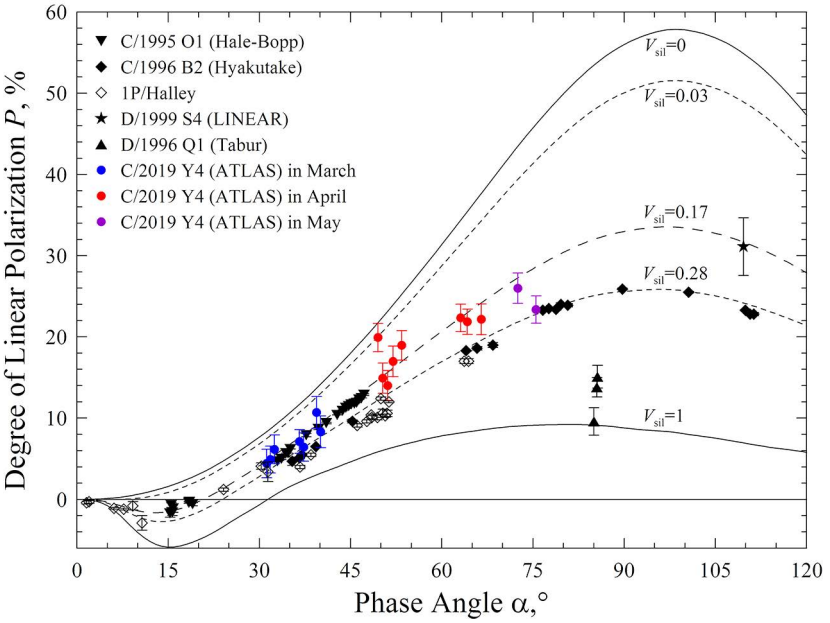

Fig. 1. Polarization *P* as a function of phase angle α in Comet ATLAS and five other comets (data adapted from [5–7]). Blue symbols correspond to Comet ATLAS prior its disintegration; whereas, red and purple ones to epochs after the disintegration began. Solid and dashed lines show results of modeling with the two-component model of cometary coma developed in [3]

Interestingly, shortly after disintegration at α = 49.5°, the polarization of Comet ATLAS was even larger than in Comet Hale-Bopp. Nevertheless, later on in April (red symbols), the polarization of Comet ATLAS was tending to converge to the Hale – Bopp. Simultaneously, it was considerably greater compared to Comet Hyakutake. However, on the last epoch of May 6, 2020, polarization of Comet ATLAS was dampened to the Hyakutake level.

As was demonstrated in [3], the angular profile of polarization of various comets can be reproduced using a mixture of weakly absorbing Mg-rich silicate particles and highly absorbing carbonaceous particles. Both materials

have long been known to be present in comets (e. g., [9]). One can explain the dispersion of P_{max} in comets through different volume fractions of their silicate and carbonaceous particles, V_{sil} and $V_{cqr} = 1 - V_{sil}$ [3]. The two solid lines of Figure 1 shows the angular profile of polarization in silicate particles ($V_{sil} = 1$) and carbonaceous particles ($V_{sil} = 0$). Within this paradigm, the intermediate volume fraction of silicate particles $V_{sil} = 0.17$ corresponds to Comet Hale – Bopp; whereas, $V_{sil} = 0.28$ corresponds to Comet Hyakutake. However, the strong polarization in Comet ATLAS shortly after disintegration suggests an extremely low relative abundance of silicates in its coma, $V_{sil} = 0.03$. It implies that the primordial dust particles are highly enriched in carbonaceous materials and, simultaneously, poor in silicate materials. Thus, the polarization maximum P_{max} may provide a means of determining the amount of time that a comet has spent in the inner Solar System. The higher P_{max} corresponds to a fresher comet. More details on this research can be found in [10].

REFERENCES:

[1] Ye Q., Zhang Q. Possible disintegration of comet C/2019 Y4 (ATLAS) // The Astronomer's Telegram. 2020. No. 13620.
[2] Bohren C. F., Huffman D. R. Absorption and scattering of light by small particles. N. Y.: Wiley, 1983. P. 547.
[3] Zubko E., Videen G., Hines D. C., Shkuratov Yu. The positive-polarization of cometary comae // Planet. Space Sci. 2016. V. 123. P. 63–76.
[4] Chornaya E. et al. Imaging polarimetry and photometry of comet 21P/Giacobini–Zinner // Icarus. 2020. V. 337. Art. ID: 113471.
[5] Kikuchi S. Linear polarimetry of five comets // J. Quant. Spectrosc. Radiat. Transfer. 2006. V. 100. P. 179–186.
[6] Kikuchi S et al. Polarimetry of comet P/Halley // Astron. Astrophys. 1987. V. 187. P. 689–692.
[7] Velichko S. F., Polarimetric and photometric characteristics of the dust in the atmosphere of splitting comets: PhD. thesis. Main Astronomical Observatory of the National Academy of Science of Ukraine, Kiev, 2010. 165 p.
[8] Hadamcik E., Levasseur-Regourd A. C. Dust evolution of comet C/1995 O1 (Hale-Bopp) by imaging polarimetric observations // Astron. Astrophys. 2003. V. 403. P. 757–768.
[9] Fomenkova M. N. et al. Compositional trends in rock-forming elements of comet Halley dust // Science. 1992. V. 258. P. 266–269.
[10] Zubko E. et al. Polarization of disintegrating Comet C/2019 Y4 (ATLAS) // Mon. Not. Roy. Astron. Soc. 2020. V. 497. P. 1536–1542.

STUDY OF THE DYNAMIC STRUCTURE OF LEO–MEO REGIONS OF THE NEAR–EARTH ORBITAL SPACE

E. V. Blinkova, A. G. Aleksandrova, T. V. Bordovitsyna, N. A. Popandopulo, I. V. Tomilova
National Research Tomsk State University, *Tomsk*, *Russia* (*zbizk322@mail.ru*)

Keywords:
near–Earth orbital space, LEO-MEO regions, resonance structure, chaotic motion

Introduction:
A study of the dynamic structure of the near-Earth orbital space is an urgent problem because the knowledge of the dynamic features of various regions of this space is necessary both for developing new satellite systems and determining zones of parking of spent objects. In the present report, results of analysis of the dynamic structure of the near–Earth orbital space in the Low Earth Orbit and Medium Earth Orbit (LEO-MEO) regions obtained by numerical simulation using methods outlined in [1–4] are presented.

RESULTS
Our investigation consisted of the following stages:

- Analysis of the dynamic structure of the orbital space using the fast Lyapunov indicator — the Mean Exponential Growth of Nearby Orbits (MEGNO) [5] — and mapping of the corresponding dynamic regions.
- Analysis of the structure of resonant perturbations affecting the motion of objects in orbital regions under consideration.
- Revealing and investigating the special features of the dynamic evolution of orbits under the influence of overlapping resonances of various types.

The motion of objects was simulated at the SKIF Cyberia cluster of Tomsk State University using the program complex "Numerical Model of AES System Motion" [6]. During simulation, perturbations from geopotential harmonics up to the 10^{th} order and degree and perturbations from the Moon and the Sun were taken into account. Together with the equations of motion, the equations for calculating the MEGNO parameters were integrated.

Tables 1 and 2 present the types of the considered secular resonances. Figures 1–4 show the distributions of the orbital and secular resonances of different types. The regions of existence of the orbital resonances have very narrow size along the semimajor axis and are designated by yellow curves on the plot scale.

Our analysis of the MEGNO maps showed that the main source of chaoticity of object motion in the examined regions of the orbital space is overlapping of stable and unstable components of multiplet orbital resonances. The chaoticity zones and the zones affected by multiplet orbital resonances practically coincided. Additional overlap of secular resonances on zones of the orbital resonance enhanced the effect of chaoticity of motion. There are also occasional phenomena of increasing the MEGNO parameters due to overlapping of a great number of stable and unstable secular resonances.

CONCLUSIONS
Thus, the dynamic structure of the zone is rather complex. This must be taken into account when developing new satellite systems and determining parking zones of spent objects.

ACKNOWLEDGEMENTS:
This work was supported by the Russian Science Foundation (Scientific Project No. 19–72–10022).

Table 1. Types Ψ_N of low-order apsidal-nodal resonances

No.	Type of resonant relationship	No.	Type of resonant relationship	No.	Type of resonant relationship
1	$\left(\dot{\Omega}-\dot{\Omega}'_{S,L}\right)+\dot{\omega}-\dot{\omega}'_{S,L}$	8	$\left(\dot{\Omega}-\dot{\Omega}'_{S,L}\right)-2\dot{\omega}-2\dot{\omega}'_{S,L}$	15	$\left(\dot{\Omega}-\dot{\Omega}'_{S,L}\right)+2\dot{\omega}'_{S,L}$
2	$\left(\dot{\Omega}-\dot{\Omega}'_{S,L}\right)-\dot{\omega}+\dot{\omega}'_{S,L}$	9	$\left(\dot{\Omega}-\dot{\Omega}'_{S,L}\right)+\dot{\omega}$	16	$\left(\dot{\Omega}-\dot{\Omega}'_{S,L}\right)-2\dot{\omega}'_{S,L}$
3	$\left(\dot{\Omega}-\dot{\Omega}'_{S,L}\right)+\dot{\omega}+\dot{\omega}'_{S,L}$	10	$\left(\dot{\Omega}-\dot{\Omega}'_{S,L}\right)-\dot{\omega}$	17	$\left(\dot{\Omega}-\dot{\Omega}'_{S,L}\right)$
4	$\left(\dot{\Omega}-\dot{\Omega}'_{S,L}\right)-\dot{\omega}-\dot{\omega}'_{S,L}$	11	$\left(\dot{\Omega}-\dot{\Omega}'_{S,L}\right)+2\dot{\omega}$	18	$\dot{\omega}-\dot{\omega}'_{S,L}$
5	$\left(\dot{\Omega}-\dot{\Omega}'_{S,L}\right)+2\dot{\omega}-2\dot{\omega}'_{S,L}$	12	$\left(\dot{\Omega}-\dot{\Omega}'_{S,L}\right)-2\dot{\omega}$	19	$\dot{\omega}+\dot{\omega}'_{S,L}$
6	$\left(\dot{\Omega}-\dot{\Omega}'_{S,L}\right)-2\dot{\omega}+2\dot{\omega}'_{S,L}$	13	$\left(\dot{\Omega}-\dot{\Omega}'_{S,L}\right)+\dot{\omega}'_{S,L}$	20	$\dot{\omega}$
7	$\left(\dot{\Omega}-\dot{\Omega}'_{S,L}\right)+2\dot{\omega}+2\dot{\omega}'_{S,L}$	14	$\left(\dot{\Omega}-\dot{\Omega}'_{S,L}\right)-\dot{\omega}'_{S,L}$		

Table 2. Types Ψ_N of secular resonances with the velocity of motion of the perturbing body of the second-fifth orders

No.	Type of resonant relationship	No.	Type of resonant relationship	No.	Type of resonant relationship
1	$\overline{n}'_{S,L}-\dot{\omega}$	7	$\overline{n}'_{S,L}+\dot{\omega}-(\dot{\Omega}-\dot{\Omega}')$	13	$\overline{n}'_{S,L}-2\dot{\omega}-(\dot{\Omega}-\dot{\Omega}')$
2	$\overline{n}'_{S,L}+\dot{\omega}$	8	$\overline{n}'_{S,L}-\dot{\omega}+(\dot{\Omega}-\dot{\Omega}')$	14	$\overline{n}'_{S,L}+2\dot{\omega}+(\dot{\Omega}-\dot{\Omega}')$
3	$\overline{n}'_{S,L}-2\dot{\omega}$	9	$\overline{n}'_{S,L}-\dot{\omega}-(\dot{\Omega}-\dot{\Omega}')$	15	$\overline{n}'_{S,L}-2\dot{\omega}+(\dot{\Omega}-\dot{\Omega}')$
4	$\overline{n}'_{S,L}+2\dot{\omega}$	10	$\overline{n}'_{S,L}+\dot{\omega}+(\dot{\Omega}-\dot{\Omega}')$	16	$\overline{n}'_{S,L}+2\dot{\omega}-(\dot{\Omega}-\dot{\Omega}')$
5	$\overline{n}'_{S,L}-(\dot{\Omega}-\dot{\Omega}')$	11	$\overline{n}'_{S,L}-2(\dot{\Omega}-\dot{\Omega}')$		
6	$\overline{n}'_{S,L}+(\dot{\Omega}-\dot{\Omega}')$	12	$\overline{n}'_{S,L}+2(\dot{\Omega}-\dot{\Omega}')$		

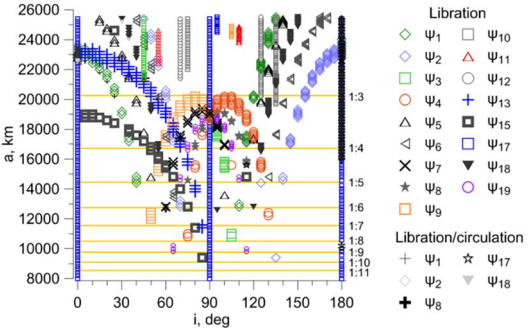

Fig. 1. Distribution of the apsidal-nodal secular resonances associated with precession of the Moon orbit and zone of existence of orbital resonances

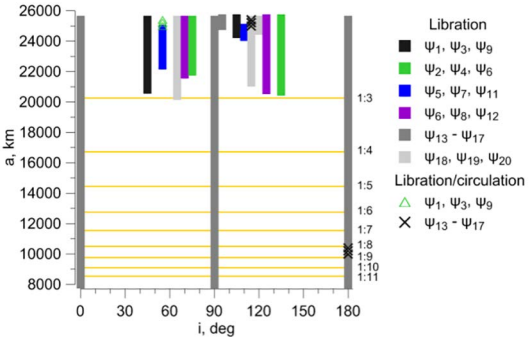

Fig. 2. Distribution of the apsidal-nodal secular resonances associated with precession of the Sun orbit and zone of existence of orbital resonances

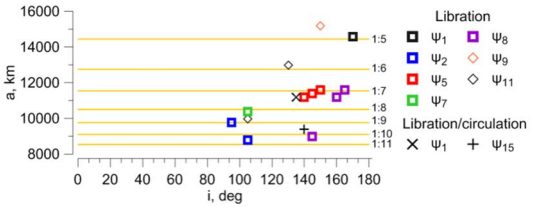

Fig. 3. Distribution of the secular resonances associated with the average motion of the Moon and zone of existence of orbital resonances

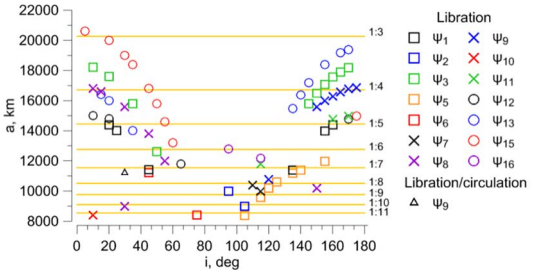

Fig. 4. Distribution of the secular resonances associated with the average motion of the Sun and zone of existence of orbital resonances

REFERENCES:

[1] Allan R. R. Resonance effects due to the longitude dependence of the gravitational field of a rotating primary // Planet. and Space Sci. 1967. V. 15. P. 53–76.
[2] Kuznetsov E. D., Zakharova P. E., Glamazda D. V., Shagabutdinov A. I., Kudryavtsev S. O. Light pressure effect on the orbital evolution of objects moving in the neighborhood of low-order resonances // Sol. Syst. Res. 2012. V. 46. Iss. 6. P. 442–449.
[3] Bordovitsyna T. V., Tomilova I .V. Special Features of the Structure of Secular Resonances in the Dynamics of Near-Earth Space Objects // Russian Physics J. 2016. V. 59. No. 3. P. 365–373.
[4] Aleksandrova A. G., Bordovitsyna T. V., Popandopulo N. A. et al. A New Approach to Calculation of Secular Frequencies in the Dynamics of Near-Earth Objects in Orbits with Large Eccentricities // Russian Physics J. 2020. V. 63, No 1. P. 64–70.
[5] Cincotta P. M., Girdano C. M., Simo C. Phase space structure of multi-dimensional systems by means of the mean exponential growth factor of nearby orbits // Physica D. 2003. V. 182. P. 151–178.
[6] Aleksandrova A. G., Bordovicy'na T. V., Chuvashov I. N. Numerical simulation in problems of near-earth object dynamics // Russian Physics J. 2017. V. 60. No. 1. P. 80–89.

ACTIVITY OF (6478) GAULT DURING JANUARY 13–MARCH, 28, 2019

Y. Skorov[1], O. Ivanova[2,3,4], I. Luk'yanyk[4], D. Tomko[2], M. Husárik[2], J. Blum[1], O. Egorov[5], O. Voziakova[5]

[1] *Technische Universität Braunschweig, Institute for Geophysics and Extraterrestrial Physics, Mendelssohnstr. 3, D–38106 Braunschweig, Germany* (*skorov@gmail.com*)

[2] *Astronomical Institute of the Slovak Academy of Sciences, SK-05960 Tatranská Lomnica, Slovak Republic*, (*oivanova@ta3.sk*)

[3] *Main Astronomical Observatory of the National Academy of Sciences of Ukraine, 27 Zabolotnoho Str., 03143 Kyiv, Ukraine*

[4] *Astronomical Observatory of Taras Shevchenko National University of Kyiv, 3 Observatorna Str., 04053 Kyiv, Ukraine*

[5] *Sternberg Astronomical Institute, Lomonosov Moscow State University, Universitetsky pr. 13, Moscow 119234, Russia*

KEYWORDS:
minor planets, photometry, asteroid (6478) Gault, data analysis, simulations

INTRODUCTION:

The main–belt asteroid (6478) Gault (hereafter Gault) was discovered on 1988 May 12 by Carolyn and Eugene Shoemaker. Its orbital semimajor axis, eccentricity, perihelion distance and inclination are 2.305 au, 0.194, 1.859 au and 22.8 degrees, respectively. Knezevic & Milani (2003) classified it as a stony S–type asteroid and a member of the Phocaea family. Ye et al., (2019) showed that the colour of Gault was more similar to that of C–type asteroids than S–types. The asteroid Gault has also been dynamically linked with the low – albedo Tamara family (Kleyna et al., 2019), which resides in the Phocaea region (Novaković, 2017). Members of this family are characterized by the highest orbital inclinations among all the families of the inner asteroid belt. The Tisserand parameter of Gault is $T_J = 3.46$. This value is significantly larger than the nominal dividing line ($T_J = 3$) that separates comets ($T_J < 3$) from asteroids ($T_J > 3$). The recent activity of Gault was detected on January 5, 2019 (Smith, Denneau, 2019). An archive-data check revealed the activity of the asteroid in December 2018. Based on a thorough analysis of the archive images taken in 2013, 2016 and 2017, Chandler et al. (2019) concluded that Gault shows sustained activity since 2013. They also noted that this asteroid is unique: we do not know other members of this family that would be active so long. This unusual behavior caused great interest.

Our observation of Gault was carried out with different telescopes. We obtained photometric data with the 2.5–m telescope of the Caucasian Mountain Observatory (CMO) of SAI MSU (Russia) and with the 1.3–m and the 0.61–m telescopes at the Skalnaté Pleso Observatory (Slovakia).

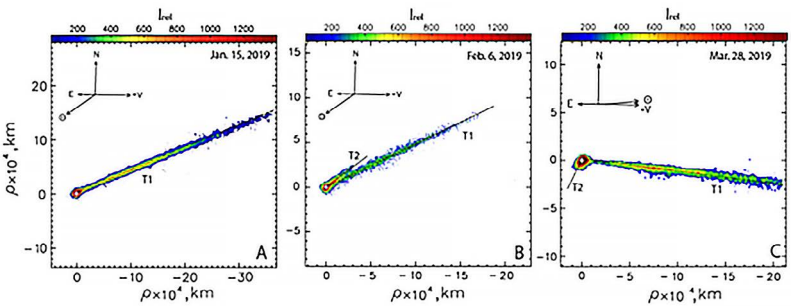

(a) (b) (c)

Fig. 1. The composite images of asteroid (6478) Gault obtained in the R filter. Panel (**a**) shows the image taken at the 2.5–m telescope (CMO) of SAI MSU on January 15, 2019; panels (**b**) and (**c**) show the images taken at 1.3m telescope (SPb) on February 6, and March 28, 2019, respectively. The optocentre of the asteroid is marked by a white cross. Black lines show the directions of the tails (T1 and T2)

R-band images of asteroid Gault are shown in Figure 1. These data were obtained at the 2.5–m (CMO) telescope of SAI MSU on January 15, 2019 (A), at the 1.3–m (SPb) telescope on February 6 and March 28, 2019 (B and C), respectively. The asteroid coma is compact and bright. On January 15, 2019, the asteroid presents only one tail T1. The asteroid exhibits a second faint tail (T2) on images obtained from the observations carried out on February 6, 2019, and on March 23, 2019. For observations made in January and February 2019, the dust tail (T1) is elongated in the anti-sunward direction, as can be seen in panels A and B. On March 28, 2019 (panel C), both tails (T1 and T2) change the orientation relative to the sun dramatically.

Using the direct images in the broad-band filters B, V and R one can evaluate the dust colour. The resulting colour-colour BV-VR diagram is shown in Figure 2.

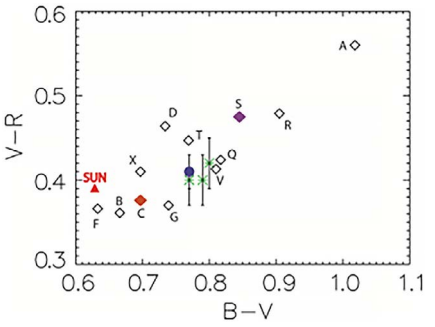

Fig. 2. Colour–colour diagram of asteroid Gault. Our results are marked by green asterisks with error bars. The result from Jewitt et al. (2019) is marked by the blue circle. The red triangle shows the colour of the Sun from Willmer (2018). We also show results (marked by diamonds) for asteroids of various spectral types A, B, C, D, F, G, Q, R, S, T, V (data from Dandy et al., 2003).

Gault usually refers to a Phocaea family and is considered as a stony S-type asteroid. However, Jewitt et al. (2019) concluded that in an optical range this asteroid is more similar to C-type asteroids. The retrieved broadband optical and near-infrared colours and optical spectroscopy (Bolin, 2019) also suggest that Gault belongs to the C-complex asteroids. From our results (Figure 2) we can see that the colour of the asteroid is bluer than that of S-type and redder than that of C–type asteroids. Colour maps were built and colour variations along the tail for the observation made on January 15, 2019 were analyzed. The Afr was calculated for the R filter, The evaluated value varies from 47 to 32 cm for the period from January to the end of March, 2019. The rotational period of the body is estimated from the light curve by different methods and is about 1.79 hr.

Undoubtedly, one of the most intriguing questions is the question of the cause (or causes) that initiated the observed dust activity. We are talking about multiple collisions colour caused by the approach of an asteroid with meteor showers produced by comet activity. We showed that there are several candidates whose orbits are close to the orbit of Gault during the periods of observed activity. For some of these candidates (for example, 73P and 380P), the resulting distances are very small. We do not claim that this mechanism successfully explains all the cases of activity, but two clusters seem to be in good agreement with this hypothesis. In Kleyna et al. (2019), Moreno et al. (2019) and Ye et al. (2019), an estimate of the total loss of matter during the observed release was obtained based on an analysis of the morphology of the tails. These results are in good agreement and suggest that the total ejection mass was about 107 kg. This value allows us to estimate the total size of the impactor (or impactors, since in the zeroth approximation we can assume that the mass of emissions adds up). Taking the qualitative estimates for a high-speed impact into a porous target, we can conclude that the total impactor volume is on the order of a few cubic meters, which seems reasonable (Vogler and Fredenburg, 2019).

REFERENCES:

[1] Bolin 2019. Apache Point Observatory visible and near-infrared photometry/spectroscopy of multi-tailed active asteroid (6478) Gault. EPSC-DPS Joint Meeting 2019, held 15–20 September 2019 in Geneva, Switzerland, id. EPSC-DPS2019–1828.
[2] Chandler C. O., Kueny J., Gustafsson A., Trujillo C. A., Robinson T. D., Trilling D. E. Six Years of Sustained Activity in (6478) Gault // The Astrophysical J. Letters. 2019. V. 877. Iss. 1. Art. L12.
[3] Dandy C. L., Fitzsimmons A., Collander-Brown S. J. Optical colours of 56 near–Earth objects: trends with size and orbit // Icarus. 2003. V. 163. Iss. 2. P. 363–373.
[4] Jewitt D., Kim Y., Luu J., Rajagopal J., Kotulla R., Ridgway S., Liu W. Episodically Active Asteroid 6478 Gault // The Astrophysical J. Letters. 2019. V. 876. Iss. 2. Art. L19.
[5] Kleyna J. T., Hainaut O. R., Meech K. J., Hsieh H. H., Fitzsimmons A., Micheli M., …, Bhatt B. C. The Sporadic Activity of (6478) Gault: A YORP-driven event? // The Astrophysical J. Letters. 2019. V. 874. Iss. 2. Art. L20.
[6] Moreno F., Jehin E., Licandro J., Ferrais M., Moulane Y., Pozuelos F. J., …, Popescu M. Dust properties of double-tailed active asteroid (6478) Gault // Astronomy and Astrophysics. 2019. V. 624. Art. L14.
[7] Novaković B., Tsirvoulis G., Granvik M., Todović A. A dark asteroid family in the Phocaea region // The Astronomical J. 2017. V. 153. Iss. 6. Art. 266.
[8] Smith K. W., Denneau L., Vincent J. B., Weryk R. (6478) Gault / Central Bureau Electronic Telegrams. 2019. 4594.
[9] Ye Q., and 15 colleagues. Multiple Outbursts of Asteroid (6478) Gault // The Astrophysical J. 2019. V. 874. Art. L16.
[10] Shock Phenomena in Granular and Porous Materials / eds. Vogler T. J., Fredenburg D. A. Springer International Publishing, 2019.
[11] Willmer C. N. The Absolute Magnitude of the Sun in Several Filters // The Astrophysical J. Supplement Series. 2018. V. 236. Iss. 2. 47.

THE DYNAMICS RESEARCH OF ASTEROIDS 3200 PHAETHON AND 2007 PR10 UNDER THE YARKOVSKY EFFECT INFLUENCE

T. Yu. Galushina[1], O. N. Letner[2]
[1] *Scientific Research Institute of Applied Mathematics and Mechanics of Tomsk State University, 36, Lenin Ave, Tomsk, Russian Federation* (*tanastra@nxt.ru*)
[2] *Scientific Research Institute of Applied Mathematics and Mechanics of Tomsk state university, 36, Lenin Ave, Tomsk, Russian Federation, +7 3822 52 97 76* (*oksana.letner@gmail.com*)

KEYWORDS:
asteroids with small perihelion distance, the Yarkovsky effect, orbit fitting, orbital evolution, 3200 Phaethon, 2007 PR10

Regular passage of the asteroid close to the Sun can lead to the acquisition of additional acceleration due to thermal radiation its rough surface heated during the day and cooling at night. This phenomenon is called the Yarkovsky effect [1]. Objects with small perihelion distances ($q < 0.15$ AU) are subject to a significant influence of the effect due to this feature of their orbits. Therefore, it is important to take this disturbing factor into account when constructing orbital evolution and detecting the features of the asteroid motion. In turn, the study of the motion of asteroids with $q < 0.15$ AU can contribute to solving the asteroid hazard problem, since such orbit feature allows them to approach from the side of the Sun to the Earth undetected.

The work is devoted to the study of dynamics and evaluation of the Yarkovsky effect influence on the motion of asteroids 3200 Phaethon and 2007 PR10 with a perihelion distance of 0.140 AU and 0.133 AU respectively. The effect was taken into account using transverse acceleration A_2, the determination algorithms of which were added to the «IDA» software [2, 3]. The transverse acceleration A_2 is included in the number of estimated parameters during solving the least squares problem. The fitting values of the asteroid coordinates, velocity components, and the A_2 parameter are found. Since the asteroid 3200 Phaethon has radar observations [4] in addition to positional ones, different sets of observations were considered for it: only positional (P) and with the addition of radar (*R*) ones. In the numerical model of asteroid motion planet ephemeris plays an important role, since in the funds available to us the coordinates of the planets are given at different time intervals and with different precision. Currently the planet ephemeris DE438 is the most precise, but the time interval is too short to build the orbital evolution of the asteroids 3200 Phaethon and 2007 PR10. Therefore, to study we used the DE431. Table 1 shows the values of parameter A_2 with its mean square errors obtained for asteroids using the two planet ephemerises DE431 and DE438, as well as the value of A2 for 3200 Phaethon, given on the NASA website.

The results lead to the following conclusions. Mean square errors in the determination of A_2 are of the same order as the values themselves, however, the inclusion of radar observations can reduce them by almost half. The results obtained with different planet ephemeris differ within uncertainty. The closest value to NASA data is obtained using the modern planet ephemeris DE438. The difference does not exceed the mean square error and can be explained by a different set of observations.

In [5] it is shown that during building the initial confidence region of 3200 Phaethon and 2007 PR10 taking into account the Yarkovsky effect leads to a decrease in the mean square error σ and the size of the region. In order to evaluate the influence of the effect on their dynamics, the orbital evolution of objects was built taking into account two sets of perturbing factors, one of which contains the effect and the other does not. The study interval was determined by the integration precision and amounted (− 1000, 7000) yr. for 3200 Phaethon and (− 6000, 5500) yr. for 2007 PR10. For both asteroids the

evolution of orbital elements is constructed and such features of motion as approaches to major planets, secular and orbital resonances, and the chaoticity manifestation are revealed. The orbital resonance was detected only for Phaethon. The asteroid moves in the vicinity of the 3 / 7 orbital resonance with Venus with an unstable behavior of the resonant characteristics [6]. Moving outside the resonance region, it enters it for a short time interval, and then again leaves it.

Table 1. The results of determining the parameter A_2, AU/day^2

	3200 Phaethon			2007 PR10	
	$A_2(P)$	$A_2(R)$	A_2(NASA)	$A_2(P)$	$A_2(R)$
DE431	−4.508 ±2.623	−3.623 ±1.648	−5.445 ±5.92	−3.866 ±1.402	
DE438	−2.307 ±2.635	−4.546 ±1.656		−3.851 ±1.401	

The study shown that evolution of asteroid orbit elements differs insignificantly for two models except semimajor axis *a.* Figure 1 presents the graphs of its evolution for asteroids 2007 PR10 and 3200 Phaethon without taking into account the Yarkovsky effect (a) and without it (b).

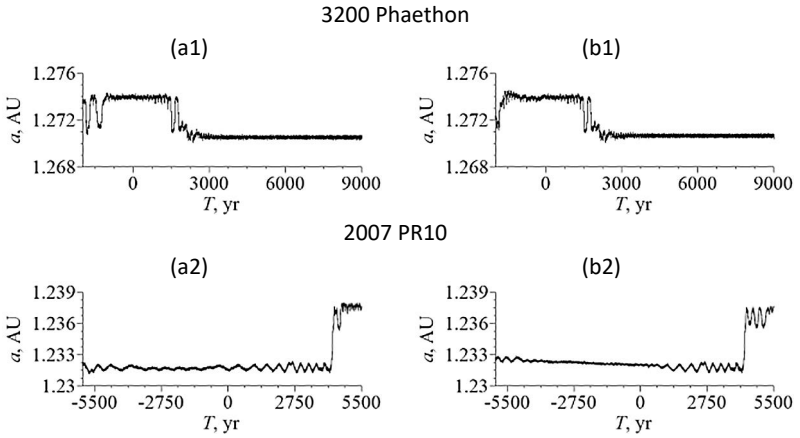

Fig. 1. The evolution of the semimajor axis *a* without taking into account the Yarkovsky effect (a1, a2) and with it (b1, b2) for asteroids 2007 PR10 and 3200 Phaethon

The figure shows that taking into account the Yarkovsky effect leads to noticeable changes in the semimajor axis evolution of both asteroids, which significantly affects the number of approaches to major planets and the distance to them. In addition, it is interesting to note that for 2007 PR10, when integrated into the future taking into account the Yarkovsky effect the precision is significantly lower than that without taking into account the effect. The decrease in the integration precision is due to that the asteroid experiences more rapprochement with Venus and Mercury and is closer to Venus.

A similar situation exists with the asteroid 3200 Phaethon, but when integrated into the past. Taking into account the Yarkovsky effect the integration precision is three orders lower than the precision without taking into account the effect. An asteroid is closer to Earth and Venus.

ACKNOWLEDGEMENTS:
This work was supported by the Russian Science Foundation (project No. 19–72–10022).

REFERENCES:

[1] Farnocchia D. et al. Near Earth Asteroids with measurable Yarkovsky effect // Icarus. 2013. V. 224. Iss. 1. P. 1–13.
[2] Galushina T., Bykova L., Letner O., Baturin A. IDA software for investigating asteroid dynamics and its application to studying the motion of 2012 MF7 // Astronomy and Computing. 2019. No. 29. Art. id. 100301.

[3] Galushina T. Yu., Syusina O. M. Comparative analysis of methods for obtaining the Yarkovsky effect parameter from observations // Russian Physics Journal. 2020. V. 63. No. 3.
[4] Yeomans D. K. et al. Asteroid and comet orbits using radar data // The Astronomical J. 1992. V. 103. No. 1. P. 303–317.
[5] Galushina T. Yu., Letner O. N. Influence of the Yarkovsky effect on motion of asteroids with small perihelion distance// Russian Physics Journal. 2020. V. 63. No. 1. P. 71–78.
[6] Galushina T. Yu., Sambarov G. E. Dynamics of Asteroid 3200 Phaethon Under Overlap of Different Resonances // Solar System Research. 2019. V. 53. No. 3. P. 215–223.

TO THE QUESTION OF PRECESSION RING AROUND DWARF PLANET HAUMEA

B. P. Kondratyev, V. S. Kornoukhov
Sternberg Astronomical Institute, Lomonosov Moscow State University, 13 Universitetskij prospect, 119992, Russia (work@boris-kondratyev.ru)

KEYWORDS:
non-planetary rings, potential, precession of Haumea's ring

The discovery in recent years of non-planetary rings around some small celestial bodies has caused great interest in the problem of the origin and evolution of such rings. We consider the problem of the precession of ring located in the gravitational field of a massive rapidly rotating triaxial ellipsoid. Our method uses the mutual energy as a perturbing function in the Lagrange equations. It was found that the precession period of Haumea's ring is 12.9 days.

POTENTIAL:
Consider a homogeneous ellipsoid with semi-axes $a_1 \geq a_2 \geq a_3$ rotating around an axis a_3. The gravitational potential is a harmonic function, it can be expanded into a series of spherical harmonics

$$\varphi = \frac{GM}{r}\left\{1 + \sum_{n=2}^{\infty}\sum_{m=0}^{n}\left(\frac{R_0}{r}\right)^n P_{nm}(\sin\theta)\left[C_{nm}\cos m\lambda + S_{nm}\sin m\lambda\right]\right\}. \quad (1)$$

Here, the potential (1) is enough to decompose to members of the fourth order: after averaging (1) over λ, the odd zonal harmonics vanish, and in cylindrical coordinates (r, z) we obtain

$$\varphi \approx \frac{GM}{r}\left\{1 + \frac{C_{20}}{2}\left(\frac{R}{r}\right)^2\left(3\left(\frac{z}{r}\right)^2 - 1\right) + \frac{C_{40}}{8}\left(\frac{R}{r}\right)^4\left(35\left(\frac{z}{r}\right)^4 - 30\left(\frac{z}{r}\right)^2 + 3\right)\right\}, \quad (2)$$

The coefficients in (2) are:

$$\left.\begin{aligned} C_{20} &= \frac{2a_3^2 - a_1^2 - a_2^2}{10R_0^2}; \\ C_{40} &= 3\frac{3\left(a_1^4 + a_2^4\right) + 8a_3^4 + 2a_1^2a_2^2 - 8\left(a_1^2 + a_2^2\right)a_3^2}{140R_0^4}. \end{aligned}\right\} \quad (3)$$

MUTUAL ENERGY:
Through the orbital elements

$$r = \frac{a(1-e^2)}{1 + e\cdot\cos\upsilon}, \quad z = r\sin(\upsilon + \omega)\cdot\sin i, \quad (4)$$

where υ is the true anomaly, ω, i, e, a — the elements of the orbit. Mutual energy of the central and test bodies

$$W_{mut} = -m\cdot\varphi(r,z), \quad (5)$$

being averaged over the average anomaly, gives the mutual energy of the central body and the Gaussian ring

$$W_{mut} = -\frac{m(1-e^2)^{3/2}}{2\pi}\int_0^{2\pi}\varphi(r,z)\frac{d\upsilon}{\left(1 + e\cdot\cos\upsilon\right)^2}. \quad (6)$$

Calculating this integral, we find

$$W_{mut} = W_0 + W_1 + W_2; \quad (7)$$

$$\left.\begin{aligned} &W_0 = -\frac{GMm}{a}, \quad W_1 = \frac{GMm}{4a} C_{20} \left(\frac{R}{a}\right)^2 \frac{3\cos^2 i - 1}{(1-e^2)^{3/2}}, \\ &W_2 = -\frac{3}{128} \cdot \frac{GMm}{a} \cdot \frac{C_{40}}{(1-e^2)^{7/2}} \left(\frac{R}{a}\right)^4 \times \\ &\times \left\{ \begin{aligned} &\left((5\cos^2 i - 1) - (7\cos^2 i - 1) \cdot 5\sin^2 i \cdot \sin^2 \omega\right) 4e^2 + \\ &+ (35\cos^4 i - 30\cos^2 i + 3) \cdot (2 + e^2) \end{aligned} \right\}. \end{aligned} \right\} \quad (8)$$

MODEL OF HAUMEA AND PRECESSION OF RING:
Defining a perturbing function for Haumea's ring as

$$L = -\frac{W_{mut}}{m}, \quad (9)$$

and substituting (9) into the Lagrange equations for osculating elements, we obtain ($n = \sqrt{GM/a^3}$ is mean motion)

$$\frac{d\Omega}{dt} = \frac{3}{2} C_{20} n \left(\frac{R}{a}\right)^2 \frac{\cos i}{(1-e^2)^2}, \quad (10)$$

The Haumea's model can be introduced by combining the ellipsoidal stone core with confocal icy shell and represents a non-uniform figure of rotating gravitating mass [1]. Then the semi-axes of the figure and the core will be related by the relations

$$a^2 = a_c^2 + \lambda, \quad b^2 = b_c^2 + \lambda, \quad c^2 = c_c^2 + \lambda. \quad (11)$$

Given the confocal nature of the outer boundaries of the stone core and the ice shell, we obtain the expressions for potential coefficient

$$\bar{C}_{n0} = C_{n0}(a_c, b_c, c_c) \cdot \left(\frac{a_c b_c c_c}{abc}\right)^{(3+n)/3} \frac{\rho_c - \rho_{sh}}{\rho} + C_{n0}(a,b,c) \frac{\rho_{sh}}{\rho}. \quad (12)$$

Then, using the generalized Maclaurin – Laplace theorem [2], instead of (12) we obtain a simpler formula

$$\bar{C}_{n0} = C_{n0}(a,b,c). \quad (13)$$

In addition, here we use the refined Haumea's parameters [3]:

$$\left.\begin{aligned} &a = 1082 \pm 15 \text{ km}, \quad b = 836 \pm 5 \text{ km}, \quad c = 511 \pm 13 \text{ km}, \\ &\rho = 2.07 \pm 0.07 \quad \text{g}\times\text{cm}^{-3}, \quad i_{ring} = 3.2 \pm 1.4^\circ, \\ &r_{ring} = 2300 \pm 60 \text{ km}. \end{aligned} \right\} \quad (14)$$

For ρ_{sh} = 1 g·cm^{-1}; ρ_c = 3 g·cm^{-1}, we get estimates for sizes of the stone core

$$a_c = 1010 \text{ km}, \quad b_c = 740 \text{ km}, \quad c_c = 331 \text{ km}. \quad (15)$$

In addition, we find that the mass of the core and shell of Haumea

$$M_c = (3.1 \pm 0.1) \cdot 10^{24} \text{ g}, \quad M_{sh} = (0.9 \pm 0.1) \cdot 10^{24} \text{ g}. \quad (16)$$

so that the ratio of shell mass to total planetoid mass is

$$\frac{M_{sh}}{M_c + M_{sh}} \approx 22.5\,\%. \quad (17)$$

The coefficients of even zonal harmonics for Haumea are

$$C_{20} = -0.225 \pm 0.009, \quad C_{40} = 0.116 \pm 0.009. \quad (18)$$

Putting the ring round, the precession rate and the precession period of the line ring nodes in the Houmea equator plane are equal to

$$\frac{d\Omega}{dt} = (-5.7 \pm 0.3) \cdot 10^{-6}\ \mathrm{s}^{-1}; \quad T_{precession} = 12.9 \pm 0.7\ \mathrm{d}. \tag{19}$$

REFERENCES:

[1] Kondratyev B. P. The near-equilibrium figure of the dwarf planet Haumea and possible mechanism of origin of its satellites // Astrophysics and Space Science. 2016. V. 361. No. 5. Art. id. 169. 9 p.
[2] Kondratyev B. P. Theory of Potential. New methods and challenges with solutions. M.: Mir, 2007. 512 p.
[3] Kondratyev B. P., Kornoukhov V. S. Determination of the figure of the dwarf planet Haumea from observations of a stellar occultation and photometry data // MNRAS. 2018. V. 478. No. 3. P. 3159–3176.

INTERSTELLAR COMET 2I/BORISOV: THE DUST COMPOSITION ESTIMATION

V. V. Busarev[1], E. V. Petrova[2], M. P. Shcherbina[1], N. P. Ikonnikova[1], M. A. Burlak[1], A. A. Belinski[1]

[1] *Lomonosov Moscow State University*, *Sternberg Astronomical Institute* (*SAIMSU*), *University Av.*, *13*, *Moscow*, *119992*, *Russia* (*busarev@sai.msu.ru*)

[2] *Space Research Institute*, *Russian Academy of Sciences* (*IKI RAS*), *Profsoyuznaya 84/32*, *Moscow*, *117997*, *Russia* (*epetrova@iki.rssi.ru*)

KEYWORDS:
Multiband photometry, comets, interstellar comet 2I/Borisov, reflectance spectra, numeric simulation, dust composition

INTRODUCTION:
Multiband photometry of the first interstellar comet 2I/Borisov (C/2019 Q4) with coma was performed with the 0.6-m telescope at the Caucasus Mountain Observatory (CMO) of SAI MSU over October-December 2019. The comparison of the integral spectral reflectance of comet 2I with its simulated reflectance spectra allowed us to assess the chemical-mineralogical composition of the cometary coma dust matter.

RESULTS OF OBSERVATIONS AND NUMERIC SIMULATION:
UBVri–observations of comet 2I/Borisov were carried out with a semi–automatic telescope RC600 [1] at CMO (a height of 2112 m above sea level) for about two months, when the comet was approaching perihelion, at 2.40–2.01 AU heliocentric distances. The specified combination of light filters covers the 0.38–0.73 mm spectral range more uniformly than those of the classic UBVRI-system (e. g., [2]). During our photometric measurements, the phase angles of comet 2I were within a range of about 20–30°. At the same time, several G-type stars were observed to determine the comet's reflectance at effective wavelengths of the photometric system. Taking into account the combined spectral transmission of light filters, spectral quantum efficiency of the CCD-matrix, and the local spectral transparency of the terrestrial atmosphere, these wavelengths were determined to be 0.376 μm (U), 0.444 (B), 0.528 (V), 0.633 (r), and 0.723 μm (i). The entire set of obtained interpolated reflectance curves of comet 2I is shown in Figure 1.

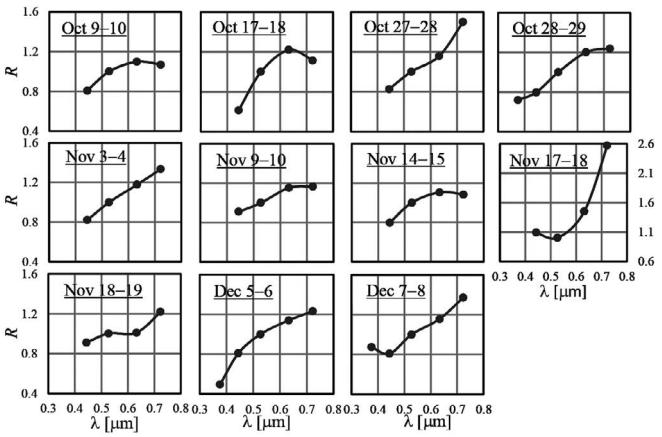

Fig. 1. Normalized (at 0.53 μm) spectral dependences of the reflectance R for comet 2I observed in October-December of 2019 at heliocentric distances changing from 2.40 to 2.01 AU

The spectral curves demonstrate a significant diversity of shapes with the comet's spinning and approaching the Sun. The effective wavelengths of the light filters are shown by dots in each of the curves. Note that some reflec-

tance curves contain only 4 dots instead of 5. It is explained by the absence of the signal from the comet in the U band (it was lower than the errors of measurements). We will return to the issue below.

The complex (aggregate) structure of cometary dust particles is confirmed by results of both remote and in situ investigations of solar system comets (see, e. g., [3–5]; and references therein). The typical morphology of cometary aggregate particles and its alteration, while the particles are moving away from a nucleus, are caused by disintegration due to evaporation of volatiles and agglomeration intensified in the plasma environment of a comet (e. g., [6, 7]). Based on a statistical fractal structure of cometary dust agglomerates (e. g., [8]), we used fractal-like clusters (A, B, C, and D in Figure 2) consisting of submicron particles. Besides, the following simplified model of comet 2I was assumed: a low albedo (0.05) nucleus with the reddish reflectance spectrum, typical of D-asteroids, is surrounded by a dust coma.

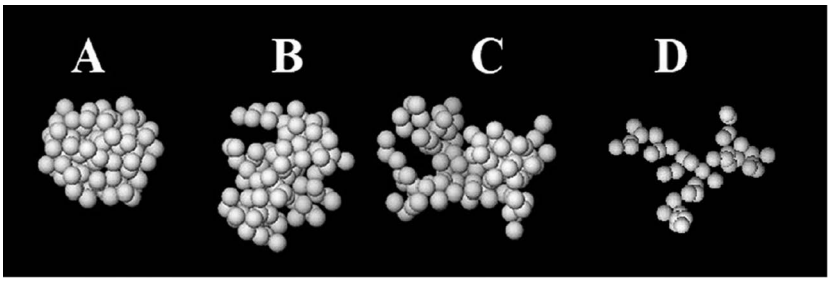

Fig. 2. Examples of the fractal-like aggregates considered

Since cometary dust particles are heterogeneous in composition and may contain both a dark (opaque) material and partially transparent silicates and volatile ices [9, 10] we consider four cases for the material of aggregates to analyze the effect of the dust composition on the spectrum shape.

1. H_2O ice (material M1); in the considered spectral range the real part of the refractive index mr weakly changes from 1.30 to 1.33 [11], while the imaginary one mi is negligible and assumed to be 0.0.
2. To show how a higher value of the wavelength-independent refractive index influences the spectrum shape, we consider a conventional material (M2) with $m_r = 1.80$ (which roughly corresponds to the mean value of m_r for Mg-Fe silicates) and $m_i = 0.10$.
3. Mg-Fe silicate (olivine) (material M3) as one of the most abundant components of the cometary dust material; m_r varies from 1.78 to 1.81, while m_i decreases with increasing the wavelength to ~0.6 μm and further changes weakly [12].
4. A mixture of different organic substances, which is collectively known in astronomy as tholins (material M4), with the strongly increasing absorption in the short-wavelength range.

The reflectance spectra of aggregates composing the coma were calculated with the superposition T-matrix method [13]. The intensity of light scattered by the coma-nucleus system was obtained with the radiative-transfer procedure, and examples of the spectra for a phase angle of 20° are shown in Figure 3. The comparison of the modeled spectra (as those in Figure 3) and the interpolated spectra of 2I (Figure 1) revealed that the typical reflectance spectra of comet 2I generally correspond to those of Fe-Mg silicate and tholine aggregates (Fig. 3, central and right columns).

CONCLUSIONS:

Thus, from the comparison of the modeled integral reflectance spectra to those of comet 2I, the following properties of the 2I coma particulate material can be distinguished.

1. No signs of small H_2O ice particles or their aggregates were found, since no negative spectral gradient and/or no characteristic maximum at 0.4 μm (as that in Figure 3, *left*) is observed in the interpolated reflectance curves of 2I (Figure 1).

2. Dust particles containing Mg-Fe silicates and tholins definitely prevail in the light scattering by the 2I coma (Figure 1), which follows from the positive gradient in the entire spectral range considered.

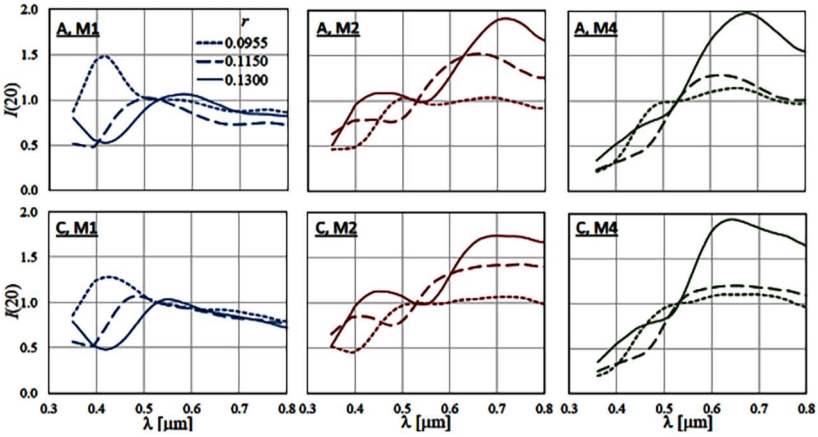

Fig. 3. Modeled spectra of the intensity of light I(20) (normalized at 0.53 μm) scattered by the coma-nucleus system at a phase angle of 20°. The coma contains aggregate structures A (top row) or C (bottom row); three cases of radii r (specified in microns) of constituent particles and three materials — water ice (M1), Fe-Mg silicates (M2), and tholins (M4) — are presented. In all of the models, the coma optical thickness is assumed to be 0.5 at 0.56 mm

3. In some measured spectra (Figure 1, plots for Nov 17–18 and Dec 7–8), the intensity starts to grow toward short wavelengths; or its decrease becomes less steep (as that for Oct 28-29). This points to the Rayleigh scattering strengthening and indicates the intense release of gaseous compounds (H_2O and others) from the 2I nucleus. The shape of the curve for Nov 17–18 may be most representative as corresponding probably to the most active area on the 2I nucleus surface.
4. A convex shape of three spectra exhibiting the maximum at 0.63 μm (for Oct 9–10, Oct 17218, and Nov 14215) characterizes a more quite state of the cometary coma. This is confirmed by a very low level of the signal in the U band. This spectrum shape is closest to the model spectra for Mg–Fe silicates in Figure 3 (central).
5. Based on this modeling, the considerable predominance of magnesium-ferrous and organic dust component in the coma of comet 2I has been determined. This conclusion is consistent with the results of direct measurements of the dust material (including the general estimate of the dust–to–volatiles ratio) of comet 67P/Churyumov-Gerasimenko (e. g., [14]), which resembles 2I by the visible-range color indices.

REFERENCES:

[1] Berdnikov L. N. et al. // Astron. Rep. 2020. V. 64. P. 310.
[2] Bessell M. S. // ARA&A. 2005. V. 43. P. 293.
[3] Fulle M. et al. // AJ. 2000. V. 119. P. 1968.
[4] Kolokolova L., Nagdimunov L., Mackowski D. // JQSRT. 2018. V. 204. P.138.
[5] Güttler C. et al. // A&A. 2019. V. 630. A24.
[6] Ivlev A. V., Morfill G. E., Konopka U. // Phys. Rev. Lett. 2002. V. 89. P. 195502.
[7] Dominik C. In: Henning T., Grün E., Steinacker J. (eds). ASP Conf. Ser. V. 414. Cosmic Dust — Near and Far, Astron. Soc. Pac., San Francisco, 2009. P. 494.
[8] Mannel T. et al. // MNRAS. 2016. V. 462. S304.
[9] Hanner M. S., Bradley J. P. In: Comets II (Festou M. et al., eds), Univ. of Arizona Press, Tucson, 2005. P. 555.
[10] Frattin E. et al. MNRAS 2017. V. 469. S195.
[11] Warren S. G., Brandt R. E., JGR. 2008. V. 113. P. 14220.
[12] Dorschner J. et al. A&A. 1995. V. 300. P. 503.
[13] Mackowski D. W., Mishchenko M. I. JQSRT. 2011. V. 112. P. 2182–2192.
[14] Rotundi A. et al. Science. 2015. V. 347. P. 3905.

VARIABILITY OF THE REFLECTANCE SPECTRA OF (1) CERES AND SOLAR ACTIVITY

V. V. Busarev[1], L. F. Golubeva[2], E. V. Petrova[3], D. I. Shestopalov[2]
[1] *Lomonosov Moscow State University*, *Sternberg Astronomical Institute*,*University Av.*, *13*, *Moscow*, *119992*, *Russia* (*busarev@sai.msu.ru*)
[2] *Shemakha Astrophysical Observatory*, *Shemakha AZ-3243*, *Azerbaijan*, (*lara_golubeva@mail.ru*, *shestopalov_d@mail.ru*)
[3] *Space Research Institute*, *Russian Academy of Sciences* (*IKI*), *Moscow*, *117997*, *Russia* (*epetrova@iki.rssi.ru)*

KEYWORDS:
spectrometry, asteroid (1) Ceres, reflectance spectra variability, solar activity

The anomalous reflectance spectra (RS) of asteroid (1) Ceres in the visible region was registered at Shemakha Astrophysical Observatory on December 26, 1989 [1]. The observed Ceres' spectra resembled the "reddish" spectra of D asteroids (i. e., objects whose spectra show a systematic increase in the scaled reflectance coefficients with increasing the wavelength). The stellar magnitude of the asteroid was 0.2 higher than the ephemeris one; therefore Ceres was noticeably redder and darker at the time of observations than usual. In addition, no variations in the asteroid's RS depending on the longitude of the central meridian were found. The spectra of Ceres obtained in the oppositions of 2007 and 2009 in a range of 0.38–0.95 μm also noticeably differ from each other [2]. While one pair of spectra (2007) was similar to the spectra of C asteroids, the other pair (2009) resembled the spectra of G asteroids. Since the spectral observations of Ceres in 2007 and 2009 corresponded to the opposite hemispheres of the asteroid, it was concluded that the oxidation state of the surface material may be different. The latter, in turn, may cause different intensities of inter-valent absorption bands in the visible RS. A few years later, the short-term variations of Ceres' RS were discovered by the other team of observers [3]. During a month (from December 18, 2012 to January 20, 2013), the spectrum of Ceres underwent changes in the slope of the spectral curve, showing either negative or positive values in a range of 0.56–0.9 μm. Note, the authors of papers [1–3] failed in searching for possible biases that might distort the resulting asteroid spectra when being calibrated by the spectra of standard stars. The same assumption was put forward in [1, 3] that temporary variations in the Ceres' reflectance spectra can be caused by the sublimation of frost on the surface of one of its hemispheres during the spring-summer season.

The RS of the illuminated and earth-facing hemisphere of Ceres (at low phase angles) obtained in different oppositions by different researchers at different telescopes are shown in Figure 1. The references to RS, observation dates, and the nearest time data on solar activity corresponding to RS in Figure 1 are given in Table 1 (see notes about the designations). According to the value of the gradient of the spectral curves in a range of 0.5−0.9 μm, the spectra may be divided into three groups:

1. Flat or "neutral" curves (Nos. 4–12, 16, 17).
2. Spectral curves with the negative slope or "bluer" (Nos. 1–3, 18).
3. Spectral curves with the positive slope or "reddish" (Nos. 13–15).

Of course, the boundaries themselves can be traced more precisely in the future, but their meaning is quite clear.

The differences in the spectral curves in Figure 1 are not due to the geometry of observations or the calibrating procedure. For Ceres, there is a certain increase in the slope of the spectral curves with increasing the phase angle. But this "reddening" effect is absent for the sample of spectra in Figure 1.

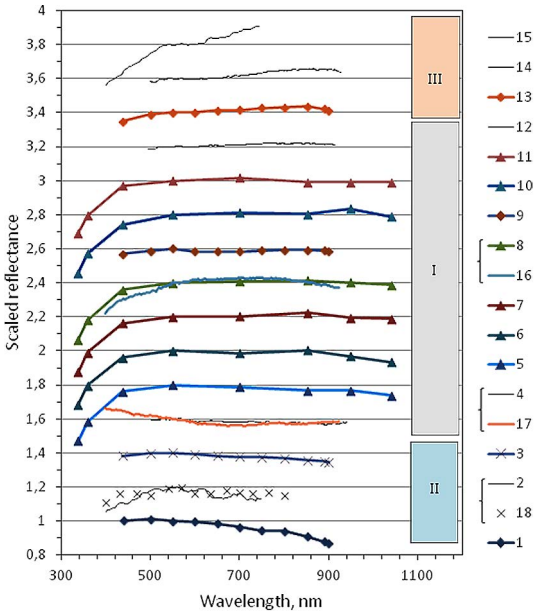

Fig. 1. Reflectance spectra of (1) Ceres. Spectral curves are shifted from each other along *y*-axis for clarity

Designations and notes for Table 1:
'SA' — solar activity; 'max' — maximum of SA; 'min' — minimum of SA; 'b' — before maximum or minimum of SA; 'a' – after maximum or minimum of SA; '+', '–' or '0' — positive, negative or neutral gradient of Ceres' RS; CME —coronal mass ejection on the Sun, H — halo-type CME; 'E' — eastward CME; 'W' — westward CME; 'Eq.' — equatorial CME; '?' — absence of data on CME; the number of X-ray flares is given according to GOES data 11 days before the date, which corresponds to time of propagation of solar wind shockwave from the Sun to asteroid with a median speed ~550 km/s; 'B' — very weak flare; 'C' — weak flare; 'M' — average flare.

Next, we tested the hypothesis stated in [1, 3], namely, whether these changes in the spectral characteristics of Ceres are associated with seasonal changes in the heat flux to its surface. The calculations of the energy irradiance of the Ceres' surface were carried out according to the theory presented in [10]. Owing to the small eccentricity of the Cererean orbit (e = 0.076) and the small inclination angle of the rotation axis of Ceres to its orbital plane ($\varepsilon = 4°$ [9]) the level of insolation of the asteroid's surface varies slightly with the change of seasons in equatorial and middle latitudes. The results of calculations of the average daily heat flux to the Ceres' surface during the Cererean year allow us to conclude that there is no regularity between the type of spectral curve and the time of year on Ceres.

Among possible reasons leading to the variability of the Ceres' reflectance spectra [11–13], we give preference to the influence of solar activity (SA). At the same time, we agree with the opinion expressed in [3] that the same processes lead to the appearance of a rarefied exosphere of Ceres and to changes in the reflectance spectra of its surface. To analyze the influence of SA to possible origin of an exosphere of Ceres since 1975 to 2013, we have used data on the number of sunspots from SILSO database (http://sidc.be/silso), data of GOES satellite on X-ray solar flares and flare-index from NOAA National Centers for Environmental Information (https://www.ngdc.noaa.gov/stp/solar/solarflares.html), and data of SOHO satellite obtained with LASCO coronagraph on solar coronal mass ejections (CMEs) (https://cdaw.gsfc.nasa.gov/CME_list/); it should be noted, the last data have been regularly archived since 1996 only. These data in abbreviated form are presented in Table 1 (last column). as is known, the sunspot number indicates the overall SA level; flares (especially in the X-ray range) and CMEs are signs of local

fast movement of magnetized plasma clumps in the upper layers of the solar atmosphere (e. g., [14]). Importantly, solar flares are often accompanied by CMEs representing eruptions into interplanetary space, which become interplanetary CMEs (ICMEs) (e. g., [15–17]). Producing shock waves in the solar wind, ICMEs are a strong factor to affect the surfaces of asteroids and other atmosphereless bodies. The key parameters of these plasma clouds are their total mass, concentration, and speed of constituent particles, which, in turn, depend on those of initial CMEs. As follows from solar observations, the estimated mass and kinetic energy of CME is proportional to the energy (W/m^2) of corresponding X-ray flare (e. g., [15, 18]; https://cdaw.gsfc.nasa.gov/CME_list/). Therefore, since the data on CMEs before 1996 is lacking, we used the number and the strength of solar flares to estimate SA in the mentioned period.

Table 1. Spectrophotometric observations of (1) Ceres and data on solar activity

No in Figure 1	Source of RS	Date	SA
1	[3]	19.12.2012	max(–), 6CME, 12 flares (B)
2	[1]	06.04.1986	min (~0), ?, no flares
4	[4]	04.07.1987	min(0), ?, 8 flares (B)
3	[3]	18.12.2012	max(–), ?, 2CME (E), 4 flares (B–C)
6	[5]	23.08.1979	b–max (0),?, 2 flares (C)
9	[3]	19–20.01.2013	max (~0), 9 CME, 9 flares (B)
5	[5]	24.12.1980	max (0), ?, 8 flares (C)
7	[5]	19.10.1980	max(0), ?, 10 flares,(C–M)
8	[5]	02.11.1980	max(0), ?, 8 flares (C)
12	[5]	13.07.1997	min (~0), CME (Eq.), no flares
10	[5]	16.09.1980	max(0), ?, 7 flares (C)
13	[3]	18.01.2013	max(+), CME (H, W), CME (E), 9 flares, (C–B)
14	[7]	20.04.1992	max(+), 6 flares, (C–B)
11	[5]	26.01.1982	max(0), ?, 7 flares (C)
15	[1]	26.12.1989	max(+),?, 10 flares (C)
16	[2]	05.10.2007	b–min (~0), no flares
17	[2]	02.04.2009	a–min (~0), no flares
18	[8]	13.10.1975 12.06.1977 15.06.1977	min (~0), no flares

Thus, the data on the above RS of Ceres and the SA level led us to the next findings.

1. Judging by the quantity and energy of corresponding X-ray flares, division of Ceres' RS into three groups (see Figure 1) agrees with different levels of SA: group I of Ceres' RS is obtained at low flare activity and corresponds probably to the characteristics of the asteroid surface itself; groups II and III of the spectra were registered at the elevated SA level and include spectral signs of the hypothetical Cererean exosphere. At growing SA, the exosphere may be a result of direct destructive action of more dense and high-speed flux of solar wind particles to the surface matter of the asteroid including phyllosilicates and ices (predominately H_2O ice).
2. According to the results of our numerical T-matrix simulations of light scattering by aggregate particles [19], RS of an asteroid surrounded by a rarefied dust exosphere composed of H_2O–ice submicron aggregates should have a distinct negative gradient, similar to those of 1 and 3 spectra of group II. These results also show that a positive gradient, like those of 13–15 RS of group III, is typical of RS of an asteroid with an exosphere consisting of Fe-Mg submicron aggregates.
3. We explain the 15^{th} anomalously red Ceres' spectrum by the predominance of globally distributed submicron Fe-Mg aggregates of particles

in the exosphere during the SA maximum. Although the data on solar flares for neighboring days did not differ significantly, the total flare-index (for a full solar disk) was extremely high two months before, namely 88.96 (https://www.ngdc.noaa.gov/stp/solar/solarflares.html). We suppose that this state of Ceres' exosphere might have lasted for about two months.

References:

[1] Golubeva L. F., Shestopalov D. I. Spectrometry of Minor Planets. The Possible Reason for Changes in Reflection Spectrum of 1 Ceres // Sol. Sys. Res. 1995. V. 29. P. 32–40.
[2] Busarev V. V. New Reflectance Spectra of 40 Asteroids: A Comparison with the Previous Results and an Interpretation // Sol. Sys. Res. 2016. V. 50. P. 13–23.
[3] Perna D., Kaňuchová Z., Ieva S. et al. Short-term variability on the surface of (1) Ceres. A changing amount of water ice? // Astron. Astroph. 2015. V. 575. Art. L1. 6 p.
[4] Vilas F., McFadden L. A.. CCD reflectance spectra of selected asteroids. I. Presentation and data analysis considerations // Icarus.1992. V. 100. P. 85–94.
[5] Zellner B., Tholen D. J., Tedesco E. F. The eight-color asteroid survey: results for 589 minor planets // Icarus.1985. V. 61. P. 355–416.
[6] Lazzaro D., Angeli C. A., Carvano J. M. et al. S3OS2: the visible spectroscopic survey of 820 asteroids // Icarus. 2004. V. 172. P. 179–220.
[7] Vilas F., Larson S. M., Hatch E. C., Jarvis K. S. CCD reflectance spectra of selected asteroids. II. Asteroid spectra and data extraction techniques // Icarus. 1993. V. 105. P. 67–78.
[8] Chapman C. R., Gaffey M. J. IV. Spectral reflectances of the asteroids // Asteroids / ed. T. Gehrels. Tucson, Arizona: Univ. Arizona Press, 1979. P. 1064–1089.
[9] Ermakov A. I., Mazarico E., Schröder S. E. et al. Ceres's obliquity history and its implications for the permanently shadowed regions // Geoph. Res. Lett. 2017. V. 44. P. 1–10.
[10] Sharonov V. V. The nature of planets. M.: GIFML, 1958. 552 p.
[11] Sizemore H. G., Schmidt B. E., Buczkowski D. A. et al. A global inventory of ice-related morphological features on dwarf planet Ceres: implications for the evolution and current state of the cryosphere // JGR Planets. 2019. V. 124. P. 1650–1689.
[12] Villareal M. N., Russell C. T., Luhmann J. G. et al. The dependence of the Cerean exosphere on solar energetic particle events // Astroph. J. Lett. 2017. V. 838. Art. L8. 5 p.
[13] Küppers M. The mystery of Ceres' activity // JGR Planets. 2019. V. 124. P. 205–208.
[14] Parker E. N. The solar-flare phenomenon and the theory of reconnection and annihilation of magnetic fields // Astroph. J. Suppl. 1963. V. 8. P. 177–211.
[15] Forbes T. G. A review on the genesis of coronal mass ejections // JGR Space Phys. 2000. V. 105. P. 23,153–23,165.
[16] Marsch E. Kinetic physics of the solar corona and solar wind // Living Rev. Solar Phys. 2006. V. 3. 100 p.
[17] Pinto R. F., Brun A. S., Rouillard A. P. Flux-tube geometry and solar wind speed during an activity cycle // A&A. 2016. V. 592. Art. A65.
[18] Hundhausen J., Burkepile J. T., Cyr O. C. St. Speeds of coronal mass ejections: SMM observations from 1980 and 1984–1989 // JGR Space Phys. 1994. V. 99. P. 6,543–6,552.
[19] Mackowski D. W., Mishchenko M. I. A multiple sphere T-matrix Fortran code for use on parallel computer clusters // J. Quant. Spectrosc. Radiat. Transfer. 2011. V. 112. P. 2182–2192.

PROTOPLANETARY DISK AT THE SNOWLINE: MODELING CLUSTERS OF REFRACTORY AND ICE PARTICLES

M. Ya. Marov[1], A. V. Rusol[1], A. B. Makalkin[2]
[1] *Vernadsky Institute of Geochemistry and Analytical Chemistry RAS, Kosygin St. 19, 119991 Moscow, Russia*
[2] *Schmidt Institute of Physics of the Earth RAS, B. Gruzinskaya St. 10-1, 123242 Moscow, Russia*

KEYWORDS:
protoplanetary disk, planetesimal formation, dust aggregate, fragmentation, snowline, fractal aggregate

INTRODUCTION

The paper deals with numerical modeling the structure of a centimeter to decimeter size dust clusters crossing the snow line of protoplanetary disk. It advances the results of previous study of particulate gas matter moving toward the protosun and contributing to the formation of planetesimals [1, 2]. The cluster is assumed to have a fractal and heterogeneous structure and consists of both refractory and water ice aggregates surviving or sublimating/completely evaporating at the snow line, respectively. Refractory and ice aggregates in the cluster have relatively low density due to a high porosity. Their sizes, composition, densities, and mass fractions in the cluster were constrained with the account of data of cometary nucleus based mostly on the results of Rosetta mission to comet 67 / P Churyumov – Gerasimenko [3]. Dust aggregates that make up the clusters were estimated to be in the range of ~0.01–1 cm. The results of modeling depend only on the ratio of aggregate to cluster radii rather than on their absolute sizes. However, the actual dimensions matter to confirm the validity of the assumption of the complete evaporation of ice aggregates at the snowline.

Fractal dimension of the clusters was taken $D_\beta = 2.75$, which corresponds to a macroporosity ~75–80 %, which is high compared to the comet nucleus macroporosity (about 40 %) [4]. Given the high macroporosity of the cluster and the rather low cluster/aggregate diameter ratio (a few hundred), in such a fractal approach the cluster possesses a high permeability. The small aggregate sizes (≤1 cm), along with the high permeability of the cluster, ensure rapid ice evaporation (within ~1 year) and provide cluster fragmentation at the snow line. Spherical shape of the aggregates that make up the cluster as well as the spherical shape of the volume enclosing the cluster was assumed. The varied parameters were as follows: refractory aggregate/ice aggregate volume ratio, aggregate/cluster volume ratio (for both aggregate types), mass fractions of refractory and icy aggregates, and density of refractory and ice aggregates with account for possible variations in the porosity. In addition, when estimating densities of refractory aggregates possible variations in their porosity and chemical composition were addressed keeping in mind cometary data which suggest that they consist of silicates, sulfides (with a possible amount of Fe, Ni metal) and organic compounds [3]. The particle size distribution in both refractory and icy aggregates was adopted in the form of the inverse power law with an exponent of 3.5 for both types of aggregates with varied ratio of maximum to minimum radii.

When constructing fractal clusters, the technique developed by the authors [5–7] was utilized that significantly accelerate the model of fractal clusters evaluation compared, for example, with the ballistic cluster-cluster aggregation (BCCA) technique and do not requires a supercomputer. No less important that our technique allows us to develop the model of heterogeneous clusters consisting of two types of aggregates of different size, density and mass fraction of composed particles. This approach has no analogs in the literature available.

RESULTS AND DISCUSSION:

The following main results of numerical simulations were obtained:

1. If sizes of refractory aggregates forming the cluster are larger than that of icy aggregates, then at the snowline the cluster breaks up into small fragments with masses of ≤0.1 % of the total mass of the refractory cluster component having sizes much smaller than the cluster diameter. It was also shown that if minimum and maximum radii in the size distribution for refractory and ice aggregates are equal, than the largest masses of fragments do not exceed 1 % of the mass of the refractory substance in the cluster. This result is fulfilled even in the case when mass fraction of silicates to ice is equal to the maximum value satisfying the cometary data (Δ = 9) [3].
2. If the minimum and maximum radii of refractory aggregates (pebbles) are significantly less than the corresponding radii of ice aggregates (of 5 or more), then providing mass fraction of refractory components is sufficient, large and relatively dense fragments form as the result of ice evaporation. The largest ones have masses of 15–45 % of the total mass of the refractory substance in the cluster, and maximum size may reach the cluster's diameter. Moreover, in the three largest fragments (which is <~1 % of the total number of fragments, more than half of the total mass of the refractory component of the cluster material is concentrated.
3. Given radius distributions of refractory and ice aggregates in a cluster, the distribution by mass and size of the fragments formed at the snowline depends on the ratios of the densities of refractory and icy aggregates and on the ratio of their mass fractions in the cluster. If in the cluster, mass fraction increases and density of the refractory substance decreases (meaning increasing the specific volume of the refractory component) then the largest fragments turn out commensurable with the cluster itself and become more massive and dense because they contain a higher mass fraction of the refractory component.
4. In the case density of refractory aggregates is three times higher than that of icy aggregates, then to obtain large massive fragments containing most of the refractory substance of mass, it is sufficient for the protoplanetary disk at the snowline to contain a relatively low mass fraction of the refractory component but with a significant mass fraction of ice. In this case, the refractory component to ice mass ratio (Δ ~2) is still consistent with the omposition of the protosolar matter. With an increase of the mass ratio of the refractory component to ice, the mass fraction concentrated in several large and massive fragments increases. When density of the refractory aggregates is an order of magnitude higher than that of ice aggregates the formation of large massive fragments that collect the bulk of refractory material of the cluster is less favorable. Formation of such massive fragments requires the largest possible mass ratio of refractories to ice value Δ from the range, but it still is in agreement with cometary data (Δ = 9).

CONCLUSION

The developed model provides an approach to understanding of fragmentation of heterogeneous clusters aggregates composed of refractory and ice solid components and having different ratio of the aggregates when crossing the snow line. Basically, fragmentation at different degrees of heterogeneity of protoplanetary matter at the level of clusters consisting of dust-ice aggregates and of different clusters' porosity is studied The latter is especially important when modeling mutual collisions of loose, "fluffy" fractal dust aggregates similar to those obtained in the authors earlier works (see, e. g., [7]). A solution to these problems is necessary for further development of methods of the protoplanetary disk evolution numerical modeling.

While the model under consideration do not focus specifically on a possible interaction of individual fragments in the course of relative motion in the gaseous protoplanetary disk, the obtained results give an opportunity to place constrains on a lower limit of mass increase caused by such an interaction. The formation of large massive refractory clusters during fragments linkage

looks quite plausible. However, this scenario looks possible only provided ice component is contained mainly in larger aggregates than refractory component behind the snowline.

One may expect that despite a rather simplified approach with the use of spline method to modeling two-component porous clusters formation, the results deduced are fully realistic and allows us to clarify the structural features of the fragments formed on the inner side of the snowline. Similarly, they give qualitative general picture of disc content transformation at the snowline involving solid and volatile mass concentrations, as well as clearly demonstrate an efficiency of the fractal dimension approach.

REFERENCES:

[1] Ida S., Guillot T. Formation of dust-rich planetesimals from sublimated pebbles inside of the snow line // Astron. and Astrophys. 2016. V. 596. Article id. L3. P. 5 id. L3.P. 5.
[2] Makalkin A. B., Artyushkova M. E. On the formation of planetesimals: radial contraction of the dust layer interacting with the protoplanetary disk gas // Sol. Syst. Res. 2017. V. 51. No. 6. P. 491–526.
[3] Fulle M., Blum J., Green S. F., Gundlach B. Herique A., Moreno F., Mottola S., Rotundi A., Snodgrasset C. The refractory-to-ice mass ratio in comets // Mon. Notic. Roy. Astron. Soc. 2019. V. 482. P. 3326–3340.
[4] Blum J., Gundlach B., Krause M., Fulle M. et al. Evidence for the formation of comet 67P/Churyumov – Gerasimenko through gravitational collapse of a bound clump of pebbles // Mon. Notic. Roy. Astron. Soc. 2017. V. 469. P. S755–S773.
[5] Marov M. Ya., Rusol A. V. Gas-dust protoplanetary disc: Modeling collisional interaction of primordial bodies // J. Modern Phys. 2015. V. 6. P. 181–193.
[6] Marov M. Ya., Rusol A. V. Gas-dust protoplanetary disc: Modeling primordial dusty clusters evolution // J. Pure Appl. Phys. 2015. V. 3. P. 16–23.
[7] Marov M. Ya., Rusol A. V. Estimating the parameters of collisions between fractal dust clusters in a gas–dust protoplanetary disk // Astron. Lett. 2018. V. 44. P. 474–481.

MIGRATION OF PLANETESIMALS TO THE EARTH FROM THE ZONE OF THE OUTER ASTEROID BELT

M. Ya. Marov, S. I. Ipatov
Vernadsky Institute of Geochemistry and Analytical Chemistry Russian Academy of Sciences, Moscow, Russia
(*marovmail@yandex.ru; siipatov@hotmail.com*)

KEYWORDS:
Planetesimals, outer asteroids belt, migration, ocean water

INTRODUCTION:
The problem of migration of bodies to the Earth from different distances beyond the ice line was considered in several papers. The review of such papers can be found in [1]. Earlier we studied migration of planetesimals mainly from beyond the orbit of Jupiter [1–4]. Below we consider migration of planetesimals from the zone of the outer asteroid belt.

THE MODEL AND INITIAL DATA USED FOR CALCULATIONS:
Migration of planetesimals under the gravitational influence of 7 planets (from Venus to Neptune) was calculated with the use of the symplectic code from [5]. In each variant of the calculations, the initial values of semi-major axes of orbits of 250 planetesimals varied from a_{min} to a_{min} + 0.1 AU, their initial eccentricities were equal to e_o, and the initial inclinations equaled to $e_o/2$ rad. In Table 1 we consider e_o = 0.02, and in Table 2 e_o = 0.15. Orbital elements of the migrated planetesimals were recorded in computer memory with a step of 500 years. Based on these arrays of orbital elements, we calculated the probabilities p_E of collisions of planetesimals with the Earth. The calculations were made similar to those in [1–4, 6–8].

RESULTS OF CALCULATIONS:
The value of p_E calculated for a run with 250 bodies could vary hundreds of times for different calculation variants with the same values of a_{min} and e_o (see lines for a_{min} equaled to 3.5, 3.8 and 3.9 AU in Table 2). Such difference was earlier found for calculations of migration of Jupiter-crossing objects [6–7]. One among hundreds or thousands of such objects moved in Earth-crossing orbits during millions or even tens of millions of years, and the probability of a collision of such object with the Earth was greater than that for hundreds or even thousands of other objects. In Tables 1–2 at time interval T = 100 Myr, the values of p_E vary from values less than 10^{-6} to values of the order of 10^{-3}, but they are often between 10^{-6} and 10^{-5}, as for many our previous calculations with $a_{min} \geq 5$ AU considered in [1–4]. In some calculations, there was a considerable growth of p_E after 10 Myr. There were more runs with $p_E > 2 \cdot 10^{-5}$ for $3.2 \leq a_{min} \leq 3.3$ AU and a_{min} = 3.5 AU than for other values of a_{min}, including the values of $a_{min} \geq 5$ AU considered in [1–4]. Typically, there was no noticeable growth of p_E after 100 Myr, but at a_{min} = 3.2 AU and e_o = 0.15 for T from 100 to 200 Myr there was a growth of p_E from $3.65 \cdot 10^{-4}$ to $1.045 \cdot 10^{-3}$. A few planetesimals could move in elliptical orbits even at 1 Gyr. For example, a planetesimal moved at 200 AU from the Sun at T = 1 Gyr, a_{min} = 4.4 AU and e_o = 0.15. In most calculation variants, the fraction of planetesimals collided with the Sun was less than 0.02 at $a_{min} \geq 3.5$ AU and e_o = 0.15, and it was less than 0.03 at $a_{min} \geq 3.5$ AU and e_o = 0.02.

CONCLUSIONS:
The probabilities of collisions with the Earth of the planetesimals with initial semi-major axes from 3.2 to 3.4 and from 3.5 to 3.6 AU were usually greater than those for the planetesimals initially located beyond the orbit of Jupiter.

ACKNOWLEDGEMENTS:
The work was carried out as a part of the state assignments of the Vernadsky Institute of RAS No. 0137-2020-0004.

Table 1. Probability p_E of a collision of a planetesimal with the Earth during time interval T. N_{ell} is the number of planetesimals left in elliptical orbits, N_{ej} is the number of planetesimals ejected into hyperbolic orbits, N_{Sun} is the number of planetesimals collided with the Sun. Initial semi-major axes of planetesimals were between a_{min} and a_{min} + 0.1 AU, and their initial eccentricities equaled to 0.02

***T*, Myr**	**1.0**	**1.0**	**10**	**10**	**100**	**100**	**100**	**100**
$a_{min,}$ AU	N_{ell}	$10^6 p_E$	N_{ell}	$10^6 p_E$	N_{Sun}	N_{ej}	N_{ell}	$10^6 p_E$
3.0	250	0	250	0	0	0	250	0
3.1	250	0	250	0	0	0	250	0
3.2	250	0	243	23.19	7	75	168	33.54
3.3	250	0	223	15.44	9	85	156	129.83
3.3	250	0	227	51.80	5	89	156	219.58
3.4	250	0	250	0	0	3	247	0
3.4	250	0	250	0	0	0	250	0
3.5	228	5.71	96	6.20	4	100	146	4009.1
3.5	224	13.6	200	14.64	0	99	152	17.33
3.6	244	0.42	213	3.38	1	55	194	3.59
3.6	245	0.66	206	1.96	0	78	172	3.15
3.7	201	2.09	143	3.26	0	174	76	5.68
3.8	170	3.08	17	11.9	1	244	5	11.93
3.8	158	18.65	16	52.12	2	247	1	72.91
3.9	137	1.01	31	1.48	1	243	6	2.45
4.0	128	1.63	22	1.92	2	244	4	3.62
4.1	73	10.73	16	352.8	2	240	8	388.7
4.1	79	7.43	11	7.47	2	247	1	7.47
4.2	230	1.52	193	2.17	0	130	120	3.40
4.3	80	0.36	23	0.46	1	246	3	0.54
4.4	75	5.60	12	7.90	2	245	3	7.92
4.5	61	1.84	9	1.84	1	248	1	1.84
4.6	72	1.62	10	1.82	1	246	3	1.83
4.7	65	4.12	9	12.90	1	247	2	12.90
4.8	73	5.40	12	0.588	1	247	2	0.66
4.9	53	4.21	7	8.08	1	247	2	8.08

References:

[1] Marov M. Ya., Ipatov S. I. Delivery of water and volatiles to the terrestrial planets and the Moon // Solar System Research. 2018. V. 52. No. 5. P. 392–400. https://arxiv.org/ftp/arxiv/papers/2003/2003.09982.pdf

[2] Ipatov S. I. Migration of bodies to the Earth and the Moon from different distances from the Sun // The Ninth Moscow Solar System Symposium 9M-S3. 2018. https://ms2018.cosmos.ru/. # 9MS3-SB-11. P. 104–106.

[3] Ipatov S. I. Migration of planetesimals to the Earth and the Moon from different distances from the Sun // 50th LPSC. 2019, #2594. https://www.hou.usra.edu/meetings/lpsc2019/pdf/2594.pdf .

[4] Marov M. Ya., Ipatov S. I. Water inventory from beyond the Jupiter orbit to the terrestrial planets and the Moon // Proc. IAU Symp. No. 345 “Origins: from the Protosun to the First Steps of Life”, ed. by Bruce G. Elmegreen, L. Viktor Tóth, Manuel Gudel, Proc. IAU. Vol. 14. Symp. S345, Cambridge University Press. 2020. P. 164–167. doi:10.1017/S1743921319001479

[5] Levison H. F., Duncan M. J. The long–term dynamical behavior of short-period comets // Icarus. 1994. V. 108. P. 18–36.

[6] Ipatov S. I., Mather J. C. Migration of Jupiter-family comets and resonant asteroids to near-Earth space // Annals of the New York Academy of Sciences. 2004. V. 1017. P. 46–65. http://arXiv.org/format/astro-ph/0308448.

[7] Ipatov S. I., Mather J. C. Comet and asteroid hazard to the terrestrial planets // Advances in Space Research. 2004. V. 33. P. 1524–1533. http://arXiv.org/format/astro-ph/0212177.

[8] Ipatov S. I. Probabilities of collisions of planetesimals from different regions of the feeding zone of the terrestrial planets with the forming planets and the Moon // Solar System Research. 2019. V. 53. N 5. P. 332–361. http://arxiv.org/abs/2003.11301.

Table 2. Probability p_E of a collision of a planetesimal with the Earth during time interval *T*. N_{ell} is the number of planetesimals left in elliptical orbits, N_{ej} is the number of planetesimals ejected into hyperbolic orbits, N_{Sun} is the number of planetesimals collided with the Sun. Initial semi-major axes of planetesimals were between $a_{\min}$ and $a_{\min}$ + 0.1 AU, and their initial eccentricities equaled to 0.15

***T*, Myr**	**1.0**	**1.0**	**10**	**10**	**100**	**100**	**100**	**100**
$a_{\min,}$ AU	N_{ell}	$10^6 p_E$	N_{ell}	$10^6 p_E$	N_{Sun}	N_{ej}	N_{ell}	$10^6 p_E$
3.0	250	0	250	0	0	16	234	3.70
3.1	250	0	250	0	0	0	250	0
3.2	250	0	225	24.19	16	116	118	365.47
3.2	250	0.15	229	39.87	22	124	104	4429.3
3.3	228	0.89	148	46.54	5	161	84	223.51
3.3	220	1.63	150	33.79	10	158	82	65.38
3.4	235	0.30	127	1.77	0	180	70	24.55
3.5	118	7.16	11	44.91	2	246	2	235.9
3.5	123	6.1	13	10.62	1	245	4	10.62
3.6	97	3.81	7	5.80	1	245	4	5.80
3.6	85	3.17	9	4.04	2	245	3	4.07
3.7	101	1.21	8	3.54	2	246	2	3.54
3.8	72	1.64	14	283	1	244	5	1243.2
3.8	61	4.71	9	5.80	0	249	1	5.80
3.9	74	178.6	9	178.6	0	247	3	178.6
3.9	58	1.57	11	1.79	0	248	2	1.80
4.0	53	0.44	7	0.44	1	243	6	2.45
4.0	60	2.24	12	2.56	1	244	12	2.56
4.1	59	2.52	5	49.93	2	247	1	50.60
4.1	69	2.17	7	2.61	1	249	0	2.62
4.2	65	1.06	4	1.08	1	247	2	1.08
4.3	66	1.43	5	1.52	1	248	1	1.52
4.4	60	2.32	6	2.97	1	248	1	2.97
4.5	54	0.46	7	6.80	4	244	2	6.80
4.6	53	1.41	3	21.80	2	247	1	21.80
4.7	53	0.53	4	0.62	0	250	0	0.62
4.8	60	0.33	1	0.35	0	250	0	0.35
4.9	67	2.42	10	3.34	0	248	2	3.34

PROBABILISTIC ANALYSIS OF THE COSMIC MASSES ACCUMULATIONS IN THE SOLAR SYSTEM

T. V. Salnikova[1], A. S. Samokhin[1,2]
[1] *Lomonosov Moscow State University, Leninskie gori, GSP-1, Moscow 119991, Russia*
[2] *Trapeznikov Institute of Control Sciences RAS, 65 Profsoyuznaya street, Moscow 117997, Russia (samokhin@ipu.ru)*

KEYWORDS:
numerical simulation, cosmic masses, asteroids, dust particles, stable configuration, elliptical orbits, circle orbits, steady states

INTRODUCTION:
Cosmic masses: asteroids, small planets, dust particles and dust clouds fill the interplanetary space. There is still no answer, why instead of one planet, we have an asteroid belt stable configuration with small planets, such as Ceres. There are many hypotheses for the belt conformation. For example, Sean N. Raymond and Andre Izidoro suggested in [1] that in fact there was no planetary embryo, and the belt was formed from the debris of the planets during their formation and immediately took its current form.

PROBLEM SETTING:
The aim of this work is an attempt to obtain stable clusters of cosmic masses of the Solar system when considering a large variety of initial conditions in a flat setting. We study the issue of gravitational capture of dust particles in the Solar system, their transition to steady states: into elliptical and circular orbits. The asteroid belt being a stable formation is a part of our numerical simulation.

Jupiter has the second mass of the Solar objects after the Sun and it attracts the attention of researchers. The steps of our numerical study begin with a consideration of the cosmic masses evolution under Sun and Jupiter attraction. Next complexification of the mathematical model occurs due to the perturbations of additional planets: Mars, Earth, Saturn and others.

RESULTS:
As a result, a statistical analysis of the cosmic masses evolution under numerous possible initial conditions with successively added disturbances is presented. The graphs of the considered dependencies are constructed numerically.

REFERENCES:
[1] Raymond S. N., Izidoro A. The empty primordial asteroid belt // Science Advances. 2017. V. 3. No. 9. 5 p. doi:10.1126/sciadv.1701138.

BEHAVIOR OF FE-CONTAINING SPECIES DURING METEOR EVENTS AND IN LASER EXPERIMENTS

A. A. Berezhnoy[1], A. M. Popov[2], J. Borovička[3], T. A. Labutin[2], S. M. Zaytsev[2], G. V. Belov[2]

[1] *Sternberg Astronomical Institute, Moscow State University, Universitetskij pr., 13, 119234 Moscow, Russia (a_tolok@mail.ru)*

[2] *Department of Chemistry, Moscow State University, Leninskie Gory 1 / 3, 119234 Moscow, Russia*

[3] *Astronomical Institute, Czech Academy of Sciences, Fričova Street 298, CZ–25165 Ondřejov, Czech Republic*

KEYWORDS:
FeO, laser experiments, thermochemistry, meteor events, quenching

Numerous emission atomic and ionic lines of iron in meteor spectra have been recognized for a long time [1]. FeO orange bands were detected, among others diatomic spectra, in Benešov bolide [2]. Thermochemical calculations of equilibrium chemical composition of bolide-produced hot clouds with usage of quenching theory were performed in order to estimate the content of main impact-produced metal oxides such as AlO, MgO, FeO, and CaO [3, 4]. Laser Induced plasma can imitate the emission of these molecules in a laboratory. High spectral and temporal resolution as well as known target composition allows ones to study a plasmachemistry of the lab experiments in great details.

For lab experiments we used setup described in [5]. For better reproducibility the radiation of the Nd:YAG laser (λ = 266 nm, E = 24±1 mJ/pulse, $\tau \sim 6$ ns) was focused at 3.5 mm below the surface of iron target, which resulted in spot diameter at the pure iron target was ~0.2 mm (laser fluence of ~75 J $\cdot$cm^{-2}). Experiments were performed at 1 bar pressure. The central part of the plasma plume was projected onto the slit of the Czerny-Turner spectrograph equipped with 1800 lines/mm grating.

The general requirement to observe molecular spectra in laser-induced plasmas is the relatively long delay time providing a low plasma temperature. The LIBS spectra with the time delay from 10 to 100 μs after laser pulse were recorded. The ratio of delay time to gate time was maintained higher than 10.

Excitation temperature of a plasma was calculated by neutral Fe lines up to delay time of 50 μs. FeO orange bands were detected at delay times between 20 and 100 μs. Peculiarities observed in the relative intensity distribution of the FeO orange bands as a function of delay time (and, respectively, a collision temperature) were analyzed.

The comparative thermochemical treatments of the equilibrium chemical composition of laser-produced and bolide clouds were performed with usage of the EQL program [6] equipped with IVTANTHERMO database [7] (see Figure). Rate constants of the relevant chemical reactions with participation of Fe–containing species were taken from [8].

Based on studies of rate constants of main reactions with participation of metal-containing species including gas-phase FeO it was found that chemical composition of impact-produced Benešov meteoroid cloud during bolide and wake phases is in the equilibrium at typical temperatures (about 3000 K) of appearance of strong molecular bands. Comparing hydrodynamic and chemical timescales during the laboratory experiments one can conclude that quenching of chemical composition of laser-produced cloud occurs at 1700–2200 K. These temperatures are significantly lower than temperature range (3100–5300 K) at which the most intensive FeO orange bands were detected during the present experiment.

Due to a higher pressure and lower temperature the FeO_2 / FeO ratio is expected to be significantly higher in laser-induced plasma in comparison with that in the Benešov wake cloud. A presumable contribution of the highest

iron oxides to the laser plasma emission detected at longest time delay (100 μs) in the region 620–640 nm has been discussed.

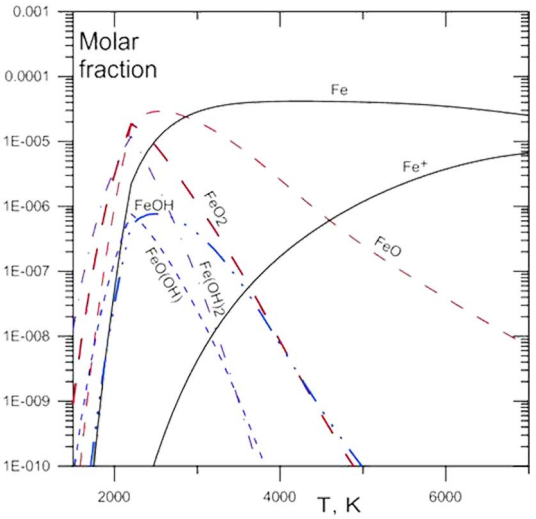

Fig. 1. Equilibrium composition of Fe-containing species as a function of temperature in the laser-induced plasma at 1 bar. Air-to-target mass ratio is 10^4

ACKNOWLEDGEMENTS:
A. M. P., T. A. L., S. M. Z., A. A. B. would like to thank financial support from RSF grant No. 18–13–00269. J. B. and A. A. B. were supported by grant No. 19-26232X from the Czech Science Foundation.

REFERENCES:

[1] Ceplecha Z. Spectral data on terminal flare and wake of double-station meteor 38421 (Ondřejov, April 21, 1963) // Bull. Astron. Inst. Czech. 1971. V. 22. P. 219–304.
[2] Borovička J., Spurný P. Radiation study of two very bright terrestrial bolides and an application to the comet S–L 9 collision with Jupiter // Icarus. 1996. V. 121. P. 484–510.
[3] Berezhnoy A. A., Borovička J. Formation of molecules during meteor events // Icarus. 2010. V. 210. P. 150–157.
[4] Borovička J., Berezhnoy A. A. Radiation of molecules in Benešov bolide spectra // Icarus. 2016. V. 278. P. 248–265.
[5] Zaytsev S. M., Popov A. M., Zorov N. B., Labutin T. A. Measurement system for high-sensitivity LIBS analysis using ICCD camera in LabVIEW environment // J. Instrumentation. 2014. V. 9. Art. P06010.
[6] Belov G. V. Iorish V. S., Yungman V. S. IVTANTHERMO for Windows — Database on thermodynamic properties and related software // Calphad. 1999. V. 23. P. 173–180.
[7] Belov G. V., Dyachkov S. A., Levashov P. R., Lomonosov I. V., Minakov D. V., Morozov I. V., Sineva M. A., Smirnov V. N. The IVTANTHERMO-online database for thermodynamic properties of individual substances with web interface // J. Phys.: Conf. Ser. 2018. V. 946. Art. 012120.
[8] NIST chemical kinetics database. 2020. Standard reference database 17, Version 7.0 (web version). Release 1.6.8.

ESTIMATION YARKOVSKY EFFECT IN 355258 (2007 LY4) AND 404118 (2013 AF40) YOUNG ASTEROID PAIR

E. Plavalova, A. Rosaev
Research and Educational Center "Nonlinear Dynamics", Yaroslavl State University
Mathematical Institute Slovak Academy of Sciences

We have studied the Yarkovsky effect on the close asteroid pair 355258 (2007 LY4) and 404118 (2013 AF40). We have found that this pair may have been formed at close encounter 8075±100 yrs ago. Using the assumption of the birth of this pair during the breakup of a recent close encounter, we have established some restrictions on the thermal parameters of these asteroids.

ABOUT IMPORTANCE OF MAGNETIC PHENOMENA FOR THE SATURN RINGS ORIGIN

V. Tchernyi[1], S. Kapranov[2], A. Pospelov, E. Chensky
[1] *Modern Science Institute SAIBR, Moscow, Russia* (*chernyv@mail.ru*)
[2] *Kovalevsky Institute of Marine Biological Research RAS, Moscow, Russia* (*sergey.v.kapranov@yandex.ru*)

KEY WORDS:
Saturn rings origin, space magnetism, space diamagnetism, space superconductivity, space ice

Presence of magnetic field of Saturn and temperature 70–100 K nearby of it give us an idea of diamagnetism and superconductivity of the rings particles. The rings could emerge from the ice particles moving on chaotic orbits around Saturn within protoplanetary cloud. After appearance of magnetic field of Saturn and diamagnetic force of expulsion at the certain time moment for the ice particles all chaotic orbits of them start to shift to the magnetic equator plane, where there is a minimum of the particles magnetic energy. Each particle comes to the stable position preventing its own horizontal and vertical shift. Particles are locked within three-dimensional magnetic well due to Abrikosov quantum vortex phenomenon for superconductor. This mechanism is valid and it works even particles have a small fraction of superconductor. Final picture is similar to the picture of iron particles forms the same shape around a magnet on laboratory table. Any other phenomena like gravity resonances, dusty plasma and others may bring some peculiarities to the final picture of the rings. It follows that magnetic field of Saturn and low temperature around of it are the main reason for the rings origin and the rings is product of the early time of the magnetic field of Saturn appearance. Additional matter to the rings also may come from the frozen water particles generated from the Saturn sputniks geysers due to magnetic coupling between planet and satellites. The data of Cassini mission to Saturn rings are conforming suggested theory.

ACKNOWLEDGEMENTS:
Part of work contributed by S. V. Kapranov was supported by the state assignment AAAA–18–118021350003–6. On 8.07.2019 4-min. movie: The Mystery of Saturn Rings Solved By Magnetism? https://www.youtube.com/watch?v=AI6AaMJoR4A

REFERENCES:
[1] Tchernyi V. V., Kapranov S. V. The Astrophysical J., 2020, V. 894, No. 1.
[2] Tchernyi V. V., Kapranov S. V., Pospelov A. Yu. arXiv.org/abs/2004.13212, 28.04.2020.
[3] Tchernyi V. V., Pospelov A. Yu. Astrophys Space Sci., 2007, V. 307, P. 347.
[4] Tchernyi V. V., Chensky E. V. GRSL, 2005, V. 2, P. 445.

DUST AND DUSTY PLASMAS IN THE SYSTEM OF MARS

S.I. Popel, A. P. Golub', L. M. Zelenyi
Space Research Institute of the Russian Academy of Sciences (IKI), 84/32 Profsoyuznaya Str, Moscow117997, Russia, (popel@iki.rssi.ru)

KEYWORDS:
Mars, Phobos, Deimos, ionosphere, dusty plasmas, waves, radiative transport.

INTRODUCTION:
Investigation of dusty plasma systems beyond the Earth's atmosphere is of considerable interest not only from the viewpoint of understanding and describing the processes occurring in nature, but also in connection with the planning of space missions, including those to Mars and its satellites, as well as with the interpretation of data obtained in the existing and future space missions. In the Martian atmosphere the dust component can play a substantial (in some cases, decisive) role in the radiation balance. Dust grains get charged under the action of solar radiation, interaction with charged particles of the atmosphere and solar wind, triboelectric effect in dust devils, and other factors [1]. Dusty plasmas are formed in a surface layer over the illuminated part of Martian satellites Phobos and Deimos owing to photoelectric and electrostatic processes [2]. According to observations made from the Viking [3, 4] as well as Phobos-2 and Mars-Express spacecrafts [5], the surfaces of Phobos and Deimos are covered with a dust consisting of small separate regolith grains formed as a result of bombardment of the surface by microscopic meteoroids [6].

The purpose of this work is a brief review of the results of studies of dust and dusty plasmas in the atmosphere of Mars and in the vicinity of its satellites Phobos and Deimos, carried out recently at the Space Research Institute of the Russian Academy of Sciences.

A SELF-CONSISTENT MODEL OF DUSTY PLASMA IN THE MARTIAN IONOSPHERE:
The model [7] describes, in particular, sedimentation of dust grains in the atmosphere, their growth in a supersaturated vapor, and dust grain charging processes, allowing for variations of the ion-subsystem composition in the atmosphere and photoelectric emission. We pay attention to condensation and absorption of carbon dioxide and water molecules by dust particles. The effect of the charges of particles on condensation processes is also taken into account. Using the modified (to the conditions of the Martian ionosphere) model we illustrate the effect of the initial distributions of dust particles, as well as the condensation and absorption of carbon dioxide and water molecules by dust particles, on the formation and evolution of dusty plasmas in the Martian ionosphere. We show that the solid carbon dioxide particles can reach the sizes of the order of 100 nm at altitudes of about 100 km. These data are in accordance with observations performed on Mars Express orbiter with the aid of the SPICAM infrared spectrometer [8]. There is a possibility of the existence in the Martian ionosphere of carbon dioxide dust clouds analogous to noctilucent clouds. Furthermore, phenomena in Martian atmosphere analogous to polar mesosphere summer echoes are also possible.

WAVE PROCESSES IN MARTIAN ATMOSPHERE:
Horizontal winds that arise in the ionosphere of Mars due to heating by solar radiation and rotation of Mars, at the initial stage of their interaction with dusty plasma clouds at altitudes of about 100 km, can lead to the emergence of conditions for the excitation of dust acoustic waves due to the development of kinetic instability [9]. The generation time of dust acoustic waves turns out to be sufficiently long so that the formation of nonlinear plasma wave structures, for example, solitons, is possible. An increase in the number density of dust particles or a decrease in the electron number density by an order of magnitude leads to an increase in the amplitude of the dust sound

soliton by about an order of magnitude. Linear and nonlinear waves in the Martian ionosphere can be recorded in measurements made by spacecraft. The possibility of the occurrence of dust acoustic wave disturbances in the ionosphere of Mars should be taken into account when processing and interpreting observational data.

RADIATIVE TRANSPORT IN THE PRESENCE OF DUST:

To calculate the radiative transport we have used the model [10] or self-consistent calculation of modification of atmosphere in the presence dust. Entrance parameters for calculations are position of the dust, the seasonal and daily time, the data about the composition of dust particles and their distribution in sizes. On the basis of this model, we calculate the radiative properties of homogeneous atmospheric layers with regard to the variation of their composition with altitude, determine the radiation fluxes and temperature changes related to radiant energy release, investigate optical-physical atmospheric characteristics in the context of attenuation of the solar radiation flux. The presence of dust in the atmosphere leads to the temperature variation of $|\Delta T|$ = 0.1-0.8 K near Martian surface. The most effective change in the temperature regime is observed under the conditions of the variations of the atmosphere parameters caused by the presence of nano- and microscale dust particles.

BEHAVIOR OF DUST AT PHOBOS AND DEIMOS:

The problem of the motion of a dust particle in the electrostatic and gravitational fields of the satellites of Mars, Phobos and Deimos, has been considered. Particle motion starts from the satellite's surface and represents damped oscillations around a stable position above the satellite's surface (Fig. 1). It has been established that damped oscillations of a particle are caused by variations in its electric charge which is calculated with taking into account the influence of the solar radiation, solar wind, and photoelectrons emitted from the satellite's surface. The time during which the particle reaches the stable position above the satellite's surface has been determined. It is noted that this time should be less than the duration of daylight hours on the satellite. For a particle on Phobos, the time to reach the stable state and its height above the surface of the satellite is less than on Deimos.

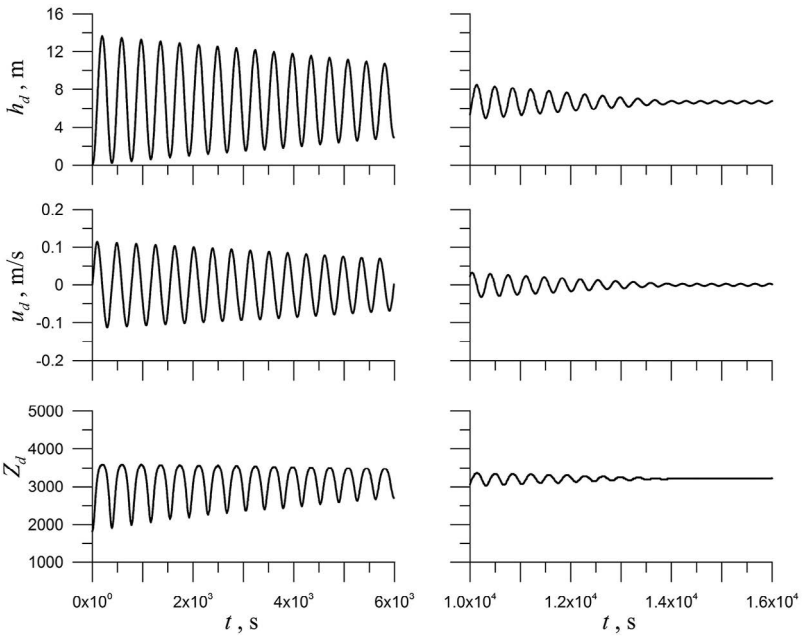

Fig. 1. The altitude (h_d), velocity (u_d), charge number (Z_d) of a dust particle with the size a=1.3 μm vs time at the surface of Phobos. The subsolar angle is 87°.

ACKNOWLEDGMENTS:
This work was supported in part by the Russian Foundation for Basic Research (project no. 18-02-00341-a).

REFERENCES:

[1] Izvekova Yu.N., Popel S.I. Plasma effects in dust vortices at the surface of Mars // Plasma Phys. Rep. 2017. V. 43. No. 12. P. 1172-1178.
[2] Popel S.I., Golub' A.P., Zakharov A.V., Zelenyi L.M. Dusty plasmas at Martian satellites // J. Phys.: Conf. Ser. 2019. V. 1147. P. 012110, 11 pages.
[3] Thomas P. Surface features of Phobos and Deimos // Icarus. 1979. V. 40.No. 2. P. 223-243.
[4] Thomas P., Veverka J. Downslope movement of material on Deimos // Icarus. 1980. V. 42. No. 2. P. 234-250.
[5] Zakharov A., Horányi M., Lee P., et al. Dust at the Martian moons and in the circummartian space // Planet. Space Sci. 2014. V. 102. P. 171-175.
[6] Popel S.I., Golub' A.P., Dol'nikov G.G., et al. On fluxes of dust particles in the system of Mars // Tech. Phys. Lett. 2020. V. 46. No. 8, in press.
[7] Reznichenko Yu.S., Dubinskii A.Yu., Popel S.I. On dusty plasma formation in Martian ionosphere // J. Phys.: Conf. Ser. 2020. V. 1556. P. 012072, 7 pages.
[8] Montmessin F., Gondet B., Bibring J.P., et al. Hyperspectral imaging of convective CO_2 ice clouds in the equatorial mesosphere of Mars // J. Geophys. Res. 2007. V. 112. P. E11S90.
[9] Izvekova Yu.N., Reznichenko Yu.S., Popel S.I. On a possibility of the existence of dust acoustic perturbations in Martian ionosphere // Plasma Phys. Rep. 2020. V. 46. No. 12, in press.
[10] Adushkin V.V., Chen B.B., Popel S.I., et al. Radiative forcing of aerosols in Central Asia // Dokl. Earth Sci. 2015. V. 460. No. 2. P. 137-141.

METEOROID PARAMETERS FROM OPTICAL DATA

A. Kartashova[1], A. Golubaev[2], O. Popova[3], G. Bolgova [1], A. Mozgova[4], I. Chuvashov[1], D. Glazachev[3], V. Efremov[3]

[1] *Institute of astronomy RAS, Moscow, Russia, (akartashova@inasan.ru)*

[2] *Institute of Astronomy of V. N. Karazin Kharkiv National University, Kharkiv, Ukraine*

[3] *Institute for Dynamics of Geospheres RAS, Moscow, Russia*

[4] *Astronomical Observatory, Taras Shevchenko Kyiv National University, Kyiv, Ukraine*

KEYWORDS:
meteoroid, bolide, trajectory, orbital elements, asteroid impact hazard

INTRODUCTION:

Meteoroids are the source of information about the origins of our Solar System. These bodies are too small for observations in the interplanetary space and all information about them are collected from meteor/fireball observations and analyzes of meteorite substance. Different methods are used for determination of fireball/meteor parameters. The high precision parameters can be obtained from bolide network observations, where ones can get the images with fireball and reference stars. But the bolide networks cover only small areas and are recording data only of small subset of bolides the flight of the fireball can be occasionally recorded by occasional dash cameras or security cameras.

One of the amazing examples of the superbolide was Chelyabinsk event (15.02.2013). The uniqueness of the Chelyabinsk event consists in the fact that it was really large and well documented. Few hundreds videos, photos and other registrations were got. A field survey was organized by Russian Academy of Sciences shortly after the event. During the expedition we were able to collect additional information and records of the superbolide. The trajectory was reconstructed by dash cameras data records and our background images (these images were made from locations of dash cameras). The number of records (as well as our background images) allowed us to determine the trajectory, orbit and other parameters with good precision (Table 1) [1]. After the Chelyabinsk event it is evident that not only large space bodies but also ~20 m size meteoroids poses a substantial hazard [2].

In the June 21 2018 (1:16 UTC) the space body entered the Earth atmosphere in the Lipetsk region. This event was registered by dash cameras too. This Ozerki event occurred early in the morning (01:16:20 UTC). The fireball was much fainter than the Chelyabinsk event, and only few video records were available in the Web. The most part of these videos were done from moving cars. Only one video from Chastaya Dubrava was obtained from the standing car. We used these video for Ozerki meteoroid parameters investigation [3]. In the result we can calculate the trajectory, orbit and other parameters with less precision in comparison with Chelyabinsk event, but nevertheless these data permitted to evaluate this event and to compare its estimates with independent ones (Table 1).

Table 1. The parameters of Ozerki and Chelyabinsk meteoroids

Meteoroid	Ozerki	Chelyabinsk
Date, Time UT, DDMMYYYY, hh:mm:ss	21062018, 01:16:20	15022013, 03:17
V_g, km/s	10.03±1	15.3±0.2
a, au	0.84±0.02	1.763
q, au	0.673±0.04	0.739±0.012
e	0.199±0.03	0.581±0.011
i, °	18.443±3.047	4.93± 0.27

Meteoroid	Ozerki	Chelyabinsk
Ω, °	89.656	326.442±0.0015
ω, °	335.286±5.147	108.3±2.3
D, m	3.65±0.45	~18-20
m, t	94±20	$(10–13)\cdot10^3$

Due to two different events, we were able to test our methods our methods for processing such data.

Monitoring of small space bodies and studying of their parameters is one of the fundamental tasks.

Knowledge of the characteristics of space objects (similar to Chelyabinsk and Ozerki meteorites), information of their origin and evolution are important for understanding of the small bodies population (meter and decameter scales) in the Solar system, as well for assessment of hazards, which they may cause.

The study of small bodies by different methods are presented.

Acknowledgements:
The work was partially supported by RFBR 16-02-00805.

References:
[1] Popova O. et al. Chelyabinsk airburst, damage assessment, meteorite recovery and characterization // Science. 2013. V. 342 (6162), P. 1069–1073.
[2] Kartashova A. et al. Study of injuries from the Chelyabinsk airburst event // Planetary and Space Science. 2018. Vol. 160, P. 107–114.
[3] Kartashova A. et al. Investigation of the Ozerki meteoroid parameters // Planetary and Space Science. 2020. DOI: 10.1016/j.pss.2020.105034.

ON THE METHYLACETYLENE ABUNDANCE AND NITROGEN ISOTOPE RATIO IN PLUTO'S ATMOSPHERE

V. A. Krasnopolsky
Moscow Institute of Physics and Technology (PhysTech), Moscow, Russia (Vlad.krasn@verizon.net)

KEYWORDS:
Pluto, atmosphere, chemical composition, photochemistry, isotope ratios, evolution

INTRODUCTION:
he recent progress in the studies of Pluto is related to the New Horizons flyby, and the solar and stellar occultations at 52–187 nm revealed vertical profiles of N_2, CH_4, C_2H_2, C_2H_4, and C_2H_6 [1-3]. The ALMA submillimeter spectroscopy [4] gave a CO profile, abundance of $HC^{14}N$, and restrictive upper limits to $HC^{15}N$ and HC_3N. The photochemical model of Pluto's atmosphere and ionosphere [5] reproduces fairly well these data. Recently methylacetylene and atomic hydrogen were detected using UV spectroscopy from New Horizons [6].

METHYLACETYLENE C_3H_4
abundance of $5{\cdot}10^{15}$ cm^{-2} observed from New Horizons is close to $7.7{\cdot}10^{15}$ cm^{-2} in our early model [7] but exceeds $9{\cdot}10^{14}$ cm^{-2} in [5]. To bring the model into agreement with the observation, rate coefficients of the three key reactions of C_3H_4 production and loss are changed to the values calculated in [8]. The calculated C_3H_4 abundance is $4.3{\cdot}10^{15}$ cm^{-2} (Figure 1).

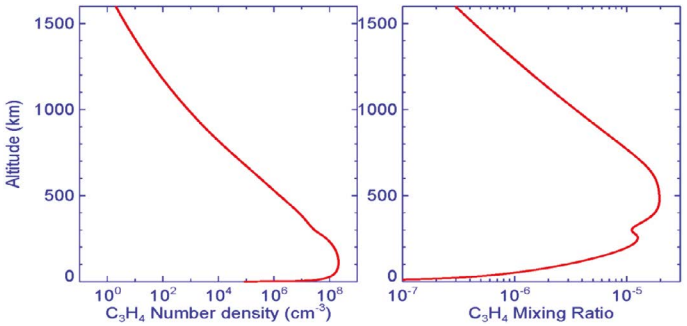

Fig. 1. Vertical profiles of C_3H_4 number density and mixing ratio

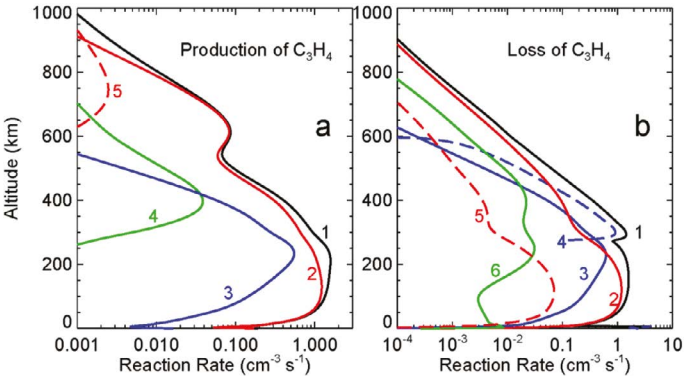

Fig. 2. Main reactions of production and loss of methylacetylene. Production (a): 1 — total; 2 — $C_3H_3 + H (+ M) \rightarrow C_3H_4 (+ M)$; 3 — $C_3H_5 + H \rightarrow C_3H_4 + H_2$; 4 — $C_2H_4 + CH \rightarrow C_3H_4 + H$; 5 — $C_4H_5 + + e \rightarrow C_3H_4 + CH$. Loss (b): 1 — total; 2 — photolysis; 3 — $C_3H_4 + H (+ M)$; 4 — condensation; 5 — $C_3H_4 + C_2H \rightarrow C_3H_3 + C_2H_2$; 6 — $C_3H_4 + CN \rightarrow C_3H_3 + HCN$

Main reactions of production and loss of C_3H_4 are shown in Figure 2. Column abundances of some species in the model and its previous version are presented along with production and loss rates, escape and precipitation flows, and chemical lifetimes. The HC_3N abundance of $2.3 \cdot 10^{13}$ cm^{-2} in the model is close to the upper limit of $2 \cdot 10^{13}$ cm^{-2} [4]. The change in the model increases H_2 and C_3H_8 by factors of 1.3 and reduces H and C_4H_2 by factors of 1.3, while the other species remain almost unchanged relative [5].

ATOMIC HYDROGEN

abundance of $(7.7 \pm 1.7) \cdot 10^{13}$ cm^{-2} at $\tau = 1$ (490 km) was measured [6] using the observed Lyman-beta emission. This value is $6.9 \cdot 10^{13}$ cm^{22} in our model and $7.3 \cdot 10^{13}$ cm^{-2} in the previous version.

REFLECTIVITY OF 0.17 AT 140-185 NM

[6] agrees with the HST value of 0.14 at 180-190 nm [9].

NITROGEN ISOTOPE RATIO:

The observed lower limit $HC^{14}N/HC^{15}N > 125$ on Pluto (Lellouch et al., 2017) agrees with $^{14}N/^{15}N$ in the planets, asteroids, comets, and the solar wind. However, it looks puzzling compared to $HC^{14}N/HC^{15}N = 60$ on Titan, because both Pluto and Titan have nitrogen-methane atmospheres with significant similarity in photochemistry. Our analysis confirms predissociation of N_2 at 80–100 nm as the major process of nitrogen isotope fractionation. The observed twofold difference on Pluto is partly caused by diffusive depletion of the heavy isotope in HCN and in predissociation of N_2. On Pluto, mean altitudes of HCN and predissociation of N_2 are 500 and 860 km, well above the homopause at 96 km. On Titan, the observations of $HC^{14}N/HC^{15}N$ refer to 90–460 km (Vinatier et al., 2007), predissociation proceed near 985 km, both below the homopause at 1000 km, and diffusive depletion does not occur. Therefore the observed limit corresponds to $^{14}N/^{15}N > 253$ for N_2 in the lower atmosphere and $^{14}N/^{15}N > 228$ in the upper layers of the N_2 ice. These limits reflect the conditions on Pluto in the last two million years. The current loss of N_2 is 37.5 $g \cdot cm^{-2} \cdot Byr^{-1}$ primarily caused by photodestruction. The calculated isotope fractionation factor of 1.96 accounts for formation and condensation of nitriles, diffusive separation, and fractionation in thermal escape. Variations of $^{14}N/^{15}N$ in the N_2 ice are relevant to evolution of the solar EUV, mixing processes in the N_2 ice, and possible periods of hydrodynamic escape that are poorly known and not considered here.

REFERENCES:

[1] Gladstone G. R. et al. 2016. Science. 351. 6279. aad8866.
[2] Young L. A. et al. 2018. Icarus. 300. 174–199.
[3] Kammer J. A. et al. 2020. Astron. J. 159. 26. 9.
[4] Lellouch E. et al. 2017. Icarus. 286. 289–307.
[5] Krasnopolsky V. A., 2020. Icarus. 335. 113374.
[6] Steffl A. J. et al. 2020. Astron. J. 159. 274. 12.
[7] Krasnopolsky V. A., Cruikshank D. P. 1999. J. Geophys. Res. 104. 21979–21996.
[8] Vuitton V. et al. 2019. Icarus. 324. 120–197.
[9] Krasnopolsky V. A., 2001. Icarus. 153. 277–284.
[10] Vinatier S. et al. 2007. Icarus. 191. 712–721.

MODELS OF H CHONDRITES GENESIS AND EVOLUTION: NEW FINDINGS

S. Voropaev[1], U. Böttger[2], S. Pavlov[2], F. Hanke[2]
[1] *GEOKHI RAS, Kosygina str. 19, 119991 Moscow, Russia,* (*voropaev@geokhi.ru*)
[2] *DLR, Institute of Optical Sensor Systems, Rutherfordstraße 2, 12489 Berlin, Germany*

KEYWORDS:
meteorite, chondrite, parent body, accretion, carbonates, fluids, volatiles

INTRODUCTION:
Markovka chondrite (H4) under investigation was a small fragment 1·2·5 cm — part of the large meteorite fall at 1967 near Markovka village, east Siberia. It was stone rain of fragmented chondrite body with the size ca. 1 m as whole. Relative fresh and unweathered sample allows us to collect detailed Raman spectra of mineral phases with Witec Alpha 300 System, DLR. The resulting chemical composition of the main minerals (olivine, pyroxenes, plagioclases etc.) was refined by the SEM-EDX method, Dept. Chemistry, Moscow State University. Also, the presence of numerous FeNi grains allowed for metallographic analysis of nickel diffusion across the grain boundary. As is well known [1], the rate of diffusion of nickel is determined by the temperature of the environment and due to the concentration' gradient the cooling history could be confidently estimated.

The basic model of H parent body assumes an onion-shells structure, where H6 corresponds "core", H5 — "low mantle", H4 — "upper mantle" and H3 — "outer crust" [2]. Generally, it reflects a negative correlation between the petrologic type and the cooling rate, that is, the deeper the layer, the slower it cools. But, there are a number of exceptions where positive correlation is present. For some cases, two stage (with impact excavation) cooling model provides T – t path consisted with Hf – W age of peak metamorphism and constraints imposed by the Pb–Pb ages of the phosphates and Ar – Ar ages of the feldspars vs. their respective closure temperatures [3]. Also, alternative model was developed in which maximum metamorphic temperatures are reached in km-sized planetesimals and slow cooling through 700 K occurs in larger bodies that accreted from these planetesimals [4].

Using new findings at Markovka' mineralogical composition we will try to remove some of the contradictions between different models of H chondrites' parent bodies.

COMPOSITION:
Raman spectra of Markovka contain lines as of main silicate groups (olivine, pyroxene, etc.) as Fe-oxides (maghemite, goethite, etc.) presented on Figure 1. Measurements of the characteristic line shift provide important information concerning chemical content and deformation state of the chondrite' rocks [5].

Olivine shows its characteristic doublet peak (DB) between 818–825 1/cm (DB1) and 847–856 1/cm (DB2). Its exact position depends on Fe–Mg concentrations vary primarily as a function of Mg/(Mg + Fe) and may be used to estimate the Fo content of the olivine. A tighter correlation was found between the DB2 peak positions Fo values for magnesian olivine

(Fo > 50), which provides Markovka' olivine composition as $Fo_{80}Fa_{20}$ From another side, the structural difference of ortho- and clinopyroxene results in a doublet for orthopyroxene between 660–680 1/cm and a weak peak at approximately 235 1/cm, where clinopyroxene shows only a single peak and no peak around 235 1/cm, respectively. So, Raman spectra of Markovka' pyroxene with peaks at 1008, 336, 232 1/cm and double peak at 680 1/cm provides clear indication of transition from low–Ca pyroxene to orthopyroxene with composition as $En_{80}Fs_{20}$. The similar Mg/Fe content of the above silicates indicates the thermal equilibration.

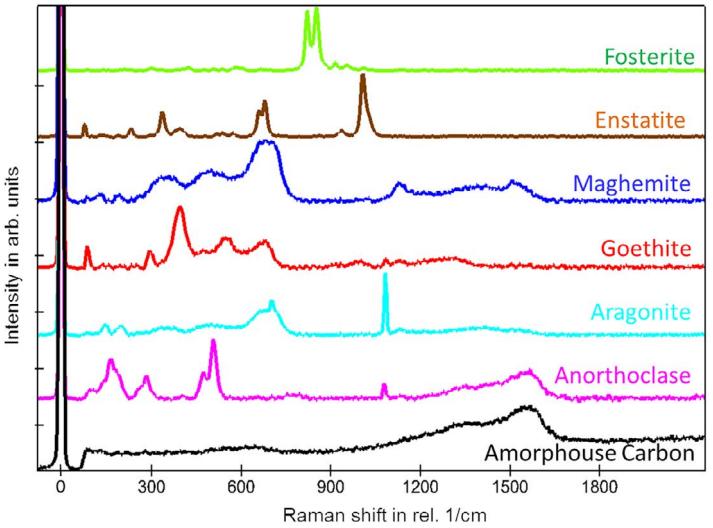

Fig. 1. Raman spectra of mineral phases of Markovka (H4) meteorite

Carbonates ($CaCO_3$) mineral' polymorphs could be identified using the positions of some of their minor Raman bands: calcite has bands at 282 and 713 1/cm and aragonite has minor bands at 207 and 704 1 / cm, respectively [6]. Markovka's spectra has characteristic peaks at 703 and 196 1/cm which indicates aragonite presence. It is high-pressure polymorph of calcite and, according its phase diagram (Figure 2), is stable starting 3 kbar, only.

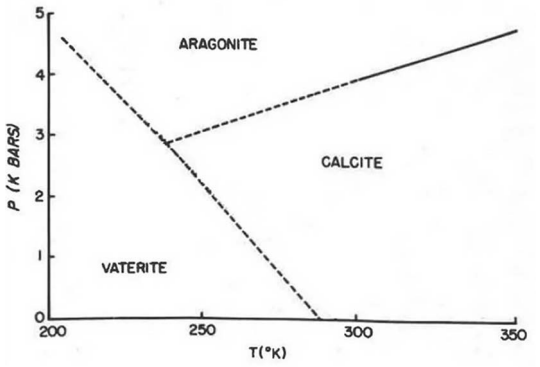

Fig. 2. Phase diagram Calcite-Aragonite-Vaterite

RESULTS AND DISCUSSION:

Aragonite presence could be explained twofold. First, huge size of the Markovka' parent body. With mean density of chondrites as 3–4 g·cm^{-3}, needed pressure as 3 kbar is possible for body with radius ca. 400 km. Current accretion models suppose quite short time interval of ca. 1–2 Mio. years (since CAI formation) and planetesimals with limited size ca. 50–200 km (in radius). Second, aragonite could be precipitated from a saturated solution under certain conditions. The Mg:Ca ratio at which the calcium carbonate mineral that has pseudohomogeneously precipitated from seawater changes from calcite to aragonite was experimentally determined as a function of temperature. Results indicate a dramatic change in the critical Mg:Ca ratio over a relatively small temperature range. So, Markovka provides new constraints on evolution processes at the early Solar system and worth for the further detailed mineralogical and geochemical analysis.

References:

[1] Wood J. A. The cooling rates and parent bodies of several iron meteorites // Icarus. 1964. V. 3. P. 429–459.

[2] Henke S., Gail H.-P., Trieloff M., Schwarz W. H. Thermal evolution model for the H chondrite asteroid — instantaneous formation versus protracted accretion // Icarus. 2013. V. 226. P. 212–228.
[3] Kleine T., Touboul M., Van Orman J. A., Bourdon B., Maden C., Mezger K., Halliday A. N. Hf–W thermochronometry: closure temperature and constraints on the accretion and cooling history of the H chondrite parent body // Earth Planet. Sci. Lett. 2008. V. 270. P. 106–118.
[4] Scott E. R. D., Rajan R. S. Metallic minerals, thermal histories and parent bodies of some xenolithic, ordinary chondrite meteorites // Geochlmica et Cosmochlmica Acta. 1981. V. 45. P. 53–67.
[5] Kaeter D., Ziemann M., Boettger U., Weber I., Hecht L., Voropaev S., Korochantsev A., Kocherov A. The Chelyabinsk meteorite: New insights from a comprehensive electron microscopy and Raman spectroscopy study with evidence for graphite in olivine of ordinary chondrites // Meteoritics and Planetary Science. 2018. V. 53. P. 416–432.
[6] White S. N. Laser Raman spectroscopy as a technique for identification of seafloor hydrothermal and cold seep minerals // Chemical Geology. 2009. V. 259. P. 240–252.

NONLINEARITY IN INVERSE ORBITAL PROBLEMS FOR POTENTIALLY HAZARDOUS ASTEROIDS

O. M. Syusina[1], V. A. Avdyushev[2]
[1] *Tomsk State University, 634050, Tomsk, Russian Federation, +73822529776 (olga_syusina@rambler.ru);=*
[2] *Tomsk State University, 634050, Tomsk, Russian Federation, +73822529776 (sch@niipmm.tsu.ru)*

KEYWORDS:
potentially hazardous asteroids, inverse problem, nonlinearity

INTRODUCTION:

In the study of the probabilistic motion of potentially hazardous asteroids, one of the important tasks is the reliable construction of confidence regions, based on which the probability of collision of objects with the Earth is evaluated. The task of confidence region construction can be solved in both linear and nonlinear statements. The choice of construction method depends on the nonlinearity of the inverse problem. With weak nonlinearity, the application of time-consuming nonlinear methods does not make sense. If the problem is strongly nonlinear, the confidence regions constructed by linear estimations will give rough results and, consequently, will cause unreliable estimations of probability of asteroid collisions with the Earth or other planets.

In the strongly nonlinear case, nonlinear stochastic methods are used [1]. They give more adequate regions than linear methods, although nonlinear methods are not always practically justified. The main reason for strong nonlinearity is the unsuccessful choice of orbital parameters [2, 3]. Consequently, nonlinearity can be significantly weakened by transforming the parameters, but it is impossible to completely get rid of it. Ultimate minimal nonlinearity, which cannot be eliminated by parametric transformations, is due to the so-called intrinsic nonlinearity [4]. Its value just predetermines the adequacy of nonlinear stochastic methods [1].

Nonlinearity is estimated using nonlinearity indicators [3, 5–8]. All of them, in fact, are a measure of the bias of parametric estimates due to nonlinearity with respect to the expected linear analogues. Nonlinearity indicators just allow making the right choice between linear and nonlinear methods for the adequate construction of confidence region.

The present research provides results of nonlinearity evaluation in inverse problems of orbital dynamics for all potentially hazardous asteroids, using new nonlinearity indicators which allowed us to evaluate both parameter-effect and intrinsic nonlinearity [9]

NONLINEARITY INDICATORS:

Total nonlinearity of inverse problem is comprised of parameter-effect and intrinsic nonlinearities [4]. The parameter-effect nonlinearity is caused by an unsuccessful choice of parametric space although, in some cases, it can be significantly reduced by parametric transformations. While the intrinsic nonlinearity is an immanent feature of any nonlinear inverse problem, and it is impossible to eliminate.

The parameter-effect and intrinsic χ nonlinearities can be estimated using the following relations [9]

$$\chi_P = \frac{\left\|\mathbf{A}\Delta q - \mathbf{\Pi}\Delta p\right\|}{\left\|\Delta p\right\|}, \quad \chi_I = \frac{\left\|\mathbf{\Pi}\Delta p - \Delta p\right\|}{\left\|\Delta p\right\|}.$$

Here $\mathbf{A} = \mathbf{p}'_q(\hat{\mathbf{q}})$ is the matrix of partial derivatives of model observation representations p with respect to parameters q at the nominal estimate $\hat{\mathbf{q}}$ determined from observations; Δq is positions of the vertices of the confidence region relative to the nominal estimate; $\mathbf{\Pi}$ is the projection matrix: $\mathbf{\Pi} = \mathbf{A}(\mathbf{A}^\mathrm{T}\mathbf{A})^{-1}\mathbf{A}$; Δp is the differences between model observation representa-

tions for the nominal estimate and those for the vertices of the confidence ellipsoid.

The nonlinearity threshold value is ascertained as $\overline{\chi} = 1.2 \cdot 10^{-3}$ [9]. All inverse problems with indicator values less than the threshold one can be considered as weakly nonlinear.

Numerical experiment:
Potentially dangerous asteroids observed in one appearance were chosen as objects of study. These objects are the most interesting in terms of nonlinearity analysis, since short observation spans are typical for such objects. Consequently, the inverse problems for them can be very strong nonlinear [2, 3]. As of June 2020, on the website Minor Planet Center (www.minorplanetcenter.net) there are 395 potentially hazardous asteroids observed in one appearance.

The orbital parameters of the asteroids were determined from their positional observations taken from the website of the Center for Minor Planets. The initial epoch for each asteroid was chosen as the arithmetic mean of all the moments of observations, since the orbital parameters assigned to it provide the weakest total (parametric) nonlinearity [3]. Asteroid orbits were simulated on the basis of differential equations of the few-body gravitational problem (the Sun, planets, the Moon, an asteroid), which were integrated numerically by the Everhart method [8, 10].

For each object, we evaluated the parameter-effect and intrinsic nonlinearities. They are presented in Figure 1 in three levels: weak, moderate, and strong at the nonlinearity indicators less than 0.001 (green), from 0.001 to 0.01 (yellow), and greater than 0.01 (red) respectively.

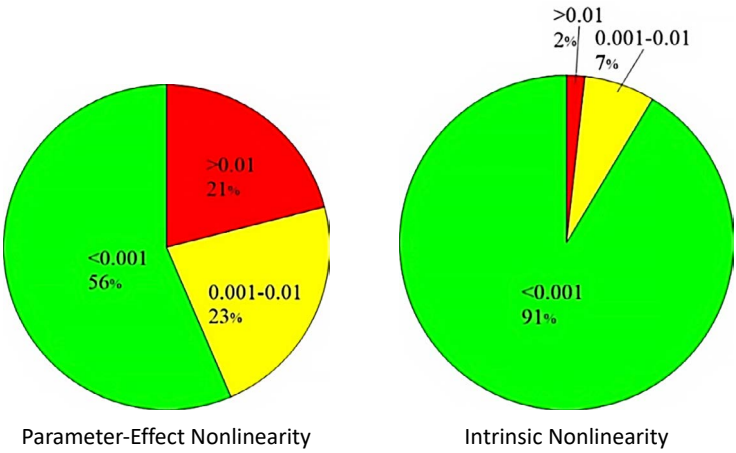

Fig. 1. Distribution of nonlinearity indicators for potentially hazardous asteroids observed in one appearance before June 2020

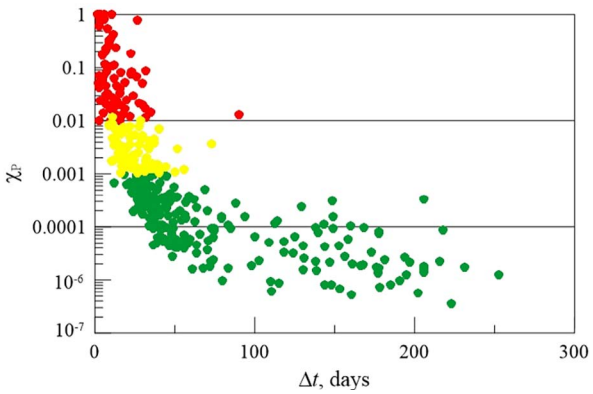

Fig. 2. Parameter-effect nonlinearity versus observation span

A general analysis showed that in probabilistic estimation problems, linear stochastic simulation of orbital uncertainty is unacceptable for almost half of the objects (44 %) (see Figure 1). However, for the vast majority of the asteroids (92 %), the intrinsic nonlinearity is weak and, therefore, non-linear methods can be used for stochastic simulation.

As can be seen in Figure 2, strong parameter-effect nonlinearity ($\chi_p > 0.01$) is manifested mainly for the objects that were observed for less than 35 days. Moderate nonlinearity ($0.001 < \chi_p < 0.01$) is for the objects with observations over spans greater than 9 but less than 73 days. Thus, when researching objects with short arcs (less than 73 days), it is first necessary to study of the nonlinearity of inverse problem so as to select the correct (linear or nonlinear) method for constructing the confidence region.

Acknowledgements:
The research was carried out within the state assignment of Ministry of Science and Higher Education of the Russian Federation (theme No. 0721-2020-0049)

References:

[1] Avdyushev V. A. Nonlinear methods of statistic simulation of virtual parameter values for investigating uncertainties in orbits determined from observations // Celestial Mechanics and Dynamical Astronomy. 2011. No. 110. P. 369–388.
[2] Chernitsov A. M., Dubas O. M., Tamarov V. A. Ways to reduce the nonlinearity of the least squares problem when constructing regions of possible asteroid motions // Izv. universities. Physics. Application. 2006. V. 49. No. 2. P. 44–51.
[3] Syusina O. M., Chernitsov A. M., Tamarov V. A. Construction of confidence regions in problem on probabilistic study into motion of minor bodies of the solar system // Sol. Syst. Res. 2012 No. 46. P. 195–207.
[4] Draper N. R., Smith H. Applied Regression Analysis. 3 ed. John Wiley and sons. 1998.
[5] Beale E. M. L. Confidence Regions in Nonlinear Estimation // J. R. Statist. Soc. 1960. V. 22. P. 41–88.
[6] Bates D. M., Watts D. G. Relative curvature measures of nonlinearity // J. Royal Statistical Society. Series B (Methodological). 1980. V. 42 No. 1. P 1–25.
[7] Avdyushev V. A. Intrinsic nonlinearity and method of disturbed observations in inverse problems of celestial mechanics // Celestial Mechanics and Dynamical Astronomy. 2017. V. 129. No. 4. P. 537–552.
[8] Avdyushev V. A. Numerical orbit simulation. Tomsk: Publishing House of Tomsk State University, 2015. 336 p.
[9] Avdyushev V. A., Syusina O. M., Tamarov V. A. Nonlinearity in inverse problems of asteroid dynamics // Sol. Syst. Res. 2020 (in press).
[10] Everhart E. Implicit Single Sequence Methods for Integrating Orbits // Celect. Mech. 1974. V. 10. P. 35–55.

COMETARY DUST MIGRATING THROUGH THE SOLAR SYSTEM

A. Kochergin[1,2], E. Zubko[3], G. Videen[3,4]
[1] *Far Eastern Federal University, 8 Sukhanova St., Vladivostok 690950, Russia* (*kochergin.av@outlook.com*)
[2] *Institute of Applied Astronomy of RAS, 10 Kutuzova Emb., Saint-Petersburg, 191187, Russia*
[3] *Humanitas College, Kyung Hee University, 1732 Deogyeong-daero, Yongin-si, Gyeonggi-do 17104, Republic of Korea* (*evgenij.s.zubko@gmail.com*)
[4] *Space Science Institute, 4750 Walnut Street, Boulder Suite 205, CO 80301, USA*

KEYWORDS:
Solar System, comets, interplanetary dust particles, zodiacal light, solar-radiation pressure

INTRODUCTION:
Zodiacal Light reveals the presence of interplanetary dust in the Solar System [1]. Such interplanetary dust particles (IDPs) may encounter the Earth [2] and Moon, providing information on their microphysics [3, 4]. The light-scattering response from IDPs is predominantly governed by submicron and micron-sized particles [5]. Furthermore, such small particles suggest a minimum dustload of interplanetary space; whereas, for example, 1-mm particles necessitate an enormous cumulative volume of IDPs, 5–6 orders of magnitude greater compared to that of submicron particles [6].

There is uncertainty as to the parent bodies of IDPs (see Table 1 of [1] for review). While some studies suggest more than half of IDPs originated from asteroids, other works suggest they are mainly of cometary origin [7]. This latter conclusion would imply, however, that the phenomenon of Zodiacal Light is almost entirely caused by dust freshly ejected from comets as submicron and micron–sized particles cannot settle in an elliptical orbit due to the effect of solar-radiation pressure [8]. The effect of radiation pressure is quantified through the ratio of the force of solar-radiation pressure to the solar-gravitation force, $\beta = F_{radiation}/F_{gravity}$. It is worth noting that the β parameter in a given particle is independent of its heliocentric distance, and $\beta < 1$ is necessary to keep the particle bound to the Solar System. However, such a constraint on the β parameter is much stricter if the particle is ejected from the parent body on its perihelion passage [8]:

$$\beta < (1 - \varepsilon)/2, \quad (1)$$

where ε stands for eccentricity of orbit. For instance, a particle ejected from Comet 67P/Churyumov – Gerasimenko ($\varepsilon = 0.641$) near perihelion must have $\beta < 0.179$. This limit is a few times smaller compared to the β parameter in micron-sized particles [9], implying such particles will get swept out of the Solar System. On the other hand, ejection near aphelion significantly relaxes the constraint on the β parameter [8]:

$$\beta < (1 + \varepsilon)/2, \quad (2)$$

yielding, in application to Comet 67P/Churyumov – Gerasimenko, $\beta < 0.821$. Therefore, particles ejected near aphelion have a much better chance of survival in the Solar System. Their orbits are much larger than those of their parent bodies. In order for IDPs to be located where Zodiacal Light arises, ~1 − 2 au, one needs to investigate the migration of IDPs throughout the Solar System. We are developing a numerical model that would be capable of such simulation. Here we present validation of this model by experimental inference of the constraints expressed in eqs. (1) and (2).

MODEL:
We model the motion of particles ejected from a parent body using an iterative time-domain approach. Such an approach makes it possible to account rigorously for three forces acting on a small dust particle: gravity of the parent

body, gravity of the Sun, and solar-radiation pressure. Within this approach, a dust particle is placed at a subsolar point of the nucleus of a comet whose location with regard to the Sun is described in terms of the position vector S_0. At the initial time $t_0 = 0$, the particle acquires an initial velocity V_0 that is set to be 1.5 of the escape velocity from the nucleus and oriented along the normal from the surface. At this initial moment in time, we calculate the resultant of all three forces acting on the dust particle. Over the increment of time Δt, the resultant force is assumed to remain constant, implying also a constant acceleration of the dust particle a_0. At the end of this increment, we update all three forces and their resultant for the current location of the particle and repeat the entire procedure. Clearly, at $\Delta t \rightarrow 0$, the model trajectory should converge to its exact profile. In practice, $\Delta t = 1$ s provides sufficient accuracy in determining orbits of ejected dust particles. Finally, it is worth noting that this code has been exploited in the analysis of astronomical observations of several comets [10, 11].

RESULTS AND DISCUSSION:

We model the motion of dust particles ejected from the nuclei of four comets: 1P/Halley, 2P/Encke, 67P/Churyumov – Gerasimenko, and 81P/Wild 2. At two points of their orbits, perihelion and aphelion, we simulate ejection of dust particles with the β parameter varying from 0.01 to 0.99 with the increment of 0.01. While searching for elliptical orbits of the ejected particles, we constrain the largest possible value of the β parameter at an accuracy of 0.01.

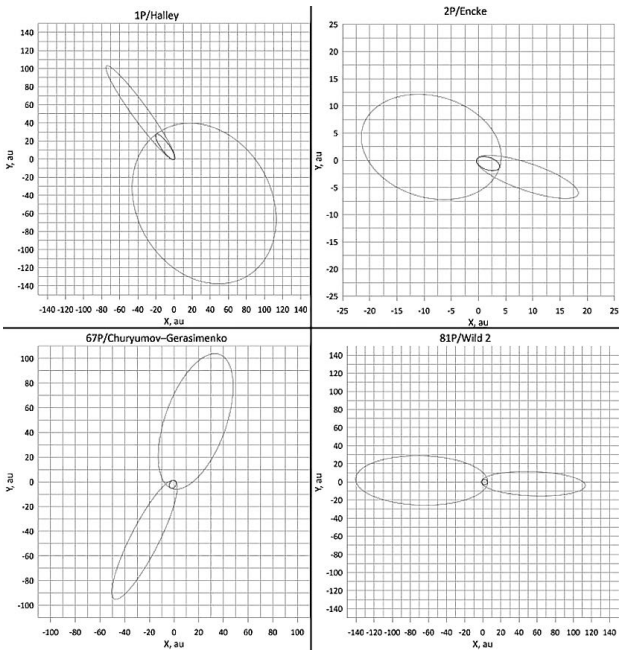

Fig. 1. Blue lines show orbits of comets 1P/Halley, 2P/Encke, 67P/Churyumov – Gerasimenko, and 81P/Wild 2 around the Sun (0,0). Red lines show elliptical orbits of dust particles ejected at perihelion and aphelion at the greatest possible values of the β parameter

Our modeling reveals that the dust particles originating from Comet 1P/Halley remain orbiting around the Sun if their $\beta \leq 0.01$ (perihelion) and 0.98 (aphelion). Their orbits are shown in the top left in Fig. 1. In the case of Comet 2P/Encke, the β parameter is limited to 0.06 at the perihelion ejection and to 0.91 at the aphelion ejection (*top right* in Figure 1). In Comet 67P/Churyumov – Gerasimenko, the β parameter is constrained to 0.17 and 0.83, respectively (*bottom left* in Figure 1). Finally, in Comet 81P/Wild 2, $\beta \leq 0.22$ and 0.76, respectively (*bottom right* in Figure 1). These retrievals appear in good quantitative agreement with the theoretical constraints expressed in eqs. (1) and (2), suggesting great accuracy of our numerical model.

Of course, these comets do not reveal significant activity at their aphelion passage. However, such activity may be significant in a fresh comet, which may remain active up to quite long heliocentric distances, even up to 26 au [12]. A fresh short-period comet may be active throughout its entire revolution around the Sun.

Finally, as one can see in Figure 1, orbits of dust particles ejected at the aphelion passage have an enormous size. Their own aphelion lies at 42.4 au (1P/Halley), 22.2 au (2P/Encke), 109.7 au (67P/Churyumov – Gerasimenko), and 140.6 au (81P/Wild 2). This suggests a long journey of those dust particles before they could settle in the inner part of the Solar System. This is a subject of future study where we will take additionally into account an impact of gravitation of all big planets and, also, the Poynting-Robertson drag force [8].

REFERENCES:

[1] Ipatov S. I. et al. Dynamical zodiacal cloud models constrained by high resolution spectroscopy of the zodiacal light // Icarus. 2008. V. 194. P. 769 –788.
[2] Love S. G., Brownlee D. E. A direct measurement of the terrestrial mass accretion rate of cosmic dust // Science. 1993. V. 262. P. 550–553.
[3] Flynn G. J., Sutton S. R. Cosmic dust particle densities — Evidence for two populations of stony micrometeorites // Lunar Planet. Sci. Conf. 1991. V. 21. P. 541–547.
[4] Busemann H. et al. Ultra–primitive interplanetary dust particles from the comet 26P/Grigg–Skjellerup dust stream collection // Earth Planet. Sci. Lett. 2009. V. 288. P. 44–57.
[5] Zubko E. et al. On the small contribution of supermicron dust particles to light scattering by comets // Astrophys. J. 2020. V. 895. Art. ID. 110.
[6] Zubko E. Absolute magnitude of small cosmic dust particles // Mon. Not. Roy. Astron. Soc. 2020. V. 492. P. 810–820.
[7] Nesvorný D. et al. Cometary origin of the Zodiacal cloud and carbonaceous micrometeorites. Implications for hot debris disks // Astrophys. J. 2010. V. 713. P. 816–836.
[8] Burns J. A. et al. Radiation forces on small particles in the Solar System // Icarus. 1979. V. 40. P. 1–48.
[9] Zubko E., at al. Comet C/2012 S1 (ISON) coma composition at ~4 au from HST observations // Planet. Space Sci. 2015. V. 118. P. 138–163.
[10] Kochergin A. et al. Velocity of dust ejected from interstellar Comet 2I/Borisov // Res. Notes of the AAS. 2019. V. 3. Article ID: 152.
[11] Luk'yanyk I. et al. Rapid variations of dust colour in comet 41P/Tuttle – Giacobini – Kresák // Mon. Not. Roy. Astron. Soc. 2019. V. 485. P. 4013–4023.
[12] Szabó Gy. M. et al. Cometary activity at 25.7 AU: Hale-Bopp 11 years after perihelion // Astrophys. J. Lett. 2008. V. 677. P. L121–L124.

APPLYING UT TO VISUAL TIMING IN OCCULTATION OBSERVATIONS

A. Dehghani Ghanatghestani[1], A. Poro[1], D. Gault[2]
[1] *The International Occultation Timing Association-Middle East Section, Iran*, (*info@iota-me.com*)
[2] *Kuriwa Observatory, Australia*

KEYWORDS:
occultation, timing, observation, visual, Universal Time

INTRODUCTION:
There are several methods of obtaining a sample of Universal Time (UT) and we also discussed the required accuracy required for both visual (eye) and video (camera) observations. Most people start their occultation observing career by using visual methods, so that is a good place to start.

References:
[1] Poro A., Maley P. D. Occultation Book. Daneshpajohan-e'javan Publishing. 2012.

ESTIMATION OF SOME NEAS' COMPOSITION BY SPECTRAL METHOD

A. A. Savelova[1], V. V. Busarev[1,2] , M. P. Shcherbina[1], S. I. Barabanov[2]
[1] *Sternberg Astronomical Institute Lomonosov Moscow State University (SAI MSU), Moscow, Russia (aa.rezaeva@physics.msu.ru)*
[2] *Institute of Astronomy, Russian Academy of Sciences, Moscow, Russia*

KEYWORDS:
asteroid, NEA, mineral, meteorite, composition, reflectance spectra, modeling

INTRODUCTION:

Nowadays new asteroids are still regularly opened. Since 1 January by 5 August 1481 NEAs have already been discovered [1]. In comparison with the past, asteroids are being detected more frequently. This fact makes scientists look for a way to accelerate the determination of parameters of asteroids.

One of the most important characteristics of asteroids is their taxonomic class. Before, we wrote a program that allows user to determine (approximately) mineral and meteorite quantitative composition of asteroids (the program was presented at previous symposia, for example [2]). The program uses reflectance spectra of meteorites or minerals from open databases ([3, 4]) and searches for the best fit of weighted sum of these reflectance spectra to the reflectance spectrum of the asteroid under study. Using this fit the program makes a conclusion about possible mineral / meteorite composition of the asteroid. The approximated asteroid composition helps to determine its taxonomic class [5]. Thus the program makes determination of taxonomic classes of asteroids faster and more precisely.

Our group collected new spectral data on some NEAs. Using the program, we found possible composition of the bodies and their taxonomic classes. Our new results are presented in the poster.

REFERENCES:

[1] The Minor Planet Center (MPC). Available at: https://minorplanetcenter.net/about (accessed 5 August 2020).
[2] Rezaeva A. A., Shcherbina M. P., Busarev V. V. Modeling of asteroid reflectance with laboratory databases of analog sample // Abstracts of the Tenth Moscow Solar System Symposium (10M–S3). Space Research Institute. Moscow. Russia. 2019. P. 439–440.
[3] NASA Reflectance Experiment Laboratory. Available at: http://www.planetary.brown.edu/relabdocs/relab_disclaimer.htm (accessed 5 August 2020).
[4] CEnter for Terrestrial and Planetary Exploration. Available at: https://ctape.uwinnipeg.ca/ (accessed 5 August 2020).
[5] Gaffey M. J., Cloutis E. A., Kelley M. S., Reed K. L. Mineralogy of asteroids // Asteroids III / eds. Bottke W. F. Jr. et al.). Tucson: Univ. of Arizona Press, 2002. P. 183–204.

NEGATIVE POLARIZATION OF ASTEROIDS (216) KLEOPATRA AND (324) BAMBERGA

A. Berdyugin[1], E. Chornaya[2,3], E. Zubko[4]
[1] *University of Turku, Vesilinnantie 5, Turku 20014, Finland* (*andber@utu.fi*)
[2] *Far Eastern Federal University, 8 Sukhanova St., Vladivostok 690950, Russia* (*ekaterina.d.chornaya@gmail.com*)
[3] *Institute of Applied Astronomy of RAS, 10 Kutuzova Emb., Saint Petersburg, 191187, Russia*
[4] *Humanitas College, Kyung Hee University, 1732 Deogyeong-daero, Yongin-si, Gyeonggi-do 17104, Republic of Korea* (*evgenij.s.zubko@gmail.com*)

KEYWORDS:
asteroids, mainbelt, regolith, polarization, taxonomy

INTRODUCTION:

Polarimetry of asteroids provides a means for their classification (e. g., [1]) and characterization of microphysical properties in their regolith (e. g., [2]). Scattering of unpolarized solar radiation by asteroidal regolith produces a partially polarized radiation that is quantitatively described in terms of the degree of linear polarization $P = (F_{\perp} - F_{||})/(F_{\perp} + F_{||})$ (e. g., [3]). Here $F_{\perp}$ and $F_{||}$ stand for the fluxes of the scattered light whose electric fields vibrate perpendicular or within the scattering plane, respectively. P is typically measured in per cent. P is a function of phase angle α; i. e., the Sun-Target-Observer angle. However, ground-based observations of the Main-Belt asteroids are limited to the range of small phase angles, $\alpha < 25°$, due to their relatively large heliocentric distance. In this short paper we report results of polarimetric observations of two Main-belt asteroids, (216) Kleopatra and (324) Bamberga. The former object belongs to M type, whereas, the later one to C type within the Tholen taxonomy [4].

OBSERVATIONS:

Polarimetric measurements were performed with the *Dipol-2* polarimeter [5] mounted on the Tohoku 60-cm telescope (T60) located at Haleakala observatory, Hawaii, in February – March of 2020. Dipol-2 is a remotely operated double-image CCD polarimeter, which is capable of measuring polarization in three *BVR* filters of the Johnson-Cousins photometric system simultaneously. The innovative design of the polarimeter, where the two orthogonally polarized images of the sky overlap on the images of the source, allows to completely eliminate the sky polarization at an instrumental stage even when it is variable, and to achieve unprecedentedly high, up to 10^{-5}, accuracy of polarimetric measurements [6–9].

Each night we obtained from 24 to 64 individual measurements of Stokes q and u parameters simultaneously in three filters. In computing the mean values of q and u we applied a "2σ" iterative weighting algorithm. The initial mean and standard deviation were obtained by applying equal weights to all points. Subsequently, on each step, individual points deviating by more than two standard deviations from the mean ($d > 2\sigma$) were given a lower weight proportional to the inverse square of the error estimate, e_x. The value $e_x = \sigma$ for $d < 2\sigma$ was assumed to increase linearly from $e_x = 1\sigma$ to 3σ with d increasing from 2σ to 3σ. Points with $d > 3\sigma$ were rejected. The procedure converges fast and values of the mean and its standard deviation are obtained within a few iterations. Under normal conditions, 6–8 % of individual points deviated by more than 2σ were given lower weight ($W < 1$). The remaining 92–94 % of points were equally weighted ($W = 1$). The weighting procedure helps to suppress effects from transient clouds, moments of bad seeing, cosmic ray events, and so on.

To calibrate our instrument, we observed ~20 unpolarized standard stars. The zero point of polarization angle was determined by observing high-polarized standards HD204827 and HD25443. The determined instrumental polarization of the telescope, <0.005 %, is negligible in the present case.

RESULTS AND DISCUSSION:

Figure 1 shows the degree of linear polarization *P* as a function of phase angle α measured with the *V* filter in asteroids (216) Kleopatra (*left*) and (324) Bamberga (*right*). Blue points here presents our own results; whereas, black symbols correspond to the data adapted from the literature, [1, 10, 11] for (216) Kleopatra and [12, 13] for (324) Bamberga.

As the error bars in our measurements, we use *standard deviation* of individual polarimetric measurements around their average on a given epoch. In Figure 1, one can see that the average values of polarization in our observations are in good quantitative agreement with other observations whenever they appear at a similar phase angle. The point is that the mean polarization can also be treated as a random number whose standard deviation is much smaller compared to the standard deviation of individual polarimetric measurements. Therefore, mean polarization is typically obtained with a high confidence. In our observations, its standard deviation does not exceed 0.09 %; whereas, in more than half of all cases, it was 0.05 % or smaller.

We note that our observations significantly extend the existing data for asteroid (324) Bamberga toward the range of small phase angle, up to α = 2.5°, making it possible to constrain a whole branch of the negative polarization in this asteroid.

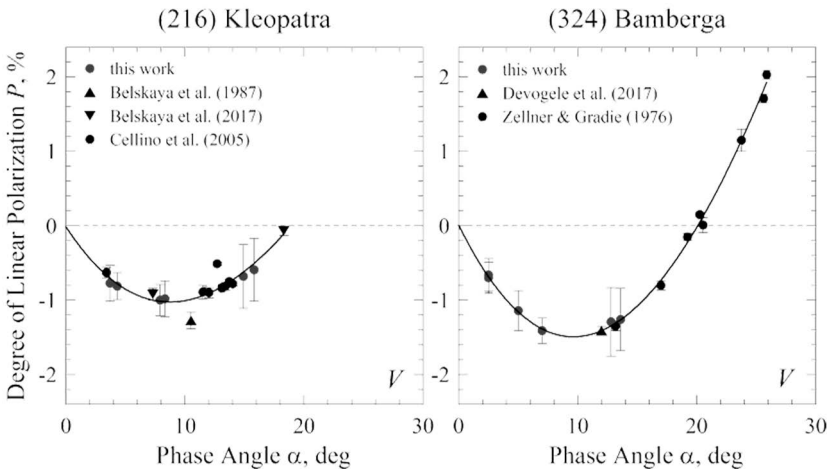

Fig. 1. Degree of linear polarization as a function of phase angle in asteroids (216) Kleopatra (left) and (324) Bamberga (right) in the *V* filter. Our data (blue points) obtained are compared versus the literature (black symbols). Solid black lines show a 3–rd degree polynomial fit to all data points

Using a third-degree polynomial and assuming $P = 0$ % at $\alpha = 0°$ that is consistent with a typical angular profile of polarization in asteroids (e. g., [1]), we search for the best fit to all available data for each asteroid. The resulting curves are shown with black solid lines in Figure 1. As one can see, such fits nearly perfectly match the vast majority of existing observations. However, the polynomial fits also allow us to constrain minimum of negative polarization P_{min} and its phase angle α_{min} in both asteroids. For instance, we find $P_{min} = -1.02$ % at $\alpha_{min} = 8.8°$ in (216) Kleopatra, and $P_{min} = -1.49$ % at $\alpha_{min} = 9.6°$ in (324) Bamberga.

Interestingly, these results are perfectly consistent with the M- and C-type asteroids within the polarimetric taxonomy of asteroids inferred in [1]. For example, in the M-type asteroids, [1] suggests $P_{min} = -(1.00\pm0.25)$ % and $\alpha_{min} = (9.0\pm2.0)°$; whereas, in the C-type asteroids, $P_{min} = -(1.55\pm0.55)$ % and $\alpha_{min} = (8.7\pm2.1)°$. Thus, our observations of (216) Kleopatra and (324) Bamberga confirm their M type and C type, respectively.

Finally, it is worth noting that we present here only part of our observations. The results obtained in the *B* and *R* filters, along with six-hour monitoring of polarization versus rotational phase, will be reported in a later publication.

References:

[1] Belskaya I. N. et al. Refining the asteroid taxonomy by polarimetric observations // Icarus. 2017. V. 284. P. 30–42.
[2] Shkuratov Yu. et al. The opposition effect and negative polarization of structural analogs for planetary regoliths // Icarus. 2002. V. 159. P. 396–416.
[3] Bohren C. F., Huffman D. R. Absorption and scattering of light by small particles. N. Y.: Wiley, 1983. 547.
[4] Tholen D. J. Asteroid taxonomy from cluster analysis of photometry. Ph.D. thesis, University of Arizona, 1984. P. 150
[5] Piirola V. et al. DIPOL-2: a double image high precision polarimeter // Proc. SPIE. 2014. V. 9147. Art. ID. 91478I.
[6] Piirola V. A double image chopping polarimeter // Astron. Astrophys. 1973. V. 27. P. 383–388.
[7] Berdyugin A. et al. High-precision broad-band linear polarimetry of early-type binaries. II. Variable, phase-locked polarization in triple Algol-type system λ Tauri // Astron. Astrophys. 2018. V. 611. Art. ID. A69.
[8] Berdyugin A. et al. Optical polarimetry: Methods, instruments and calibration techniques // Astrophys. Space Sci. Library. 2019. V. 460. P. 33–65.
[9] Piirola V. et al. High-precision polarimetry of nearby stars (d < 50 pc). Mapping the interstellar dust and magnetic field inside the Local Bubble // Astron. Astrophys. 2020. V. 635. Art. ID. A46.
[10] Belskaya I. N. et al. Polarimetry of CMEU asteroids. I. Number of M – type asteroids // Kinemat. Fiz. Neb. Tel. 1987. V. 3. No. 2. P. 19–21.
[11] Cellino A. et al. Asteroid polarimetric observations using the Torino UBVRI photopolarimeter // Icarus. 2005. V. 179. P. 304–324.
[12] Zellner B., Gradie J. Minor planets and related objects. XX. Polarimetric evidence for the albedos and compositions of 94 asteroids // Astron. J. 1976. V. 81. P. 262–280.
[13] Devogele M. et al. The Calern Asteroid Polarimetric Survey using the Torino polarimeter: assessment of instrument performances and first scientific results // Mon. Not. Roy. Astron. Soc. 2017. V. 465. P. 4335–4347.

SCALING RELATIONS FOR SPATIAL HETEROGENEITY OF SHOCK WAVE EFFECTS FROM THE IMPACT OF COSMIC OBJECTS OF DIFFERENT SIZES

D. O. Glazachev, O. P. Popova, E. D. Podobnaya, N. A. Artemieva, V. V. Shuvalov
Geophysics of Natural and Man-Made Effects RAS, Leninsky pr. 38(*1*), *Moscow 119334*, *Russia* (*glazachevd@gmail.com*)

KEYWORDS:
asteroid, comet, asteroid-comet hazard, shock wave, crater, scaling relations, overpressure distribution

INTRODUCTION:

The impact-induced shock wave in the atmosphere is referred to as the air blast or blast wave. The intensity of the blast depends on the energy released during the impact and the height in the atmosphere at which the energy is deposited [1].

Damage on the ground produced by pressure pulses of shock waves is one of the most important dangerous effects of asteroid and comet airbursts and crater-forming impacts. It was the only one in the case of the small Chelyabinsk event. The Chelyabinsk airburst resulted in little structural damage, other than broken windows, window frames and doors [2].

The effects of the blast wave may be estimated based on the data on nuclear explosions [3] or based on the especially elaborated model [4].

Systematic numerical simulations of the interaction of the cosmic objects with atmosphere in a frame of hydrodynamic model were conducted in [5, 6]. Considered scenario included 39 asteroidal, 39 cometary bodies and 3 intermediate variants with density 2630 kg / m3 with different entry angles and velocities. The considered sizes were in the range from 20 m to 3 km and the kinetic energies covered broad range 0.5 Mt TNT — 2.2 Tt TNT. These simulation results provided the basis, on which scaling relations for the most important parameters of the shock wave were constructed. Thorough impact risk assessment is a significant computational challenge and this motivates the need for simplified approaches and fast damage calculators, where suggested scaling relations may be used.

The energy release during the impact differs from the point explosions, and impact effects demonstrate spatial heterogeneity. There is symmetry in the direction perpendicular to the trajectory of the cosmic object. But along the trajectory the overpressure distribution may be divided on two different areas by the point of maximal energy release for airbursts or center of crater for crater forming impacts. The inclusion of heterogeneity of the overpressure into suggested approximations allows us to obtain better agreement.

Suggested scaling relations are dependent only on the properties of the entering object (size, density, velocity and entry angle). These relations incorporated in special project called the Impact effects Calculator. It is available at the link: http://AsteroidHazard.pro.

REFERENCES:

[1] Shuvalov V. V., Popova O. P., Svettsov V. V. et al. Determination of the height of the “meteoric explosion” // Sol Syst Res. 2016. V. 50. No. 1. P. 3-14.
[2 Popova O. P. et al. Chelyabinsk Airburst, Damage Assessment, Meteorite Recovery, and Characterization // Science. 2013. V. 342 No. 6162 P. 1069–1073.
[3] Collins G. S., Melosh H. J., Marcus R. A. Earth Impact Effects Program: A Web-based computer program for calculating the regional environmental consequences of a meteoroid impact on Earth // Meteoritics & Planetary Science. 2005. V. 40 No. 6 P. 817–840.
[4] Shuvalov V. V., Svetsov V. V., Artemieva N. A. et al. Asteroid Apophis: Evaluating the impact hazards of such bodies // Sol Syst Res. 2017. V. 51 No. 1. P. 44–58.

[5] Artemieva N., Shuvalov V. Atmospheric shock waves after impacts of cosmic bodies up to 1000 m in diameter // Meteoritics & Planetary Science. 2019. V. 54, No. 3. P. 592–608.
[6] Artemieva N., Shuvalov V., Svetsov V. Hazardous Effects Caused by Impacts of Small Cosmic Bodies: Shock Waves on the Surface // 48th Lunar and Planetary Science Conference, held 20–24 March 2017. Woodlands, Texas. LPI Contribution. 2017. No. 1964. id. 1514.

YOUNG ASTEROID FAMILY RAMPO AND CASCADE DISRUPTION

E. D. Kuznetsov[1], A. E. Rosaev[2], E. Plavalova[3], M. A. Vasileva[1]
[1] *Ural Federal University, Lenina Avenue, 51, Yekaterinburg 620000, Russia,* (*eduard.kuznetsov@urfu.ru*; *maxa1907@icloud.com*)
[2] *Yaroslavl State University, Sovetskaya Street,14, Yaroslavl 150000, Russia,* (*hegem@mail.ru*)
[3] *Mathematical Institute of the Slovak Academy of Sciences, Stefanikova 848/49, 81473, Bratislava, Slovakia* (*plavalova@komplet.sk*)

KEYWORDS:
asteroid family, numerical simulation, cascade disruption, Yarkovsky effect, Kholshevnikov metrics, Hill radius, escape velocity

INTRODUCTION:
Some observed asteroid families in the main asteroid belt are each composed of bodies that are thought to originate from the catastrophic disruption of larger parent bodies (e. g., [1]). Daughter fragments produced by breakup of a parent asteroid will appear as a group in the space of the proper elements, even Gyrs after the original collision (e. g., [2]). Very young families with age less than 1 Myr, for which the member orbits have not had time to differentially precess away from each other, can also be identified as groups in the space of the osculating orbital elements [3].

Rampo family was discovered by Pravec and Vokrouhlicky [4] with only three members. Since that number of members belonging to this cluster has increased up to seven [5]. Recently, six new members were discovered [6]. So, at present, 13 members of the Rampo family are known (Table 1).

Table 1. Osculating orbital elements of the Rampo family members at epoch 6 July 1998 (JD 2451000.5)

Asteroid	ω, deg	Ω, deg	*i*, deg	*e*	*a*, au
(10321) Rampo	278.15537	54.08063	6.065299	0.094372	2.32898
(294272) 2007 UM101	280.10595	53.36877	6.053119	0.094215	2.32981
2006 UA169	272.04861	58.62852	6.075379	0.094235	2.32809
(451686) 2013 BR67	266.11447	61.89185	6.097731	0.093416	2.32803
2014 HS9	270.80450	58.71640	6.082418	0.094256	2.32790
2016 TE87	272.01456	58.19967	6.077982	0.095052	2.32905
2015 HT91	265.97106	62.32508	6.091863	0.094187	2.32853
2009 SR371	274.40377	57.02508	6.072834	0.947422	2.32906
2013 RL101	266.96515	61.88935	6.090348	0.093699	2.32773
2013 VC30	270.30822	59.59185	6.082108	0.094323	2.32798
2015 TA367	278.96654	53.46620	6.063380	0.094523	2.32906
2015 TM372	272.64769	57.86332	6.079069	0.093989	2.32864
2017 UH21	268.82520	60.55940	6.087524	0.093442	2.32880

Pravec et al. [5] gave formal age estimate age of this family as 780±130 kyrs (The method of clone convergences in the secular angles). However, they provide very different age values for each pair in cluster: four of the six secondaries converged with the primary about 1400 kyr ago. It is interesting to study convergence six new members discovered in [6].

METHOD:
We use the numerical simulation to study the dynamic evolution of members of the Rampo family to estimate their age and test the hypothesis about the possible formation of this cluster due to cascade disruption of the parent body.

We integrate orbits of Rampo cluster in Mercury package in 1800 kyrs interval with all major planets' perturbations. We use the convergence of orbital

elements and velocity relative to the family's primary member — (10321) Rampo.

We analyze the possibility of approaching asteroids in pairs, and we consider the possibility of approaching asteroid orbits in the past. We performed numerical simulations of orbital evolution for asteroids to find close encounters between paired objects and estimate the conditions of such approaches. For this purpose, the motion equations were integrated within 1 Myr interval in the past by Orbit 9 software as a part of the OrbFit [7] package. Initial orbital elements were chosen from the AstDyS database. Equations of motion for asteroids, eight major planets and dwarf planet Pluto were integrated simultaneously. Perturbations from the Sun oblateness, relativistic effects, and the influence of the diurnal Yarkovsky effect were considered.

For high-precision modeling of the dynamic evolution of asteroids, it is necessary to know the values of the drift velocity of the orbits' semimajor axes under the influence of the diurnal Yarkovsky effect. We estimated the maximal absolute values due to the Yarkovsky effect, assuming that the axis of rotation of the asteroid is orthogonal to its orbit plane. Follow [8], we base on data on physical parameters and drift velocity for asteroid (101995) Bennu.

We assess the age of asteroid pairs under the assumption that the pair forms due to the destruction of the parent body. It is the time when the distance between the asteroids is comparable with the radius of the Hill sphere relative to the Sun for the primary (more massive) asteroid, and their relative velocity is comparable to the escape velocity.

To study the orbital evolution of asteroid pairs, we have analyzed the behavior of the Kholshevnikov metrics ρ_2 [9] defined in the five-dimensional space of Keplerian orbits (the position of asteroids in orbits is not considered).

RESULTS:

The estimations of the orbital convergence ages for the Rampo family members with (10321) Rampo are given in Table 2.

Table 2. The orbital convergence for the Rampo family members with (10321) Rampo

Asteroid	Age [kyrs]		
	Nodes and pericenters convergence	Relative velocity	Pravec et al. [5]
(294272) 2007 UM101	500	500	660
2006 UA169	750	750	1665
(451686) 2013 BR67	~1000	~1000	1378
2014 HS9	750		1239
2016 TE87	750		852
2015 HT91	750		1151
2009 SR371	550		
2013 RL101	500		
2013 VC30	950		
2015 TA367	1000		
2015 TM372	800		
2017 UH21	>1800		

As a result, we note first that orbit of 2017 UH21 is not converged in considered time interval: if this asteroid belongs to a cluster, it is older than 1800 kyrs. Secondly, we outline three groups of orbits converged about 500 kyrs ((294272) 2007 UM101, 2009 SR371, 2013 RL101) and 750 kyrs (2006 UA169, 2014 HS9, 2016 TE87, 2015 HT91, 2015 TM372), and 1000 kyrs ((451686) 2013 BR67, 2013 VC30, 2015 TA367) accordingly. The orbital convergence is obvious, and ages estimation is confirmed by the relative velocity method. There is a tiny possibility that the Rampo family was born in a single breakup event.

PROPOSAL:

The Rampo family is a suitable target for the in-situ study of collisional families' origin with spacecraft. The mission **RAFAEL** (**RA**mpo **F**amily **A**ge **E**stimation **L**aboratory) may include multiplying encounters with the family members using low thrust maneuvers between near-coplanar orbits. An estimation of the formation ages of the asteroid family members can be used to constrain how the population of the cluster collisionally evolved over time and how asteroid surfaces age by space weathering.

ACKNOWLEDGEMENTS:

The study was funded by RFBR (the research project no. 18–02–00015).

REFERENCES:

[1] Farinella P., Davis D. R., Marzari F. Asteroid families, old and young. ASP Conf. Ser. 107. Completing the Inventory of the Solar System. Astronomical Society of the Pacific, San Francisco, 1996. P. 45–55.
[2] Milani A., Knezević Z. Asteroid proper elements and the dynamical structure of the asteroid belt // Icarus. 1994. V. 107. P. 219–254.
[3] Nesvorný D., Brož M., Carruba V. Identification and dynamical properties of asteroid families // Asteroids IV. Univ. of Arizona, Tucson, 2015. P. 297–321.
[4] Pravec P., Vokrouhlický D. Significance analysis of asteroid pairs // Icarus. 2009. V. 204. P. 580–588.
[5] Pravec P., Fatka P., Vokrouhlický D. et al. Asteroid clusters similar to asteroid pairs // Icarus. 2018. V. 304. P. 110–126.
[6] Kuznetsov E. D., Vasileva M. A. On new members of asteroid clusters similar to asteroid pairs // Meteoritics and Planetary Science. 2019. V. 54. Iss. S2. Art. id. A229.
[7] Orbfit Consortium, OrbFit: Software to Determine Orbits of Asteroids. Astrophysics Source Code Library. 2011. arXiv:1106.015.
[8] Spoto F., Milani A., Knezevic Z. Asteroid family ages // Icarus. 2015. V. 257. P. 275–289.
[9] Kholshevnikov K. V., Kokhirova G. I., Babadzhanov P. B., Khamroev U. H. Metrics in the space of orbits and their application to searching for celestial objects of common origin // MNRAS. 2016. V. 462. P. 2275–2283.

FORMATION OF WATER AND HYDROXYL IONS IN SIMULATED PLASMA OF (MICRO)METEORITE IMPACT

V. S. Cheptsov[1,2], A. E. Chumikov[1], N. G. Managadze[1], G. G. Managadze[1]
[1] *Space Research Institute, Russian Academy of Sciences, Moscow 117997, Russia (cheptcov.vladimir@gmail.com);*
[2] *Lomonosov Moscow State University, Russia, Moscow, 119991, Leninskie Gory, 1*

KEYWORDS:
water formation, meteorite impact, hypervelocity impact, laser plasma, LASMA

INTRODUCTION:
Water is one of the most plenty substances in the Universe, and the questions about its origin and abundance in the space attract interest through decades. To date several routes of water formation in hot and cold gas clouds and on the surface of dust grains are revealed [1]. Nevertheless, it is generally agreed that these processes of water formation have insufficient efficiency to explain the high water abundance observed in the space.

We propose one more route of the water formation in space — synthesis of OH and H_2O in plasma which occurs at (micro)meteorite impacts. Impact events are numerous and diverse in the space, and collisions at speeds > 1 km/s can generate impact plasma [2, 3]. It is known that a diverse substances can be synthesized at adiabatic expansion of impact plasma [4] and laser plasma [5–8], which is considered like the best model of the impact plasma [6, 7]. Thus, the water formation in impact processes in space is expectable, but such mechanism of water synthesis was not earlier considered. We performed laser modeling of micrometeorite hypervelocity impacts to check feasibility of the water formation in impact plasma.

MATERIALS AND METHODS:
Modeling of impact plasma formation was performed using laser-ablation mass-reflectron LASMA [9]. LASMA instrument is equipped with Nd:YAG laser which produces pulses at 1.064 μm wavelength with 7 ns pulse duration and with a power density of ~10^9 W·cm^{-2}. Such an effect causes complete atomization and ionization of the sample substance and emission of the formed ions as a plasma torch. High-speed ions in the free expansion mode fall into the time-of-flight mass analyzer, where they are separated by the time of flight. The ions separated in time, after their reflection in the retarding field of the electrostatic reflector, are registered by a secondary electron multiplier. Further the signal goes to a high-speed analog–to –digital converter and is stored in the device's memory as a single spectrum. By the time of flight of ions and signal intensity, it is possible to determine ions masses and relative concentrations with high accuracy.

Experiments were performed with the several targets of different composition:

1. Mixture of SiO_2 and TiH_2 powders in the ratio 1:1 (w/w);
2. Mixture of SrO and TiH_2 powders in the ratio 2:1 (w/w);
3. Mixture of SiO_2 and TiH_2 powders in the ratio 6:1 (w/w);
4. Allende meteorite fragment;
5. $KMnO_4$ powder.

For the experiments the mixtures of powders were pressed into tablets, and a fragment was cleaved from Allende meteorite. Further the tablets or the meteorite fragment were placed into vacuum chamber of LASMA, the air was pumped out to ~$3\cdot10^{-6}$ Torr, and the series of laser shots with simultaneous registering of mass-spectra were performed. The laser spot diameter was 30−50 μm, pulses frequency was ~0.1 Hz. Registration of the positive ions with energies 60 − 74 eV was performed. At least 200 laser pulses for each target were carried out.

RESULTS AND CONCLUSION:

The experiments were started with analyzing of SiO_2 + TiH_2 in 1:1 ratio mixture. The mass-spectra obtained did not contain the peaks with m/z of 17 and/or 18, corresponding to OH^+ and/or H_2O^+. Due to this result the experiments with mixture of SrO and TiH_2 powders were performed. 500 laser shots were performed with the target SrO+TiH_2, and 16 spectra with signs of OH^+ and H_2O^+ ions along with H^+, O^+, Sr^+, and Ti^+, were found (Figure 1). It testified that hydroxyl and water formation is possible in the laser plasma.

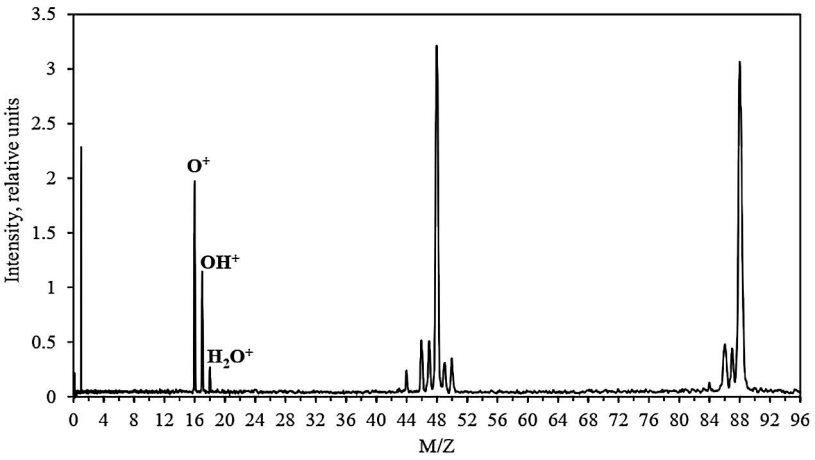

Fig. 1. Single mass-spectrum obtained at laser shot to target composed of SrO and TiH_2

It was hypothesized that OH^+ and H_2O^+ formation absence in experiments with SiO_2+TiH_2 in 1:1 ratio was due to high concentration of TiH_2, which absorbs laser energy well, and a few ionization of SiO_2 caused by it. Therefore the mixture of SiO_2 and TiH_2 powders in the ratio 6:1 was tested. The series of 500 laser shots was performed, and 11 spectra containing mass-peaks characteristic for OH^+ and H_2O^+ were registered.

^{17}O and ^{18}O isotopes could be responsible for signals at 17 and 18 m/z. So the determination of isotopic relative sensitivity coefficients for the oxygen isotopes was performed using $KMnO_4$ as a target. It was found that contribution of ^{17}O and ^{18}O into 17 and 18 m/z signals in the experiments above was negligible. It testified that effect of laser shots modeling micrometeorite impact has led to the formation of hydroxyl and water from predominantly silicate target considered like simple model of meteorite.

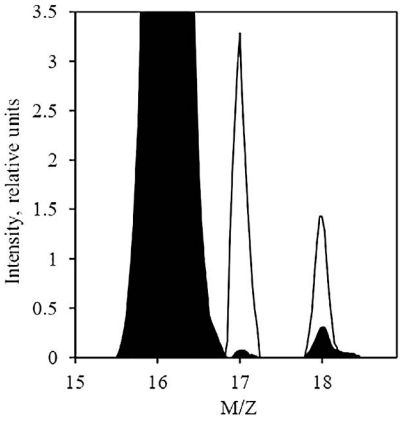

Fig. 2. Part of summarized mass-spectrum of $KMnO_4$ (filled with black color) along with part of single mass-spectrum of Allende meteorite (solid line). The spectra are normalized by integrals of $^{16}O^+$. The figure demonstrates contribution of $^{17}O^+$ and $^{18}O^+$ ions into the signals at 17 and 18 m/z, respectively

To prove the results, the experiment was reproduced using Allende carbonaceous chondrite fragment as the target. Among the series of 600 laser shots to Allende meteorite surface the 21 spectra with relatively large 17 and 18 m/z peaks were registered. The signals obtained were distinct and significantly — on the average in ~32 and ~2.5 times — exceeded the possible contribution of $^{17}O^+$ and $^{18}O^+$, respectively (Figure 2).

Thus, it is experimentally shown that hydroxyl and water formation is possible in laser plasma, which testifies feasibility of the same process in impact plasma. Taking into account widespread of impact events in the Universe it could has a considerable contribution to the water formation in general. At the same time determining of the hydroxyl and water yields from single events as well as at formation of particular planet or moon and in all the Universe is difficult. The mechanisms of water formation in impact events and effectiveness of the processes dependences on characteristics of the impact (composition of target and projectile, speed, angle, etc.) are also unrevealed. A lot of factors need to be further studied in detail.

REFERENCES:

[1] Van Dishoeck E. F. et al. Interstellar water chemistry: from laboratory to observations // Chem. Rev. 2013. V. 113. P. 9043 – 9085.
[2] Grün E. et al. Dust in interplanetary space and in the local galactic environment. In Astrophysics of Dust. ASP Conference Series. 2004. V. 309. P. 245–263.
[3] Meyer-Vernet N., Zaslavsky A. In situ detection of interplanetary and Jovian nanodust with radio and plasma wave instruments. In Nanodust in the solar system: discoveries and interpretations. Astrophysics and Space Science Library. 2012. V. 385. P. 133–160.
[4] Managadze G. G. et al. Excess of L-alanine in amino acids synthesized in a plasma torch generated by a hypervelocity meteorite impact reproduced in the laboratory // Planet. Space Sci. 2016. V. 131. P. 70–78.
[5] Burakov V. S. et al. Plasma chemistry in laser ablation processes // Spectrochim. Acta B. 2001. V. 56. P. 961–971.
[6] Ferus M. et al. Prebiotic synthesis initiated in formaldehyde by laser plasma simulating high-velocity impacts // Astron. Astrophys. 2019. V. 626. Art. A52.
[7] Managadze G. Plasma and collision processes of hypervelocity meteorite impact in the prehistory of life // Intern. J. Astrobiol. 2010. V. 9. P. 157–174.
[8] Zhang R. et al. Laser ablation mass spectrometry of pyrolyzed Koppers coal-tar pitch: a precursor for fullerenes and metallofullerenes // J. Phys. Chem. B. 1999. V. 103. P. 9450–9458.
[9] Managadze G. G. et al. Study of the main geochemical characteristics of Phobos' regolith using laser time-of-flight mass spectrometry // Solar Syst. Res. 2010. V. 44. P. 376–384. doi:10.1134/S0038094610050047.

FEATURES OF MESURING THE MECHANICAL PROPERTIES OF METEORITES L-TYPE

A. P. Krivenko[1], I. I. Nugmanov[2], S. A. Voropaev[1], N. V. Dushenko[1]
[1] *Vernadsky Institute of Geochemistry and Analytical Chemistry of Russian Academy of Sciences (superb92@yandex.ru)*
[2] *Kazan Federal University, Kazan, Russia*

KEYWORDS:
mechanical properties, meteorites, asteroids, Earth, Moon, L5

INTRODUCTION:
Data on the mechanical properties of a chondrite meteorite are very important, as they provide information on the composition and evolution of small celestial bodies [1]. Such data help us understand the problems of the growth of planetesimals and the evolution of the inner structure of growing planet in the early solar system. The formation of the crust of the Moon, the Earth and other internal planet was accompanied by mechanical destruction of the primary chondritic substance by global gravitational processes [2]. Geological deformation, tectonic and formation of the primary atmosphere caused by such processes was determined by the tensile strength of the material and growth of major cracks in large blocks of the growing crust.

METHODS:
The determination of splitting stretching tensile strength (Brazilian test)
by applying compressed force across diameter of disk shaped sample in according to ASTM D3967–08. The thickness to diameter ratio of the disk shaped sample is from 0,2 to 0,75. The diameter of sample must be at least tenth of linear grain size (heterogeneity) of formation. Measuring was carried out in state of natural saturation. The determination of sample' density was performed by method hydrostatic weighing in fluid with determined density at current temperature (22 °C).

The sample with disk shape is placed in the device uniaxial tension of the installation GTYAN.441179.050 and fixed in radial direction. Important that the loading line was lie transverse to bedding. The load increases at a given strain rate until the specimen breaks. The tensile stretching strength is determination in according to ASTM D3967 method.

Determination of elastic deformation properties under conditions of triaxial compression
were carried out in accordance with ASTM D7012–1. A cylindrical sample was used for testing, with a ratio of height to diameter of at least 2 : 1. The sample preparation for testing consisted of drilling cylindrical samples with a diamond crown with an external diameter of 30 mm; reduction to the required length on the cutting machine and grinding of the end surfaces with an accuracy of 0.005 mm. The tests were performed for 3 loading and unloading cycles, with the achievement of the conditional compressive strength at stages 1 and 2 and the destruction of the sample at stage 3. The tests were performed according to the method of multi-stage triaxial tests [3].

The tests were carried out in a state of natural saturation at various effective pressures in the range of 10-20 MPa for multi-stage triaxial tests. The measurement of elastic and strength properties is carried out in a chamber of triaxial axisymmetric compression using axial and radial (ring) linear displacement sensors.

A sample with installed sensors was placed in a triaxial compression chamber of the GTYAN.441179.050 installation, which is then filled with a crimp fluid (PMS–50). At all stages of testing, the values of axial pressure, axial and radial deformation are recorded. The fracture pressure values are recorded. The values of static and dynamic elastic moduli under given conditions are determined according to the methods of ASTM D7012 and ASTM D2845.

The propagation velocity of the longitudinal (P wave) and transverse (S wave) ultrasonic waves was determined using the PIK-UZ-EP installation. Having set

the height value of the sample using the PIK-UZ-EP program, the speed of *P* and *S* waves is automatically calculated. The calculation of dynamic elastic modules (Young and Poisson's ratio) was carried out according to formulas (1) and (2):

$$R = \frac{V_p}{V_s} = \sqrt{\frac{2(1-\mu)}{(1-2\mu)}}, \quad (1)$$

$$E = V_p^2 \rho \frac{(1+\mu)\cdot(1-2\mu)}{(1-\mu)}, \quad (2)$$

where, R is the ratio of longitudinal and transverse waves, V_p is the velocity of longitudinal waves (m/s), V_s is the velocity of transverse waves (m/s), μ is the dynamic Poisson's ratio (CU), E is the dynamic Young's modulus (GPa), ρ is the rock density (g/cm^3).

RESULTS:

Determination of sample density by hydrostatic weighing are presented in Table 1.

Table 1. Geometrical and physics parameters

Sample number	Sample mass in air, mg	Sample mass in aqua at 22 °C, mg	Fluid density g/cm^3	Fluid temperature, °C	Calculated density, g/cm^3
L5_1	40.611	28.667	0.9978	22	3.393
L5_2	43.368	30.623	0.9978	22	3.395
L5_3	147.158	103.884	0.9978	22	3.393

The results of determining the speed of passage of ultrasonic waves are made for the sample "L5_3" and are presented in table 2.

Table 2. The results of determining the velocity and dynamic elastic parameters of the sample L5_3

Length, mm	Diam, mm	Hydrostatic pressure, MPa	Speed of transverse wave, m/s	Speeg of longitudal wave, m/s	Young moduli, GPa	Poissons ratio, CU
63.690	29.445	0	3651.950	6349.950	112.390	0.253
		10	3694.320	6349.950	114.220	0.244
		20	3737.680	6349.950	116.050	0.235
		30	3737.680	6349.950	116.050	0.235
		40	3737.680	6479.150	117.520	0.251
		50	3737.680	6479.150	117.520	0.251

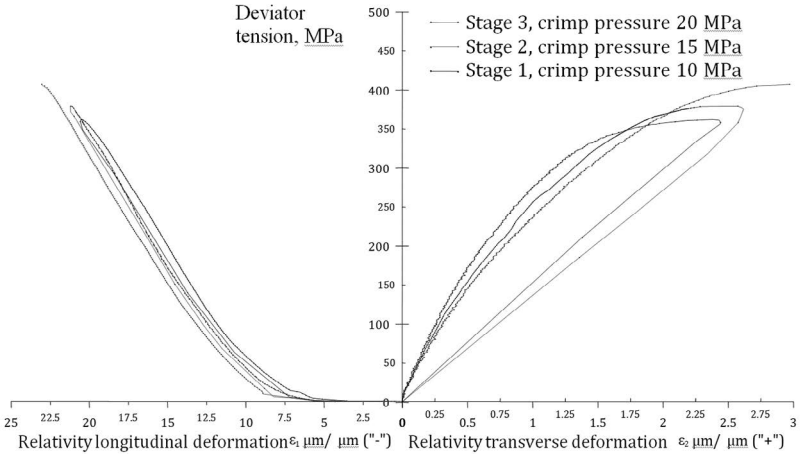

Fig. 1. Plot stress-strain for uniaxial tests

According to ASTMD7012-14 (Figure 1), the results of volumetric compression are presented in graphical form in the format of the curves of total stresses and strains.

DISCUSS:

The study of samples in industrial installation has a number of limitations regarding the size of the sample. It should be at least 25 mm in diameter and 50 mm in length. But often the surface of a fallen meteorite is damaged by cracks and chips. And in order to experimentally evaluate the mechanical properties, it is necessary to study very small parts of the meteorite. For this, we are developing a setup that allows us to measure the mechanical properties of samples with a diameter of 5 mm and a length of 10 mm or more. The limiting factor is only the size of the chondrules, typical size is about 1 mm. At the developed installation, tests can be carried out in accordance with regulatory documents.

REFERENCES:

[1] Yomogida K., Matsui T. Physical properties of ordinary chondrites and their implications // J. Geophysical Research. 1983. V. 88(10). P. 9513–9533.
[2] Voropaev S. et al. // Doklady Physics. 2017. V. 62. No. 10. P. 486–487.
[3] McPhee C. Core analysis: A Best Practice Guide. Elsevier, 2015.

DUST ACOUSTIC WAVES AND SOLITONS IN MARTIAN IONOSPHERE

Yu. S. Reznichenko[1, 2], Yu. N. Izvekova[1], S. I. Popel[1]
[1] *Space Research Institute, Russian Academy of Sciences, Moscow 117997, Russia (besedina_yn@mail.ru)*
[2] *Moscow Institute of Physics and Technology, Institutskiy Pereulok 9, Dolgoprudny, Moscow Region 141701, Russia (dvju@yandex.ru)*

KEYWORDS:
dusty plasmas, dust acoustic waves, solitons, Mars, ionosphere

Interest in planetary ionosphere dusty plasmas has substantially increased in 2000s [1–4]. In recent years significant attention is paid to Mars exploration. Spacecrafts MarsExpress, ExoMars Trace Gas Orbiter, Mars Exploration Rover Opportunity, Mars Science Laboratory Curiosity, etc, are operating successfully.

There is an ionosphere on Mars conditionally at altitudes of 80 to 400 km [5]. At altitudes of about 100 km in the ionosphere, where the temperature is sufficiently low for carbon dioxide freezing, there are clouds formed by dust carbon dioxide grains with a size of about 80–130 nm and number density of about 1 cm^{-3} [6]. In addition, clouds of micron-sized grains were observed at altitudes of about 80 km [7].

Therefore, investigation of the Martian atmosphere at altitudes of about 100 km is quite challenging for dusty plasma processes. Here, we estimate possibilities of dust acoustic wave appearance at these altitudes at night time.

According to existing ideas [8], as a result of solar radiation and Martian rotation there are horizontal winds with the characteristic velocity of propagation m/s. Thus, there is a possible situation, when dusty clouds appear at the region of action of homogeneous horizontal winds. This effect can lead to the development of perturbation in plasmas as it takes place, for example, near the lunar surface [9].

We find that these winds can result in dust kinetic perturbations. The condition for the excitation of perturbations is where τ is the characteristic time of development of the perturbation and ν_{dn} is the frequency of collisions of dust particles with neutrals. For Martian parameters $T \approx 90$ K, $n_n = 10^{12}$ cm^{-3}, $m_n \approx 7 \cdot 10^{-23}$ g, $u \approx 100$ m/s, $n_d \approx 1$ cm^{-3}, $a \sim 100$ nm (here a is the characteristic size of a dust particle) this condition is satisfied and there is a possibility of dust acoustic structure formation. The linear dispersion relationship in this case is that for dust acoustic waves and has the form

$$\omega_k = \frac{\omega_{pd}\lambda_D k}{\sqrt{1+k^2\lambda_D^2}},$$

where ω_{pd} is the dust plasma frequency,

$$\frac{1}{\lambda_D^2} = \frac{1}{\lambda_{D_e}^2} + \frac{1}{\lambda_{D_i}^2},$$

$\lambda_{e(i)}$ is the electron (ion) Debye length.

Furthermore, there is a possibility of nonlinear wave generation. An important kind of nonlinear waves in plasmas is solitons. We consider dust acoustic solitons at altitudes of about 100 km in Martian ionosphere.

One-dimensional propagation of dust acoustic solitons is described by the set of equations, which includes the continuity equation, Euler equation, as well as Poisson equation. Furthermore, we use Boltzmann distribution for electrons and ions. We analyze this set of equations using Sagdeev potential technique and find that amplitude of soliton increases with the increase in dust particle number density. We show that amplitude of soliton increases with the decrease in electron number density.

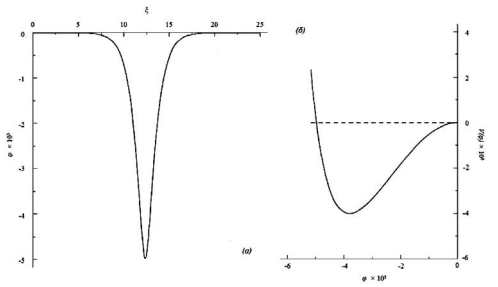

Fig. 1. An example of soliton and Sagdeev potential profiles at altitudes of about 100 km at night time. Here, n_{e0} = 1000 cm^{-3}, n_{d0} = 1 cm^{-3}, $T_e = T_i$ = 90 K, a = 100 nm

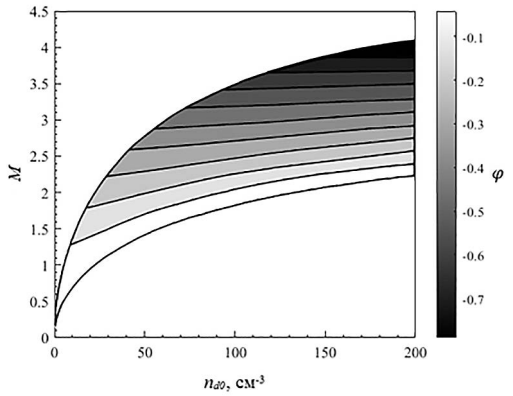

Fig. 2. Soliton amplitude versus and at altitudes of about 100 km at night time. Here, n_{e0} = 1000 cm^{-3}, n_{e0} = 1000 cm^{-3}, $T_e = T_i$ = 90 K, a = 100 nm

ACKNOWLEDGEMENTS:
This work was supported in part by the Russian Foundation for Basic Research (project No. 18–02–00341).

REFERENCES:

[1] Shukla P. K., Mamun A. A. // Introduction to Dusty Plasmas Physics. Bristol/Philadelphia: Institute of Physics Publishing, 2002.
[2] Tsytovich V. N., Morll G. E., Vladimirov S. V., Thomas H. // Elementary Physics of Complex Plasmas. Berlin; Heidelberg: Springer, 2008.
[3] Fortov V. E., Ivlev A. V., Khrapak S. A., Khrapak A. G., Morll G. E. // Phys. Reports. 2005. V. 421. P. 1.
[4] Popel S. I., Kopnin S. I., Yu M. Y., Ma J. X., Huang F. // J. Phys. D: Applied Phys. 2011. V. 44. Art. 174036.
[5] Withers P. // Adv. Space Res. 2009. V. 44. P. 277. 2009.04.027.
[6] Montmessin F., Bertaux J. L., Quemerais E., Korablev O., Rannou P., Forget F., Perriera S., Fussend D., Lebonnoisc S., Reberaca A. // Icarus. 2006. V. 183. P. 403.
[7] Montmessin F., Gondet B., Bibring J. P., Langevin Y., Drossart P., Forget F., Fouchet T. // J. Geophysical Research. 2007. V. 112. Art. E11S90.
[8] Bougher S. W., Engel S., Roble R. G., Foster B. // J. Geophysical Research. 1999. V. 104. P. 16,591.
[9] Popel S. I., Morozova T. I. // Plasma Physics Report. 2017. V. 43. P. 566.
[10] Popel S. I., Kopnin S. I., Kosarev . N., Yu M. Y. // Adv. Space Res. 2006. V. 37. P. 414.

ON POSSIBILITY OF THE EXISTENCE OF OSCILLATIONS IN SCHUMANN CAVITY AT MARS

Yu. N. Izvekova[1], S. I. Popel[1], O. Ya. Izvekov[2]
[1] *Space Research Institute, Russian Academy of Sciences, Moscow 117997, Russia (besedina_yn@mail.ru)*
[2] *Moscow Institute of Physics and Technology, Dolgoprudnyi, Moscow obl. 141700, Russia*

KEYWORDS:
Schumann oscillations, dust in Martian atmosphere, dust devils, electric field generated in vortices

INTRODUCTION:
The possibility of existence of oscillations in a Schumann cavity in the atmosphere of Mars is discussed. On Earth, the main source of energy in the resonator cavity are thunderstorms at tropical latitudes. On Mars, electric phenomena are possible during dust events such as dust devils and dust storms. The charging of dust grains in a dust devil on the surface of Mars is considered and the possible values of the electric fields generated by the vortex are determined. Estimates of the amplitude of oscillations in a Schumann cavity on Mars are obtained and compared with the amplitudes of oscillations in a Schumann cavity on Earth.

According to [1], when the electric field reaches its breakdown value pd < 200 (where p is the pressure in Torr and d is the electrode gap in cm), a glow discharge is ignited. At values of the discharge pd > 103 follows the streamer – leader mechanism (a spark discharge). In the atmosphere of Mars, pd ~105 (at discharge length of approximately 1 km). However, there is no unequivocal experimental evidence confirming the existence of lightning discharges in the atmosphere of Mars. Non-thermal microwave radiation during a Martian dust storm was recorded by a radio telescope in 2009 [2], and peaks were discovered in the recorded radiation spectrum in the vicinity of the predicted values of the first three modes of Schumann resonances on Mars. However, measurements conducted during 5 years using the Mars Express orbiter [3] did not record any signals that can be interpreted as Schumann resonances. We note that although the measurements from the orbit of Mars were conducted during the same time interval as measurements with the radio telescope, at the exact times when the authors of [2] conducted their measurements, the authors of [3] were not recording. To determine whether lightning discharges are possible on Mars, it is necessary to conduct measurements of the electric fields on Mars surface. Such measurements are planned during the second stage of the ExoMars mission.

ELECTRIC FIELDS IN DUST DEVILS:
Dust devils occur above well-heated surfaces as a result of convective instability. The rising air flows drag along the particles of the underlying surface. During collisions in the air flow, mostly in the surface layer, dust grains become charged. This process is usually explained by the triboelectric effect due to which during grain collisions, an electric charge flows from one grain to another. When two grains from the same material collide, the smaller

grain gains a negative charge and the larger one gains a positive charge. Under the action of gravity, the heavier positively-charged grains gather mostly in the lower part of the column while the lighter negatively charged grains gather in the upper part of the column. The space charge separation in the rising flow generates an electric field, while the rotation of the charged particles in the column produces a magnetic field.

We build a model of the electric field distribution in the dust devil and its vicinity taking the finite conductivity of the atmosphere into account by using the following approach, which allows one to account for the dipole structure of the charged dust column. The simulations are carried out in a cylindrical-

ly symmetric approximation. The vortex is represented as a cylinder within which the spatial charge separation occurs. At the initial moment, the charge of the plasma column is zero. The charge in the dust devil is created by the two equal cylinders placed one above the other. The upper cylinder carries a negative charge while the lower cylinder carries a positive charge and the absolute values of both charges increase with time. The absolute value of the local charge density decreases from the center of the cylinder by the Gauss curve and smoothly transitions from the positive charge to the negative charge by the linear law along the vertical axis. Let us determine the average charge density as ρ_q. The charge separation rate $\partial\rho_q/\partial t$ can vary depending on the conditions of grain charging. The efficiency of the tribo charging and the relative velocity of different types of particles are the important parameters that determine the duration of the process and the final values of the fields and the charges.

We use the Poisson equation and the equation for the electric field and charge relaxation. The Poisson equation is solved by the difference method over a uniform 500·500 mesh. The partial derivatives are replaced with differential relationships; as a result, we obtain a linear system of algebraic equations for the values of the potential at the nodes of the mesh. This system is solved by the iteration method. The boundary condition is that the partial derivative of the potential by radius is zero at the axis of the cylinder. The values of the potential at the outer boundary of the cylinder are obtained by integrating over the known charge density distribution in the cylinder volume.

The breakdown values of the electric field on Mars, according to estimates of different authors, are in the range from 16 to 25 kV/m. The calculated maximum charge accumulated in the half of the vortex corresponding to $7.4\cdot10^{-11}$ C·m^{-3}·s^{-1} is of 5.37 C and the maximum charge accumulated in the half of the dust devil corresponding to $3.7\cdot10^{-11}$ C·m^{-3}·s^{-1} is of 2.68 C. It is seen that at large values of it is possible to reach the breakdown value of the electric field, while at lower charge separation rates the achieved maximum field is lower. In cases where the field in the dust devil reaches the breakdown value lightning discharges are possible.

The amplitudes of Schumann oscillations:

The energy released in lighting discharges on an ideally conducting surface can be estimated as

where Q is the charge (C) carried by the discharge and l is the discharge length (m). For average lightning on Earth (Q = 20 C and l = 4 km), we have $W_E \approx 2\cdot10^9$ J [4]. According to simulations carried out in the previous section, for the dust devil on Mars, Q = 20 C and l = 5 km, and the estimated energy of a possible single discharge is $W_M \approx W_E/20$. According to [4], a major fraction of the discharge energy is used to ionize and heat the plasma in the discharge channel, another fraction is used for Ohmic losses and the creation of shock waves in the atmosphere, and only 0.01–0.1 % of the discharge energy is pumped into the resonator.

$$W = \frac{1}{8\pi\varepsilon_0}\cdot\frac{Q^2}{l},$$

The ratio of electric field amplitudes can be estimated via the formula $E_M/E_E \approx \left(\nu_M W_M/\nu_E W_E\right)^{1/2}\left(V_E/V_M\right)^{1/2}$, were ν_E (ν_M) is the discharge frequency on the Earth (Mars), V_E (V_M) is the volume of the Earth (Martian) resonator. Possible discharge frequency can be estimated on the speed of reaching the electric field breakdown values due to charge separation. Let us estimate the required number of dust vortices, in which the electric field reaches breakdown values, so that the amplitude of Schumann resonances on Mars is comparable to that on the Earth. We set $\left(\nu_M W_M/\nu_E W_E\right)^{1/2}\left(V_E/V_M\right)^{1/2} = 1$ thus $V_M \approx 5.7V_E$, from where we get the estimate for the number of dust vortices $N \approx 5.7\nu_E\Delta t_M$. For the characteristic frequency of discharges on Earth $\nu_E \approx 100$ s^{-1}, and the time of charge separa-

tion in the Martian vortex $\Delta t_M \approx 10$ s, the number of suitable dust vortices that must simultaneously be on the surface of Mars is $N \approx 5.7 \cdot 10^3$.

Let us now consider a dust storm that can periodically cover nearly all of the surface of the planet. Let us estimate the possible discharge frequency in a dust storm. Let the area of the storm be S and the height of the dust layer be *a*. Lightning with a length a (the shortest distance between opposite charges) can charge the region of the dust layer with a volume approximately and the dust layer is separated into N independent storm cells. Let us estimate the amplitude of Schumann resonances on Mars compared with that on the Earth. If the dust storm is approximated with a flat condenser, then the maximum charge separated in a single storm cell is $Q_M \approx \varepsilon_0 E a^2 \approx 217$ C at the breakdown field $E = 20$ kV/m and dust layer thickness $a = 20$ km. At $\nu_M = 0.6$ s^{-1} we get the ratio $E_M/E_E \approx 0.52$ and at $\nu_M = 5.9 \cdot 10^2$ s^{-1} we get .

It should be noted that the estimates given above are approximate. as an example, we assume that the discharge carries all the charge that was separated in the dust devil or storm cell of a dust storm. However, in [17] an example was considered in which a single discharge may carry only a quarter of the total charge.

ACKNOWLEDGEMENTS:
This work was supported in part by the Russian Foundation for Basic Research (project No. 18-02-00341).

REFERENCES:

[1] Bazelyan E. M., Raizer Yu. P. Fizika Molnii i Molniezashchity. M.: Fizmatlit, 2001 [in Russian].
[2] Ruf C., Renno N. O., Kok J. F., Bandelier E., Sander M. J., Gross S., Skjerve L., Cantor B. Emission of non-thermal microwave radiation by a Martian dust storm // Geophys. Rev. Lett. 2009. V. 36. Art. L13202.
[3] Gurnett D. A. , Huff R. L. , Morgan D. D. , Persoon A. M. , Averkamp T. F. , Kirchner D. L. , Duru F. , Akalina F. , Kopf A. J. , Nielsen E. , Safaeinili A. , Plaut J. J., Picardi G. Non-detection of impulsive radio signals from lightning in Martian dust storms using the radar receiver on the Mars Express spacecraft // Adv. Space Res. 2008. V. 41. Art. 1335.
[4] Bliokh P. V., Nikolaenko A. P., Filippov Yu. F. Global'nye Elektromagnitnye Rezonansy v Polosti Zemlya – Ionosfera (Global Electromagnetic Resonancs in the Earth–Ionosphere Cavity). Kiev: Naukova Dumka, 1977 [in Russian].

CURRENT STATUS OF ULTRAVIOLET SPECTROGRAPH FOR EXOPLANET (UVSPEX) FOR WSO-UV

S. Kameda[1], A. Tavrov[2], T. Muraoka[1], A. Nakayama[3], G. Murakami[4], T. Kodama[5], M. Ikoma[3], K. Enya[4], N. Narita[3], N. Terada[6], H. Fujiwara[7], M. Sachkov[8], O. Korablev[2]

[1] *Rikkyo University, Japan* (*kameda@rikkyo.ac.jp*)
[2] *Space Research Institute, Russian Academy of Sciences* (*IKI*), *Moscow, Russia*
[3] *The University of Tokyo, Japan*
[4] *ISAS/JAXA, Japan*
[5] *Universite de Bordeaux*
[6] *Tohoku University, Japan*
[7] *Seikei University, Japan*
[8] *Institute of Astronomy of the Russian Academy of Sciences* (*INASAN*), *Moscow, Russia*

KEYWORDS:
exoplanet, exosphere, oxygen, ultraviolet, space telescope

Introduction:

Many Earth-sized planets have been discovered and exist in the habitable zone. Moreover, several Earth-sized planets were recently detected around low-temperature stars near the solar system. However, it is difficult to characterize them as the Earth-like, Venus-like or others. Transit spectroscopy for exoplanetary atmosphere has been performed to characterize larger exoplanets but it requires very high accuracy because of their small size. Hydrogen exosphere has been detected around Neptune-sized exoplanet [1], but an Earth-sized exoplanetary exosphere has not been detected. Recently, Earth's hydrogen exosphere was re-investigated and it was revealed that the Earth's exosphere is extended to ~ 38 Earth radii [2]. On the other hand, Venus' and Mars' hydrogen exosphere is not so much extended because of its low temperature of upper atmosphere. This is caused by the difference in mixing ratio of CO_2 in the upper atmosphere. Venus and Mars have CO_2-rich atmospheres with a lower exospheric temperature. On Earth, CO_2 was removed from its atmosphere by a carbon cycle with its ocean and tectonics. Translating these arguments to exoplanets in a habitable zone presents a possible marker to distinguish an Earth-like planet from a Mars-like or Venus-like planet. The expanded exospheres can be observed in UV, during the exoplanet transit event in a primary eclipse. It reduces the stellar flux when an exoplanet orbiting in front of the host star.

INSTRUMENTATION:

High sensitivity (photon counting) is required for low-temperature star especially faint in UV. Spectral resolution of 0.3 nm is required for separating major emission lines of exospheric atoms. The spectral resolution will be achievable by spectrometers in the main WUVS block, however, it is difficult to measure the weak stellar emission from low-temperature stars without a photon-counting detector. To realize exoplanet transit observations in oxygen spectral lines with the required accuracy, we are developing the Ultraviolet Spectrograph for Exoplanets (UVSPEX) for the WSO-UV telescope. The engineering requirements for the UVSPEX are following. The spectral resolution is better than 0.3 nm to separate O I line from other spectral lines. The spectral range is to exceed the wavelengths from 115 to 135 nm to detect at least H Lyman alpha 121.6 nm to O I 130 nm. The throughput is better 0.3 % accounting more than four terrestrial exoplanets distanced at 5 pc. To achieve these requirements, a simple spectrograph design is proposed, containing the slit, the concave (toroidal) grating as a disperse element and the imaging detector. This optical concept is conventional and used in the other space missions for UV spectroscopy.

Spectrometer slit is aligned at primary focus of the telescope from off-axial sub-FoV. Slit width is 0.2 mm, corresponding to 2.4 arcsec. The concave grating is brazed type with groove density of 2400 grooves per mm. It has a toroidal shape. The effective area has nearly Ø30 mm and the focal length is ~200 mm. The surface is coated by Al + MgF_2 to increase the reflectance, and diffraction efficiency of ~29 % can be achieved.

UVSPEX is planned to be a part of Field Camera Unit (FCU). In this presentation, we show the configuration of UVSPEX instrument and its science objectives.

REFERENCES:

[1] Ehrenreich D. et al. A giant comet-like cloud of hydrogen escaping the warm Neptune-mass exoplanet GJ436b // Nature. 2015. V. 522. P. 459–461.
[2] Kameda S. et al. Ecliptic North-South Symmetry of Hydrogen Geocorona // Geophysical Research Letters. 2017. V. 44. Iss. 23. P. 11,706–11,712.

EXOPLANETARY DUST PHENOMENA IN TRANSIT PHOTOMETRY

M. L. Khodachenko[1,2,3], O. V. Arkhypov[1], I. F. Shaikhislamov[4]
[1] *Space Research Institute, Austrian Academe of Sciences, Graz, Austria* (*maxim.khodachenko@oeaw.ac.at*)
[2] *Institute of Astronomy RAS, Moscow, Russia*
[3] *Institute of Nuclear Physics, Moscow, Russia*
[4] *Institute of Laser Physics SB RAS, Novosibirsk, Russia*

KEYWORDS:
transit photometry, exoplanets, exodust, mass loss

INTRODUCTION:
It was argued theoretically [1] and experimentally [2] that there is the dust component at altitudes ~3000 km and above gaseous giant exoplanets. Such dust could be involved in the escaping flow of upper atmospheric planetary material driven by stellar XUV-radiation and tidal forces. As other sources of the dust at giant exoplanets might be the erosion of moonlets by meteoroids and plasma, evaporation of heated and liquefied satellites, satellite volcanic activity, magnetosphere capturing of interplanetary dust. The dust product of any of these processes can be manifested as a dusty obscuring matter (DOM), which transits over a stellar disk and results in additional absorption of the light distorting the regular shape of the transit light curves (TLCs), especially before and after exoplanetary eclipses. Hitherto the out-transit parts of TLCs were studied only for the search of cumulative effect of exomoons [3], but here we report on the analysis of individual cases of the transit-vicinities. To detect photometric effects of DOM structures co-moving with the transiting object we search for flux variations a short time before the ingress of the planet on the stellar disk and after the egress [4].

STELLAR SET AND METHOD:
We use the publicly available light curves from the *Kepler* mission (NASA Exoplanet Archive: https://exoplanetarchive.ipac.caltech.edu/) after Pre-search Data Conditioning (PDCSAP flux F_{PDC}) [5]. The analyzed data set includes TLCs of 118 Kepler objects with sufficiently high signal-noise-ratio supplemented also with ones from the list in [6]. Our survey uses the long-cadence data with exposure period of δt = 29.4 min. To remove the residual instrumental drifts as well as the stellar variability at timescales longer than the transit duration, we approximate the normalized light curve of each individual transit $F_{PDC}(t_k)/\langle F_{PDC}(t_k)\rangle$, which covers a time interval $\pm 10\Delta t_{tr}$ centered at the transit mid-time, with a 6th order polynomial $F_0(t_k)$. Here t_k is the flux count time, and Δt_{tr} is the transit duration. After the iterative exclusion of outliers, we use the finally obtained $F_0(t_k)$ as a reference level for the flux decrease during the individual transits $\Delta F_k = [F_{PDC}(t_k)/\langle F_{PDC}(t_k)\rangle] - F_0(t_k)$ and prepare the phase-folded TLC (Figure 1).

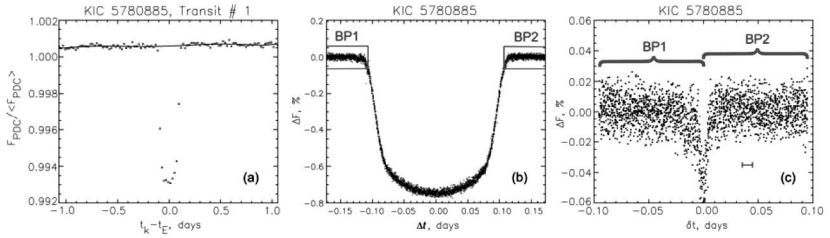

Fig. 1. Example of the light curve processing: *a* — polynomial approximation of the TLC background (solid line); *b* — phase-folded TLC with the indicated near-transit border parts BP1, BP2 (blue boxes); *c* — clipped border parts (labeled) vs. the border distance δt

To detect the dust extinction, the linear gradients $G_{1,2} \equiv \partial(\Delta F)/\partial(\delta t)$ were found for the clipped TLC in the time intervals $-\tau_{max} < \delta t < -\tau_{min}$ before ingress

(index "1") and $\tau_{min} < \delta t < \tau_{max}$ after egress (index "2"). Here $\delta t = \Delta t \pm 0.5\Delta t_{tr}$ is the border distance time counted from the transit border in folded TLC, calculated with the cumulative transit duration Δt_{tr} from the NASA Exoplanet Archive. The gradients G_1 and G_2, were calculated for two time intervals: (a) from 0.03 to 0.16 days and (b) from 0.01 to 0.05 days, which characterize, respectively, the *distant* and *adjoining* regions near the transiting object corresponding to the planetocentric distances from ~2 to ~17 typical planetary radii of hot jupiters.

RESULTS:

The gradients G_1 and G_2 in the *distant* region all clustered around zero, revealing the absence of signs of dusty obscuring matter (DOM) there. However, in the *adjoining* region, 17 cases of hot jupiters showed significantly negative gradients G_1, while the values of G_2 remained around zero (Figure 2). Visual analysis of individual cases also revealed the sporadic pre-transit decrease of flux, which systematically decreases G_1 (Figure 3). This effect was reproduced with the models using a stochastic obscuring precursor ahead of the planet. Such phenomena may be caused by dusty atmospheric outflows, erosion and/or tidal decay of moonlets, or background circumstellar dust accumulated in electrostatic or magnetic traps in front of the mass-losing exoplanet.

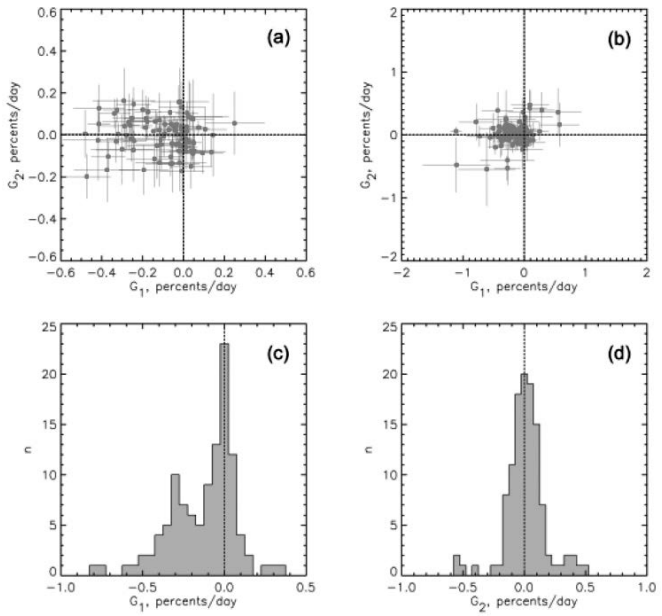

Fig. 2. Distributions of pre-ingress (G_1) and post-egress (G_2) gradients in the adjoining regions (τ_{min} = 0.01, and τ_{max} = 0.05 days): *a* — G_2 vs. G_1 for 90 KOIs with $G_{1,2}$ errors < 0.2 %/day; *b* — G_2 vs. G_1 for all considered KOIs; *c* — histogram of G_1 for all considered KOIs; *d* — histogram of G_2 for all KOIs. The value n is the number of estimates within a bin of histogram

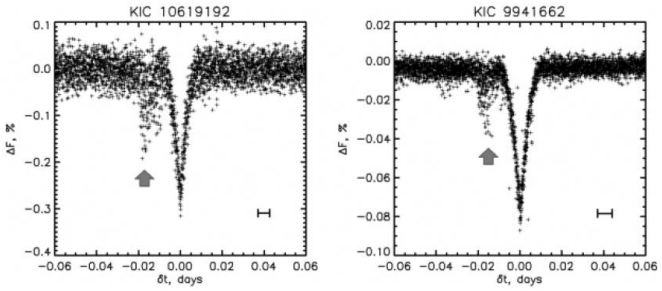

Fig. 3. Examples of DOM manifestations (arrowed) in the pre-ingress parts of folded and clipped TLCs, resulting in significant values of gradient G_1

A special study reveals that all significantly (above three standard errors) negative values of G_1 are associated with the Jupiter-type planets with radii $10 < R_p < 25$ in units of the earth's radius at extremely short orbits with radii $0.026 < a_{orb} < 0.065$ au. The estimated effective area $S_{DOM} \sim -00.1\pi \cdot G_1 \tau_{max} R_s^2$ obscured by DOM on the stellar disk expressed in percent of the planetary cross-section with $\tau_{max} = 0.05$ days and particular stellar radii R_s from the NASA Archive viries in the considered set of objects from 0.4 % achieved for KOI 1.01, up to the 3.3 % for KOI 203.01.

The phenomenology of detected DOM was also simulated assuming an obscuring precursor ahead the real transiting planet (KIC 10619192) which imitates the integral effect of a dust cloud at a distance of 5 planetary radii. Since the same flux drop could be obtained with very different geometries and transparency of cloud, the equivalent opaque circular disk of the precursor was assumed for the simulation simplicity (Figure 4). The realistic results were obtained only for stochastic behavior of precursor: the radius of precursor was randomly taken in the range $[0; 0.5R_p]$ with the appearance time randomized in the range [0; 375 days] with average interval 0.0375 days between individual DOM events. The duration of each DOM event was 0.02 days with a constant area of DOM for each individual event.

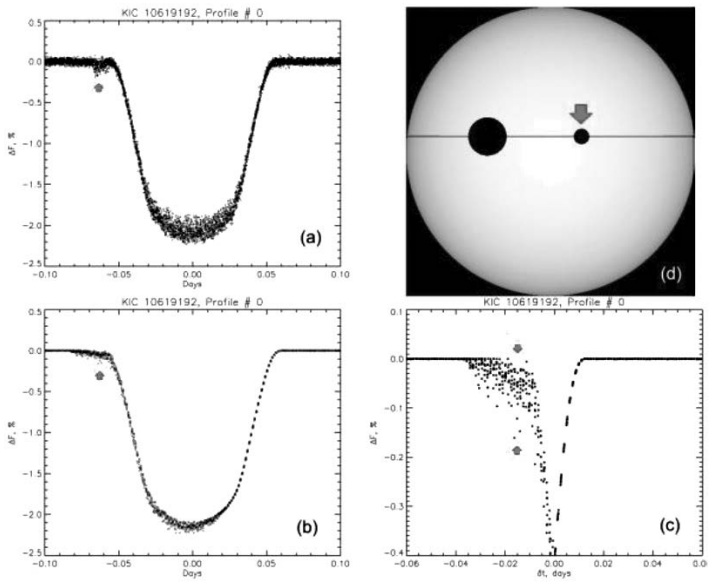

Fig. 4. Modeling of pre-transit manifestations of DOM in KIC 10619192: *a* — real folded TLC; *b* — model-based synthetic folded TLC; *c* — clipped TLC to visua-lize the synthetic DOM effect; *d* — model geometry with the planet, crossing the stellar disk along the solid line and a sporadic DOM precursor (arrowed)

CONCLUSIONS:

1. The absence of systematic deviation of the out-of-transit gradients G_1 and G_2 from zero in the distant regions, and the same in the adjoining post-transit region, but only for G_2, means that there are no detectable DOM manifestations far from exoplanets, and in the closer regions behind them. This assures also the absence of influential artifacts from photometry or light curve processing.

2. Since the discovered significant irregular drops of stellar radiation flux take place only before the ingress in close vicinity of the transit border of only short-period giant exoplanets, we deal here with a new aspect of hot Jupiter nature requiring investigation.

3. The entirely pre-transit location of the found peculiarities excludes the possibility that these are photometric or processing artifacts or the manifestation of orbiting bodies (exomoons, moonlets, exorings, etc.) as a source of obscuring matter.

ACKNOWLEDGEMENTS:
The authors acknowledge the projects No. I2939-N27 and S11606-N16 of the Austrian Science Fund (FWF) for support. MLK is grateful also to the grant No. 18-12-00080 of the Russian Science Foundation and acknowledges the project "Study of stars with exoplanets" within the grant No. 075-15-2019-1875 from the government of Russian Federation.

REFERENCES:
[1] Wang L., Dai F. // Astrophys. J. Let., 2019, V. 873, L1.
[2] Huitson C. M., Sing D. K., Vidal-Madjar A., et al. // MNRAS, 2012, V. 422, 2477.
[3] Teachey A., Kipping D. M., Schmitt A. R. // Astron. J., 2018, V. 155, 36.
[4] Arkhypov O. V., Khodachenko M. L., Hanslmeier A., // A&A, 2019, V. 631, A152.
[5] Jenkins J. M., Douglas A., Chandrasekaran H., et al., // ApJ. Let., 2010, V. 713, L87.
[6] Aizawa M., Masuda K., Kawahara H., Suto Y., // Astron. J., 2018, V. 155, 206.

CLASSIFICATION OF EXOPLANETS

E. Plávalová
Mathematical Institute Slovak Academy of Sciences, *Slovakia*,
Štefánikova 49, *814 73 Bratislava* (*plavalova@mat.savba.sk*)

While studying different types of exoplanets, exoplanetary systems or working with a bunch of databases, we often come across the problem of mistaken identity. It would be very useful to have a taxonomy scale (classification), which is easy and quick to interpret, comprehensible and should capture the most relevant information about exoplanets. We have focused on the classification by Plávalová (2012), which is a five parameter system, categorising parameters such as mass, semi-major axis and temperature. If the specific attributes of the surface are known, we are able to add this as a fifth parameter using a symbol like “i” for example to represent an ice planet. The finished result would look something like this; Earth is E0W0t, Neptune is N1.5F0i, and exoplanet 55 Cnc e is E-1.8R1.

LIGHT CURVE ANALYSIS AND RADIUS STUDY OF 16 TRANSITING EXOPLANETS WITH GROUND-BASED DATA FROM ETD

P. Mirshafiekhozani[1,2], F. Davoudi[1,2,3], A. Poro[1,2,3], E. Paki[2], F. Ahangarani[2], A. Farahani[2], M. Roshana[2], F. Abolhasani[2], Sh. Zamanpour[2], E. Lashgari[2], S. Modarres[2], A. Mohandes[2], S. J. Jafarzadeh[1,3], O. Basturk[4], S. Mesforoush[3], A. Fasihi Harandi[3], M. J. Gozarandi[1,3], Z. Zare Mehrjardi[1,3], P. D. Maley[5], S. Khakpash[3,6], K. Rokni[3,7], A. Sarostad[3]

[1] *The International Occultation Timing Association-Middle East section* (*peg.mirshafie@gmail.com*)
[2] *Exoplanet Transit Project* (*ETP*), *Transit department*, *IOTA-ME*, *Iran*
[3] *The Six Summer School of Astronomy*, *Khayyam Observatory*, *Mahdasht*, *Iran*
[4] *Ankara University*, *Faculty of Science*, *Astronomy and Space Sciences Department*, *TR-06100*, *Tandogan*, *Ankara*, *Turkey*
[5] *The International Occultation Timing Association*, *Carefree AZ*, *USA*
[6] *Department of Physics*, *Lehigh University*, *16 Memorial Drive East*, *Bethlehem*, *PA 18015*, *USA*
[7] *Iranian Space Agency*, *Tehran*, *Iran*

KEYWORDS:
transit, ETD, Exofast, Radius

INTRODUCTION:

Throughout the transit of an exoplanet passing in front of the disk of its' host star, it blocks a small portion of light from the star with the change in flux at mid-transit known as the transit depth (Rice, 2014). Transit photometry is a powerful technique for studying exoplanets and deriving the orbital and absolute parameters of exoplanets. Since the first step to derive the parameters of exoplanets is observation, we collect light curves of ground-based observations that are available on the Exoplanet Transit Database (ETD, http://var2.astro.cz/) website. ETD, preserved by the Czech Astronomical Society (CAS), is one of the free databases of the transiting observations which makes the raw transit data available. This online web application provides some useful information for researchers such as time of the transit start, center, end, duration, and the depth of each transit that named as transit prediction.

We did a project in two parts to compare values of the exoplanets' output parameters with that from the NASA Exoplanet Archive (NEA, https://exoplanetarchive.ipac.caltech.edu/) database.

In the first part of our project, we have studied six exoplanets includes HAT-P-8b (Latham et al., 2009), HAT-P-16b (Buchhave et al., 2010), HAT-P-21b (Bakos et al., 2011), HAT-P-22b (Bakos et al., 2011), HAT-P-28b (Buchhave et al., 2011), and HAT-P-30b (Johnson et al., 2011) whose light curves are taken from ETD. We chose these planets because the number of light curves of their transits is appropriate and their observations have been made in the last ten years. They have suitable brightness to enable ground-based observations (maximum magnitude 15). In addition to the suitability of data quality, we made a selection by eye; For example, we chose those for analysis that have sufficiently out-of-transit data points and show an obvious decrease in the brightness in the light curve during the transit. The orbital period of each exoplanet is less than 5 days. Duration of transits is less than 0.2 day and these planets only orbit around one star. After investigating the transit light curves from ETD, we analyzed transit data of these exoplanets by using the AstroImageJ (AIJ) software package. AIJ is a graphical software package for general image processing. It simplifies light curve plotting, especially for applications requiring ultra-precise light curves such as exoplanet transits (Mandel and Agol, 2002). We studied 82 light curves and extracted parameters from them such as R_p, k, $t14$, T_c, and i by using AIJ and their uncertainties only by fixing the parameter values found in the analysis in EXOFAST.

In the second part of our project, we analyzed 14 light curves of 10 hot jupiter exoplanets available on ETD. We know hot jupiters as a class of giant gassy exoplanets. They are the easiest planets to detect because of their large size (with masses greater than or equal to 0.25 Jupiter mass) and short orbital period (with period between 0.8–6.3 days) (Becker et al., 2015). At first, we chose some exoplanets of the list which we come across by visiting ETD and then we analyzed the raw transiting data and reduced observational data from their light curves. Then, we compared values of the Radius of planets, which is one of the most important parameters that can be derived in high accuracy of transiting photometry, from a web-based tool, EXOFAST (https://exoplanetarchive.ipac.caltech.edu/cgi-bin/ExoFAST/nph-exofast) (A Fast Exoplanetary Fitting Suite in IDL) with the parameters from the Extrasolar Planets Encyclopedia (http://exoplanet.eu/) database and we used a file includes BJDTDB, Flux, and its' Error as input for EXOFAST.

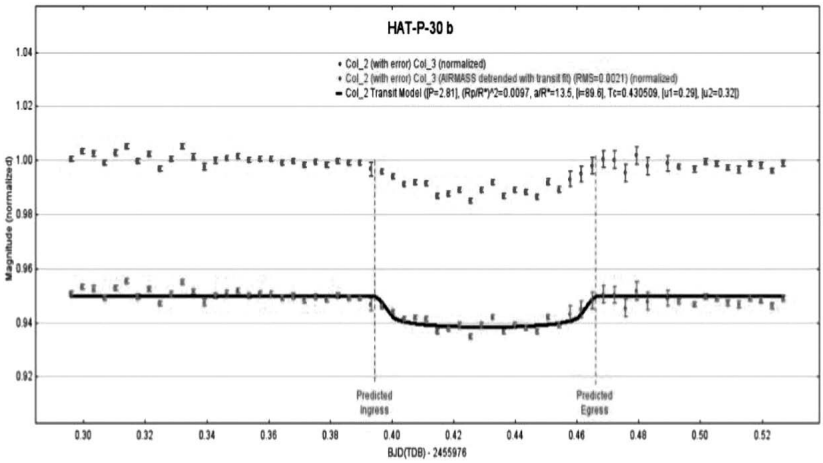

Fig. 1. Multi-plot example for HAT-P-30b transit using the airmass detrend parameter. The raw data are shown as solid blue dots which are plotted with no fit, while the solid red dots show the same data assuming that it will reflect a dip in brightness due to the exoplanet's transit, which is shown by the black line through the data

CONCLUSION:

The results show that the parameters of exoplanets obtained from ground-based observation with small telescopes are comparable to their values in NEA in this study. They also prove the follow-up potential of amateur and university observatories in providing system parameters. These results are important because they can show the role of observations with small telescopes to study more discovered planets.

Table 1. Radius Comparison of 16 Exoplanets from NEA vs. Exofast and AstroImageJ's results in our study

Planets	RP(RJ) from NEA	RP(RJ) in our study
CoRot-12b	1.44 (±0.13)	1.8058 (±0.2109)
HAT-P-52b	1.009 (±0.072)	1.0964 (±0.0750)
HAT-P-57b	1.413 (±0.054)	1.4751 (±0.1124)
HATS-28b	1.194 (±0.07)	1.2139 (±0.0750)
HATS-34b	1.43 (±0.19)	1.3289 (±0.0950)
KELT-3b	1.345 (±0.072)	1.3706 (±0.1032)
WASP-61b	1.24 (±0.03)	1.1478 (±0.0474)
WASP-67b	1.4 (+0.3, –0.2)	0.9970 (±0.0676)
WASP-122b	1.743 (±0.047)	1.7442 (±0.0802)
WASP-140b	1.44 (+0.42, –0.18)	1.1990 (±0.0735)

Planets	RP(RJ) from NEA	RP(RJ) in our study
HAT-P-8b	1.40 (±0.13)	1.46 (±0.11)
HAT-P-16b	1.289 (±0.066)	1.31 (±0.06)
HAT-P-21b	1.11 (±0.16)	1.11 (±0.16)
HAT-P-22b	1.15 (±0.19)	1.11 (±0.06)
HAT-P-28b	1.212 (+0.113, –0.082)	1.25 (±0.09)
HAT-P-30b	1.44 (±0.15)	1.38 (±0.26)

REFERENCES:

[1] Rice K. The detection and characterization of extrasolar planets // Challenges. 2014. V. 5(2), P. 296–323.
[2] Latham D. W., Bakos G. A., Torres G., Stefanik R. P., Noyes R. W., Kovács G., Pál A., Marcy G. W., Fischer D. A., Butler R. P., Sipőcz B., Discovery of a transiting planet and eight eclipsing binaries in HATNet field G205 // The Astrophysical J. 2009. V. 704. Iss. 2. P. 1107.
[3] Buchhave L. A., Bakos G. Á., Hartman J. D., Torres G., Kovács G., Latham D. W., Noyes R. W., Esquerdo G. A., Everett M., Howard A. W., Marcy G. W. HAT-P-16b: A 4 MJ planet transiting a bright star on an eccentric orbit // The Astrophysical J. 2010. V. 720. Iss. 2. P. 1118.
[4] Bakos G. Á., Hartman J., Torres G., Latham D. W., Kovács G., Noyes R. W., Fischer D. A., Johnson J. A., Marcy G. W., Howard A. W., Kipping D. HAT-P-20b – HAT-P-23b: Four massive transiting extrasolar planets // The Astrophysical J. 2011. V. 742. Iss. 2, P. 116.
[5] Buchhave L. A., Bakos G. Á., Hartman J. D., Torres G., Latham D. W., Andersen J., Kovács G., Noyes R. W., Shporer A., Esquerdo G. A., Fischer D. A. HAT-p-28b and HAT-p-29b: Two sub-Jupiter mass transiting planets // The Astrophysical J. 2011. V. 733. Iss. 2. P. 116.
[6] Johnson J. A., Winn J. N., Bakos G. Á., Hartman J. D., Morton T. D., Torres G., Kovács G., Latham D. W., Noyes R. W., Sato B., Esquerdo G. A. HAT-P-30b: a transiting hot Jupiter on a highly oblique orbit. // The Astrophysical J. 2011. V. 735. Iss. 1. P. 24.
[7] Mandel K., Agol E. Analytic light curves for planetary transit searches // The Astrophysical J. 2002. V. 580. Iss. 2. P. L171.
[8] Becker J. C., Vanderburg A., Adams F. C., Rappaport S. A., Schwengeler H. M. WASP-47: A hot Jupiter system with two additional planets discovered by K2 // The Astrophysical J. Letters. 2015. V. 812. Iss. 2. Art. L18.

"DETECTABILITY WINDOW" REGULARIZATION ALGORITHM TO ACCOUNT FOR OBSERVATION SELECTION IN STATISTICS OF RV-EXOPLANETS

A. Ivanova[1], V. Ananyeva[1], I. Shashkova[1], A. Tavrov[1], J.-L. Bertaux[2].
[1] *Space Research Institute, Russian Academy of Sciences, Moscow, Russia* (*ctf.i.a.e@gmail.com*)
[2] *LATMOS/IPSL/CNRS/UVSQ, 78280, Guyancourt, France*

KEYWORDS:
exoplanets, mass statistic, RV exoplanets, comparative planetology

The key problem in studying exoplanets statistics is the inhomogeneity of observation data (NASA Exoplanet Archive. URL: exoplanetarchive.ipac.caltech.edu). The main reasons for the inhomogeneous data are: different sensitivity of spectrographs, different time of observations and different methods of processing the obtained data. There are several approaches to solve the problem of data regularization, one of which is the "detectability window" method, which is herewith presented.

This method was considered in [1–2]. In [1] a binary border "detectability window" was used, because of this severity (this makes a pessimistic approach) a rather large number of planets felt out of consideration. In [2] the authors applied a "probability window" (similar to the recently used "detectability window", however that probabilistic border makes an optimistic approach), which allowed to take into account much larger number of planets. In [2], the authors interest was concentrated solely on the planets circulating around red dwarfs (class M stars).

In the present study, the method of "probability window" [2] has been extended to regularize the statistics of all RV- exoplanets known up-to-date. It has been applied to all the exoplanets discovered by the method of radial velocities, with the exception of exoplanets with a period less than 1 day or more than 10,000 days, and with the exception of exoplanets with a mass less than 0.011 masses of Jupiter or more than 13 masses of Jupiter. Thus, out of all the 716 exoplanets, 696 exoplanets remain for consideration.

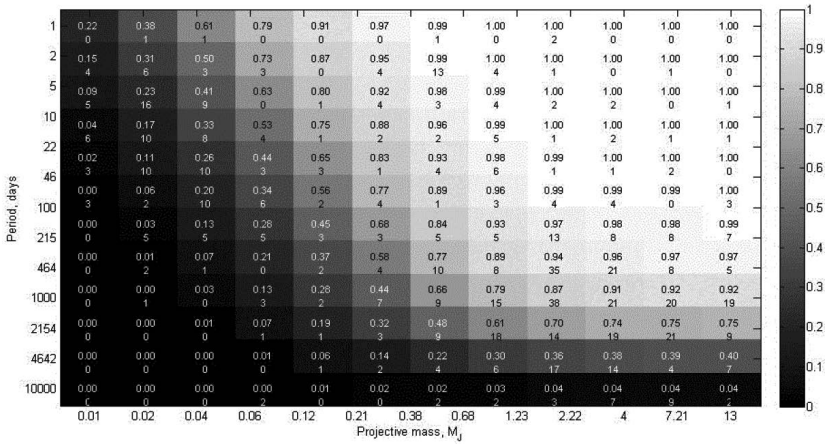

Fig. 1. Detectability window built according to 696 exoplanets. Along the horizontal axis the projective mass of the exoplanet in the masses of Jupiter (M_J) units is shown. Along the vertical axis the observation program duration in the Earth day units. In cell, the upper number is the detection probability, the lower number is the number of considered exoplanets. The cell background color corresponds the probability of detection in correspondence to the colorbar at right

To build the "probability window" it is necessary to have a list (an array) of the exoplanets with known orbital periods and masses as well as data on ob-

servation programs: observation period, spectrograph error, etc. These data are partially displayed in NASA Exoplanet Archive, but some parameters were needed to be taken from the original articles devoted to particular exoplanets discoveries.

One knows these parameters and sets the “detectability” criteria, the “probability window” can be build. The criteria used by us were: the fraction of the intersection of the orbital period of the exoplanet and the observation period, the ratio of the radial velocity half-amplitude and σ of the survey program. An example of the built “probability window” is shown in Figure 1. After the “probability window” is formed according to the criteria, we proceed to forming a histogram. If the value of the “probability window” cell to which the exoplanet should enter is greater than 0, then the exoplanet gets weight inversely proportional to the cell value.

ACKNOWLEDGEMENTS:
Authors acknowledge the support from the Government of Russian Federation and Ministry of Education and Science of Russian Federation (grant No. 2020-1902-01-133).

REFERENCES:

[1] Ananyeva V. I., Venkstern A. A., Churbanov D. V., Shashkova I. A., Tavrov A. V., Korablev O. I., Bertaux J.-L. The distribution of exoplanet giants by the true and projective masses. Accounting observational selection // Solar System Research. 2019. V. 53. No. 2. P. 124–137.

[2] Tuomi M., Jones H. R.A., Butler R. P., Arriagada P., Vogt S. S., Burt J., Laughlin G., Holden B., Shectman S. A., Crane J. D., Thompson I., Keiser S., Jenkins J. S., Berdiñas Z., Diaz M., Kiraga M., Barnes J. R. Frequency of planets orbiting M dwarfs in the Solar neighbourhood: arXiv:1906.04644. 2019. https://arxiv.org/abs/1906.04644.

RADIAL VELOCITY-EXOPLANETS DISTRIBUTIONS BY MASSES AND BY ORBITAL PERIODS

V. Ananyeva[1], A. Ivanova[1], I. Shashkova[1], A. Tavrov[1], J.-L. Bertaux[2]
[1] *Space Research Institute, Russian Academy of Sciences, Moscow, Russia* (*a-lada@yandex.ru*)
[2] *LATMOS/IPSL/CNRS/UVSQ, 78280, Guyancourt, France*

KEYWORDS:
exoplanets, mass statistics, period statistics, RV exoplanets

To date, almost 800 exoplanets with a known projective mass have been discovered by the radial velocity (RV-) technique. However, there are strong selection effects that distort the true (original) exoplanets statistics e.g. mass- and period statistics as seen in the observed mass- and period distribution of exoplanets. We have corrected the observed mass- and period distributions by the "detectability window" regularization algorithm.

We considered RV-exoplanets with periods 1-10^4 days and masses 0.011–13 mJ (Jupiter mass). We divided each range into 12 logarithmically equal bins. For each area on the plane "orbital period (P) – projective mass (m)" we determined the probability of discovery a planet within the cell (P, m). The algorithm is described in detail in A. Ivanova report "Detectability window regularization algorithm to account for observation selection in statistics of RV-exoplanets" during the same meeting.

Some matrix elements (detection probability cells) of "detectability window" are zeros. There's a zero chance of finding the planet with the given (P, m). We identified this area as a blind spot. As the number of planets in the blind spot is unknown, we have considered two options: the distribution of planets of all masses with periods of 1–100 days, and the distribution of planets of all periods with masses more than 21 Earth masses (Figure 1, 2).

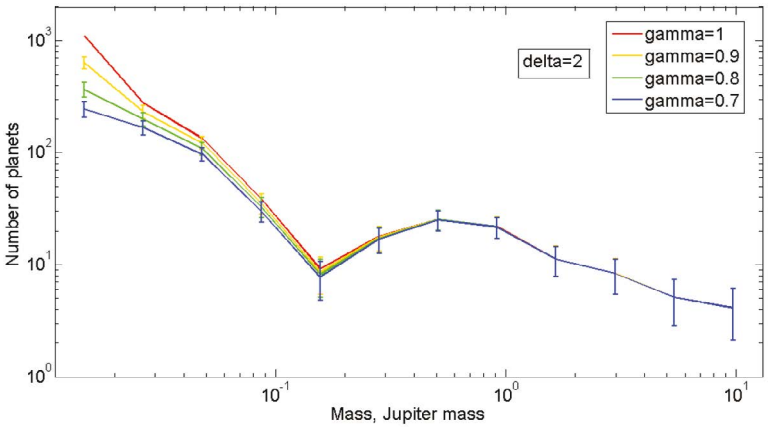

Fig. 1. The distribution of planets of all masses with orbital periods of 1–100 days

Since the distribution in the range of small masses strongly depends on the coefficient gamma, which is part of the expression for the boundary of the "detectability window" (K > gamma × sigma(O–C)), we considered a sample of planets with small values sigma: sigma(O–C) < 4 m/s and periods of 1–100 days, for which the blind spot is absent.

This result in the small mass area is consistent with the mass distribution of the transit exoplanets of Kepler [1]. The distribution of planets of all periods with masses more than 21 Earth masses follows a power law with fractures at ~0.135 Jupiter masses and ~2 Jupiter masses, which is consistent with the prediction of the C. Mordasini's theory of population synthesis [2].

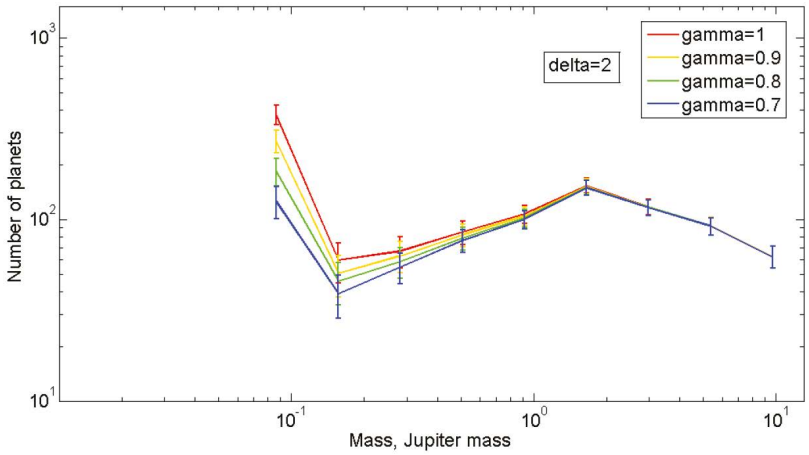

Fig. 2. The distribution of planets of all periods with masses more than 21 Earth masses

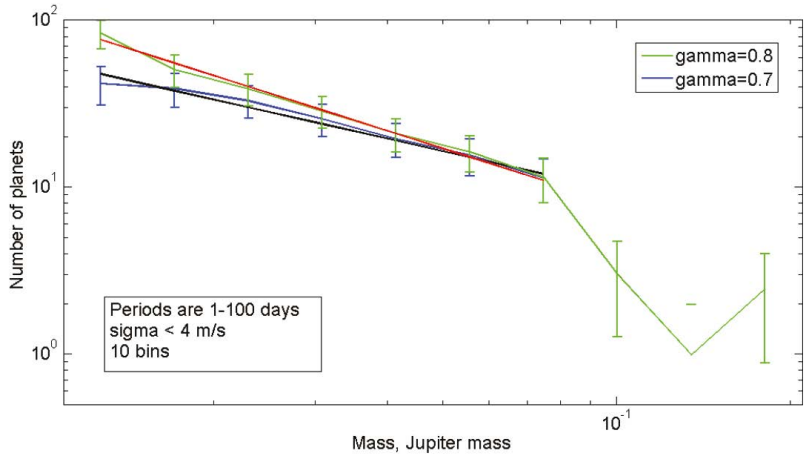

Fig. 3. Distribution of planets with masses 0.011–0.3 m_J and periods of 1–100 days, for which sigma(O–C) < 4 m/s. In the range of 0.011–0.0866 m_J (3.5–27.5 Earth masses) the distribution follows the power law with the index of –1.78 for gamma = 0.7 and –2.1 for gamma = 0.8, on average –2

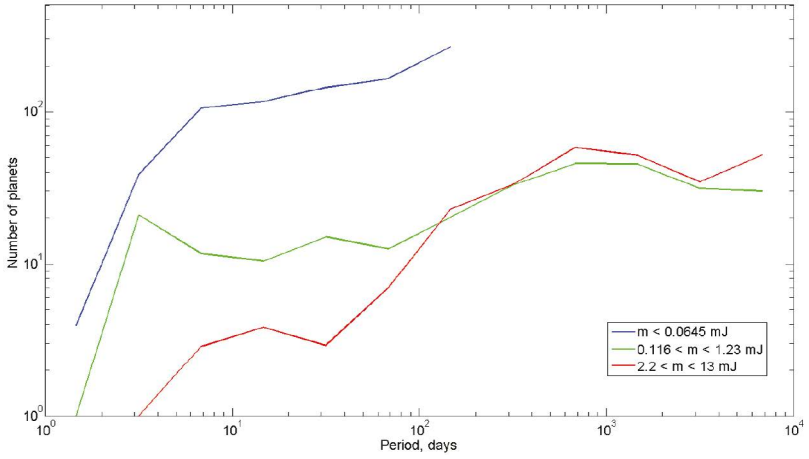

Fig. 4. The distribution by orbital periods of planets with masses less than 20.5 Earth masses (blue line), 0.116–1.23 Jupiter masses (green line) and more than 2.2 Jupiter masses (red line). Planets with masses near breakpoints are excluded from consideration

As can be seen in Figure 4, the mass distribution differs for the three mass ranges: $m < 0.135\ m_J$, $0.135 < m < 2\ m_J$, and $m > 2\ m_J$. The distribution of orbital periods for the planets in each mass range also differs.

Authors acknowledge the support from the Government of Russian Federation and Ministry of Education and Science of Russian Federation (grant No. 2020-1902-01-133).

REFERENCES:

[1] Ananyeva V. I., Ivanova A. E., Venkstern A. A., Shashkoval A., Yudaev A. V., Tavrov A. V., Korablev O. I., Bertaux J.-L. Mass distribution of exoplanets considering some observation selection effects in the transit detection technique // Icarus. 2020. V. 346. Art. 113773. DOI: 10.1016/j.icarus.2020.113773.

[2 Mordasini Ch. Planetary Population Synthesis // Handbook of Exoplanets / eds. H. J. Deeg, J. A. Belmonte. 2018. P. 2425–2474. doi:10.1007/978-3-319-30648-3_143-1.

STUDY OF THE MASS DISTRIBUTION OF TRANSIT EXOPLANETS VIA MASS-RADIUS DEPENDENCE

O. Y. Yakovlev[1], A. E. Ivanova[1], V. I. Ananyeva[1], A. V. Tavrov[1], J.-L. Bertaux[2]
[1] *Space Research Institute of the Russian Academy of Sciences, Moscow, Russia, 117997 (yko-v@ya.ru)*
[2] *LATMOS/IPSL/CNRS/UVSQ, 78280, Guyancourt, France*

KEYWORDS:
exoplanets, mass distribution, mass-radius exoplanets dependence

The report is devoted to the study of the mass distribution of transit exoplanets detected by Kepler and TESS space telescopes. Among these planets, the mass is quite reliably known for 386 planets out of 2771. The key idea of the study is to include in the distribution the remaining 2385 exoplanets with calculated masses by their radius.

Review of various mass-radius models was carried out and 3 models from publications were selected [1–3]. In addition, a simple mass-radius relation was defined using averaged data from the NASA Exoplanet Archive (NASA Exoplanet Archive: exoplanetarchive.ipac.caltech.edu/).

Using these several models (Figure 1), the exoplanets' guess masses were calculated and five distributions were constructed (Figure 2): the initial distribution (about 386 planets) and four distributions by mass-radius relations. Using the maximum likelihood estimate (MLE), the power law distribution parameters α, M_{min} are determined, the probability density function of which is determined:

$$p(M) = -\frac{1+\alpha}{M_{min}^{1+\alpha}} M^{\alpha}, \quad (1)$$

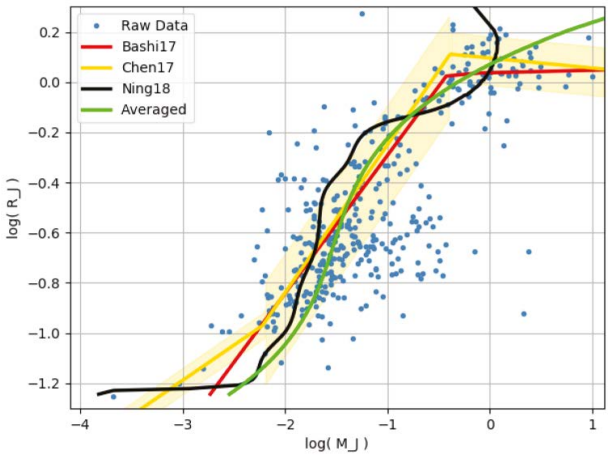

Fig. 1. Mass-radius (*M*-*R*) plane, axes shown in Jupiter units, in logarithmic scale. Dots denote exoplanets detected by Kepler and TESS space telescopes (archive Raw Data, NASA Exoplanet Archive: exoplanetarchive.ipac.caltech.edu/) and the lines show the mass-radius relations Bashi17 [1], Chen17 [2], Ning18 [3], Averaged (by Raw Data averaging)

For each distribution, the parameters α, M_{min} are defined, which were verified using the Kolmogorov-Smirnov test (KST) [4]. The found values are compared with the results presented in [5]. The results do not coincide, but, for the distributions determined by the model [1] ($\alpha = -1.787 \pm 0.036$, $M_{min} = 0.02 M_j$) and by the averaged mass-radius relation ($\alpha = -1.767 \pm 0.038$, $M_{min} = 0.05 M_j$), the exponents differ little ($\alpha = -1.90 \pm 0.06$, $M_{min} = 0.02 M_j$ [5]).

Further, following to [5], the distributions were constructed taking into account exoplanets that cannot be detected by the transit method due to the orientation of their orbital plane, using transit detection probability. For these distributions, it was established by KST that the approximation in the considered mass range by the power law is improper.

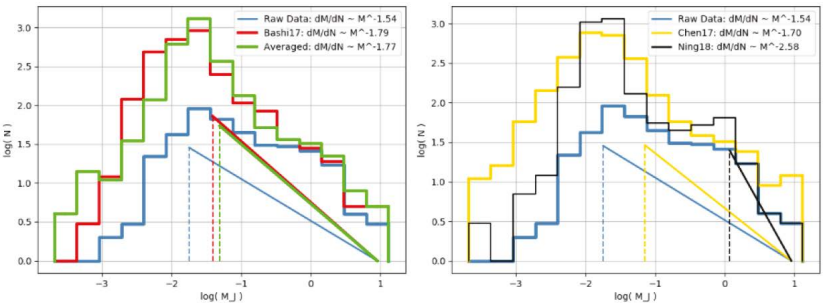

Fig. 2. Mass distributions of exoplanets detected by Kepler and TESS space telescopes (Raw Data); distributions with addition masses calculated by mass-radius relations to the Raw Data: Bashi17 [1], Chen17 [2], Ning18 [3], Averaged (by Raw Data averaging). The vertical dotted lines indicate M_{min}, which correspond to the optimal α in the distribution law $\partial M/\partial N \sim M^{\alpha}$ represented by oblique lines

In [6], the mass distribution was obtained by the method of planetary population synthesis, which was approximated by a broken power law (with transition points M_t). For the distribution using the model [3], power law parameters were determined using the MLE and compared with [6] (Figure 3).

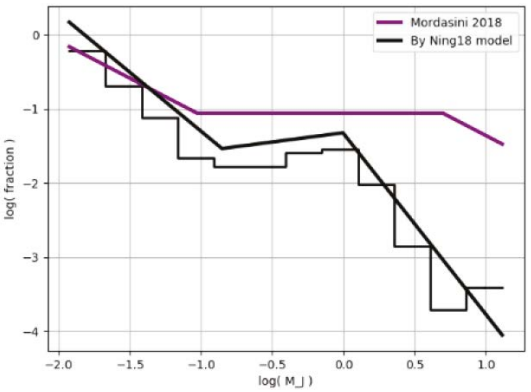

Fig. 3. De-biased mass distribution with masses calculated by mass-radius relations Ning18 [3] and the resulting broken power law (α = –2.59, –0.75, –3.44; M_t = 0.14, 0.99M_j); broken power law by [6] (α = –2, –1, –2; M_t = 0.094; 5M_j)

We show that the mass distributions using the averaged mass-radius dependence and the more complex mass-radius model [1–3] are close to each other and to the previously obtained statistics [5] using the «mass determination» correction factor. The distribution using mass-radius model [3] is closest to the semitheoretical model [6].

ACKNOWLEDGMENTS:
This work was supported by the Government of Russian Federation and Ministry of Education and Science of Russian Federation (grant No. 2020-1902-01-133).

REFERENCES:

[1] Bashi D., Helled R., Zucker S., Mordasini C. Two empirical regimes of the planetary mass-radius relation // Astronomy and Astrophysics. 2017. V. 604.
[2] Chen J., Kipping D. Probabilistic forecasting of the masses and radii of other worlds. // The Astrophysical J. 2017. V. 834. P. 17–30.
[3] Ning B., Wolfgang A., Ghosh S. Predicting Exoplanet Masses and Radii: A Non-parametric Approach // Astrophysical J. 2018. V. 869. No. 1. P. 5–25.

[4] Clauset A., Shalizi C., Newman M. Power-Law Distributions in Empirical Data // Society for Industrial and Applied Mathematics Review. 2009. V. 51. No. 4. P. 661–703.
[5] Ananyeva V. I., Ivanova A. E., Venkstern A. A., Shashkova I. A., Yudaev A. V., Tavrov A. V., Korablev O. I., Bertaux J.-L. Mass distribution of exoplanets considering some observation selection effects in the transit detection technique // Icarus. 2020. V. 346. No. 4. P. 1–18.
[6] Mordasini C. Planetary Population Synthesis // Handbook of Exoplanets / eds. Deeg H., Belmonte J. Springer, 2018. P. 2425–2474.

ACTIVITY OF TWO STARS WITH PLANETARY SYSTEMS IN TUC – HOR GROUP

I. S. Savanov[1], E. S. Dmitrienko[2]
[1] *Institute of Astronomy, Russian Academy of Sciences, Pyatnitskaya ul. 48, Moscow, 119017 Russia* (*igs231@mail.ru*)
[2] *Sternberg Astronomical Institute, Moscow State University, Universitetskii pr. 13, Moscow, 119992 Russia*

KEYWORDS:
exoplanet, stellar activity, young moving groups, spots, rotation, flares, activity cycles

INTRODUCTION:
The TESS space mission provides a unique opportunity to investigate the photometric variability of stars (including those with planetary systems) in young moving groups (YMGs). YMGs are dynamically unbound associations of stars that are identified based on their common motion. The ages of YMGs reach 300 Myr and they probe a more continuous range of ages than do young star clusters. The stellar environments in YMGs also differ from those found in high-density star clusters, such as Praesepe or Pleiades. The YMG clusters are less compact and, therefore, stellar dynamical interactions in them are less frequent. As a result, they may be more characteristic of the precursors of exoplanetary systems that orbit typical field stars. Dynamical studies indicate that stellar interactions in open clusters are unlikely to disrupt planetary systems, but milder impacts, such as changes in the eccentricity of planetary orbits, are quite possible. Finally, most known YMGs are substantially less distant than star clusters. This provides additional advantages for detailed characterization of the exoplanetary systems in YMGs through such techniques as transmission spectroscopy and radial velocity monitoring.

We report the results of our analysis of the activity of two stars with planetary systems in 45 Myr Tuc – Hor group.

DS TUC:
A close-in exoplanet with a radius between those of Neptune and Saturn was discovered around star DS Tuc (DS Tuc A, HD 222259A) which is a member of the Tucana – Horologium (Tuc – Hor) group with an age of 45 Myr. DS Tuc is a visual binary consisting of a G6V primary and a K3V secondary. The G6V-type component may be considered as the prototype of a young Sun, while the planetary system itself may be considered as the prototype of a young Solar system. We analyzed the activity of the hot G6V component. The data processing is analogous to that performed by us previously when analyzing the data from the Kepler Space Telescope archive and the archive of TESS observations. According to our estimate, the stellar rotation period is $P = 2.85 \pm 0.18$ days, which coincides with its published estimates. If the appearance of the second peak corresponding to a period of 3.4 days in the power spectrum is interpreted as evidence for the presence of differential stellar rotation, then the differential rotation parameter of DS Tuc is $\Delta\Omega = 0.357 \pm 0.010$ rad/day. We performed a further analysis of the star's photometric variability with a mean photometric period of 2.85 days. The light curve was analyzed in detail by the method of solving the inverse problem of reconstructing the maps of surface temperature inhomogeneities. We showed that, as a rule, there are concentrations of spots at two longitudes on the surface maps. The spot positions and sizes undergo changes and are sometimes unstable. The fraction of the spotted stellar surface S is about 3.3 %. We studied the object's position on the S — age, S — rotation period, and S — Rossby number diagrams and concluded that it corresponds to the general pattern of the dependences established by us previously for young stars with planetary systems. For the first time we have estimated the possible activity cycle of DS Tuc, 1610 days (4.4 years), based on All Sky Automated Survey observations (astrouw.edu.pl/asas).

AB PIC:

On the base of high-precision data from the archive of the TESS mission the photometric variability of K1 dwarf K1 AB Pic (HD 44627), a member of the Tuc – Hor Association and the host of the distant giant planet with a mass of 13.5 Jupiter masses, was studied. During the observation interval with the TESS mission 48 superflares with energy $6.1 \cdot 10^{32}$–$3.4 \cdot 10^{35}$ erg were registered. Estimates of the period of rotation of the star $P = 3.860 \pm 0.020$ days and of the amplitude of the brightness variability were made. The area of spots on the surface of AB Pic significantly exceeds that ones on the Sun, spottedness A varies between 54,000 and 95,000 MSH. It is suggested that during the observation interval the area of spots on the surface of the star had cyclical changes lasting 233 days which can be regarded as the analog of the Rieger cycle on the Sun. Estimates of longer AB Pic activity cycles were based on data from the All Sky Automated Survey observation archive and indicated possible activity cycles of 258 days, 1120 days (3.1 year) and 2640 days (7.2 year).

NON-THERMAL ATMOSPHERIC LOSS FOR EXOPLANET GJ 436B: H_2 PHOTODISSOCIATION INPUT

V. I. Shematovich[1], A. A. Avtaeva[1]
[1] *Institute of Astronomy of the Russian Academy of Sciences, Moscow, Russia* (*shematov@inasan.ru*)
[2] *Sternberg Astronomical Institute, Moscow State University, Moscow, Russia*

KEYWORDS:
hot exoplanets, sporadic stellar activity, atmospheric mass loss, aeronomic kinetic model

INTRODUCTION:
Exoplanets with substantial hydrogen/helium atmospheres have been discovered in abundance, many residing extremely close to their host stars. Their atmospheres are forced by the extreme irradiation levels resulting in the formation of the extended planetary envelopes due to the thermal and non-thermal atmospheric escape. Ongoing atmospheric escape has been observed to be occurring in a few nearby exoplanet systems through transit spectroscopy both for hot jupiters and for lower-mass super-earths and mini-neptunes [1, 2].

It is currently known from observations and theoretical studies that molecular hydrogen does not completely dissociate in the upper atmosphere of Gliese 436b and is carried far away from the planet [3]. Numerical modeling by gas-dynamic models had shown that the Gliese 436b exoplanet should be surrounded by an extended, relatively cold, dense partially ionized gas envelope with the presence of molecular hydrogen, covering the entire disk of the star [3, 4].

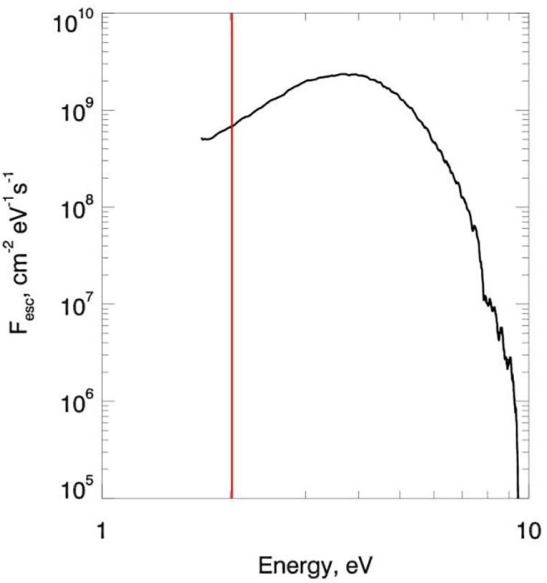

Fig. 1. The energy spectrum of the atomic hydrogen flux escaping from the upper atmosphere of GJ 436b due to photodissociation processes. The vertical red line shows the escape energy of hydrogen atoms at the upper boundary of the model atmosphere at distance of ~2 planetary radii

The results of calculations of the effect of the extreme ultraviolet (UV) stellar radiation on the production of the suprathermal fraction of atomic hydrogen in the $H_2 \rightarrow H$ transition region in the upper atmosphere of warm neptune

GJ 436b are given in this report. The formation of the escaping flux of H atoms created by this effect was also studied and the production rate and energy spectrum of the hydrogen atoms with excess kinetic energy during the dissociation of H_2 was calculated. Using the numerical stochastic model for a hot planetary corona [5], we had investigated the kinetics and transfer of suprathermal hydrogen atoms in the upper atmosphere and the flux of atoms escaping from the atmosphere was calculated (Figure 1). The latter is estimated as $6.7 \cdot 10^6$ $cm^{-2} \cdot s^{21}$ for a moderate stellar activity level of UV radiation, which leads to an atmospheric evaporation rate of $8.1 \cdot 10^6$ $g \cdot s^{-1}$ due to the process of H_2 photodissociation. This estimate is close to the lower boundary of observational estimates in the range ($3.7 \cdot 10^6$–$1.1 \cdot 10^9$) $g \cdot s^{21}$ for the rate of atmospheric loss for GJ 436b [4].

Additional non-thermal escape processes such as the photoelectron impact and the precipitation of high-energy charged and neutral particles from stellar wind into the extended atmosphere of exoplanet GJ 436b are also discussed.

This study was carried out in the framework of the project “Study of stars with exoplanets” under a grant from the Government of the Russian Federation for scientific research conducted under the guidance of leading scientists (agreement No. 075-15-2019-1875).

REFERENCES:

[1] Shematovich V. I., Marov M. Ya. Escape of planetary atmospheres: physical processes and numerical models // Physics Uspekhi. 2018. V. 61. P. 217.
[2] Owen J. E. Atmospheric Escape and the Evolution of Close-In Exoplanets // Ann. Rev. Earth and Planetary Sciences. 2019. V. 47. P. 67–90.
[3] Kulow J. R., France K., Linsky J., Loyd R. O. P. Ly-α Transit Spectroscopy and the Neutral Hydrogen Tail of the Hot Neptune GJ 436b // Astrophysical J. 2014. V. 786. P. 132.
[4] Berezutsky A. G., Shaikhislamov I. F., Miroshnichenko I. B., Rumenskikh M. S., Khodachenko M. L. Interaction of the Expanding Atmosphere with the Stellar Wind around Gliese 436b // Solar System Research. 2019. V. 53. P. 138.
[5] Shematovich V. I. Suprathermal hydrogen produced by the dissociation of molecular hydrogen in the extended atmosphere of exoplanet HD 209458b // Solar System Research. 2010. V. 44. P. 96–103.

3D MODELING OF TRANSIT ABSORPTION OF GJ3470B IN HYDROGEN AND HELIUM LINES

I. F. Shaikhislamov[1], M. L. Khodachenko[2], A. G. Berezutsky[1], I. B. Miroshnichenko[1], M. S. Rumenskikh[1]
[1] *Institute of Laser Physics SB RAS, Novosibirsk, Russia* (*ildars@ngs.ru*)
[2] *Space Research Institute, Austrian Academy of Sciences, Graz, Austria*

KEYWORDS:
exoplanets, planetary wind, transit absorption

INTRODUCTION:
Salz et al. (2016) performed aeronomy hydrodynamic simulations of the escaping atmospheres of 18 hot gas planets in the solar neighborhood with the aim to find ideal observational targets. This study revealed that the warm Neptune GJ 3470b should have one of the largest mass loss rates due to its low mass, close orbit and relatively high activity of the host star. The Ly-α observation of GJ 3470b reported in Bourrier et al. (2018) revealed large absorption depths of ~35 % in the blue wing [–94; –41] km/s of the line. Different to similar warm Neptune GJ 436b, significant absorption depth of ~23 % was detected also in the red wing [23; 76] km/s, as well as a relatively short transit duration of ~2 hours without any distinct early ingress and extended egress phases.

Thus, GJ 3470b appears to be the second hot exoplanet with a large hydrogen envelope extending far beyond the Roche lobe. Moreover, besides of the hydrogen related Ly-α, also the absorption in line 10830 Å of metastable helium has been detected for this planet. Ninan et al. (2019) reported about 1 % absorption at averaged over the line width of 1.2 Å taking place mostly at the blue wing [–36; 9] km/s of the line. The simulation, based on 1D profiles of helium atoms and ions performed in Salz et al. (2016) assuming standard abundance He/H = 0.1, yielded the column density of He(2^3S) atoms one order of magnitude larger than that inferred from the observations. Very recently new three transits at the 10830 Å line have been reported by Palle et al. (2020). The spectro-photometric light curve has been obtained, which shows that absorption by He(2^3S) atoms coincides with the expected ingress and egress times. The spectrally resolved absorption at transit shows the depth of 1.5 % around the line center restricted by the interval [–30; 20] km/s, while the half width interval is [–22; 10] km/s.

In the present paper we use a 3D global hydrodynamic multifluid code which allows fully self-consistent calculation of the formation of escaping planetary wind (PW) of hot exoplanets and its interaction with the stellar wind (SW). Previously we employed this code to interpret the Ly-α absorption at GJ 436b Khodachenko et al. (2019) and the absorption in HI, OI, CII, SiIII resonant lines at hot Jupiter HD209458b Shaikhislamov et al. (2020). For the GJ 3470b, we calculate the absorption in both, Ly-α and He 10830 Å lines. A number of simulations runs with different modelling parameter sets has been performed, assuming slow and fast SW conditions and using the estimated XUV and Ly-α fluxes of the star.

RESULTS
The obtained results show that planetary material of upper atmosphere of GJ3470b extends very far from the planet (Figure 1). Similar to our previously studied case of GJ436b (Khodachenko et al. 2019), the Ly-α transit for GJ3470b is produced by ENAs formed in course of the interaction between the escaping PW and surrounding SW. As in the case of our previously reported studies of HD20458b and GJ436b, the role of the radiation pressure in the acceleration of ENAs in the case of GJ3470b has been found to be insignificant.

The applied model is able to reproduce, within the measurements error margins (bar), the 10 % Ly-α absorption at the red-shifted velocities of about 80 km/s, as well as 20 % absorption, averaged over the whole red wing of the line (Figure 2). The red-shifted Ly-α absorption is produced in the shocked

region by ENAs, which have sufficiently high velocity dispersion to provide absorption in the blue and red parts of the line. Simulation runs with different modelling parameter sets revealed that the observed fast decay of the Ly-α absorption in the egress part of the transit light-curve can be the result of sufficiently high ram pressure of fast SW, which rapidly blows away from the orbital line the trailing tail of escaping planetary atmospheric material (Figure 3). The best fit parameters of the SW correspond in the temperature and velocity to the fast Solar wind and imply for the parent star of GJ3470b the total mass loss rate of 0.1 of the Solar value, which is compatible with the smaller than the Sun size of the star.

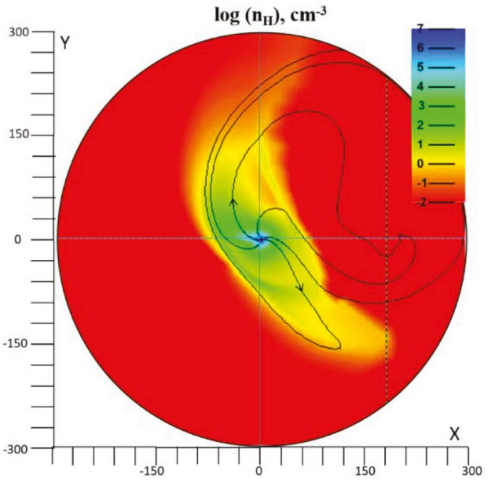

Fig. 1. Distribution of atomic hydrogen density. The distance is scaled in units of planet radius. The planet is located at the center of the coordinate system and moves anti-clockwise; the star is to the right, at X = 190. Black lines show the streamlines

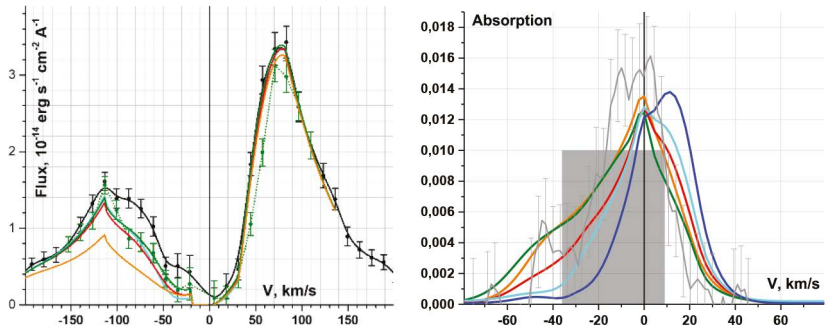

Fig. 2. The absorption profiles of Ly-α line in Doppler shifted velocity units simulated with following parameters: F_{XUV} = 4 erg·cm^{-2}·s^{-1}, n_{sw} = 1.8·10^3 cm/s (blue line); F_{XUV} = 6, n_{sw} = 3.5·10^3 (cyan); F_{XUV} = 6, n_{sw} = 7·10^3 (orang); F_{XUV} = 8, n_{sw} = 7·10^3 (red); F_{XUV} = 10, n_{sw} = 1.4·10^4 (olive) (*left panel*). Other parameters were He/H = 0.013; V_{sw} = 520 km/s; T_{sw} = 0.65 MK; black and green dots with error-bars show the out-of-transit and mid-transit measurements, respectively, reproduced from Bourrier et al. (2018). The absorption profiles of He 10830 Å line, calculated at the same parameter sets. The shaded area represents the measurements by Ninan et al. (2019). The grey line with error bars represents the measurement by Palle et al. (2020) (*right panel*).

Similarly to 1D modeling of Ninan et al. (2019) and Palle et al. (2020), we found that He(2^{3}S) atoms produced by GJ3470b outflow extend to the distances of at least 10 planet radii. To fit the He(2^{3}S) absorption at the same parameters, as those derived to fit the Ly-α absorption, the helium abundance in the upper atmosphere of GJ3470b should be He/H ≈ 0.015, i.e. about an order of magnitude lower than the Solar value. At the same time, a good agreement of the simulated absorption profile with the measurements was found.

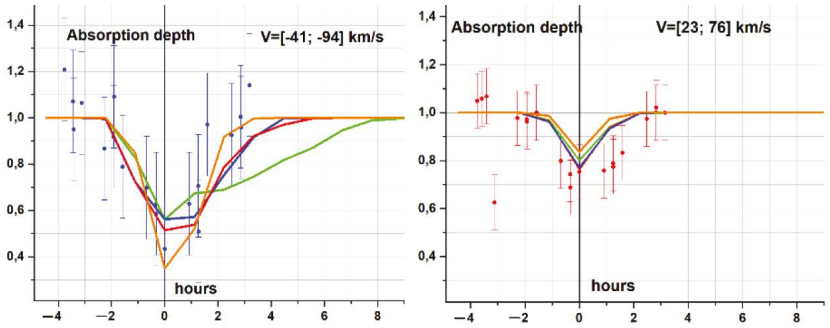

Fig. 3. The simulated and measured transit light-curves of GJ3470b in the Ly-α line averaged over the blue wing [–94; –41] km/s (*left panel*) and over the red wing [23; 76] km/s (*right panel*). Dots with error-bars show the measured values reproduced from Bourrier et al. (2018). The simulated transits are shown in different colors, coded similar to Figure 2

The comparative study of various pumping and depopulation processes of He(2^3S) state has shown that the interpretation of the measured absorption in 10830 Å line can be quite intricate, because in different regions of the escaping planetary material, as well as in the shocked region, different processes are responsible for the production of absorbing agent. Altogether, the performed 3D self-consistent multi-fluid simulations of the expanding and escaping upper atmosphere of GJ3470b and the related spectral absorption features and transit light-curves have shown that the available observational data can be relatively well interpreted within the range of reasonable values of physically justifiable parameters related with the planetary atmospheric composition, stellar XUV flux and SW plasma flow.

ACKNOWLEDGEMENTS:
This work was supported by the Russian Science Foundation RSF (project No. 18-12-00080) and in part by RFBR (project No. 20-02-00520). Parallel computing has been performed at Computation Center of Novosibirsk State University and Siberian Supercomputer Center of SB RAS.

REFERENCES:
[1] Bourrier V. et al. (2018). A&A, 620, A147.
[2] Khodachenko M. L. et al. (2019). ApJ, 885(1), 67.
[3] Ninan J. P. et al. (2019). preprint arXiv:1910.02070.
[4] Palle E. et al. (2020). A&A, 638, A61.
[5] Salz M. et al. (2016). A&A, 586, A75.
[6] Shaikhislamov I. F. et al. (2020). MNRAS, 491(3), 3435.

STUDY OF TRANSIT TIMING VARIATION IN FIVE HOT JUPITER PLANETS

F. Davoudi[1], O. Basturk[2], H. Safari[1], E. Murat Esmer[2], S. Yalçınkaya[2]
[1] *Department of Physics, P. O. Box 45371-38791, University of Zanjan, Zanjan, Iran (fa.davoudi@gmail.com)*
[2] *Ankara University, Faculty of Science, Astronomy and Space Sciences Department, TR-06100, Tandogan, Ankara, Turkey*

KEYWORDS:
new ephemeris, hot jupiter, transiting exoplanets, TTV

INTRODUCTION:
Ground-based telescopes and space missions such as the Transiting Exoplanet Survey Satellite (TESS) provided good potential for finding transiting exoplanets. 4171 exoplanets have been confirmed so far which the most are transiting exoplanets.

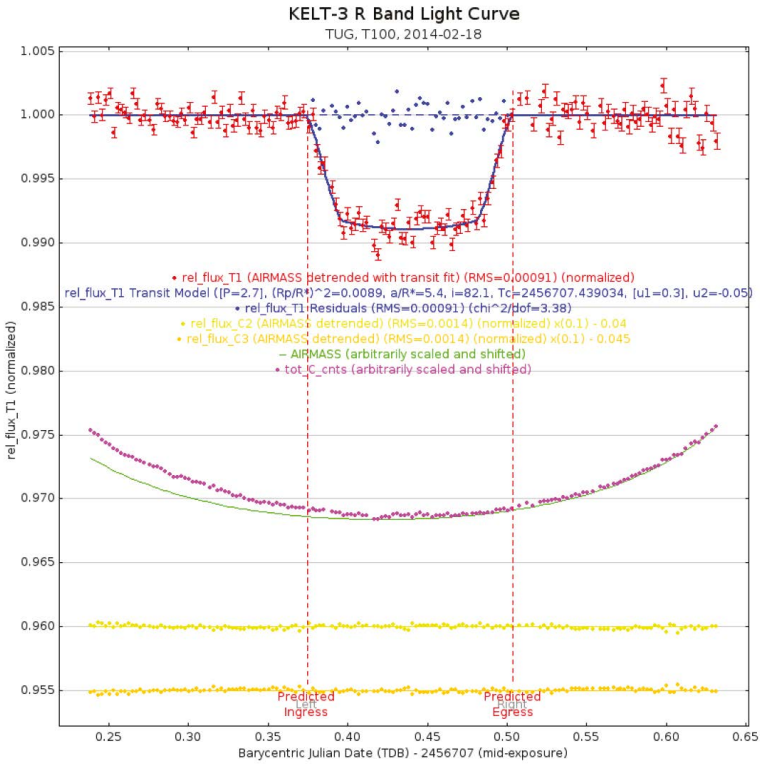

Fig. 1. A ground-based light curve of KELT-3b

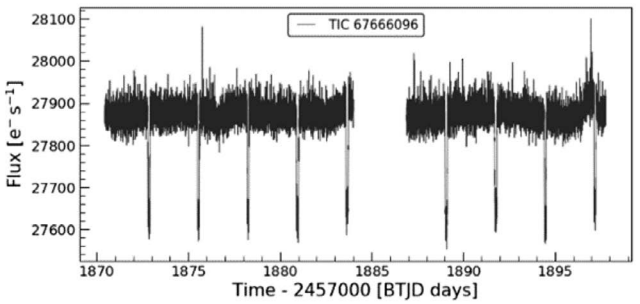

Fig. 2. TESS light curve of KELT-3b

The transit occurs when the outer planet is nearly aligned with the barycentre of the inner binary and its motion during the transit is essentially transverse to the line of sight. There are several physical effects, cause transit timing variations (TTV). Such as the "Romer Delay" due to the change in light travel time caused by the reflex motion of the inner binary creates TTV, this effect is present in the absence of deviations from a keplerian orbit because of the inner binary orbits about the center of mass [2]. The best way to detect the effect may be to observe many transits and calculate the standard deviation of the observed transit timing deviations over many orbits. We will present TTVs and refine update the ephemeris of 5 transiting exoplanets: KELT-3b, XO-2b, WASP-43b, TrES-1b, HAT-P-10b/WASP-11b.

We collect all previous observations from the literature and all the space and the ground-based transit light curves of systems, observed during TESS 2-minute cadence. Also, we use observational facilities in Turkey, such as 1 m Turkish telescope T100, located in the Bakırlıtepe campus of TÜBİTAK National Observatory of Turkey (TUG) and 35 cm telescope T35 in Ankara University Kreiken Observatory (AUKR). Also, we use the light curves of amateur astronomers presented in the Exoplanet Transit Database (ETD, URL: http://var2.astro.cz/ETD/) [2]. For example, In the following figures, light curves of KELT-3b observed by T100 telescope and TESS space data for this system (TIC ID: 67666096) were displayed.

First, we convert time references of data in BJD_TDB and measure mid-transit times from all space and ground-based light curves and correct the linear ephemeris information. We refine the ephemeris information (reference epoch T0, and orbital period P) and we prepare TTV diagrams based on Monte Carlo Markov Chain (MCMC) approach.

REFERENCES:

[1] Bartolini C., Zoffoli M. Light-time effect in IM Aurigae // Astronomy and Astrophysics. 1986. V. 168. P. 377–379.
[2] Poddaný S., Brát L., Pejcha O. Exoplanet Transit Database. Reduction and processing of the photometric data of exoplanet transits // New Astronomy. 2010. V. 15. Iss. 3. P. 297–301.

THERMAL ATMOSPHERIC LOSS FOR CLOSE-IN EXOPLANETS

E. S. Kalinicheva, V. I. Shematovich
Institute of Astronomy of the Russian Academy of Sciences, *Moscow*, *Russia*
(*kalinicheva@inasan.ru*)

KEYWORDS:
hot jupiters and neptunes, sporadic stellar activity, atmospheric mass loss, aeronomic kinetic model

INTRODUCTION:
Theoretical studies of thermal atmospheric loss for close-in exoplanets (see, e.g., [1]) are showing that lower-density planets like sub-neptunes or super-earths with a large volatile envelope may be most significantly affected by evaporation, leading in the more extreme cases to a massive erosion of the atmosphere and the formation of rocky remnant cores.

The hot neptune GJ436b was recently found to have an escaping atmosphere producing an extended transit that absorbs more than 50% of its host star's Ly-α emission [2]. Numerical modeling by gas-dynamic models had shown that hot neptune Gliese 436b should be surrounded by an extended, relatively cold, dense gas envelope with the presence of molecular hydrogen, covering the entire disk of the star [2, 3].

The developed self-consistent 1D model of hydrogen-helium atmosphere with suprathermal electrons taken into account [4] was used to calculate the thermal atmospheric loss rate for a close-in neptune. The two-scale structure of the close-in (hot) neptune atmosphere was found. The lower part of the atmosphere is more massive and its density is decreasing exponentially with height, while the density of the upper part of the atmosphere, the corona, varies with height according to a power law. Such two-scale density profile is caused by the local extreme heating resulting in the formation of the planetary wind [3]. Therefore, number density of atmospheric gas in the corona is varying with height according power law.

Additional non-thermal escape processes such as the precipitation of high-energy charged and neutral particles from stellar wind into the extended atmosphere of close-in exoplanets are also discussed.

ACKNOWLEDGEMENTS:
This study was carried out in the framework of the project "Study of stars with exoplanets" under a grant from the Government of the Russian Federation for scientific research conducted under the guidance of leading scientists (agreement No. 075-15-2019-1875).

REFERENCES:
[1] Owen J. E. Atmospheric Escape and the Evolution of Close-In Exoplanets // Annu. Rev. Earth Planetary Sciences. 2019. V. 47. P. 67–90.
[2] Kulow J. R., France K., Linsky J., Loyd R. O. P. Ly-α Transit Spectroscopy and the Neutral Hydrogen Tail of the Hot Neptune GJ 436b // Astrophysical J. 2014. V. 786. P. 132.
[3] Berezutsky A. G., Shaikhislamov I. F., Miroshnichenko I. B., Rumenskikh M. S., Khodachenko M. L. Interaction of the Expanding Atmosphere with the Stellar Wind around Gliese 436b // Solar System Research. 2019. V. 53. P. 138.
[4] Ionov D. E., Shematovich V. I., Pavlyuchenkov Ya. N. Influence of Photoelectrons on the Structure and Dynamics of the Upper Atmosphere of a Hot Jupiter // Astronomy Reports. 2017. V. 61. Art. 387.

THE ORBITAL EVOLUTION OF EXTRASOLAR THREE-PLANETARY SYSTEM GJ 3138

A. S. Perminov, E. D. Kuznetsov
Ural Federal University, *620000*, *51 Lenin Avenue*, *Ekaterinburg*, *Russia*
(*perminov12@yandex.ru; eduard.kuznetsov@urfu.ru*)

KEYWORDS:
semi-analytical motion theory, dynamical evolution, stability, extrasolar planetary system, GJ 3138

INTRODUCTION:
Several dozens of extrasolar systems with three and four planets have been discovered to the present time and require study. The semi-analytical motion theory of the second order in planetary masses is constructed for the investigation of the orbital evolution of non-resonant extrasolar planetary systems with moderate orbital eccentricities and inclinations. The osculating Hamiltonian of the four-planetary problem is written in the Jacobi coordinate system and expanded into the Poisson series in the small parameter and all orbital elements of the second Poincare system [1]. This canonical system has only one angular element — mean longitude, that allows to sufficiently simplify an angular part of the expansion. The ratio of the sum of planetary masses to the mass of the star plays the role of the small parameter. The averaged Hamiltonian and the equations of motion in averaged orbital elements are constructed by Hori-Deprit method [2], the essence of which is to exclude from osculating Hamiltonian all short-periodic perturbations, defined by fast variables (mean longitudes). It allows us to sufficiently increase the integration step of the equations of motion. An application of the four-planetary motion theory to modelling of the orbital evolution of the Solar system's giant planets is considered in [3].

The equations of motion constructed up to the second order in the small parameter and the fifth degree in eccentric and oblique Poincare orbital elements are used for the modelling of the orbital evolution of extrasolar planetary system GJ 3138. The semi-major axes and eccentricities of planetary orbits in this system are known with errors. The orbital inclinations, the arguments of the pericenters and the longitudes of the ascending nodes are not determined due to the specificity of the observation methods. All unknown and known with errors orbital elements vary within allowable limits to determine the set of initial conditions for the numerical integration of the equations of motion. The limits of the change of the orbital elements are determined depending on the initial conditions of the integration. The assumption about the stability of observed planetary systems allows us to exclude the initial conditions leading to the extreme growth of the orbital eccentricities and inclinations, that to identify those under which these elements are conserved small. It is possible to narrow the possible range of unknown orbital elements and determine their most probable values in terms of stability.

VARIATION OF ORBITAL ELEMENTS:
Star GJ 3138 is a red dwarf of spectral type M0V with mass of 0.681 Solar masses. Three sub-Neptune planets orbiting around GJ 3138 was discovered from variations of the radial velocity of the star with the HARPS spectrograph in 2017 [4]. Since all planets were discovered via Doppler spectroscopy, only lower limits $M \sin I_p$ of their masses are known (here I_p is an unknown inclination of the orbital plane to the plane of the sky). Observed semi-major axes a, eccentricities e, orbital periods P and masses of planets are given in Table 1 according to [4].

To define the reference frame in which the planetary motion be considered, the orbital plane of the innermost planet is chosen as the reference plane. Thus, without loss of generality, the orbital inclinations and the longitude of the ascending node of the innermost planet is equal to 0 at the initial moment. The orbital inclinations of both outer planets are equal and vary from 0° with a step of 5°. Different spatial configurations of the planetary or-

bits are achieved by varying both the longitudes of the ascending nodes and the arguments of the pericenters with a step of 45°. All orbital eccentricities are specified to be equal minimum, mean, and maximum values. The masses of planets are altered according to their initial orbital inclinations. The semi-major axes are not varied.

Table 1. Known orbital elements and planetary masses

Planet	$M \sin I_p$ [$M_{Jupiter}$]	a [AU]	e	P [days]
GJ 3138c	$0.056^{+0.0011}_{-0.0010}$	0.00197±0.0005	$0.19^{+0.18}_{-0.13}$	1.22003^{+6e-5}_{-4e-5}
GJ 3138b	0:0132±0.0019	0.057±0.001	$0.11^{+0.11}_{-0.07}$	5.974±0.001
GJ 3138d	$0.033^{+0.0071}_{-0.0066}$	$0.698^{+0.018}_{-0.019}$	$0.32^{+0.20}_{-0.21}$	$257.8^{+3.6}_{-3.5}$

The estimates of the theoretical radii of the convergence R_e, R_I for the series representing the equations of motion in the orbital eccentricities and inclinations are calculated according to [5] and given in Table 2. If the values of the orbital eccentricities and inclinations are less than corresponding radii R_e, R_I, it is guaranteed the convergence of the series of the equations of motion and the suitability of the motion theory.

Table 2. Theoretical radii of the convergence

Planet	GJ 3138c	GJ 3138b	GJ 3138d
R_e	0.66	0.38	0.66
R_I, °	80	44	80

NUMERICAL INTEGRATION AND RESULTS:

The equations of motion in averaged elements are numerically integrated by the Everhart method of 7th order. The modelling interval is 1 Myr, that corresponds to $300 \cdot 10^6$ revolutions of planet GJ 3138 c around the host star, $60 \cdot 10^6$ and $1.4 \cdot 10^6$ revolutions for planets *b* and *d* respectively.

Table 3. Maximum values of the averaged eccentricities and inclinations

	e_0	0.06		0.19		0.37	
GJ 3138c	I_0, °	e_{max}	I_{max}, °	e_{max}	I_{max}, °	e_{max}	I_{max}, °
	0	0.06–0.09	0	0.19–0.28	0	0.37–0.56	0
	5	0.06–0.09	16	0.19–0.28	16	0.37–0.56	18
	10	0.06–0.10	32	0.19–0.29	32	0.37–0.57	37
	15	0.06–0.10	48	0.19–0.30	50	0.37–0.58	54
	e_0	0.04		0.11		0.22	
GJ 3138b	I_0, °	e_{max}	I_{max}, °	e_{max}	I_{max}, °	e_{max}	I_{max}, °
	0	0.04–0.05	0	0.11–0.14	0	0.22–0.29	0
	5	0.04–0.05	13	0.11–0.14	13	0.22–0.29	13
	10	0.04–0.05	26	0.11–0.15	26	0.22–0.29	26
	15	0.04–0.05	39	0.11–0.15	39	0.22–0.29	39
	e_0	0.11		0.32		0.52	
GJ 3138d	I_0, °	e_{max}	I_{max}, °	e_{max}	I_{max}, °	e_{max}	I_{max}, °
	0	0.1102	0	0.3203	0	0.5205	0
	5	0.1102	5	0.3203	5	0.5205	5
	10	0.1102	10	0.3203	10	0.5205	10
	15	0.1102	16	0.3204	16	0.5205	16

Table 3 present the maximum values of averaged orbital eccentricities e_m and inclinations I_m achieved by each planet on the modelling interval. De-

pending on the initial values of the orbital eccentricities e_0 and inclinations I_0, each tabular cell contains the highest values e_m and I_m determined for all initial combinations of the arguments of the pericenters and the longitudes of the ascending nodes. Note that the observational uncertainties of masses of planets b and d in the system is about 15 % according to Table 1. It means that the values of e_m and I_i obtained for minimal possible value of planetary mass M (in the case of $I_p = 90°$) are reliable for larger mass of a planet with a smaller value of I_p (not less than 60°).

There is the set of initial combinations of the longitude of the ascending node and the argument of the percenter providing the stability of dynamical evolution of the system. At the same time, for $I_0 > 20°$ there are initial conditions that lead to extreme growth of the orbital eccentricities and possibly to flips of the orbits (transitions between prograde and retrograde motion). Note, that flips and extremely values of the eccentricities (close to 1) can be manifested as an artefact of the analytical theory, since, such inclinations and eccentricities exceed the radii of the convergence. In this case the real orbital evolution, including the real presence of flips, can be studied only by using numerical methods.

The method shown in this article allows us to determine the most probable values of unknown orbital nodes and pericenters and narrow the range of possible values of the orbital eccentricities and inclinations.

ACKNOWLEDGMENTS:
The study was supported by the Ministry of Science and Education (the project “Theoretical and experimental studies of the formation and evolution of extrasolar planetary systems and characteristics of exoplanets”, application No. 2020-1902-01-133).

REFERENCES:

[1] Perminov A. S., Kuznetsov E. D. Expansion of the Hamiltonian of the planetary problem into the Poisson series in elements of the second Poincare system // Solar System Research. 2015. V. 49. No. 6. P. 430–441.
[2] Perminov A. S., Kuznetsov E. D. The Hori-Deprit method for averaged motion equations of the planetary problem in elements of the second Poincare system // Solar System Research. 2016. V. 50. No. 6. P. 426–436.
[3] Perminov A. S., Kuznetsov E. D. Orbital evolution of the Sun – Jupiter – Saturn – Uranus – Neptune four-planet system on long-time scales // Solar System Research. 2018. V. 52. No. 3. P. 241–259.
[4] Astudillo-Defru N., Forveille T., Bonfils X. et al. The HARPS search for southern extra-solar planets. XLI. A dozen planets around the M dwarfs GJ 3138, GJ 3323, GJ 273, GJ 628, and GJ 3293 // Astronomy and Astrophysics. 2017. V. 602. Art. id. A88.
[5] Kholshevnikov K. V. The Hamiltonian in the planetary or satellite problem as a d’Alembertian function // Astronomy Reports. 2001. V. 45. No. 7. P. 577–579.

PROBABILITIES OF COLLISIONS OF EXOPLANETESIMALS WITH EXOPLANETS IN THE PROXIMA CENTAURI PLANETARY SYSTEM

S. I. Ipatov
Vernadsky Institute of Geochemistry and Analytical Chemistry of RAS, *Moscow*, *Russia* (*siipatov@hotmail.com*)

KEYWORDS:
Proxima Centauri planetary system, exoplanets, exoplanetesimals, probabilities of collisions

Initial data for calculations: Migration of exocomets in the Proxima Centauri system was studied in [1]. The exoplanet "*b*" with a semi-major axis $a_b = 0.0485$ AU located in a habitable zone, and the exoplanet "*c*" with a semi-major axis a_c from 0.06 to up to 0.3 AU (for test calculations up tyo 0.7 AU) were considered in [1]. Now it is considered [2, 3] that $a_c = 1.489 \pm 0.049$ AU. I made two series of calculations of migration of planetesimals from the vicinity of the orbit of the exoplanet "c". In both series I considered a star with a mass equal to 0.122 of the solar mass. **In the first series** of calculations, as in [2], the following initial semi-major axes and masses of two exoplanets were considered: $a_b = 0.0485$ AU, $a_c = 1.489$ AU, $m_b = 1.27 m_E$ and $m_c = 12 m_E$, where m_E is the mass of the Earth. For the exoplanet "*b*", the initial eccentricity e_b and initial inclination i_b were considered to be equal to 0, and the initial eccentricity e_c of the exoplanet "*c*" equaled to 0 or 0.1. Initial inclination of the exoplanet "c" was considered to be $i_c = e_c/2 = 0.05$ rad or $i_c = e_c = 0$. For interest, I also considered $i_c = 152°$; such calculations characterize the case when orbits of planetesimals were inclined to the orbit of the exoplanet. **In the second series** of calculations, as in [3], I considered $a_b = 0.04857$ AU, $e_b = 0.11$, $m_b = 1.17 m_E$, $a_c = 1.489$ AU, $e_c = 0.04$, $m_c = 7 m_E$. I supposed that $i_b = i_c = 0$. **In both series of calculations**, the density of the exoplanets "*b*" and "*c*" were considered to be equal to densities of the Earth and Uranus, respectively. In each calculation variant, initial semi-major axes of planetesimals were in the range from a_{min} to $a_{min} + 0.1$ AU, with a_{min} from 1.2 to 1.7 AU with a step of 0.1 AU. Initial eccentricities e_o of planetesimals equaled to 0 or 0.15 for the first series of calculations, and $e_o = 0.02$ or $e_o = 0.15$ for the second series. Greater initial eccentricities could be a result of the mutual gravitational influence of planetesimals. Initial inclinations of the planetesimals equaled to $e_o/2$ rad. 250 planetesimals were considered in each calculation variant. The motion of planetesimals under the gravitational influence of exoplanets was calculated with the use of the symplectic code from [4]. Based on the obtained arrays of orbital elements of migrated planetesimals stored with a step of 100 yr, I calculated the probabilities of collisions of planetesimals with the exoplanets. For masses, orbits, and radii of the star and the exoplanets, the calculations were made similar to those in [5–7], which had been made for the planets of the solar system.

RESULTS OF CALCULATIONS:
For the second series of calculations, the probability p_b of a collision of one planetesimal, initially located near the orbit of the exoplanet "*c*", with the exoplanet "*b*" was non-zero in 5 among 18 variants at $e_o = 0.02$ and in 3 among 6 variants at $e_o = 0.15$. In one of 24 variants $p_b = 0.008$, in three $p_b = 0.004$, and in other four variants p_b it was between to $4 \cdot 10^{-6}$ and $3 \cdot 10^{-4}$. For all three variants of **the first series** presented in Table 1 at $e_c = 0.1$ and $e_o = 0.15$, the values of p_b were in the range 0.008–0.019. For other calculations of the first series, $p_b = 0$. **For the second series**, only one of several hundreds of planetesimals reached the orbit of the exoplanet "*b*", but the probability p_b of a collision of one planetesimal with this exoplanet (averaged over thousands planetesimals) is greater than the probability of a collision with the Earth of a planetesimal from the zone of the giant planets in the solar

system. The latter probability for most calculations with 250 planetesimals was less than 10^{-5} per one planetesimal [8]. The probability p_d of a collision of a planetesimal from the zone of the orbit of the exoplanet "*c*" with the exoplanet "*d*" (a_d = 0.02895 AU, $m_d = 0.29m_E$, $e_d = i_d = 0$) was nonzero only for seven variants (among 24). The mean values of p_b and pd averaged over 6000 planetesimals equaled to $8.5 \cdot 10^{-4}$ and $7.0 \cdot 10^{-4}$. Therefore, a lot of icy material could be delivered to the exoplanets "*b*" and "*d*".

Table 1. Probability p_c of a collision of a planetesimal with the exoplanet with a_c = 1.489 AU, $e = e_c$, $i_c = e_c/2$, $m_c = 12m_E$ during time interval T (in Myr). Initial semi-major axes of planetesimals in AU were between a_{min} and a_{min} + 0.1, and their initial eccentricities equaled to e_o. N_{el} is the number of planetesimals left in elliptical orbits, N_{ej} is the number of planetesimals ejected into hyperbolic orbits, N_{st} is the number of planetesimals collided with the star

		T	**1**	**1**	**10**	**10**	**50**	**50**	**50**	**50**
a_{min}	e_c	e_o	N_{el}	p_c	N_{el}	p_c	N_{st}	N_{ej}	N_{el}	p_c
1.5	0	0.15	146	0.084	3	0.100	0	249	1	0.107
	0.1		74	0.010	4	0.011	1	248	1	0.021
	0.1		80	0.020	6	0.024	5	242	3	0.033
1.6	0.1		76	0.040	3	0.043	4	243	3	0.043

For the first series of calculations at $i_c = e_c = 0$ and e_o = 0.15, the values of the probability p_c of a collision of one planetesimal, initially located near the second exoplanet, with this exoplanet were about 0.06–0.1. For $i_c = e_c/2 = 0.05$ and e_o = 0.15, p_c was about 0.02–0.04. **For the second series** of calculations, p_c was about 0.1–0.3, exclusive for a_{min} = 1.4 AU and e_o = 0.02 when p_c was about 0.7–0.8 (and the main growth was before T = 1 Myr). Usually there was a small growth of p_c after 20 Myr. **For both series** of calculations, most of planetesimals were ejected into hyperbolic orbits in 10 Myr. The ratio of planetesimals ejected into hyperbolic orbits usually exceeded the number of planetesimals collided with the exoplanets if the number of planetesimals decreased by a factor of several. For variants in Table 2, this ratio was much less than 1 only at a_{min} = 1.4 AU and e_o = 0.02. Note that the real number of ejected planetesimals can be smaller than N_{ej} in the tables because it is need to take into account that some planetesimals ejected in our runs already collided with exoplanets. In some calculations a few planetesimals could still move in elliptical orbits after 100 Myr.

Table 2. Probability p_c of a collision of a planetesimal with the exoplanet "c" with a_c = 1.489 AU, e_c = 0.04, i_c = 0, and $m_c = 7m_E$ during time interval T (in Myr). Initial semi-major axes of planetesimals in AU were between a_{min} and a_{min} + 0.1, and their initial eccentricities equaled to e_o. Designations N_{el}, N_{ej} and N_{st} are the same as for Table 1

e_o = 0.02

T	**0.1**	**1**	**1**	**10**	**10**	**20**	**20**	**20**	**20**
a_{min}	p_c	N_{el}	p_c	N_{el}	p_c	N_{st}	N_{ej}	N_{el}	p_c
1.2	0.0010	248	0.013	129	0.095	0	158	92	0.098
	0.0013	247	0.069	90	0.152		178	72	0.152
	0.0004	247	0.028	79	0.121		183	67	0.138
1.3	0.0172	236	0.068	15	0.169	0	247	3	0.170
	0.0121	236	0.048	26	0.092		243	7	0.092
	0.0156	240	0.041	15	0.086	1	245	4	0.086
1.4	0.1700	243	0.706	81	0.776		181	68	0.776
	0.1694	238	0.711	70	0.783	0	191	59	0.783
	0.1633	237	0.663	81	0.738		189	61	0.741
1.5	0.0120	239	0.053	48	0.143	0	210	40	0.212
	0.0232	239	0.079	51	0.247		211	39	0.258
	0.0354	238	0.104	54	0.203		212	38	0.234

T	**0.1**	**1**	**1**	**10**	**10**	**20**	**20**	**20**	**20**
1.6	0.0105	242	0.040	24	0.222	0	246	4	0.222
	0.0225	236	0.092	15	0.147		245	5	0.150
	0.0121	237	0.060	12	0.129		244	6	0.129
1.7	0.0040	238	0.118	55	0.218	0	207	43	0.220
	0.0051	236	0.116	49	0.212		210	40	0.212
	0.0020	248	0.098	52	0.184		205	45	0.184

e_o = 0.15

T	**0.1**	**1**	**1**	**10**	**10**	**20**	**20**	**20**	**20**
$a_{\min}$	p_c	N_{ell}	p_c	N_{ell}	p_c	N_{st}	N_{ej}	N_{ell}	p_c
1.2	0.0142	234	0.133	24	0.212	0	229	21	0.212
1.3	0.0128	226	0.067	13	0.088		248	2	0.088
1.4	0.0231	222	0.088	22	0.130		243	7	0.131
1.5	0.0229	224	0.094	19	0.163		245	5	0.168
1.6	0.0253	214	0.110	17	0.148		247	3	0.148
1.7	0.0214	227	0.117	49	0.319	1	212	37	0.322

ACKNOWLEDGEMENTS:
The work was carried out as a part of the state assignments of the Vernadsky Institute of RAS No. 0137-2020-0004 and was supported by the grant No. 13.1902.21.0039 “Theoretical and experimental studies of the formation and evolution of extrasolar planetary systems and characteristics of exoplanets” of the Russian Ministry of Education and Science.

REFERENCES:

[1] Schwarz R., Bazso A., Georgakarakos N. et al. Exocomets in the Proxima Centauri system and their importance for water transport // Monthly Notices of the Royal Astronomical Society. 2018. V. 480. P. 3595–3608.
[2] Kervella P., Arenou F., Schneider J. Orbital inclination and mass of the exoplanet candidate Proxima c // Astronomy and Astrophysics. 2020. V. 635. Art. L14.
[3] Benedict G. F., McArthur B. E. A Moving Target – Revising the Mass of Proxima Centauri c // Research Notes American Astronomical Soc. 2020. V. 4. No. 6. Art. Id. 86. doi:10.3847/2515-5172/ab9ca9.
[4] Levison H. F., Duncan M. J. The long-term dynamical behavior of short-period comets // Icarus. 1994. V. 108. P. 18–36.
[5] Ipatov S. I., Mather J. C. Migration of Jupiter-family comets and resonant asteroids to near-Earth space // Annals of the New York Academy of Sciences. 2004. V. 1017. P. 46–65. http://arXiv.org/format/astro-ph/0308448.
[6] Ipatov S. I., Mather J. C. Comet and asteroid hazard to the terrestrial planets // Advances in Space Research. 2004. V. 33. P. 1524–1533. http://arXiv.org/format/astro-ph/0212177.
[7] Ipatov S. I., Probabilities of collisions of planetesimals from different regions of the feeding zone of the terrestrial planets with the forming planets and the Moon // Solar System Research. 2019. V. 53. No. 5. P. 332–361. http://arxiv.org/abs/2003.11301
[8] Ipatov S. I. Migration of planetesimals to the Earth and the Moon from different distances from the Sun // 50th Lunar and Planetary Science Conf. 2019. Art. 2594.

MOTION OF FAST EXOPLANETS AND ROTATION OF THE EARTH

V. A. Kotov
Crimean Astrophysical Observatory, *Nauchny*, *Crimea 298409*, *Russia*
(*vkotov@craocrimea.ru*)

KEYWORDS:
Sun, Earth, rotation, exoplanets, gravitation

Substantial part of the fast exoplanets move with periods commensurate with timescales P_G and/or $2P_G/\pi$, where P_G = 9601(35) s coincides with $1/9^{th}$ of the terrestrial day and the period of solar pulsations, P_0 = 9600.606(12) s. There is also a noticeable lack of exoplanetary orbits with periods $P \approx 3\pi P_G \approx 1.05$ days, which copies the "period gap" of cataclysmic variables at $P \approx 0.11$ days; it is also noted the ratio of central periods of two gaps is equal to π^2. The exoplanet phenomenon is supposed to be caused by coherent, with P_0 timescale, oscillations of gravity, operating within the extra-solar planetary systems.

Hypotheses are advanced that (a) "solar" pulsations have cosmic origin: the P_0 timescale characterizes oscillations of G or/and a tendency of cosmic objects, physical processes and structures of the Universe to recur in time and space with the P_0 timescale, and (b) the cosmic timescale P_0, spin period of the Sun (27.027(6) days, synodic) and both periods of the Earth's motion (axial and orbital) are fundamental constants of Nature. True origin of the ubiquitous P_0 phenomenon, however, is yet far from clear.

CORONAGRAPH WITH WAVEFRONT CORRECTION FOR EXOPLANET DIRECT IMAGING

A. V. Yudaev[1], O. Y. Yakovlev[2], A. V. Tavrov[2]
[1] *Moscow Institute of Physics and Technology*, *Dolgoprudny*, *Moscow Region*, *141701*, *Russia*
[2] *Space Research Institute of the Russian Academy of Sciences*, *Moscow*, *Russia* (*tavrov@iki.rssi.ru*)

KEYWORDS:
exoplanets, direct Imaging, wavefront correction, adaptive optics

Active coronagraph is deemed to play a key role for the next generation of high-contrast instruments. The report is devoted to the study of the LC phase-only SLM applied as the pixilated wavefront corrector aiming the direct imaging of exoplanets. Space telescopes with the mirror diameter more than 1 m has critical the primary mirror figure error as well as the reflecting surface micro-roughness. Both factors cause the wavefront perturbation and the contrast degradation if the coronagraph aims to achieve the desired image contrast for an exoplanet imaging.

Figure 1 demonstrates several evaluated PSFs related to the WSO-UV mission (1.7-m primary mirror telescope). The contrast enhancement with passive coronagraphs w/o any wavefront correction optics attains 2–3 orders, which might be insufficient to detect an exoplanet with 10e-10 flux relative to its parent star flux (at PSF peak).

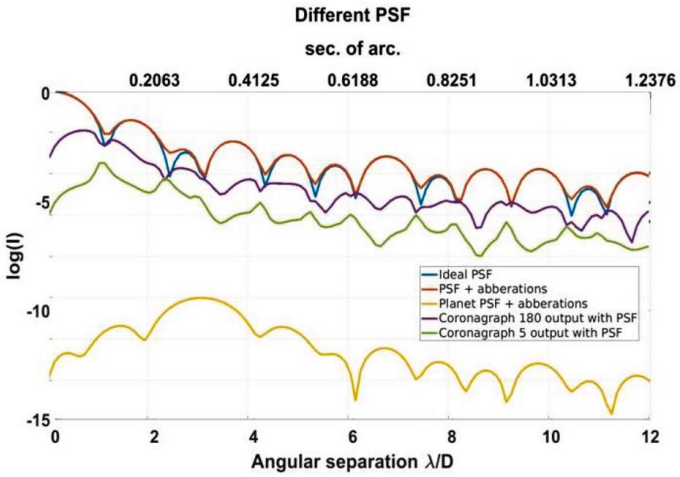

Fig. 1. Point spread functions (PSFs) after 1.7-meter telescope to consider an Earth-like exoplanet imaging by a passive coronagraph (w/o wavefront correction)

Wavefront quality has to be obtained at level about λ/1000 p-v (peak-to-valley) to be able to reduce the speckle noise from an unsuppressed stellar PSF to image faint exoplanet companion.

In the Lab. set-up (Figure 2), an incident collimated beam with the monochromatic wavefront about 2λ p-v we succeeded to relax the wavefront perturbations to the level better than λ/50 p-v, less than by 50 iterations (Figure 3). It was detected by an implemented Shack-Hartmann wavefront sensor with micro-lenses array.

Then we sent the corrected wavefront to the coronagraph. Currently we study further operations possibilities including the correction of non-common-path wavefront error (caused by coronagraph optics), achromatic schemes and other features to finalize an adaptive optics stellar coronagraph.

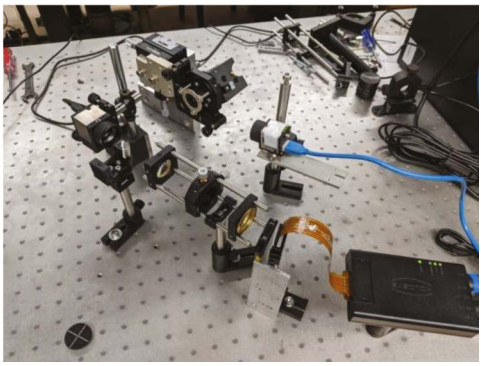

Fig. 2. Laboratory set-up

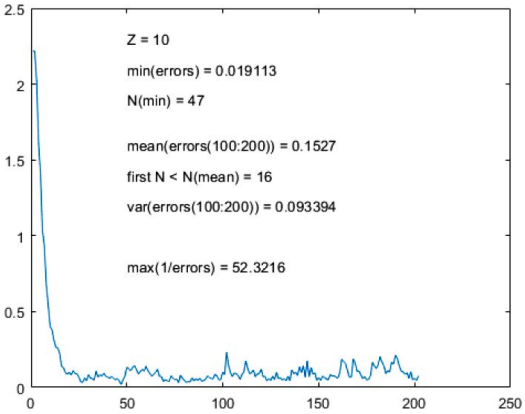

Fig. 3. Wavefront correction result and legend, Vertical: PV (peak-to-valley) wavefront level, Horizontal: Iteration number

ACKNOWLEDGMENTS:
This work was supported by the Government of Russian Federation and Ministry of Education and Science of Russian Federation (grant No. 2020-1902-01-133).

REFERENCES:

[1] Tavrov A., Kameda Sh., Yudaev A., Dzyuban I., Kiselev A., Shashkova I., Korablev O., Sachkov M., Nishikawa J., Tamura M., Murakami G., Enya K., Ikoma M., Narita N. Stellar imaging coronagraph and exoplanet coronal spectrometer: two additional instruments for exoplanet exploration onboard the WSO-UV 1.7-m orbital telescope // J. Astronomical Telescopes, Instruments, and Systems. 2018. V. 4. Iss. 4. Art. 044001. https://doi.org/10.1117/1.JATIS.4.4.044001.

[2] Kühn J., Patapis P., Lu X., Arikan M. SLM-based digital adaptive coronagraphy: current status and capabilities // Proc. Advances in Optical and Mechanical Technologies for Telescopes and Instrumentation III Conf. 2018. V. 10706. Art. 2N. https://doi.org/10.1117/12.2312554.

NUMERICAL SIMULATION OF HELIUM-RICH ATMOSPHERES OF HOT EXOPLANETS

M. S. Rumenskikh[1,2], A. G. Berezutsky[1,2], I. B. Miroshnichenko[1], I. F. Shaikhislamov[1]
[1] *Institute of Laser Physics SB RAS, Novosibirsk, Russia* (*marina_rumenskikh@mail.ru*)
[2] *INASAN, Moscow, Russia*

KEYWORDS:
exoplanets, hot jupiters, ionospheres, cosmic plasmas, numerical modelling

INTRODUCTION:
The investigation of the atmospheres of close-orbit exoplanets and their interaction with incoming stellar wind is becoming more important due to the planned launches of new space telescopes and large ground-based instruments. Hot jupiters and warm neptunes located at a distance of <0.05 AU from parent star experience strong heating of atmosphere by ionizing radiation and the interaction of planetary and stellar winds can be considered as the interaction of plasma flows.

Ly-α observations have been immensely valuable for providing evidence of atmospheric escape. However, there are inherent limitations of using this line. Lyα suffers from extinction by the interstellar medium and contamination from geocoronal emission, rendering the signal from the Lyα line core — and the valuable information content it might carry — irretrievable [1].

The use of the metastable helium line to investigate atmospheres of hot jupiters, such HD 209458b, using transit measurements was proposed in [2]. The 10830 Å line is intense enough in the stellar spectrum to be detected by ground-based telescopes, and does not undergo significant distortion passing through the interstellar medium. Data obtained during the transit observations will help to estimate such parameters as temperature, pressure, and density around the planet. This line may provide a new wavelength window for studying the hydrodynamic escape and atmospheric mass loss. Its main advantages over the UV lines are weaker interstellar absorption and the possibility of ground-based observations.

Here we investigate the excitation and depopulation processes of the metastable helium in the atmospheres of hot exoplanets, which prove to be rather complex. The interpretation of absorption in 10830 Å line requires 3D modeling including interaction of planetary outflow with the stellar wind, which we demonstrate for the warm Neptune GJ 4370 b.

ACKNOWLEDGEMENTS:
The research was carried out in the framework of the project “Study of stars with exoplanets0 under a grantfrom the Government of the Russian Federation for scientific research conducted under the guidance of leading scientists (agreement No. 075-15-2019-1875) also by the RNF project No. 18-12-00080 and RFBR project.

REFERENCES:
[1] Ehrenreich D., Bourrier V. A giant comet-like cloud of hydrogen escaping the warm Neptune-mass exoplanet GJ 436b // Nature. 2015. V. 522. P. 459–461.
[2] Seager S., Sasselov D. D. Theoretical Transmission Spectra during Extrasolar Giant Planet Transits // Astrophysical J. 2000. V. 537. P. 916.

INVESTIGATING THE IMPACT OF EXOPLANETS PARAMETERS ON THEIR HABITABILITY

F. JahediParizi, B. Sakhaei, J. Jafarzadeh, A. Poro
The International Occultation Timing Association-Middle East Section, Iran
(*info@iota-me.com*)

KEYWORDS:
exoplanets, habitable, planets, climate models

INTRODUCTION:
Today, as more exoplanets are discovered, the desire for finding habitable one's increases. There are many climate models for assessing the habitability and climate changes of exoplanets. One of the simplest, yet accurate enough models is the latitudinal energy balance model. It is a diffusion-like process, which simulates the temperature profile over the planet's surface. In this study, our purpose is to investigate the impact of some parameters of exoplanets on their temperature and habitability. Our exoplanet candidates are GJ 273b, Trappist-1d, 'Tau Ceti-e, GJ 3323b, and the studied parameters are planet eccentricity, diurnal period, obliquity and its fraction of ocean. In each case, the selected parameter was varied in a wide range. Finally, the probable descriptions of results are presented.

REFERENCES:
[1] Kasting J. F., Whitmire D. P., Reynolds R. T. Habitable zones around main sequence stars // Icarus. 1993. V. 101. Iss. 1. P. 108–128.
[2] Forgan D. Assessing circumbinary habitable zones using latitudinal energy balance modelling // Monthly Notices of the Royal Astronomical Soc. 2013. V. 437. Iss. 2. P. 135221361.
[3] Dressing C. D. et al. Habitable climates: the influence of eccentricity // The Astrophysical J. 2010. V. 721. Iss. 2. Art. 1295.
[4] Vladilo G. et al. The habitable zone of Earth-like planets with different levels of atmospheric pressure // The Astrophysical J. 2013. V. 767. Iss. 1. Art. 65.

ESTIMATION OF THE TOTAL MASS OF TEN EXOPLANETS AND THEIR HOST STARS BASED ON THE PRIMARY TRANSIT METHOD

Z. Zarei[1,2], A. Poro[1,2], M. Hedayatjoo[1,2], Y. Dashti[1,2], F. Mohammad Zadeh[1,2], M. Hashemi[1,2], E. Rajaei[1,2], A. Kazemi[2], A. Sarostad[2], M. Nastaran[2], A. Dehghani Ghanatghestani[2]

[1] *The International Occultation Timing Association-Middle East section* (*info@iota-me.com*)

[2] *Exoplanet Transit Project* (*ETP-1*), *Transit department*, *IOTA-ME*, *Iran*

KEYWORDS:
photometry, EXOFAST, mass, metallicity

INTRODUCTION:

Ever since the first discoveries were made about exoplanets in 1992, many researchers have been studying their properties by using data provided from different sources (Swift, 2010). A part of these sources is the ground-based observations, conducted in small observatories around the world. Even though space missions such as TESS are able to survey a great percentage of the sky and provide us with more reliable data, these observatories show great potential for producing data on brighter stars and have contributed immensely to this field (Davoudi, 2020).

Throughout this article, we analyzed the parameters of the following exoplanets: CoRoT-12b, HAT-P-52b, HAT-P-57b, HATS-28b, HATS-34b, KELT-3b, WASP-61b, WASP-67b, WASP-122b, and WASP-140b. All of the planets were discovered through the primary transit method, between the years 2010 and 2016. Their orbital periods range from 1.710 to 4.674 days, and their host stars' apparent magnitudes are between 9.8 to 15.52 (The Extrasolar Planets Encyclopaedia (http://exoplanet.eu)). In order to calculate their parameters and carry out a detailed analysis, we got the raw data from the Exoplanet Transit Database (ETD, URL: http://var2.astro.cz/ETD). Then we proceeded with data reduction using the Phoebe 0.32 software (http://phoebe-project.org/1.0/download). Therefore, we gave the normalized data to EXOFAST (https://exoplanetarchive.ipac.caltech.edu/cgi-bin/ExoFAST/nph-exofast) software and obtained the parameters for the planets. The purpose of this study is to make a comparison of some of the exoplanets' parameters with other studies.

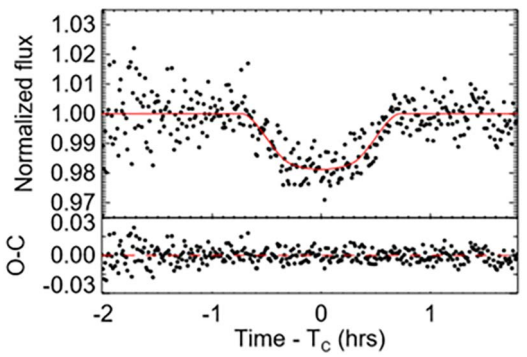

Fig. 1. An example of an observational and theoretical light curve provided by Exofast software for WASP-140 b (Clear filter)

RESULT:

To calculate the total mass of stars and planets, Visual Basic language software was designed (Figure 2). Features of this software: Converting required units, calculating the mass of stars and planets, and comparing the calculated mass through observation with the mass calculated based on reference. The results are shown in Table 1.

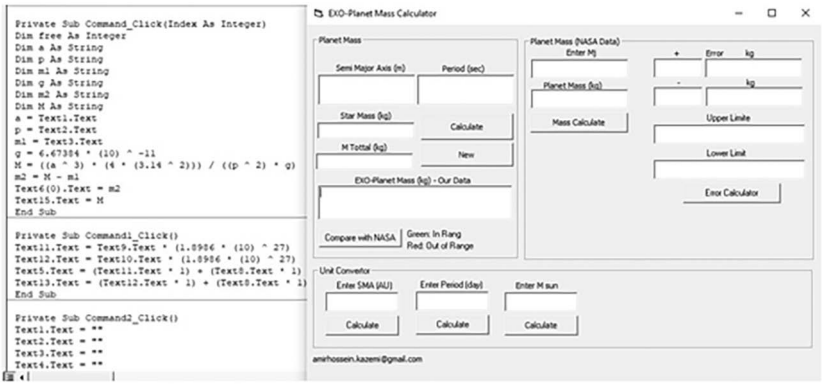

Fig. 2. An image of the software environment designed to calculate the total mass

Table 1. Calculations of the total mass by the software designed in this study

Planet	Semi-Major Axis (m)	Period (sec)	Total Mass (kg)
CoRoT-12b	5971647802.6026	239252.3532	2.19843494365844E+30
CoRoT-12b	5971647802.6026	239252.3532	2.19843494365844E+30
HAT-P-52b	5570426313.3852	232954.137	1.88220942193734E+30
HAT-P-52b	5570127117.6438	232954.137	1.88190614956745E+30
HAT-P-52b	5570127117.6438	232954.137	1.88190614956745E+30
HAT-P-57b	899472755762.303	208564.38	9.88615146224498E+36
HATS-28b	6242719144.311	269119.1988	1.98506862337482E+30
HATS-34b	4783990307.1153	178181.2206	2.03793585713948E+30
KELT-3b	6171959351.4699	228706.794	2.65616185953124E+30
KELT-3b	6171809753.5992	228706.794	2.65596872158041E+30
WASP-61b	7671528407.3667	326209.14	2.5072459528813E+30
WASP-67b	7798536999.591	390379.932	1.83911099012456E+30
WASP-122b	4432285713.0996	144670.8222	2.45846959546179E+30
WASP-140b	4845325434.1023	189164.1618	1.87860135329608E+30
HAT-P-57b	5652256348.6581	208564.38	2.45317635666998E+30

REFERENCES:

[1] Davoudi F., Jafarzadeh S. J., Poro A., Basturk O., Mesforoush S., Harandi A. F., Gozarandi M. J., Mehrjardi Z. Z., Maley P. D., Khakpash S., Rokni K. Light curve analysis of ground-based data from exoplanets transit database // New Astronomy. 2020. V. 76. Art. 101305.

[2] Swift D. C., Eggert J. H., Hicks D. G., Hamel S., Caspersen K., Schwegler E., Collins G. W., Nettelmann N., Ackland G. J. Mass-radius relationships for exoplanets // The Astrophysical J. 2011. V. 744. Iss. 1. Art. 59.

PERIOD STUDY BY THE TRANSIT METHOD WITH GROUND-BASED OBSERVATIONS

A. Poro[1,2], Elmi Kanklou F.[1,2], Ranjbaryan Iri Olya S.[2], N .Dashan[2], F. Ansarinia[2], F. Abdollahi[2], A. Haselpour[2], Dehghanizadeh Baghdadabad F.[2], F. Jahediparizi[2], A. Gardi[2], Hossein vand A.[2]

[1] *The International Occultation Timing Association-Middle East section* (*info@iota-me.com*)

[2] *Exoplanet Transit Project* (*ETP-2*), *Transit department*, *IOTA-ME*, *Iran*

KEYWORDS:
photometry, EXOFAST, orbital parameters, transit

INTRODUCTION:

Throughout this study, we analyzed the orbital parameters of the following exoplanets: CoRoT-11b, CoRoT-12b, CoRoT-20b, HAT-P-52b, HAT-P-57b, HATS-28b, HATS-34b, KELT-3b, Kepler-19b, Kepler-20c, WASP-7b, WASP-61b, WASP-67b, WASP-107b, WASP-108b, WASP-121b, WASP-122b, WASP-140b, and WASP-163b. All of the planets were discovered through the primary transit method, between the years 2008 and 2018. Their host stars' apparent magnitudes are between 9.51 to 15.52 (http://simbad.u-strasbg.fr/simbad/).

In order to calculate their parameters and carry out a detailed analysis, we got the raw data from the Exoplanet Transit Database (ETD, URL: http://var2.astro.cz/). Then we proceeded with data reduction use the Phoebe 0.32 software (http://phoebe-project.org/). Therefore, we gave the normalized data to EXOFAST online software (https://exoplanetarchive.ipac.caltech.edu/cgi-bin/ExoFAST/nph-exofast) and obtained the parameters for the planets. The purpose of this study is to make a comparison of some of the planet's parameters with other studies based on the Extrasolar Planets Encyclopedia.

ANALYSIS AND CONCLUSION:

A) Period accuracy

We compared periods calculated by Exofast online software with their values on the Extrasolar Planets Encyclopedia (https://exoplanetarchive.ipac.caltech.edu/cgi-bin/ExoFAST/nph-exofast). In the Table 1, the first column is the name of the planet, the second column is the period calculated from the observations, and the third column is the period are compared. The results of observations from each planet are averaged. As can be seen, the periods of all the planets match and they are comparable.

Table 1. Compare the values of the period obtained from the observation with the Extrasolar Planets Encyclopaedia

Planet	Period of observation (day)	Comparison period (day)
CoRoT-11b	2.99433	2.994325 (±2.1e-05)
CoRoT-12b	2.828042	2.828042 (±1.3e-05)
CoRoT-20b	9.24285	9.24285 (±0.0)
HAT-P-52b	2.753595	2.753595 (±9.4e-06)
HAT-P-57b	2.4653	2.465295 (±3.2e-06)
HATS-28b	3.181078	3.181078 (±3.9e-06)
HATS-34b	2.106161	2.106160 (±4.7e-06)
KELT-3b	2.70339	2.703390 (±1e-05)
Kepler-19b	9.28716	9.286994 (±8.8e-06)
Kepler-20c	10.854091	10.854091 (-2.6e-06+3.03e-06)
WASP-7b	4.954642	4.954641 (±3.5e-06)
WASP-61b	3.8559	3.8559 (±3e-06)
WASP-67b	4.61442	4.61442 (±1e-05)
WASP-107b	5.72149	5.72149 (±2e-06)
WASP-108b	2.675546	2.675546 (±2.1e-06)

Planet	Period of observation (day)	Comparison period (day)
WASP-121b	1.274926	1.274925 (±2.5e-07)
WASP-122b	1.710057	1.710056 (±3.6e-06)
WASP-140b	2.235983	2.235983 (±8e-06)
WASP-163b	1.609688	1.609688 (±1.5e-06)

B) Calculating T_c

Time of transit, T_c, is the time that conjunction happens. It is represented the time of transit center and the minimum of the planet transit light curve. T_c is reported in Barycentric Julian Date that is expressed as Barycentric Dynamical Time (Davoudi et al., 2019). We calculated T_c for all of our observations and shows it in the Table 2.

Table 2. Calculate the mid-time (T_c) of the transit for observations

Planet	T_c	Planet	T_c
CoRoT-11b	2456091.829404 (±0.001026)	KELT-3 b	2456715.551831 (±0.001899)
CoRoT-12b	2457014.579814 (±0.002255)	Kepler-19 b	2456129.893894 (±0.002722)
CoRoT-20b	2455968.465498 (±0.002736)	Kepler-20 c	2457207.554245 (±0.002246)
CoRoT-20b	2455968.471144 (±0.002502)	WASP-7 b	2457953.561049 (±0.001250)
CoRoT-20b	2456726.347691 (±0.002966)	WASP-61 b	2456950.759645 (±0.001194)
CoRoT-20b	2455968.458761 (±0.006091)	WASP-61 b	2456950.747158 (±0.001281)
HAT-P-52 b	2458140.342804 (±0.001007)	WASP-67 b	2458002.381915 (±0.000671)
HAT-P-52 b	2457724.552899 (±0.001222)	WASP-67 b	2456798.021280 (±0.000965)
HAT-P-52 b	2458520.336274 (±0.000948)	WASP-107 b	2458545.543719 (±0.000550)
HAT-P-57 b	2458663.509091 (±0.000652)	WASP-108 b	2458262.537298 (±0.001543)
HAT-P-57 b	2458668.440058 (±0.002275)	WASP-108 b	2457534.842474 (±0.001069)
HATS-28 b	2457571.883928 (±0.001015)	WASP-108 b	2457850.562043 (±0.000589)
HATS-34 b	2457989.119324 (±0.000909)	WASP-121 b	2457794.618947 (±0.000250)
HATS-34 b	2458871.602190 (±0.001336)	WASP-122 b	2458862.643263 (±0.000692)
KELT-3 b	2457126.464382 (±0.000550)	WASP-140 b	2457755.318812 (±0.000607)
		WASP-163 b	2458702.378044 (±0.001795)

C) Calculating T_{depth}

We calculated the transit depth values. There are also transit depth values of the Czech Astronomical Society (ETD) are present in the Table 3. There may be several observations for each planet, an average of which has been calculated.

Table 3. Transit depth values obtained in observations and its values in ETD

Planet Name	Transit Depth (Observation)	Transit Depth (ETD)
CoRoT-11b	0.010352 (±0.000505)	0.018075 (±0.00126)
CoRoT-12b	0.017022 (±0.002778)	0.026933 (±0.00442)
CoRoT-20b	0.020805 (±0.005372)	0.0323 (±0.0044)
HAT-P_52b	0.014011 (±0.000634)	0.01873208 (±0.002096)
HAT-P_57b	0.010690 (±0.000539)	0.01545 (±0.001325)
HATS-28b	0.017898 (±0.000685)	0.0217 (±0.0011)
HATS-34b	0.018625 (±0.000935)	0.014113 (±0.001133)
KELT-3b	0.009705 (±0.000369)	0.011197 (±0.001060)
Kepler-19b	0.007244 (±0.000795)	0.0107 (±0.0015)
Kepler-20c	0.007541 (±0.000475)	0.0103 (±0.0013)
WASP-7b	0.016220 (±0.000188)	0.00646 (±0.00043)
WASP-61b	0.010062 (±0.000282)	0.001125 (±0.00075)
WASP-67b	0.013701 (±0.000605)	0.01645 (±0.001)
WASP-107b	0.025798 (±0.000456)	0.03295 (±0.0007)

Planet Name	Transit Depth (Observation)	Transit Depth (ETD)
WASP-108b	0.015107 (±0.000431)	0.01675 (±0.00125)
WASP-121b	0.005584 (±0.000048)	0.0207 (±0.00055)
WASP-122b	0.014602 (±0.000320)	0.012 (±0.000625)
WASP-140b	0.019769 (±0.000624)	0.021575 (±0.00135)
WASP-163b	0.008744 (±0.000980)	0.0213333 (±0.003233)

REFERENCE:

[1] Davoudi F., Jafarzadeh S. J., Poro A., Basturk O., Mesforoush S., Fasihi Harandi A., Gozarandi M. J., Zare Mehrjardi Z., Maley P. D., Khakpash S., Rokni K., Sarostad A. Light Curve Analysis of Ground-Based Data from Exoplanets Transit Database // New Astronomy. 2020. V. 76.

DEVELOPMENT OF RADIATION BLOCK FOR NON-HYDROSTATICAL GCM OF VENUS' ATMOSPHERE

M. V. Razumovskiy[1], B. A. Fomin[1], A. V. Rodin[1,2]
[1] *Moscow Institute of Physics and Technology, Institutskii per. 9, Dolgoprunyi, Moscow obl., 141701 Russia;*
[2] *Space Research Institute, Russian Academy of Sciences, Profsyuznaya ul. 84/32, Moscow, 117997 Russia*

KEYWORDS:`
Venus, Atmospheres, Radiative transfer, General Circulation Model

INTRODUCTION:
Non-hydrostatic general circulation models adapted for the atmospheres of Earth-like planets are new generation of models gaining popularity in modern planetary science. Familiar class of objects to study with a 3D non-hydrostatic GCM is the atmospheres of extrasolar "hot Jupiters". However in the last decade such models were successfully employed for exploring atmospheres of Earth-like Solar System planets (e.g. Venus and Titan) and Super-Earth exoplanets [1, 2]. Recent studies on general circulation of Venus' atmosphere [3, 4] with MIPT/PGI GCM were based on usage of the simplistic Newtonian thermal forcing scheme that is not applicable for complete description of the atmospheric dynamics. In this study we present ideas of building full-valued thermal forcing scheme for the Venus' atmosphere. We focused on following features of the atmosphere: much greater, compared to the Earth's atmosphere, vertical inhomogeneity and deeper cloud layer. For considering gaseous absorption in scattering atmosphere we use the method of k-distributions. However, for getting "k-distributions" we follow the work [5] instead of familiar technique "correlated-k" that results in the error growth with increasing inhomogeneities. For validation of the fast calculations we employ etalon simulation algorithm based on line-by-line opacity integration and Monte Carlo simulations of scattering processes[6].

REFERENCES:
[1] Mingalev I.V., Rodin A.V. and Orlov K.G. Numerical Modeling of the General Circulation of the Atmosphere of Titan at Equinox. Solar System Research. 2019. V. 53. No. 4. P. 278-293.
[2] Razumovskiy M.V., Rodin A.V. Modeling the Atmospheres of Tidally Locked Super-Earths Orbiting Low-Mass Host Stars Using a Non-hydrostatic General Circulation Model. Astronomy Letters, 2020. V. 46. No. 6. P. 400-406.
[3] Mingalev I.V., Rodin A.V. and Orlov K.G. Numerical Simulations of the Global Circulation of the Atmosphere of Venus: Effects of Surface Relief and Solar Radiation Heating. Solar System Research, 2015. V. 49 No. 1 P. 24-42.
[4] Mingalev I.V., Rodin A.V. and Orlov K.G. A Non-hydrostatic Model of the Global Circulation of the Atmosphere of Venus. Solar System Research, 2012. V. 46 No. 4 P. 263-277.
[5] Fomin, B.A., A k-distribution technique for radiative transfer simulation in inhomogeneous atmosphere: 1. FKDM, fast k-distribution model for the longwave, J.Geophys.Res.,109, D02110, doi:10.1029/2003JD003802, 2004.
[6] Fomin, B.A., Monte-Carlo algorithm for line-by-line calculations of thermal radiation in multiple scattering layered atmospheres, J.Quant.Spectrosc.Rad.Transfer 2471, DOI.1016/j.jqsrt.2005.05.078.

LONG-TERM VARIATIONS OF ZONAL WIND SPEED AT THE CLOUD TOP LEVEL OVER MISSION TIME FROM VMC/VENUS EXPRESS AND UVI/AKATSUKI UV IMAGES

M. V. Patsaeva, I. V. Khatuntsev, A. V. Turin, L. V. Zasova
Space Research Institute RAS, Moscow, 117997, Russia
(*marina@irn.iki.rssi.ru*)

KEYWORDS:
Venus, mesosphere, dynamics, topography

INTRODUCTION:

UV (365 nm) images obtained by Venus Monitoring Camera (VMC) onboard Venus Express spacecraft from 2006 to 2013 and by Ultraviolet Imager (UVI) onboard Akatsuki from December 2015 to November 2018 were used to study the mesosphere dynamics. Wind vectors obtained by data processing of 262 orbits of VMC [1, 2, 4] and of 66 orbits of UVI were derived by digital tracking technique.

Analysis of the cloud top zonal wind in equatorial latitudes extracted from VMC images showed that zonal wind deceleration above Aphrodite Terra (the highest region in equatorial latitudes) is associated with influence of the surface [3, 4]. At the same time, results obtained from UVI images in [5] didn't reveal the influence of topography on the cloud top winds.

To study the factors, which allow to detect the influence of topography on dynamics of the upper clouds, we divided a long 8-years period of VMC observation, when the mean zonal wind speed increases [1], in two four-year intervals of observation. In turn, a 3-year period of Akatsuki observation was divided in two 1.5-year intervals. As a result we have got a possibility to investigate the dependence of zonal winds on topography for different time intervals from 2006 to 2018. The behavior of the zonal wind in the first 4 years and the last 4 years of Venus Express mission and in the first 1.5 years and the next 1.5 years of Akatsuki mission was investigated separately.

RESULTS:

An increase in the mean zonal wind speed was detected in equatorial latitudes during the Venus Express mission from 2006 to 2013 [1]. Akatsuki spacecraft, which continued observations of Venus since 2015, makes it possible to trace the change in the average zonal wind over a long time. Figure 1 shows that since 2015 there was a decrease in the mean zonal wind speed.

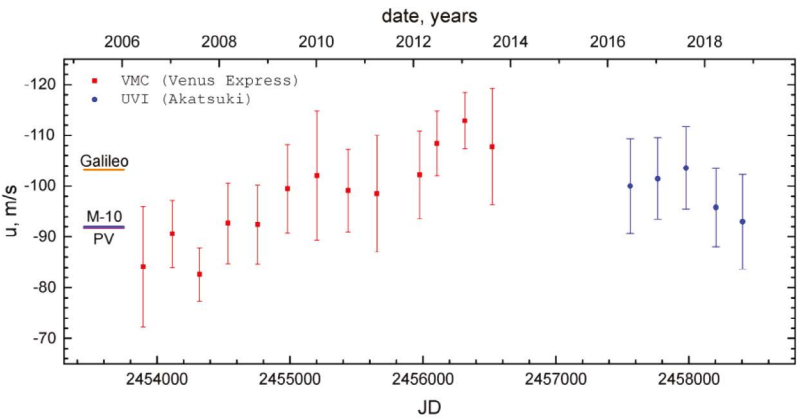

Fig. 1. Variations of the mean zonal wind speed at 20±2.5° S over the mission time. Red squares show zonal wind averaged through the Venusian year derived from VMC images, blue circles are the same for UVI. The results from the Mariner-10 (92 m/s), Pioneer-Venus (91.8±3 m/s) and Galileo (103 m/s) missions for the same latitude zone are shown at the left edge of the plot for comparison.

A study of the longitudinal dependence of the mean zonal speed in the latitudinal zone 10±5° S (which corresponds to the highest region in equatorial latitudes) shows the presence of zonal speed minimum over Aphrodite during the first 4 years of the Venus Express mission. The mean zonal speed is 91.2 m/s, the difference between minimum and maximum is 18.4 m/s. During the last 4 years of the mission, the speed minimum shifts from Aphrodite Terra, and the mean zonal speed increases up to 106.5 m/s. At that time, a maximum of the mean zonal speed is observed over Aphrodite Terra, and the difference between the maximum and minimum decreases to 14.9 m/s. During the first 1.5 years of the Akatsuki mission, when the mean zonal speed was 101.6 m/s, a shift of minimum parallel with the appearance of a zonal speed maximum over Aphrodite Terra are also observed. When the mean zonal speed decreased to 97.9 m/s in the next 1.5 years, a speed minimum appeared over Aphrodite Terra again (Figure 2). In this case, the difference between minimum and maximum of the mean zonal speed increased from 6.1 m/s to 9.8 m/s. Thus, as the mean zonal wind speed decreases, the influence of the surface becomes more pronounced.

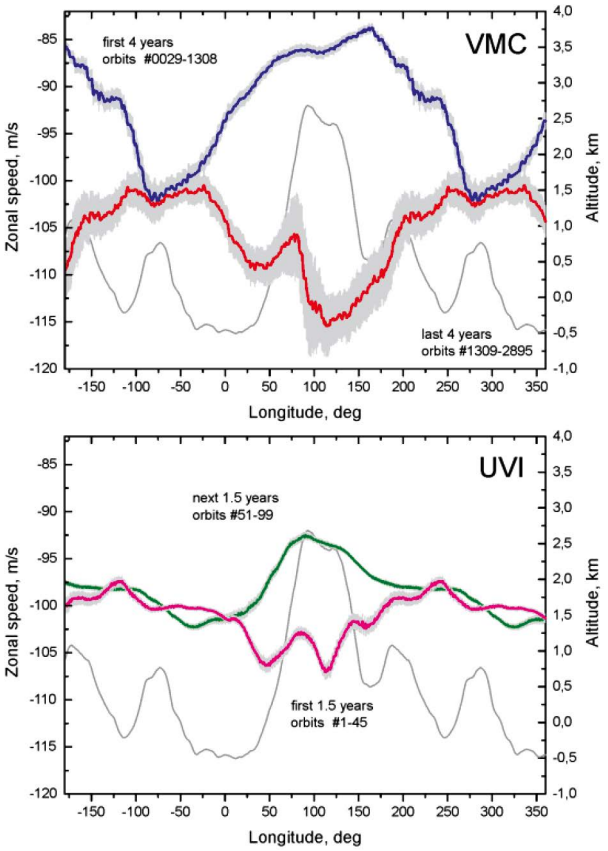

Fig. 2. Mean profiles of zonal wind speed for first 4 years of VMC (blue line, top panel), last 4 years of VMC (red line, top panel), first 1.5 years of UVI (pink line, bottom panel), next 1.5 years of UVI (green line, bottom panel) averaged within latitude zone 10±5° S. The error bars correspond to 3*SEM, where SEM is standard error of the mean. The gray line (top and bottom panels) shows the mean surface topography at the same latitude zone.

CONCLUSIONS:

1) In 2006-2013 the VMC registered a monotonous increase of the mean zonal wind speed: during almost 10 Venusian years of observations, the mean zonal speed changed from 85 to 115 m/s [1]. On the contrary, in 2016-2018 (5 Venusian years) the mean zonal wind speed obtained from UVI images, manifests a downward trend from 103 to 92 m/s.

2) The zonal wind deceleration caused by the influence of the surface [3, 4] was observed over Aphrodite Terra when the mean zonal wind decreased. A comparison of the results of the zonal wind speed behavior during the separated periods of observation for VMC and UVI shows that for both cameras a correlation of wind speed in the upper cloud layer above Aphrodite Terra with the surface relief was observed (more pronounced for VMC). It depends on the mean zonal wind speed in such a way, that during the period of lower mean wind speed a minimum of zonal wind speed was observed above the maximum altitude of Aphrodite for both VMC and UVI observations. Vice versa, during the higher mean wind speed period a maximum of wind speed was close to the position of maximum altitude of Aphrodite.

ACKNOWLEDGEMENTS:
The authors would like to thank the program No. AAAA-A18-118052890092-7 of the Ministry of Science and Higher Education of the Russian Federation for the support.

REFERENCES:

[1] Khatuntsev I. V., Patsaeva M. V., Titov D. V., Ignatiev N. I., Turin A. V., Limaye S. S. et al. Cloud level winds from the Venus Express Monitoring Camera imaging // Icarus. 2013. V. 226. No. 1. P. 140–158. https://doi.org/10.1016/j.icarus.2013.05.018.

[2] Patsaeva M. V., Khatuntsev I. V., Patsaev D. V., Titov D. V., Ignatiev N. I., Markiewicz W. J., Rodin A. V. The relationship between mesoscale circulation and cloud morphology at the upper cloud level of Venus from VMC/Venus Express // Planetary and Space Science. 2015. V. 113–114. No. 08. P. 100–108. https://doi.org/10.1016/j.pss.2015.01.013.

[3] Bertaux J.-L., Khatunstsev I. V., Hauchecorne A., Markiewicz W. J., Marcq E., Lebonnois S., Patsaeva M., Turin A., Fedorova A. Influence of Venus topography on the zonal wind and UV albedo at cloud top level: The role of stationary gravity waves // J. Geophysical Research Planets. 2016. V. 121. P. 1087–1101. https://doi.org/10.1002/2015JE004958.

[4] Patsaeva M. V., Khatuntsev I. V., Zasova L. V., Hauchecorne A., Titov D. V., Bertaux J.-L. Solar Related Variations of the Cloud Top Circulation Above Aphrodite Terra From VMC/Venus Express Wind Fields // J. Geophysical Research: Planets. 2019. V. 124. P. 1864–1879. https://doi.org/10.1029/2018JE005620.

[5] Horinouchi T., Kouyama T., Lee Y. J., Murakami S., Ogohara K. Mean winds at the cloud top of Venus obtained from two-wavelength UV imaging by Akatsuki // Earth, Planets and Space. 2018. V. 70. 19 p. https://doi.org/10.1186/s40623017-0775-3.

HORIZONTAL WINDS IN THE LOWER CLOUDS ON THE NIGHTSIDE OF VENUS FROM VIRTIS/VEX 1.74 μm DATA

D. A. Gorinov, I. V. Khatuntsev, L. V. Zasova, M. V. Patsaeva, A. V. Turin
Space Research Institute RAS, *Moscow*, *Russia* (*dmitry_gorinov@rssi.ru*)

KEYWORDS:
Venus, cloud layer, dynamics, wind tracking

INTRODUCTION:
The Visible and Infrared Thermal Imaging Spectrometer (VIRTIS) instrument onboard Venus Express obtained images of Venus atmosphere in a visible and an infrared channel, sampling it on different levels. Nightside images in 1.74 μm correspond to the lower cloud level at 44–48 km altitude above surface. By tracing the displacement of cloud features on these images, it is possible to retrieve horizonal wind velocity vectors. In this work for the first time the entire VIRTIS dataset (2006–2008) was analyzed, expanding on previous analysis of partial datasets [1–2]. By retrieving velocity vectors, we were able to view and analyze mean atmospheric circulation in the lower clouds in the Southern Hemisphere. This atmospheric layer is in constant superrotation mode with a westward mean speed of 60–65 ms^{-1} in the latitudes up to 60°, with a 1–5 ms^{-1} westward deceleration across the nightside. The meridional motion is significantly weaker, with mean values of 0–3 ms^{-1} (poleward). Its direction changes to equatorward in the equatorial latitudes, which could indicate lower boundary of a cloud level Hadley cell. a diurnal gradient in the meridional speed was also detected, as the poleward motion is strongest near the morning terminator, and changes to poleward near the evening terminator. Significant longitudinal variations were detected, however their interpretation as the influence of topography-induced stationary gravity waves was not identified.

REFERENCES:
[1] Sánchez-Lavega A., Lebonnois S., Imamura T., Read P., Luz D. The atmospheric dynamics of Venus // Venus III. 2017. P. 1541–1616.
[2] Hueso R., Peralta J., Sánchez-Lavega A.Assessing the long-term variability of Venus winds at cloud level from VIRTIS – Venus Express // Icarus. 2012. V. 217. P. 575–598.

VENERA-D: A PERSPECTIVE PLANETARY MISSION

L.V. Zasova
Space Research Institute, RAS, 117997, Moscow, Profsoyuznaya 84/32, (lzasova@gmail.com)

KEYWORDS:
Venus, JSDT, Venera-D, Roscosmos, NASA, mission, sample return

INTRODUCTION:
A return of samples of Venus atmosphere and soil back to the Earth is a strategical aim of the Roscosmos program of Venus exploration. This ambitious aim is difficult and risky to be realised by a single mission to Venus. For the last 35 years there were only remote observations from orbit and ground based observations. For a representative choice of a landing site suitable for soil sampling, it is necessary to study the surface in detail and carefully. Together with 'hellish' (T= 470°C and P=92 bar) condition on the surface, Venus is covered by 20 km thick sulfuric acid clouds. Measurements in-situ in the atmosphere (by balloons and during the descent of the landers) and on the surface (by landers and long-lived stations) are especially important together with the simultaneous remote observations from the orbit. Previous studies carried out on the surface of Venus, took place almost 40 years ago with the equipment of that time, gave only the most general characteristics of the surface conditions due to large measurement errors.

VENERA-D MISSION:
The Venera-D mission, developed by IKI/NPOL/Roscosmos - HASA Joint Science Definition Team (JSDT) [1,2] may be the first mission on the route to Venus samples return. The fundamentally new scientific tasks of the conception of Venera-D mission were formulated on the basis of the knowledge and experience of the entire world scientific community [3, 4] . Venera-D includes, besides orbiter, the elements for in-situ measurements, cited above: aerial platforms, lander with connected to it Long Lived In-situ Solar System Explorer (60 days on the surface), LLISSE, NASA. It is also planned to include several others long lived stations, which will work for 120 days on the surface, (1 Venus day=117 earth days) Seismic and Atmospleric Explorer of Venus, SAEVe, NASA. They will measure during the whole Venus day vatiations of wind, temperature, pressure, solar and thermal fluxes, composition, thermal tides and waves. It will help to identify the most favorable local time for landing and soil sampling.

In comparison with previous expeditions, it is well developed and substantiated, and, undoubtedly, will be ready to implemente in 2029.

Thus, Venus-D mission , as it is developed by JSDT, can be the first, unconditionally decisive step in preparation of the return of soil and atmosphere samples from Venus.

REFERENCES:
[1] Phase I repot of the Venera-D Joint Science Definition Team https://www.lpi.usra.edu/vexag/reports/Venera-D-STDT013117.pdf
[2] Phase II repot of the Venera-D Joint Science Definition Team http://www.iki.rssi.ru/events/2019/Venera-DPhaseIIFinalReport.pdf
[3] Venera-D. Venus modeling workshop" Proceedings. IKI RAS, 2018. http://venera-D.cosmos.ru/fileadmin/user_upload/documents/Workshop2017_Proceedings.pdf
[4] Venera-D Landing Sites selection and Cloud Layer Habitability Workshop. October 2-5, 2019. IKI, Moscow, Russia. http://venera-d.cosmos.ru/uploads/media/VeneraD_2019Wkshp_techRp.pdf

LANDING ON THE VENUS SURFACE WITH GRAVITY ASSIST

V. A. Zubko, A. A. Belyaev, N. A. Eismont, K. S. Fedyaev, L. V. Zasova, D. A. Gorinov
Space Research Institute of the Russian Academy of Sciences (*IKI*), *Moscow*, *Russia*

KEYWORDS:
Venus, Venera-D, atmosphere, landing, gravity assist, orbital mechanics

INTRODUCTION:

The research provided a solution of the problem to maximize accessible landing areas on the Venus surface for a mission of the Venera-D project. Launch windows from 2029 to 2034 are considered. Simultaneously the constraints on minimum demanded payload mass are taken into account. Maximum allowed value of overload at atmospheric reentry is considered as additional requirements. The list of parameters to be chosen for satisfying project demands, includes launch and arrival dates to Venus. trajectories are analyzed for those such scenarios with reaching Venus on the first and second semi-orbits.

Characteristic velocity required for launch phase has been estimated in order to determine payload mass values Oxygen-hydrogen propellant was supposed for upper stage putting payload from near Earth orbit to Venus transfer trajectory. For near Venus orbital maneuvers a propulsion system with specific impulse around 320 seconds is supposed.

The research demonstrates possibility of radical extension of landing areas compared to standard methods. The main idea of such extension includes usage of a gravity assist maneuver that gives a possibility to transfer the spacecraft to the resonant orbit with 1:1 ratio to the Venus orbital period. Such situation allows to access almost all the points on the Venus surface, but to fulfill such scenario duration of mission increases by the Venus orbital period. The new method doesn't require additional fuel costs. The maximum value of overload at atmosphere reentry doesn't exceed 180 g.

LLISSE: DEVELOPMENT STATUS

T. Kremic, G. Hunter, C. Tolbert
NASA Glenn Research Center, *Cleveland*, *OH* (*Tibor.Kremic@nasa.gov*)

KEYWORDS:
Venus surface, LLISSE, high-temp electronics, GEER, super-rotation, climate, evolution, surface-atmosphere interaction, weathering

INTRODUCTION:
Exploration to better understand the deep Venus atmosphere and surface have been long standing objectives of the Venus science community as stated in Venus Exploration Analysis Group (VEXAG) documents [1] and the Planetary Decadal Survey Report [2]. The extreme environmental conditions at the surface of Venus, coupled with the thick clouds and dense atmosphere, have made achieving surface science objectives very challenging. Landed missions to date have not been able to last more than about 2 h [3]. Recent advances in high-temperature electronics [4, 5] and the addition of new capabilities to simulate Venus conditions, such as provided by the Glenn Extreme Environment Rig (GEER) [6], are helping change our outlook on feasibility of long duration Venus landers.

NASA's Long-Lived In-situ Solar System Explorer (LLISSE) project has been developing the needed capabilities to enable future Venus surface science exploration [7]. LLISSE has a goal of developing an engineering model fidelity lander with a target life of 60 days at Venus surface conditions (Figure 1) by the mid 2020's. LLISSE will accomplish its goals by leveraging high-temp electronics, sensors, power, and communications. Instruments/sensors are being developed concurrent with the small lander itself. These science sensors target the following key Venus Exploration Analysis Group (VEXAG) questions: better knowledge of super-rotation of the atmosphere (Goal 1, Objective B), the climate and its evolution (Goal 1, Objective B), and surface — atmosphere interaction/weathering (Goal 3, Objective B).

Table 1. LLISSE Science Objectives, Notional concept of the Long-Life In-situ Solar System Explorer Venus Lander

Decadal Survey Goals	LLISSE Science Objectives	Measurements	Instrument Requirements
A) Define the current climate on the terrestrial planets	1) Acquire temporal meteorological data	Measurement of p, T, u, v and light	3-axis wind sensor measurements, radiance
	2) Estimate momentum exchange between the surface and the atmosphere	Same as above	Same as above
B) Understand chemistry of the middle, upper and lower atmosphere	3) Determine the key atmospheric species at the surface over time	Measure the abundance of gases H_2O, SO_2, CO, HF, HCl, HCN, OCS, NO, O_2	Chemical sensor measurements
Determine how solar energy drives atmospheric circulation and chemical cycles	4) Determine the rate of solar energy deposition at the Venus surface	Measure incident and reflected solar energy	Measurements of radiance

Fig. 1. The purpose of this briefing is to provide an update on the develop status of LLISSE, and its enabling capabilities

LLISSE SUMMARY/OVERVIEW:

The LLISSE project includes the design and demonstration of a prototype instrument suite and supporting systems to function at the surface conditions of Venus and communicate periodic measurements of temperature, pressure, wind velocity and direction, atmospheric chemical composition, and solar radiation to an orbiter [7] (see Figure 1). Measurements are taken only while transmissions are occurring. Lander life is selected so that duration covers a Venus day-light period and at least one terminator, the goal of LLISSE is to operate for approximately 60 Earth days. In the configuration envisioned for Venera-D, LLISSE will have an expected mass of ~10 kg and is expected to be attached to the exterior of the main Venera-D lander.

LLISSE DEVELOPMENT STATUS:

LLISSE system operation depends on high temperature electronics based on SiC materials and have shown extended operation in Venus relevant conditions [4,5]. These circuits continue to be upscaled in complexity and have seen ~2 order magnitude improvement through the LLISSE project. Electronics have demonstrated successful operations in simulated Venus conditions without any environmental protection [8]. The complexity of the circuitry in the current design cycle is of the order needed to accomplish LLISSE goals. The integrated circuit capability enables a wide range of very compact onboard mission electronics, including sensor signal amplification, digitization, and wireless transmission integrated circuits [4, 5].

LLISSE development includes ongoing iterations of design and test and evolving the core components of the LLISSE system. Progress continues to be made on the sensor systems for surface wind speed, temperature and pressure, as well as specific sensors for atmospheric chemical composition. Viability of each sensor approach has been shown although sensors are at differing levels of matureity due to complexity or the amount time in the development cycle.

The development of other LLISSE components is also progressing. For example, a high temperature battery is in development and stable chemistries have been identified. Life testing at cell levels are nearing the desired life goals for Venus conditions. Further, communication system designs including transmitter components and antennas are maturing in the development process.

REFERENCES:

[1] Venus Exploration Analysis Group reports. 2009–2011. reports/archive.
[2] National Research Council. Vision and Voyages for Planetary Science in the Decade 2013–2022. The National Academies Press, 2011. URL: https://doi.org/10.17226/13117.
[3] Venus Flagship Mission Study. 2009.
[4] Neudeck P. et al. Prolonged silicon carbide integrated circuit operation in Venus surface atmospheric conditions // AIP Advances. 2016. URL: http://aip.scitation.org/doi/10.1063/ 1.4973429.
[5] Spry D. et al. Presented at 2017 Intern. Conf. Silicon Carbide and Related Materials. Sept. 17–22. Washington, DC. To appear in Mat. Sci. Forum. 2018.
[6] Kremic T. 2017. GEER Status Update, VEXAG presentation: https://www.lpi.usra.edu/vexag/ meetings/archive/vexag_15/presentations/31-Kremic-GEER.pdf.
[7] Kremic T. et al. 2017. Long-Lived In-Situ Solar System Explorer. VEXAG presentation located at: https://www.lpi.usra.edu/vexag/meetings /archive/vexag_15/presentations/8-Kremic-LISSE.pdf.
[8] http://www.sciencemag.org/news/2017/11/armed-tough-computer-chips-scientists-are-ready-return-hell-venus, and publication in preparation.
[9] Courtesy of Makel Engineering, Inc.

VENUS, AN ASTROBIOLOGY TARGET

S. S. Limaye and colleagues
University of Wisconsin, SSEC, 1225 West. Dayton Street, Madison, Wisconsin 53706, USA (*sslimaye@wisc.edu*)

KEYWORDS:
Venus, cloud habitability, astrobiology, exoplanets

INTRODUCTION:
Assessment of available data and models of Venus reveal some gaps and assumptions about of our knowledge and understanding of the cloud cover of Venus considering that it presently harbors a potential habitable zone. We propose a four-fold theme for the exploration of Venus as an astrobiology target — (i) investigations focused on the likelihood that liquid water existed on the surface in its past leading to a potential for the origin and evolution of life, (ii) investigations into the potential for habitable zones within Venus' clouds and Venus-like atmospheres, (iii) theoretical investigations into how active aerobiology may impact the radiative energy balance of Venus' clouds and Venus-like atmospheres, and (iv) application of these investigative themes towards better understanding the atmospheric dynamics and habitability of exoplanets. The proximity of Venus to Earth, guidance for exoplanet habitability investigations, access to the cloud habitable layer and surface for in-situ extended measurements, make the planet a very attractive target for near term astrobiological exploration.

The rationale for considering Venus for astrobiology exploration is discussed in greater detail by [1].

REFERENCES:
[1] Limaye S. S. et al. Venus, an astrobiology target. Submitted to Astrobiology. 2020.

A TEMPERATE CLIMATE HISTORY OF VENUS

M. J. Way[1,2]
[1] *NASA/Goddard Institute for Space Studies, 2880 Broadway, New York, New York, USA (michael.way@nasa.gov)*
[2] *Theoretical Astrophysics, Department of Physics & Astronomy, Uppsala University, Uppsala, Sweden*

KEYWORDS:
Habitability, Volatile Cycling, Volcanism

INTRODUCTION:
Today Venus presents us with a hothouse world whose origins remain shrouded in mystery and ambiguity. Two competing visions rule the scientific discourse today. In one Venus has been bone dry for the past 4+ billion years having lost all of its water during a long magma ocean phase [1]. In the second Venus had a short-lived magma ocean phase like Earth, condensable water on its surface and a period with habitable conditions of unknown length [2,3]. In this work we focus on the second more optimistic view of Venus backed by what little observational data we have and via a series of 3-D general circulation model experiments. We use Earth as a guide to many of our choices since its shares a similar mass, density and likely geochemical composition. We show that Venus could have had habitable conditions throughout much of its history. We also emphasize that increasing solar luminosity through time is not the primary driver of dramatic climate change.

We hypothesize that Venus went through three post-magma ocean evolutionary changes in its history (See Figure 1).

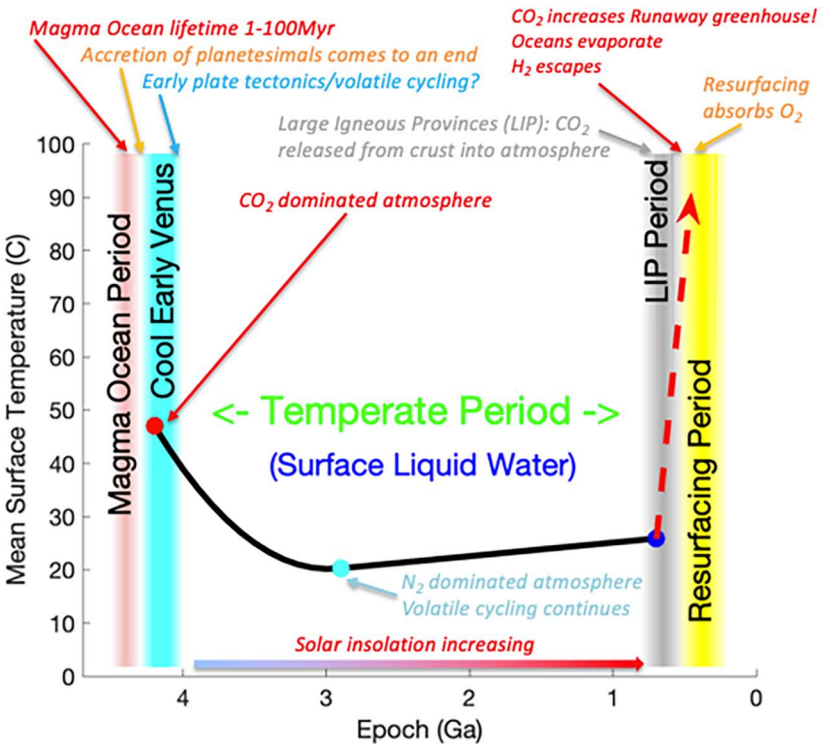

Fig. 1.

1. A period of temperate conditions whose length is currently impossible to estimate. Our General Circulation Model simulations show Venus could be temperate as long as 3 billion years. Volatile cycling akin to that of subductive plate tectonics is required, as it is on Earth, to keep the climate stable over geological time scales.

2. A transition period where large scale volcanism takes place akin to that of Large Igneous Provinces (LIPs) on Earth. These LIPs would release large quantities of CO_2 previously locked up in crustal units. This CO_2 would in turn drive the planet into an extreme moist or runaway greenhouse state. Much of its water would be lost via hydrogen escape to space over possibly 100s of millions of years. Plate tectonics would shut down without surface water, preventing any further volatile cycling.
3. A final period where the planet would resurface nearly 80% of its surface through widescale volcanism we now see as the large basaltic flats. The oxygen remaining in the atmosphere from the oceans would in turn be absorbed by this period of large-scale volcanism over 100s of millions of years. This explains why Venus presently has very little oxygen in its atmosphere – a long standing problem with the temperate Venus scenario.

We will discuss the many simulations performed, the assumptions behind our choices and the observational requirements needed to test this hypothesis.

REFERENCES:

[1] Hamano K., Abe, Y, Genda, H. Emergence of two types of terrestrial planet on solidification of magma ocean. // Nature 2013. V. 497. P. 607.
[2] Way, M. J., Del Genio A.D., et al. Was Venus the first habitable world of our Solar System? // Geophysical Research Letters, V. 43. P. 8376–8383 https://doi.org/10.1002/2016GL069790
[3] Way, M. J., Del Genio A.D. Venusian Habitable Climate Scenarios: Modeling Venus Through Time and Applications to Slowly Rotating Venus-Like Exoplanet // Journal of Geophysical Research Planets. 2020. V. 125, https://doi.org/10.1029/2019JE006276

THE YOUNG VOLCANIC RISES AS SUITABLE LANDING SITES FOR FUTURE VENUS MISSIONS: SCIENTIFIC RELEVANCE IN THE DEBATE BETWEEN THE EQUILIBRIUM AND CATASTROPHIC RESURFACING HYPOTHESES

P. D'Incecco[1], I. Lopez[2], J. Filiberto[3], G. Komatsu[1]
[1] *International Research School of Planetary Sciences, Università d'Annunzio, Viale Pindaro 42, 65127 Pescara, Italy* (*piero.dincecco@unich.it*)
[2] *Universidad Rey Juan Carlos, Madrid, Spain*
[3] *Lunar and Planetary Institute, USRA, 3600 Bay Area Blvd Houston, TX 77058*

KEYWORDS:
Venus, geology, volcanism, stratigraphy, landing sites

INTRODUCTION:
During the last decades, the geologic history of Venus has been characterized by a major debate on whether the planet underwent a catastrophic or equilibrium resurfacing. While the random global distribution of impact craters indicates that a global rejuvenation of the crust took place about 300–600 Myr ago [1, 2], which supports a catastrophic resurfacing [3]; the number and non-random distribution of volcanoes on Venus seem to be in contrast with this hypothesis [1] and favor instead a more steady (equilibrium) resurfacing.

GEOLOGIC DATING OF VOLCANIC RISES:
The VIRTIS instrument of the Venus Express mission observed high 1 mm emissivity anomalies which indicate the presence of chemically unweathered lavas at Imdr, Themis, and Dione Regiones [4, 5]. The emissivity anomalies observed by VIRTIS are likely due to the occurrence of recent volcanic activity [4, 5].

Recent laboratory studies have demonstrated that basalt and olivine would take only weeks to months to oxidize under Venus-like surface conditions [7, 8], while weathering of pyroxene would take longer time [8]. The results of those studies imply that volcanism over areas with values of 1 mm emissivity comparable to those of Imdr, Themis and Dione Regiones may be actually no more than a few years old [7, 8].

Compared to the other volcanic rises of Venus, Imdr Regio is the one with the smallest amount of associated volcanics, with an approximate volume of $48 \cdot 10^6$ km^3 [4]. This region is also associated with geologically recent tectonic (as well as volcanic) activity [9].

Wrinkle ridges predate the formation of the topographic swell and have been uplifted for about 200 m [4]. The density of wrinkle ridges at Imdr is smaller than in the neighboring areas [6]. One possibility is that part of the wrinkle ridges within Imdr Regio has been covered by subsequent volcanic eruptions.

IMDR, THEMIS AND DIONE REGIONES AS SUITABLE LANDING SITES:
Venus is characterized by a dry atmosphere, while it is still an object of debate whether its mantle is comparably dry [1, 2, 10, 11]. Understanding whether the most recent surface volcanic deposits on Venus formed from dry or wetter magmas would provide important clues about the current presence or absence of a weak Earth-like asthenosphere. A hydrated mantle might in fact favor the presence of a weak asthenosphere and a more steady (equilibrium) volcanic resurfacing, while dry conditions would cause overheating of the mantle with potentially consequent catastrophic resurfacing. Recent studies have observed the presence of pyroclastic deposits on Venus [12, 13], a fact that might imply the localized presence of volatiles in the mantle, however the volatiles maybe in the form of CO_2 rather than water. Furthermore,

reanalyzes from Venera and Vega landers, compared with experiments for terrestrial magmas also suggests dominance of CO_2 for the Venera-13 landing site, but did not rule out some amount of water in the interior as well [11].

A lander would unveil the chemical properties of the surface material of potentially young volcanic rises such as Imdr, Themis, and Dione Regiones, and comparing the chemistry of those lavas with similar magmas on Earth and experimental results [11, 14, 15] can constrain the first order volatile content of such magmas — either hydrous or not.

The chemical composition and volatile content of possibly young lavas would provide unprecedented information about the rheology of the Venusian mantle, and the evolution of both the mantle and the crust.

REFERENCES:

[1] Strom R. G., Schaber G. G., Dawson D. D. The global resurfacing of Venus // J. Geophysical Research. 1994. V. 99. Iss. E5. P. 10899–10926. doi:10.1029/94JE00388.
[2] Nimmo F., Mckenzie D. Volcanism and tectonics on Venus // Annu. Rev. Earth and Planetary Sciences. 1998. V. 26. P. 23–51. doi:10.1146/annurev.earth.26.1.23.
[3] Turcotte D. L., Morein G., Roberts D., Malamud B. D. Catastrophic Resurfacing and Episodic Subduction on Venus // Icarus. 1999. V. 139. Iss. 1. P. 49–54. http://dx.doi.org/10.1006/icar.1999.6084.
[4] Smrekar S. E. et al. Recent hot-spot volcanism from VIRTIS Emissivity data // Science. 2010. V. 328. Iss. 5978. 605–608.
[5] D'Incecco P., Mueller N., Helbert J., D'Amore M. Idunn Mons on Venus: location and extent of recently active lava flows // Planetary and Space Science. 2017. V. 136. P. 25–33. http://dx.doi.org/10.1016/j.pss.2016.12.002.
[6] Bilotti F., Suppe J. The Global Distribution of Wrinkle Ridges on Venus // Icarus. 1999. V. 139. Iss. 1. P. 1372157. http://dx.doi.org/10.1006/icar.1999.6092.
[7] Filiberto J., Trang D., Treiman A. H., Gilmore M. S. // Science Advances. 2020. V. 6. Art. eaax7445.
[8] Cutler K. S., Filiberto J., Treiman A. H., Trang D. Experimental Investigation of Oxidation of Pyroxene and Basalt: Implications for Spectroscopic Analyses of the Surface of Venus and the Ages of Lava Flows // The Planetary Science J. 2020. V. 1(1). 10 p.
[9] D'Incecco P., López I., Komatsu G., Ori G. G., Aittola M. Local stratigraphic relations at Sandel crater, Venus: Possible evidence for recent volcano-tectonic activity in Imdr Regio // Earth and Planetary Science Letters. 2020. V. 546. Art. 116410. URL: https://doi.org/10.1016/j.epsl.2020.116410; https://doi.org/10.1016/j.epsl.2020.116410.
[10] Karimi S., Dombard A. J. Studying lower crustal flow beneath Mead basin: implications for the thermal history and rheology of Venus // Icarus. 2017. V. 282. P. 34–39.
[11] Filiberto J. Magmatic diversity on Venus: Constraints from terrestrial analog crystallization experiments // Icarus. 2014. V. 231(0). P. 131–136.
[12] Ghail R. Rheological and petrological implications for a stagnant lid regime on Venus // Planetary and Space Science. 2015. V. 113–114. P. 2–9. URL: http://dx.doi.org/10.1016/j.pss.2015.02.005.
[13] Ghail R., Wilson L. A pyroclastic flow deposit on Venus // Volcanism and Tectonism Across the Inner Solar System / eds. Platz T., Massironi M., Byrne P. K., Hiesinger H. L.: Geological Society, 2015. V. 401. P. 97–106. URL: http://dx.doi.org/10.1144/SP401.1.
[14] Kargel J. S., Komatsu G., Baker V. R., Strom R. G. The Volcanology of Venera and VEGA Landing Sites and the Geochemistry of Venus // Icarus. 1993. V. 103(2). P. 253–275.
[15] Treiman A. H. Geochemistry of Venus surface: Current limitations as future opportunities // Exploring Venus as a Terrestrial Planet / eds. L. W. Esposito, E. R. Stofan, T. E. Cravens. 2007. P. 250. Geophysical Monograph Ser.

VOLCANIC HISTORY OF THE DERCETO CORONA EVENT, ASTKHIK PLANUM, VENUS

L. M. MacLellan[1], R. E. Ernst[1,2], H. El Bilali[1], R. C. Ghail[3]
[1] *Department of Earth Sciences, Carleton University, 1125 Colonel By Drive, Ottawa, Ontario K1S5B6, Canada* (*laurenmaclellan@cmail.carleton.ca; Richard.Ernst@Carleton.ca*)
[2] *Faculty of Geology and Geography, Tomsk State University, 36 Lenin Avenue, Tomsk 634050, Russia*
[3] *Department of Earth Sciences, Royal Holloway University of London, Egham, United Kingdom*

KEYWORDS:
Venus, planetary geology, flood basalt, Derceto Corona, Kallistos Vallis, Ubastet Fluctus, Hanghepiwi Chasma, Vaidilute Rupes, caldera

INTRODUCTION:
Detailed 1:500,000 mapping of a major-scale volcanic centre on Venus provides a complementary view to that of terrestrial large igneous provinces (LIPs): on Venus, the surface flood basalt relationships are preserved owing to the absence of erosion, but the plumbing system is only indirectly revealed. Herein we report on detailed mapping of the southern portion of the major Derceto Corona (DC) volcanic event located in southern Astkhik Planum (our map area: 1,920,000 km^2) using full resolution (75 m/pixel) Magellan SAR images [1].

SUMMARY OF VOLCANIC HISTORY:
Thirty-seven distinct lava flow units together with those associated with grabens were mapped and grouped into eight main and multiple minor volcanic stages. On the east side of DC, the Eastern Stage flows extend for 750 km and are fed from NNW-NW-trending grabens (overlying dykes) and from more local (small shield) sources. The Kallistos-Ubastet Stage consists of the 1200 km long Kallistos Vallis and its flow field containing the overflow Ubastet Fluctus pulse, are all fed from an irregular chamber 30×10 km long on the south side of DC. Lavas of both the Eastern Stage and the Kallistos-Ubastet Stage flowed over a section of Vaidilute Rupes (escarpment) and spread out on its eastern side. A Western Stage flow field (>1000 km long) was sourced from the elliptical fracture system of DC; after flowing downslope it swings almost 180 degrees to follow a pre-existing rift, Hanghepiwi Chasma. On the north side of DC, a laterally propagating NE-trending graben set (overlying a dyke swarm) produces a 90 km long and 5 km wide "Great Dyke" that feeds a flow field.

PLUMBING SYSTEM LINKS:
Two flow stages (Western Stage-1 and the Great Dyke/NE-trending dyke swarms) are inferred to be fed from the elliptical-shaped down-sag caldera collapse of DC. The Eastern Stage flows are fed mostly from a region to the east of the corona, whereas the rest of the flows are fed via an older regional NW-trending graben system that was reused for magma transport from underlying chambers or laterally from the collapse of the central chamber. The total areal extent of the flows is 534,650 km^2 with an inferred volume of 26,730 km^3 (assuming an average flow thickness of 50 m); this is consistent with LIP-scale area and also with LIP-scale volume if the expected underlying plumbing system was catalogued.

REFERENCES:
[1] MacLellan L. M., Ernst R. E., El Bilali H., Ghaili R. Volcanic history of the Derceto large igneous province, Astkhik Planum, Venus // Earth-Science Reviews (submitted).

TESSERAE ON VENUS MAY PRESERVE EVIDENCE OF FLUVIAL EROSION

R. E. Ernst[1,2], S. Khawja[1], C. Samson[1], P. K. Byrne[3], R. C. Ghail[4], L. M. MacLellan[1]

[1] *Department of Earth Sciences, Carleton University, 1125 Colonel by Drive, Ottawa, Ontario K1S 5B6, Canada* (*Richard.Ernst@Carleton.ca*)

[2] *Faculty of Geology and Geography, Tomsk State University, 36 Lenin Avenue, Tomsk 634050, Russia*

[3] *Department of Marine, Earth, and Atmospheric Sciences, North Carolina State University, Raleigh, NC 27695, USA*

[4] *Department of Earth Sciences, Royal Holloway University of London, Egham, United Kingdom*

KEYWORDS:
Tesserae, plains volcanism, fluvial erosion, climate change, paleo-valley

INTRODUCTION:
Fluvial erosion is absent on Venus at present, precluded by a high surface temperature of ~450° C. This interpretation is supported by the abundance of uneroded volcanic flows. Recent climate modeling, however, has suggested the possibility of Earth-like climatic conditions on Venus for much of its earlier history, prior to a catastrophic runaway greenhouse effect.

FLUVIAL EROSION IN TESSERAE:
We observe that within some tesserae — the stratigraphically oldest and most complex geological units—there are valleys that are morphologically similar to those resulting from fluvial erosion on Earth. Given poor topographic resolution we use an indirect technique to recognize paleo-valleys, observing the pattern of lava flooding of the margins of tesserae by adjacent plains volcanism. Eight areas were studied (1 in Salus, 5 in Manatum and 2 in Ananke tesserae), and these reveal paleo-valley patterns that are morphologically similar to 5 of the 6 main types of terrestrial stream patterns. We attribute these patterns to a combination of the initial rock types (including possible layered sequences of sedimentary and volcanic rocks [1]), affected by folding and faulting, followed by erosion by fluvial (and, to a lesser extent, wind) action. This proposed fluvial erosion in tesserae provides support for climate models that suggest cooler conditions prevailed on Venus in the past, before the onset of major effusive volcanism that gives the surface its relatively young average model age.

FUTURE MISSIONS:
Higher-resolution radar images and topographic data acquired by future missions to Venus will provide the basis for testing the hypothesis of fluvial reshaping of the enigmatic tesserae.

REFERENCES:
[1] Byrne P. K., Ghail R. C., Gilmore M. S., Şengör A. M. C., Klimczak C., Solomon S. C., Senske D. A., Whitten J. L., Khawja S., Ernst R. E. Venus tesserae feature layered, folded, and eroded rocks // Geology. 2020 (in press).

FIRST EXPERIMENTS WITH A MINIATURIZED 3D HEAT FLUX SENSOR FOR PLANETARY REGOLITH

M. Domínguez-Pumar[1], J. A. Rodríguez-Manfredi[2], V. Jimenez[1], S. Bermejo[1], J. Pons-Nin[1]
[1] *MNT-Group. Polytechnic University of Catalonia*, *Barcelona*, *SPAIN*
[2] *Centro de Astrobiología* (*INTA-CSIC*), *Torrejón de Ardoz*, *SPAIN*
(*manuel.dominguez@upc.edu*)

KEYWORDS:
Heat flux sensor, regolith, thermal inertia, planetary exploration, miniaturized sensor

INTRODUCTION:
The objective of this work is to present the first experimental and analytical results obtained with a 3D heat flux (HF) sensor for regolith. The sensor provides heat flow magnitude and angle in 3 dimensions.

The sensor may provide information on the local thermal environment surrounding the lander. It may also be used to obtain the thermophysical properties of the regolith. Since the sensor is simple it may be used in particularly difficult planetary exploration, such as in the case of Venus. The potential limits in terms of accuracy are yet to be determined.

To the best knowledge of the authors, this is the first 3D heat flux sensor for regolith ever published.

SENSOR DESCRIPTION:
The sensor structure is based on a 3D wind sensor for Mars [1–2]. The sensor is a 10 mm diameter sphere composed of 4 equally shaped sectors, that are placed on two superimposed boards, which act as supporting structure and provide signal routing (see Figure 1, Top). A customized silicon die, which includes a Pt resistor, is attached to each sector in order to sense temperature and provide heating power. Finally, two additional dice are placed on the supporting boards in order to control the temperature at the core of the sphere. The sensor is operated at constant temperature, which must be above that of the surrounding regolith. Sensor information is retrieved from the power signals delivered to each one of the sectors. The incoming heat flux generates an asymmetry in the power signals of the sensor.

MAIN RESULTS:
An analytical solution of a conducting sphere buried in the regolith has been obtained. The solution shows that, for this geometry, the heat flux asymmetry generated on the surface is independent of the thermal conductivity of the surrounding regolith. This implies that the sensor is a heat flux sensor and not a temperature gradient sensor, which would therefore require an accurate estimation of the thermal conductivity of the regolith to obtain heat flux.

Fig. 1. Photograph of the 4-sector spherical sensor (10 mm diameter), before being wrapped and inserted into the regolith simulant

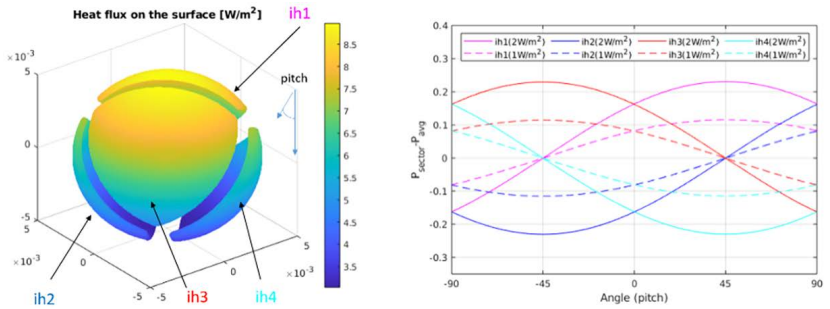

Fig. 2. Heat flux on the surface of the sphere for a thermal conductivity of the regolith of k_r = 0.003 W/(mK), ΔT = 10 K and two heat fluxes Q_0 = 1–2 W/m^2 (Left). Integral of the heat fluxes differences on each of the sectors over the average, for pitch rotations under the same conditions (Right)

By integrating the heat flux analytical solution on the surface of the sectors it is possible to obtain the power delivered at each sector for keeping the temperature constant. The average power in the sectors depends on the thermal conductivity of the regolith, as expected. On the other hand, the power differences between sectors are independent of the thermal conductivity of the regolith. This way, the optimal signals for inferring the heat flux modulus and angle are the differences between the power delivered at each sector and the average power delivered to all sectors.

Figure 2 shows results obtained from the analytical solution. Figure 2, left shows the heat flux at each point of the surface of the sphere, which depends on the average temperature overheat over the temperature of the surrounding regolith, DT, the thermal conductivity of the regolith, kr, and the incoming heat flux to be measured. Figure 2, right shows the power increase, predicted by the analytical solution, at each sector over the average in all sectors, for different angles and two vertical heat fluxes in the regolith: 1 or 2 W/m^2. This set of signals is independent of the thermal conductivity of the regolith.

EXPERIMENTAL RESULTS:

Experimental results have been obtained in a laboratory setup in which the heat flux could be controlled and the sensor rotated in order to analyze the sensor response to angle and magnitude. Glass microbeads of 40–70 mm have been used as regolith simulant. A thermopile was placed on the surface of the simulant to have an independent heat flux measurement. The sensor has been operated above the temperature of the surrounding regolith by approximately 6° C.

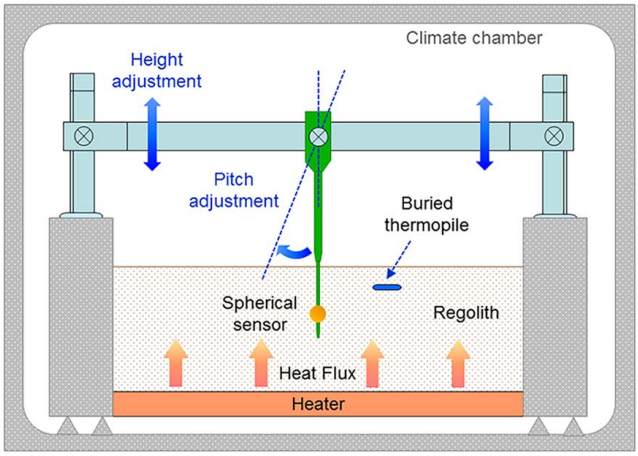

Fig. 3. Schematic of the experimental setup. The complete structure has been placed in a climate chamber. The temperature of the bottom plate allows to set different heat fluxes in the regolith

Figure 3 shows the evolution of the powers injected in the sectors for two heat fluxes magnitudes and different angles. The sensor behavior matches very well the expected response predicted by the analytical solution.

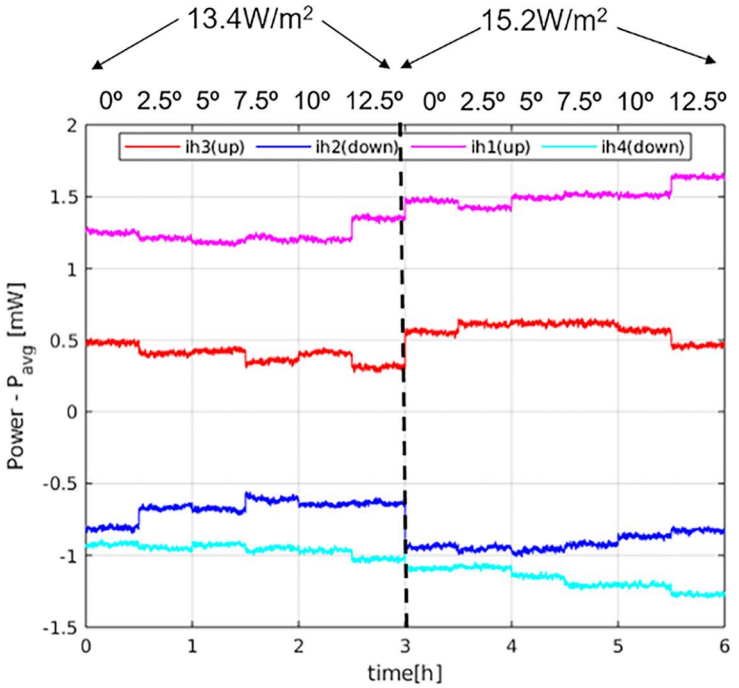

Fig. 4. Concatenation of 30 min time intervals in which a steady state has been achieved in a 170 h experiment. HF magnitude and angle are changed as a function of time

REFERENCES:

[1] Kowalski L. et al. (2016), IEEE Sensors Journal, 16, 1887–1897.
[2] Dominguez-Pumar M. et al. (2016), IEEE Trans. Ind. Electr., 64 (1), P. 664–673.

VENUS SURVEYOR FOR PLANETARY EXPLORATION RESEARCH (VESPER)

S. T. Port, T. DeMichael, D. Sadhukhan, I. Haskin, J. Jordan, C. Liebfried, J. Romanin, B. Rosenthal, S. Vivod, A. Wroblewski, S. Jansen, K. Martin, T. Kremic, G. Hunter
NASA Glenn Research Center, 21000 Brookpark Rd, Cleveland, OH 44135

KEYWORDS:
Venus, imaging system, surface, geology, morphology, weathering, camera, imager, harsh environment

INTRODUCTION:
The surface of Venus has only ever been imaged six times by four different landers [1–2]. The final image was obtained by Venera 14 in 1982, nearly 40 years ago [2]. These low-resolution images provided researchers with the first evidence of weathering on Venus [1–2]. Such evidence included fine particles on the surface and rocks with pitting and rounded edges [1–2]. Venera 9's images showed the presence of mass wasting [1]. However, many details may have been lost due to the low-resolution of these cameras [1–3].

Over the past 40 years advances in technology have allowed researchers to send multiple landers equipped with high-resolution cameras to Mars, including the Mars Science Laboratory mission's Curiosity rover which can take images with a resolution as high as 150 micron/pixel at 2 meters [4]. For Venus, new, higher resolution images are essential in order to characterize different rock types and identify chemical and mechanical weathering processes that may have been unobservable by past landers. This data could be obtained using a more advanced imager system with a resolution higher than the original Venera cameras encapsulated inside a vessel able to survive for several minutes at Venus surface conditions. Such a concept is the core of this paper.

INSTRUMENT:
The Venus Surveyor for Planetary Exploration Research (VeSPER) camera system is a short-lived imaging system that can be attached to a Venus lander. The camera was originally designed to be externally attached to the Seismic and Atmospheric Exploration of Venus (SAEVe), a mission concept involving two Venus landers. However, due to its small size, VeSPER can be attached to any future lander. VeSPER is designed to withstand Venus surface conditions for 90 minutes. To date, VeSPER has only been tested in a furnace at Venus temperature (460°C), but ambient pressure and in air. In the future, VeSPER will undergo further testing under Venus conditions, including possible testing in the Glenn Extreme Environment Rig (GEER) at Venus temperature, pressure, and atmospheric chemical composition.

MISSION OVERVIEW:
VeSPER was designed relevant to SAEVe to obtain five images of Venus at wavelengths between 550–1020 nm. These images include two images taken during descent (~5 km and 400 m from the surface) and three images from the surface. The motive behind the two images during descent is to ascertain the landing site morphology. One of the instruments onboard SAEVe is a seismometer. Thus, the next two images taken by VeSPER will be of the ground before and after the deployment of the seismometer to check instrument coupling. These images will be used not only to observe where the seismometer has landed, but to also take higher quality images of the surface than the images obtained by the Venera landers. These images can be used to further understand the composition and mechanical and chemical weathering processes occurring on Venus. The last image taken by VeSPER will be of the horizon. This image will be used to study the topography and morphology of the surface.

FUTURE WORK:
As mentioned previously, VeSPER has not been exposed to Venus pressure or atmospheric chemical composition. Future experiments at these condi-

tions will be completed with possible testing in the GEER located at NASA Glenn Research Center. Further advancements are planned to extend the lifetime and the performance of the system (such as improvements in image compression and transfer). These advancements would allow for the acquisition of additional images of the surface of Venus.

REFERENCES:

[1] Florensky C. P., Ronca L. B., Basilevsky A. T. et al. The surface of Venus as revealed by Soviet Venera 9 and 10. // Geological Society of America Bulletin. 1977. V. 88. P. 1537–1545.
[2] Basilevsky A. T., Kuzmin R. O., Nikolaeva O. V. et al. The surface of Venus as revealed by the Venera landings: Part II // Geological Society of America Bulletin. 1985. V. 96. P. 137–144.
[3] Garvin J. B., Mouginis-Mark P. J., Head J. W. Characterization of Rock Populations on Planetary Surfaces: Techniques and a Preliminary Analysis of Mars and Venus // The Moon and Planets. 1981. V. 24. P. 355–387.
[4] Bell J. F., Godber A., McNair S. et al. The Mars Science Laboratory Curiosity rover Mastcam instruments: Preflight and in-flight calibration, validation, and data archiving // Earth and Space Science. 2017. V. 4. P. 396–452.

TARGETS OF HIGH RESOLUTION RADAR ANALYSIS ON VENUS FOR THE ENVISION MISSION

A. Kereszturi
Konkoly Observtory, *CSFK*, *H-1121 Budapest*, *Konkoly Thege 15-17*, *Hungary*
(*kereszturi.akos@csfk.mta.hu*)

KEYWORDS:
Venus, EnVision mission, geology, geomorphology, radar

INTRODUCTION

Range of questions on the geological history of Venus could be answered by high resolution radar dataset from future missions, like the planned EnVision ESA mission [1, 2]. Related example topics are listed in this work.

METHODS

To evaluate the possibility of identifying candidate surface features on Venus in the future, information on small-scale surface features from Earth based radar observations (Space Shuttle base radar data — SRTM) was used, comparing to already observed surface features of Venus. Using the experiences gained by the author during the compilation of the *Encyclopedia of planetary landforms* for Springer [3] important knowledge gaps could be identified, where radar morphology could identify certain surface features and thus clarify some aspects of the geological history.

RESULTS

Surface features, below the spatial resolution of Magellan data, but above the planned resolution of EnVision were surveyed, among them some, which related to major questions are presented in Table 1.

Table 1. Candidate surface features could be identified by detailed radar survey

feature type	expected characteristics	inferred findings
tesserae	folding, depositional and lava flow features	formation conditions, origin, timing of old tectonic events
signatures of ancient ocean	possible abrasion features at high elevation edges of tesserae	link to planetary geological history and climatic changes
pyroclastic deposits	evaluation of morphology, location, elevation and age of pyroclastic deposits	estimated volatile content, its change along with time, threshold elevation change along with atmospheric pressure change
lava plains	survey of highly deformed craters, stratigraphy of flows	reconstruction of catastrophic resurfacing
100 m scale lava channel features	reconstruction of multiple flow episodes and viscosity	reconstruction of embayment and global resurfacing
freshmost lava flow morphology	suggestion on viscosity, accurate stratigraphy	lava chemistry, comparison to older lavas, timing sequence of activity
height dependent weathering morphology	erosion / deposition at different elevation, current role of pressure and wind, high altitude condensation	surface modification and weathering, contribution to the understanding of chemical cycling
identification of sedimentary structures	layering, stratigraphy, classification by morphology	connection to geological history, targeting future landers

The example surface features, which could be potentially identified by EnVision radar data support the understanding of the following major questions:

1. Tesserae: origin by reconstruction of lava flows, deformation history.
2. Signs of ancient oceans: searching for abrasion features at high elevations.

3. Reconstruction of global resurfacing by high resolution stratigraphy.
4. Evaluation of unique surface modifications by sedimentary analysis.

Several unique new features might be observable by future radar research, including remnants of old climatic regime different from the current one. Sedimentary features are almost missing from the earlier observations with few possible exceptions [4] where in the identification beside the radar based morphology polarimetry could also help with the identification of low density face material [5], and correlation with subsurface radar sounder results (10 m vertical resolution) also improves the work.

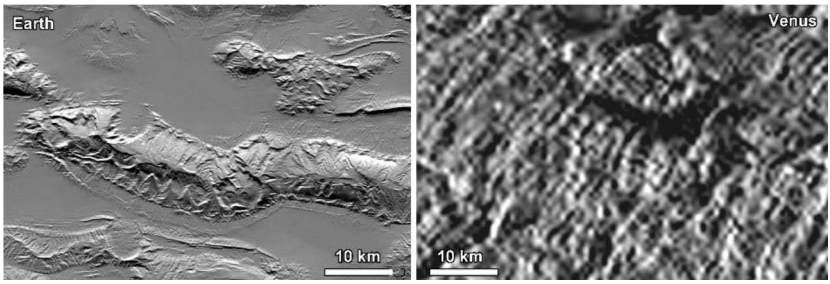

Figure 1. Potential Earth based example on the expected improvement in the spatial resolution of radar images. Right: Magellan based radar image of Laima Tessera (51.5° N, 48.2° E, NASA/JPL). Left: SRTM shaded relief radar image of Zagros Mountain. The folded sedimentary layers could be identified in the image of the Earth with plastic salt flow feature. The SRTM image has only twice worse spatial resolution than expected from EnVision

ANSWERS FROM ENVISION MISSION

The EnVision is a proposed ESA orbiter mission equipped with S-band Synthetic Aperture Radar (VenSAR), a Subsurface Radar Sounder (SRS) and VenSpec, spectrometers for rough surface composition VenSpec-M (Infrared Imager). The expected spatial resolution of radar data ranges from 30 m regional coverage to 1–5 m images of specific targeted surveys [6].

Stereo radar based imaging and nadir altimetry will improve topographic information [7] what would be important to identify sedimentary units and their stratigraphic relation (see an example in Figure 1). Better identification of grain transport modes [8], reconstruction of multiple flow episodes at channels [9] will be possible, as well as the understanding the origin of plains, identify subunits and stratigraphic connection to channels and lava flows [10] will enrich the knowledge on the geological history.

CONCLUSION

With the radar survey of the proposed EnVision ESA mission, improvement of two orders of magnitude relatively to Magellan images are expected at selected areas. Survey of high resolution SRTM data will provide examples for the radar based appearance of such small (100 m scale) features, which could improve the understanding the major questions in the geology of Venus, as well as answers to fundamental questions on the evolution of rocky planets are expected.

ACKNOWLEDGEMENT:

This work was supported by the GINOP-2.3.2-15-2016-00003 fund of NKFIH.

REFERENCES:

[1] de Oliveira M. R. R., Gil P. J. S., Ghail R. A novel orbiter mission concept for Venus with the EnVision proposal // Acta Astronautica 2018. V. 148. P. 260–267.
[2] Wilson C., Ghail R., Widemann T., Titov D., Bruzzone L., Helbert J., Carine V. A., Marcq E., Dumoulin C., Rosenblatt P. Envision M5 Venus orbiter proposal. EPSC-DPS2019-1611. 2019.
[3] Encyclopedia of Planetary Landforms / eds. Hargitai H., Kereszturi A. New York: Springer, 2015. 2460 p.
[4] Senske D. A., Plaut J. J. The Tellus Region of Venus: processes in the formation and modification of tessera terrain // Lunar and Planetary Science Conference. 2000. V. 31. Art. 1496.
[5] Carter L.M Using Radar Polarimetry to Understand Surface Deposits on Venus // Paris Conference. 12–14 Feb. 2000.

[6] Ghail R. et al. EnVision — Understanding why most Earth-like planet neighbour is so different. ESA M5 proposal.. 2017
[7] Kieffer H. High Resolution Topography as a Constraint on Venus Tectonic Processes // Paris Conference. 12–14 Feb. 2000.
[8] Carpy S. et al. Sand Transport Regime on Venus: Analytical Approach // Paris Conference. 12–14 Feb. 2000.
[9] Komatsu G. Channels on Venus: What We Know Before Revisiting With EnVision // Paris Conference. 12–14 Feb. 2000.
[10] Gregg T. K. P. The Importance of Plains // Paris Conference. 12–14 Feb. 2000.

LEAVES — A LOW-MASS ATMOSPHERIC SENSOR PLATFORM CONCEPT FOR DISTRIBUTED EXPLORATION AT VENUS

J. A. Balcerski[1], K. L. Jessup[2], G. W. Hunter[3], A. J. Colozza[4], M. G. Zborowski[4], D. A. Makel[5]
[1] *Ohio Aerospace Institute, Cleveland, OH (jeffreybalcerski@oai.org)*
[2] *Southwest Research Institute, Boulder, CO*
[3] *NASA Glenn Research Center, Cleveland, OH*
[4] *HX5, LLC, Cleveland, OH*
[5] *Makel Engineering, Inc, Chico, CA*

KEYWORDS:
Venus, exploration, swarm, sensors, atmosphere, picosat, leaves

INTRODUCTION:
The LEAVES (Lofted Environmental and Atmospheric VEnus Sensors) architecture is a "swarm" approach to obtaining key, *in-situ*, Venus atmospheric data for exceptionally low cost and risk. This is made possible by an ultra-lightweight, passively-lofted, inexpensive atmospheric sensor package that can be deployed directly from orbit without an aeroshell and is sensitive enough to yield valuable new, transformative information on planetary atmospheres. LEAVES uniquely enables atmospheric sensing through combining miniaturized sensors, electronics, and communications on a lightweight physical "kite" that acts as a passive, drifting body when in the presence of a substantial planetary atmosphere, like the cloud-bearing upper and middle atmosphere of Venus. LEAVES utilizes components appropriate for Venus such as high precision, targeted, chemical species sensors [1, 2] which are now commercially available or have been matured to TRL 5–6 by other applications and programs (i. e. NASA SBIR and HOTTeCH).

PROBE DESIGN:
Comparison with other platforms:
- Single trajectory platforms (probes, dropsondes, landers): cover a range of altitudes, but need multiple (expensive) units to cover diverse local solar times.
- Cloud/Boundary layer aerial platforms (balloons, planes, dirigibles): cover a broad range of local solar times, but mainly over a limited ~20 km altitude range.
- LEAVES provides an opportunity to combine broad local time coverage (through multiple coordinated orbital deployments) and altitude coverage (by slow-descent gliding) which could allow redundancy in altitude, local solar time, and/or increased latitude coverage.

Each lightweight atmospheric probe is made of a ~100 g, high-drag structure and a 20 g science payload consisting of at least two highly-sensitive, chemical species sensors (e. g. SO_2 and CO at better than 1 ppm resolution), temperature and pressure sensors, 6-axis inertial measurement unit, a microprocessor, 400 MHz transmit-only radio, and coin cell battery power supply. The remarkably low ballistic coefficient of 0.173 allows for both a direct orbital deployment (i. e. without aeroshell) and a long duration period of science operations in Venus' atmosphere [3].

UNPRECEDENTED ATMOSPHERIC DATA:
During a host spacecraft's aerobraking or orbital science campaign, cohorts of a dozen or more probes are released from their compact, flat-packed storage unit at an altitude of ~150 km. If the carrier spacecraft is in a polar orbit, the deployment sequence can be timed to space out the probes over 10–20° of latitude. The LEAVES' orbit then decays over several days until they reach their target operational altitude of 100 km. For the next 9–10 hours, they each collect around 1 MB of data, comprised of > 1000 repeated sensor measurements. These data span 60 km of altitude (including the clouds) and 1500 km of lateral travel (roughly 30 degrees of longitude, assuming ascending and descending orbital deployment).

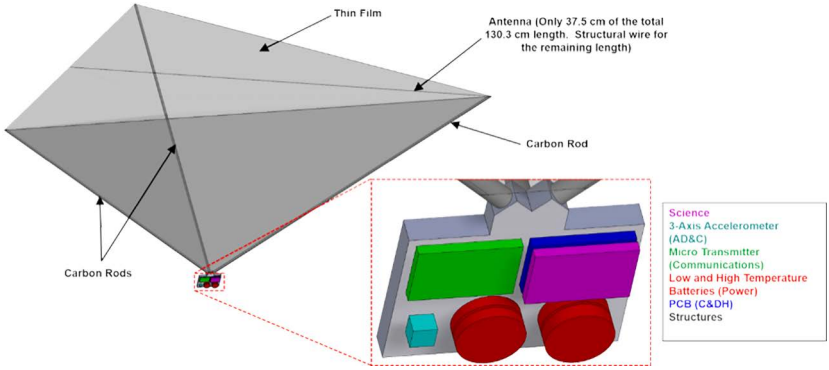

Fig. 1

APPLICATIONS TO VENUS EXPLORATION:

Current development is focused on environmental details (i. e. T, P, wind measurements along with atmospheric gas or aerosol abundances). Additional sensors that may be included on the LEAVES platform are: imagers functioning at optical or UV wavelengths, micron level imagers, and UV flux sensors. With adequate outfitting LEAVES could be an integral part of characterizing the properties of Venus' unknown UV absorber and ultimately identifying its composition and physical state as aerosol/gas/particle. In fact, with only slight modification multiple high-priority Venus atmospheric investigations could be enabled by the LEAVES platform including: density profiles of trace gases (SO_2, OCS and Cl_2) directly linked to the sulfur aerosol chemistry; the N_2 density gradient from ~100 km to 30 km [4, 5]; characterization of UV absorption variability relative to environmental conditions[6] as well as aerosol properties (density profiles, particle size and shape per altitude and/or local time); and characterization of relative abundance of organic and/or life supporting agents such as: CH_4, H_2O, P, and pH [7].

REFERENCES:

[1] Makel D., Carranza S., Venus Science Priorities for Laboratory Measurements Hampton, VA, 2015.
[2] Hunter G. , New Frontiers 4 Technology Workshop, Washington, DC, 2016.
[3] Balcerski J. A. et al., "LEAVES - Lofted Environmental Atmospheric Venus Sensors NIAC Phase I Final Report," 20190002495.
[4] Marcq E. et al., Nat. Geosci., vol. 6, no. 1, pp. 25–28, Jan. 2013.
[5] Peplowski P. N. et al., 51st LPS, 2020.
[6] Jessup K. L. , 49th LPS, 2018, The Woodlands, TX, 2018.
[7] Limaye S. S. , 16th Annual VEXAG Meeting, Laurel, MD, 2018

CLOUD LEVEL WINDS FROM VMC (VENUS EXPRESS) AND UVI (AKATSUKI) IMAGING

I. V. Khatuntsev, M. V. Patsaeva, A. V. Turin, L. V. Zasova
Space Research Institute RAS, Profsoyuznaya 84/32, 117997 Moscow, Russia (*khatuntsev@iki.rssi.ru*)

KEYWORDS:
Venus, atmosphere, dynamics, wind tracking techniques

INTRODUCTION:
Images of the day side of Venus obtained in the UV (365 nm) spectral range have maximum contrast (>30 %) due to dark cloudy details. These details, observed at the cloud tops (70±2 km), are formed by an unknown UV absorber. Digital tracking technique of contrasting details in the upper clouds provide important information about the cloud level circulation winds derived by a digital tracking technique from UV (365 nm) images captured by the Venus Monitoring Camera (VMC) onboard the Venus Express spacecraft from 2006 through 2013 were used to study the atmospheric circulation (see details in [1 – 3]). About $5 \cdot 10^5$ raw vectors were obtained from VMC images. After filtering we use about $1.9 \cdot 10^5$ vectors.

In December 2015, Akatsuki (JAXA) entered a highly elliptical orbit around Venus. The Ultraviolet Imager (UVI) onboard Akatsuki obtained a large number of UV (365 nm) images of Venus. Images obtained from first 100 orbits (12.2015–11.2018) were processed by us using the same digital tracking technique as VMC images. About 10^6 vectors were obtained from UVI images.

Thus, we can compare the results obtained, excluding the subjective factor of the processing technique used.

RESULTS:
The polar orbit of Venus Express with pericentre at the North pole provides optimal conditions for observations of the Southern hemisphere. For this reason, VMC observed mainly Southern hemisphere: from the equator to near-polar latitudes ~80°. The plane of the Akatsuki orbit is located near the plane of the equator of Venus (inclination is 3°), so UVI has the ability to observe both hemispheres in the range of latitudes from –70° to +70°.

The average fields of zonal and meridional velocities demonstrate solar related variations. Figure 1 shows the average zonal and average meridional velocities in latitude — local time coordinates obtained by averaging UVI and VMC data over the entire observation interval. The color scale is the same for both missions. In the Southern Hemisphere, the maximum of the mean zonal speed is observed in the afternoon: for VMC (~100 m/s) — at 15 h at latitude of –40°, associated with the middle latitude jet, for UVI (105 m/s) — 16 h 30 m at latitude of –35°. Moreover, in the case of UVI, the evening maximum speed extends north to latitude of +35°. The other connected to the solar related features may be in the case of VMC a maximum of the zonal wind speed reaching of 100 m/s in equatorial region at 8–10 h and minimum of less than 90 m/s at noon (the last associated also with Aphrodite Terre [3]). The meridional velocity component also shows structural identity and differences in detail. VMC detects a maximum meridional velocity of –10 m/s ("–" indicates flow transfer towards the South Pole) at 14–15 h at latitude of − 50°. UVI captures the maximum meridional velocity (− 9 m/s) at 12–13 h at latitude of –55°. In the Northern Hemisphere, a region of a maximum of +11 m/s is observed 13–14 h at latitude of +50°.

CONCLUSIONS:
The data on the circulation of the atmosphere of Venus on the cloud top level, obtained by VMC onboard Venus Express in 2006–2013 and UVI onboard Akatsuki in 2015–2018, require joint analysis. Throughout the entire observation period, the influence of thermal tide is detected. The structural differences in the mean velocity fields obtained by VMC and UVI indicate long-term variations in the circulation parameters and require careful analysis.

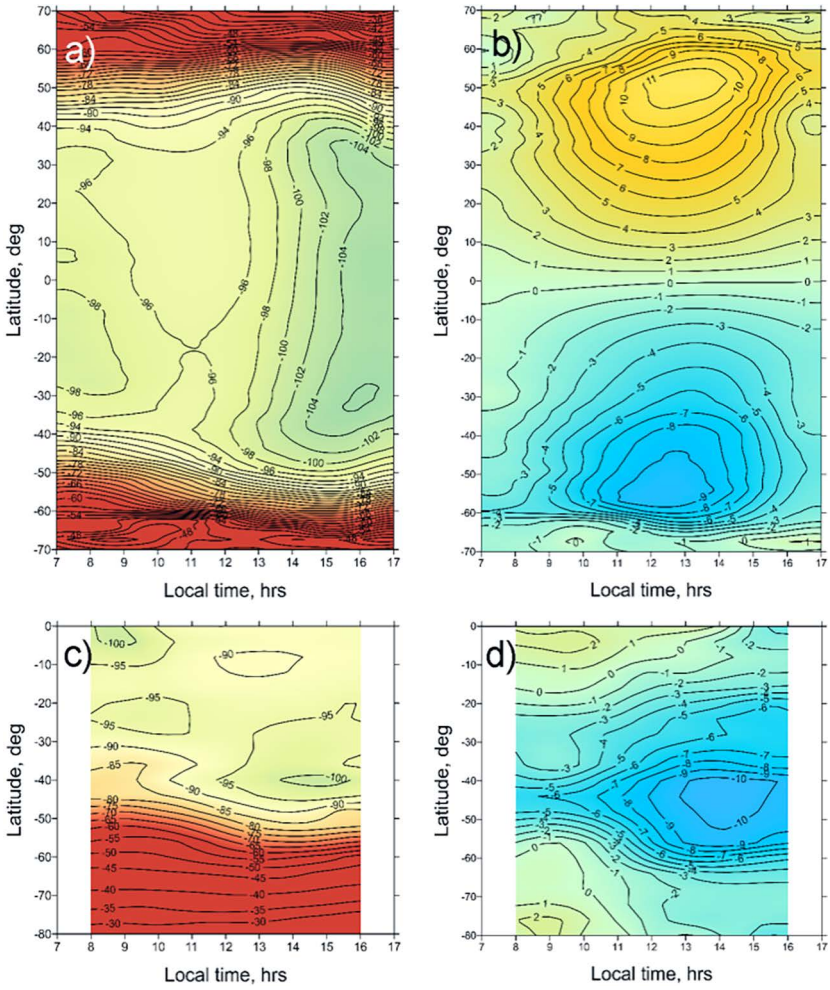

Fig. 1. Diurnal variations of the mean zonal (a, c) and meridional (b, d) wind components obtained with UVI/Akatsuki (a, b) and VMC/Venus Express data

REFERENCES:

[1] Khatuntsev I. V., Patsaeva M. V., Titov D. V., Ignatiev N. I., Turin A. V., Limaye S. S. et al. Cloud level winds from the Venus Express Monitoring Camera imaging. // Icarus. 2013. V. 226. No. 1. P. 140–158. https://doi.org/10.1016/j.icarus.2013.05.018.

[2] Patsaeva M. V., Khatuntsev I. V., Patsaev D. V., Titov D. V., Ignatiev N. I., Markiewicz W. J., Rodin A. V. The relationship between mesoscale circulation and cloud morphology at the upper cloud level of Venus from VMC/Venus Express. // Planetary and Space Science. 2015. V. 113–114. No. 08. P. 100–108. https://doi.org/10.1016/j.pss.2015.01.013.

[3] Patsaeva M. V., Khatuntsev I. V., Zasova L. V., Hauchecorne A., Titov D. V., Bertaux, J.-L. Solar Related Variations of the Cloud Top Circulation Above Aphrodite Terra From VMC/Venus Express Wind Fields // J. Geophysical Research: Planets. 2019. V. 124. P. 1864–1879. https://doi.org/10.1029/2018JE005620.

EMISSIONS IN THE IR CO_2 BANDS OUTGOING THE PLANETARY ATMOSPHERE WITH MACROSCOPIC WIND VELOCITY GRADIENT

V. P. Ogibalov[1,2,3], Yu. I. Bordovskaya[3]
[1] *St. Petersburg State Forest Technical University, Institutsky per., 5, St. Petersburg, 194021 Russia* (*vpo563@mail.ru*)
[2] *Admiral Makarov State University of Maritime and Inland Shipping, Dvinskaya st., 5/7, St. Petersburg, 198035 Russia*
[3] *Department of Atmospheric Physics, St. Petersburg State University, Ulyanovskaya st., 1, St. Petersburg-Petrodvorets, 198504 Russia*

KEYWORDS:
Radiative transfer, planetary atmospheres, wind field gradient, Venus, molecular bands, carbon dioxide

INTRODUCTION:
So far, a number of issues concerning the energy and dynamics of the atmosphere of Venus remain not fully understood. Among them is the phenomenon of superrotation which consists in a presence of wind currents with significant velocities in the narrow altitude region above the top of cloud layer at low latitudes in the Venusian atmosphere [1–2]. For the slant pathways of photons, there exists a non-zero wind speed projection. Due to the Doppler effect, this produces frequency shifts in value of the volume absorption coefficient which depend on altitude and both zenith angle and azimuth angle of photon pathways. Therefor an existence of wind fields with macroscopic altitude gradients can effect on the transfer of radiation, in particular, at frequencies close to narrow cores of spectral lines within the infrared vibrational bands of CO_2. To estimate for the first time a possible influence of strong winds to the radiation outgoing from a planetary atmosphere, a simple model of the vertical wind profile with Gaussian distribution was formulated and the applied for a simplified problem of the transfer of radiative in a spectral line belonging to the different near-infrared (NIR) vibrational bands of CO_2 molecule. In this study, the first results of modeling the NIR emissions outgoing at different directions and different frequencies from a planetary atmosphere consisting of pure CO_2 gas are presented and discussed. It is inferred that an existence of macroscopic wind fields with velocity values about the sound speed can produce significant changes in the spectra of outgoing radiation at frequencies which are located from the central frequency of a spectral line in distances about some units of the Doppler halfwidth.

REFERENCES:
[1] Lebonnois S., Hourdin F., Eymet V., Crespin A., Fournier R., Forget F. Superrotation of Venus' atmosphere analyzed with a full general circulation model // J. Geophysical Research. 2010. V. 115. E06006. doi:10.1029/2009JE003458.
[2] Mendonça J. M., Read P. L. Exploring the Venus global super-rotation using a comprehensive general circulation model // Planetary and Space Science. 2016. V. 134. P. 1–18. doi:10.1016/j.pss.2016.09.001.

THE CHOICE OF THE REFERENCE SURFACE FOR VENUS

V. N. Zharkov, T. V. Gudkova, T. I. Menshchikova
Schmidt Institute Physics of the Earth RAS, B. Gruzinskaya, 10, Russia
(*zharkov@ifz.ru*)

KEYWORDS:
gravity field, theory of figure, topography, interior structure, Venus

INTRODUCTION:
Joint analysis of the topography and the gravitational potential of a planet provides one of the few available means of remotely probing the planetary interiors We use the gravity and topography data obtained by Magellan mission: the global topography model (SHTJV360u) [1] and gravity field model (SHGJ180u) [2]. The data are available at the Planetary System data (http://pds-geosciences.wustl.edu).

INTERIOR STRUCTURE MODEL:
The interior structure models of Venus consist of the crust, the mantle and the core. Taking into account the uncertainty in the crustal thickness, we take several interior structure models of Venus from [3] with the thickness of the crust (hcr) varying from 30 to 100 km, while its density being equal to 2800 kg m^{-3}. The density in the mantle is defined by the coefficient A: $\rho_m(P) = \rho(P)A$, where $\rho(P)$ is the density function of PVM model from [4]. Table 1 contains crustal thickness and density, the core radius, the coefficient A, the moment of inertia, and elastic Love numberk2.

Table 1. Trial interior structure models of Venus [3]

Model	h_{cr}, km	ρ_{cr}, kg/m^3	R_{core}, km	I/MR^2	k_2^e	Coef. A
V_5	70	2800	3200	0.3341	0.2542	1.001
V_16	30	2800	3300	0.3318	0.2661	0.982
V_17	100	2800	3300	0.3312	0.2658	0.986

THE CHOICE OF A REFERENCE SURFACE:
Observational gravity field of a planet can be represented as a superposition of two components: the gravity field of a hydrostatically equilibrium planet, and the deviation of gravity field from the hydrostatic equilibrium, which is called non-equilibrium part. Analyzing of gravity and topography data needs the choice of a reference surface. As in [5], we consider the Venus as a model. We assume that the gravity field of the Venus was a twin of the Earth at some earlier epoch. We use the Earth-like venusian interior structure model [3], satisfying the mass and Love number k_2 [6], and construct equilibrium figure surface for such a planet. An outer surface of a hydrostatical equilibrium model is defined as [5, 7]:

$$r(s_1,\theta) = s_1\left\{1 + s_0(s) + s_2(s)P_2(t) + s_4(s)P_4(t) + \ldots\right\}, \quad (1)$$

where s_1 is the mean radius (the radius of an equivolume sphere) and $P_2(t)$ and $P_4(t)$ are the first even ordinary Legendre polynomials, which depend on even degrees of $t = \cos\theta$, θ is the polar distance.

The calculated functions s_2 and s_4 for the model V_5 are plotted in the figure. Table 2 contains the parameters of the equilibrium figure of Venus at the surface and equilibrium values of J_2^0 and J_4^0. for density distributions of trial Earth-like interior structure models, listed in Table 1.

The parameters are calculated in the second approximation of the theory of figure. Two values of the small parameter of figure are present in Table 2: 1) the small parameter of figure corresponding to the present rotation period of Venus ($m = 6.1\cdot10^{-8}$) and 2) the small parameter of figure for effectively equilibrium Venus ($m = 1.5\cdot10^{-5}$) [8]. In [8] the authors pointed out that during the cooling the interiors of Venus became too solid (or very viscous),

and the figure of the planet was fixed as it was at that time, and it does notcorrespond to the present angular velocity of the planet, The value of the small parameter of figure for effectively equilibrium Venus is conserved from that time.

Table 2. Parameters of the equilibrium figure of Venus for the interior structure models from [3] (see Table 1)

Model	$m = 6.1\cdot10^{-8}$				$m = 1.5\cdot10^{-5}$			
	$-s_2$, 10^{-8}	$-s_4$, 10^{-15}	J_2^0, 10^{-8}	$-J_4^0$, 10^{-16}	$-s_2$, 10^{-6}	$-s_4$, 10^{-11}	J_2^0, 10^{-6}	$-J_4^0$, 10^{-11}
V5	3.97	1.41	1.94	9.57	9.77	8.53	4.77	5.79
V16	3.94	1.40	1.91	9.32	9.69	8.44	4.69	5.64
V17	3.93	1.39	1.90	9.23	9.67	8.39	4.67	5.58

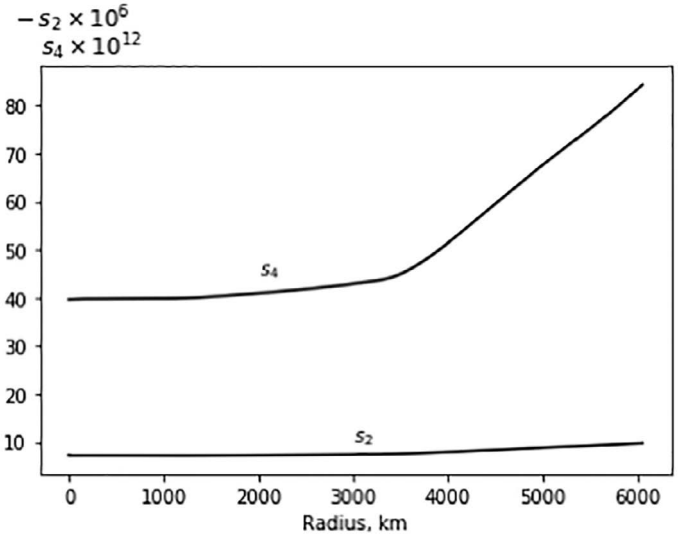

Fig 1. The functions of s_2 and s_4 along the radius of Venus

Moments J_n are related to normalized tesseral gravitational moments C_{no} as $J_n = -(2n+1)^{1/2}C_{no}$. Substituting the values of C_{no} from the model of gravity field (modelSHGJ180u) [2], we get the observed values of gravitational moments at present time: $J_2^{obs} = 4.4\cdot10^{-6}$ and $J_4^{obs} = -2.14\cdot10^{-6}$. The observed value of the zonal quadrupole gravitational moment J_2^{obs} corresponds to the model value for effectively equilibrium Venus ($m = 1.5\cdot10^{-5}$) at some earlier epoch when the Venus was not slowed by tidal friction.

The shape of Venus is very close to a sphere. That is why one often takes a sphere of mean radius R for the reference surface [9]. In the present paper, we consider an equilibrium spheroid $r(s, \theta)$ with mean radius R (see (1)) as a reference surface.

The hydrostatically equilibrium part of the Venusian gravitational field V_0 includes GM/r, the term proportional J_2^* and the term of order $m^2 - J_4^*$. As noted above current value of J_2 corresponds to effectively equilibrium Venus at earlier epoch when Venus was not slowed by tidal friction. We take $J_2^* = J_2^{obs}$, $J_4^* = J_4^0$ for effectively equilibrium Venus. The value of J_4^* significantly differs from the observed zonal gravitational moment J_4.

The values of tesseral gravitational moments C_{g20} and C_{g40} are related to the values of zonal gravitational moments as $C_{g20} = -J_2^0/\sqrt{5}$, $C_{g40} = -J_4^0/3$. We take for the coefficients C_{g20}^0 the following values (see the Table 2): $C_{g20}^0 = -2.13\cdot10^{-6}$, $C_{g40}^0 = -1.93\cdot10^{-11}$.

The hydrostatic equilibrium part of the Venusian gravitational field V_0 can be represented as

$$V^0(r,\varphi)=\frac{GM}{r}\left(1+\left(\frac{R_e}{r}\right)^2 C^0_{g20}P_{20}(\sin\varphi)+\left(\frac{R_e}{r}\right)^4 C_{g40}P_{40}(\sin\varphi)\right).$$

ACKNOWLEDGEMENTS:
The study was performed under a government contract of the Schmidt Institute of Physics of the Earth of the Russian Academy of Sciences.

REFERENCES:

[1] Rappaport N. J., Konopliv A. S., Kucinskas A. B. An improved 360 degree and order model of Venus topography // Icarus. 1999. V. 139. P. 19–31. doi:10.1006/icar.1999.6081.
[2] Konopliv A. S., Banerdt W. B., Sjogren W. L. Venus gravity: 180th degree and order model // Icarus. 1999. V. 139. P. 3–18. doi:10.1006/icar.1999.6086.
[3] Gudkova T. V., Zharkov V. N. Models of the internal structure of the Earth-like Venus // Solar System Research. 2020. V. 54. No. 1. P. 20–27.
[4] Zharkov V. N., Zasurskii I. Ya. A physical model of Venus // Solar System Research. 1982. V. 16. P. 14–22.
[5] Zharkov V. N., Gudkova T. V. On the model structure of the gravity field of Mars // SSolar System Research. 2016. V. 50. No. 4. P. 235–250.
[6] Konopliv A. S., Yoder C. F. Venusian k2 tidal Love number from Magellan and PVO tracking data // Geophysical Research Letters. 1996. V. 23. P. 1857–1860.
[7] Zharkov V. N., Trubitsyn V. P. Fizika planetnykh nedr (Physics of Interior of Planets). M.: Nauka, 1980.
[8] Zharkov V. N., Gudkova T. V. On Parameters of the Earth-like model of Venus // Solar System Research. 2019. V. 53. P. 1–4.
[9] Zharkov V. N. Gravity field, loading coefficients, anomalous density waves and the case of long waves // Venus geology, geochemistry and geophysics research results from the USSR / eds. Barsukov V. L., Basilevsky A. T., Volkov V. P., Zharkov V. N. University of Arizona Press, 1992. P. 219–228.

DATA ANALYSIS OF THE GRAVITY FIELD OF VENUS

T. I. Menshchikova, T. V. Gudkova, V. N. Zharkov
Schmidt Institute Physics of the Earth RAS, B.Gruzinskaya, 10, Russia
(*ms.tamm@mail.ru*)

KEYWORDS:
gravity field, topography, geoid, gravity anomalies, interior structure, Venus

INTRODUCTION:
In the absence of seismic data, the joint analysis of the topography and gravity data of Venus helps us to get the knowledge on its interiors. When analyzing the gravity and topography data, one has to choose a reference surface. In this study we use an outer surface of a hydrostatical equilibrium model for Earth-like Venus as a reference surface [1]. Only non-equilibrium components of gravity and topography fields have been considered. The geoid heights and gravity anomalies for the model of Venus are calculated.

DATA:
We use the gravity and topography data provided by the Magellan mission: the spherical harmonic global topography model (SHTJV360u) [2] and gravity field model (SHGJ180u) [3]. The data are available at the Planetary System data (http://pds-geosciences.wustl.edu).The trial interior structure model of Venus V_5 from [4] is used. Figure 1 shows a map based on the data for the heights of the surface relief of Venus after expansion to degree and order 70. The heights are calculated relative to the hydrostatical equilibrium figure, the parameters of which are defined in [1]. The map demonstrates main geological structures of the Venusian topography. Some of them are the Ishtar Terra, where the Maxwell Montes (the highest mountains on Venus) are located, the Beta Regio — the volcanic feature similar to the Earth, and Aphrodite Terra — the large "continent" spreading along the equator between 60 and 210° longitudes.

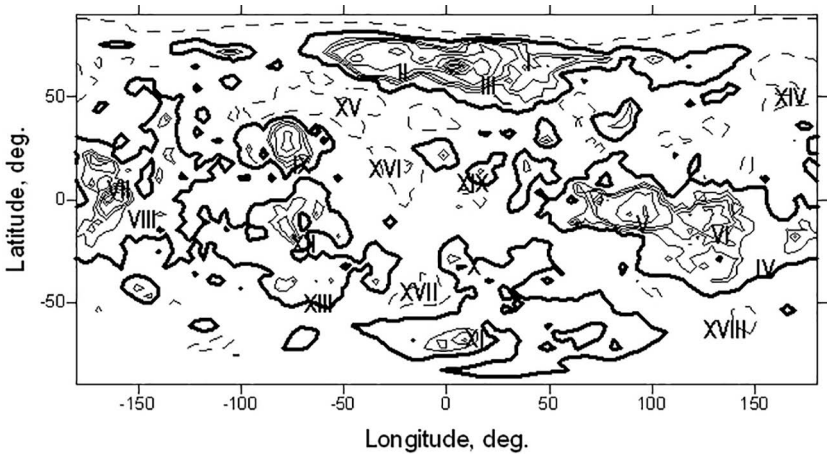

Fig. 1. Contour map of height sof the surface relief of Venus to degree and order 70. The zero level (thick solid line) corresponds to the equilibrium figure. The solid lines correspond to positive heights; the dashed ones, to negative heights. The map legend: I — Ishtar Terra, II — Lakshmi Planum, II — Maxwell Montes, IV — Aphrodite Terra, V — plateau Ovda, VI — Thetis Regio, VII — AtlaRegio, VIII — Maat Mons, IX — Beta Regio, X — Alpha Regio, XI — Lada Terra, XII — Pheobe Regio, XIII — Thetis Regio, XIV — Atalanta Planitiae; XV — Sedna Planitia; XVI — Guinevere Planitia; XVII — Lavinia Planitia; XVIII - Aino Planitia; XIX – Eistla Regio

GEOID HEIGHTS:
The geoid heights of Venus are of about few tens meters (Figure 2), the same as for the Earth. Contrary to the Earth, the geoid of Venus well correlates to the topography features. In the geoid map one can clearly see some

so-called “continents” — Ishtar Terra, Beta Regio and Aphrodite Terra. The maximum local anomalies are associated with such regions as Beta Regio and OvdaRegio, and the zones of the “continents” — Aphrodite Terra, Ishtar Terra and Lada Terra. The lowlands have negative geoid heights. The dynamical scale of geoid heights relative to the equilibrium surface is about 200 meters.

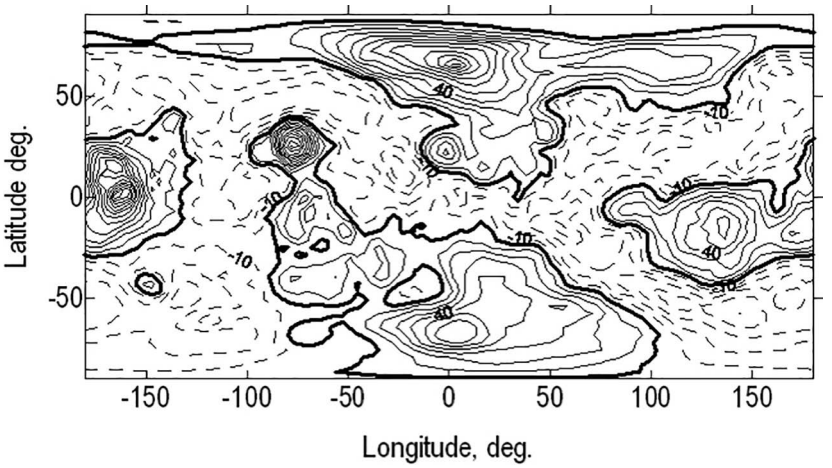

Fig. 2. Map of Venus geoid heights for harmonics of degree 2 through 70 relative to the equilibrium figure. The solid lines correspond to positive heights, the dashed ones, to negative heights: the zero level is shown by a thick solid line. The interval between the contour lines is 10 m

GRAVITY ANOMALIES:

Figure 3 shows a map of the gravity anomalies contours on the surface of Venus. Lowlands have negative gravity anomalies. The gravity anomalies of highlands are not large (the possible isostatic compensation), volcanic uplifts are characterized by larger gravity anomalies. The maximum intensity inferred in the Atla Regio and Beta Regio, Maxwell Montes and some smaller volcanic uplifts. In general, the gravity disturbances are rather small, as a consequence of the smooth relief. Maximum values are up to 250 mGal. Most of gravity anomalies and geoid heights are correlated to the topographic structures.

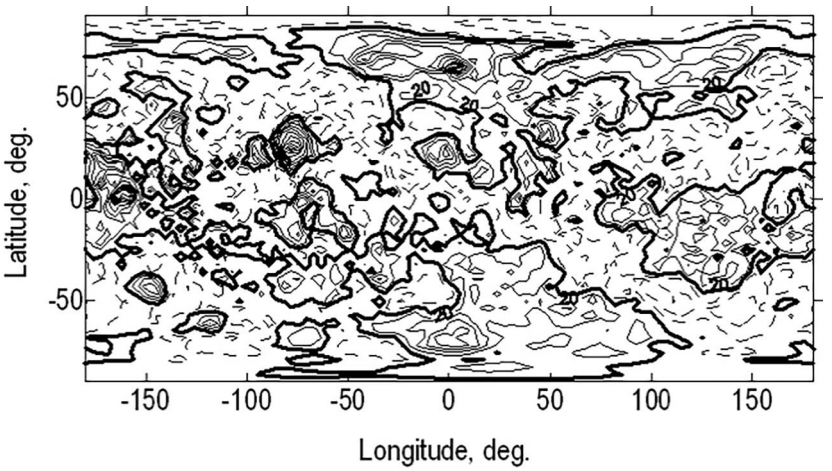

Fig. 3. Map of the deviations of the gravity from the hydrostatic-equilibrium valueson the surface of Venus for harmonics of degree 2 through 70. The solid lines correspond to positive values; the dashed lines, to negative ones. The interval between the contour lines is 20 mGal

The maps of geoid heights and gravity anomalies allow one to judge if there is a correlation between the gravity field and topography, as it takes place

in the case of weak isostatic compensation. The geoid heights are higher in the areas where the gravity disturbances are increased (where there is some additional uncompencated mass). In the map of the Earth geoid heights, the continents and mountains are not seen. In the map of Venusian geoid heights one can see “continents” (the uplift zones). This means that the isostatic compensation in the Earth is higher then for Venus.

ACKNOWLEDGEMENTS:
The study was performed under a government contract of the Schmidt Institute of Physics of the Earth of the Russian Academy of Sciences.

REFERENCES:

[1] Zharkov V. N., Gudkova T. V., Menshchikova T. I., The choice of the reference surface for Venus // 11th Moscow Solar System Symp.: Abstract . Moscow, IKI RAN, Oct. 8–12, 2020. M.: IKI RAN, 2020.
[2] Rappaport N. J., Konopliv A. S., Kucinskas A. B. An improved 360 degree and order model of Venus topography // Icarus. 1999. V. 139. P. 19–31. doi:10.1006/icar.1999.6081.
[3] Konopliv A. S., Banerdt W. B., Sjogren W. L. Venus gravity: 180th degree and order model // Icarus. 1999. V. 139. P. 3–18. doi:10.1006/icar.1999.6086.
[4] Gudkova T. V., Zharkov V. N. Models of the internal structure of the Earth-like Venus // Solar System Research. 2020. V. 54. No. 1 P. 20–27.

RESULTS OF GEOLOGIC ANALYSIS OF THE CORONAE OF DIFFERENT TOPOGRAPHIC CATEGORIES ON VENUS

E. N. Guseva, M. A. Ivanov
Vernadsky Inst., *RAS*, *Moscow*, *Russia* (*guseva-evgeniya@ya.ru*)

KEYWORDS:
Venus, coronae, topography, geological structures, stratigraphic position

INTRODUCTION:
Coronae are large circular volcano-tectonic structures that can reach ~2500 km in diameter [1]. The defining element of coronae is an annulus consisting of densely packed grooves and sometimes ridges [2–4]. The annulus surrounds the coronae interiors, where features of volcanic origin dominate [4]. In some coronae, individual lava flows extend beyond the annulus and overlay the surrounding plains [5]. The concentric shape of the coronae, their nonrandom spatial distribution [6], as well as pronounced volcanic and tectonic components indicate that the coronae represent the surface manifestation of mantle diapirs [7–9]. In the framework of this interpretation of coronae, their topographic configuration is important since it can reflect various stages of the evolution of the parent diapir [10]. Numerical modeling of its evolution indicates a successive change of the topographic profiles that correspond to different phases of the evolution of the coronae [10]. In our previous work [11], we investigated the topographic configuration of all cataloged coronae in order toclassify them according to their characteristic topographic profile and, on this basis, estimate the possible stages of evolution of mantle diapirs. In this work, we analyzed the geological settings in which each of the studied coronae occurred in order to establish the stratigraphic position of coronae of the different topographic categories.

METHODS:
We used published catalogues of coronae [4, 12]. We inspected these catalogues to exclude repetitions and combined the catalogues together into one list of structures. We studied geology of each coronae from this list using C1-MIDR images (resolution 225 m/px) in order to determine their outer borders and specific units that coronae are in contact with. These images and the global geological map of Venus [13] were used to estimate the stratigraphic position of the studied coronae.

TOPOGRAPHIC AND GEOLOGICAL GROUPS OF CORONAE:
We investigated 550 coronae (Table 1) of five topographic categories.

Table 1. Geological characteristics of coronae of different categories

topographic categories	all coronae	structures %	grp.1	grp. 2	grp. 3	grp. 4	volcanism
D-shaped	99	18	44	37	6	12	26
W-shaped	188	34	130	17	13	28	12
W-W-shaped	18	3	9	6	2	1	1
W-V-shaped	59	11	45	9	1	4	8
U-shaped	186	34	118	12	3	53	10
Total	550	100	346	81	25	98	57
%			63	15	5	18	10

(1) Dome-shaped coronae (99 structures or ~18 % of the analyzed population). (2) W-shaped coronae (188 or ~34 %). (3) W–W-shaped coronae (18 or ~3 %). (4) W–V-shaped coronae (59 or ~11 %). (5) U-shaped coronae (186 or ~34 %). In turn, the surroundings of the coronae and the nature of their annulus define four specific geological groups of coronae.

Group 1 — structures with the annulus represented by groove belts, in all cases, flooded by the material of the surrounding regional plains and/or de-

formed by wrinkle ridges. These coronae are the most abundant features (346 out of 550 or 63 %). *Group 2* — structures with annulus consisting of rift-related fractures that deform the regional plains and in some cases are flooded by lobate plains. These coronae compose about 1/5 of all analyzed structures (81 or 15 %). *Group 3* — structures of the "transitional" type, the annulus of which partially consists of the older groove belts and partly of the younger rift zones (25 or 5 %). *Group 4* — structures that do not have a morphologically pronounced outer border or are flooded by material of shield and/or regional plains (98 or 18 %). For each category of coronae, we calculated the number of structures spatially associated with lobate plains (volcanism in Table 1).

TOPOGRAPHIC CONFIGURATION OF DIFFERENT GEOLOGICAL GROUPS OF CORONAE:

Group 1 (*"pre–rift" coronae*)*: these structures* most often have the W-shaped (130 structures) and U-shaped (118 structures) topographic profiles that correspond to the late model evolutionary phases of coronae (Figure 1 e–g). "Pre-rift" coronae are probably the older structures at the regressive stage of evolution of the parent diapir.

Group 2 (*"rift–shaped" coronae*)*: these structures* are mostly have the dome-shaped topographic profile (D-shaped coronae, 37 structures). Such a topographic profile correspond to the initial model phases of evolution the diapir (Figure 1a–c). Thus, the rift-shaped coronae likely represent progressive stages of the diapir evolution. The D–shaped coronae are most often spatially associated with the lobate plains (26 structures), which are manifestations of the younger volcanic activity [14].

Group 3 (*"transitional" coronae*)*: these structures* are more often characterized by the W-shaped topographic profile (13 structures), as well, as the "pre-rift" coronae whose structures they probably inherit.

Group 4 (*"depression–like" coronae*)*:* the absolute majority of these structures show the U- and W-shaped topographic profiles (86 feature out of 98) that correspond to the final phases of evolution of the parent diapir (Figure 1 f, g).

DISCUSSION:

The evolutionary stages of the coronae-forming parent diapirs and their progressive and regressive phases are illustrated by a series of model topographic profiles (Fig.1, [10]). The initial phases of the progressive stage characterized by the growth of dome-shaped structures above the diaper, which abuts against the bottom of the lithospheric rheological barrier (Figure 1a–c). This characteristic topographic profile corresponds to D-shaped coronae. According to the results of numerical simulation [10], these coronae represent the stage of evolution when the parent diaper still has sufficient positive buoyancy to be able to warp the lithospheric barrier upward. About one fifth of the entire population of coronae belongs to this category. The dome-shaped coronae (their characteristic diameter is 175–225 km) are concentrated in the Beta–Atla-Themis region (BAT). This region bounded is outlined by large branches of rift zones and characterized by abundant fields of lobate plains [15, 10]. Both rifts and lobate plains are characteristic features of the late network rifting-volcanism regime of resurfacing [14; 16]. The close spatial association of dome-shaped coronae with the BAT region suggests that about 20 % of the coronae on Venus formed during the late resurfacing regime.

For all other coronae, the main feature of their topographic configuration is a longer wavelength topographic depression in the interior of a corona, which is complicated by shorter wavelength positive topographic details.

According to the model results [10], the presence of the sagging interior indicates that such coronae are at the regressive stages of evolution when the parent diaper lost its positive buoyancy due to heat loss.

The W–W and W-shaped coronae make up ~37 % of the entire population of coronae and may correspond to the earlier phases of the regressive stage (Figure 1d, e). About half (45 %) of the analyzed coronae are annular struc-

tures or topographic depressions without an annulus (categories W–V and U, Figure 1f, g), which may correspond to the latest phases of the regressive stage of the evolution [10].

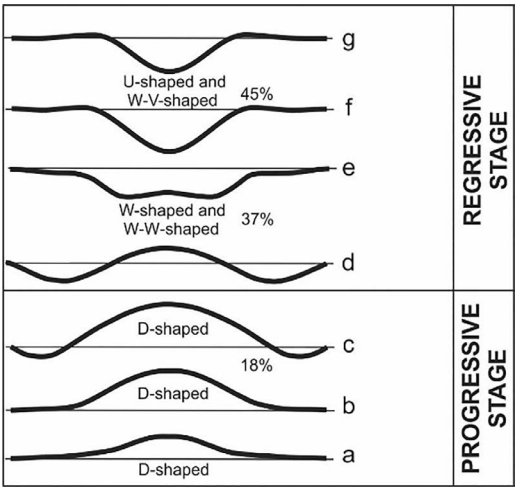

Fig. 1. Topographic profiles of coronae at different stages of their evolution (modified from [10])

Our results show that most of the coronae on Venus are manifestation of the later stage of the evolution of mantle diapirs when they acquired negative buoyancy. The vast majority of these coronae are spatially associated with groove belts and characterize later episodes of the tectonic regime of resurfacing [16]. The number of coronae that can appear in the early and late stages of the regressive stage is approximately the same (37 % and 45 %, respectively). This suggests that the parent coronae-forming diapirs formed in a wider time interval near the end of the tectonic regime, but this activity mostly ceased prior to the emplacement of extensive lava plains of the volcanic regime of resurfacing (shield and regional plains) that partly embayed and flooded the tectonic components of most coronae.

REFERENCES:

[1] Head J. W., Crumpler L. S., Aubele J. C., Guest J., Saunders R. S. Venus Volcanism: Classification of volcanic features and structures, associations, and global distribution from Magellan data // J. Geophysical Research. 1992. V. 97. P. 13.153–13.197.

[2] Barsukov V. L., Basilevsky A. T., Burba G. A. et al. (27 others) The geology and geomorphology of the Venus surface as revealed by the radar images obtained by Venera 15 and 16 // J. Geophysical Research. 1986. V. 91. NB4. P. D378–D398.

[3] Pronin A. A., Stofan E. R. Coronae on Venus: Morphology and distribution // Icarus. 1990. V. 87. P. 452–474.

[4] Stofan E. R., Sharpton V. L., Schubert G., Baer G., Bindschadler D. L., Janes D. M., Squyres S. W. Global distribution and characteristics of coronae and related features on Venus: Implications for origin and relation to mantle processes // J. Geophysical Research. 1992. V. 97. No. E8. P. 13347–13378.

[5] Ivanov M. A., Head J. W. Geology of Venus: Mapping of a global geotraverse at 30N latitude // J. Geophysical Research. 2001. V. 106. No. E8. P. 17515–17566.

[6] Phillips R. J., Raubertas R. F., Arvidson R. E., Sarkar I. C., Herrick R R., Izenberg N., Grimm R. E. Impact craters and Venus resurfacing history // J. Geophysical Research. 1992. V. 97. N. E10. P. 15.923–15.948.

[7] Janes D. M., Squyres S. W., Bindschadler D. L., Baer G., Schubert G., Sharpton V. L., Stofan E. R. Geophysical models for the formation and evolution of coronae on Venus // J. Geophysical Research. 1992. V. 97. No. E10. P. 16055–16068.

[8] Jellinek A. M., Lenardic A., Manga M. The influence of interior mantle temperature on the structure of plumes: Heads for Venus, tails for the Earth // Geophysical Research Letters. 2002. V. 29. No. 11. P. 27-1–27-4.

[9] Johnson C. L., Richards M. A. A conceptual model for the relationship between coronae and large-scale mantle dynamics on Venus // J. Geophysical Research. 2003. V. 108. N. E6. P. 12-1–12-18.
[10] Smrekar S. E., Stofan E. R. Corona formation and heat loss on Venus by coupled upwelling and delamination // Science. 1997. V. 277. P. 1289–1294.
[11] Guseva E. N., Ivanov M. A. Topographic configuration of coronae on Venus: supporting evidence for time-dependent styles of resurfacing // 10th Moscow Solar System Symp. 2019. IKI RAS. 10MS3-PS-31.
[12] Crumpler L. S., Aubele J. Volcanism on Venus // Encyclopedia of Volcanoes / eds. B. Houghton, H. Rymer, J. Stix, S. McNutt, H. Sigurdson. San Diego, San Francisco, New York, Boston, London, Sydney, Toronto: Acad. Press, 2000. P. 727–770.
[13] Ivanov M. A., Head J. W. Global geological map of Venus // Planetary and Space Science. 2011. V. 59. P. 1559–1600.
[14] Ivanov M. A., Head J. W. The history of volcanism on Venus // Planetary and Space Science. 2013. V. 84. P. 66–92.
[15] Squyres S. W., Janes D. M., Baer G., Bindschandler D. L., Shubert G., Sharpton V. L., Stofan E. R. The morphology and evolution of coronae on Venus // J. Geophysical Research. 1992. V. 97. P. 13.611–13.634.
[16] Ivanov M. A., Head J. W. The history of tectonism on Venus: A stratigraphic analysis // Planetary and Space Science. 2015. V. 113–114. P. 10–32.

INVESTIGATION OF DESIGN CHARACTERISTICS OF A LANDER FOR MANEUVERABLE DESCENT TO THE VENUS SURFACE

A. V. Kosenkova, A. B. Martynov
Lavochkin Association, *Russia*, *Khimki*, *Leningradskaya 24*, *141402*
(*tarasovaAV@laspace.ru*)

KEYWORDS:
Venus, lander, maneuverable descent, lateral maneuver, design

INTRODUCTION

Venus exploration can be interesting not only from the viewpoint of fundamental science but also from the viewpoint of comparative planetology. There are various projects such as Venera–D [1], EnVision [2], Venus Flagship Mission [3], VERITAS, DAVINCI+ [4], CubeSat UV Experiment, Venus Mobile Explorer, Venus Origins Explorer that are being considered nowadays in Russia and abroad, also using international collaboration.

And despite the successful operation of recently launched Venus-Express (2005) [5] and Akatsuki (2010) [6] orbiters, the fundamental questions related to the origin and evolution of Venus, its atmosphere and climate, as well as studying the problems of the Earth's climate, cannot be solved on the basis of observations only from orbit. Direct measurements are needed in the atmosphere and on the Venus surface using atmospheric probes and landers.

In this connection, the issues of creating a lander to the Venus surface become relevant. The last and the only landers were developed in the USSR — Vega-1/ 2 missions (1984 year), there were also some probes in Pioneer Venus-2 mission (USA, 1978). But all soviet landers made landings in low latitudes: from +30° to –30°. At the same time, for today, scientists are interested in various parts of the Venus surface [7, 8], which should be studied for one reason or another. Therefore, the issue of expanding the coverage of landing areas and ensuring the achievement of the most interesting for studying landing area is very important.

LANDER FOR MANEUVERABLE DESCENT

This paper proposes different types of a lander to be considered for the possibility of making maneuverable descent and proposes "lifting body" type of a lander [9] as the most perspective, which, with an allowable complication of the design, have a sufficiently high lift-to-drag ratio at hypersonic velocities, sufficient to solve the current maneuvering tasks in the planet's atmosphere in order to reach the desired landing area and also to increase the breadth of coverage of potential landing zones while carrying out an expedition to Venus.

The use of spherical (Soviet ones) and conical (American ones) landers at the initial stages of the Venus exploration was related to the simplicity and reliability of their structure, as the primary task for the lander was to reach the surface with working equipment. The first generation of landers could not maneuver in the atmosphere and deviate from the ballistic trajectory. to land the vehicle in the planned landing zone, it is proposed to use landers capable of maneuvering in the atmosphere. Landers that have a certain lift-to-drag ratio at hypersonic velocity range have this capability. However, ensuring a required lift-to-drag ratio means that the lander mass increases and its structure becomes more complex. A trade-off solution would be to use "lifting body" type of a lander. The complication of the structure of such lander is permissible and it has a lift-to-drag ratio sufficient for solving the existing maneuvering tasks in the Venus atmosphere.]

The paper includes a comparative analysis of the landers to the Venus surface, consideration of different types of a lander for the maneuverable descent to the Venus surface, their comparative analysis in terms of maneuverability, mass-dimensional and aerodynamic characteristics based on various comparative parameters and criteria-based assessments, calculation of the aero-

dynamic characteristics, ballistic and thermal modes of the descent process and shows advantages of using “lifting body” type of a lander comparing to the previously used ballistic type of a lander.

REFERENCES:

[1] Phase II report of the Venera-D Joint Science Definition Team. URL: https://www.pi.usra.edu/vexag/reports/Venera-DPhaseIIFinalReport.pdf.
[2] Ghail R. C. et. al. VenSAR on EnVision: Taking earth observation radar to Venus // Intern. Applied Earth Observation and Geoinformation. 2018, V. 64. P. 365–376. https://doi.org/10.1016/j.jag.2017.02.008.
[3] Venus Flagship Mission Study: Report of the Venus Science and Technology Definition Team. URL:https://www.researchgate.net/publication/41626005_Venus_Flagship_Mission_Study_Report_of_the_Venus_Science_and_Technology_Definition_Team.
[5] Venus Express mission. URL: http://www.esa.int/Enabling_Support/Operations/Venus_Express.
[6] Venus Climate Orbiter Akatsuki. URL: http://akatsuki.isas.jaxa.jp/en/.
[7] Ivanov M. A., Head J. W. Global geological map of Venus // Planetary and Space Science. 2011. V. 59. P. 1559–1600. doi:10.1016/j.pss.2011.07.008.
[8] Venera-D Landing Sites selection and Cloud Layer Habitability Workshop. October 2–5, 2019. IKI, Moscow, Russia. URL: http://www.venera-d.cosmos.ru/index.php?id=workshop2019andL=2.
[9] Kosenkova A. V. Investigation of the possibilities of aerodynamic forms of a lander capable of maneuverable descent in the Venus atmosphere // AIP Conf.: Proc. 2019. 2171. 160005. https://doi.org/10.1063/1.5133309.

SOME PLATFORMS TO OBSERVE VENUS AS A SYSTEM

A. B. Martynov, A. V. Kosenkova
Independent researcher, *Russia*, *Khimki* (*morf.me@gmail.com*)

KEYWORDS:
Venus, lander, orbiter, ground system, orbital system, design

INTRODUCTION

During the first half century of space exploration, over two dozen of spacecraft have explored Venus. In recent years many new missions have been considered or designed, almost all of which have a single spacecraft per launch or per mission departing for the initial Soviet tradition of two nearly identical missions per launch opportunity. Almost all of them have included a small or medium size satellite and/or a lander. And as it is expected, larger spacecraft can carry more instruments, operate longer and have a greater scientific impact due to the greater technical possibilities (more fuel, more lifetime, more power, more transmitting speed etc).

The investigation of VEXAG [1] and Venera-D mission work-group (LAV, IKI RAS, NASA, etc. [2, 3]) shows that there are approximately 40 technical and scientific goals which has never been done before and about 50 which were briefly performed by missions of the past and currently active missions [4]. The missions in the past had limited list of scientific tasks that were solved due to the lack of materials and technologies that could withstand the Venusian conditions or observe Venus through the “thick” and “heavy” atmosphere.

Nowadays with the significant progress by the last decades in electronics, mechanisms and materials it is possible to create much smaller spacecraft with the same scientific impact and technical possibilities — as a one large single unit has. Moreover, deploying a few of them as a system will yield far more science measurements than a single unit. For example, such system (constellation, net etc.) of small spacecraft in different landing sites can offer greater spatial and local time coverage enabling a better investigation of temporal evolution of key scientific quantities.

This paper describes systems of various mission elements that could be used for Venus exploration.

REFERENCES:

[1] Venus exploration analysis group. URL: https://www.lpi.usra.edu/vexag/.
[2] JSDT Report 1. URL: http://www.iki.rssi.ru/events/2017/venera_d.pdf.
[3] JSDT Report 2. URL: https://www.lpi.usra.edu/vexag/reports/Venera-DPhaseIIFinalReport.pdf.
[4] Venus targets and goals. URL: https://github.com/wohaco/despace/blob/master/venus.md#venus-exploration.

INFORMATION

address:
Space Researh Institute (IKI)
Profsoyuznaya street 84/32
post code 117997
metro station: Kaluzhskaya
Moscow, Russia

ИКИ РАН
площадь академика Келдыша
Метро"Калужская", первый вагон из центра, по тоннелю — прямо,
по второму поперечному тоннелю- направо, выход на площадь,
далее по стрелкам на схеме

IKI RAS
You should get off at "Kalyzhskaya" metro station using the southern exit.
After leaving a station lobby through glass doors you should go straight
to the end of the tunnel, then take right and use the stairs to get to the surface.
From this point you may follow either arrow on this map

MOSCOW METRO SCHEME

СХЕМА МОСКОВСКОГО МЕТРОПОЛИТЕНА

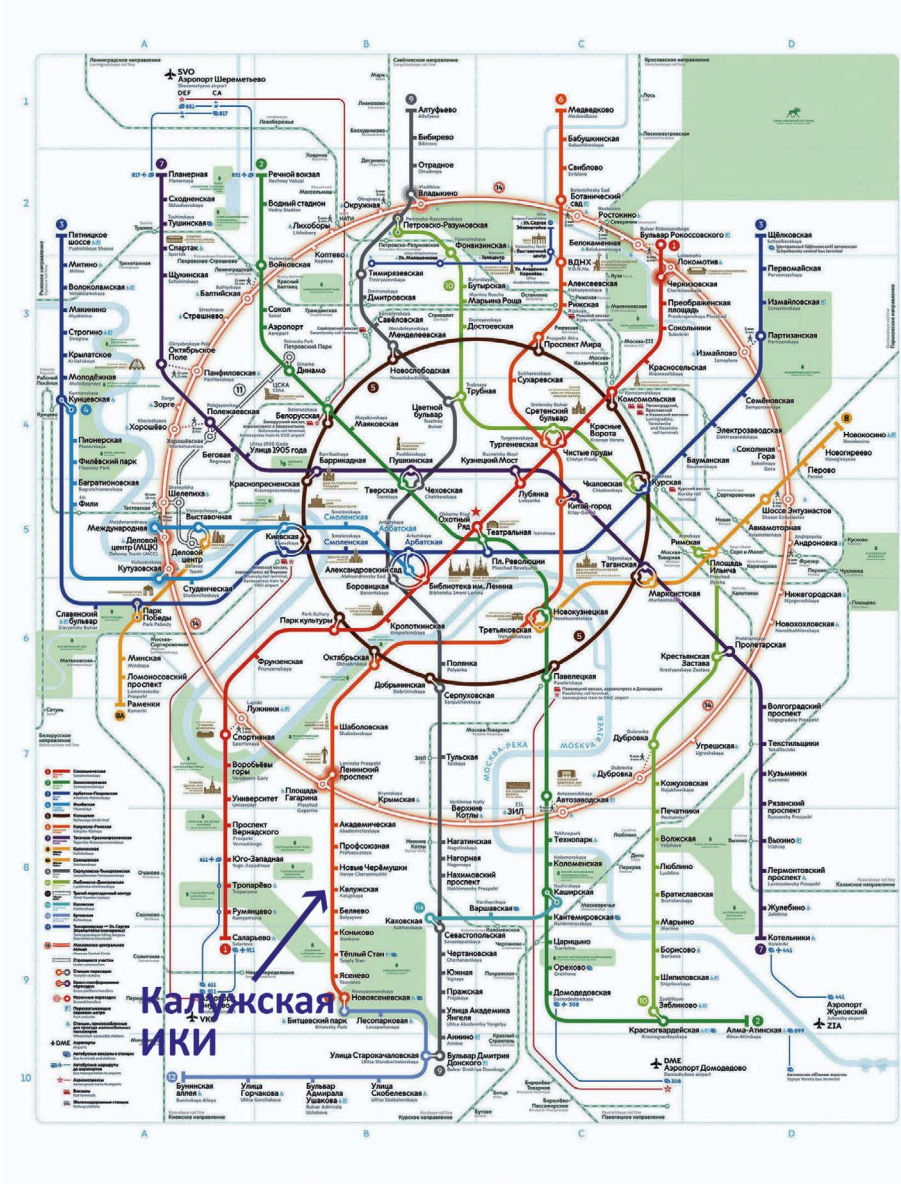

REGISTRATION AND INFORMATION DESK

location: IKI, entrance A-4
time:
5 october, 8:30–18:00
6-9 october, 9.00–18.00

ORAL SESSIONS

location: IKI conference hall, second floor

POSTER SESSIONS

online discussion

COFFEE BREAKS, WELCOME PARTY, RECEPTION

location: IKI exhibition hall, ground floor

INTERNET ACCESS AND WIFI

there is Internet access in and near the conference hall

4 OCTOBER, SUNDAY	5 OCTOBER, MONDAY	6 OCTOBER, TUESDAY	7 OCTOBER, WEDNESDAY
THE BOLSHOI THEATRE https://www.bolshoi.ru/en/timetable/			
19.00 new stage **IOLANTA** *Opera in two acts*			**19.00** **historic stage** **EUGENE ONEGIN** *Liric scenes in three acts* **19.30** **Beethoven Hall** **LUDWIG VAN BEETHOVEN AND HIS GREAT CONTEMPORARIES** *Bolshoi Theatre Orchestra Artists Concert*
MALY THEATRE https://www.maly.ru/en			
18.00 main stage **Nikolai GOGOL** **THE GAMBLERS** *A comedy*		**19.00 main stage** **Nikolai GOGOL** **THE GOVERNMENT INSPECTOR** *A comedy in 5 acts* **19.00 Main stage** **Nikolai GOGOL** **THE HANDSOME MAN** *A Comedy in 4 Acts* *PREMIERE*	**19.00 main stage** **Eduardo De FILIPPO** **CHRISTMAS AT THE CUPIELLO'S** *PREMIERE* **19.00 Ordynka stage** **Jean-Baptiste POQUELIN** **TARTUFFE, OR THE IMPOSTOR** *A comedy in 5 acts*
MOSCOW CONCERT HALL 'ZARYADYE' https://zaryadyehall.com/			
18.00 grand hall **Lucas DEBARGUE** **Alexandre CASTRO-BALBI** **David CASTRO-BALBI**	**19.00 gand hall** **Johann STRAUSS** **OPERETTA "THE FLITTERMOUSE"**	**19.00 grand hall** **piano** **B. BEREZOVSKIY and A. GINDIN**	**19.00 Small Hall** **Jean-Baptiste THE MATHEMATICIAN** *Opera* **19.00 grand hall** **DAVE BRUBECK'S 100TH ANNIVERSARY**

SOCIAL PROGRAM

for additional information please contact Mrs Tatiana Zharkova,
e-mail: zharkovaiki@yandex.ru

8 OCTOBER, THURSDAY	9 OCTOBER, FRIDAY	10 OCTOBER, SATURDAY
THE BOLSHOI THEATRE https://www.bolshoi.ru/en/timetable/		
19.00 historic stage **EUGENE ONEGIN** *Liric scenes in three acts*	**19.00 historic Stage** **EUGENE ONEGIN** *Liric scenes in three acts*	**12.00 new stage** **THE FLAMES OF PARIS** *Ballet in two acts*
19.00 chamber stage **Boris POKROVSKY** **IL TURCO IN ITALIA** *Opera in two acts*	**19.00-20.00** **chamber stage** **Boris POKROVSKY** **IL TURCO IN ITALIA** *Opera in two acts*	**19.00 historic stage** **Eugene Onegin** *Liric scenes in three acts*
		19.00 new stage **THE FLAMES OF PARIS** *Ballet in two acts*
MALY THEATRE https://www.maly.ru/en		
15.00 Main stage **HURRY UP! DISCOVER AN AMAZING WORLD OF THE THEATRE** *Sightseeing tour of the Historical building of the Maly Theatre*	**19.00 Main stage** **Friedrich DÜRRENMATT** **THE VISIT OF THE OLD LADYOF THE THEATRE** *A Tragic Comedy in Three Acts*	**18.00 Main Stage** **Aleksey KONSTANTINOVICH TOLSTOY** **TSAR BORIS** *A tragedy in 2 Acts*
15.00 main stage **Alexander OSTROVSKY** **ENOUGH STUPIDITY IN EVERY WISE MAN** *A comedy in 5 acts*	**19.00 ordynka Stage** **Anton CHEKHOV** **WEDDING! WEDDING! WEDDING!** *Sketches, short two-act comedies*	**18.00 ordynka stage** **Alexander OSTROVSKY** **IT'S A FAMILY AFFAIR - WE'LL SETTLE IT OUR-SELVES** *A comedy in four acts*
19.00 ordynka stage **Robert THOMAS** **EIGHT LOVING WOMEN** *A comedy in 5 acts*		
MOSCOW CONCERT HALL 'ZARYADYE' https://zaryadyehall.com/		
	19.00 grand hall **MARIAM MERABOVA & MIRAIF**	**14.00 small hall** **Kuzma BODROV** **I AM COMPOSER!",** *series of concerts*

Точки питания вблизи ИКИ/ Lunch points nearest to IKI

1.ИНСТИТУТ КОСМИЧЕСКИХ ИССЛЕДОВАНИЙ РАН, столовая, 1 этаж, секция А3
SPACE RESEARCH INSTITUTE, Food center, Ground Floor, Section A3

2. ТЦ “КАЛУЖСКИЙ” , ул. Профсоюзная, 61А, зона ресторанов, 2 этаж
“KALUZHSKIY” Market Center, Profsoyuznaya Street, 61A, 2 Floor

3.Кафе”АндерСон” , ул. Обручева, 30/1
Café “AnderSon”, Obrucheva street, 30/1

4. ИНСТИТУТ ПРИКЛАДНОЙ МАТЕМАТИКИ РАН, столовая, 1 этаж
INSTITUTE OF APPLIED MATHEMATICS, Food center, Ground Floor

SPACE RESEARCH INSTITUTE OF RUSSIAN ACADEMY OF SCIENCES
THE ELEVENTH MOSCOW SOLAR SYSTEM SYMPOSIUM (11M-S3)
5–9 October 2020
IKI, MOSCOW

The Program and the collection of Abstracts of the 11th Moscow Solar System Symposium (11M-S3).
Keywords: Solar System, planets, extrasolar planets, astrobiology.
The symposium was funded by Russian Academy of Sciences and by RFBR according to the research project № 20-02-22024.

ИНСТИТУТ КОСМИЧЕСКИХ ИССЛЕДОВАНИЙ РОССИЙСКОЙ АКАДЕМИИ НАУК
ОДИННАДЦАТЫЙ МОСКОВСКИЙ МЕЖДУНАРОДНЫЙ СИМПОЗИУМ ПО ИССЛЕДОВАНИЯМ СОЛНЕЧНОЙ СИСТЕМЫ (11M-S3)
5–9 октября 2020 года
ИКИ РАН, Москва

Сборник содержит программу и тезисы докладов одиннадцатого московского международного симпозиума по исследованиям Солнечной системы (11M-S3).
Ключевые слова: Солнечная система, планеты, внесолнечные системы, астробиология.
Мероприятие проводится при финансовой поддержке Российской академии наук, Российского фонда фундаментальных исследований, проект № 20-02-22024.

ISBN 978-5-00015-050-4
DOI: 0.21046/11MS3-2020
подписано в печать 21.09.2020
заказ 4185
гарнитура Calibri
формат 135×240.
издатель: ИНСТИТУТ КОСМИЧЕСКИХ ИССЛЕДОВАНИЙ РОССИЙСКОЙ АКАДЕМИИ НАУК (ИКИ РАН),
117997, Москва, Профсоюзная ул., 84/32

Дизайн издания: *Давыдов В.М.*
Компьютерная вёрстка: *Кораблева Е.О.*

Москва
2020